

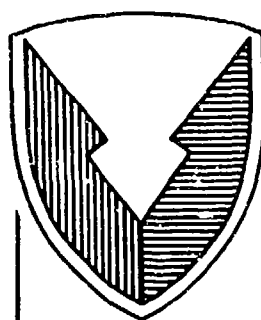
AD-A185 896

12

RD & E

C E N T E R

Technical Report



No. 12844

EXPERIMENTAL AND THEORETICAL INVESTIGATION

OF MECHANICALLY FASTENED COMPOSITES

CONTRACT NO. DAAE07-85-C-R037

FEBRUARY 1987

Gary Cloud
David Sikarskie
Madhukar Vable
Pedro Herrera Franco
Michael Bayer

Metallurgy, Mechanics and
Materials Science Dept.
Michigan State University

By E. Lansing, MI 48824

DTIC
ELECTE
OCT 13 1987
S D

APPROVED FOR PUBLIC RELEASE:
DISTRIBUTION UNLIMITED

U.S. ARMY TANK-AUTOMOTIVE COMMAND
RESEARCH, DEVELOPMENT & ENGINEERING CENTER
Warren, Michigan 48397-5000

87 10 6 126

NOTICES

This report is not to be construed as an official Department of the Army position.

Mention of any trade names or manufacturers in this report shall not be construed as an official endorsement or approval of such products or companies by the U.S. Government.

Destroy this report when it is no longer needed. Do not return it to the originator.

REPORT DOCUMENTATION PAGE				Form Approved OMB No 0704-0188 Exp Date Jun 30 1986	
1a. REPORT SECURITY CLASSIFICATION Unclassified			1b. RESTRICTIVE MARKINGS None		
2a. SECURITY CLASSIFICATION AUTHORITY			3. DISTRIBUTION/AVAILABILITY OF REPORT Approved for public release: distribution unlimited		
2b. DECLASSIFICATION/DOWNGRADING SCHEDULE			5. MONITORING ORGANIZATION REPORT NUMBER(S) TACOM T. R. 12844		
4. PERFORMING ORGANIZATION REPORT NUMBER(S)			7a. NAME OF MONITORING ORGANIZATION TACOM AMSTA-TMC		
6a. NAME OF PERFORMING ORGANIZATION Michigan State University		6b. OFFICE SYMBOL (if applicable)		7b. ADDRESS (City, State, and ZIP Code) TACOM Attn: AMSTA-TMC Warren, MI 48397-5000	
6c. ADDRESS (City, State, and ZIP Code) Dept. of Met. Mech. & Mat. Sci. Michigan State University E. Lansing, MI 48824-1226		8a. NAME OF FUNDING/SPONSORING ORGANIZATION same as #7		8b. OFFICE SYMBOL (if applicable)	
8c. ADDRESS (City, State, and ZIP Code)		9. PROCUREMENT INSTRUMENT IDENTIFICATION NUMBER Contract DAAE07-35-C-R037			
		10. SOURCE OF FUNDING NUMBERS			
		PROGRAM ELEMENT NO. 1L162601	PROJECT NO AH91	TASK NO	WORK UNIT ACCESSION NO
11. TITLE (Include Security Classification) Experimental and Theoretical Investigation of Mechanically Fastened Composites (U)					
12. PERSONAL AUTHOR(S) Cloud, Gary; Sikarskie, David; Vable, Madhukar; Herrera Franco, Pedro; and Bayer, Michael					
13a. TYPE OF REPORT Final		13b. TIME COVERED FROM 5/85 TO 12/86		14. DATE OF REPORT (Year, Month, Day) 1987 February	
				15. PAGE COUNT 380	
16. SUPPLEMENTARY NOTATION					
17. COSATI CODES			18. SUBJECT TERMS (Continue on reverse if necessary and identify by block number)		
FIELD	GROUP	SUB-GROUP	Composites, Fastener, Moire, Finite Element, Boundary Element, Fastener Arrays, Washers		
19. ABSTRACT (Continue on reverse if necessary and identify by block number) The contractors conducted an experimental and analytical study of the mechanics of fasteners in FGRP composites. Areas of study considered in the contract included multiple-fastener arrays, load-spreading washers of three types, bolt preload effects, field measurement, development of analytical and experimental methods, parametric studies, and creation of design codes. A comprehensive study of literature pertaining to methods of mechanically fastening composites was undertaken, and a summary survey is included herein. Experimental methods consisted primarily of high-sensitivity, three-axis moire interferometry with digital data acquisition and data reduction. The appropriate apparatus and procedures were established as part of the contract effort. Analytical methods centered upon the boundary-element approach. Algorithms and codes which yield stress-strain fields for anisotropic materials in multiply connected geometries were created. A bolt load transducer was developed for determining joint loads in the field. Resistance strain gages were used to verify in-plane strains measured by moire methods. Poorly fitted pins or					
20. DISTRIBUTION/AVAILABILITY OF ABSTRACT <input checked="" type="checkbox"/> UNCLASSIFIED/UNLIMITED <input type="checkbox"/> SAME AS RPT <input type="checkbox"/> DTIC USERS			21. ABSTRACT SECURITY CLASSIFICATION Unclassified		
22a. NAME OF RESPONSIBLE INDIVIDUAL Donald Ostberg			22b. TELEPHONE (Include Area Code) 313-574-5814		22c. OFFICE SYMBOL AMSTA-TMC

19. Abstract (Continued)

tilted pins affect strain field drastically. Strain gage results were between the ideal case and the tilted-pin strain readings. Stress concentrations were reduced by judicious use of fastener arrays and conical washers with high bolt tension.

PREFACE

The research described in this report was conducted at Michigan State University in the Department of Metallurgy, Mechanics, and Materials Science and in the Composite Materials and Structures Center; and at Michigan Technological University in the Department of Mechanical Engineering and Engineering Mechanics.

Investigators at Michigan State University included Dr. Gary Cloud, Professor; Dr. Pedro Herrera Franco, Research Assistant; Mr. Michael Bayer, Research Assistant; and Ms. Kristin Zimmerman, Research Aide. At Michigan Technological University, the researchers were Dr. David Sikarskie, Dean of Engineering; Dr. Madhu Vable, Associate Professor; and Mr. Yikhan Zhang, Research Assistant.

This page left blank intentionally

TABLE OF CONTENTS

Section	Title	Page
1.0.	Introduction	25
1.1.	Project Summary	25
1.2.	Background	26
1.3.	Organization of Report	27
1.4.	Literature Relevant to Joint Design	28
1.4.1.	Introduction	28
1.4.2.	Review of Terms	28
1.4.3.	Riveted Connections	29
1.4.4.	Bolted Connections	32
1.4.5.	Locally Reinforced Bolted Connections	41
1.5.	Literature Concerning Applications of Composites	53
1.6.	Literature Relevant to Mechanics of Joining	56
1.7.	Other References	58
1.8.	Principal Results	58
1.9.	Recommended Further Research	61
2.0.	Characterization of the Material	63
2.1.	Elastic Properties of Composites	63
2.2.	Stress and Strain in the Laminate	64
2.3.	Experimental Evaluation of Material Properties	65
2.3.1.	Specimen Dimensions	65
2.3.2.	Experimental Procedure	69
2.3.3.	Results	69
2.4.	Failure Modes	69
3.0.	Analytical Study	76
3.1.	Introduction	76
3.2.	Problem Formulation	78
3.3.	The Green's Function	80
3.4.	Problem Descretization	82
3.5.	Numerical Results	84
3.5.1.	Test Problems	84
3.5.2.	Square Geometry	84
3.5.3.	Circular Geometry	88
3.5.4.	A Circular Hole in Infinite Plate Under Uniaxial Tension	90
3.6.	Coupon Geometries	90
3.6.1.	Test 1	91
3.6.2.	Test 2	91
3.6.3.	No Load on Pin Hole Boundary	91
3.6.4.	Load on Pin Hole Boundary	93
3.6.5.	Displacement Boundary Conditions	104
3.7.	Conclusions	104

TABLE OF CONTENTS (continued)

Section	Title	Page
4.0.	Experimental Procedures and Apparatus	105
4.1.	Choice of Experimental Technique	105
4.2.	Moire Interferometry	105
4.3.	Construction of the Moire Interferometer	106
4.4.	Adjustment of Interferometer	111
4.5.	Fabrication of Moire Specimen	114
4.6.	Specimen Gratings	116
4.7.	Grating Replication Process	117
4.8.	Moire Fringe Photography	120
4.9.	Data Reduction	122
4.10.	Digitizing Moire Test Data	124
4.11.	Data Reduction and Plotting Strains	124
5.0.	Experimental Study of Hole Arrays	128
5.1.	Objectives and Scope	128
5.2.	Two Holes in Tandem; Both Loaded	128
5.3.	Two Holes in Tandem; Lower Loaded	143
5.4.	Two Holes in Tandem; Upper Loaded	151
5.5.	Two Holes in Parallel; Both Loaded	158
5.6.	Three Hole Staggered Array; All Loaded	175
5.7.	Summary and Conclusions	192
6.0.	Experimental Study of Washers and Clamping Force	205
6.1.	Objectives and Scope	205
6.2.	Approach to the Problem	205
6.3.	Choice of Method	207
6.4.	Surface Regions of Interest	207
6.5.	Influence of Misaligned Pin	209
6.6.	Influence of Bolt Design	219
6.7.	Influence of Torque	219
6.8.	Testing of Washer Designs	219
6.8.1.	Joint with Flat Washer	226
6.8.2.	Joint with Conical Washer Down	226
6.8.3.	Joint with Conical Washer Up	226
6.9.	Comparison of Pin With Bolt and Washer	226
6.10.	Comparison of Different Types of Washers	246
6.11.	Conclusions and Recommendations	253
7.0.	Model Field Study	256
7.1.	Approach	256
7.2.	Bolt Load Transducer	257
7.3.	Strain Gage Measurements	260
7.4.	Summary and Conclusions	270

TABLE OF CONTENTS (continued)

Section	Title	Page
References		273
Appendix A. Mathematical Expressions of Green's Function		A-1
Appendix B. Analytical Expressions of Integrals and singularities		B-1
Appendix C. BEM Computer Program		C-1
Appendix D. Moire Interferometry		D-1
Appendix E. Processing of Agfa 8E75 Moire Masters		E-1
Distribution List		Dist-1

This page left blank intentionally

LIST OF ILLUSTRATIONS

Figure	Title	Page
1-1.	Selection of some of the Most Common Flush Head Fasteners Developed for Composites	30
1-2.	Stress-Wave Rivet System	30
1-3.	Metal Fastener Installed in Composite Structure Illustrating the Most Common Types of Damage	31
1-4.	Composite Fastener	33
1-5.	Post Initial-Failure Behavior; Type A Lay-Up, 16-mm Good-Fit Washers	34
1-6.	Variation of Failure Load with Bolt Clamping Load, 16-mm Good-Fit Washers	35
1-7.	Variation of Failure Load with Washer Size; Constant Clamping Pressure	36
1-8.	Static Hole Elongation for Several Clamp Conditions. "T" is the Applied Bolt Torque	37
1-9.	Static Failure Modes (suggested by Crews)	38
1-10.	The Effect of End Distance on Bearing Strength	39
1-11.	The Effect of Joint Width on Bearing Strength	40
1-12.	The Effect of d/t Ratio on Bearing Strength	42
1-13.	The Effect of Stacking Sequence in Case of No Lateral Constraint; Pin-Loaded Hole in GFRP	42
1-14.	Bearing Strength Depends on Load Path	43
1-15.	Laminate Tailoring Alters Internal Load Path in a Multifastener Joint	44
1-16.	Multiple-Fastener Joint Test Results. Specimen Under Tensile Load	45
1-17.	Multilayer Square Reinforcement Graphite Showing the Layers which are Bonded onto the Surface; Surface Reinforcement . . .	46

LIST OF ILLUSTRATIONS (continued)

Figure	Title	Page
1-18.	Multilayer Butterfly Reinforcements using Different Materials and Layup. The Layers are Bonded onto the Surface of the Laminate	47
1-19.	Shim Joint Concept for a Double Lap Connection; Middle Reinforcement	49
1-20.	The Effect of Local Shim Reinforcement on Bearing Strength in GFRP Laminates	50
1-21.	Schematic Diagram of Edge-Reinforced Fiber Composite	50
1-22.	Benefits of Glass Fiber Softening Strips in Graphite-Epoxy Composites	51
1-23.	Stress Concentration Relief by Delamination	52
1-24.	Stress Concentration Factor along Line in the Direction of the Load Located in the Ligament Area. Insert Diameter at $x/a = 1.5$	54
1-25.	Bearing Stress Concentration Factor. Insert Diameter at $x/a = 1.5$	55
1-26.	Shear Strains along Locus of Shear-Out Failure. Insert Diameter at $y = -0.225$	56
2-1.	Specimen Dimensions and Location of Strain Gages	68
2-2.	Photograph of Specimen Showing Strain Gages	70
2-3.	Overall View of Specimen and Loading Rig	71
2-4.	Typical Tensile Stress-Strain Plots for Determination of Mechanical Properties of Orthotropic Composites Used in this Research	72
2-5.	Stress Channels Produced by Impact at the Edge of Composite Plate. Deformation Runs Through the Material along the Fibers rather than in the Direction of Impact	73
2-6.	Freedom of Stress and Strain Distribution in Bending of a Composite Beam Relative to the Linear Distribution in Conventional Materials	73

LIST OF ILLUSTRATIONS (continued)

Figure	Title	Page
2-7.	Illustration of the Three Basic Failure Modes	75
3-1.	Insert Problem	79
3-2.	Geometry of Test Problems	85
3-3.	Geometry of Coupons	92
3-4.	Result for Single Hole with No Pin Load	94
3-5a.	Results for Parallel Holes with No Pin Load	95
3-5b.	Results for Parallel Hole with No Pin Load	96
3-6.	Results for Tandem Holes with No Pin Load	97
3-7.	Results for Single Hole with Pin load	98
3-8a.	Results for Parallel Holes with Pin Load	99
3-8b.	Results for Parallel Holes with Pin Load	100
3-9a.	Results for Tandem Holes with Pin Loads	101
3-9b.	Results for Tandem Holes with Pin Loads	102
3-9c.	Results for Tandem Holes with Pin Loads	103
4-1.	Overall View of the Experimental Setup Incorporating the Moire Interferometer	107
4-2.	Schematic of the Basic Idea used in the Construction of the Moire Interferometer	108
4-3.	Arrangement of the Optical Elements of the Moire Interferometer	109
4-4.	Mechanical Elements Used in the Positioning of Optical Elements of the Moire Interferometer	112
4-5.	Joint Geometry and Nomenclature	115
4-6.	Photomicrograph of Two-Way Phase Grating Taken with Scanning Electron Microscope	118

LIST OF ILLUSTRATIONS (continued)

Figure	Title	Page
4-7.	Production and Replication of Moire Gratings	119
4-8.	Specimens Showing Reflective Gratings on Their Surfaces . . .	121
4-9.	Steps in the Reduction of Moire Data used to Determine Strains in Pin-Loaded Holes	123
4-10.	Microdatatizer System	125
5-1.	Stress Resultants for Two Tandem Holes Equally Loaded	129
5-2.	Moire Fringes of Displacement Parallel to Direction of Load when Both Holes are Loaded	130
5-3.	Strain ϵ_y along Lines Parallel to Direction of Load	132
5-4.	Moire Fringes of Displacement Perpendicular to Direction of Load for Hole Array in Tandem when Both Holes are Loaded	133
5-5.	Moire Fringes of Displacement at 45° to Direction of Load . .	134
5-6.	Strain ϵ_x along Lines Perpendicular to Direction of Load Near Upper Hole	136
5-7.	Strain ϵ_x along Lines Perpendicular to Load Between Holes . .	137
5-8.	Strain ϵ along Lines Perpendicular to Direction of Load in Lower Bearing Region	138
5-9.	Strain ϵ_{45} along Lines 45° to Direction of Load Near Lower Hole	139
5-10.	Strain ϵ_{45} along Lines 45° to Direction of Load	140
5-11.	Strain ϵ_{45} along Lines 45° to Direction of Load	141
5-12.	Strain ϵ_{45} along Lines 45° to Direction of Load	142
5-13.	Stress Resultants for Two Tandem Holes; Lower Loaded	144

LIST OF ILLUSTRATIONS (continued)

Figure	Title	Page
5-14.	Moire Fringes of Displacement Parallel to Direction of Load for Specimen with Tandem Hole Array when Lower Hole is Loaded	145
5-15.	Moire Fringes of Displacement Perpendicular to Direction of Load for Specimen with Tandem Hole Array when Lower Hole is Loaded	146
5-16.	Moire Fringes of Displacement 45° to Direction of Load for Specimen with Tandem Hole Array when Lower Hole is Loaded . .	147
5-17.	Strain ϵ_y along Lines Parallel to Direction of Load	148
5-18.	Strain ϵ_y along Lines Parallel to Direction of Load	149
5-19.	Strain ϵ_y along Lines Parallel to Direction of Load	150
5-20.	Strain ϵ_x along Lines Perpendicular to Direction of Load . .	152
5-21.	Strain ϵ_{45} along Lines 45° to Direction of Load	153
5-22.	Stress Resultants for Two Tandem Holes Upper Loaded	154
5-23.	Moire Fringes of Displacement Parallel to Direction of Load for Specimen with Tandem Hole Array when Upper Hole is Loaded	155
5-24.	Moire Fringes of Displacement Perpendicular to Direction of Load for Specimen with Tandem Hole Array when Upper Hole is Loaded	156
5-25.	Moire Fringes of Displacement at 45° to Direction of Load for Specimen with Tandem Hole Array when Upper Hole is Loaded	157
5-26.	Strain ϵ_y along Lines Parallel to Direction of Load	159
5-27.	Strain ϵ_x along Lines Perpendicular to Direction of Load . .	160
5-28.	Strain ϵ_{45} along Lines 45° to Direction of Load	161

LIST OF ILLUSTRATIONS (continued)

Figure	Title	Page
5-29.	Stress Resultants for Two Parallel Holes Equally Loaded . . .	162
5-30.	Moire Fringes of Displacement Parallel to Direction of Load for Specimen with Two-Hole Parallel Array	164
5-31.	Moire Fringes of Displacement Perpendicular to Direction of Load for Specimen with Two-Hole Parallel Array	165
5-32.	Moire Fringes of Displacement at 45° to Direction of Load for Specimen with Two-Hole Parallel Array	166
5-33.	Strain ϵ_y along Lines Parallel to Direction of Load	167
5-34.	Strain ϵ_y along Lines Parallel to Direction of Load	168
5-35.	Strain ϵ_y along Lines Parallel to Direction of Load	169
5-36.	Strain ϵ_y along Lines Parallel to Direction of Load	170
5-37.	Strain ϵ_x along Lines Perpendicular to Direction of Load . .	171
5-38.	Strain ϵ_x along Lines Perpendicular to Direction of Load . .	172
5-39.	Strain ϵ_{45} along Lines 45° to Direction of Load	173
5-40.	Strain ϵ_{45} along Lines 45° to Direction of Load	174
5-41.	Strain ϵ_{45} along Lines 45° to Direction of Load	176
5-42.	Strain ϵ_{45} along Lines 45° to Direction of Load	177
5-43.	Stress Resultants for Three Staggered Holes Equally Loaded	178
5-44.	Moire Fringes of Displacement Parallel to Direction of Load for Specimen with Three-Hole Staggered Array	179
5-45.	Moire Fringes of Displacement Perpendicular to Direction of Load for Specimen with Three-Hole Staggered Array	180

LIST OF ILLUSTRATIONS (continued)

Figure	Title	Page
5-46.	Moire Fringes of Displacement 45° to Direction of Load for Specimen with Three-Hole Staggered Array	181
5-47.	Strain ϵ_y along Lines Parallel to Direction of Load	182
5-48.	Strain ϵ_y along Lines Parallel to Direction of Load	183
5-49.	Strain ϵ_y along Lines Parallel to Direction of Load	184
5-50.	Strain ϵ_y along Lines Parallel to Direction of Load	186
5-51.	Strain ϵ_y along Lines Parallel to Direction of Load	187
5-52.	Strain ϵ_y along Lines Parallel to Direction of Load	188
5-53.	Strain ϵ_y along Lines Parallel to Direction of Load	189
5-54.	Strain ϵ_x along Lines Perpendicular to Direction of Load	190
5-55.	Strain ϵ_x along Lines Perpendicular to Direction of Load	191
5-56.	Strain ϵ_x along Lines Perpendicular to Direction of Load	193
5-57.	Strain ϵ_x along Lines Perpendicular to Direction of Load	194
5-58.	Strain ϵ_x along Lines Perpendicular to Direction of Load	195
5-59.	Strain ϵ_x along Lines Perpendicular to Direction of Load	196
5-60.	Strain ϵ_{45} along Lines 45° to Direction of Load	197
5-61.	Strain ϵ_{45} along Lines 45° to Direction of Load	198
5-62.	Strain ϵ_{45} along Lines 45° to Direction of Load	199
5-63.	Strain ϵ_{45} along Lines 45° to Direction of Load	200

LIST OF ILLUSTRATIONS (continued)

Figure	Title	Page
5-64.	Strain ϵ_{45} along Lines 45° to Direction of Load	201
5-65.	Strain ϵ_{45} along Lines 45° to Direction of Load	207
6-1.	Specific Regions of Interest for Measuring Strain in the Vicinity of the Fastener	208
6-2.	The Locations of the Chosen Axes for the Digitizing and Strain Readout are Shown and Labeled in Correlation with the Labeling in the Strain Plots	210
6-3.	Moire Fringe Patterns of Displacement in all Three Directions (Y, X, 45°) for the Tilted Pin. Left: No-Load; Center: 100 lbs.; Right: 200 lbs.	211
6-4a.	Comparison of the Strain Profiles of a Regular Pin	212
6-4b.	Comparison of the Strain Profiles with a Tilted Pin	213
6-4c.	Comparison of the Strain Profiles in the Y-Direction	214
6-4d.	Comparison of the Strain Profiles in the 45° Direction	215
6-5.	Effect of Tilted Pin-Deviation of Surface Strain by Shifted Bearing Area	216
6-6.	Axial Strain ϵ_y of Tilted Pin	217
6-7.	Influence of Specimen Mount on the Axial Strain Distribution; Comparing a Pin and Grips Qualitatively	218
6-8.	Bolt Assembly Used in Early Tests. A Standard Hex-Socket-Head was Used with Plastic Washers	220
6-9.	Early Fringe Patterns for the Displacement in Y and 45° Directions of the Bolt	220
6-10.	Influence of Torque on the Displacement Field. Left: No-Load, Low Torque; Center: High Torque, No-Load; Right: High Torque, At-Load (200 lbs.)	221
6-11.	Sectional View of the Bolt and the Clamping Mechanism Integrating a Thrust Bearing and a Clamping Pressure Transducer	222

LIST OF ILLUSTRATIONS (continued)

Figure	Title	Page
6-12.	Washer Designs Tested	224
6-13.	(a) Moire Fringe Pattern of Displacement in Y-direction . . .	227
	(b) Strain ϵ_y along Lines Parallel to the Direction of the Load for 200-lbs and 400-lbs loads. A Low Torque was Applied onto the Bolt	
6-14.	(a) Moire Fringe Pattern of Displacement in X-Direction . . .	228
	(b) Strain ϵ_x along Lines Transverse to the Direction of Load for 200-lb and 400-lb Loads. A Low Torque was Applied onto the Bolt	
6-15.	(a) Moire Fringe Pattern of Displacement in 45°-Direction . .	229
	(b) Strain ϵ_{45} along Lines 45° to the Direction of Load for 200-lb and 400-lb Loads. A Low Torque was Applied onto the Bolt	
6-16.	(a) Moire Fringe Pattern of Displacement in Y-Direction . . .	230
	(b) Strain ϵ_y along Lines Parallel to the Direction of Load for 200-lb and 400-lb Loads. A Low Torque was Applied onto the Bolt	
6-17.	(a) Moire Fringe Pattern of Displacement in Y-Direction . . .	231
	(b) Strain ϵ_y along Lines Parallel to the Direction of Load for 200-lb and 400-lb Loads. A High Torque was Applied onto the Bolt	
6-18.	(a) Moire Fringe Pattern of Displacement in X-Direction . . .	232
	(b) Strain ϵ_x along Lines Transverse to the Direction of Load for 200-lb and 400-lb Loads. A Low Torque was Applied onto the Bolt	

LIST OF ILLUSTRATIONS (continued)

Figure	Title	Page
6-19.	(a) Moire Fringe Pattern of Displacement in X-Direction . . .	233
	(b) Strain ϵ_x along Lines Transverse to the Direction of Load for 200-lb and 400-lb Loads. A High Torque was Applied onto the Bolt	
6-20.	(a) Moire Fringes of Displacement in 45°-Direction	234
	(b) Strain ϵ_{45} along Lines at 45° to Direction of Load for 200-lb and 400-lb Loads. A Low Torque was Applied onto the Bolt	
6-21.	(a) Moire Fringe Pattern of Displacement in 45°-Direction . .	235
	(b) Strain ϵ_{45} along Lines at 45° to Direction of Load for 200-lb and 400-lb Loads. A High Torque was Applied onto the Bolt	
6-22.	(a) Moire Fringe Pattern of Displacement in Y-Direction . . .	236
	(b) Strain ϵ_y along Lines Parallel to the Direction of Load for 200-lb and 400-lb Loads. A Low Torque was Applied onto the Bolt	
6-23.	(a) Moire Fringe Pattern of Displacement in Y-Direction . . .	237
	(b) Strain ϵ_y along Lines Parallel to the Direction of Load for 200-lb and 400-lb Loads. A High Torque was Applied onto the Bolt	
6-24.	(a) Moire Fringe Pattern of Displacement in X-Direction . . .	238
	(b) Strain ϵ_x along Lines Transverse to the Direction of Load for 200-lb and 400-lb Loads. A Low Torque was Applied onto the Bolt	
6-25.	(a) Moire Fringe Pattern of Displacement in X-Direction . . .	239
	(b) Strain ϵ_x along Lines Transverse to the Direction of Load for 200-lb and 400-lb Loads. A High Torque was Applied onto the Bolt	

LIST OF ILLUSTRATIONS (continued)

Figure	Title	Page
6-26.	(a) Moire Fringe Pattern of Displacement in 45°-Direction . .	240
	(b) Strain ϵ_{45} along Lines at 45° to Direction of Load for 200-lb and 400-lb Loads. A Low Torque was Applied onto the Bolt	
6-27.	(a) Moire Fringe Pattern of Displacement in 45°-Direction . .	241
	(b) Strain ϵ_{45} along Lines at 45° to Direction of Load for 200-lb and 400-lb Loads. A High Torque was Applied onto the Bolt	
6-28.	Comparison of Strain ϵ_y in the Ligament Area	242
6-29.	Comparison of Strain ϵ_y in the Bearing Region or Lower Zone	243
6-30.	Comparison of Strain ϵ_x in the Bearing Region or Lower Zone	244
6-31.	Comparison of Strain ϵ_{45} at the Locus of Shear-Out Failure	245
6-32.	Strain ϵ_y in the Bearing Zone Comparing the Different Washer Designs	247
6-33.	Strain ϵ_y in the Ligament Regions Comparing Washer Designs	248
6-34.	(a) Strain ϵ_{45} Indicating Shear Strain at a Low Torque . . .	249
	Clamping Condition and Characteristic ϵ_{45}	
	(b) Schematic of Washer Setup	
6-35.	Strain ϵ_y in the Top Zone Indicating an Increase of Tensile Bearing with Higher Clamping Forces	250
7-1.	Bolt Load Transducer Designs	258

LIST OF ILLUSTRATIONS (continued)

Figure	Title	Page
7-2.	Section View Showing The Placement of Strain Gages	259
7-3.	Individual Gage Outputs from Transducer in Given Orientation	261
7-4.	Individual Gage Outputs from Transducer in Given Orientation	262
7-5.	Individual Gage Outputs from Transducer in Given Orientation	263
7-6.	Individual Gage Outputs from Transducer in Given Orientation	264
7-7.	Individual Gage Outputs from Transducer in Given Orientation	265
7-8.	Individual Gage Outputs from Transducer in Given Orientation	266
7-9.	Individual Gage Outputs from Transducer in Given Orientation	267
7-10.	Locations of Resistance Strain Gages	268
D-1.	Phase Relation Between Rays from Two Grating Grooves	D-4
D-2.	Three-Dimensional Geometry of the Incident and Diffracted Rays of a Grating	D-6
D-3.	Oblique Incidence on a Plane Grating	D-8
D-4.	Constructive and Destructive Interference Produced by the Combination of Two Wavefronts	D-12
D-5.	Three-Beam Arrangement of the Moire Interferometer	D-14
D-6.	Geometrical Representation of the Deformation of the Grating	D-15
D-7.	Geometry of the Incident and Diffracted Rays from a Grating Deformed by ϵ_x when Analyzed by Beams A0 and B0	D-18

LIST OF ILLUSTRATIONS (continued)

Figure	Title	Page
D-8.	Optical Arrangement Used to Create an Image of the Interference Pattern Produced by Two Diffracted Orders . . .	D-21
D-9.	Geometry of the Incident and Diffracted Rays from a Grating Deformed by ϵ_y when Analyzed with Beams AO and BO	D-24
D-10.	Geometry of the Incident and Diffracted Rays from a Grating Deformed by γ_{xy} when Analyzed with Beams AO and BO	D-26
D-11.	Geometry of the Incident and Diffracted Rays Affected by Rigid-Body Rotation of the Grating when Analyzed by Beams AO and BO	D-27
D-12.	Schematic of the Angles of Incidence of the Moire Interferometer when Analyzing the Specimen Grating with Beams AO and CO	D-29
D-13.	Geometry of the Incident and Diffracted Rays from a Grating x' Deformed by ϵ_x , when Analyzing with Beams AO and CO . . .	D-31
D-14.	Geometry of the Incident and Diffracted Rays Affected by a Rigid-Body Rotation of the Grating when Analyzing with Beams AO and BO	D-33
D-15.	Geometry of the Incident and Diffracted Rays from a Grating Deformed by $\epsilon_{x'y'}$, when Analyzing with Beams AO and CO	D-34
D-16.	Formation of Moire Fringes Caused by Pitch and Rotation Mismatch	D-38
D-17.	Geometry of the Incident and Diffracted Rays Affected by a Fictitious Strain Produced by a Frequency and Rotational Mismatch when Analyzing with Beams BO and CO	D-40
D-18.	Geometry of the Incident and Diffracted Rays from a Grating Affected by Strain Plus Mismatch when Analyzing with Beams BO and CO	D-42
D-19.	Moire Fringes of Displacement for Two Different Amounts of Mismatch and Same Loading Conditions	D-44
D-20.	Strain ϵ_y Obtained from Two Sets of Moire Patterns from . . . the Same Specimen with Different Amounts of Mismatch	D-45

This page left blank intentionally

LIST OF TABLES

Table	Title	Page
3-1.	Material Properties for Test Problems	86
3-2.	Matrix Condition Number for Square Geometry	86
3-3.	Percentage Error in σ_{yy} for Square Geometry	87
3-4.	Matrix Condition Number for Circular Geometry	88
3-5.	Percentage Error in σ_{yy} for Circular Geometry	89
3-6.	Stress Concentration Factor for a Hole in an Infinite Medium	90
3-7.	Material Properties for Coupon Problems	91
3-8.	Stress Concentration Factors for Coupons	93
5-1.	Comparison of Stress Concentration Factors	203
5-2.	Comparison of Stress Concentration Factors	203
5-3.	Comparison of Stress Concentration Factors	203
6-1.	Testing Parameter Matrix Assigning each Strain Plot to a Specific Test	225
6-2.	Comparison of Peak and Average Strain Values Along the Most Interesting Axes for All Tested Washers	251
7-1.	Strain Gage Results Compared with Moire Results for Well-Fitted Pin and Tilted Pin	269

This page left blank intentionally

1.0. INTRODUCTION

1.1. Project Summary

The contractors, Michigan State University, conducted an experimental and analytical study of the mechanics of fasteners in glass-fiber-reinforced epoxy composite laminate. The research described in this report was begun in April 1985 under contract DAAEO7-85-C-R037. Extensions without added cost resulted in a termination date of 31 December 1986. Mr. Donald Ostberg was TACOM technical representative on the project.

The research reported herein extended the work performed in the period September 1982 to September 1983 under contract DAAEO7-82-C-4091 and described in the contract report [1.1] (see note below). TACOM technical representatives on that contract were Mr. Robert Ellis and Mr. Avery Fisher.

Areas of study considered in the contract included multiple-fastener arrays, load-spreading washers of three types, bolt preload effects, field measurement, development of analytical and experimental methods, parametric studies, and creation of design codes. A comprehensive study of literature pertaining to methods of mechanically fastening composites was undertaken, and a summary survey is included. Experimental methods consisted primarily of high-sensitivity three-axis moire interferometry with digital data acquisition and data reduction. The appropriate apparatus and procedures were established as part of the contract effort. Analytical methods centered upon the boundary-element approach. Algorithms and codes which yield stress-strain fields for anisotropic materials in multiply connected geometries were developed.

Many publications have resulted from the contract research. Several were derived from the initial 1982-83 contract [1.1-1.5] and these are mentioned several times in this report since the current research is built upon the previous effort. A number of other publications and presentations have already been derived from the current contract [1.6-1.15]. It is expected that several archival journal publications will be produced within the coming year as the work is brought to full maturity.

While this effort was very successful in terms of methodology and results, it must be viewed as an important step in a comprehensive program. This program is at the stage where it is contributing significantly to the solution of urgent problems in the design of composites structures and vehicles. In support of this claim, this report demonstrates that the investigators have begun to look at real problems, including for example the use of concave washers to improve

NOTE: numbers in square brackets refer to articles which are collected in the List of References

joint efficiency, which have been described many times but which have never been explored in a systematic way. The results of the investigation are surprising and show that some published preconceptions are not correct. The researchers believe strongly that additional major practical benefits will flow from research yet to be done.

1.2. Background

Since engineers learned to reinforce plastic materials with fibrous components some decades ago, an exciting and rewarding evolution has taken place. It is possible now to create materials and structures which fit specific and complex applications. Owing to lower manufacturing costs, improved strength/weight performance, and greater design flexibility, composites are replacing metals in many fields. The increasingly large range of ingredients available, the improving quality of resin and fiber materials, and the increasing knowledge of the mechanics of fiber-reinforced materials further expands the potential range of applications.

The automotive and defense industries, which use composite materials widely, seek improved design criteria and design guidelines. In order to exploit the potential benefits offered by composites, it is necessary to have joining methods which are efficient from both the mechanics and production viewpoints. For reasons of maintainance, repair, and assembly, adhesive joining is often not appropriate. Mechanically fastened joints are necessary. Concern arises because the organized internal structure of the composite is disturbed or even destroyed by the cutouts, holes, or other discontinuities required for the mechanical connectors.

Composite materials are frequently joined by single or multiple bolts or rivets. The strength of such joints depends in complex ways upon the number and spacing of the bolts, end distance, bolt clearance, load distribution, material properties, hole treatment, presence of washers, preloads, and so on. While the design problems have received much attention, and, indeed, some successful design techniques have been devised, a design approach which is based upon scientific knowledge, as opposed to phenomenological testing, is not yet available. Therefore, the full potential of composite materials in structural and vehicular applications cannot be realized.

What is lacking is a thorough knowledge of the interaction of mechanical fasteners and the composite material. Since this comprehensive understanding is missing for even the simplest cases, there is little probability that a generally useful design code can be developed, and designers are stuck with the cycle of guessing and testing. Modeling of fastener/material interactions, and experimental inquiry with emphasis on stress, strain and failure are necessary steps which will lead to the desired design protocol. Given the large number of relevant parameters, gaining the needed experimental mechanics data and devising appropriate computational models are forbidding tasks. Significant progress has been made. This project was undertaken in order to further the advance.

1.3. Organization of Report

A large number of problems related to mechanical joining of composites were investigated during the project. This comprehensive report is lengthy and complex. As an aid to TACOM representatives and other readers, this overview, which outlines the plan of the report and relationships between sections, is included.

The first chapter contains introductory material including the results of the comprehensive search of literature related to mechanical joining of composites and techniques to improve joint efficiency. The sections on relevant literature form a sort of survey paper on the topic of mechanical joining.

Chapter one also contains a summary of the main findings of the research and recommendations for further study of fastening problems.

Chapter two specifies the material used in the research and describes the experimental measurement of constitutive parameters which are needed for comparison of experimental and analytical results.

The third chapter discusses the analytical approach, algorithms, and results for the fastener array problem. This section is closely tied to Appendices A, B, and C, which contain the necessary mathematical developments and the computer program.

Chapter four discusses the experimental methods and procedures. This chapter is tied to Appendices D and E. Appendix D is a comprehensive treatment of three-axis moire interferometry.

The fifth chapter is a description of the experimental investigation of strains near fastener arrays. Results and conclusions on this topic are given at the end of the chapter.

The sixth chapter is devoted to the experimental investigations of load-bearing washers and bolt preloads. Results are reported at the end of the section. Chapter seven deals with investigation of a model field study.

All the references for the report, including appendices, appear following chapter seven. Given the complexity and length of the report, it seemed best to group the literature citations by chapter, as in a textbook, and they are so numbered. Most of the references are for chapter one, of course, since it deals with general principles and techniques of mechanical joining. For the sake of completeness and to enhance utility of this survey section, some useful articles which are not specifically discussed in the text are included. The citations for the remaining chapters deal primarily with techniques, specific problems, and results obtained by others which are relevant mainly to that chapter. This approach to grouping references means that a few citations appear more than once if they happen to be used in more than one chapter.

1.4. Literature Relevant to Joint Design

1.4.1. Introduction. Interpreting the term literally, composite structural materials are not new or unfamiliar. Fibrous, reinforced composites have been used for decades in such forms as plywood, cord-filled rubber, plaster, asphaltic felts, high-pressure paper laminates and bagasse board. What is new, however, is the advent of manufactured fibers possessing uniquely high levels of strength and stiffness. These have made possible the production of structural composites with extraordinary properties and, further, they suggest that an exciting new field of materials technology is beginning to develop.

In fact, no comprehensive, rigorous stress analysis of fiber-reinforced composite materials has been achieved. A good reason for this is that it would require taking into account many extremely complicated factors: elastic and inelastic behavior, residual stresses from fabrication, effectiveness of bond between components, and imperfect alignment of fibers, to name a few. In spite of this situation, the combination of available analytical methods and developmental testing has produced a number of composite structures with impressive performance characteristics.

In this literature search just one problem associated with anisotropic structural materials will be discussed. This problem is that elaborate design procedures, based on experimental and theoretical analysis, must be undertaken to account for the effects of discontinuities such as mechanical fasteners.

1.4.2. Review of Terms. In the following an excerpt of available literature is given starting at the year 1976. Published works, mostly experimental, relating to various aspects of mechanically fastened joints in glass fiber-reinforced epoxy and polyester resin are reviewed. The literature search concentrates on effects of fastener and design parameters. Fastener parameters are understood as fastener type (screw, bolt, rivet, pin), fastener size, clamping force, washer size, hole size and tolerances. Design parameters are joint type (single lap, single cover butt, etc.), laminate thickness, geometry (pitch, edge distance, hole pattern), load direction, load rate, static or dynamic load, and failure criteria. Inclusion of material parameters (fiber type, fiber form, resin type, laminate stacking sequence, etc.), which enormously affect joint strength, would have increased the number of variables beyond practicality. Only a limited number of materials systems were considered; these were the so-called glass fiber reinforced polyester (GRP), glass fiber reinforced epoxy (GFRP), and carbon fiber reinforced epoxy (CFRP) materials (definitions according to [1.16]).

Composites with an epoxy resin matrix are generally made from unidirectional prepeg with either carbon or glass fiber to produce laminates of glass fiber-reinforced epoxy (GFRP) or carbon fiber-reinforced epoxy (CFRP). Woven glass cloth, in contrast, is almost always laminated with polyester resin to produce laminates of glass fiber-reinforced polyester (GRP). In general, GRP tends to be used in

thicknesses of greater than 5 mm, whereas GFRP tend to be used for thinner, high-duty laminates.

In joining there is a choice between rivets, bolts and locally reinforced bolted connections. Their different behaviors and applications will be discussed in the following sections.

1.4.3. Riveted Connections. Applications for rivets can be found most frequently in the aircraft industry where riveted joints appear to give adequate strength in high-duty CFRP laminates in thicknesses up to about 3 mm. There is a choice between a large number of different fasteners, see Figure 1-1, varying in head size, shape and type. Most of them are for use in aircraft structures. In the case of rivets, the riveting operation may cause damage to the laminate. Matthews [1.17] and Webb [1.18] indicated these problems. Also Matthews showed that the joint strength is related to the degree of clamping imposed by the riveting operation. Due to the nature of the riveting process the closing force is not readily controlled.

The degree of clamping pressure in these operations is determined by washer size, as noted by Kingston-Lee and Rogers [1.19] who show that there is an increase in joint strength with CFRP when using washers.

Cole, et al., [1.20] identifies four basic problems when using fasteners in composites, particularly in the aircraft industry. They are named as galvanic corrosion, galling, installation damage, and low pull-through strength. For this review some of the most important aspects of his extensive paper are selected. He shows that interference fits are less desirable since the rivets cause delamination during the application procedure because of the low interlaminar strength of composite materials. The main advantage of interference fits lies in their extremely extended fatigue life compared with net or loose-fit connections, as Sendekyj and Richardson show [1.21]. For some applications a special stress-wave rivet system has been demonstrated as at least one possible solution to avoid installation damage, (see Figure 1-2. Also in the figure, a special rivet, the so called Cherry Buck, is shown. This one-piece rivet has a high-strength shank (Ti6Al-4V) with a ductile tail section (TiNb). It is ideally suited for composites to avoid installation damage because the harder shank does not expand during tail formation. The problem with most of the other systems is that they are too expensive if one considers that 100,000 to 200,000 rivets are needed in an average airplane.

The most often used low-load transfer composite-to-composite fastener is the flush-head fastener, Figure 1-1. It offers the greatest potential benefits from improvement as Cole, et al., [1.20] indicate.

Tanis and Poullos [1.22] discuss the use of composite fasteners and explain clearly the different types of damage introduced by metallic fasteners. Figure 1.3. shows some of them. Tanis, et al., show that most of the damage is done by the riveting operation, i.e., by vibrations and by excessive compressive forces from the rivet shank and head. He suggests fasteners out of composites to avoid these problems.

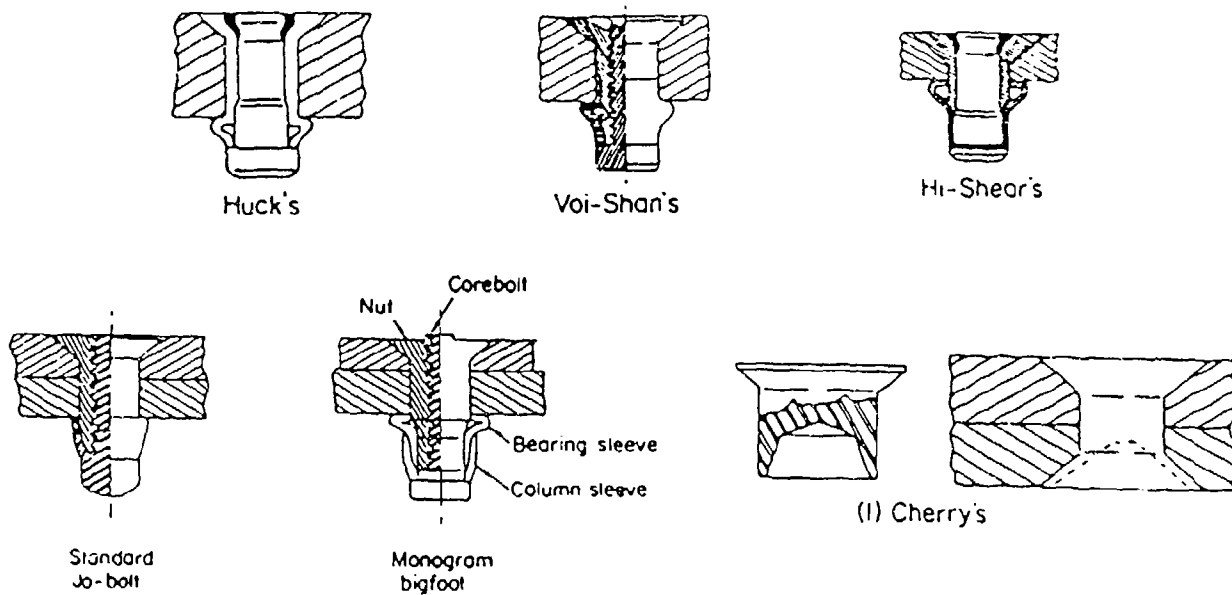


Figure 1-1. Selection of some of the Most Common Flush Head Fasteners Developed for Composites

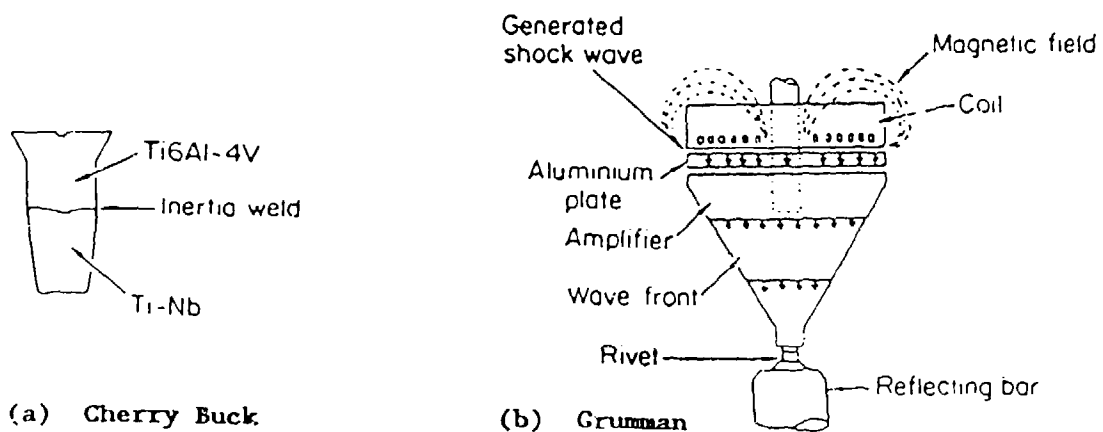


Figure 1-2. Stress-Wave Rivet System

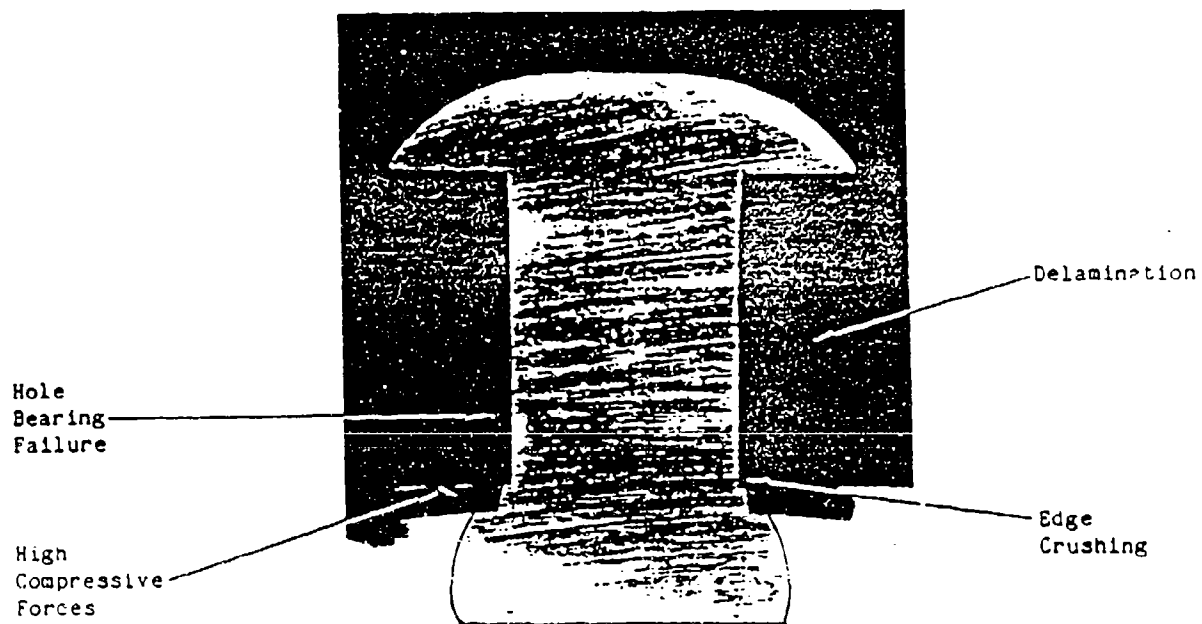


Figure 1-3. Metal Fastener Installed in Composite Structure Illustrating the Most Common Types of Damage

Figure 1-4. shows the design of such a composite fastener indicating that a totally different riveting process is used.

1.4.4. Bolted Connections. In the following section the phenomena of bolted connections are discussed thoroughly and the most important background data for this project are given.

Bolts offer the greatest strength for mechanically fastened joints in composites. Unless excessively overtightened no damage is done to the composite during assembly. The clamping pressure can be very accurately controlled, and the whole assembly is a very easily repeatable process. It is important, however, as reported by Kingston-Lee and Rogers [1.19], and Stockdale and Matthews [1.23] that the bolt is a good fit into the (preferably) reamed hole. The latter authors and Collings [1.24] noted that increasing the bolt tightening torque, and hence clamping pressure, increases the bearing strength, (see Figure 1-5 and Figure 1-6). The increase is due to a combined effect of restraint provided by the washer and frictional resistance to slip. Webb and Smith [1.25] said that there is an optimal clamping pressure for joint strength, and that at considerably higher clamping loads compressive damage may be done by the washer digging into the surface of the laminate. The washer size can influence strength, but it is more important that the hole in the washer has a close fit to the bolt as Stockdale and Matthews [1.23] already showed (see figure 1-7). Rufolo [1.26] covers bolted joints in GRP and comes to similar conclusions. Crews [1.27], who was investigating bolt-bearing fatigue of a graphite/epoxy laminate, found out that the static pre-initial- failure elongation of the bolt hole can be increased by higher clampup conditions, (see Figure 1-8). This improvement is caused by an increase in ductility or a mechanism of compliance. For cyclic loading as well, Crews comes to similar results.

He also suggests three failure modes depending on the clampup condition, (see Figure 1-9). But several investigators [1.24, 1.28, 1.29, 1.30] show a strong dependency of the failure mode on material properties, especially the fiber orientation. The most important factor influencing the failure mode is not the clamp-up condition but the ratio of end distance to hole size (e/d), as Schjelderup and Jones [1.31] prove.

Geometric effects are investigated by a number of authors. Among them count Collings [1.24], Matthews [1.17], Rufolo [1.26], Porter [1.32]. They all agree that there is a certain minimum value of the ratio e/d , i.e., end distance to diameter of the hole, for full bearing strength to be developed, (see Figure 1-10). Basically the same is true for the value of the ratio w/d , i.e., joint width to diameter of the hole, (see Figure 1-11).

The minimum values suggested for GFRP with pseudo-isotropic layups, were found to be:

$$e/d > 3$$

$$w/d > 5.$$

In the case of this investigation these values were set to

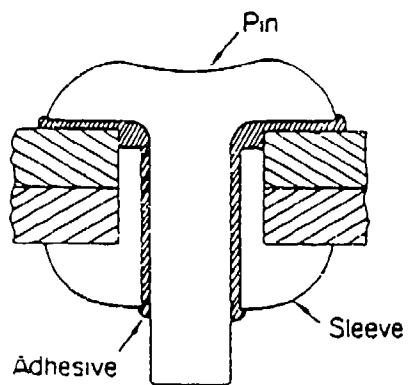


Figure 1-4. Composite Fastener

Crosshead displacement

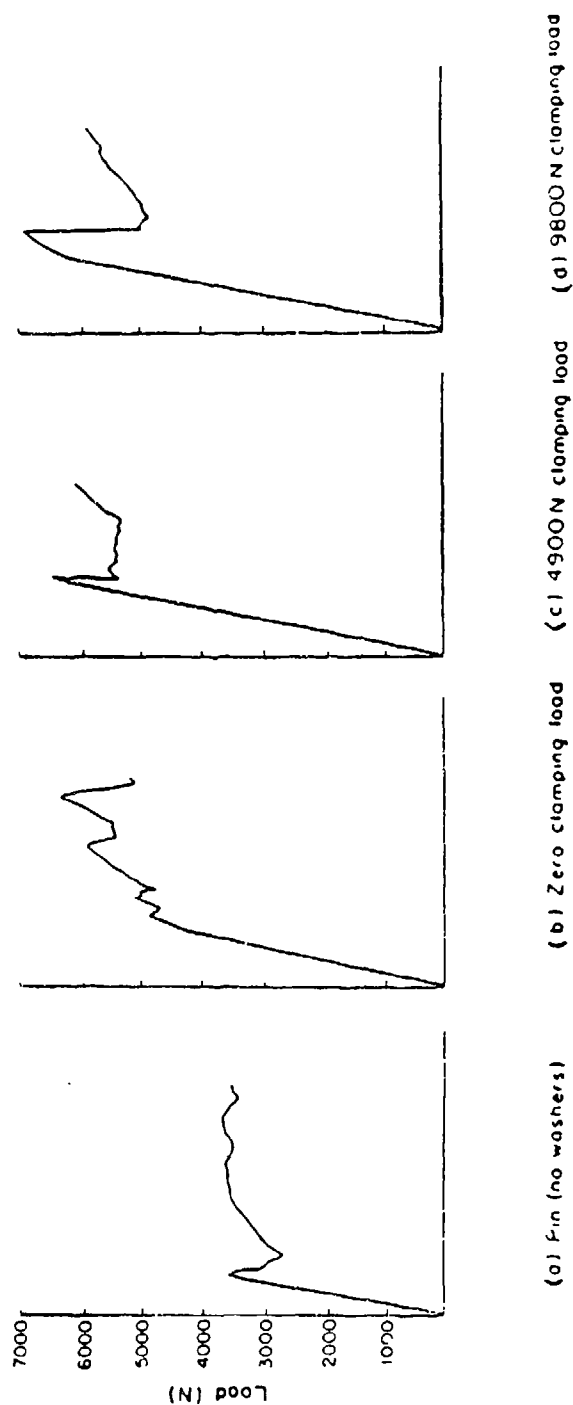


Figure 1-5. Post Initial-Failure Behavior; Type A Lay-Up, 16-mm Good-Fit Washers

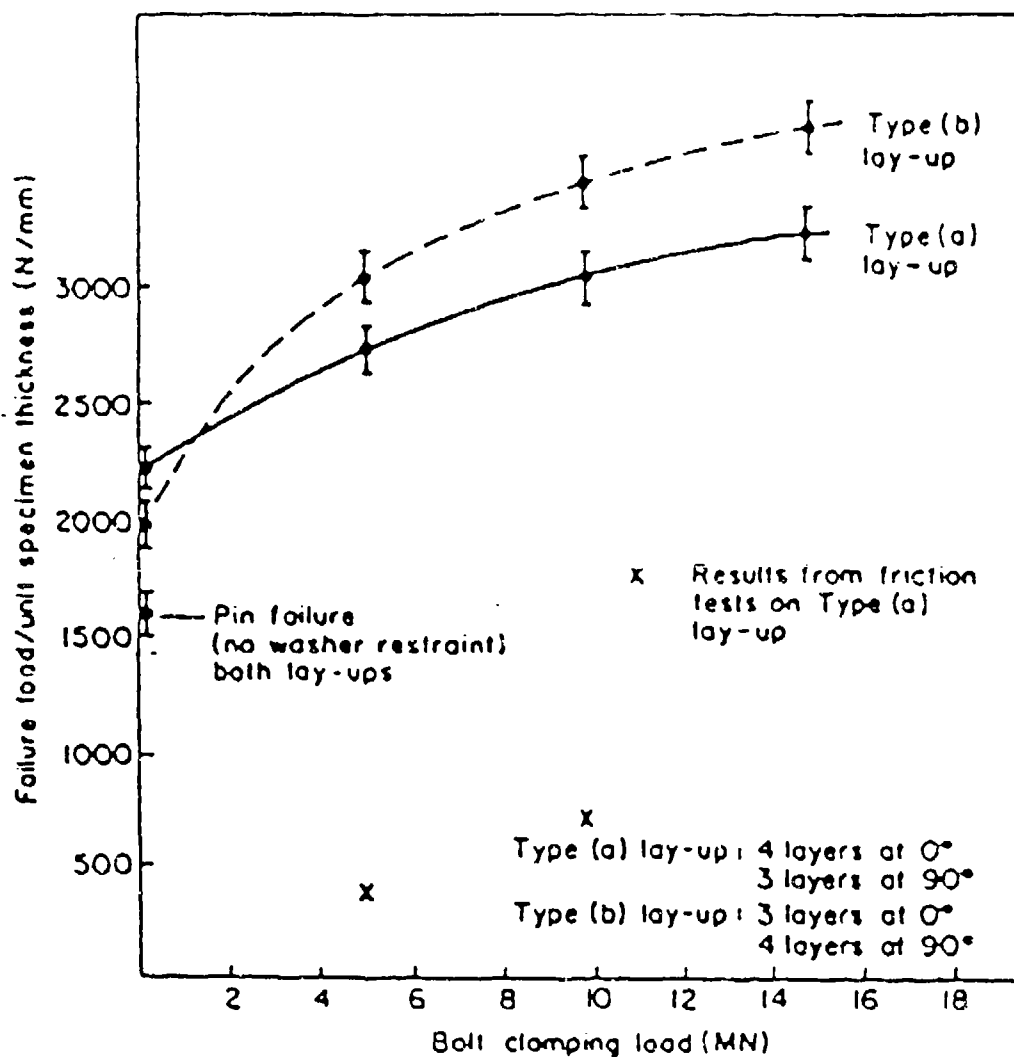


Figure 1-6. Variation of Failure Load with Bolt Clamping Load, 16-mm Good-Fit Washers

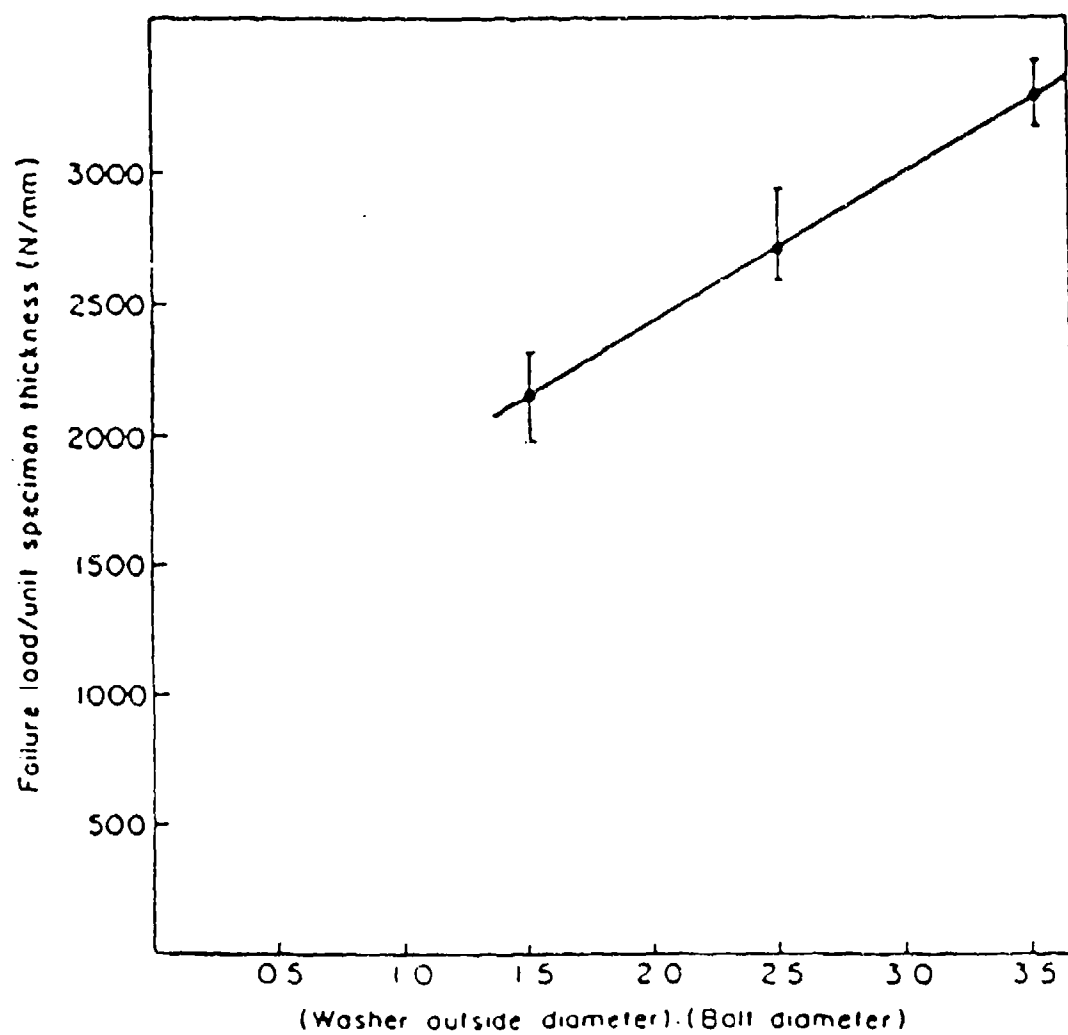


Figure 1-7. Variation of Failure Load with Washer Size; Constant Clamping Pressure

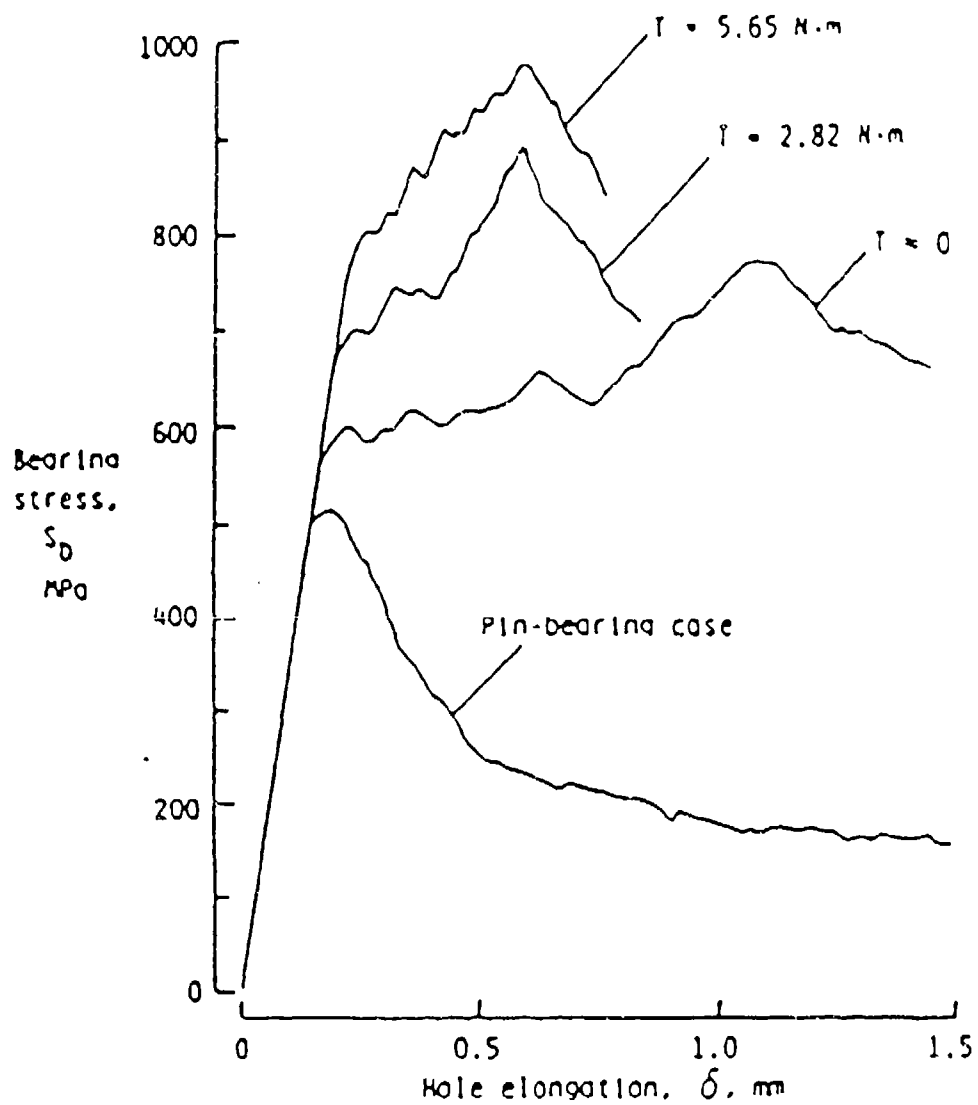
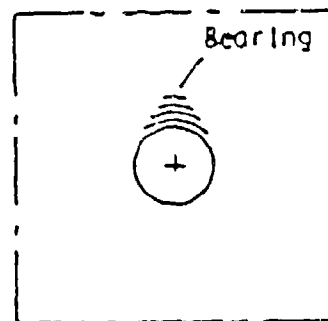
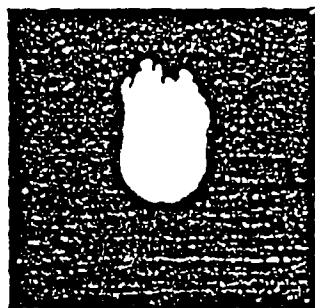
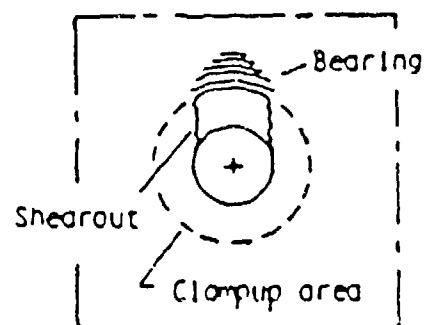
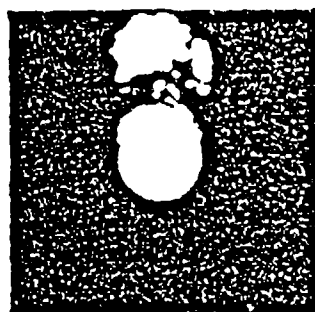


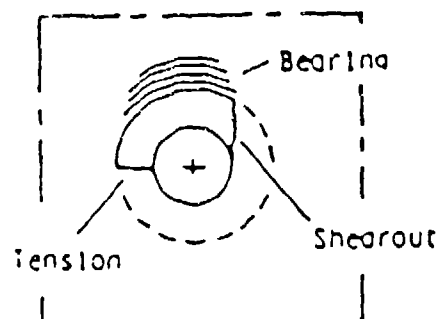
Figure 1-8 Static Hole Elongation for Several Clamp Conditions. "T" is the Applied Bolt Torque



(a) Bearing failure mode (pin bearing).

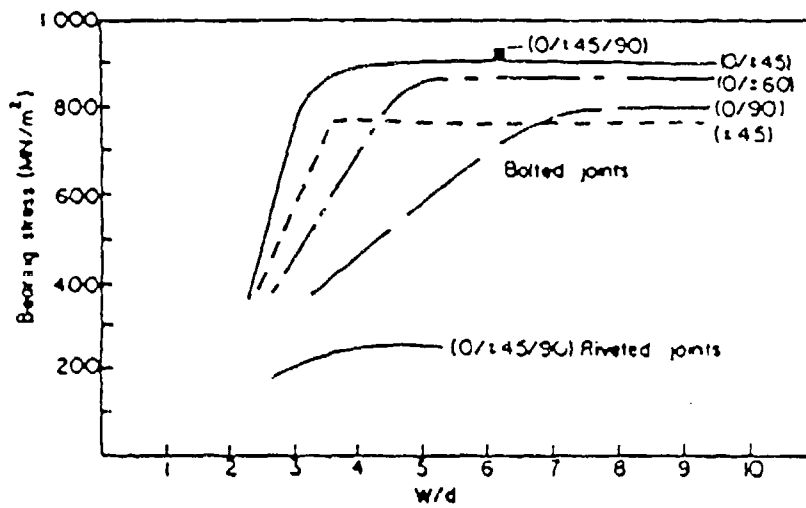


(b) Shearout-bearing failure mode (moderate clumpup).

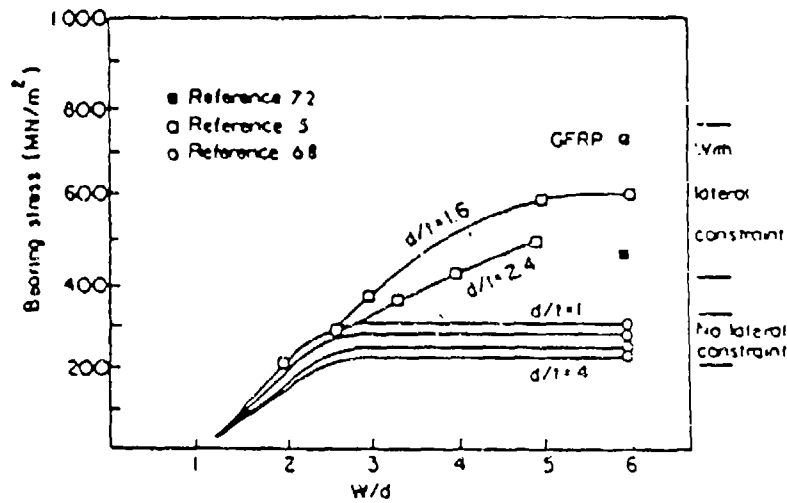


(c) Shearout-tension-bearing failure mode (high clumpup).

Figure 1-9 Static Failure Modes (suggested by Crews)

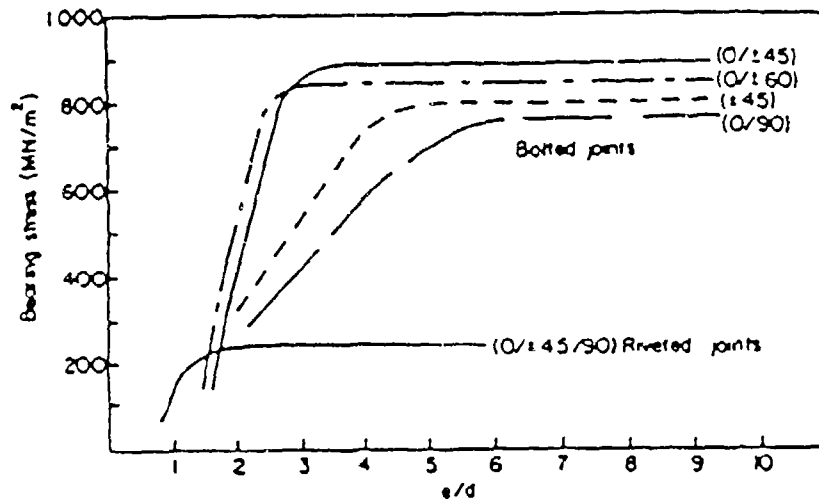


(a) CFRP

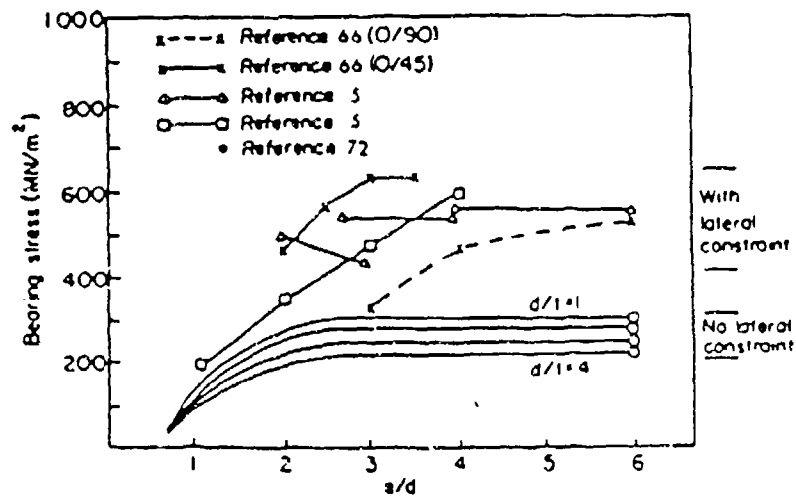


(b) GFRP

Figure 1-10 The Effect of End Distance on Bearing Strength



(a) CFRP



(b) GFRP

Figure 1-11 The Effect of Joint Width on Bearing Strength

$$e/d=4 \quad \text{and} \quad w/d=8.$$

The influence of d/t values, i.e., diameter of the hole to thickness of the laminate, was investigated by Saddler and Barnard [1.33], Collings [1.24], Dastin [1.34], and Oleesky and Moor [1.35]. The d/t value is of minor influence on bearing strength in cases of sufficient lateral constraint for GFRP as well as for CFRP, (see Figure 1-12). The stacking sequence does not have any influence either, but for fasteners without lateral constraint it appears beneficial, at least for GFRP, to place 90-degree layers at or near the surface, as indicated in Figure 1-13. A 90-degree layer means that the fiber orientation of the layer is perpendicular to the direction of the load.

When the geometric requirements are fulfilled and inter-laminar failure can be avoided by sufficient compression in the clamped area, full bearing strength is ensured. In general a value of 5 diameters would cover both distances (e , w) for most materials and layouts.

For example, an adequately tightened bolt in CFRP can be expected to have a maximum bearing strength (the definition is according to [1.16]) of 800-930 N/mm. Similar fastening in GFRP can be expected to have 550-700 N/mm. With GRP the strength range is much wider, being between 200 and 600 N/mm. Pin-loaded or riveted joints reach at the most 60 percent of the above values.

1.4.5. Locally Reinforced Bolted Connections. Some consideration is given to local reinforcement of the hole by several workers. Such an approach to improve composite bolted joint efficiency was investigated by Eisenmann and Leonhardt [1.36]. Their concept is based on tailoring the laminate in a composite structures to uncouple the local bearing capacity from the influence of the laminate axial strain level, as shown in Figure 1-14. A typical composite bolted joint exhibits a strong coupling between axial strain and bearing capacity. The development of stress channels along the fibers in the laminate makes the material very dependent on the way the load paths are formed, (see Figure 1-15). As a result, the design-allowed strain levels are often inefficiently low. By tailoring the laminate these strain levels can be successfully raised without any loss of safety. Tailoring requires special planning, designing and manufacturing of the whole composite structure.

In the vicinity of the bolt the plies of the laminate are laid out to have high load-bearing capacity. Within the compound they are flanked by high tensile modulus laminate (the so-called primary region) which carries and bypasses the axial strains. The results show that this sophisticated method is worth the effort in certain applications where efficiency and weight reduction are major goals. Some examples of the applications and improvements are shown in Figure 1-16.

Another method of reinforcement is presented in a paper by Kocher and Cross [1.37]. In their case the specimen, already in its final shape, was locally reinforced around its drilled hole. Several multilayered composite reinforcements, as shown in Figure 1-17, as well as thin metallic disks, (see Figure 1-18), were bonded on the

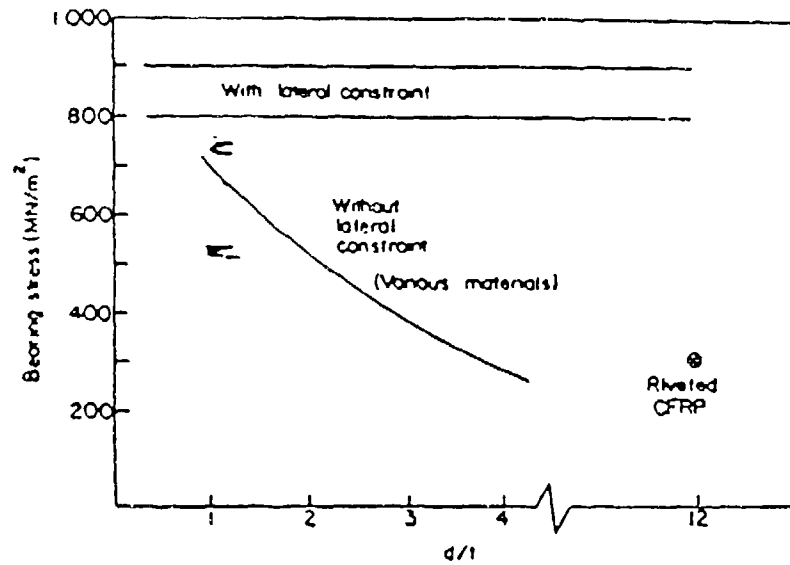


Figure 1-12 The Effect of d/t Ratio on Bearing Strength

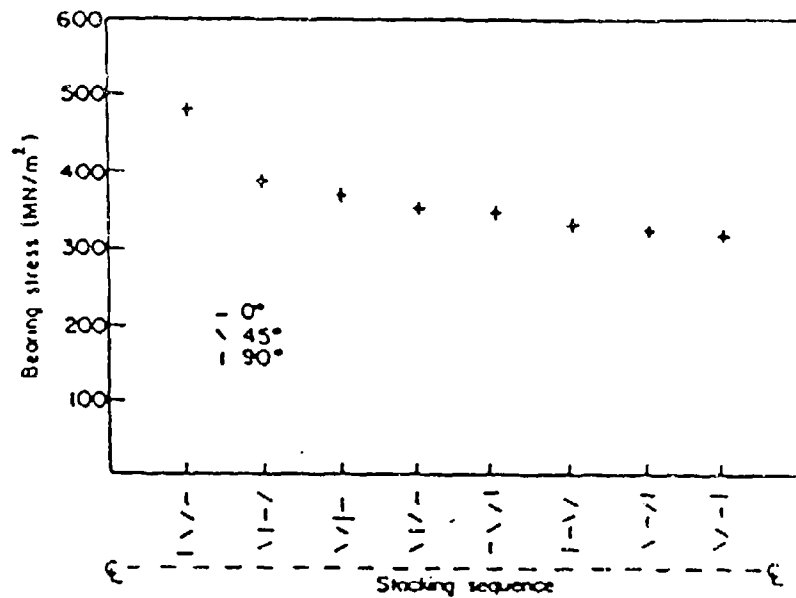


Figure 1-13 The Effect of Stacking Sequence in Case of No Lateral Constraint; Pin-Loaded Hole in GFRP

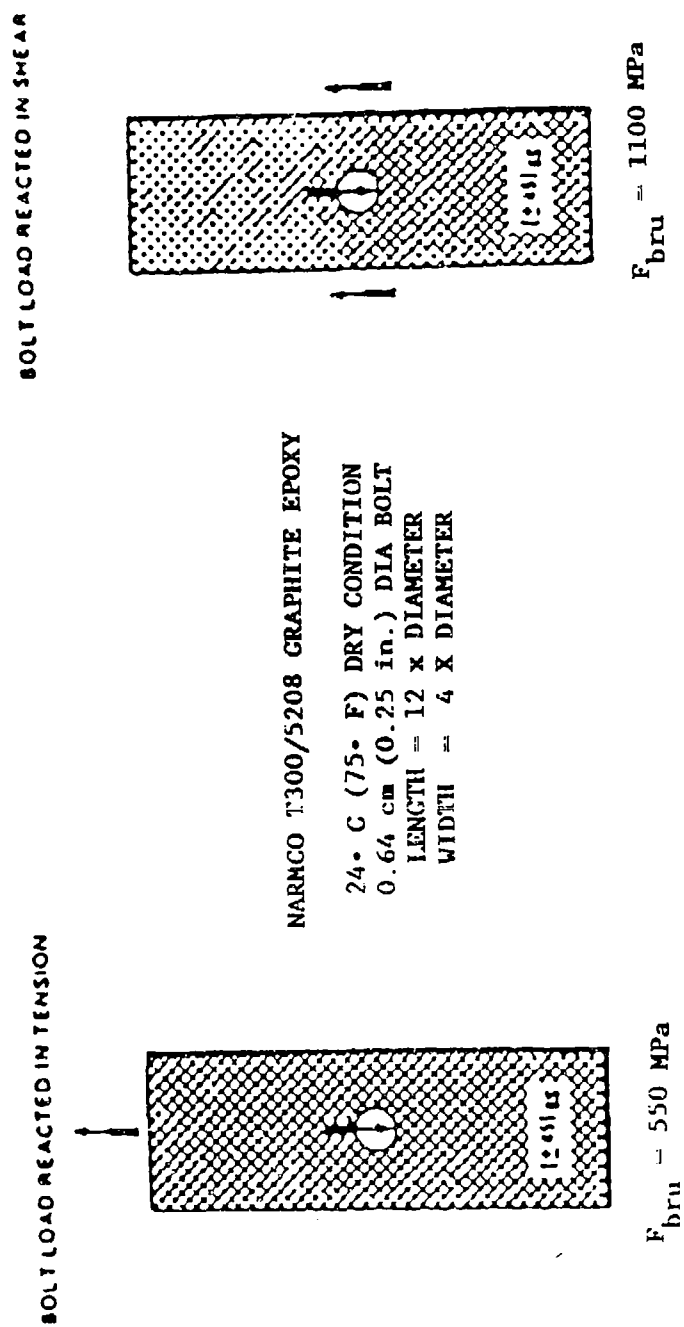


Figure 1-14 Bearing Strength Depends on Load Path

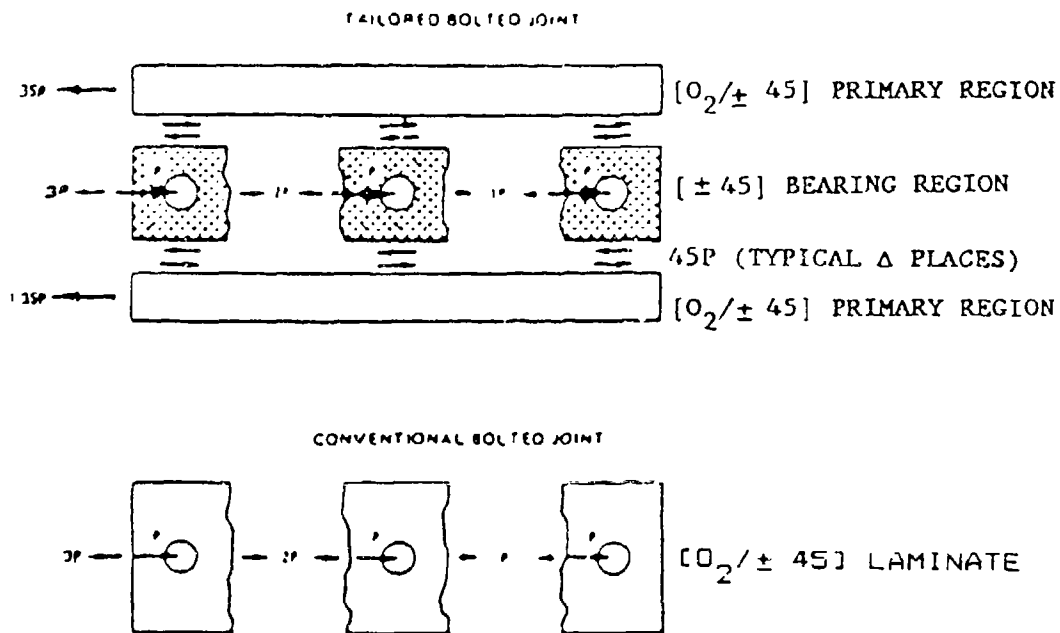
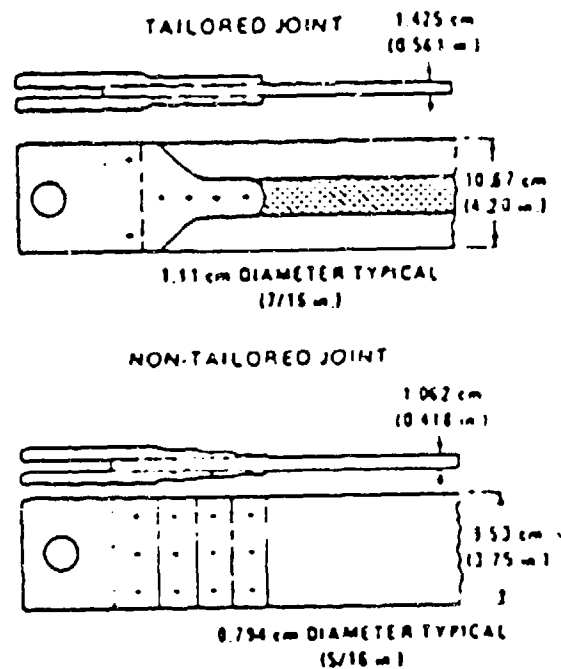


Figure 1-15. Laminate Tailoring Alters Internal Load Path in a Multifastener Joint



	TAILORED JOINT	NON-TAILORED JOINT
LAMINATE THICKNESS	1.425 cm (0.561 in.)	1.062 cm (0.418 in.)
% 0-DEGREE PLYS	47	52
JOINT LENGTH	17.5cm (6.89in.)	13.0cm (5.12in.)
NUMBER OF BOLTS	6	12
MAXIMUM STRAIN	0.651%	0.370%
MAXIMUM BEARING STRESS	854.3 MPa (123.9ksi)	330.3 MPa (47.9 ksi)
WIEGHTS:		
LAMINATE	0.4264 kg (0.9402 lb)	0.2062 kg (0.4546 lb)
ALUMINUM PLATES	0.3630 kg (0.8004 lb)	0.2815 kg (0.6206 lb)
BOLTS	0.0977 kg (0.2154 lb)	0.0987 kg (0.2177 lb)
NUTS	0.0181 kg (0.0406 lb)	0.0218 kg (0.0480 lb)
TOTAL	0.9052 kg (1.9968 lb)	0.6082 kg (1.3409 lb)
TEST LOAD	622.7 kN (140000 lb)	333.6 kN (75000 lb)
TEST LOAD PER BOLT	102.3 kN (23000 lb)	27.8 kN (6250 lb)
TEST LOAD-JOINT WEIGHT	70146	55932

Figure 1-16 Multiple-Fastener Joint Test Results. Specimen Under Tensile Load

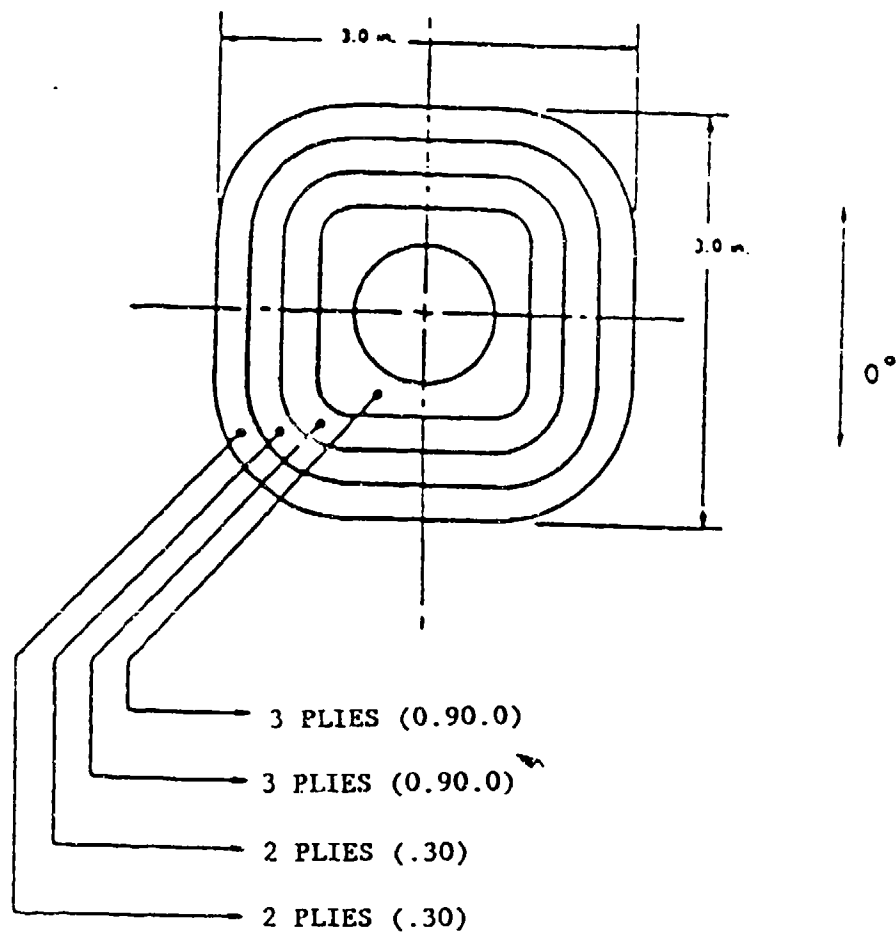


Figure 1-17 Multilayer Square Reinforcement Graphite Showing the Layers which are Bonded onto the Surface; Surface Reinforcement

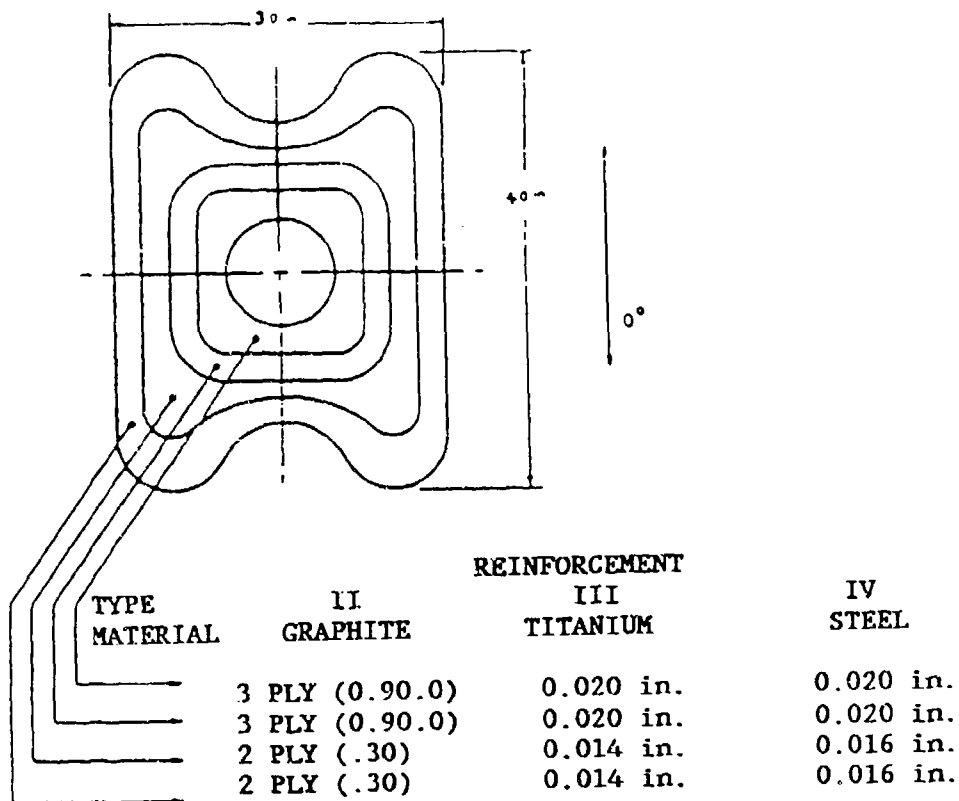


Figure 1-18 Multilayer Butterfly Reinforcements using Different Materials and Layup. The Layers are Bonded onto the Surface of the Laminate.

surface around the hole. It was shown that up to 90 percent of the parent laminate strength (no cutout) was achieved with the reinforced cutout specimens. The best and most efficient cutout reinforcements examined were the interspersed graphite composite buildup shown in Figure 1-18. This and several similar shim reinforcement methods, (see Figure 1-19), were rejected because of major disadvantages, i.e., the costly manufacturing and weight penalties, as Webb [1.18], Strauss [1.38], Clayton and Jones [1.39], and Schjelderup and Jones [1.31] prove. Figure 1-20 illustrates the idea.

A relatively low-cost, low-weight reinforcement method is explained by Padaver [1.40]. A major disadvantage is the rather sophisticated manufacturing process. Transversely isotropic boron film was used to reinforce the laminate in the areas of fastener holes, as shown in Figure 1-21. The film increased locally the existing laminate by 6-12 volume percent. The main features of the boron film were found in its high bearing strength and resistance to shear distortion. The results of Padaver's experiments show that the addition of film plies to a highly directional fiber laminae can increase the joint strength and stiffness up to 150 percent. In this case the weight penalties and the costly manufacturing might be negligible.

In contrast to local reinforcements, the idea of softening the composite in the vicinity of the hole, which means reducing the stress concentration factor, seems attractive. Clayton and Jones [1.39] suggest using GFRP to soften CFRP. The basic concept is presented in Figure 1-22. Strips of glass fibers replacing those graphite plies aligned with the load and only four bolt-diameters wide have been found by test to effectively eliminate any sign of stress concentration factor in the graphite epoxy.

Also, Hart-Smith [1.41] discusses this method of softening a composite locally. He shows evidence that the greater delaminations associated with glass epoxy than with graphite epoxy play a substantial role in adding to the relief provided by the lower modulus and the much greater failure strain of the glass fibers. His tests show improvements on bolted joints in such hybrid laminates with respect to an all-CFRP laminate. There were no substantial changes in bearing strength, but there was a greater tendency to fail in bearing rather than by the more catastrophic net-tension mode.

Hart-Smith indicates another way of stress concentration relief in composites by softening the laminate through delamination, (see Figure 1-23). He collected data from the Langley Research Center which indicated much stronger joints when using interference fits than with net or loose-fit fasteners. Hart-Smith disclosed that the prime factor for this strength improvement is delamination of the resin, introduced when installing the fastener. It appears necessary not to damage the fibers when this delamination occurs. Apparently, a very high local stress concentration factor develops in the fiber aligned with the load immediately outside the hole. If the first failure is by intraply or interply delamination rather than of fiber breakage, a much higher load can be resisted if the region is softened by delamination. While the

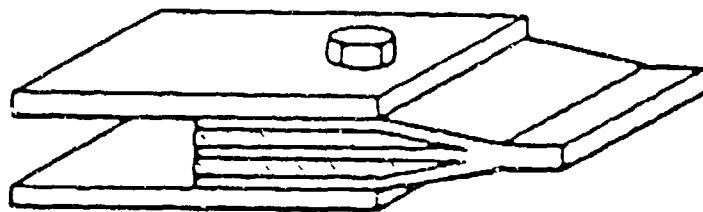


Figure 1-19 Shim Joint Concept for a Double Lap Connection; Middle Reinforcement

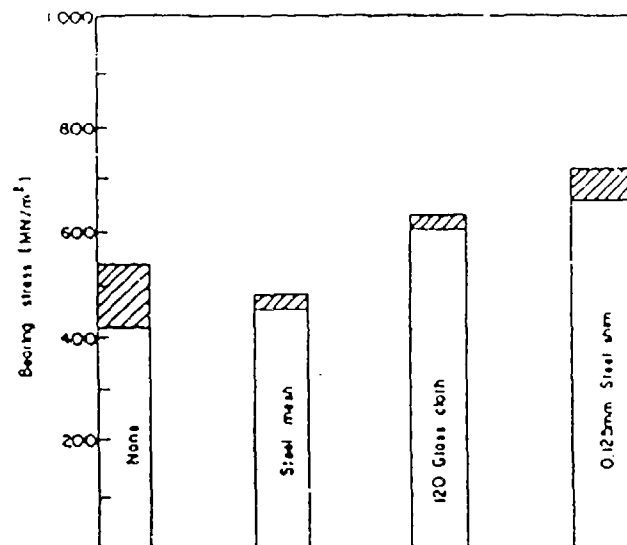


Figure 1-20. The Effect of Local Shim Reinforcement on Bearing Strength in GFRP Laminates

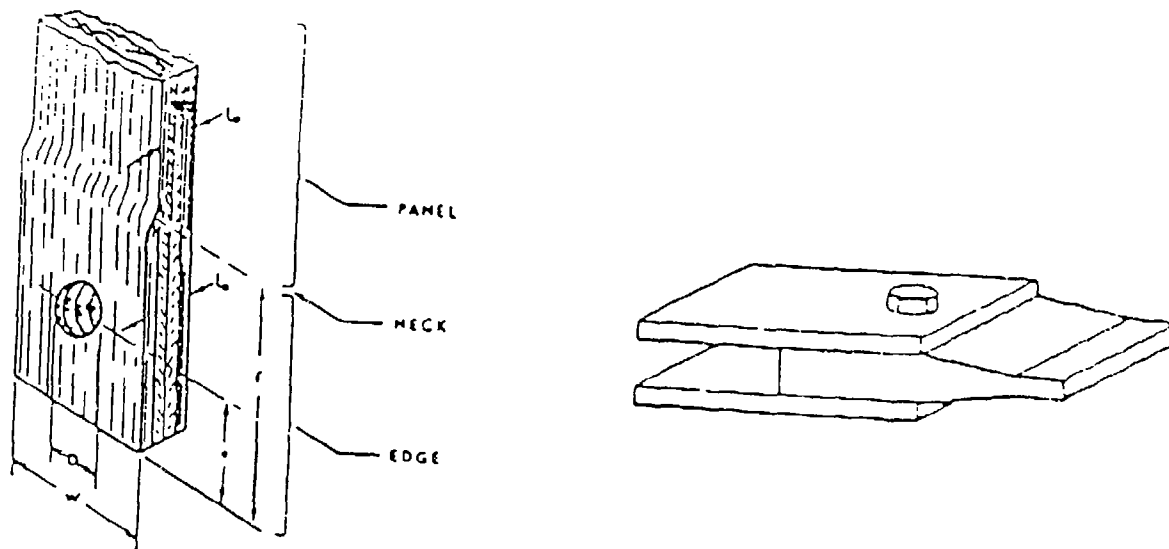


Figure 1-21 Schematic Diagram of Edge-Reinforced Fiber Composite

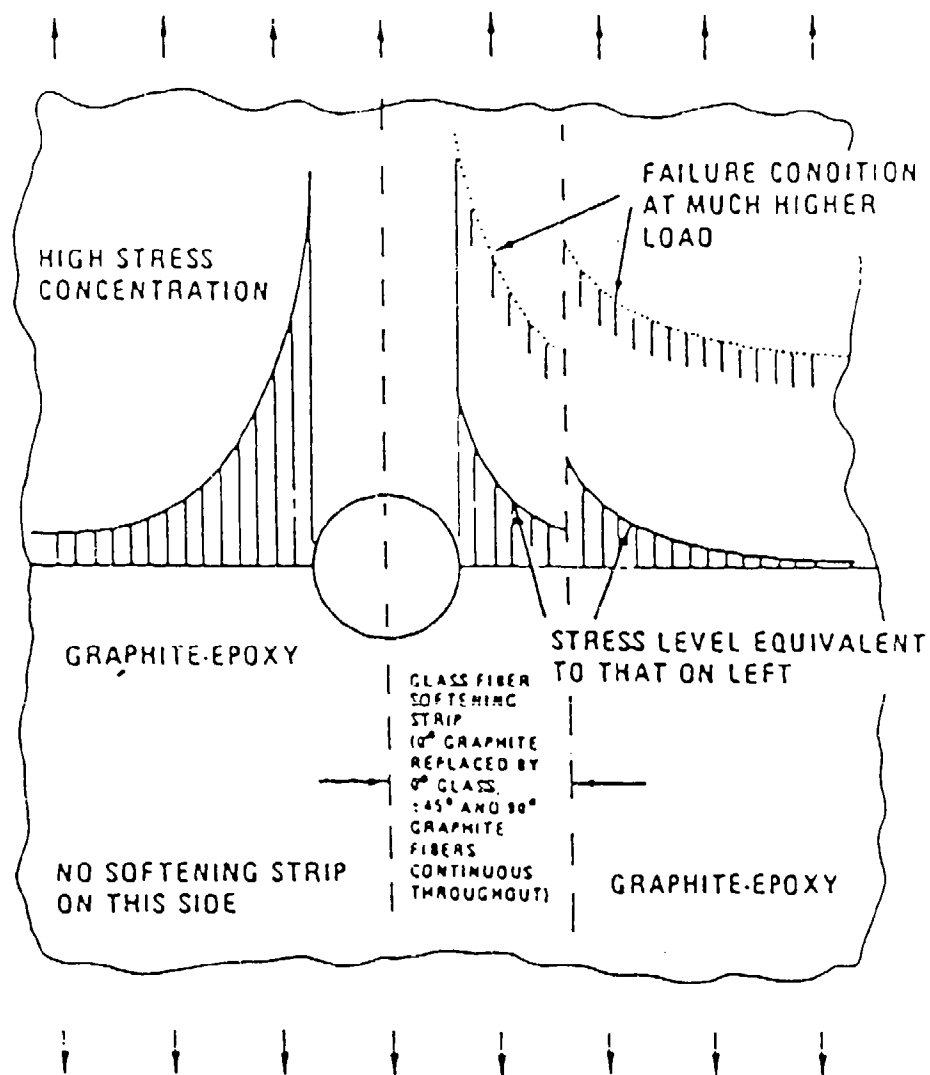


Figure 1-22. Benefits of Glass Fiber Softening Strips in Graphite-Epoxy Composites

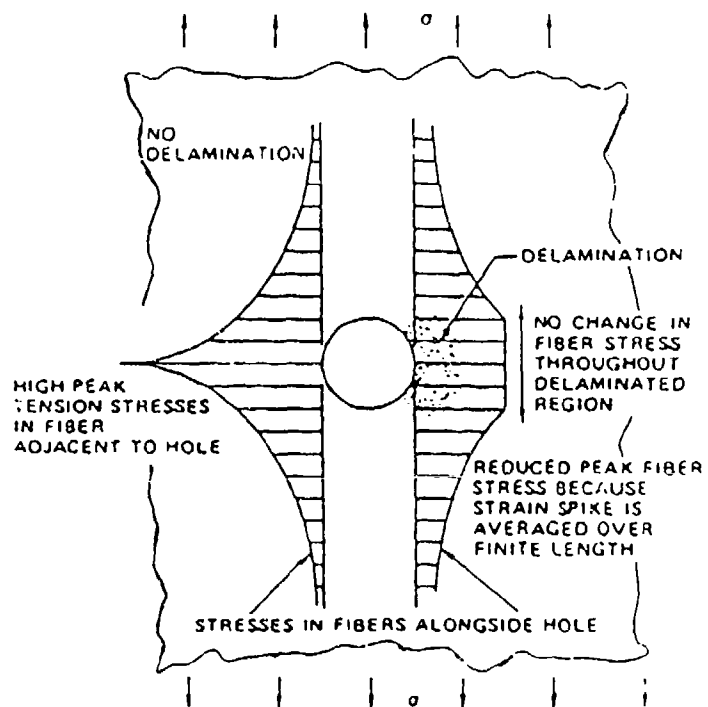


Figure 1-23 Stress Concentration Relief by Delamination

results with near-isotropic fiber patterns show consistent strength improvements of about 100 percent, other results with markedly orthotropic fiber patterns have exhibited static strength losses of as much as 25 percent.

Some interesting work was done by Herrera [1.6] who investigated loaded pins and inserts. His results show a 50 to 70 percent reduction in strain concentration factors when using aluminum bushings. Excerpts of this work appear as Figures 1-24 to 1-26. These results helped in evaluating bearing strains which are of partial interest for bolted connections. Most of the other work which was done on pin-loaded holes is summarized in his paper.

1.5. Literature Concerning Applications of Composites

One of the principal stimuli to the growth of high-performance fibrous composites has been the availability of fibrous glass under mass-production conditions. Strong, cheap, versatile, light, relatively inert and stiff, it has become an important material for automotive, marine, aircraft and space uses. A measure of its acceptance is found in the expansion which the field has undergone: in the 10 years from 1955 to 1965, the world's production of GFRP has approximately tripled to a level of 144,000 tons [1.42]. That happened 20 years ago. Unfortunately no numbers about today's production could be found, but certainly there has been a tremendous increase.

There are many reasons for the use of fibrous, composite structural materials, among the more interesting of which may be the following:

- Strengthening an otherwise weaker matrix.
- Stiffening a more flexible matrix.
- Achieving controlled mechanical and physical properties.
- Enhancing the ratios between mechanical properties and the specific weight of a structural material.
- Attaining manufacturing cost reductions while maintaining mechanical and other properties.

For the interested reader some unique examples might be given out of the huge range of applications.

Not cheap, but of extraordinary strength and relatively high ductility, are the high-duty aramid fiber composites. Most of the fiber is produced and supplied by DuPont Co. which has it comprehensively patent protected [1.43]. The production volume for the fibers is 12,000 tons per year with a sales increase of 30 percent in the last few years.

Especially in the aircraft industry the structural applications for high-strength, low-weight composites, i.e., carbon and aramid fiber laminates, are countless, ranging from rudder units, landing flaps, and

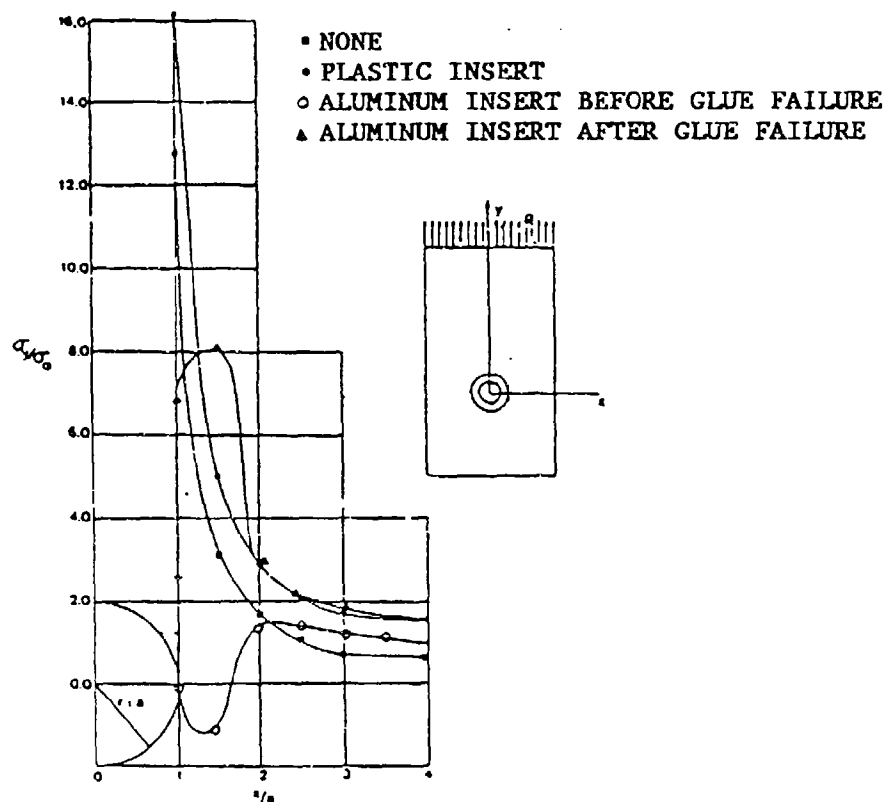


Figure 1-24 Stress Concentration Factor ALong Line in the Direction of the Load Located in the Ligament Area. Insert Diameter at $x/a = 1.5$

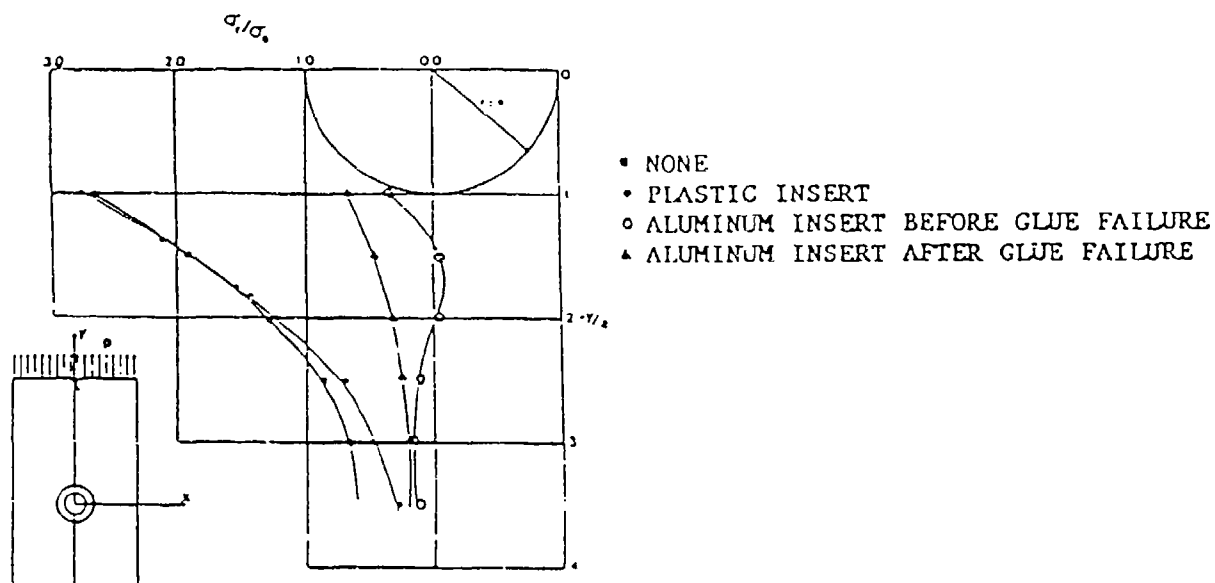


Figure 1-25. Bearing Stress Concentration Factor. Insert Diameter at $x/a \approx 1.5$

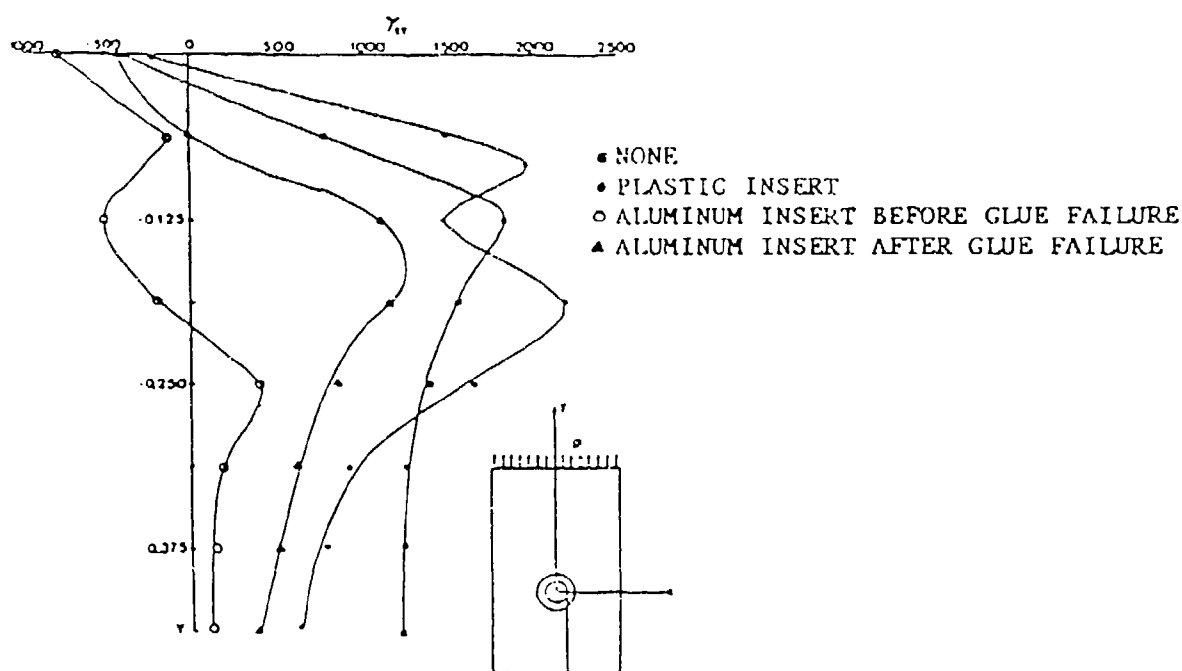


Figure 1-26 Shear Strains Along Locus of Shear-Out Failure. Insert Diameter at $y/a \approx -0.225$

elevators to window blinds [1.44, 1.45, 1.46]. The reasons for this are the high design and manufacturing allowable expenses depending on the importance of weight reduction [1.47]. In the automotive industries the allowable costs for weight savings do not yet justify the use of these high-duty fibers. This situation will probably change with the development of other high-duty fibers, thereby creating a competitive market and lower prices. Despite the extraordinary costs, the demand for Aramid fibers still is strong. This becomes clear when looking at a simple example for the achieved weight savings. A simple redesigned window blind in an aircraft has 1.0 kg less weight per window [1.44]. At this point the dimension of weight savings for large components becomes imaginable. It was estimated that an airplane which weighs 30 tons can weigh 20 tons with the rigorous application of composites. Right now, the developed know-how is not sufficiently anchored to meet the high safety requirements. Investigations on mechanical fasteners are playing a major role since they have to be used for reasons of maintenance and assembly. They are required to connect the composite structural members safely to the frame or body of the aircraft.

1.6. Literature Relevant to Mechanics of Joining

Numerous previous studies of mechanical joints and the associated problem of bolt or pin-loaded holes have been conducted. Some of the most relevant articles are mentioned here. Bickley [1.48], studied the problem of an infinite plate containing a loaded hole. For the case of a push fit he presumed contact over an arc of 180° and a cosine distribution for the contact pressure. He obtained a solution in the form of polar trigonometric series by means of a Fourier analysis in a full 0 to 360° range. He also considered a clearance fit, proposing a pressure distribution by analogy with the Hertzian solution, and proceeding as in the previous case to obtain a stress function.

The problem of a smooth, loose, rigid pin pressed against the edge of a circular hole in an infinite plate was studied analytically by Tiffen and Sharfuddin [1.49]. They obtained an integro-differential equation for which there is no known solution except in the case when the region of contact can be taken to be equal to a semi-circle. The problem of a rough, loosely fitted pin, pressed against one portion of the boundary of the hole was studied analytically by Sharfuddin [1.50]. This solution considers a specified displacement on the contact area while the rest of the boundary is stress free, but it does not permit sliding in the rough contact zone. Theocaris [1.51] gives an exact analytical solution for the stress distribution resulting from loading a perforated strip in tension through a rigid pin filling the hole. He assumed an angle of contact between pin and hole of 180° , no slip, and identical mechanical properties for pin and plate. It should be mentioned that these first four references used isotropic materials only.

More recent studies have used numerical methods and computer techniques to solve pin fastener problems. Waszczak and Cruse [1.52] used finite elements in an attempt to further understand the failure characteristics of bolted joints. A cosine distribution of normal stresses acting over half of the hole surface was used to simulate the stress distribution

caused by the bolt. De Jong [1.53] investigated the stress distribution around a pin-loaded hole in an elastically orthotropic or isotropic plate with a rigid pin and frictionless interface, using Lekhnitskii's method of complex functions. Wong and Matthews [1.54], used a two-dimensional finite element analysis for problems of bolted joints in fiber-reinforced plastic, and some correspondence is demonstrated between the calculated and experimental data for fiber-glass-reinforced epoxy resin. Matthews, et al. [1.55], employed a three-dimensional finite element analysis and showed that the stress distribution around a loaded hole depends on whether the load is applied via a pin or a bolt. Wilkinson and Rowlands [1.56] used a finite element analysis to study stresses and strains associated with a single-fastener mechanical joint in wood; and they evaluated the effects of friction and variation in joint geometry as well as ratio of pin- to-hole diameter. They also presented experimental verification by means of the Moire technique.

Analytical approaches, including boundary collocation and finite element methods, were presented by Oplinger [1.57] to study the effects of edge distance and width in single-fastener lugs. Comparison of single-fastener and parallel fastener configurations was also made, and the analytical results were compared with Moire technique results. Chang et al. [1.58] presented a method to first determine the stress distribution in the laminate by the use of a finite element method, and the failure mode and failure load are predicted. For this purpose they used Yamada's failure criterion [1.59], which is based on the assumption that, just prior to failure of the laminate, every ply has failed as a result of cracks along the fibers. Pradhan and Ray [1.60] also investigated the stress distribution around pin-loaded holes for isotropic as well as fiber-reinforced plastic composite materials. The case of full-contact angle, i.e. 180° , and that of partial contact, i.e., the case for an angle of contact less than 180° between hole and pin, was considered. They concluded that the maximum circumferential stress at the edge of the hole depends strongly on the material properties and on the ratio of hole diameter to width of plate, as well as on the angle of contact between pin and the hole. Chang and Scott [1.61, 1.62] presented a method based on finite elements to calculate the failure strength and the failure mode in the laminate. First, they determined the stress distribution and then they predicted the failure load and the failure mode by means of a proposed failure hypothesis together with the Yamada-Sun Failure Criterion. They also present a method to size laminates containing more than two pin-loaded holes which will result in the maximum failure load and the maximum failure load per unit of weight. Zhang and Ueng [1.63] obtained an analytical solution of stresses around a pin-loaded hole in orthotropic plates by the use of complex stress functions which satisfy the displacement boundary conditions along the hole boundary. Frictional effects are included. They also concluded that the distribution of stress around the pin-loaded hole is strongly affected by the presence of friction and the properties of the orthotropic material, i.e., the ratio of moduli of elasticity along the two principal axes of the joint.

There have also been experimental studies of the pin-loaded hole problem. Frocht and Hill [1.64] used photoelasticity and strain gages

on isotropic materials to study the influence of the material on the state of stress, and they also considered the effects of geometrical parameters of the joint. Also using photoelasticity, Lambert and Brailey [1.65] and Jessop, Snell and Holister [1.66] studied the reduction in stress concentration factors resulting from the introduction of an interference-fit pin in a circular hole. Cox and Brown [1.67] used a photoelastic analysis to study the effects of variations in pin clearance and plate width. Nisida and Saito [1.68] combined photoelasticity and interferometry to separate the stresses in the neighborhood of pin-loaded holes in tensile plates. These studies were done using isotropic materials. More recent experimental studies have been applied to the problem of pin-loaded holes on anisotropic materials. Oplinger, et al., [1.69] utilized the Moire technique together with finite element techniques to study pin-loaded composite plates. Wilkinson, et al., [1.70] and Rowlands, et al. [1.71], used the Moire technique and finite elements to analyze orthotropic materials for single-bolted and double-bolted mechanical fasteners in order to develop design information. Phabhakaran [1.72] used photo-orthotropic elasticity to study bolted joints in composites. Quasi-orthotropic and unidirectionally reinforced specimens were also tested for different end-distance-to-bolt-hole ratios. Cloud, et al [1.73] in a combined experimental-theoretical research program which included classical Moire techniques, boundary-element and finite elements, studied the mechanics of fasteners in orthotropic composites to obtain stress-strain fields in the vicinity of pin-type fasteners. Serabian [1.74] also utilized classical Moire techniques in order to experimentally verify Oplinger's assumptions pertaining to bolted joints on non-linear behavior observed in 0/90 and ± 45 -degree laminates. The first laminate type is in shear primarily in the region in front of the pin, while the second laminate is in tension in the ligament area. Katz [1.75], described a semi-automatic system for data reduction of Moire fringe photographs from work on pin-loaded holes.

1.7 Other References

While not specifically discussed in the above survey, several other articles have been helpful in guiding this research. These works are included in the list of references (1.76-1.109) for reasons of completeness and utility.

1.8. Principal Results

The general findings and conclusions of the research are summarized below. As mentioned above, this project involved several areas of study pertinent to mechanical fastening of composites. Detailed results, conclusions, and qualifications are presented at the ends of chapters which deal with the specific areas.

The mechanical properties of the laminate used in all the studies were measured to be:

$$\begin{aligned} E_1 &= 3.188 \times 10^6 \text{ psi (21.98 GPa)} \\ E_2 &= 3.082 \times 10^6 \text{ psi (21.25 GPa)} \\ \nu_{12} &= 0.11 \quad \nu_{21} = 0.11 \end{aligned}$$

A unique moire interferometer system and computer-based data acquisition and reduction capability for measuring surface strains along three directions over a region was developed and proven to have the correct sensitivities for research on composites.

Surface strain maps were obtained by the moire methods for single-pin, two-hole tandem, two-hole parallel, and three-hole staggered joint configurations. These maps include strains along the longitudinal, transverse, and 45-degree directions for the entire region of the joint.

A table of stress concentration factors for single-pin joints and for fastener arrays in various load configurations was developed from moire investigations of the strain fields in the joint regions. For the single-pin, the stress concentration factor (SCF) was 14. For the two-hole tandem pattern with both holes loaded, the maximum SCF was 5.6. The two-hole parallel pattern gave a maximum SCF of 1.16. The maximum SCF for the three-hole staggered array was 2.95.

Since multiple-fastener arrays result in a statically indeterminate situation, the effect on SCF of manufacturing imperfections, which cause most of the load to be concentrated at one pin of the array, must be considered. The experiments showed that, for the two-hole tandem array, the SCF increases to 9.2 when the lower hole only is loaded. With the upper hole loaded, the maximum SCF is 12, which approaches the single-pin result.

A computer code has been developed which can predict stresses in multiply connected composite material problems. It produces very good results for pure traction boundary conditions. For mixed boundary conditions, more development is necessary. The analysis of the variable-stiffness concept has been coded but not adequately tested.

The computer code was employed to calculate SCF's for single-pin and hole arrays. The values cannot be strictly compared with the experimental values given, since one of the material constants was not determined during the period of the contract. Some key values are worth noting. The SCF for the single-pin is predicted to be 8.8; for the two-hole parallel pattern, the SCF is 5.5; and for the two-hole tandem array, the SCF is 6.2. The three-hole BEM analysis was not completed at contract end.

Allowing for the difference in material properties used, the agreement between theory and experiment is encouraging, with the possible exception of the two-hole parallel array results. Agreement should improve as the exact properties are entered into the computer code.

The effects on stress concentrations of flat and conical load-bearing washers and two degrees of bolt torque were investigated using the moire technique. A key finding is that a combination of "conical washer up" (cone edges away from composite) plus "high" clamping force gives the best balance of ligament stress, bearing stress, shear stress in the shear-out zone, and tensile stress in the top zone. Next best is the

flat washer with high clamping force, and the "conical washer down" with high clamping force is third.

Bolting with low torque so as to give low clamping force is always worse than using high clamping torque, although in the low clamping force situation there are still gains if conical or flat washers are used.

Overly large bolting torques increase the risk of shear-out failure. There is an optimum level of clamping force for a given joint. The correct values for even simple joints have not yet been determined.

The twisting effect in the laminate that is induced by applying torque to a bolt has a serious effect on the surface strain field. The effect on joint performance is yet to be determined. Effective and practicable ways to eliminate the effect should be sought. One technique for laboratory use was devised during the research.

Single resistance strain gages plus the strain maps obtained through laboratory experiment and/or computation can be used to establish fastener loads in vehicles in the field. The uncertainty would be about 50 percent.

A simple bolt-load transducer was designed, constructed, and tested to obtain field measurements of fastener loads in vehicles.

A bolt-load transducer of the sort described will give field bolt load measurements with an uncertainty of about 30 percent provided it is properly oriented and the bolt tightening torque is known.

The bolt-load transducer will indicate both clamping force and joint slippage when clamping force is used.

Fasteners that are not at right angles to the specimen surface, as would be caused by misaligned holes, crooked holes, or other causes can cause deviations in the stress values in excess of 200 percent of the values measured or calculated for ideal cases. Similar effects are observed for holes that are tapered or bell-shaped.

The well-fitted pin peak strains obtained by moire techniques are higher than those observed for ill-fitting pins, and they can probably be taken as accurate worst-case strain distributions. That is, design errors caused by ignoring pin tilt are probably on the safe side. This tentative finding should be subjected to further study before it is accepted into design methodology.

The results obtained for well-fitted pins and for tilted pins probably can be used as suitable upper and lower bounds on the magnitudes of stresses that will be realized in comparable design situations.

Interior strains in the poorly-fitted pin case are likely comparable to surface strain for the well-fitted pin, but this assertion needs more study.

Measurements of surface strain can be catastrophically misleading for laminated composites unless test conditions are carefully established and unless care is taken with interpretation of test results.

1.9. Recommended Further Research

As the current contract is brought to a close, it is appropriate to mention related research ideas which should be pursued in order to: (a) gain maximum design utility from the research which has already taken place, and, (b) achieve greater understanding of the mechanics of fasteners in composite materials. Several such ideas are mentioned below with little regard to priority.

- Correlate analytical and experimental results from the current contract research on fastener arrays with the goal of optimizing array patterns, hole treatment, washers, and clamping force.
- Perform additional strain gage and transducer studies to clearly connect laboratory and analytical results with vehicle applications.
- Examine the effects of out-of-plane loads on stress magnitude and distribution.
- Measure strain fields produced in one or two of the optimum hole arrays patterns.
- Continue the assembly of design codes for mechanical fasteners in composites.
- Measure strain fields in cases where strain-relief techniques are utilized to improve the efficiency of multiple fastener patterns.
- Test and debug the computer code for the variable stiffness design concept.
- Conduct a limited parametric study involving material properties and fastener/insert radii.
- Conduct detailed parametric studies on single- and multiple- fastener arrangements.
- Undertake the development of computer code to handle the 3-dimensional fastener problem via the following steps:
 - modifying the structure of the current code,
 - testing the new code for isotropic materials for which Green's functions are known,
 - deriving Green's function for 3-dimensional orthotropic material,
 - evaluating integrals containing the derived Green's functions for fixed geometry,
 - coding the results and beginning testing.
- Continue development of a three-dimensional Moire or speckle technique for use on composites.

- Conduct 3-dimensional experimental studies using the developed optical technique plus an array of embedded strain gages.
- Test to failure the specimens used for surface strain analysis to establish failure criteria, morphology, and correlation with two-dimensional experimental and analytical stress/strain mapping already carried out.
- Examine further the effect of hole profile and tilted pins on both the magnitude and distribution of stress.
- Investigate the effects of bolt torque on joint performance, especially in terms of fatigue behavior when conical or flat washers are used.
- Develop practical methods to reduce the joint twisting action that is introduced as tightening torque is applied to a bolted joint.
- Determine whether strain-relief inserts are effective in reducing stress concentrations in multiple-fastener arrays while at the same time reducing the deleterious effects of misaligned holes and poorly shaped holes.

2.0. CHARACTERIZATION OF THE MATERIAL

The material used in this investigation was a fiber glass-epoxy laminate with woven fibers (R1500/1581, 13 plies, 0.14 in. thick) supplied by CIBA-GEIGY, Composite Materials Department, 10910 Talbert Avenue, Fountain Valley, California 92708.

In order to calculate stresses in the material, it was necessary to know with precision the material properties of this composite laminate. A review of simple concepts of the theory of elasticity for anisotropic bodies was utilized to characterize the material used in this research, and also to set the theoretical foundations of the experimental method used to measure its mechanical properties. No information about the material properties was available from the manufacturer.

2.1. Elastic Properties of Composites

Generally, composites are anisotropic materials, i.e., their strength and stiffness vary with the direction in which they are measured. If the matrix is a resin, the behavior in any direction, is in fact, visco-elastic. In most calculations, however, elastic constants are used. At low loads, for short duration and within a small temperature range, it is appropriate to use Hooke's law for the description of the anisotropic behavior [2.1].

$$\sigma_i = C_{ij} \epsilon_j$$

or

$$\epsilon_i = S_{ij} \sigma_j$$

where $i, j=1,2,\dots,6$, and σ_i are the stress components, ϵ_j are the strain components, C_{ij} is the stiffness matrix and S_{ij} is the compliance matrix. The double subscript indicates a summation. Referring to the above equations, it can be shown that the compliance matrix S_{ij} has 36 constants. However, less than 36 of the constants can be shown to be actually independent for elastic materials when the strain energy is considered, and it is shown that S_{ij} is symmetric i.e. $S_{ij} = S_{ji}$. Thus, in the compliance matrix only 21 of the constants are independent.

The reinforcing material of the composite used here was a cloth composed of two sets of interwoven fibers at right angles to each other. This means that each ply can be considered as an orthotropic material. For the assembly of plies, there are two orthogonal planes of material property symmetry, and symmetry will exist relative to a third mutually orthogonal plane. Also, if the principal material axes are aligned with the natural axes of the specimen used to characterize the material properties, each lamina can be called specially orthotropic. The stress-strain relations in coordinates aligned with the principal material directions, i.e., parallel to the intersections of three orthogonal planes of material symmetry, are:

$$\begin{aligned}
\epsilon_1 &= S_{11}\sigma_1 + S_{12}\sigma_2 + S_{13}\sigma_3 \\
\epsilon_2 &= S_{12}\sigma_1 + S_{22}\sigma_2 + S_{23}\sigma_3 \\
\epsilon_3 &= S_{13}\sigma_1 + S_{23}\sigma_2 + S_{33}\sigma_3 \\
\epsilon_4 &= 2\epsilon_{23} = \gamma_{23} = S_{44}\tau_{23} \\
\epsilon_5 &= 2\epsilon_{31} = \gamma_{31} = S_{55}\tau_{31} \\
\epsilon_6 &= 2\epsilon_{12} = \gamma_{12} = S_{66}\tau_{12}
\end{aligned}$$

where the γ_{ij} ($i \neq j$) represents engineering shear strain, ϵ_{ij} ($i \neq j$) represents tensor shear strain, and ϵ_i is the contracted notation. It should be noticed that there is no interaction between normal stresses $\sigma_1, \sigma_2, \sigma_3$ and shearing strains $\gamma_{23}, \gamma_{31}, \gamma_{12}$. Similarly, there is no interaction between shearing stresses and normal strains in different planes. There are now only nine independent constants in the compliance matrix S_{ij} . For a lamina in the 1-2 plane, a plane stress state is defined by setting $\sigma_3 = 0, \tau_{23} = 0, \tau_{31} = 0$ and the above equation expressed in matrix form reduces to:

$$\begin{bmatrix} \epsilon_1 \\ \epsilon_2 \\ \gamma_{12} \end{bmatrix} = \begin{bmatrix} S_{11} & S_{12} & 0 \\ S_{12} & S_{22} & 0 \\ 0 & 0 & S_{66} \end{bmatrix} \begin{bmatrix} \sigma_1 \\ \sigma_2 \\ \tau_{12} \end{bmatrix}$$

and

$$\begin{aligned}
\epsilon_3 &= S_{13}\sigma_1 + S_{23}\sigma_2 \\
\gamma_{23} &= 0 \quad \gamma_{31} = 0
\end{aligned}$$

2.2. Stress and Strain in the Laminate

Knowledge of the variation of stress and strain through the laminate is essential to the definition of the extensional and bending stiffnesses of a laminate. Inversion of the above equation yields:

$$\begin{bmatrix} \sigma_1 \\ \sigma_2 \\ \tau_{12} \end{bmatrix} = \begin{bmatrix} Q_{11} & Q_{12} & 0 \\ Q_{12} & Q_{22} & 0 \\ 0 & 0 & Q_{66} \end{bmatrix} \begin{bmatrix} \epsilon_1 \\ \epsilon_2 \\ \gamma_{12} \end{bmatrix}$$

where the Q_{ij} , the so-called reduced stiffnesses, are

$$Q_{11} = \frac{E_1}{1 - \nu_{12}\nu_{21}} \quad Q_{22} = \frac{E_2}{1 - \nu_{12}\nu_{21}}$$

$$Q_{12} = \frac{\nu_{12} E_2}{1 - \nu_{12} \nu_{21}} \quad \text{or} \quad Q_{12} = \frac{\nu_{21} E_1}{1 - \nu_{12} \nu_{21}}$$

$$Q_{66} = G_{12}$$

and E_1, E_2 - Young's Moduli in 1, 2 directions respectively.

ν_{ij} - Poisson's ratio for transverse strain in the
j-direction when stress is in the i-direction.

G_{12} - Shear Moduli in the 1-2 plane.

In this study the fibers in the material used to construct the specimens are aligned with the edges of the specimen; thus, there is no need to use transformation of coordinates to find the stresses and strains along the fiber orientations. Now, the stress-strain relation of the nth layer of a multilayered laminate is written as

$$\sigma_n = Q_n \epsilon_n$$

From lamination theory, the resultant forces and moments acting on the laminate are given by,

$$\begin{bmatrix} N_x \\ N_y \\ N_{xy} \end{bmatrix} = \begin{bmatrix} A_{11} & A_{12} & A_{16} \\ A_{12} & A_{22} & A_{26} \\ A_{16} & A_{26} & A_{66} \end{bmatrix} \begin{bmatrix} \epsilon_x^0 \\ \epsilon_y^0 \\ \gamma_{xy}^0 \end{bmatrix} + \begin{bmatrix} B_{11} & B_{12} & B_{16} \\ B_{12} & B_{22} & B_{26} \\ B_{16} & B_{26} & B_{66} \end{bmatrix} \begin{bmatrix} \kappa_x \\ \kappa_y \\ \kappa_{xy} \end{bmatrix}$$

$$\begin{bmatrix} M_x \\ M_y \\ M_{xy} \end{bmatrix} = \begin{bmatrix} B_{11} & B_{12} & B_{16} \\ B_{12} & B_{22} & B_{26} \\ B_{16} & B_{26} & B_{66} \end{bmatrix} \begin{bmatrix} \epsilon_x^0 \\ \epsilon_y^0 \\ \gamma_{xy}^0 \end{bmatrix} + \begin{bmatrix} D_{11} & D_{12} & D_{16} \\ D_{12} & D_{22} & D_{26} \\ D_{16} & D_{26} & D_{66} \end{bmatrix} \begin{bmatrix} \kappa_x \\ \kappa_y \\ \kappa_{xy} \end{bmatrix}$$

where;

$$A_{ij} = \sum_{n=1}^N (Q_{ij})_n (z_n - z_{n-1})$$

$$B_{ij} = \frac{1}{2} \sum_{n=1}^N (Q_{ij})_n (z_n^2 - z_{n-1}^2)$$

$$D_{ij} = \frac{1}{3} \sum_{n=1}^N (Q_{ij})_n (z_n^3 - z_{n-1}^3)$$

The A_{ij} are the extensional stiffnesses, the B_{ij} are called the coupling stiffnesses and the D_{ij} are called the bending stiffnesses. The laminate used in this study can be considered to be "balanced," i.e., one that contains an equal number of laminae of $+\theta$ degrees and $-\theta$ degrees fiber orientation. For this type of laminate, the shear coupling stiffnesses terms A_{16} and A_{26} can be shown to vanish [2.1].

Also since all the laminae within the laminate are positioned symmetrically with respect to the laminate midplane, the coupling terms B_{ij} vanish. It is important to note that the twisting-bending terms D_{16} and D_{26} vanish. This type of laminate could therefore be called a "specially orthotropic laminate." All of this means that extension forces will produce only extensions and bending moments will produce only curvature.

The S_{ij} or compliance constants can be expressed in terms of engineering material properties as:

$$S_{11} = \frac{1}{E_1}$$

$$S_{12} = -\frac{\nu_{21}}{E_2} = -\frac{\nu_{12}}{E_1}$$

$$S_{22} = \frac{1}{E_2}$$

$$S_{66} = \frac{1}{G}$$

For the class of fibrous laminates where the tensile and compressive elastic properties are identical, the compliance matrix S_{ij} is symmetric. Hence $S_{12} = S_{21}$, and,

$$\frac{\nu_{12}}{E_1} = \frac{\nu_{21}}{E_2}$$

The fundamental principle underlying test methods to characterize laminated composites states [2.2]: The single lamina is the building block of the multidirectional laminate. Therefore, characterization of lamina material properties allows predictions of the properties of any

laminate. Then a tensile test can be performed to determine uniaxial strength, effective Young's modulus and Poisson's ratio. For the case of uniaxial tension, σ_1 in the 1-direction in conjunction with the engineering constants yields:

$$\epsilon_1 = \frac{1}{E_1} \sigma_1$$

$$\epsilon_2 = - \frac{\nu_{12}}{E_1} \sigma_1$$

$$\nu_{12} = - \frac{\epsilon_2}{\epsilon_1}$$

Similarly, a uniaxial tension σ_2 in the 2-direction yields:

$$\epsilon_2 = \frac{1}{E_2} \sigma_2$$

$$\epsilon_1 = - \frac{\nu_{21}}{E_2} \sigma_2$$

$$\nu_{21} = - \frac{\epsilon_1}{\epsilon_2}$$

2.3. Experimental Evaluation of Material Properties

2.3.1. Specimen Dimensions. There are two goals in the design and test of a tensile specimen. First, the existence of a statically determinant uniaxial state of stress within the test section must be assured. However, producing such a state of stress in the laboratory is not a trivial task. The second goal is to assure that the elastic responses in the in-plane shear and transverse tension modes are constant and that failure will occur within the specimen test section. With this in mind, the dimensions of the specimen should be chosen very carefully.

Several analytical studies have revealed that these goals may be accomplished by establishing the specimen geometry such that the length-to-width ratio is a practical maximum [2.3, 2.4]. Also, Horgan [2.5], has shown that when working with composites, the end effects persist over distances of the order of several widths of the specimen. Thus, to be safe, the specimen should be designed to be quite long and narrow. In the current study, the maximum length was chosen to be 12 inches and the width 1 inch. Figure 2-1 shows the dimensions of the specimens.

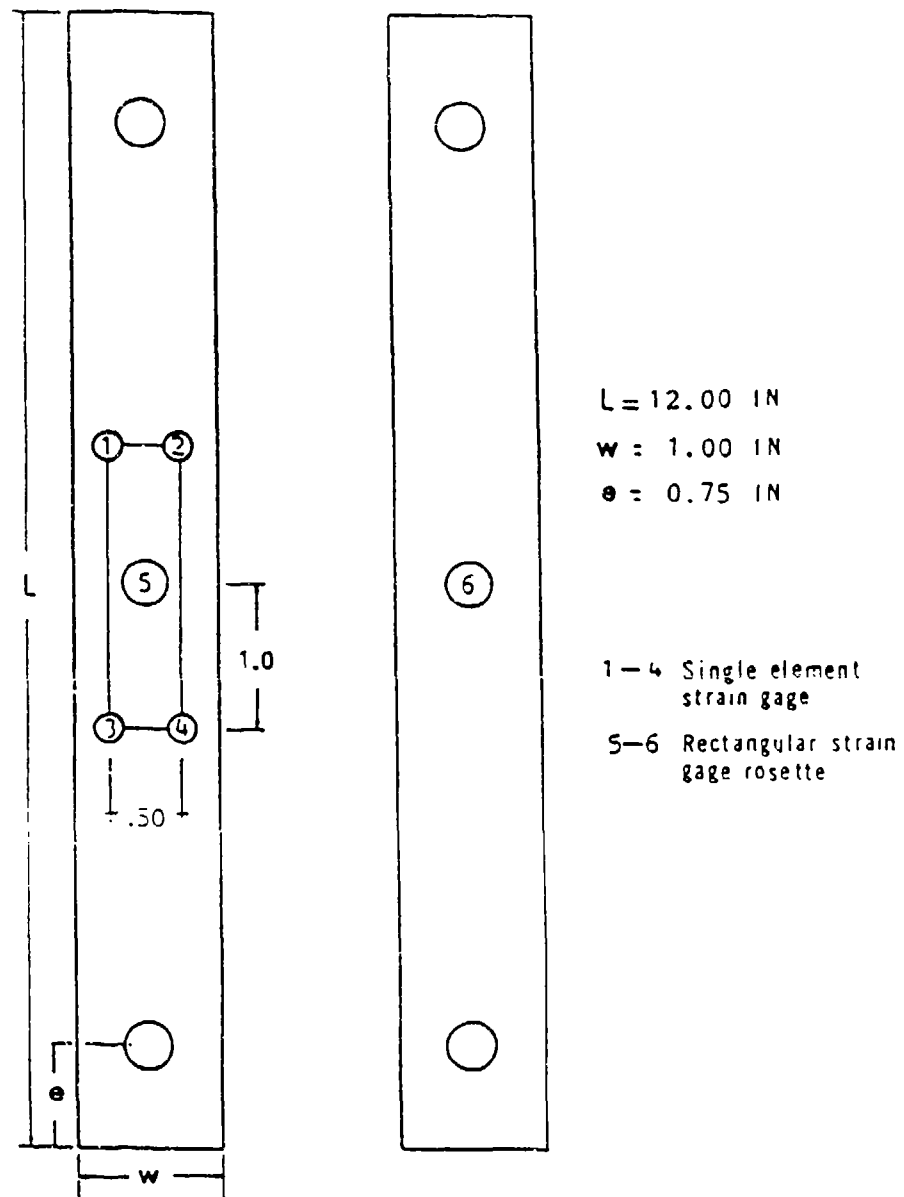


Figure 2-1. Specimen Dimensions and Location of Strain Gages

2.3.2. Experimental Procedure Determination of E_1 , E_2 and ν is quite straightforward. Two tensile tests are required, and for this purpose two specimens were constructed with dimensions as outlined above. One had the warp fibers oriented along the direction of the loading (for determination of E_1 and ν_{12}), and the other had the woven (weft) fibers in the direction of loading (for the determination of E_2 and ν_{21}). As shown also in Figures 2-1 and 2-2, four single-element strain gages, type EA-13-075AA-120 from Micromeasurements, were used to check the uniformity of the stress field. Strain gage rosettes (Micromeasurements type CEA-06-062UR-120) were also used on both faces of the specimen, first to determine any effect of bending of the specimen during loading because of any possible misalignment of the loading fixture, and then to obtain the measurements needed to perform calculations. Effects of transverse sensitivity were checked and found negligible.

The specimens were mounted in a loading frame using grips especially designed to allow rotations, thus avoiding any end effects (see Figure 2-3).

Every specimen was loaded in increments up to 500 pounds (2224 Newtons) and then unloaded and reloaded to the same stress. The tests were performed at room temperature (75°F or 23.8°C). The strain readings were made with digital strain indicators from Northern Technical Services, Inc. Figure 2-4 shows typical plots of stress vs. strain obtained from this experiment.

2.3.3 Results

The results obtained for Young's modulus and Poisson's ratio are as follows:

$$E_1 = 3.188 \times 10^6 \text{ p.s.i. (21.9804 GPa)}$$

$$E_2 = 3.0824 \times 10^6 \text{ p.s.i. (21.2523 GPa)}$$

$$\nu_{12} = 0.11 \quad \nu_{21} = 0.11$$

2.4. Failure Modes

Brief attention is given to two features describing the practical aspects of the material behavior. One is the formation of stress channels along the fibers, see Figure 2-5, and individual layers [2.6], see Figure 2-6.

With composites there is the additional application complication that, for a given failure mode, the definition of failure load is not necessarily obvious and may depend on the purpose of the joint. For



Figure 2-2. Photograph of Specimen Showing Strain Gages

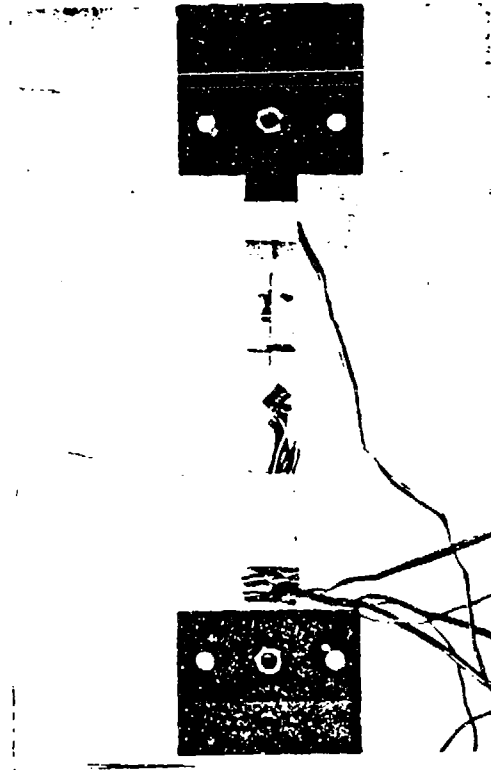
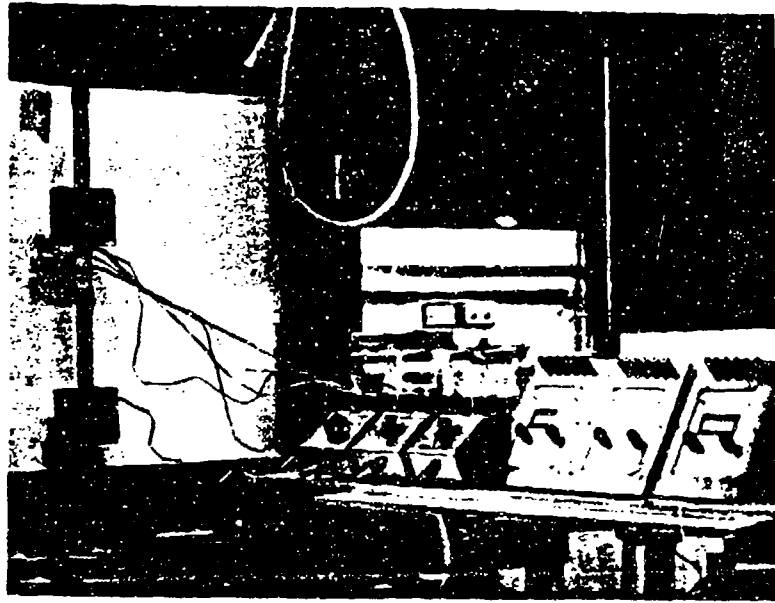


Figure 2-3. Overall View of Specimen and Loading Rig

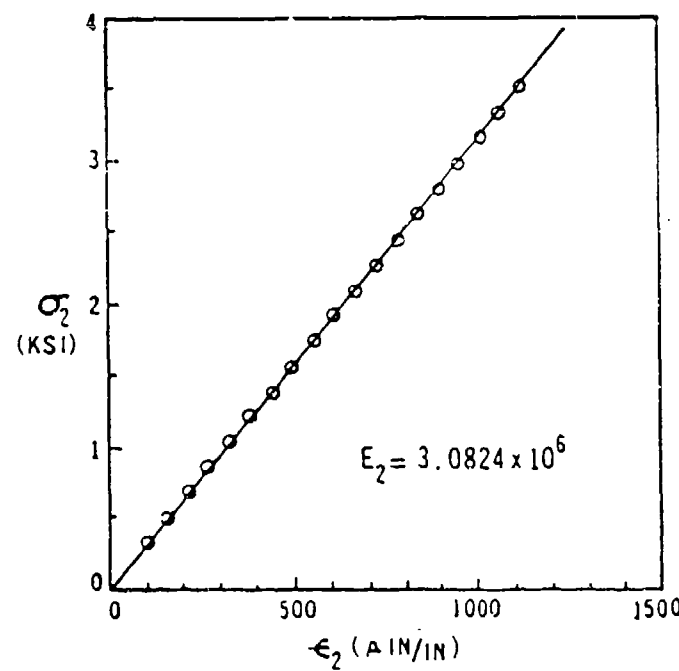
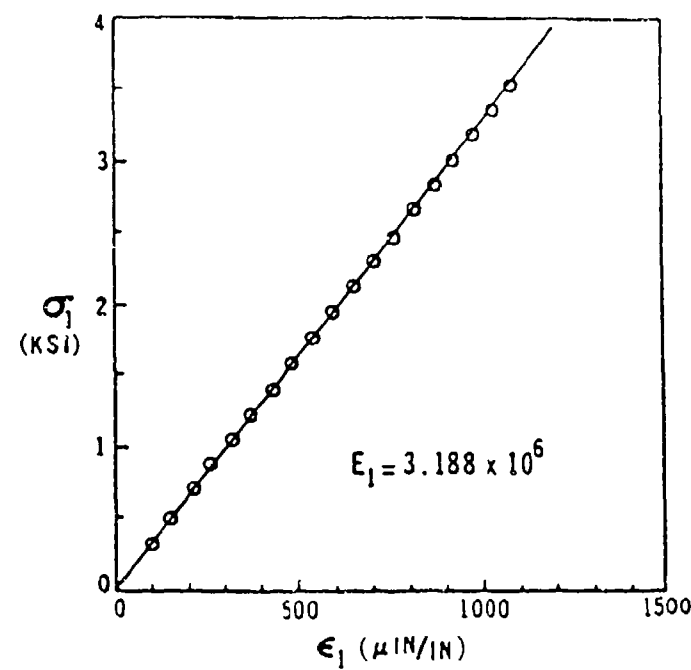
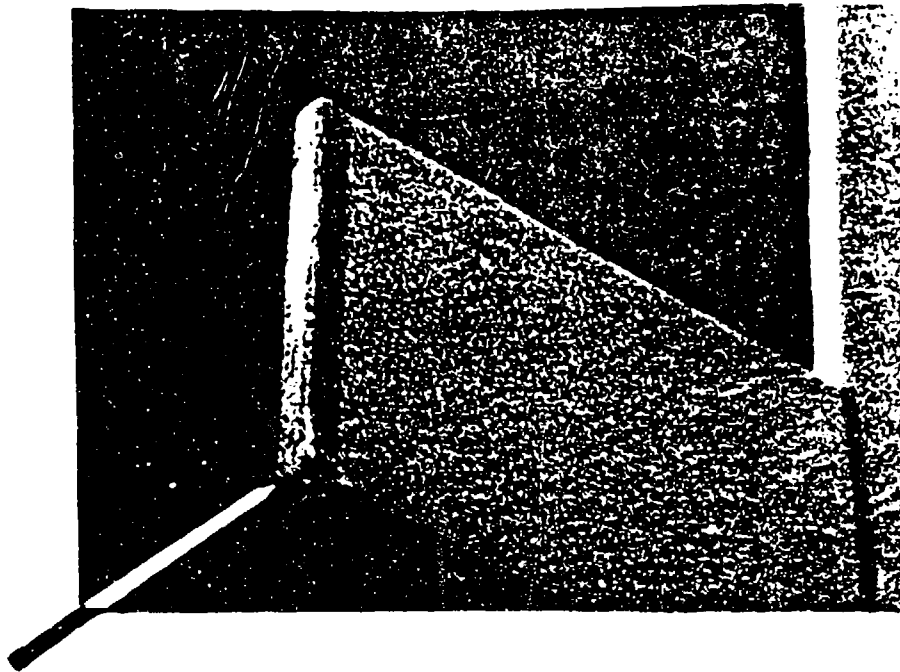


Figure 2-4. Typical Tensile Stress-Strain Plots for Determination of Mechanical Properties of Orthotropic Composites Used in this Research



DIRECTION OF IMPACT

Figure 2-5. Stress Channels Produced by Impact at the Edge of Composite Plate. Deformation Runs Through the Material Along the Fibers rather than in the Direction of Impact

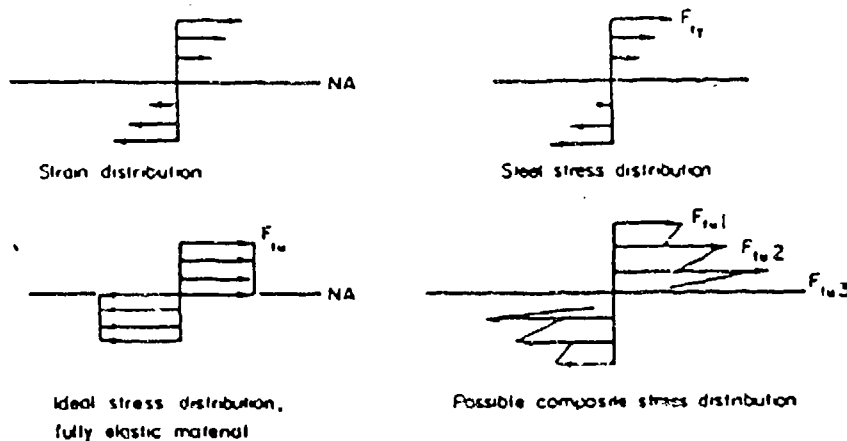


Figure 2-6. Freedom of Stress and Strain Distribution in Bending of a Composite Beam Relative to the Linear Distribution in Conventional Materials

example, In some instances it may be undesirable to have any cracking of the matrix, or more than a stated deformation of the fastener hole. The problem of defining failure as, for example, first delamination, first ply failure, total breakage, or a maximal hole elongation for evaluating joint efficiency is avoided in this investigation by establishing elastic strain as a measure of whether a joint can be used more efficiently than another one.

Mechanically fastened joints under tensile loads generally fail in three basic modes referred to as tension mode, shearout mode, and bearing mode. The type of damage resulting from each of these modes is illustrated in Figure 2-7.

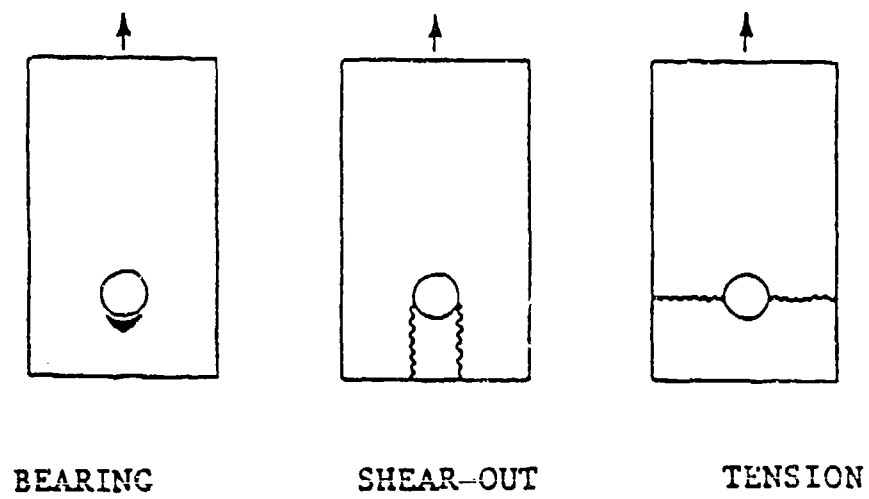


Figure 2-7. Illustration of the Three Basic Failure Modes

3.0. ANALYTICAL STUDY

3.1. Introduction

The general objective of the contract (DAAE07-85-C-R037) was to develop and use a computer code to study fastener arrays in joint design. Beside fulfilling most of the original objectives, some significant additional work has been done. The computer code is based on the Boundary Element Method (BEM). The choice of BEM over the finite element method was based on the consideration of the accuracy and cost per analysis.

The stress computed by the finite element method is some weighted average over an element. Thus, to compute high-stress gradients, like those near a pinhole, the size of the element must be reduced. But beyond a certain limit the gain achieved by reducing the size of element is offset by the increase in round-off error.

The BEM starts with the statement of the problem in terms of an integral equation. The integrand of the integral is a product of a known Green's function and an unknown function. The Green's function by definition satisfies the differential equations exactly. Hence, the solution of stresses satisfies the differential equation exactly. Thus, the resolution of high stress gradients by the BEM is very good. In composite material this particular advantage is important. Composites are usually brittle and are sensitive to high stress concentration.

The integration in the integral equation of the BEM is around the boundary of the body. Thus, for numerical purposes when the discretization needs to be performed, it need be done only on the boundary. This procedure is in contrast to the finite element method in which the discretization is done over the entire body. The net result of this difference is that the BEM requires less human and machine effort to solve a problem. In the detailed parametric study planned for the next phase of this project, this particular advantage should result in significant savings in cost.

The BEM, however, is not without its own share of problems. Though the BEM has been used extensively for isotropic problems, literature on its application in composite material problems is very sparse. This sparsity has generated some unique research challenges elaborated below.

To formulate a boundary value in terms of an integral equation, we need to know the Green's function for an infinite body made from the same material as the finite body. The form of Green's function in isotropic material is independent of the material properties. That is, the Green's function for isotropic material is a linear combination of some singular functions. The material constants of isotropic material affect only the constants of the above-mentioned linear combination. However, in orthotropic material, the nature and the form of singular functions also change with the material constants. The dependence of the form of Green's function on material constant has been known for a long time [3.13.4].

For plane, linear, orthotropic, and elastic material there are three forms of Green's function depending upon the relationship of the four material constants. In the past, [3.1,3.2] algorithms based on BEM have been designed using one of the three forms of Green's function and hence are restricted to analysis of a material of a particular kind. Composite material in general, and short fiber composites in particular, are prone to substantial variation in mechanical properties. Furthermore, we plan to use the code for the design of mechanical joints in any orthotropic composite material. The above two reasons compel one to design a code for a greater generality than the ones of the past. This is a significant departure from the original objective which was the stress analysis in glass-reinforced epoxy. The generality was achieved by rederiving the three forms of Green's function using the technique of Fourier Transform [3.5]. Care was taken in identifying the part of Green's function that would or would not change with the relationship of the material constants. This was a prelude towards designing an efficient algorithm by exploiting the common features of the three forms of Green's function.

The next step in the development of the efficient algorithm is tied to the evaluation of the integral in the integral equation. The usual numerical approach is to approximate the unknown function in the integrand by a linear combination of known polynomials. This results in a linear expression in the unknown constants of the linear combination. The unknown constants are evaluated by satisfying the boundary condition at a finite number of points. The coefficients of the unknown constants are integrals containing the Green's function and the polynomials. These integrals are usually evaluated numerically. The advantage of numerical integration is that the order of polynomial and the shape of boundary can be of any complexity. However, in practice, only a cubic polynomial and a quadratic boundary shape have been used for isotropic material. For orthotropic material the unknown function has been assumed constant over straight line segments [3.1,3.2]. The disadvantage of numerical integration is that another source of error has been introduced into the process due to the approximation of the integrand for numerical integration. The singular nature of the Green's function further exacerbates this disadvantage, particularly when stresses need to be found near the boundary. The above mentioned disadvantages of numerical integration were overcome by evaluating the integrals analytically. The unknown function is assumed to vary piecewise linearly, while the boundary has been approximated by a sum of straight lines. Comparison for problems for which the solution is known show excellent correlation as seen in par. 3.5.

Another problem encountered and partially overcome is described next. By discretizing the problem as described in the previous paragraph, we reduce the integral equations to a set of linear algebraic equations. The accuracy of the solution is dependent upon the conditioning of the matrix in the algebraic equations. Conditioning of a matrix is a measure of the diagonal dominance in the matrix. The higher the condition number (lower the diagonal dominance) greater is the sensitivity of the solution to round off errors and errors or changes in the input data. An algorithm was used [3.6] that improves the conditioning of the matrix. But there

are problems which generate poorly conditioned matrix because of something intrinsic. Such poor conditioning cannot be cured by the algorithm. In this project the above described problem arose when an attempt was made to impose displacement boundary conditions in order to simulate a pin. The problem and steps needed to cure it, and what needs to be done further will be elaborated in par. 3.6.5.

3.2. Problem Formulation

Let σ_{ij} and ϵ_{ij} represent the Cartesian stresses and strains at a point. It is assumed throughout this paper that the Cartesian axes and the material axes are parallel. The strains and stresses in an orthotropic material are related as:

$$\begin{aligned} \epsilon_{xx} &= C_{11}\sigma_{xx} + C_{12}\sigma_{yy} \\ \epsilon_{yy} &= C_{12}\sigma_{xx} + C_{22}\sigma_{yy} \\ \epsilon_{xy} &= C_{33}\sigma_{xy} \end{aligned} \quad (1)$$

where the C's are the material constants. Let $R_k(P)$ represent a point load in the direction k applied at a point P . Let $H_{ijk}(Q,P)$ and $U_{ik}(Q,P)$ represent the Green's functions, i.e., solution of stresses and displacements caused by unit force at the point P in an infinite region. They are discussed in further detail in the next section. By distributing the unknown force on the boundary B , we obtain integral expressions given as follows:

$$\sigma_{ij}(Q) = \oint_B H_{ijk}(Q,P) R_k(P) ds \quad i,j,k = x,y \quad (2)$$

$$u_i(Q) = \oint_B U_{ik}(Q,P) R_k(P) ds \quad i,k = x,y \quad (3)$$

where $u_i(Q)$ represent the displacement in the i direction of Point Q . The unknown function (force) R_k is determined by satisfying boundary conditions. The traction boundary conditions are

$$\sigma_{ij}(Q) n_j(Q) = p_i(Q) \quad i,j = x,y \quad (4)$$

where $p_i(Q)$ are the applied tractions at the point Q on the boundary B . $n_j(Q)$ are the direction cosines of the unit normal at the point Q .

The displacement boundary conditions are

$$u_i(Q) = \bar{u}_i(Q) \quad i = x,y \quad (5)$$

where \bar{u}_i is the specified displacement.

The boundary conditions such as those on the pin hole can be written in normal and tangential direction as

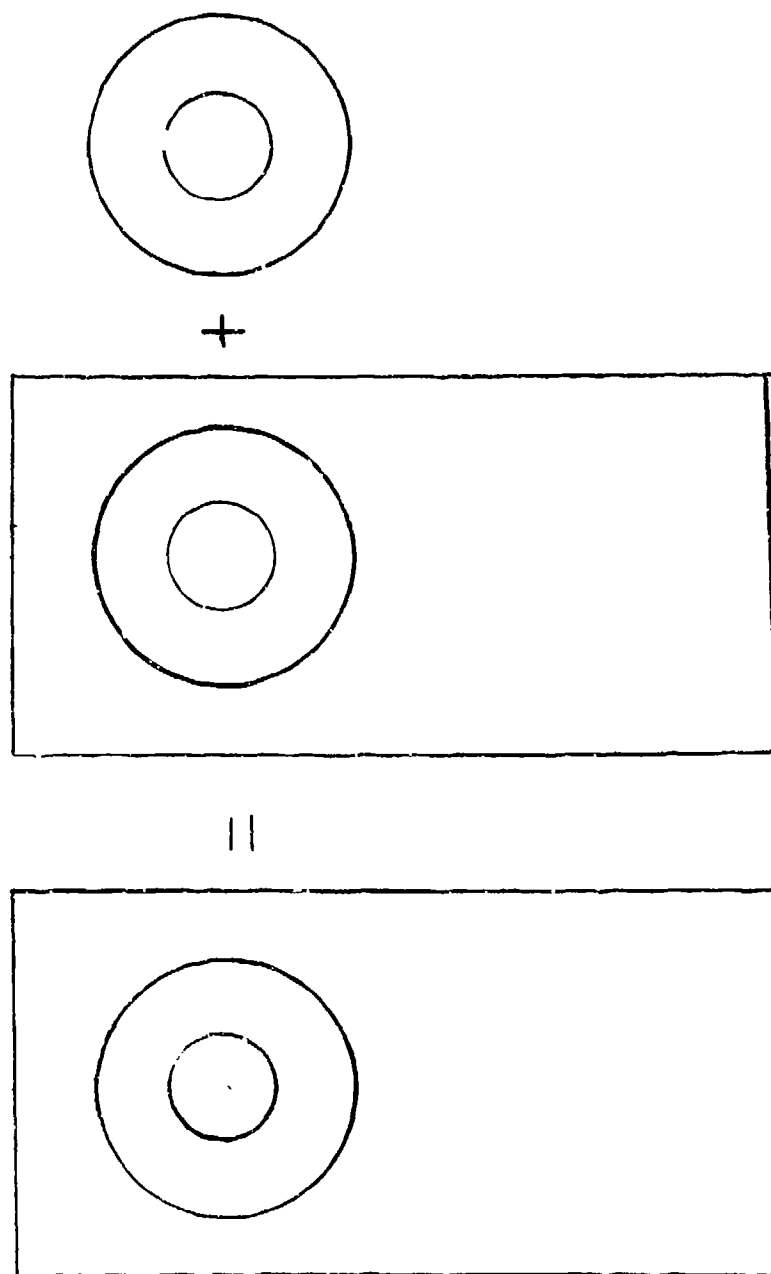


Figure 3-1. The insert problem.

$$u_i(Q) n_i(Q) = \bar{u}_n(Q) \quad i = x, y \quad (6)$$

$$(\epsilon_{ki} n_k(Q) - \mu_f n_i(Q)) \sigma_{ij}(Q) n_j(Q) = \sigma_t(Q) \quad i, j, k = x, y \quad (7)$$

where ϵ_{ki} and μ_f are the alternating tensor and the coefficient of friction respectively, u_n and $\bar{\sigma}_t$ are the imposed normal displacement and tangential stress, respectively. Usually both will be zero on the hole boundary.

To complete the formulation we next consider the variable stiffness insert problem. Figure 3-1 shows the geometry that needs to be analyzed for a variable stiffness insert. Region 1 represents the insert. Region 2 represents the composite material. The problem can be viewed as a sum of two problems, as shown in Figure 3-1. For each of these problems we write expressions for stresses and displacement analogous to equation (2) and (3) with the difference that for each region we need a different Green's function. The boundary conditions on B_3 are of the type given by equation 3. On boundary B_1 we have mixed boundary conditions. But at the interface boundary B_2 , the conditions are on continuity of displacement and tractions given below

$$(\sigma_{ij}(Q) n_j(Q))_1 = (\sigma_{ij}(Q) n_j(Q))_2 \quad (8)$$

Q on B_2

$$(\bar{u}_i(Q))_1 = (\bar{u}_i(Q))_2 \quad (9)$$

where the subscript 1 and 2 refer to region 1 and 2, respectively. Thus there are two fundamental differences. One is the nature of boundary conditions and the other is different Green's function for different regions. These fundamental differences required major reconstruction of the computer code. These features have been incorporated into the code, but the code has not been tested for these new features.

3.3. The Green's Function

To find the Green's function, a two-dimensional infinite orthotropic plane is considered. The equilibrium equation, the compatibility equation, and the boundary condition at infinity are solved using the technique of Fourier Transforms. The boundary conditions at infinity are that the stresses and their first derivative go to zero.

Three forms of Green's function were found and are given in detail in Appendix A. These three forms of Green's function correspond to the nature of the roots of the following equation.

$$C_{11} \mu^4 + 2(C_{12} + C_{33})\mu^2 + C_{22} = 0 \quad (10)$$

The difference in Equation (4) from previous work [3.1-3.3] is due to the use of tensor definition of strain in place of engineering definition of strain.

The four roots of Equation (4) may be symbolically written as:

$$\mu_1 = \bar{i}\lambda_1(\cos \delta_1 + \bar{i} \sin \delta_1) \quad (11a)$$

$$\mu_2 = -\bar{i}\lambda_1(\cos \delta_1 - \bar{i} \sin \delta_1) \quad (11b)$$

$$\mu_3 = \bar{i}\lambda_2(\cos \delta_2 + \bar{i} \sin \delta_2) \quad (11c)$$

$$\mu_4 = -\bar{i}\lambda_2(\cos \delta_2 - \bar{i} \sin \delta_2) \quad (11d)$$

where $\bar{i} = \sqrt{-1}$

CASE I: $\left(\frac{C_{12} + C_{33}}{C_{11}}\right)^2 > \left(\frac{C_{22}}{C_{11}}\right)$

For this case, $\delta_1 = \delta_2 = 0$ and

$$\lambda_{1;2} = \sqrt{\frac{C_{12} + C_{33}}{C_{11}}} \pm \sqrt{\left(\frac{C_{12} + C_{33}}{C_{11}}\right)^2 - \frac{C_{22}}{C_{11}}} \quad (12)$$

The roots have no real part and are purely imaginary.

CASE II: $\left(\frac{C_{12} + C_{33}}{C_{11}}\right)^2 = \left(\frac{C_{22}}{C_{11}}\right)$

For this case, $\delta_1 = \delta_2 = 0$, and

$$\lambda_1 = \lambda_2 = \sqrt{\frac{C_{12} + C_{33}}{C_{11}}} \quad (13)$$

At first glance it would appear that this case is a degenerate case of case I. This indeed is the case for terms T_1 , T_3 , and T_7 (see Equation A-9, A-10), (A-12), and (A-13)) of the Green's function in (A-1) and (A-2). However, for the terms T_2 , T_4 , T_6 , and T_8 , there is a significant difference. Isotropic material belongs to this case and they correspond to $\lambda_1 = \lambda_2 = 1$.

Problems with material properties belonging to this case can also be solved by scaling the original geometry. For example, by scaling the y-coordinate by the factor given in Equation (13), the problem can be reduced to an isotropic case. A strategy used in Reference [3.8] for solving an orthotropic plate problem by the boundary element method.

CASE III:
$$\left(\frac{C_{12} + C_{33}}{C_{11}}\right)^2 < \left(\frac{C_{22}}{C_{11}}\right)$$

For this case, $\lambda_1 = \lambda_2 = \lambda$, and $\delta_1 = \delta_2 = \delta$

where
$$\cos \delta = \sqrt{\frac{1}{2} \left(\sqrt{\frac{C_{22}}{C_{11}}} + \frac{C_{12} + C_{33}}{C_{11}} \right)}$$
 (14)

$$\sin \delta = \sqrt{\frac{1}{2} \left(\sqrt{\frac{C_{22}}{C_{11}}} - \frac{C_{12} + C_{33}}{C_{11}} \right)}$$

Thus the roots in Equation (5) have a real and an imaginary part. In the past [3.1], the Green's function for this case has been written in a very complicated form. From Equation (A-9), (A-10) and (A-16), (A-17), one sees that case I and III have very similar terms.

3.4. Problem Descretization

To solve the boundary value problem given by Equation (2) through (7) numerically, we need to reduce the integral expressions of Equation (2) and (3) to a linear algebraic expression. This is accomplished as follows:

ASSUMPTION 1:

Assume that the fictitious traction f_k is linearly piecewise continuous over M segments of the boundary.

$$f_k(p) = \frac{d_k^{(m+1)} - d_k^{(m)}}{S_{m+1} - S_m} (s - S_m) + d_k^{(m)} \quad (15)$$

$$S_m \leq s \leq S_{m+1}.$$

$$m = 1, 2, \dots, M.$$

$$k = x, y.$$

where S_m is the value of s at m th node and $d_k^{(m)}$ are the unknown constants to be determined.

ASSUMPTION 2:

Assume that the m^{th} boundary segment can be represented by straight line segments. This assumption does not introduce any more unknowns but permits a better approximation of the shape of the boundary. As shown in Reference [3.7], the result is higher accuracies. Rewriting Equation (15)

about the midpoint of each subdivision and substituting in Equation (2) and (3), we obtain :

$$\sigma_{ij}(Q) = \sum_{m=1}^M \sum_{n=1}^{N_m} \left[\frac{d_k^{(m+1)} - d_k^{(m)}}{S_{m+1} - S_m} (\bar{s}_n - S_m) + d_k^{(m)} \right] M_{ijk}(Q, S_n) \\ + \frac{d_k^{(m+1)} - d_k^{(m)}}{S_{m+1} - S_m} M_{ijk}^{(1)}(Q, S_n) \quad (16)$$

$$u_i(Q) = \sum_{m=1}^M \sum_{n=1}^{N_m} \left[\frac{d_k^{(m+1)} - d_k^{(m)}}{S_{m+1} - S_m} (\bar{s}_n - S_m) + d_k^{(m)} \right] N_{ik}(Q, S_n) \\ + \frac{d_k^{(m+1)} - d_k^{(m)}}{S_{m+1} - S_m} N_{ik}^{(1)}(Q, S_n) \quad (17)$$

where $\bar{s}_n = (S_n + S_{n+1})/2$ and

$$M_{ijk}^{(q)}(Q, S_n) = \int_{S_n}^{S_{n+1}} (s - \bar{s}_n)^q H_{ijk}(Q, P) ds \quad (18)$$

$$N_{ik}^{(q)}(Q, S_n) = \int_{S_n}^{S_{n+1}} (s - \bar{s}_n)^q U_{ik}(Q, P) ds \quad (19)$$

The integrals $M_{ijk}^{(q)}$ and $N_{ik}^{(q)}$ can be found by substituting the appropriate formulas given in Appendix A and B. For a closed boundary, continuity requires:

$$d_k^{(M+1)} = d_k^{(1)} \quad (20)$$

Thus there are M unknowns in each direction in Equation (16) and (17). To determine them we satisfy the boundary condition at M points in a collocation sense. The result is a set of linear algebraic equations that can be solved for the unknown constants $d_k^{(m)}$. Once they are known, the stresses are evaluated from Equation (16).

3.5. Numerical Results

The numerical results are presented in two parts. In the first part, those problems for which analytical results are known are considered. These problems represent the tests the computer code was subjected to. The second part of the section contain problem geometries on which actual experiments were conducted.

3.5.1. Test Problems: The geometries analyzed in the test problems are the generic units from which the coupons are constructed. Each problem was analyzed for four material cases given in Table 3-1. Case (2a) refers to a special orthotropic material for which we need only three material constants. Case (2b) refers to an isotropic material. All material constants are non dimensionalized by the constant C_{11} . All stresses are non dimensionalized by the maximum applied normal stress.

In all problems, the matrix condition number was calculated. The matrix condition number is defined as

$$\text{condition number} = ||A|| \quad ||A^{-1}|| \quad (21)$$

where $||A||$ and $||A^{-1}||$ are the norms of the matrix and its inverse respectively. The norm of the matrix is defined as

$$||A|| = \max_i \sum_{j=1} |A_{ij}|. \quad (22)$$

3.5.2. Square Geometry: The geometry analyzed is shown in Figure 3-2. The boundary conditions imposed correspond to a unit compressive stress in the x-direction and a unit tensile stress in the y-direction. The four boundary conditions imposed for each material case are as follows:

- a. Pure traction in x and y-direction.
- b. Displacement in the x- direction and traction in the y-direction.
- c. Traction in the x-direction and displacement in the y-direction.
- d. Pure displacement in x and y-direction.

In Table 3-2. the matrix condition number for each material case and each boundary condition is reported. In Table 3-3. the percentage error in σ_{yy} along the diagonal for each case is reported. The column headings are to be interpreted as follows: The numerics or letters before the hyphen refers to the material case of Table 3-1. The letter after the hyphen refers to the type of boundary condition described above. Thus, the heading 2A-a refers to material case 2A with pure traction boundary conditions.

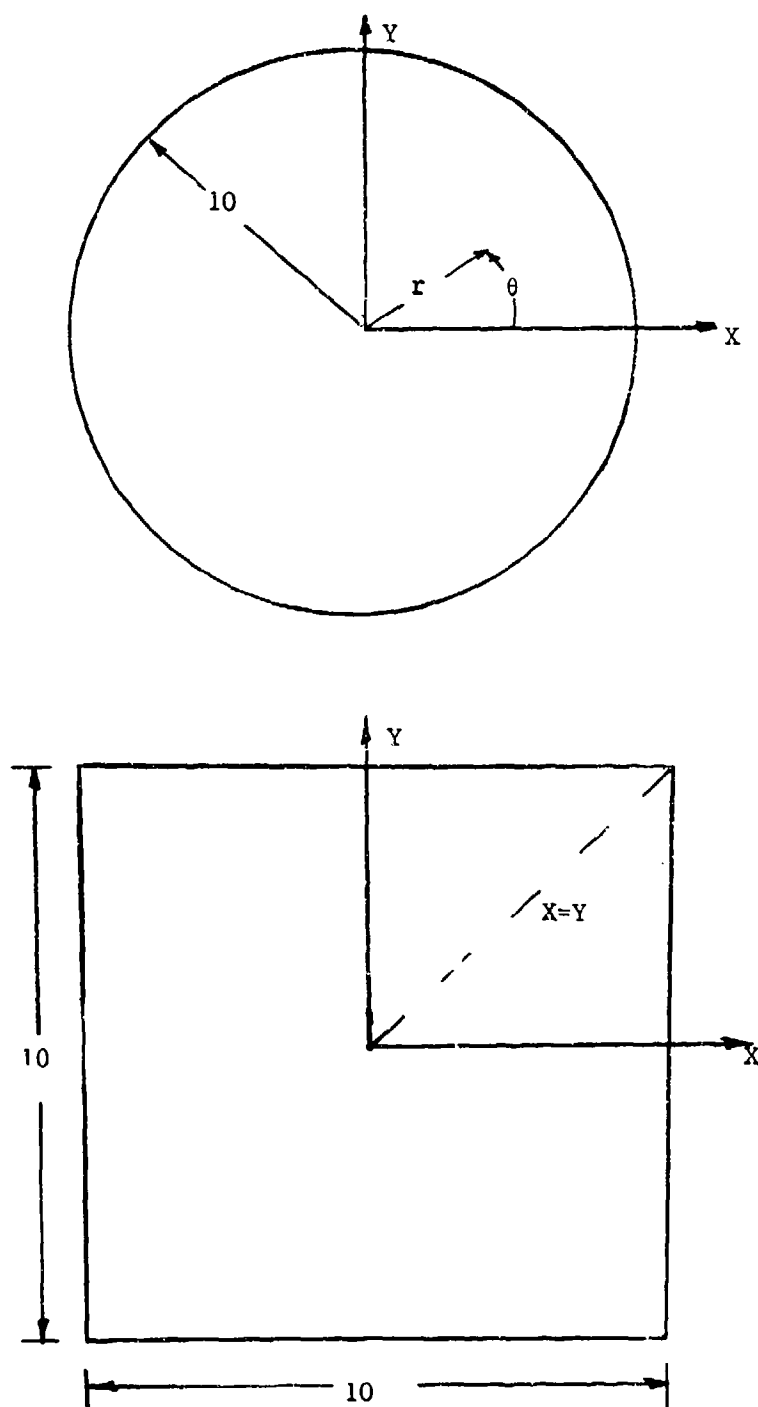


Figure 3-2. Geometry of test problems.

Table 3-1. Material Properties for Test Problems

Material	C ₁₁	C ₁₂	C ₂₂	C ₃₃
Case 1	1	-0.25	1	1.65
Case 2a	1	-0.25	1.96	1.65
Case 2b	1	-0.25	1	1.25
Case 3	1	-0.25	1.96	1.25

Table 3-2. Matrix Condition Number for Square Geometry

Material	Boundary Condition			
	a	b	c	d
1	78	312	312	303
2A	95	355	299	355
2B	77	279	275	279
3	95	823	616	823

Table 3-3. Percentage error in σ_{yy} for square geometry.

$x=y$	1-a	1-b	1-c	1-d	2A-a	2A-b	A-c	2A-d	B-a	2B-b	2B-c	2B-d	3-a	3-b	3-c	3-d
0	1.1	2.2	2.2	.22	.25	4.1	1.7	.01	1.2	3.0	2.8	0.0	.37	5.0	2.0	.09
1.0	.68	2.5	2.5	.39	.52	4.2	1.6	.01	.68	3.3	2.6	0.0	.64	4.9	1.7	.01
2.0	.51	3.4	3.4	.98	1.3	4.5	1.3	.01	.65	3.8	2.2	.02	1.4	4.9	.82	.39
3.0	2.6	5.0	5.7	2.4	2.9	5.5	.95	.04	3.0	5.1	1.8	.13	3.1	5.5	.58	1.7
4.0	9.5	9.7	11.	6.6	8.1	9.5	.68	.34	10.	9.5	.05	.10	8.4	8.7	4.2	5.8
4.5	23.	24.	13.	6.1	16.	20.	8.9	7.2	23.	24.	10.	9.1	16.	20.	13.	20.
4.7	24.	29.	22.	12.9	15.	24.	7.3	7.6	25.	31.	9.7	11.	15.	24.	12.	30.

The error is small in the center of the square but increases as we move towards the corner of the square. This is not surprising or a cause of concern. At the corner we have very sharp changes in both the geometry as well as the imposed loading. Furthermore, the mesh description used was not very fine near the corner intentionally. In our analysis of coupons the region of interest is near the pin hole boundary not the corner regions.

There is another trend of greater importance as it is an indication of a difficulty to be encountered in coupon analysis. The matrix condition number is higher when displacement boundary conditions are imposed. The matrix condition number is lowest for pure traction boundary conditions and highest for pure displacement boundary condition. The mixed boundary condition cases fall between those two extremes, but have the highest percentage error as seen in Table 3-3. Discussion of this trend will be deferred until Section 3.6.5.

3.5.3. Circular Geometry. The geometry analyzed is shown in Figure 3-2. The boundary conditions imposed correspond to a unit tensile stress in the x and y direction. The four boundary conditions imposed were on tractions and displacements in the normal and tangential direction of the boundary. The four cases are:

- e. Pure traction in normal and tangential direction.
- f. Normal displacement and tangential traction.
- g. Normal traction and tangential displacement.
- h. Pure displacement in normal and tangential directions.

Table 3-4. Matrix Condition Number For Circular Geometry

Material	Boundary Condition			
	e	f	g	h
1	10	114	565	1205
2A	11	153	816	850
2B	10	100	442	1211
3	12	146	1021	985

Tables 3-4. and 3-5. show the matrix condition number and percentage error in σ_{yy} along the line $\theta = 0^\circ$ for all cases except those in which tangential displacements are imposed. For material cases 2A and 2B, the error is small even when tangential displacements are imposed. But for material cases 1 and 3, the results are nonsensical. The possibility of a bug in the computer code always exists, but it is very unlikely. Each part of the code used in instances of nonsensical solutions are used in some form for the other 12 cases which produce very accurate results. It is more likely that there is something intrinsic to tangential displacement conditions that causes these large errors. It is worthwhile noting

Table 3-5. Percentage error in σ_{yy} for circular geometry.

r	1-e	1-f	1-g	1-h	2A-e	2A-f	2A-g	2A-h	2B-e	2B-f	2B-g	2B-h	3-e	3-f	3-g	3-h
0	.36	.03	21.	1.4	.39	.01	.37	.01	.38	.03	.37	.03	.41	.01	27.	.62
2	.36	.03	12.	15.	.39	.01	.36	.01	.38	.03	.37	.02	.41	.01	22.	2.8
4	.36	.03	8.0	35.	.39	.01	.34	.01	.38	.03	.37	.02	.41	.01	17.	7.5
6	.36	.03	1.2	51.	.39	.01	.31	.01	.38	.03	.37	.02	.41	.01	12.	13.
8	.36	.03	15.	69.	.39	.02	.26	.02	.38	.03	.36	.01	.41	.02	3.0	17.
9	.36	.05	28.	60.	.41	.04	.25	.04	.40	.06	.37	.02	.44	.06	2.6	15.
9.5	.37	.07	37.	49.9	.42	.06	.24	.05	.42	.08	.38	.04	.46	.08	5.4	13.
9.7	.39	.07	41.	42.	.42	.06	.24	.04	.42	.08	.38	.03	.46	.08	6.6	11.
9.9	.38	.07	46.	31.	.42	.05	.24	.04	.41	.08	.38	.02	.45	.08	7.8	9.0

that the matrix condition number is higher when displacement (particularly tangential) boundary conditions are imposed.

3.5.4. A Circular Hole in Infinite Plane Under Uniaxial Tension. The geometry for this case was simulated by defining $D = 1$, $E = 50$, $H = 50$, $W = 100$ in Figure 3-3. A uniform tension of $\sigma_\infty = 1$ was applied in the y -direction. The analytical solution to this problem is known [3.3] and is given below.

$$K = \frac{\sigma_\theta}{\sigma_\infty} = \sqrt{2 \frac{C_{33} + C_{12}}{C_{22}}} + 2 \sqrt{\frac{C_{11}}{C_{22}}} + 1 \quad \text{at } \theta = 0^\circ.$$

where σ_θ is the tangential stress on the hole boundary and K is the stress concentration factor. The problem was solved with 168 ($M = 84$ in Equation (10)), and each problem took less than 6 minutes of CPU time on the IBM 4081 computer. Results for the stress concentration factor are shown in Table 3-6 for the various material constants. As can be seen there is very good agreement between analytical and computed solution by the BEM.

Table 3.6. Stress Concentration Factor For a Hole in Infinite Medium

Case 1		Case 2a	
Analytical	Computed	Analytical	Computed
3.191	3.053	2.690	2.604
Case 2b		Case 3	
Analytical	Computed	Analytical	Computed
3.000	2.894	2.565	2.604

3.6. Coupon Geometries

The three coupon geometries shown in Figure 3-3. were analyzed. All length dimensions have been non dimensionalized by dividing by the diameter of the pin hole. To simulate the geometries of coupons on which experiments were conducted the following were the values of the various parameters in Figure 3-3:

$$E = 4 \quad H = 20 \quad W = 8 \quad d_x = 2.5 \quad d_y = 2.5.$$

Each geometry was analyzed for three material cases given in Table 3-7. The values of the material constants C_{11} , C_{12} , and C_{22} are those for the glass-reinforced epoxy actually used in the experiment. As the constant C_{33} was not known, all three material cases were considered for each geometry. It was assumed that the fiber and the loading are in the y -direction. Two tests were devised to check the validity of the solution.

Table 3-7. Material Properties for Coupon Problems

Material	C ₁₁	C ₁₂	C ₂₂	C ₃₃
Case 1	1	-0.11	0.9669	1.0
Case 2	1	-0.11	0.9669	1.0933
Case 3	1	-0.11	0.9669	0.5

3.6.1. Test 1. This test was designed by starting with a desired solution and working backward to get the appropriate boundary conditions. The desired solution sought for all geometries is $\sigma_{xx} = \sigma_{yy} = \sigma_{xy} = 1$. The corresponding tractions and displacements are:

$$P_x = P_y = n_x + n_y \quad (21)$$

$$\text{and} \quad u_x = (C_{11} + C_{12})x + C_{33}y/2 \quad (22a)$$

$$u_y = (C_{12} + C_{22})y + C_{33}x/2 \quad (22b)$$

If the boundary conditions are in normal and tangential directions, the equations (21) and (22) are transformed to yield the appropriate conditions. Depending upon the nature of the boundary conditions in the actual problem, appropriate boundary conditions were chosen for this test. The numerical solution was compared with the unit value of stresses and the percentage error printed.

3.6.2. Test 2. If we integrate the normal stress σ_{yy} across the width of the coupon, then we would obtain the force acting in the y-direction on the line of integration. This should be in static equilibrium with the applied load. Trapezoidal rule was used in calculating the integral of σ_{yy} .

Stress concentrations factors were found at the points marked in Figure 3-3.

$$K = \frac{\sigma_{yy}}{\sigma_{\infty}} \quad (23)$$

3.6.3. No Load on Pin Hole Boundary. A uniform tensile load $\sigma_{\infty} = 1$ was applied at $y = +H$ and $y = -E$ in Figure 3-3. The pin hole boundaries were traction free. This is the classical mechanics problem. Table 3-8. shows the stress concentration factors for various geometries and material properties. Note that for both the two hole problems the stress concentration factors at A and B are nearly the same. For the tandem hole problem this is to be expected from the symmetry of the problem. For the two parallel holes, this is suprising. The implication of the result is that there is no interaction between the holes. The conclusion is at odds with the observations in the experiment. Discussion of this difference is deferred until the end of the next section.

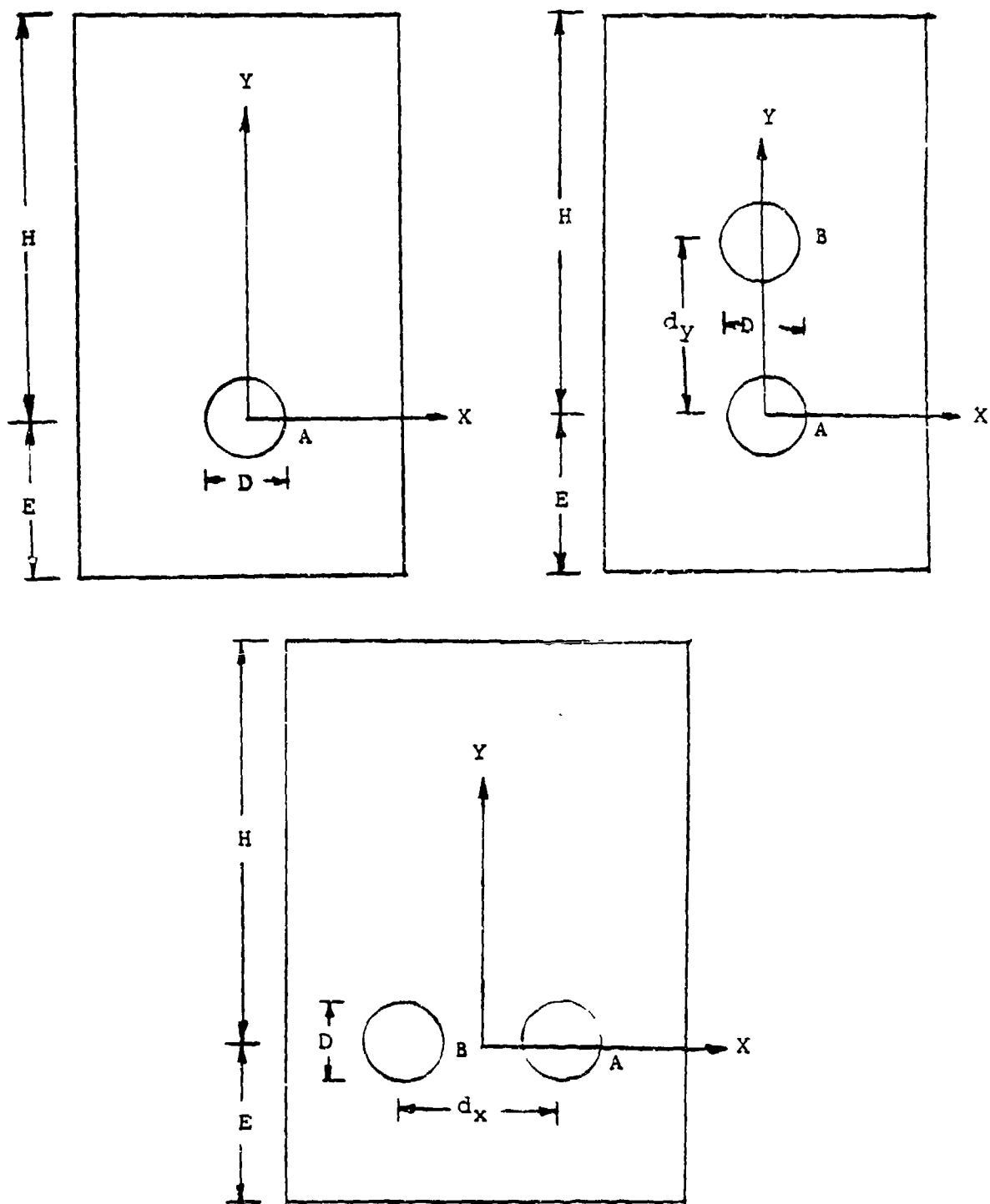


Figure 3-3. Geometry of coupons.

Note that in all geometries the material case 1 had the highest stress concentration factor while case 3 had the lowest. Hence, we conclude that as the compliance constant C_{33} increases (that is, the shear modulus decreases) the stress concentration factor increases.

The variation of σ_{yy} at various sections is shown in Figures 3-4., 3-5., and 3-6. It should be remembered that the stresses and the length variables are nondimensionalized as described in par. 3.6. Nothing unusual is seen in the various graphs. The two tests described earlier showed no abnormalities for any geometry or material.

Table 3.8. Stress Concentration Factors for Coupons

Material	Single Hole		Two Parallel Holes				Two-Tandem Holes					
	No Load		Load		No Load		Load		No Load		Load	
	K _A	K _A	K _A	K _B	K _A	K _B	K _A	K _B	K _A	K _B		
1	3.2	8.8	3.3	3.2	5.4	5.5	2.9	2.9	3.0	6.2		
2	3.0	8.1	3.1	3.1	5.0	5.1	2.8	2.8	2.9	5.7		
3	2.7	6.8	2.8	.27	4.3	4.4	2.6	2.5	2.6	4.8		

3.6.4. Load on Pin Hole Boundary. A uniform tensile load of $\sigma_{\infty} = 1$ was applied at $y = H$. For static equilibrium, a cosine distribution was applied on the lower edge of the boundary. The cosine distribution simulates the pin [9]. For the two parallel holes, each pin would support half the total force applied. However, for the tandem hole problems, it can be expected that the upper pin will carry more load than the lower pin. Nevertheless, for demonstration purposes, it was assumed that both pins carried equal loads.

From Table 3-8. it can be seen that the observations made in the previous section are valid here too. The expected difference is that the upper hole in the tandem hole geometry yields higher stress concentration factors than the lower hole. The variation the σ_{yy} across various sections is given in Figures 3-7., 3-8., and 3-9. No unusual behavior was found in the graphs or the tests of pars. 3.6.2 and 3.6.3.

The stress concentration factors for the parallel hole are nearly the same. As was remarked earlier, the conclusion that there is no interaction between the holes is at odds with experimental observations. There are two factors that could account for the difference. The value of C_{33} will influence the length over which the interaction will take place. But a more important factor is the assumption of cosine distribution for the normal traction. This distribution may be enforcing symmetry that does not exist. A more likely situation is: the lower part of the hole boundary which is closer to the other hole supports more load than the far side. The degree of interaction will be dictated by the lopsidedness of the normal traction behavior on the lower hole boundary.

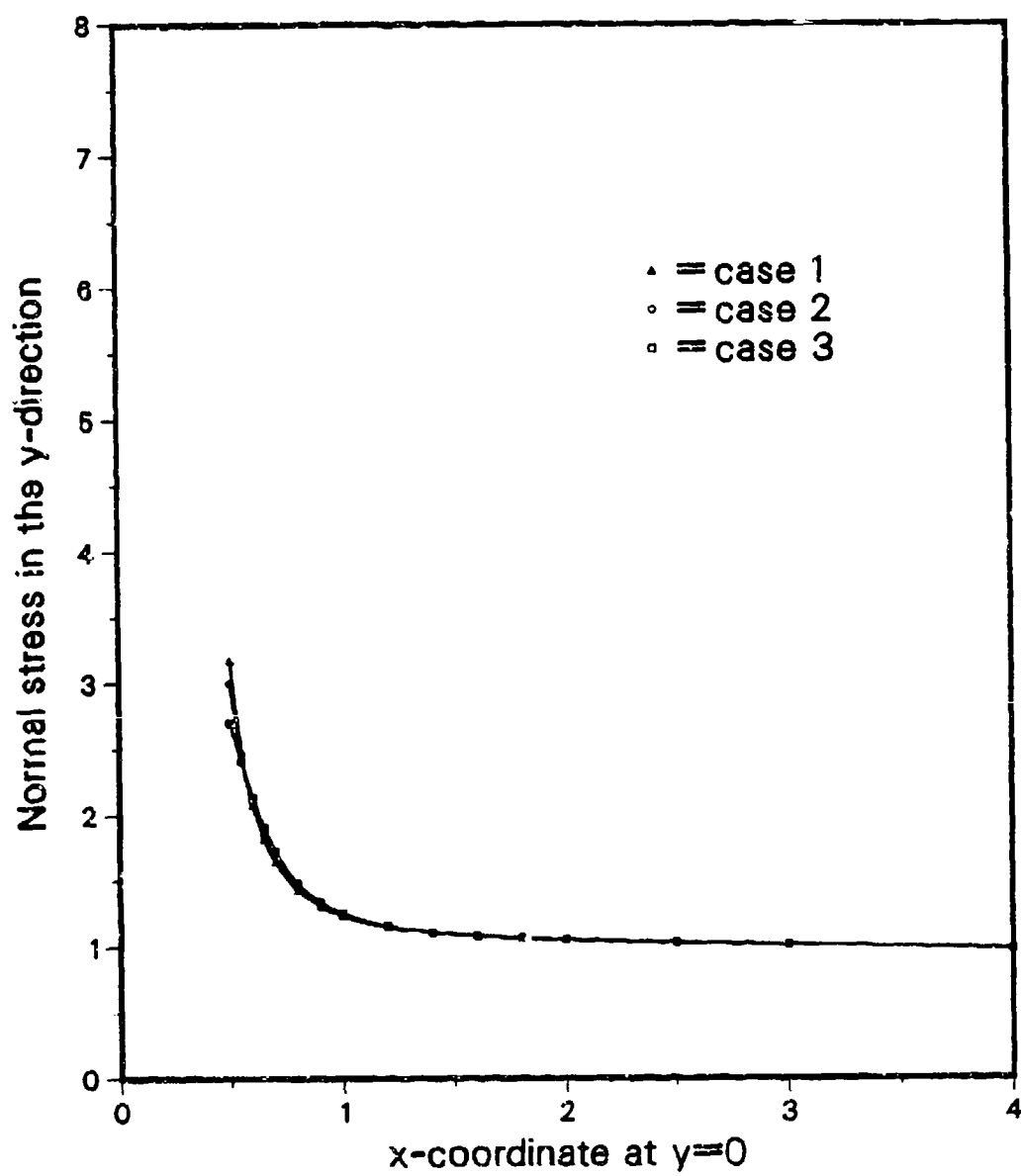


Figure 3-4. Results for single hole with no pin load.

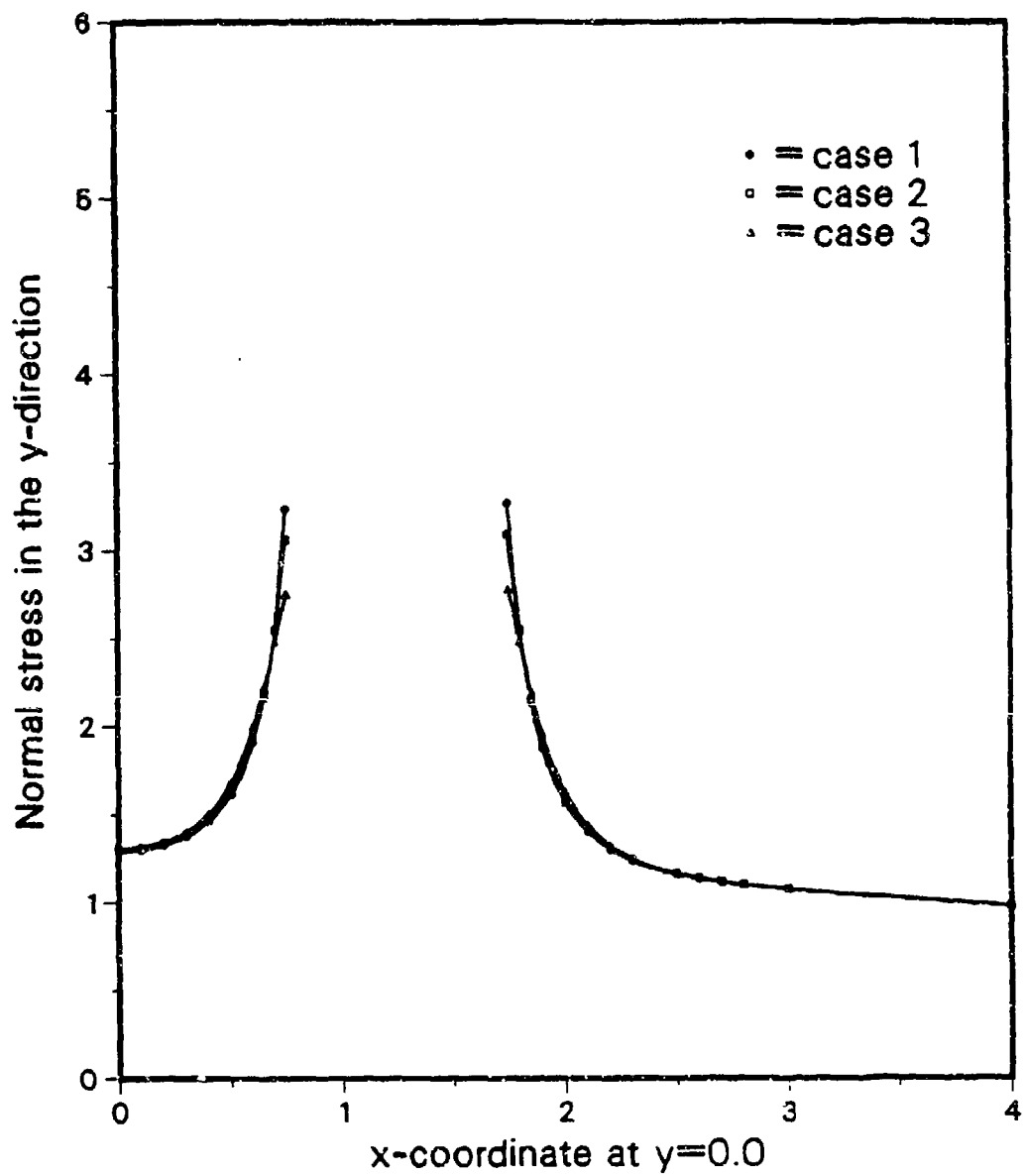


Figure 3-5a. Results for parallel holes with no pin load.

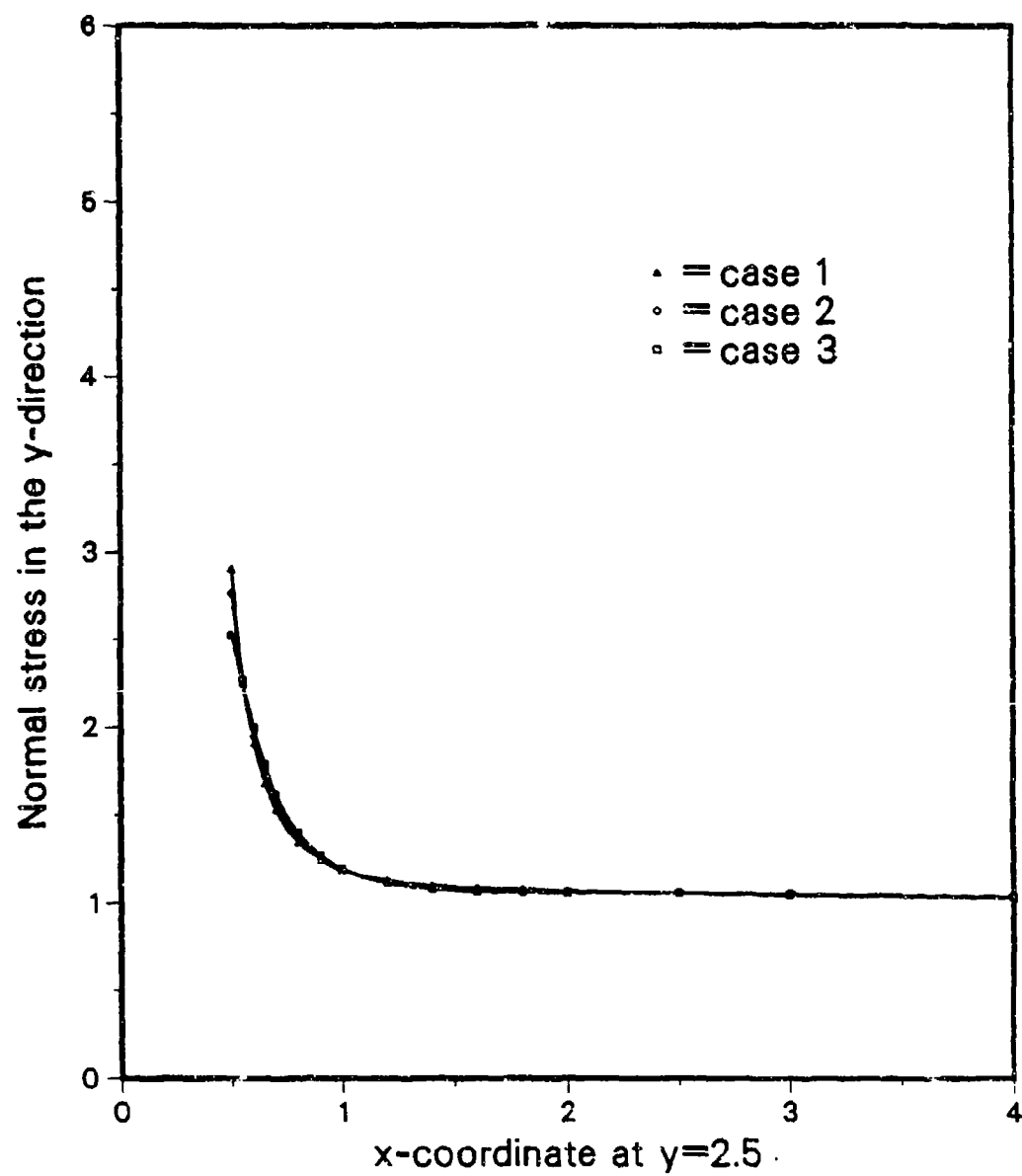


Figure 3-5b. Results for parallel holes with no pin load.

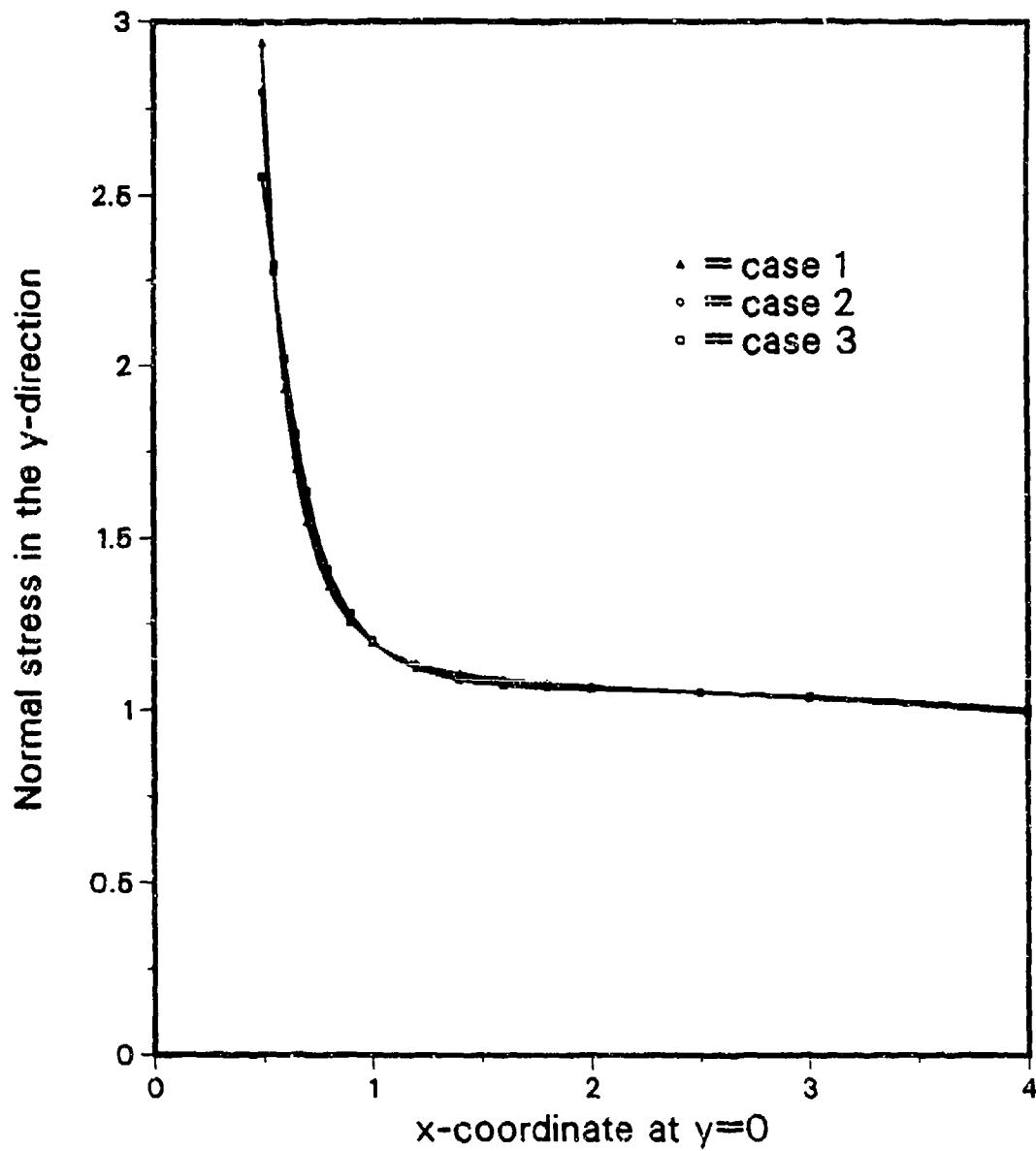


Figure 3-6. Results for tandem holes with no pin loads.

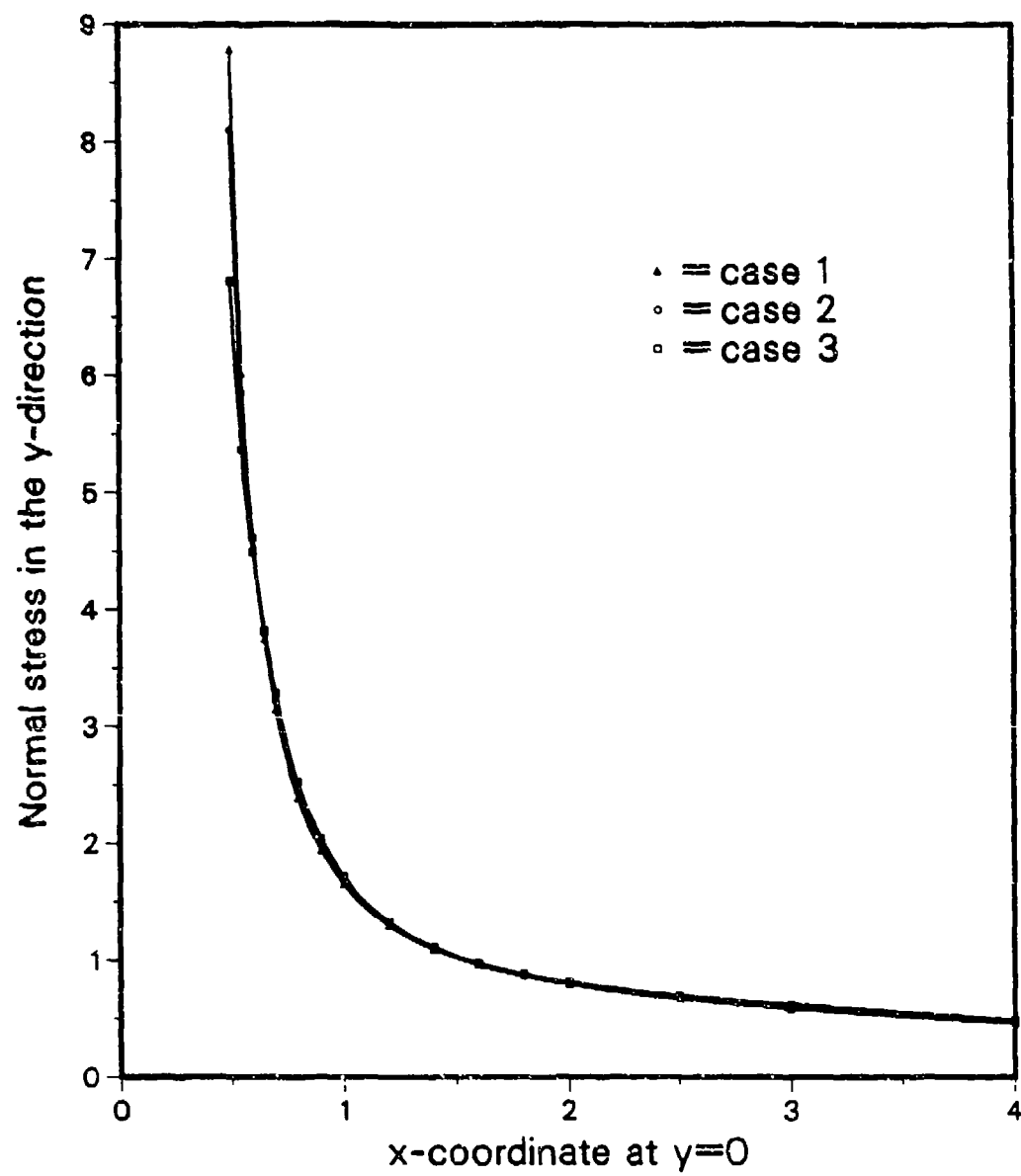


Figure 3-7. Results for single hole with pin load.

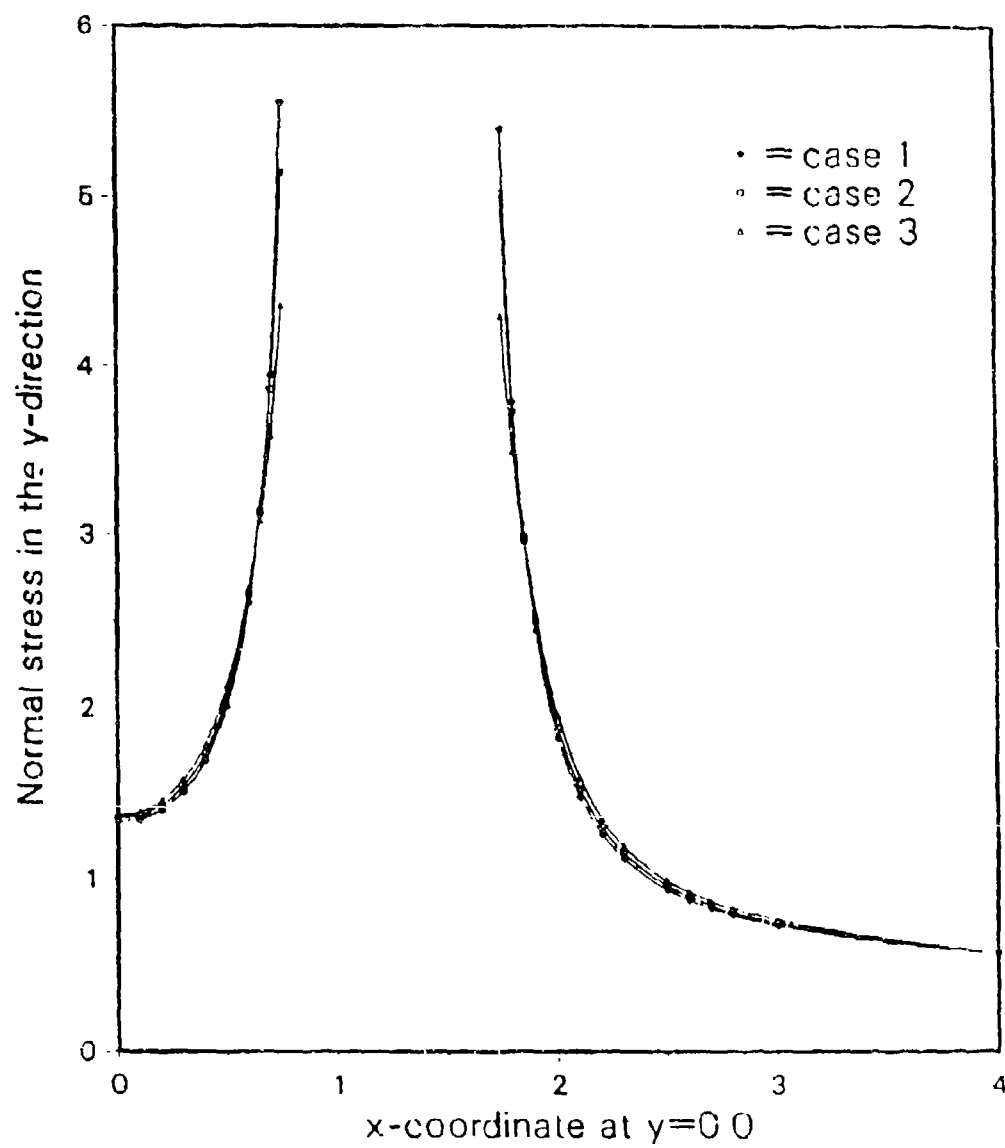


Figure 3-8a. Results for parallel holes with pin loads.

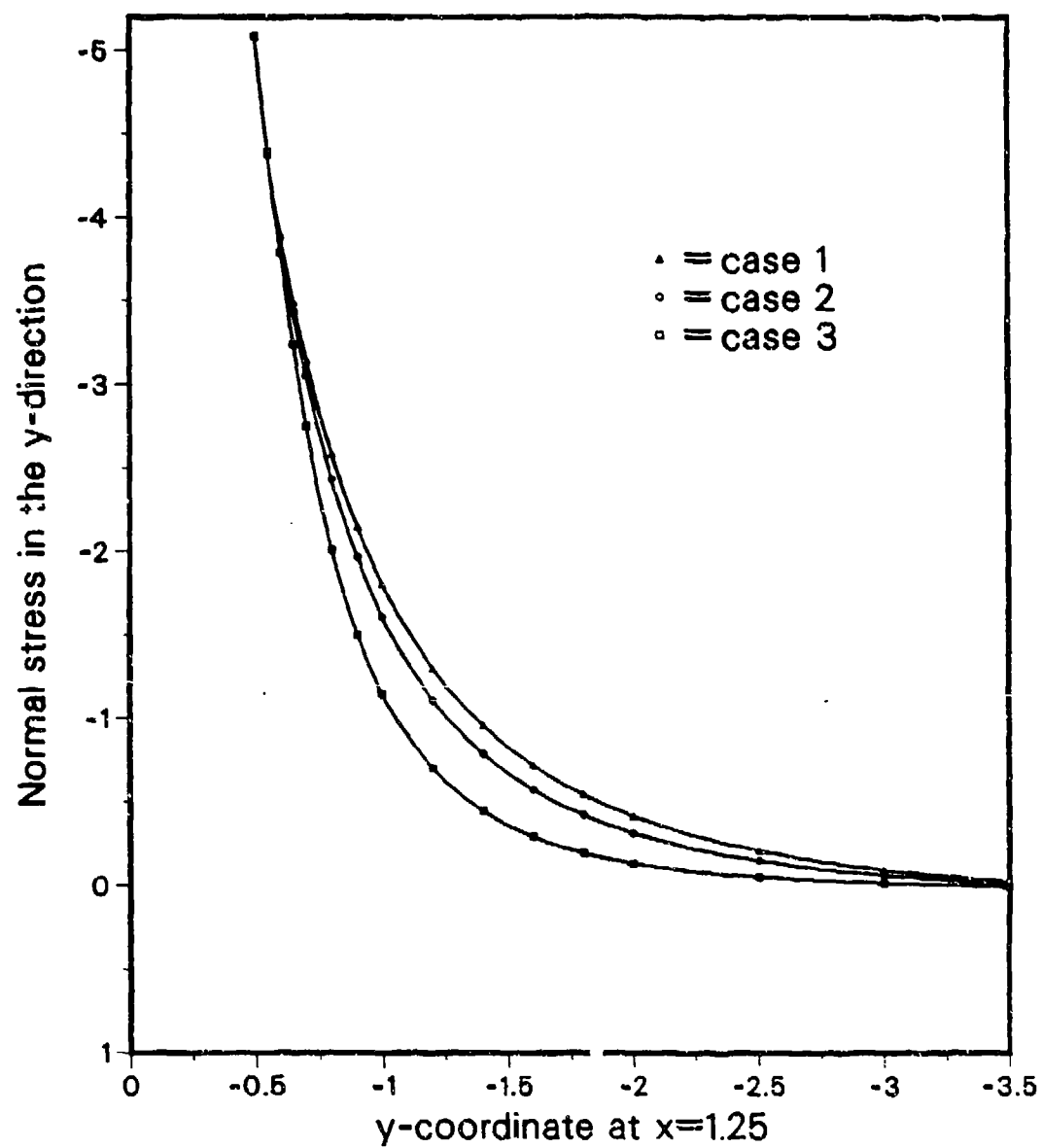


Figure 3-8b. Results for parallel holes with pin load.

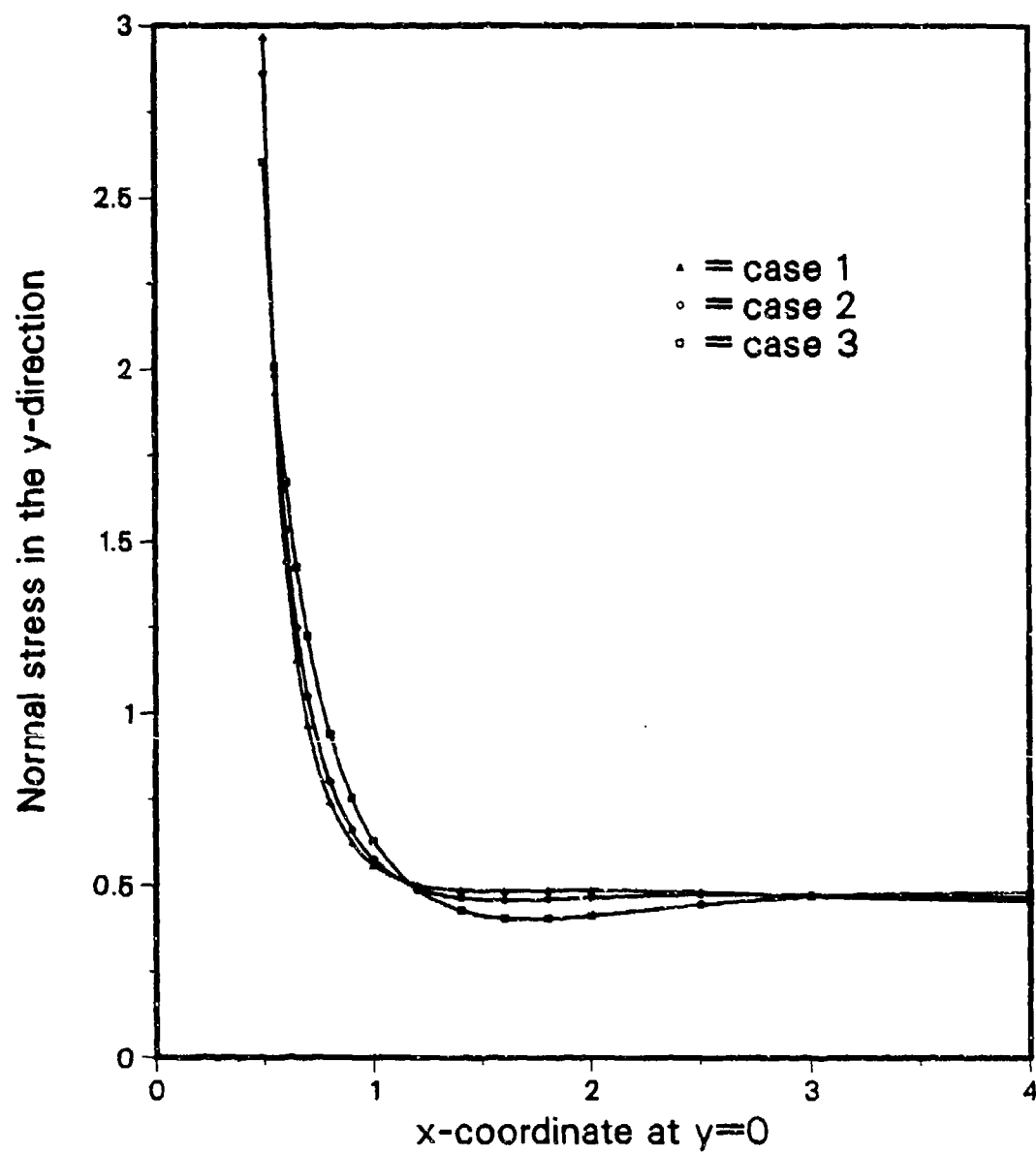


Figure 3-9a. Results for tandem holes with pin loads.

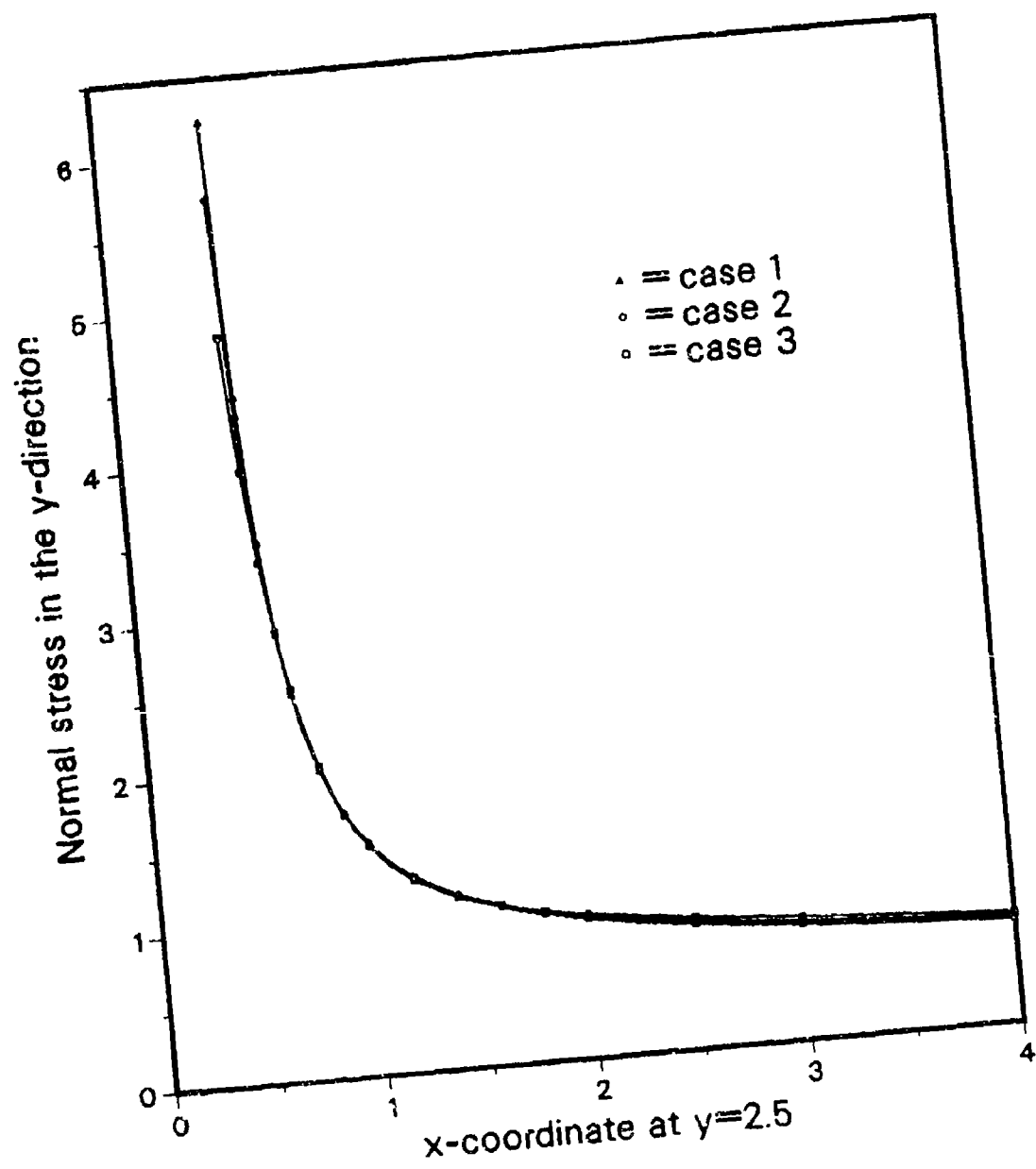


Figure 3-9b. Results for tandem holes with pin loads.

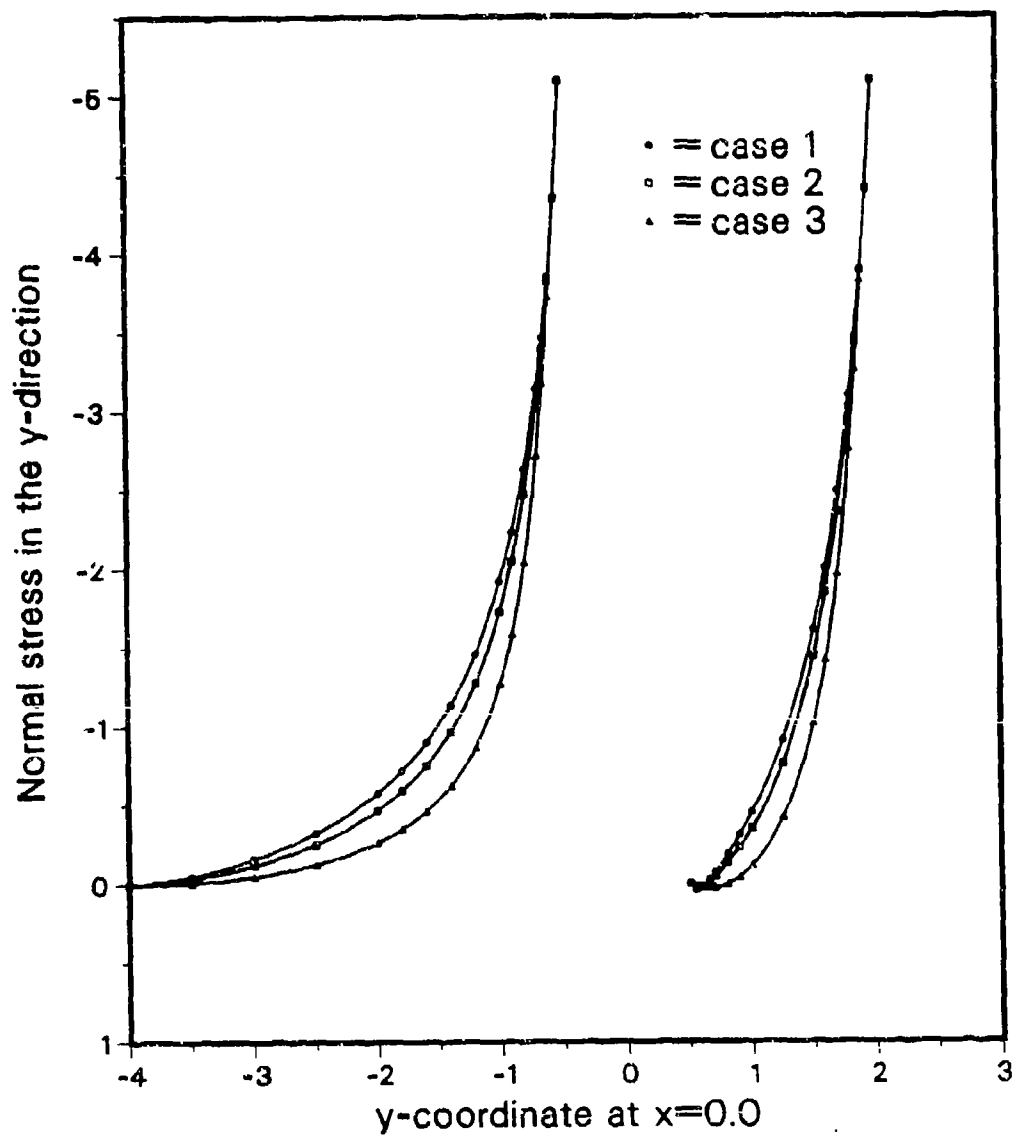


Figure 3-9c. Results for tandem holes with pin loads.

3.6.5. Displacement Boundary Conditions. Each coupon problem is a statically indeterminate problem. If one were to assume an exact fit between the pin and the hole boundary, then the correct boundary conditions will be: the normal displacement u_n and the tangential stress τ_t in Equations (6) and (7) should be zero. The problem of single hole geometry was solved using these boundary conditions but assuming no friction. The results obtained were nonsensical, and the solution failed the test described in par. 3.6.1. The matrix condition number increased from 359 to 8,592. In test problems it was also seen that whenever displacement boundary conditions are imposed the matrix condition number increases dramatically. The result of this increase can at times increase the roundoff error to a point that it overwhelms the actual solution. The problem arises from the fact that the Green's function used in the formulation results in weak singular integral equations. There are several possible cures to this problem.

- . Use a higher order singularity in the formulation. The implementation of this idea would require rederiving the Green's function and its integral over boundary segments (see Equations (18) and (19)).
- . Since u_n is zero everywhere on the lower boundary of the hole, therefore $du_n/ds = 0$. This would generate the higher order Green's function we need and would require far less modification than suggestion 1. Implementing this suggestion will be the first task of the next phase. However, it must be remarked that this is a short term solution as it cannot be used for solving problems with interference or loose fits.
- . Apply Galerkin's idea to the integral equations. This suggestion has the added advantage of reducing the collocation error. That is, error introduced due to the fact that we satisfy boundary conditions at finite number of points. The difficulty is that in BEM, the Galerkin technique has seldom been used even for isotropic problems. Dr. Vable has done some work on this issue, and if the ideas succeed in isotropic problems, then they will be adapted to the project.

3.7. Conclusions

A computer code given in Appendix C has been developed which can analyze stresses in multiply connected composite material problems. It produces very good results for pure traction boundary conditions. For mixed boundary conditions more work needs to be done. The analysis of the variable insert concept has been coded, but the additional features have not been tested.

4.0. EXPERIMENTAL PROCEDURES AND APPARATUS

4.1. Choice of Experimental Technique.

To predict the strength of the mechanical joint, determination of the deformation fields, which are probably nonlinear, is required. A full-field analysis seems to be the most suitable approach. Transmission photoelasticity has been successfully utilized in studying isotropic-material mechanical joints [4.1-4.5] but it cannot be used to study opaque composite materials. Photoelastic coatings have been applied to measurements in composites [4.6-4.7], but they present problems on the free edges, producing distortions in the displacement field, especially in the boundary. The extension of transmission photoelasticity techniques to birefringent composites offers another method to determine stresses in composite joints. This novel technique is called photo-orthotropic elasticity [4.8]. The major problem with this technique is to find a suitable combination of birefringent materials which will best serve to model the actual composite to be tested. Holography and Speckle interferometry have also been applied to perform measurements of strain in composites, but they lack the desired strain sensitivity [4.9-4.10]. The Moire method yields full-field information of the in-plane surface displacements, and it appears to be the most suitable optical technique for this study [4.11-4.15, 4.16]. It has a great potential for the macroscopic strain analysis of composites, and it does not suffer any limitations from anisotropy, inhomogeneity, or inelasticity of the composite material.

4.2. Moire Interferometry

The basis of any moire method is the grating which is attached to the specimen surface, allowed to deform with the specimen, and compared with its undeformed state.

In-plane moire interferometry fringes depict in-plane displacements of every point on the surface as maps of equal displacement [4.17]. This idea can be expressed quantitatively as,

$$U_x = dN_x = \frac{1}{F} N_x$$

$$U_y = dN_y = \frac{1}{F} N_y$$

where: U_x , U_y are components of displacement in the x and y directions respectively; N_x and N_y are the fringe orders when lines of the reference or analyzer grating are perpendicular to the x and y directions respectively; d is the pitch or distance between lines of the reference grating; and F is the frequency of the reference grating.

In the interferometric technique, the specimen carries a phase-type grating possessing a symmetrical corrugated surface which alters the phase of the incident light in a regular, repetitive way. When the specimen is deformed, the grating on its surface deforms with it. The specimen grating will change in frequency and direction systematically from point to point. Consequently, plane wavefronts illuminating the specimen grating will be diffracted; but, because of the localized changes in frequency and direction of the grating lines, the emergent wavefronts will be slightly warped. The resulting interference fringe pattern of these warped wavefronts is a contour map of the angular separation λN_x or λN_y , of the two diffracted orders, since bright fringes of constructive interference separate dark zones of destructive interference whenever N_x or N_y is an integer.

4.3. Construction of the Moire Interferometer

The main objectives pursued in the construction of the Moire interferometer were: (1) to avoid a rigid connection between the optical elements and the specimen being tested, (2) to be able to perform measurements in three different directions, (3) to obtain a good efficiency of light utilization, and (4) to develop an experimental set up suitable to be adapted to perform measurements in environments not so ideal as an optics laboratory.

Figure 4-1 shows a photograph of the overall view of the experimental apparatus. Figure 4-2 shows a two-dimensional schematic of the basic idea of the experimental apparatus as follows: a 20-mW Helium-Neon laser 1 produced a beam of coherent light having a wavelength of 632.8 nm

(24.913×10^{-6} in.). Using two front-surface mirrors 2 and 3, the beam was directed to the spatial filter where it was filtered and expanded with a 40x microscope objective and a pinhole 4. A collimating lens 5 (a 13 in.-diameter plano-convex lens, focal length= 1.0 m) changed the expanding beam into a parallel beam. This collimated beam reached two first-surface-flat mirrors 6 and 7 oriented at 45° with respect to the optical axis of the lens. Each of these two mirrors directed portions of the parallel rays to another two mirrors 8 and 9 which could be oriented easily to direct the light towards the specimen grating 10, and to obtain the desired angle of interference between the two beams. These two beams incident onto the specimen grating were diffracted. The diffracted rays passed through a converging lens 11 (focal length= 75 cm.), and were directed by a front surface mirror, oriented at 45° with respect to the normal of the grating, to the observing system or photographic camera. The beam narrowed and passed through an aperture before reaching the camera.

Figure 4-3 shows the arrangement, viewed along the z-axis, of the elements forming the interferometer. In order to describe the orientation of the flat mirrors, consider a set of axes with the positive z-axis going into the page, and the x and y axis located on the plane of the paper as a reference system.

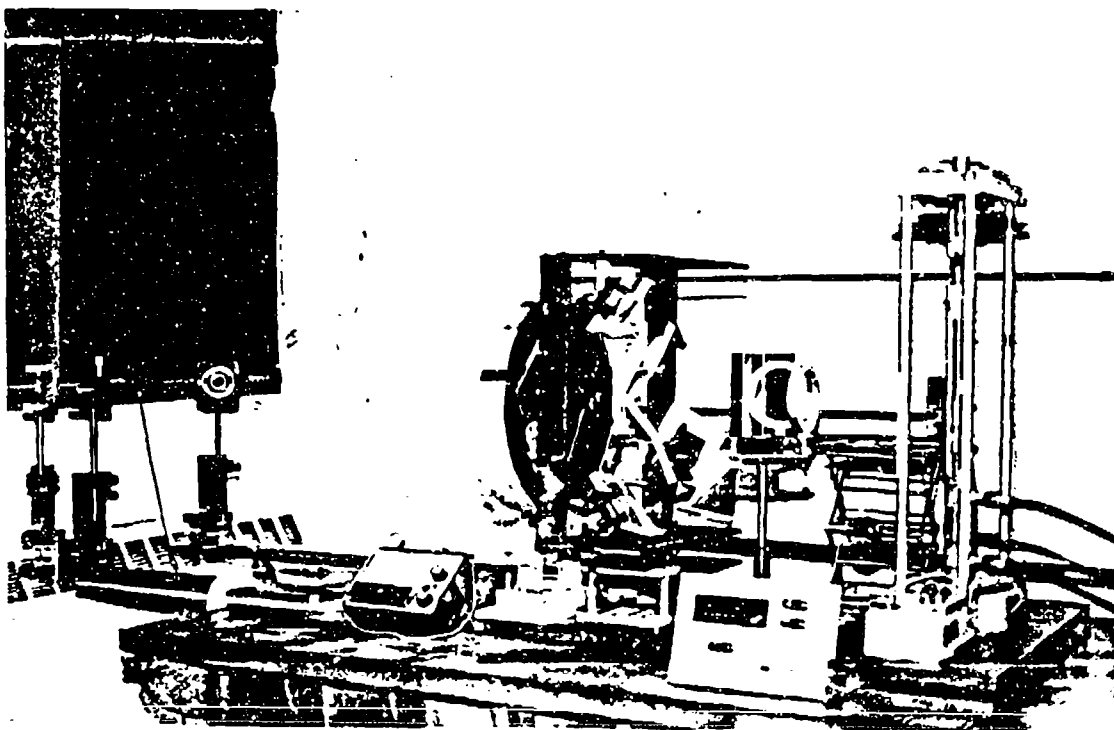


Figure 4-1. Overall View of the Experimental Setup Incorporating the Moire Interferometer

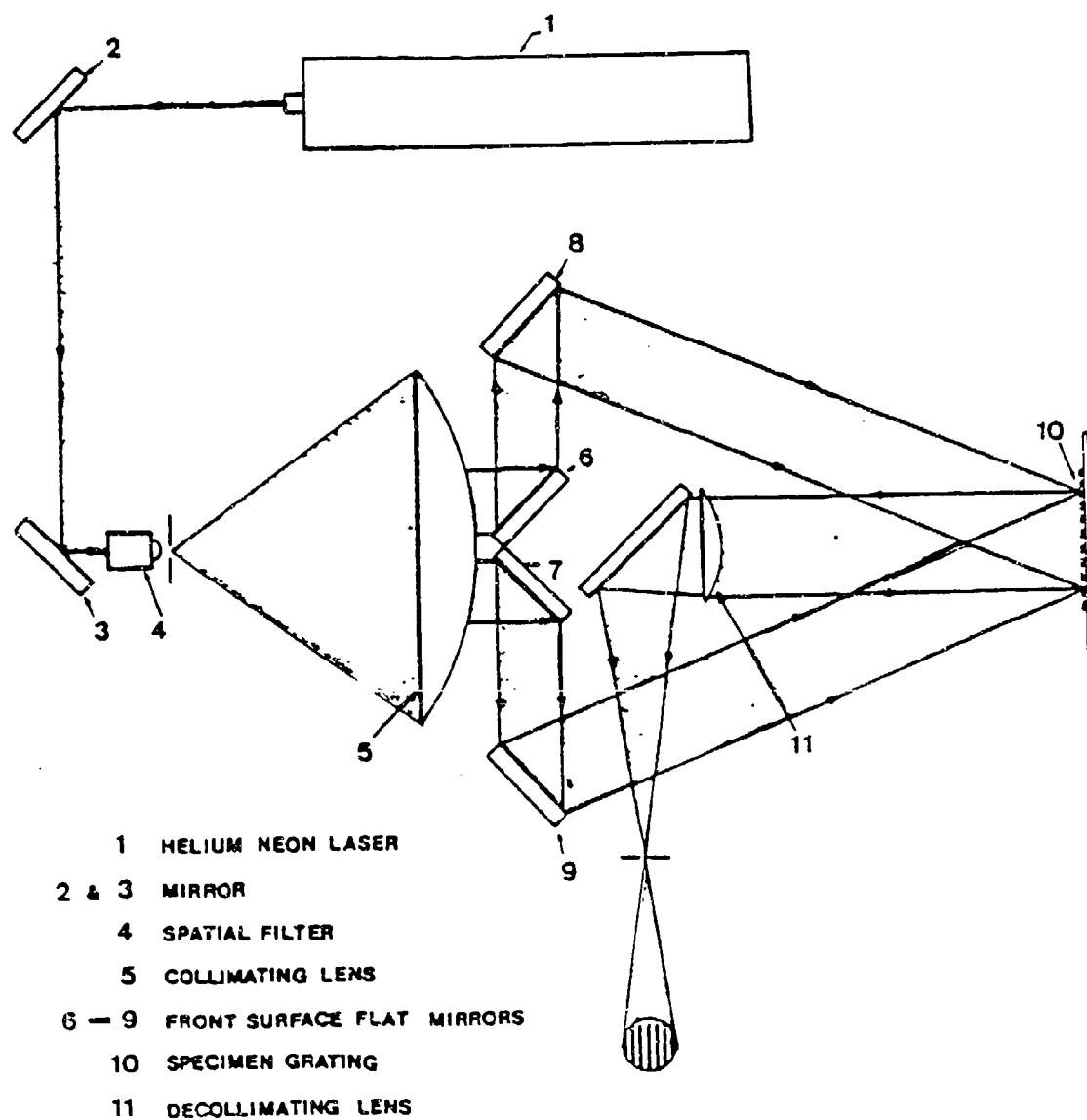
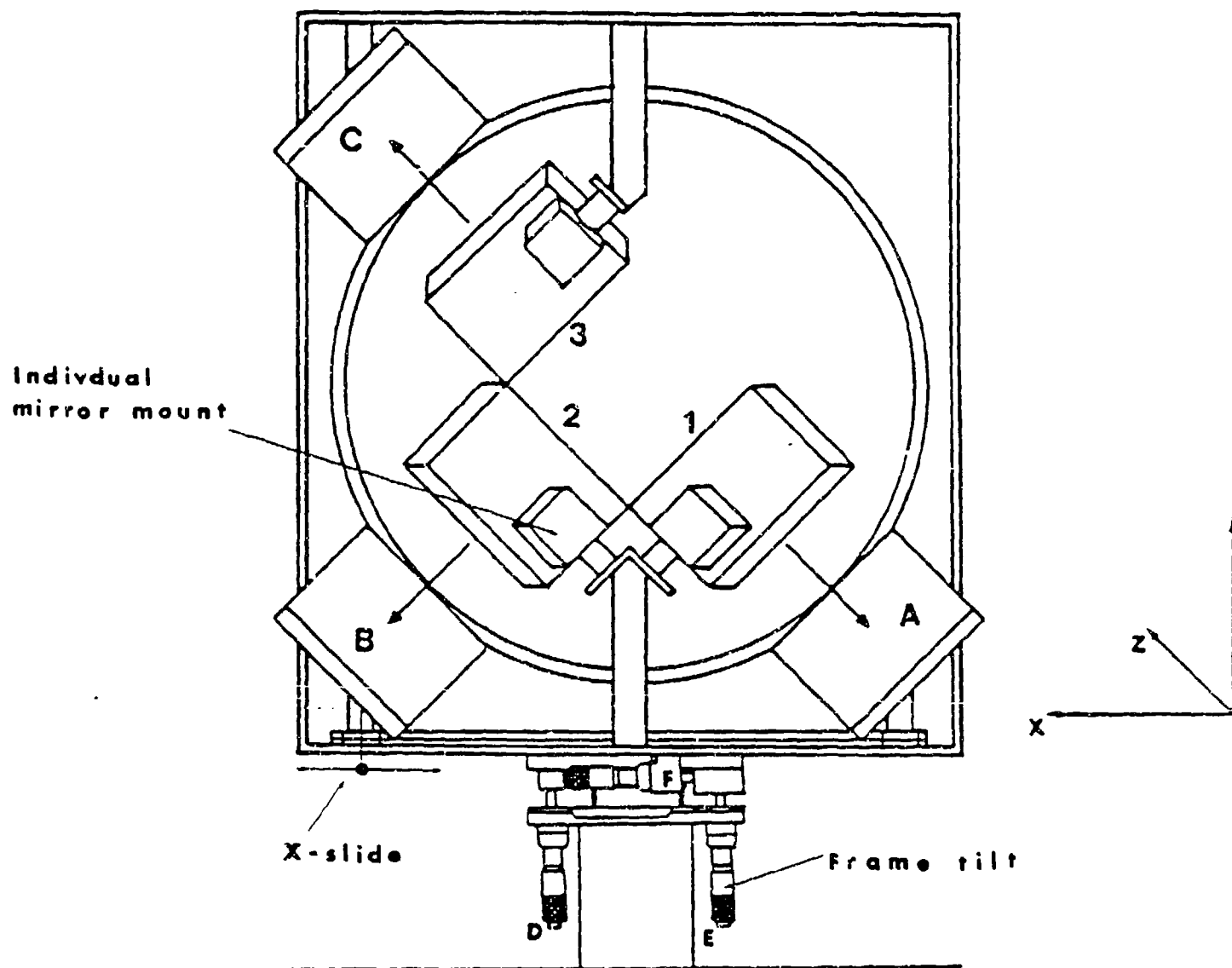


Figure 4-2. Schematic of the Basic Idea used in the Construction of the Moire Interferometer



(A), (B), (C) and 1,2,3 Correspond to Mirrors Located in the Interferometer

Figure 4-3. Arrangement of the Optical Elements of the Moire Interferometer

The three flat mirrors upon which the plane wavefront from the collimator is incident are denoted by the numbers 1, 2 and 3. The other three mirrors used to direct the beams of light towards the specimen grating are denoted by the letters A, B, and C.

To direct a portion of the light to mirror A, mirror 1 is rotated 45° from the xy-plane in the clockwise direction as viewed from the positive y-axis and also rotated 45° counterclockwise from the xy-plane as viewed from the positive z-axis. In order to direct light to mirror B, mirror 2 is rotated 45° from the xy-plane counterclockwise as viewed from the positive y-axis and 45° from the xy-plane in the clockwise direction as viewed from the positive z-axis. Similarly, mirror 3 is rotated 45° counterclockwise from the xy-plane as viewed from the positive y axis and 45° from the xy-plane counterclockwise as viewed from the positive z-axis to direct a portion of the light to mirror C.

Mirrors A, B, and C are located at three corners of a square. The distance between their centers can be adjusted easily. For this research, it was set at 11 inches. These three mirrors provide the three beams of light which converge on the surface of the specimen forming three sides of a square-based pyramid. The angle of interference between them can be adjusted by changing the distance between the interferometer and the specimen grating according to the equation in Appendix D which relates the angle of incidence and the desired interference frequency.

All the mechanical components used to position and mount the mirrors were purchased from the Newport Corporation, 18235 Mt. Baldy Circle, Fountain Valley, CA 92708. The mirrors were purchased from Melles Griot, Optical Components, 1770 Kettering Street, Irving, California 92714. They are front-surface mirrors. Their flatness is one quarter of a wavelength, and their dimensions are 100 by 100 mm. All the mirrors were glued onto Newport type MM-2 mirror mounts. The glue used was Pliobond Adhesive, manufactured by the Goodyear Tire & Rubber Company, Akron, Ohio, 44301. The tilting element of the mirror mounts provided a kinematic orthogonal adjustment using balls that are spring-loaded between a conical recess and a flat. Orientation is easy to adjust with low friction, fine pitch (80 threads per in.), lapped stainless steel drive screws, which push the alignment mechanism via hardened steel balls. The angular range is $\pm 4.45^\circ$ about each of the orthogonal axes. The root-mean-square sensitivity is $2/3.5$ arc-seconds. Mirror mounts 1, 2 and 3 are fixed permanently to the supporting aluminum frame of the interferometer. Mirrors A, B, C are connected to the aluminum frame by support posts which are held by post holders (Newport type VPH). The posts are held together using universal clamps (Newport model CA-2). These universal clamps allow free positioning and orientation of mirrors A, B, and C. The post holders of mirrors A and B are mounted on optical carriers (Newport type MTF) which allow horizontal adjustment up to 0.25 inch by an 80-pitch screw. These

carriers are mounted on an optical rail (Newport model MRL-12). The post holder for mirror C is fixed directly to the aluminum frame using a screw which can slide horizontally. The aluminum frame holding all the optical components is mounted on a tilt platform (Newport model 37) which offers three axis adjustments: two tilts, and one in-plane rotation. The tilt range in each direction is -6 to +8 degrees. The body of the platform is hard anodized aluminum and it has hardened steel inserts to interface with the micrometer spherical tips. The platform is oriented to provide tilt about the x and z axes and in-plane rotation (xz-plane) about the y-axis.

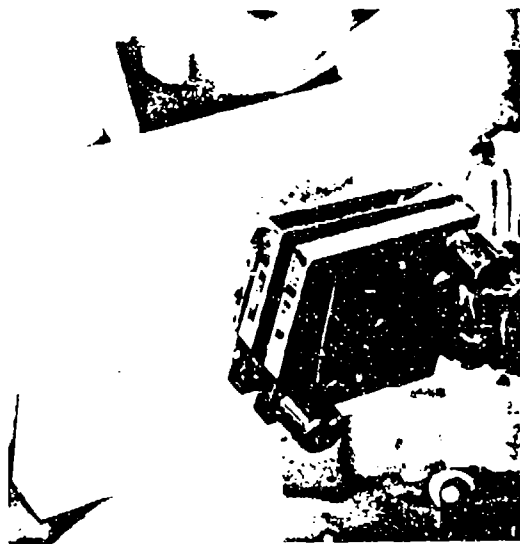
4.4. Adjustment of Interferometer.

In order to adjust the positions of the mirrors A, B and C, the following procedure was used:

- Using the formula given in equation D.9 (Appendix D), calculate the distance from the interferometer to the specimen grating that will render the desired angle of interference between the two incident beams.
- Using this result, move the specimen together with the loading frame to the calculated distance. Loosen the universal clamps and orient manually the mirrors to direct the light towards the specimen grating. Care should be taken to avoid touching the surfaces of the mirrors, since any hand grease cannot be removed without damage to the optical surfaces. This positioning will give a rough adjustment of the orientations of the mirrors. To describe the process of fine adjustment of the orientation of the mirrors, let the knobs of the mirror mount adjustment screws be denoted by a_1 and a_2 , b_1 and b_2 , c_1 and c_2 , for mirrors A, B and C respectively. (see Figure 4-4.a).
- On the focal plane of the decollimating lens, notice three bright spots. They correspond to the first diffraction orders of the three incident beams. Adjust mirrors B and C first. Block the light from mirror A, then only two bright spots will remain on the focal plane of the decollimator. These bright spots should be in a vertical position, that is, one above the other. In order to get the correct sign of the pitch mismatch, that is, the mismatch that will result in an increase in the number of fringes per unit of space due to a tensile strain, and a decrease in the number of fringes per unit of space due to a compressive strain, the bright spot corresponding to the diffracted order OB' should be located above the one corresponding to the diffracted order OC'. Then, both spots should be identified before continuing. The position and orientation of the bright spot OB' can be adjusted using knobs b_1 and b_2 . Knob b_1 will control the separation between the two bright spots. A clockwise rotation of this knob will move the bright spot OB' upwards. The angular orientation of the bright spot can be adjusted with knob b_2 . A clockwise rotation of this knob will rotate the interference



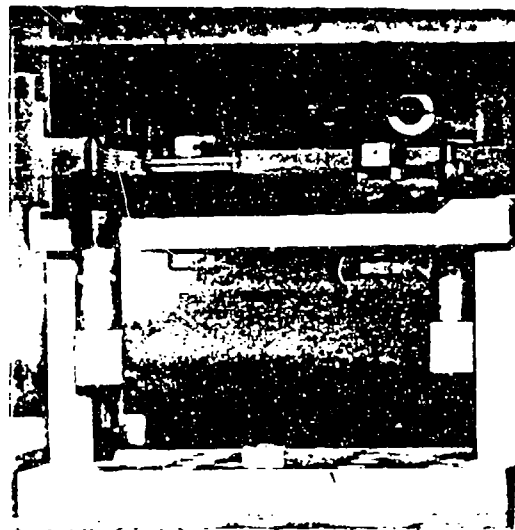
(a) Mirror Setup and Orientation



(b) Mirror Mount



(c) Loading Frame



(d) Micrometer Mirror Base

Figure 4-4. Mechanical Elements Used in the Positioning of Optical Elements of the Moire Interferometer

fringes clockwise as viewed from the camera. The function of the first knob is to produce extensional pitch mismatch and rotational pitch mismatch is produced by the second, as in traditional Moire. Once the two bright spots have been positioned correctly, the resulting interference pattern should be in the form of horizontal fringes.

- Now, to adjust mirrors A and B, block the light from mirror C and uncover mirror A. In this step, mirror B should not be touched at all, since that would produce a misalignment of the horizontal fringes. Next, block any of the two mirrors to identify their corresponding diffraction orders. Again, to get the correct sign of the pitch mismatch, spot OA' should be to the right of spot OB', that is, in a horizontal position. Knob a_2 can be used to produce extensional pitch mismatch, and a clockwise rotation will move spot OA' farther to the right of spot OB'. Knob a_1 will produce a rotational pitch mismatch and a clockwise rotation of it will produce a counterclockwise rotation of the interference pattern as viewed from the camera. When these two bright spots have been positioned correctly, the resulting interference pattern should be formed of vertical fringes.
- After adjusting mirrors A and B, and B and C, for vertical and horizontal fringes respectively, a third set of interference fringes can be obtained at 45° . To obtain this set of fringes, simply block the light reaching mirror B and uncover mirror C. While doing this, extreme care should be taken to avoid disturbing the adjustments for the other two orientations.
- Also, for further alignment of the fringe pattern, the micrometers of the tilt table on which the frame is mounted can be used. These micrometers add three degrees of freedom and are denoted by D, E, and F. Micrometer D provides tilting about the z-axis and will rotate the interference pattern in the xy-plane, that is, in the surface of the specimen, as viewed from the camera. Micrometer E tilts the interferometer about the x-axis and it will produce both extensional and rotational pitch mismatch. Micrometer F will rotate the interferometer in the xz-plane. This rotation is used to position the surface of the specimen grating perpendicular to the optical axis of the collimator. For the no-load stage, the diffracted orders should retrace their path to the pinhole of the spatial filter.
- A 35mm Canon A-1 Camera and a 70-210mm zoom lens with a 2x focal length converter were used to record the fringe patterns. A cable shutter release was used to avoid any vibration of the camera.

The specimen was loaded using a modified loading frame manufactured by Scott-Engineering Sciences, 1400 S. W. 8th. Street, Pompano Beach, Florida, 33060. Tension was applied using a hydraulic (double-acting) cylinder ram with the hydraulic pressure supplied by a hand pump.

To measure the applied load, a force transducer was made by the investigator. This transducer was connected to a strain indicator model 3270, made by Daytronic Corporation, Miamisburg, Ohio. The span of the conditioner was adjusted to display the actual magnitude of the applied load. The sensitivity of this transducer was ± 5 pounds, and the range was $\pm 2,200$ lbs.

The virtues of this system can be summarized as follows:

- It allows a good efficiency of light utilization.
- No rigid connection is required between the specimen and the system.
- With small improvements, it can be utilized to perform measurements in environments not so ideal as an optics laboratory.
- Grating frequencies are easily adapted to suit the problem.
- Measurements can be performed in three different directions giving a map of strains in the same number of directions and allowing calculations of maximum strains.
- Pitch mismatch can be easily adjusted.
- It is amenable to various methods of data recording, such as film, television camera, etc.

4.5. Fabrication of Moire Specimen

The dimensions of a test coupon should be selected very carefully in order to assure that the planned test will yield results which truly represent the expected material behavior. When working with composites, care should be taken when dimensioning the test coupon. Horgan [4.18], showed that end effects are more severe for fiber-reinforced composites than for isotropic materials. Also, it is the geometric factors that usually render one of the failure modes predominant. These factors are the width of the specimen and the distance between hole center and the free end which is perpendicular to the loading axis. Figure 4-5 shows these geometric parameters considered in the design of the specimen.

The effect of end distance was investigated by Collings [4.19]. He suggested that a minimum ratio $e/d > 3$ was needed to develop full bearing strength. He also studied the effect of specimen width in single-hole specimens. A minimum w/d of 8 was required if full bearing strength was to be developed.

The dimensions of the specimen adopted in this study are also shown in Figure 4-5. In the spirit of avoiding end effects and to provide full bearing strength, the specimen used to obtain the stress and strain distribution around the pin-loaded hole was: 50.8 mm (2.0 in.) wide, 203.2 mm (8.0 in.) long; a 6.35-mm (0.25 in.)-diameter hole was drilled through this composite laminate, and the distance from the center of the hole to the free end was 25.4 mm (1.0 in.).

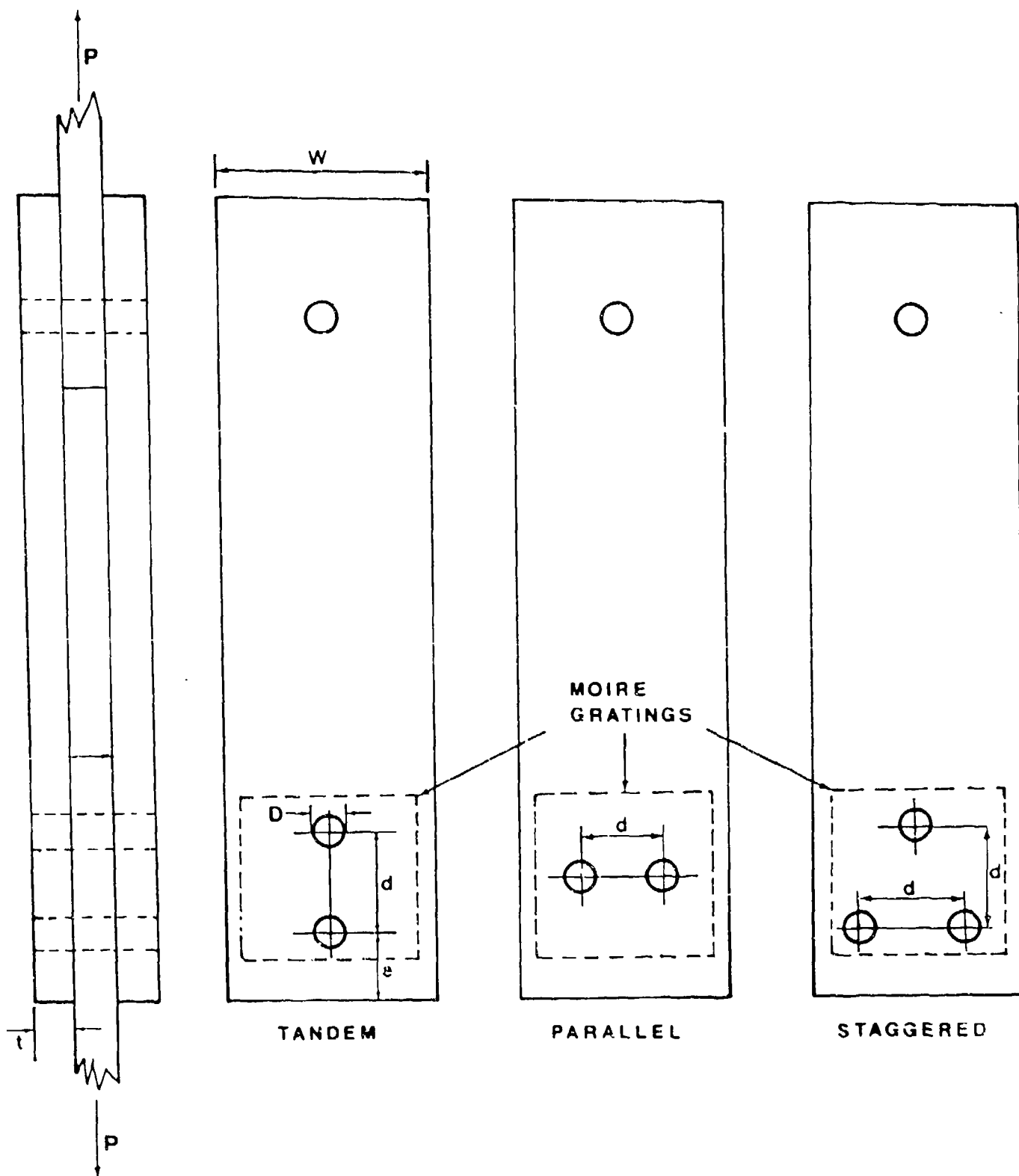


Figure 4-5. Joint Geometry and Nomenclature

The specimens were cut slightly oversized, with fibers perpendicular and parallel to the axis of loading, from a large panel using a band saw. The cutting process was carried out slowly, and the composite was frequently wetted with water to prevent both the saw and the laminate from overheating. The sides were finished by hand to the specified dimensions, using first a wet/dry, 200-grit paper, and, for final finish, a wet/dry, 400-grit paper. Again, water was used to prevent overheating. Since the finishing procedure was performed by hand, in order to obtain square sides, the composite laminate was sandwiched between two steel templates, whose edges had been aligned, one with respect to the other. During this cutting and finishing procedure, extra caution was required to avoid delamination of the material. Also, the drilling process had to be carried out with extreme care. The finished blank was sandwiched between one of the steel templates and a piece of particle board, and clamped together. This pressure helped to avoid delaminations during the drilling operation. The steel template was used as a reference to position the holes in the specimen.

4.6. Specimen Gratings

Application of the Moire effect to any problem depends on the successful deposition of line grids (or dots) on the surface of the specimen material.

All specimens in this study used reflective diffraction gratings. Following a method developed by Basehore and Post [4.20], the master gratings or molds were produced as follows: A high-resolution photographic plate (Agfa type 8E75), was exposed to two beams of collimated coherent laser light. The two beams intersected at the surface of the emulsion. These interfering beams generated a three-dimensional pattern of constructive and destructive interference. The frequency of this interference pattern could be calculated using the equation in Appendix D. When the exposed plate was developed, a silver compound remained in the areas exposed to constructive interference, while the silver was washed out elsewhere. Upon drying, the gelatin of the emulsion shrunk, but a reinforcing effect of the silver crystals on the exposed areas caused a nonuniform shrinkage, which is termed the lenticulation effect. The effect was a textured surface which had the same frequency as the interference system. Since a cross-line grating was desired, the plate was rotated 90° after the first exposure and a second exposure was made.

In order to produce these photoplates, the moire interferometer was used. It was adjusted to produce two horizontal beams using mirrors A and B, following the procedure described above. Since no reference grating of the desired known frequency was available, the angles were adjusted, and, using a traveling microscope with a 40x microscope objectives and with a scale in millimeters, the number of fringes per millimeter in the interference system was counted. Then, the mirrors were fine-adjusted until the desired frequency was obtained. A second checking was done on the previous counting results using a 75x microscope objective lens. As a final verification step, a small piece

of the overcoated plate was placed in a scanning electron microscope, and a photomicrograph (Figure 4-6) with a precisely known magnification was taken. Based on this photomicrograph, calculation of the frequency of the grating was verified. The frequency used in this study for the specimen gratings was 640 lines per mm (16,256 lines per inch).

The diffraction efficiency of a grating depends partly on the depth of its corrugations. This characteristic was controlled by the amount of exposure of the photoplate. The best time was worked out by trial and error.

Details of the photographic process to produce the high-resolution plates are given in Appendix E.

It has been reported elsewhere [4.20], that bleaching can be used to increase the depths of the corrugations of the grating. In this case, bleaching did augment the diffraction efficiency. But at the same time, the resultant texture of the photoplate surface did not produce a highly reflective grating; instead it produced a very diffusive surface, so bleaching was not used.

Next, a thin film of aluminum was deposited on the whole surface of the photoplate. Aluminum was chosen because it has the ability to resist tarnishing, it is highly reflective in thin films, and it is low in cost. An additional requirement which was satisfied by the use of aluminum was that the metallic film should not contribute a significant reinforcing effect to the specimen.

The grating on the photoplate was coated with aluminum in a vacuum deposition unit (Denton D. V. high-vacuum evaporator). The tungsten coil containing a small piece of aluminum was located 10 cm (4.0 inches) approximately above the photoplate. The chamber was evacuated to 10^{-5} torr or less, and a current of approximately 30 amperes was passed through the tungsten filament. The thickness of the aluminum film was determined by trial and error. The overcoated photoplate was stored in a dust-free environment to await replication on the specimen.

4.7. Grating Replication Process

Figure 4-7 summarizes the manufacture and replication process of the grating on the surface of the specimen. A small amount of photoelastic cement, PC-10C from Measurements Group, Photoelastic division, Rayleigh, North Carolina, was mixed according to the manufacturer's instructions. It was poured onto the specimen, which had been positioned next to two steel blocks used as a reference to position the grating at the proper angle with respect to the specimen. The angle between the longitudinal axis of the specimen and the edges of the photoplate was 45 degrees. Next, the aluminum-coated plate was placed on the specimen facing down. Excess cement was squeezed out by applying a pressure of 10 psi approximately to the glass plate/specimen sandwich. Curing time for the epoxy was about 4 hours, but the plates were removed after 12 hours.

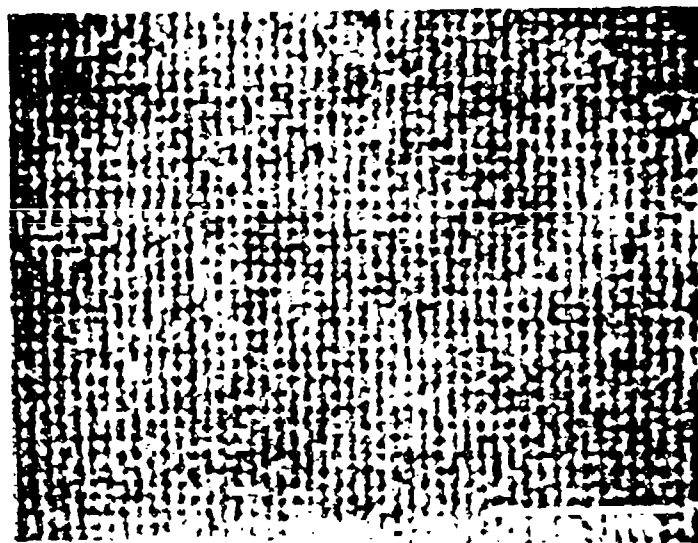


Figure 4-6. Photomicrograph of Two-Way Phase Grating Taken with Scanning Electron Microscope

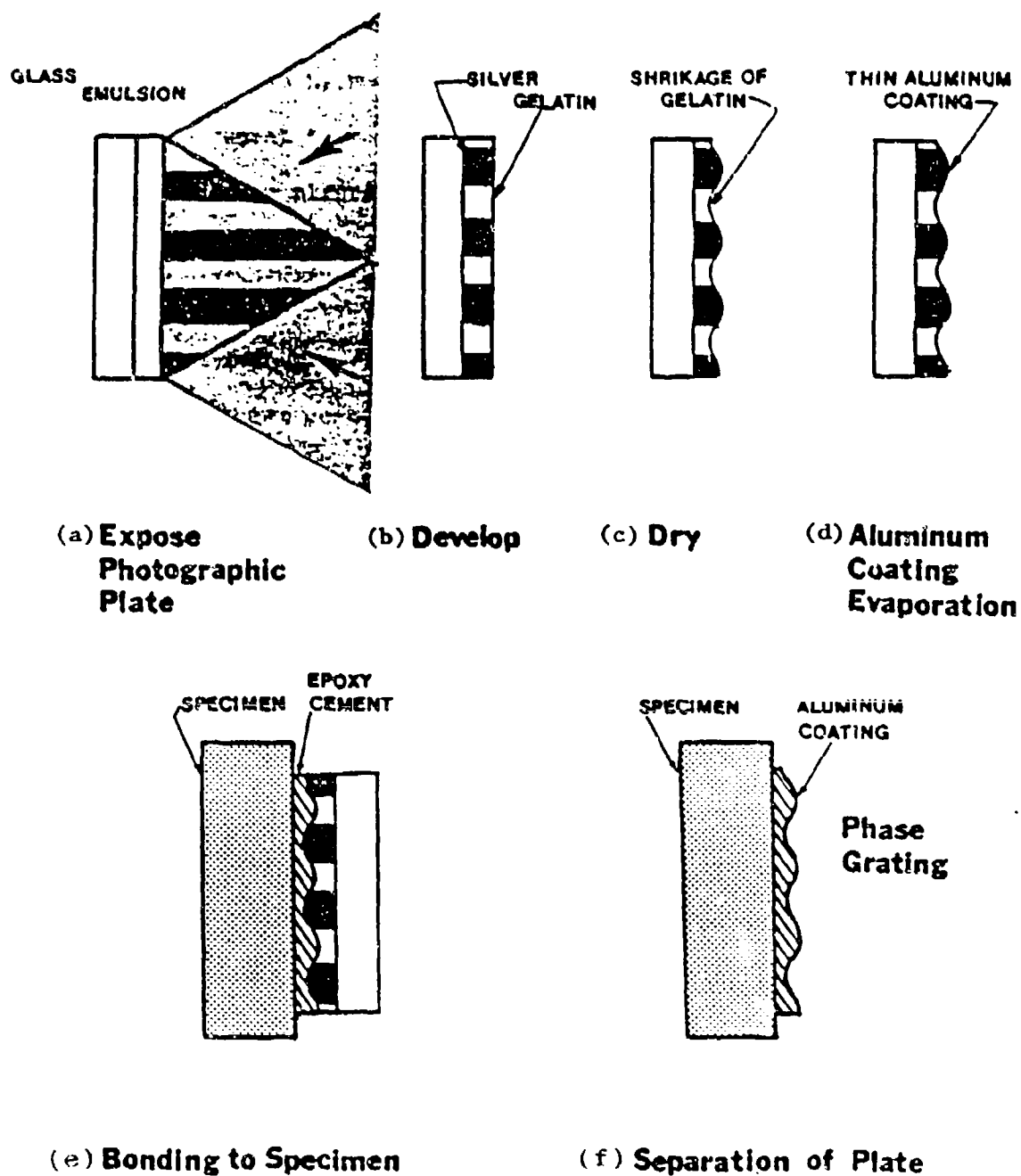


Figure 4-7. Production and Replication of Moire Gratings

When the epoxy had hardened, the photoplate was removed by a twisting-prying action. The thin film of aluminum adhered to the epoxy and this resulted in a highly reflective phase grating on the surface of the specimen.

Before the gluing operation, some important preparation steps were taken. First, the specimen was cleaned thoroughly with Freon TF degreaser (marketed by Measurements group, Photoelastic Division). To prevent the cement from filling the hole in the laminate, it was filled first with molding plastic. This molding plastic was given a concave shape on its upper surface to avoid spreading it out on the surface of the specimen during subsequent cleaning. Also, to avoid having some of the squeezed-out epoxy adhere permanently to the edges and bottom of the specimen, these were covered with Teflon tape, held in place with masking tape. As a final cleaning step, the specimen was sprayed directly with the freon TF degreaser and the surface wiped off with single strokes using gauze sponges. This last step was repeated 10 or 15 times, taking care not to contaminate the surface of the specimen with the molding plastic.

After removing the photoplate, excess epoxy that was squeezed out and was adhered to the masking tape was removed easily. Because the epoxy was brittle, it could be broken free from the specimen edges.

At this point, the specimen was ready to be labeled and to be tested. Care was taken to avoid contamination of the surface of the grating by either fingerprints or airborne dust. Figure 4-8 shows two specimens with reflective gratings printed on their surfaces.

4.8. Moire Fringe Pattern Photography

After all the adjustments of the interferometer were completed, a final check for alignment was performed. Black and White Kodak Technical Pan film 2415 (ESTAR-H Base) was loaded in the Canon camera and the test was ready to begin.

First, the specimen was loaded with a modest force (no more than 5 pounds) to keep it in a fixed position and to avoid any rigid-body rotation. Next the fringe patterns in all three directions were checked to verify that the initial loading did not introduce any rotational mismatch. Such rotation was common to all three fringe patterns, and it was corrected by rotating the tilt table about an axis perpendicular to the specimen surface.

Data was recorded by photographing the fringe patterns and hand recording the magnitude of the applied loads. Photographs were taken for 50-pounds increments, up to a maximum load of 250 pounds. Then, the load was returned to zero and the fringes were checked again for rotation.

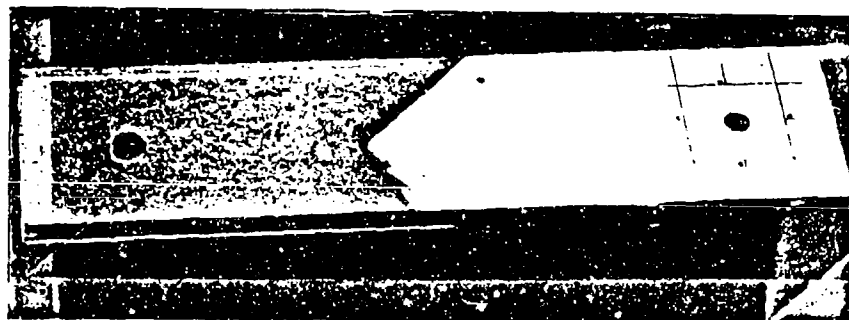
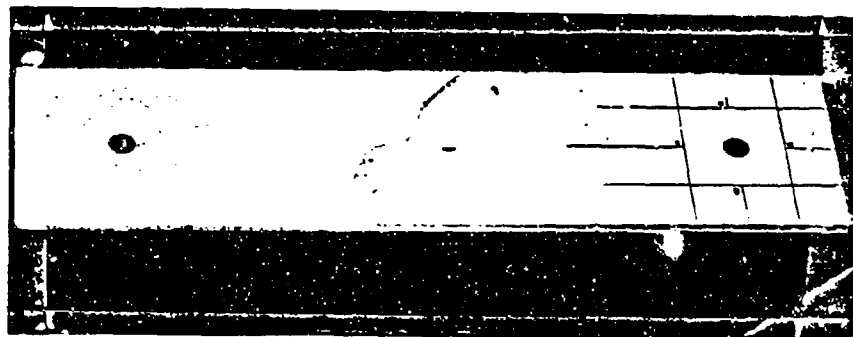


Figure 4-8. Specimens Showing Reflective Gratings on Their Surfaces

The first set of photographs corresponded to the base (no-load) for all three fringe patterns. The next set corresponded to the first increment of 50 pounds. This procedure was repeated for each level of loading.

The camera was focused on the plane of the image of the surface of the specimen. The fiducial marks on the specimen served as a guide to adjust the focus of the camera. Also, to avoid losing the focus, the shutter was released using a cable. Care had to be taken to wait a few seconds after loading to avoid unwanted vibration which could have affected the sharpness of the fringes.

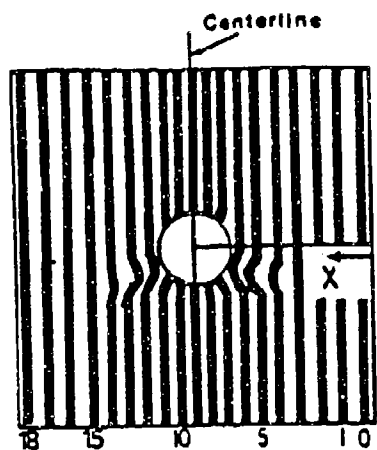
The time of exposure was set by the automatic mode of the camera with the film ASA set at 125 and the exposure corrected by a factor of 0.5. This feature of the camera was very useful, since the diffraction efficiency of the gratings was noticed to vary slightly with the direction of illumination, thus time and film were conserved.

The film was processed according to the manufacturer-recommended developing and fixing times. Kodak D-19 developer was used to obtain maximum contrast, and fixing was in Kodak fixer solution. Next, all the fringe patterns were printed on Kodak Kodabromide F-5 paper for maximum contrast. The fringe pattern photographs were then ready to be digitized.

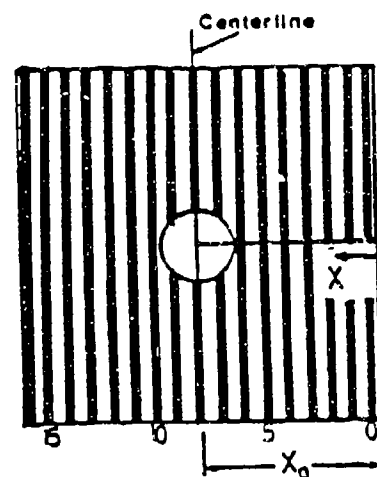
4.9. Data Reduction

In Appendix D, it was shown that, using a small amount of mismatch, the map of displacements could be determined more accurately. An initial Moire fringe pattern, produced by using some mismatch, was obtained. Its initial fringe density had to be measured and subtracted from all subsequent fringe densities recorded under "at-load" conditions. This subtraction effectively defined the strain produced by the deformation caused by the applied loading. Ideally, if the fictitious strain were homogeneous, the fringe density would be constant over the area viewed on the specimen by the Moire setup. However, due to imperfections in the lenses, the beam expanders and the mirrors, the fringe density was not constant over the length viewed. The subtraction of fringe densities between the "at-load" plus mismatch and the "mismatch only" states (the former referred to as data and the latter as base), had to be done locally. In schematic form, this procedure is illustrated in Figure 4-9.

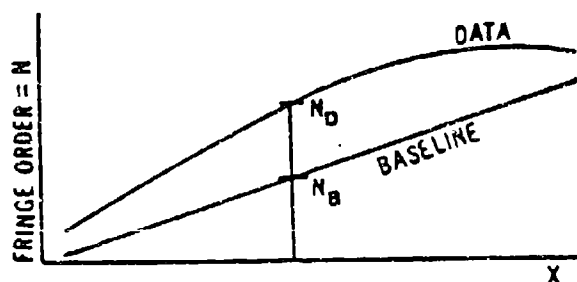
Three direct derivatives must be determined for the Moire rosette method. Various methods of differentiation may be utilized, including graphical differentiation where (1) displacement curves are plotted from fringe data, (2) tangents are estimated, and (3) their slopes are measured. For most experimental strain analyses, a large volume of data must be analyzed. With large volumes, the graphical techniques are excessively tedious and slow. Numerical methods have the advantage of being easily adapted to a computer which allows power and versatility. Keeping in mind the inherent inefficiency of the differentiation of experimental data, a computer-assisted data reduction system



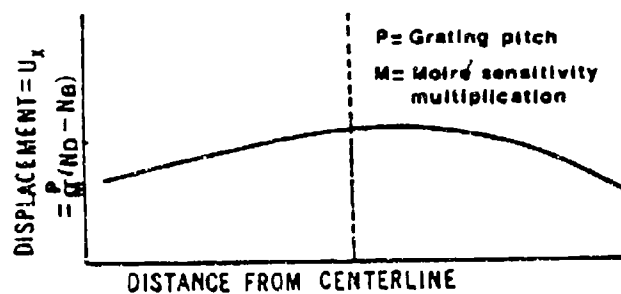
(a) FRINGE PATTERN = DATA



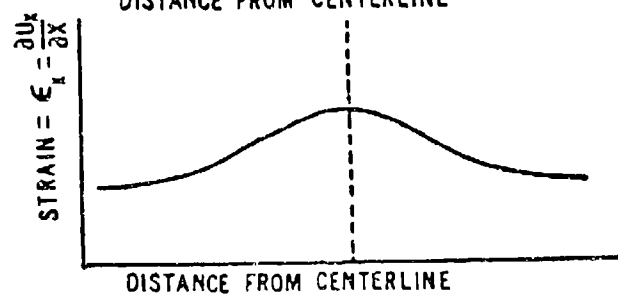
(b) FRINGE PATTERN = BASELINE



(c) FRINGE ORDER PLOT



(d) DISPLACEMENT PLOT



(e) STRAIN PLOT

Figure 4-9. Steps in the Reduction of Moiré Data used to Determine Strains in Pin-Loaded Holes

(combination of graphical and numerical methods), was employed to fit and smooth the experimental data, thereby improving the accuracy of displacement information and consequently its derivatives.

4.10. Digitizing Moire Test Data

Photographs of Moire patterns were prepared for digital data reduction to obtain strains in three different directions. The first step was to number the moire fringes and identify the various fiducial marks and the orientation of the specimen in the photographs. This preparation had to be done for a data photograph (at-load) and for its matching baseline (no-load) fringe pattern. Numbering of the fringes is usually an easy process. The displacements and components of displacements within the boundaries of the specimen are continuous and single-valued. They are continuous, and, therefore, on a line between any two points with different displacements, displacements with intermediate values must occur. They are single-valued, and, therefore, no two fringe orders can occupy the same location on the deformed body [4.17]. These considerations follow directly from the assumption of continuity. From these properties, it follows that the isothetic (locus of points exhibiting the same displacement component) lines of different values do not intersect. Assigning a displacement value to the first fringe can be completely arbitrary, since it only defines the reference point, i.e., absolute fringe number is not important. Consecutive fringes will have a difference in displacement equal to the space between reference grating lines. It is important, however, that numbers or fringes be not repeated or skipped.

Digitization from the fringe photographs was done using a Micro Datatizer (software specifications for Michigan State University, S. O. No. 178058 by GTCO Corporation, Rockville, Maryland). The microdatatizer system in schematic form is shown in Figure 4-10. The photograph to be digitized was divided into a series of axes oriented perpendicular to the direction of the reference grating lines. For this particular problem the axes were spaced at 0.0625-inch intervals. The photographs were placed on the digitizing tablet and digitization of points one-by-one was done by placing a cross-hair over the point or any of the fiducial marks and identifying labels. Scaling to specimen dimensions was done automatically. The required scaling factors were based on two digitized points and the corresponding specimen coordinates for each. Each axis was digitized and the point coordinates dumped to punch cards. These cards allowed easy data manipulation.

4.11. Data Reduction and Plotting Strains.

The Moire data analysis computer program, developed and extensively used by Cloud and colleagues [4.11-4.15], was utilized with some minor modifications to subtract the initial mismatch and to obtain the desired strain maps. The operations performed by the analysis routines are as follows.

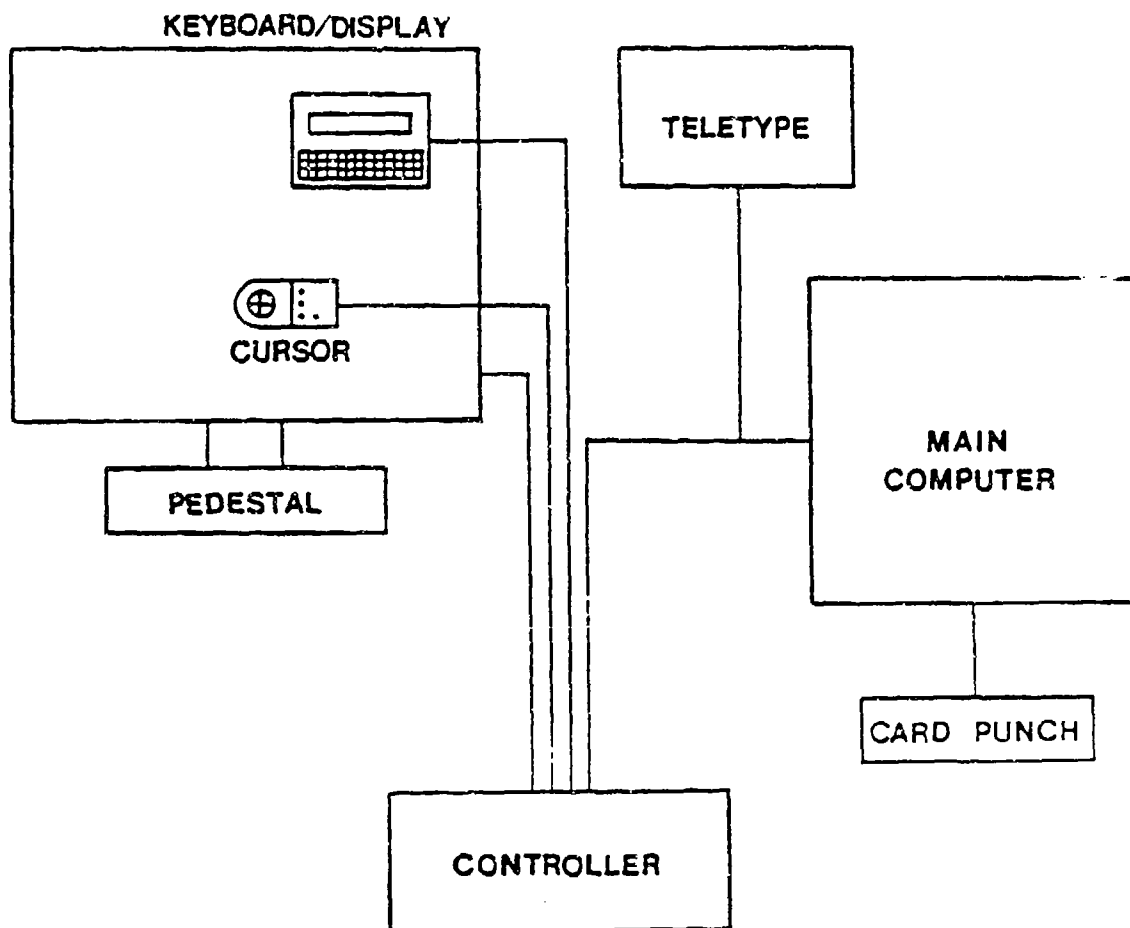


Figure 4-10. Microdatatizer System

- Read in the data containing specimen identifiers, the moire sensitivity multiplication factor and the spatial frequency of the reference grating. Then, for an "at-strain" fringe pattern, the distance between two fiducial marks, the maximum fringe order to be entered, and positions of each moire fringe along the axis under consideration are entered. The maximum fringe order and the fringe positions must then be entered for the matching base line fringe pattern.
- Generate fringe order numbers for each fringe position entered.
- Fit the "at-load" data and "baseline" data with two smooth continuous curves by means of a cubic spline fitting and smoothing routine.
- The curves are interpolated to obtain the fringe number as a function of distance from a reference line at 100 points on both the data and baseline curves. The maximum range of the curves is sorted out and divided by 100 to establish the nodes, which must be common to both data and baseline curves.
- Subtract the baseline fringe order (no-load) from the data fringe orders at load, for each of the 100 points. Each difference is divided by the reference grating spatial frequency (i.e., multiplied by the reference grating pitch), and then divided by the sensitivity multiplication factor to obtain the displacement function U for the chosen axis.
- To have all results reported in terms of distance from an important specimen feature, subtract the position of each nodal position value from the distance of the first fiducial mark to the important specimen feature.
- Using third-and fourth-order finite differences, calculate the first derivative of displacement with respect to position along the appropriate axis. This result is the strain at each of the 100 nodes.
- Print all values of input fringe orders and strains.
- Plot strain ϵ , as a function of the distance along the axis.
- Repeat the process for each axis.

The plots of strain vs. position obtained have the advantage of displaying results for several lines of the same specimen. Thus, the strain at any point on the same specimen can be seen on a single plot.

The modifications made to the computer program as developed by Cloud [4.11] were:

- All the arrays were modified to store up to 150 values. This allowed the handling of relatively dense Moire fringe patterns.

- The differentiation subroutine was changed from a first-order forward difference computation to the following: (a) for the first 3 nodes, the derivative is computed using a third-order forward differences algorithm; (b) for the next 94 nodes, the derivative is computed using a fourth-order central differences algorithm; and (c), for the last 3 nodes, the derivative is computed using a third-order backward differences algorithm. The differentiation process carried out before used the following finite-difference expression:

$$f'(x) = \frac{f(x+h) - f(x)}{h} + O(h)$$

This derivative of f with respect to x is accurate to within an error of the order of h . Since it had been employed by Cloud [4.11] in the analysis of specimens which had undergone large plastic deformations, and since the analysis was performed over very short lengths, that accuracy was not a drawback in the results.

When dealing with composite materials and especially with the pin-loaded hole problem, the first-order differences would yield good results only in a region where ϵ is "large." More accurate expressions should be used. The needed accuracy can be found by using higher order finite-differences expressions, which are obtained by taking more terms in the Taylor series expansion [4.21]. The expressions used are:

Third-order forward differences,

$$f'(x) = \frac{2f(x+3h) - 9f(x+2h) + 18f(x+h) - 11f(x)}{6h} + O(h^3);$$

Fourth-order central differences,

$$f'(x) = \frac{f(x-2h) - 8f(x-h) + 8f(x+h) - f(x+2h)}{12h} + O(h^4);$$

Third-order backward differences,

$$f'(x) = \frac{11f(x) - 18f(x-h) + 9f(x-2h) - 2f(x-3h)}{6h} + O(h^3).$$

- A plotting routine, PLOTP, which gave multiple plots of strain vs. position was added.

5.0. EXPERIMENTAL STUDY OF HOLE ARRAYS

5.1. Objectives and Scope

The main objective in this portion of the research is to gain insight into the stress-strain field in the vicinity of hole arrays. Three configurations are considered. The first has two holes in a row parallel to the direction of the load. Ideally in this case, if all of the pins are identical and if the pin-hole interactions are the same, symmetry can be assumed. Then each pin will carry one-half of the load applied to the plate. However, in less ideal conditions, some load misalignment can exist, thus producing a nonuniform distribution of the load between the two pins. In order to simulate the worst condition, the holes were loaded individually.

In the second case, two holes are in a row perpendicular to the direction of the load, and both holes were loaded equally.

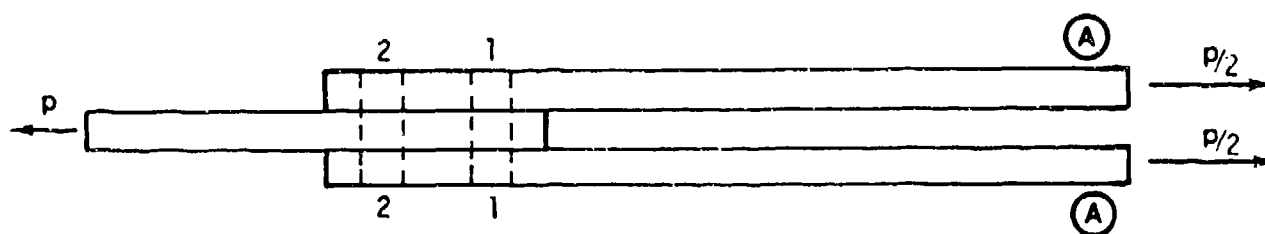
The third configuration considered has three holes in a staggered or triangular configuration. All three holes were loaded equally and simultaneously.

2. Two Holes in Tandem: Both Loaded

The first test was performed on the specimen with the two holes arranged in a row parallel to the loading axis. Both holes were loaded at the same time and subjected to a tensile load of 444 N. (100 lb.)

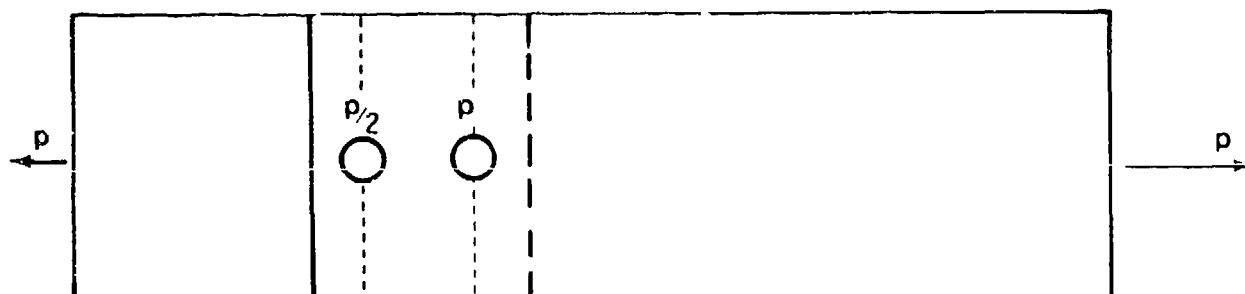
In an ideal situation, if all the pins are identical and the pin/hole interactions are the same, symmetry can be assumed. Then, the load applied to the joint is equally divided between the pins and, in this case each pin will carry one half of the applied load. Based on this assumption of symmetry, the load transmitted to each net section can be calculated as shown in Figure 5-1. In the laminate A, section 1-1 transmits the total load P , while section 2-2 transmits only part of it ($P/2$). Thus, each plate A will carry only $P/2$ in section 1-1 and $P/4$ in section 2-2. This indicates that the stress in the net area of section 1-1 is twice as large as the stress in the net section 2-2. This situation of equal load in each pin was simulated using cables and pulleys to divide the load.

Figure 5-2 shows a typical Moire fringe pattern of displacements parallel to the direction of the applied load. In this figure it can be seen that the number of fringes per unit of length has increased in the edges of the horizontal diameter of both holes. This is an indication that there exists a tensile stress in both areas. Also, in the bearing region of both holes, the number of fringes per unit of length has decreased, and this is an indication of the presence of a compressive stress. It is noticed that the shape of the fringe changes drastically on both sides of the bearing region, and this bending of the fringes should be produced by a high shear deformation on the specimen. Also



(a) Side View

section stress
resultants



(b) Top View

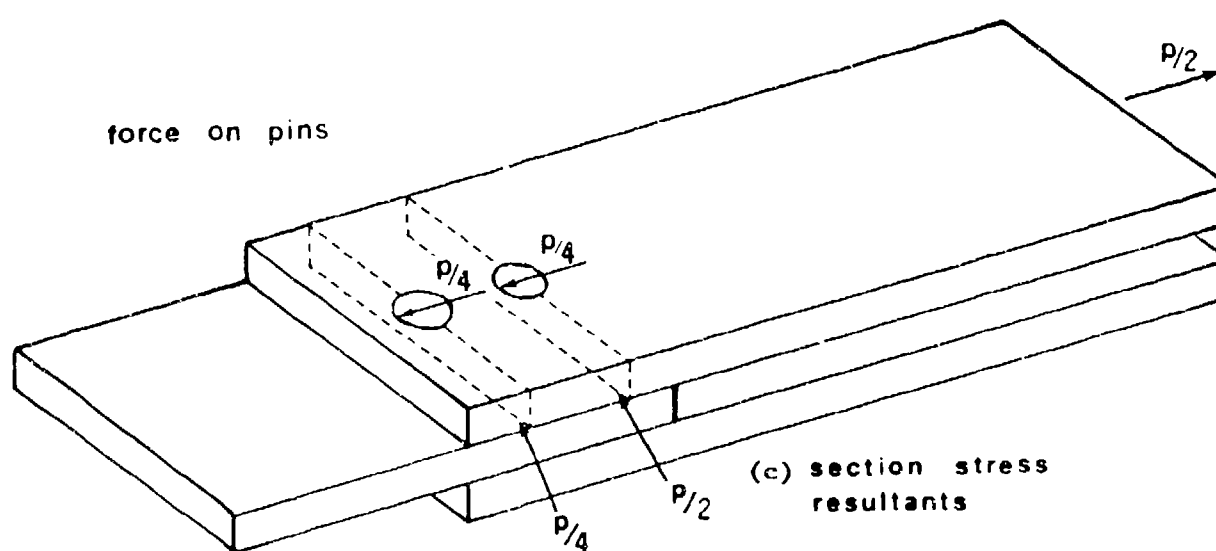


Figure 5-1. Stress Resultants for Two Tandem Holes Equally Loaded

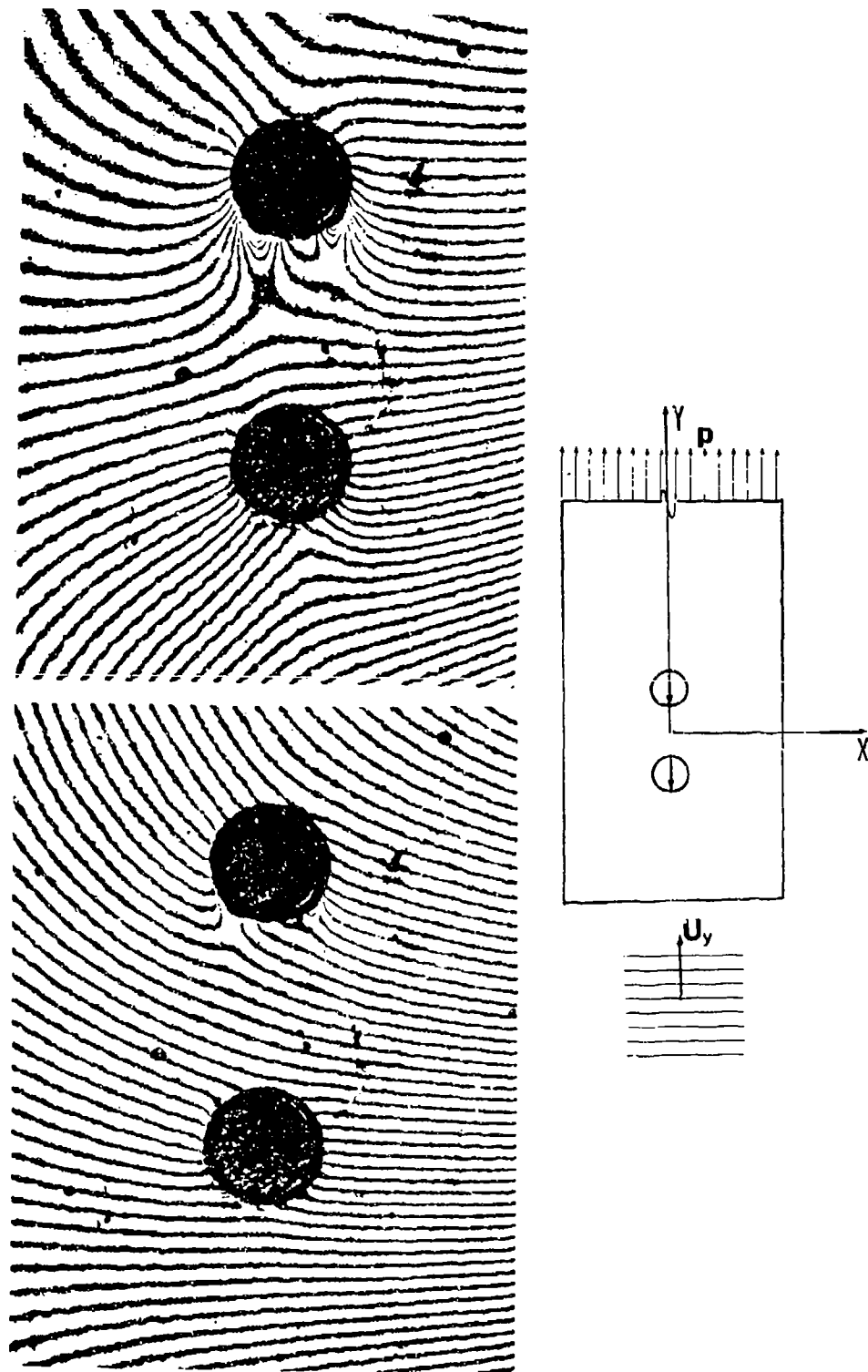


Figure 5-2. Moire Fringes of Displacement Parallel to Direction of Load when Both Holes are Loaded

notice that the effect of the loading is more noticeable on the upper hole.

Figure 5-3 shows strain ϵ_y along several lines parallel to the direction of the load. It should be pointed out that in the following figures of strain, obtained from the photographs, the strain is referred to a centerline, which is a line perpendicular to the direction of the strain under consideration and it is indicated in the legend drawing in the upper right-hand corner of the figures.

In Figure 5-3 it can be seen from line $X_2=0.125$ that the maximum strain occurs at $Y=0.285$, i.e., slightly below the horizontal diameter of the upper hole. The strain changes to negative in the bearing region, and its sign changes again to tensile strain slightly above the horizontal diameter of the lower hole. For the second hole, the maximum strain is attained also below its horizontal diameter. In the region between the two holes, the compressive strain attains a minimum value close to the upper hole, and then it becomes less compressive. At this point the strain curve has an inflection point after which the strain curve has another minimum value. The strain at the edge of the upper hole is 2.9 times larger than the maximum tensile strain at the edge of the lower hole.

In order to better understand the behavior of the joint, the stress concentration factor (SCF) at the edge of the holes in the direction of loading are calculated. In order to non-dimensionalize the numerical results, the far-field stress defined as $\sigma_0 = P/wt$ is used. The local stress is calculated using Hooke's Law for the orthotropic material and the strain values obtained from the figures. The SCF is defined as $k = \sigma/\sigma_0$. For this specimen, the calculated values of the SCF are as

follows: for the upper hole $k = 5.57$, and for the lower hole $k = 1.91$. This indicates that even when the same load is applied to each hole and the load transmitted by each section 1-1 has been estimated to be twice as large as that in section 2-2, the resulting stress is different from those estimated theoretically.

Hyer and Liu [5.1] indicated that the load sharing always approached 50-50 to within 10 percent, based on the position of an isotropic point in the region between the two holes. It might be interesting to study the effect of the pin/hole interactions due to the reduction of the contact area between pin and hole on the proportion of the load transmitted to each section of the joint.

Figures 5-4 and 5-5 show typical Moire fringe patterns of displacement perpendicular and at 45° to the direction of the applied load. In Figure 5-4 it can be seen that the number of fringes increases in the bearing region of both holes and it decreases in their ligament areas. The decrement is caused by a compressive strain in the x-direction. The fringes are also bent on both sides of the bearing region of both holes. This indicates that there exists high shear deformations in the region. Similarly, in Figure 5-5 it is very noticeable which areas are under a

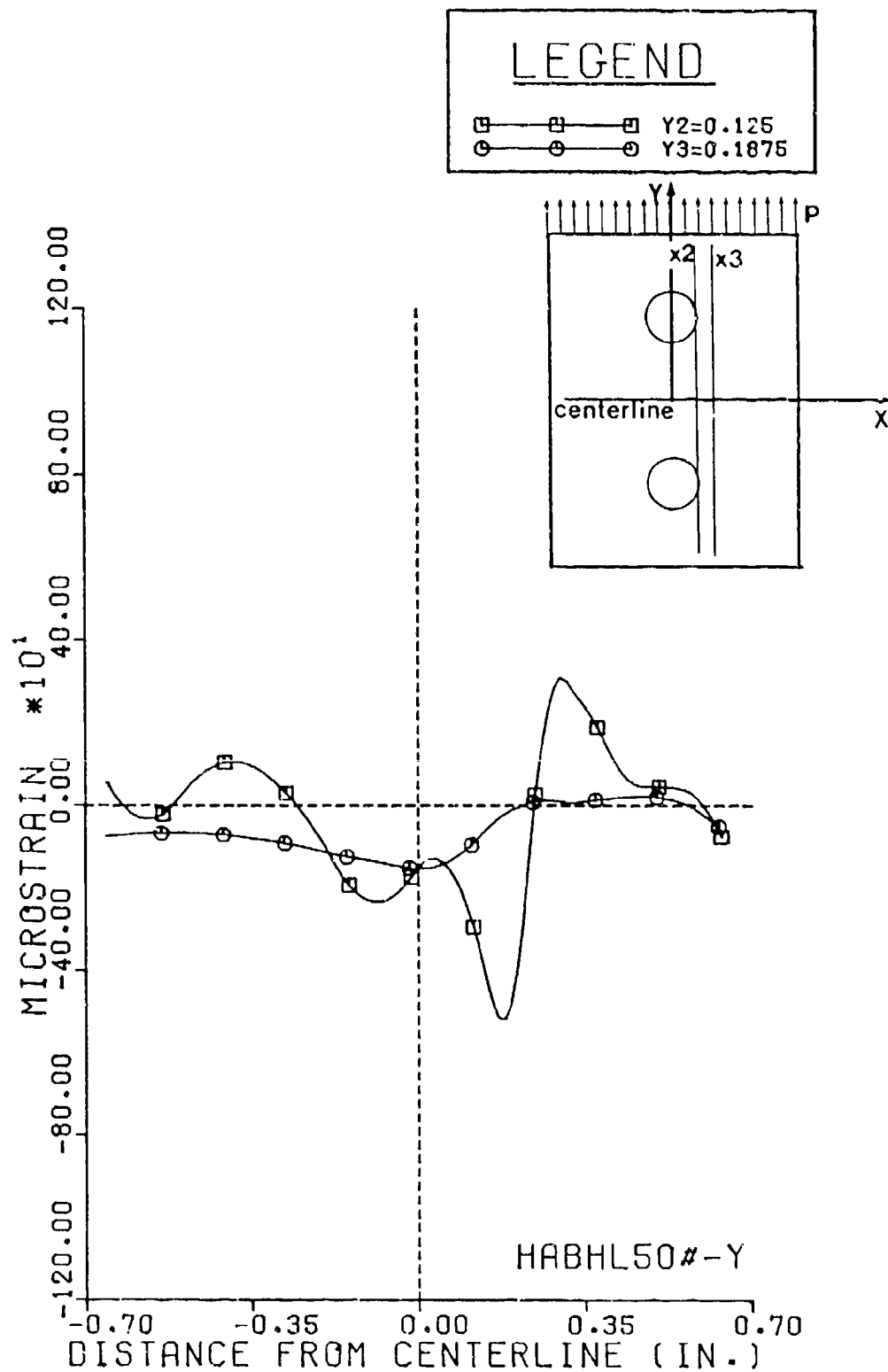


Figure 5-3. Strain ϵ_y along Lines Parallel to Direction of Load

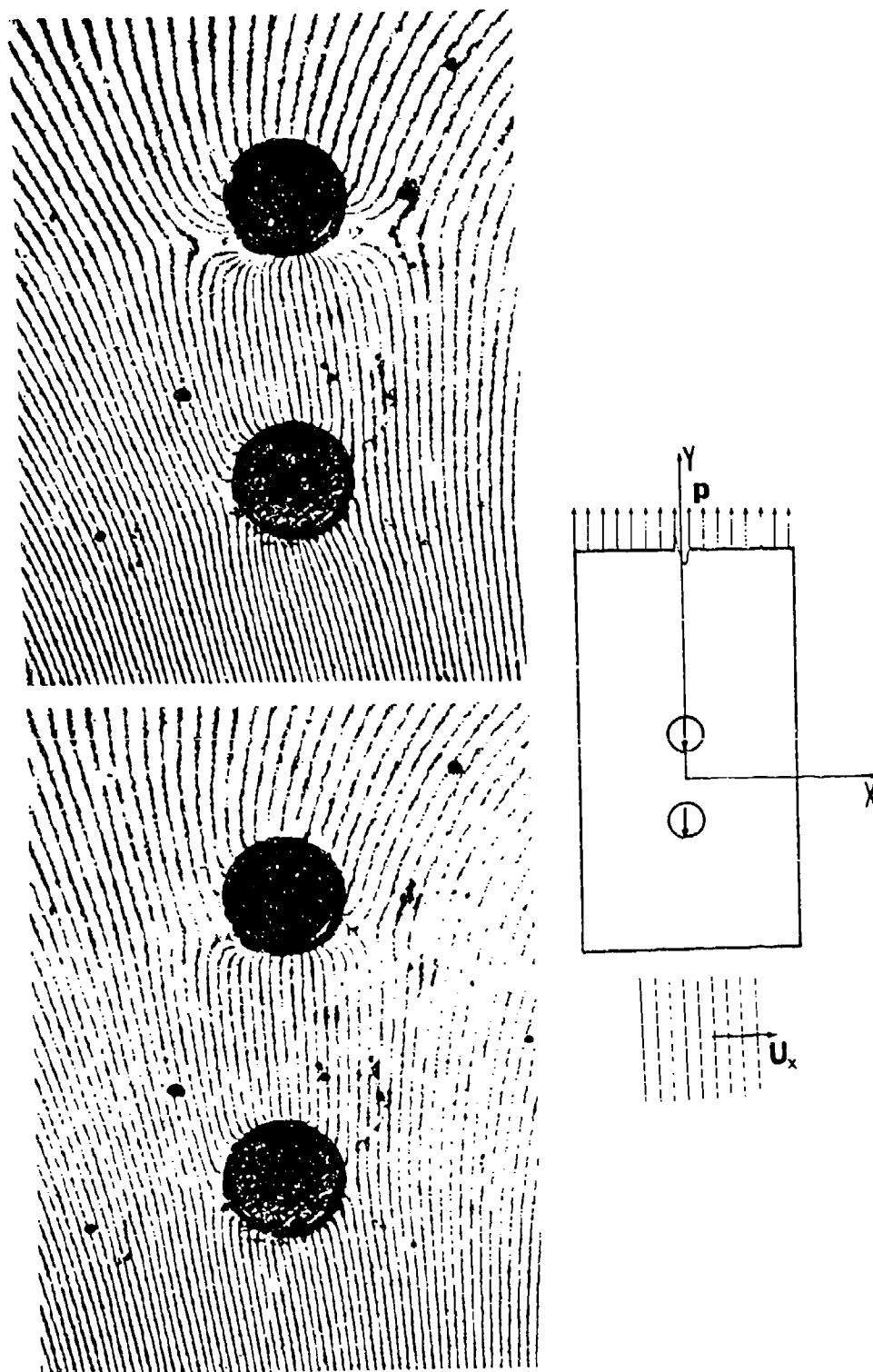


Figure 5-4. Moire Fringes of Displacement Perpendicular to Direction of Load for Hole Array in Tandem when Both Holes are Loaded

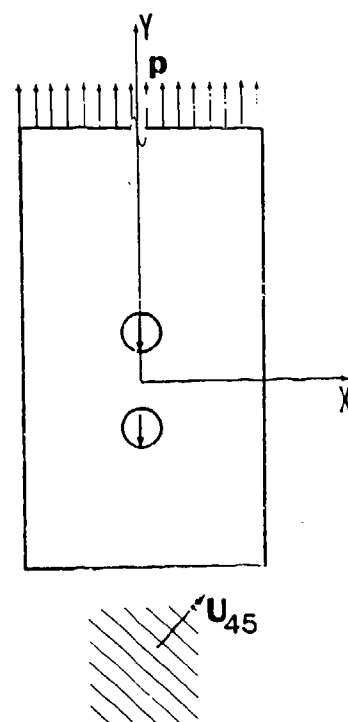
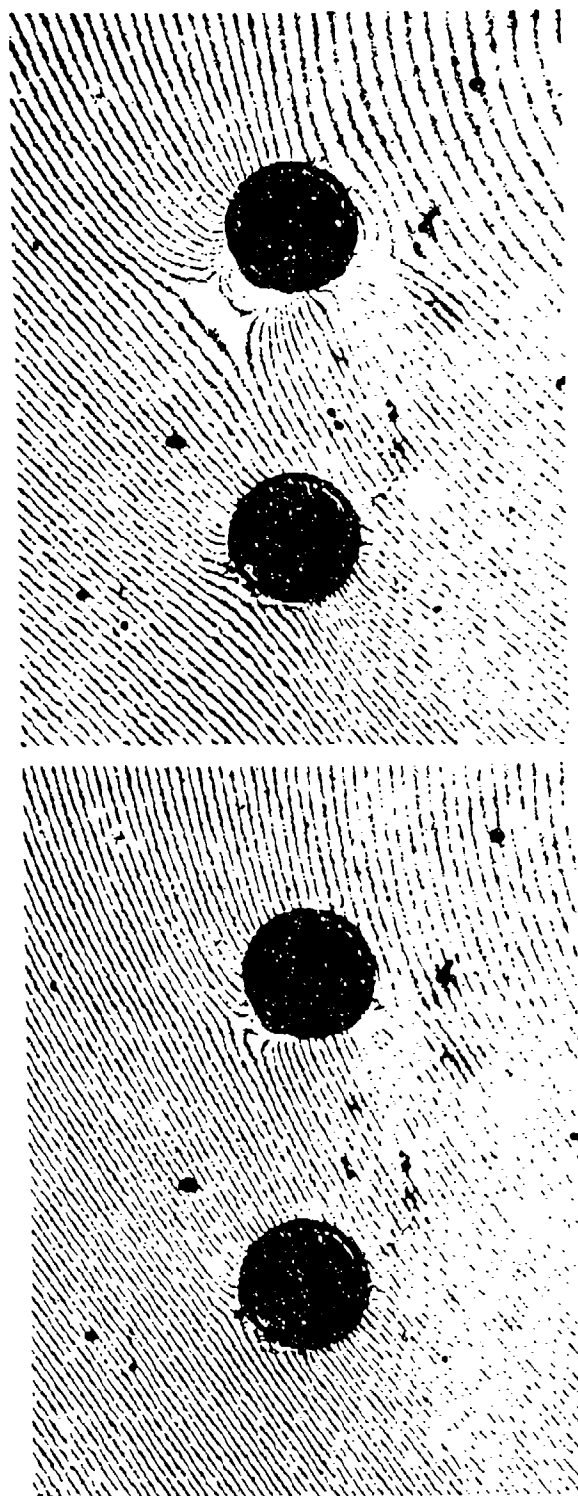


Figure 5-5. Moiré Fringes of Displacement at 45° to Direction of Load

tensile stress or a compressive stress. Figures 5-6 and 5-7 show strain ϵ_x for parallel lines perpendicular to the direction of loading and located in the bearing region of the upper hole. In this region ϵ_x is positive and on both ligament areas, it is negative. Figure 5-7 shows that ϵ_x approaches an average negative value in the area close to the upper edge of the lower hole.

In the case of a single pin-loaded hole there exists a small change of the sign in the strain on the upper portion of the hole, but in this case the nature of the strain in the region between the two holes appears to be governed by the bearing strain of the upper hole.

Figure 5-8 shows strain ϵ_x for parallel lines located in the bearing region of the lower hole. ϵ_x presents the same characteristics as at the upper hole. The only difference between both holes is the relative magnitude of the tensile strain ϵ_x in the bearing region, with ϵ_x in the upper hole approximately four times larger than the strain in the lower hole. It was also noticed that in Figures 5-6 and 5-8, the location of the point where ϵ_x changes from positive to negative coincides with the location of the point where ϵ_y also changes in sign. In the ligament areas on both sides of the holes, a fair symmetry is noticed in the strain distribution. Figure 5-9 shows strain ϵ_{45} for lines located in the bearing region of the lower hole. On the right-hand-side ligament of the lower hole, ϵ_{45} is negative. It has been shown for the case of the single hole [5.2] that on that location ϵ_{45} is tensile, but in this case there is an interaction with the bearing strain of the upper hole resulting in a compressive strain. For lines encompassing the regions of the lower hole, ϵ_{45} changes from negative to a maximum tensile strain and then it goes back to a compressive strain.

Figures 5-10, 5-11 and 5-12 show strain ϵ_{45} for parallel lines located in the bearing region of the upper hole and also at half the distance between the two holes. As can be seen in Figures 5-10 and 5-11, ϵ_{45} is highly tensile in the lower left edge, and more towards the left it becomes negative then it increases again but it still remains negative. Figure 5-12 shows very little variation except for lines y'5 and y'6 which show a slight increase to a positive value near the locus of maximum shear strain. Then the locus of the end of the bearing region and the beginning of the tensile area of the upper hole and the strain remain negative.

These cases suggest that the bearing region of the upper hole does affect the strain distribution of the lower hole. Further study is recommended to determine the effect of the distance between centers, that is, P/D and d/D on the interactions of the strains, in order to design parameters of multiple-hole arrays.

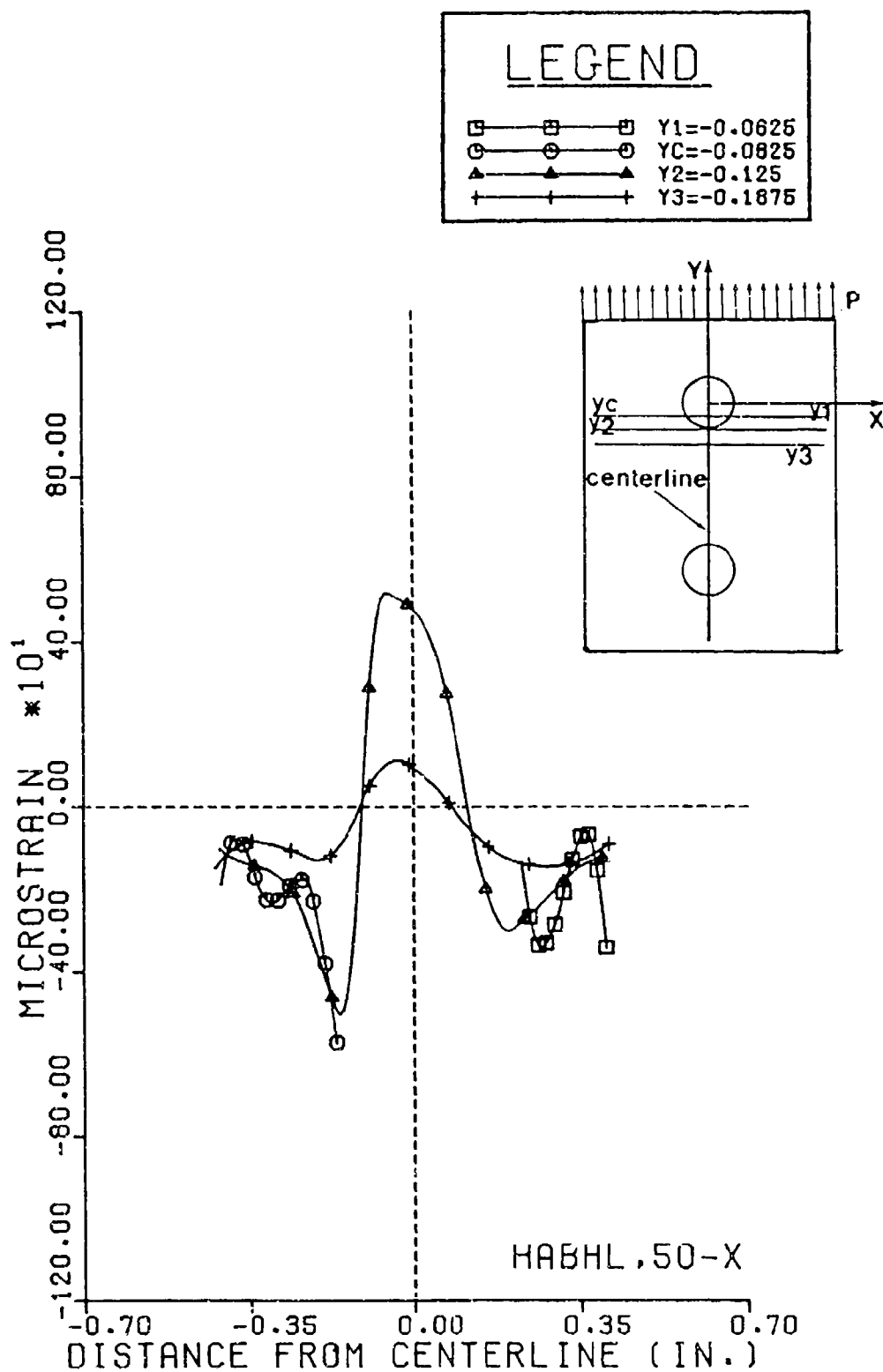


Figure 5-6. Strain ϵ_x along Lines Perpendicular to Direction of Load Near Upper Hole

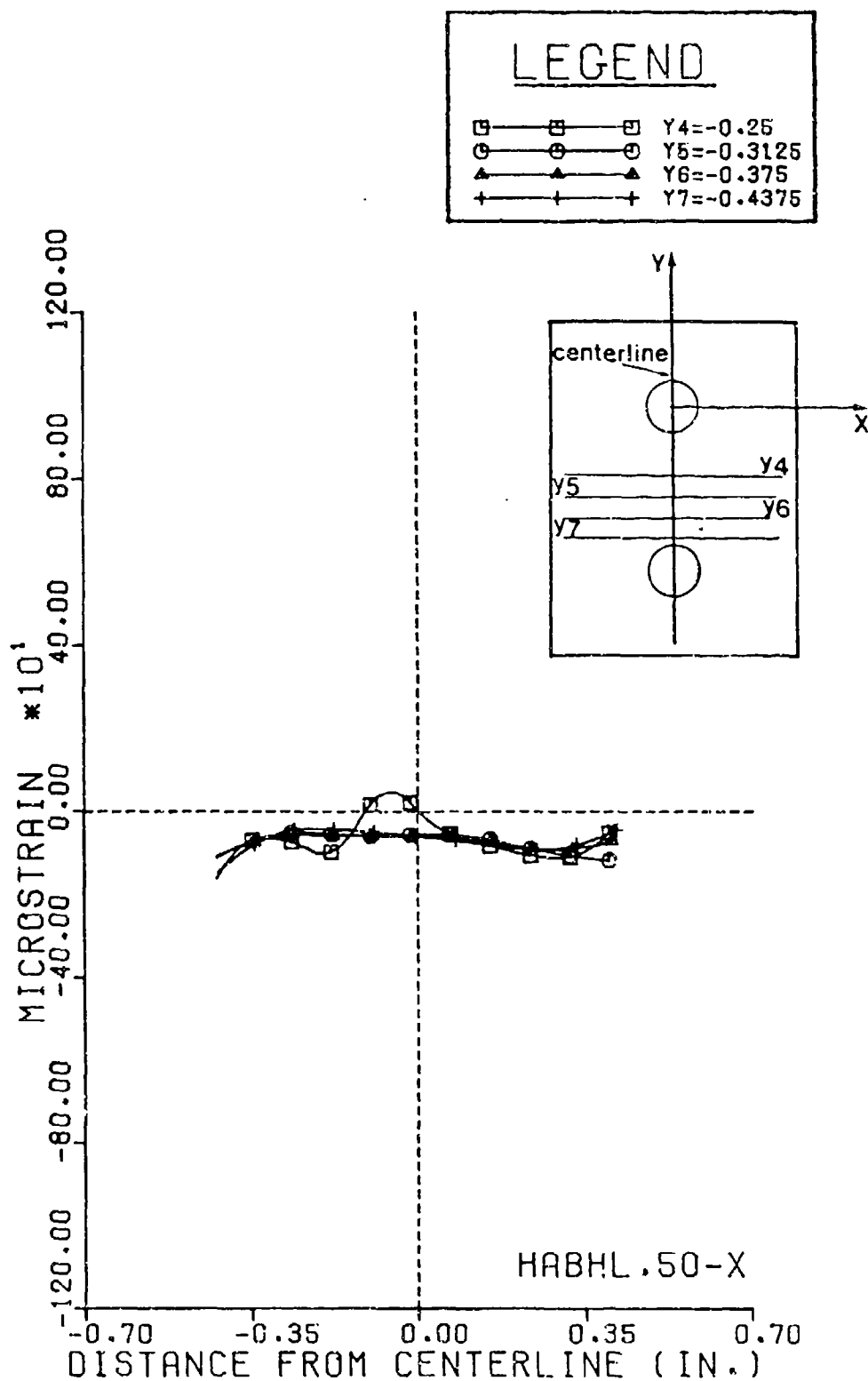


Figure 5-7. Strain ϵ_x along Lines Perpendicular to Load Between Holes

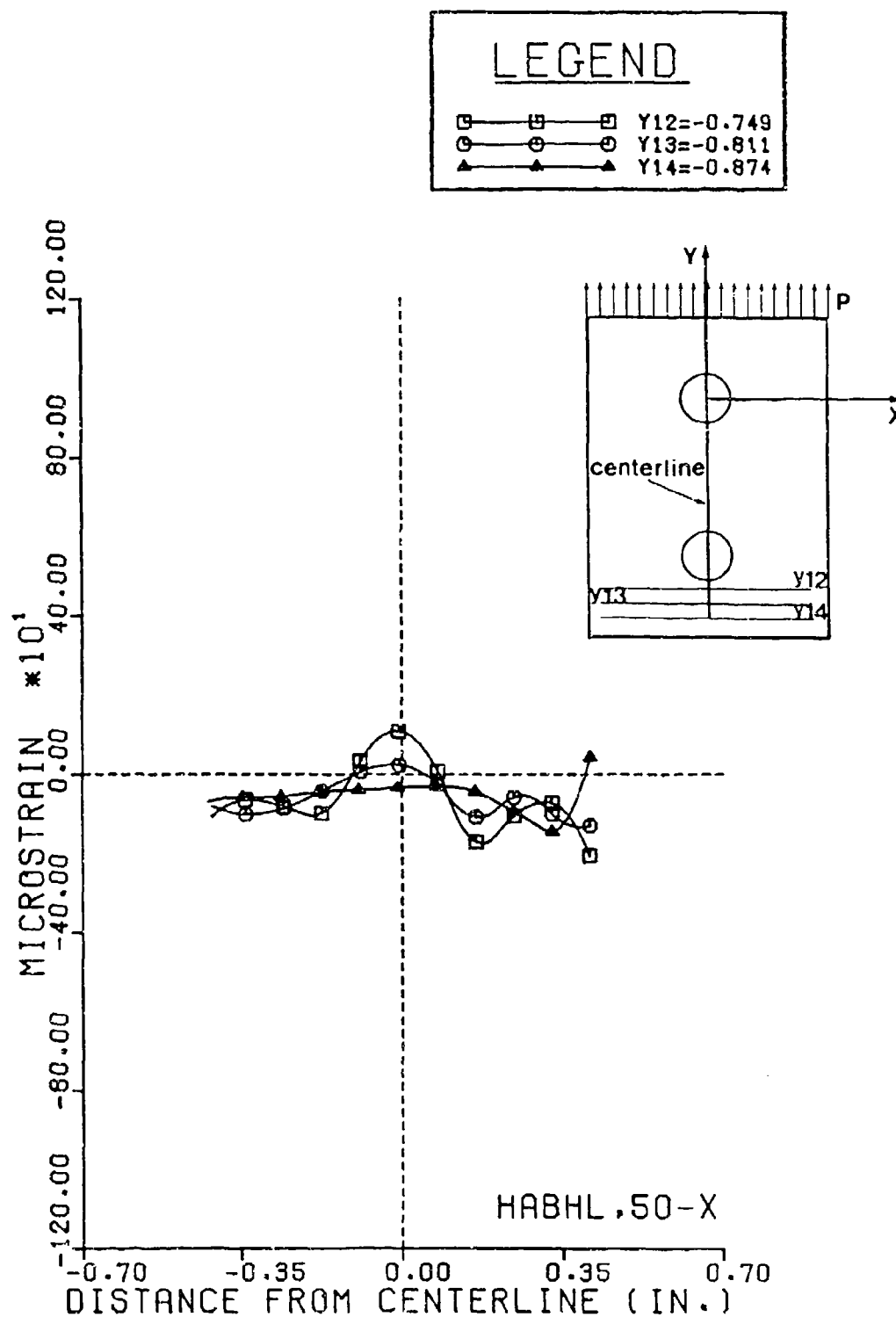


Figure 5-8. Strain ϵ_x along Lines Perpendicular to Direction of Load in Lower bearing Region

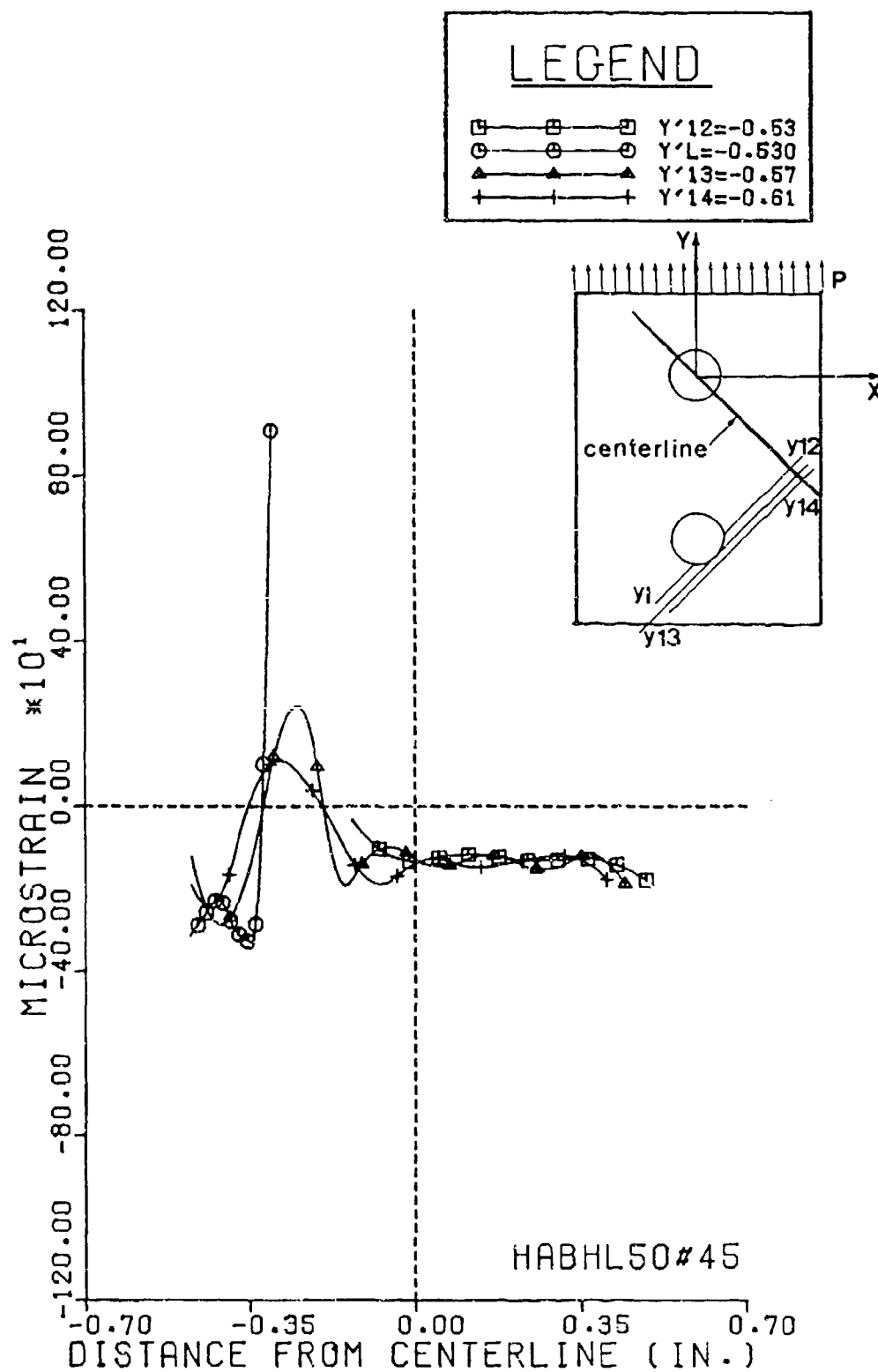


Figure 5-9. Strain ϵ_{45} along Lines 45• to Direction of Load Near Lower Hole

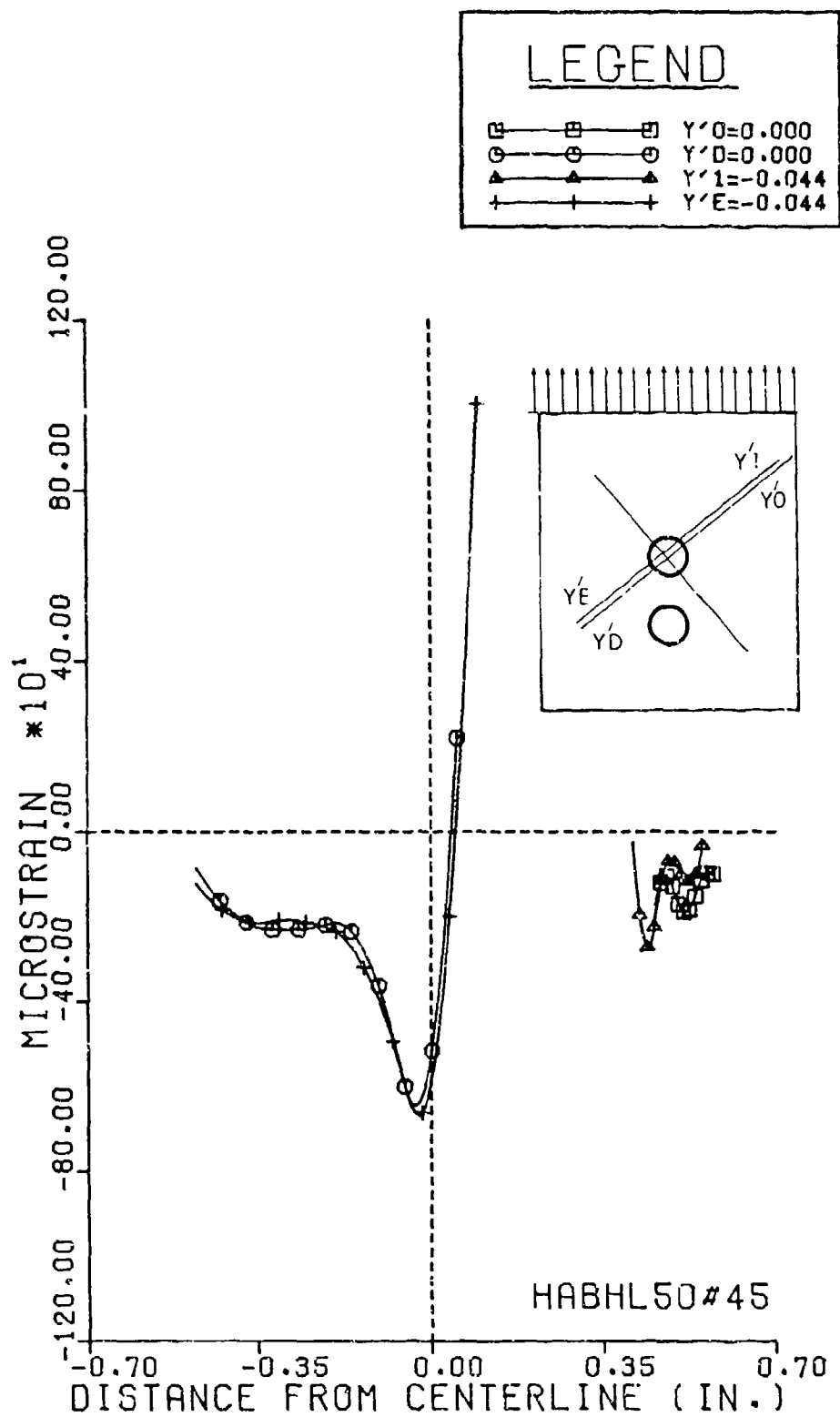


Figure 5-10. Strain ϵ_{45} along Lines 45° to Direction of Load

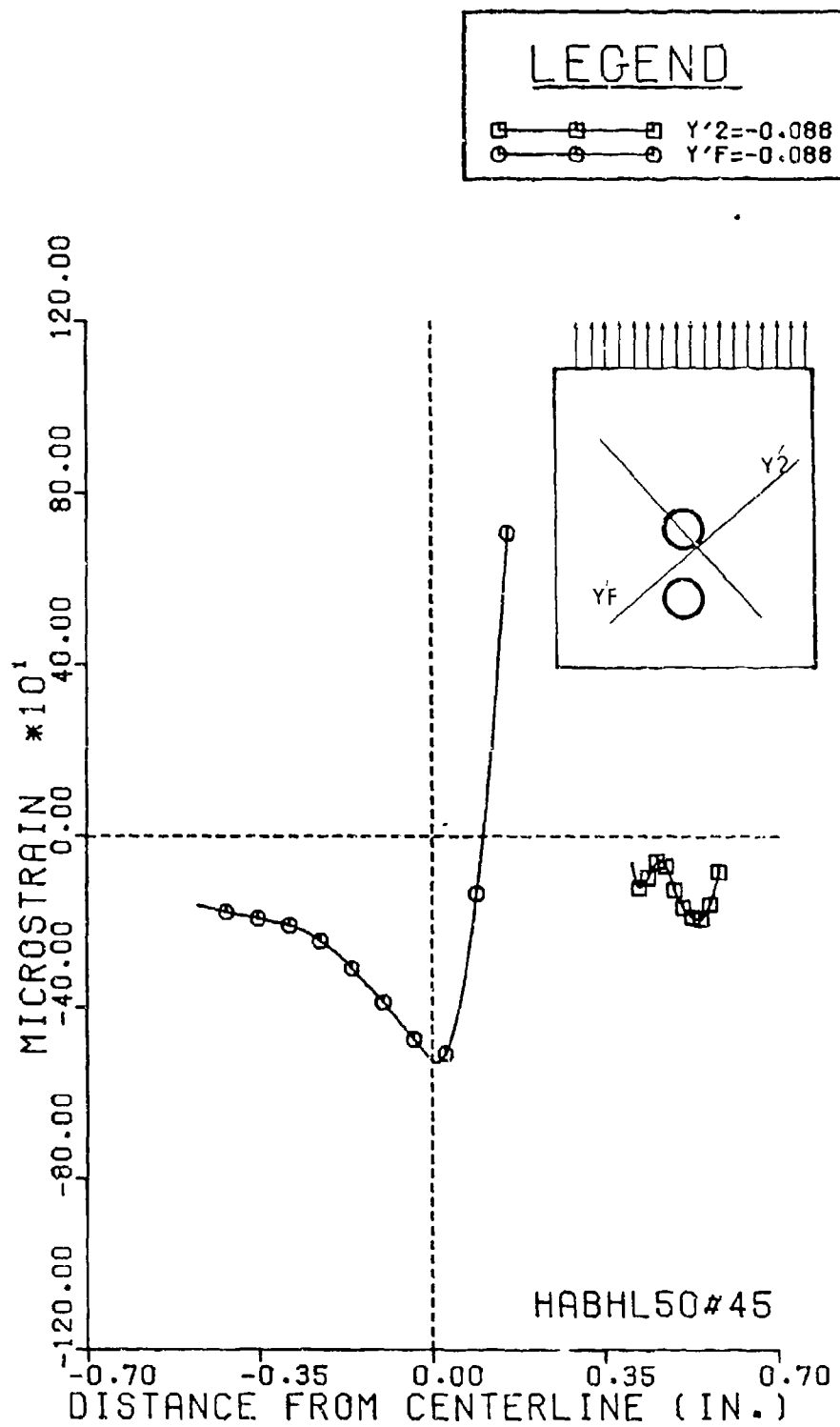


Figure 5-11. Strain ϵ_{45} along Lines 45• to Direction of Load

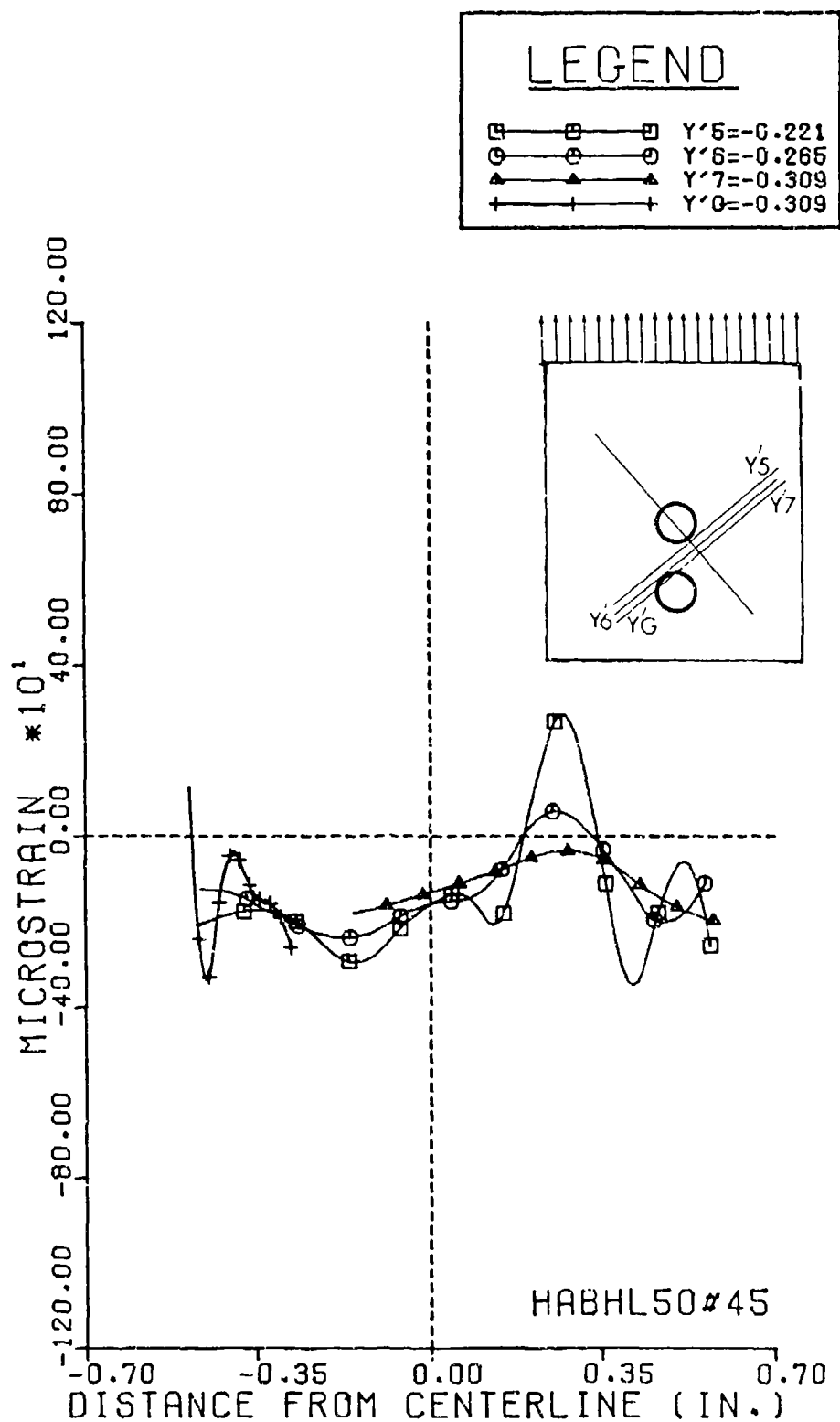


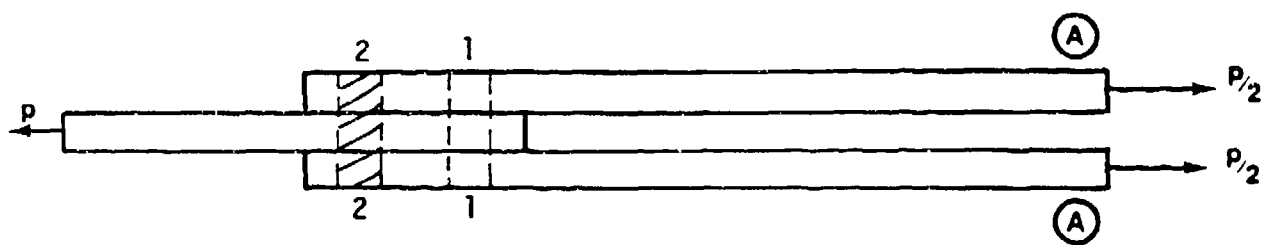
Figure 5-12. Strain ϵ_{45} along Lines 45- to Direction of Load

5.3. Two Holes in Tandem: Lower Loaded

In order to simulate a condition of misalignment between two different laps, both holes were loaded separately, one at a time in tension, using a force of 444N. This condition may well be present in actual conditions of operation in any joint which is assembled under not-so-ideal conditions. When only one hole is being loaded because of the misalignment, the load is introduced to the joint by one pin only. In this case the load transmitted to each section in the two-hole joint is shown in Figure 5-13. The net section of the loaded holes carries the total load. The unloaded hole will act only as a stress raiser.

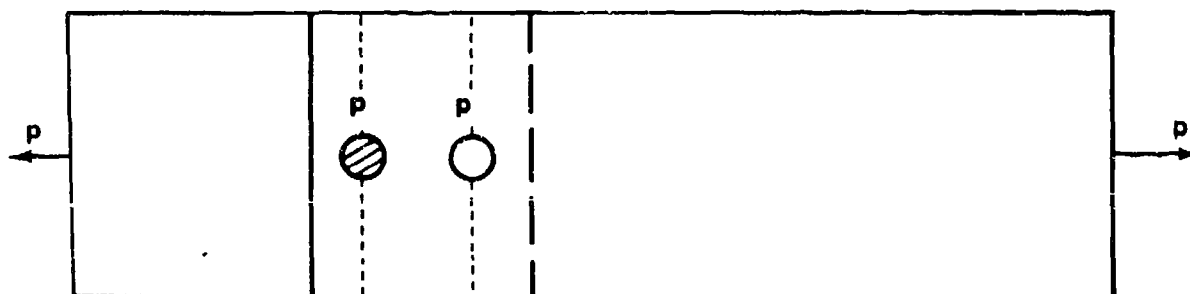
Figures 5-14, 5-15 and 5-16 show Moire fringe patterns of displacement parallel, perpendicular, and at 45° to the direction of loading for this specimen. In Figure 5-14 there is a noticeable increase in the number of fringes in the ligament areas of both holes but especially for the lower hole. This is an indication of a tensile deformation. In the bearing region of the lower hole the decrease in the number of fringes is quite noticable but not in the lower portion of the upper hole. This is an indication of high compressive strain at the edge of the lower hole. Also, the fringes in the upper portions of both holes and in the bearing region of the lower hole are not bent, thus indicating the presence of a high shear deformation. In Figure 5-15 there is a noticeable increase in the number of fringes in the bearing area of the lower hole, but it is difficult to say for the upper hole because of the fringe density. In Figure 5-16 there is a reduction in the number of fringes on the lower left portion of the lower hole and also an increase in the number in the lower right portion, indicating a high compressive strain in the lower left portion and a high tensile strain in the right portion of the lower hole. Figure 5-17 shows strain ϵ_y along several lines located in the ligament region to the right of the two holes. In line $x_2 = 0.125$ which is tangent to both holes, two maximum strains are noticed. For the unloaded hole, the maximum strain occurs at $x = -0.2363$, i.e., below the horizontal diameter of the unloaded hole. For the loaded hole the maximum strain occurs at $x = -0.33$, i.e., below the horizontal diameter of the loaded hole. The magnitude of the strain ϵ_y at the edge of the loaded hole is 1.84 times larger than that at the edge of the unloaded hole. The stress concentration factor for the upper hole is $k = 4.97$ and for the lower hole is $k = 9.16$.

As can be seen in Figure 5-18, there exists above the unloaded hole a tensile strain; but, closer to the upper edge, the strain becomes negative. Below the unloaded hole the strain fluctuates from negative to positive, becoming zero and then increasing again. This point where the strain is zero was also noticed by Hyer and Liu [4.23] in an isotropic specimen. They showed that this point (an isotropic point) will have a position between the two holes which depends on the ratio of loads shared by each hole. Beneath the loaded hole the strain is compressive as expected. For lines closer to the long edges of the specimen the strain takes an average value (see Figure 5-19). The case of a homogenous or orthotropic body for an infinite plate with a

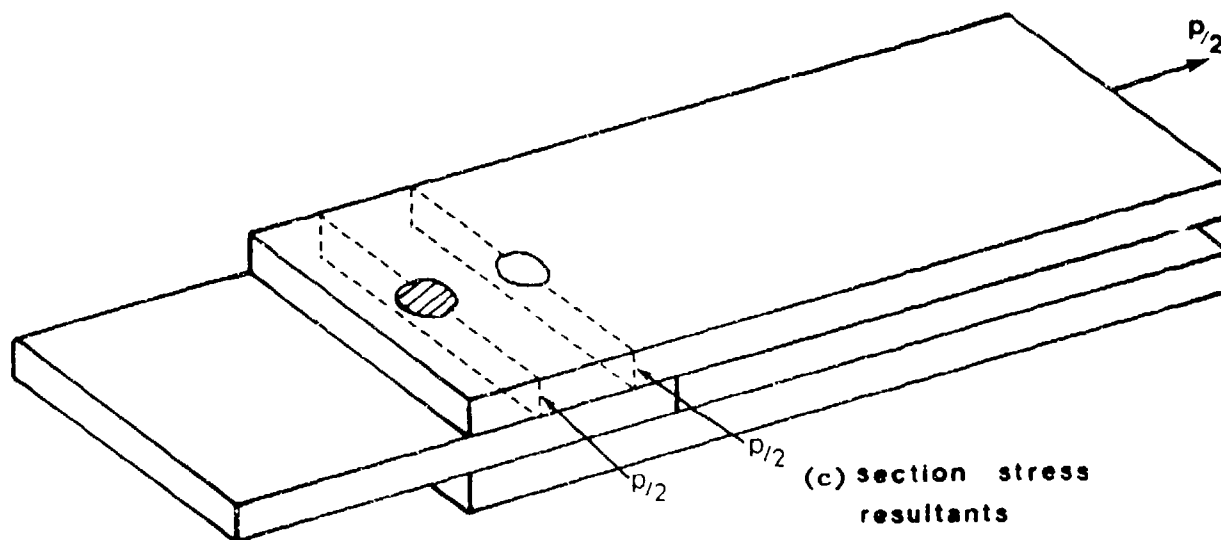


(a) Side View

section stress
resultants



(b) Top View



(c) section stress
resultants

Figure 5-13. Stress Resultants for Two Tandem Holes: Lower Loaded

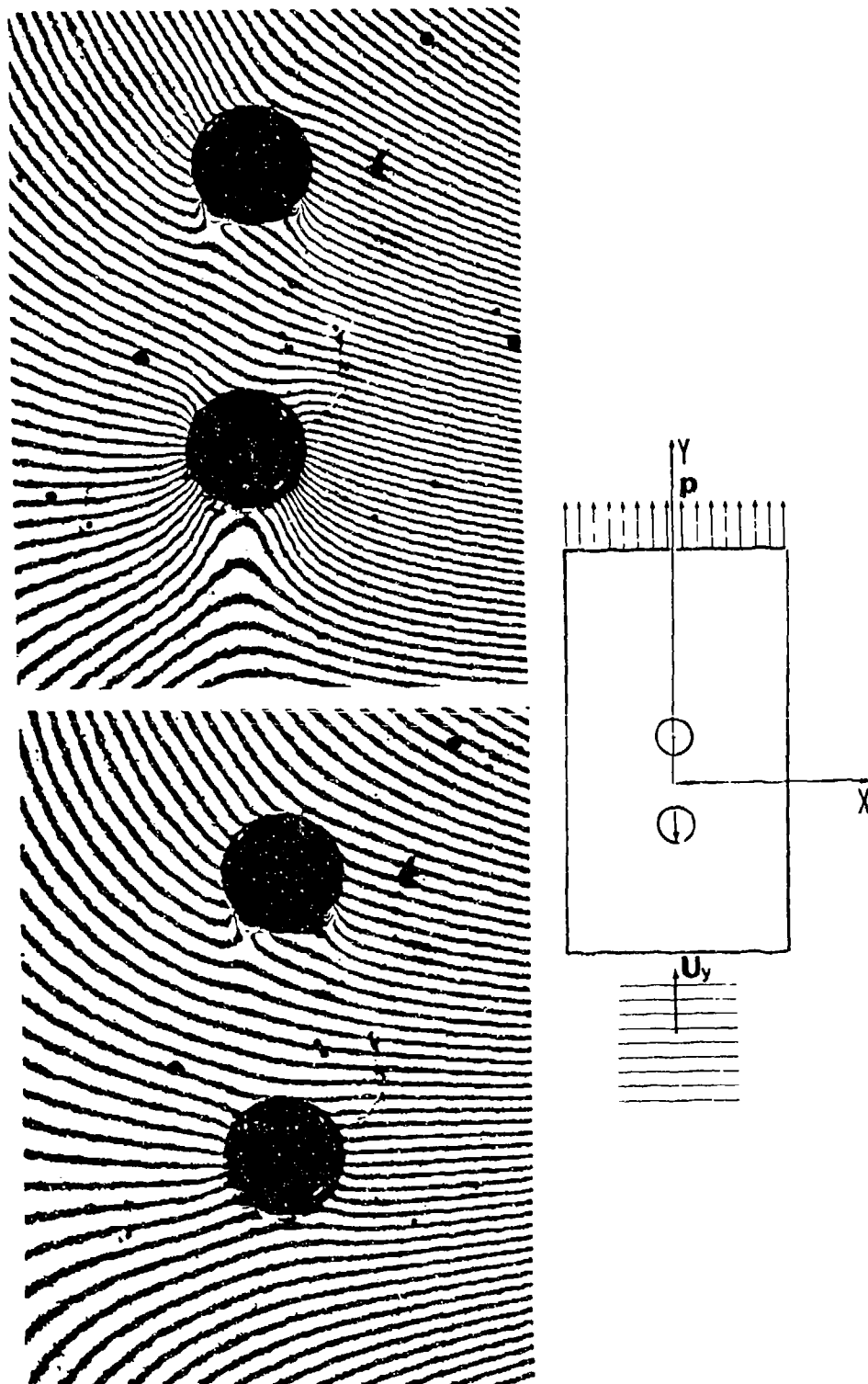


Figure 5-14. Moire Fringes of Displacement Parallel to Direction of Load for Specimen with Tandem Hole Array when Lower Hole is Loaded

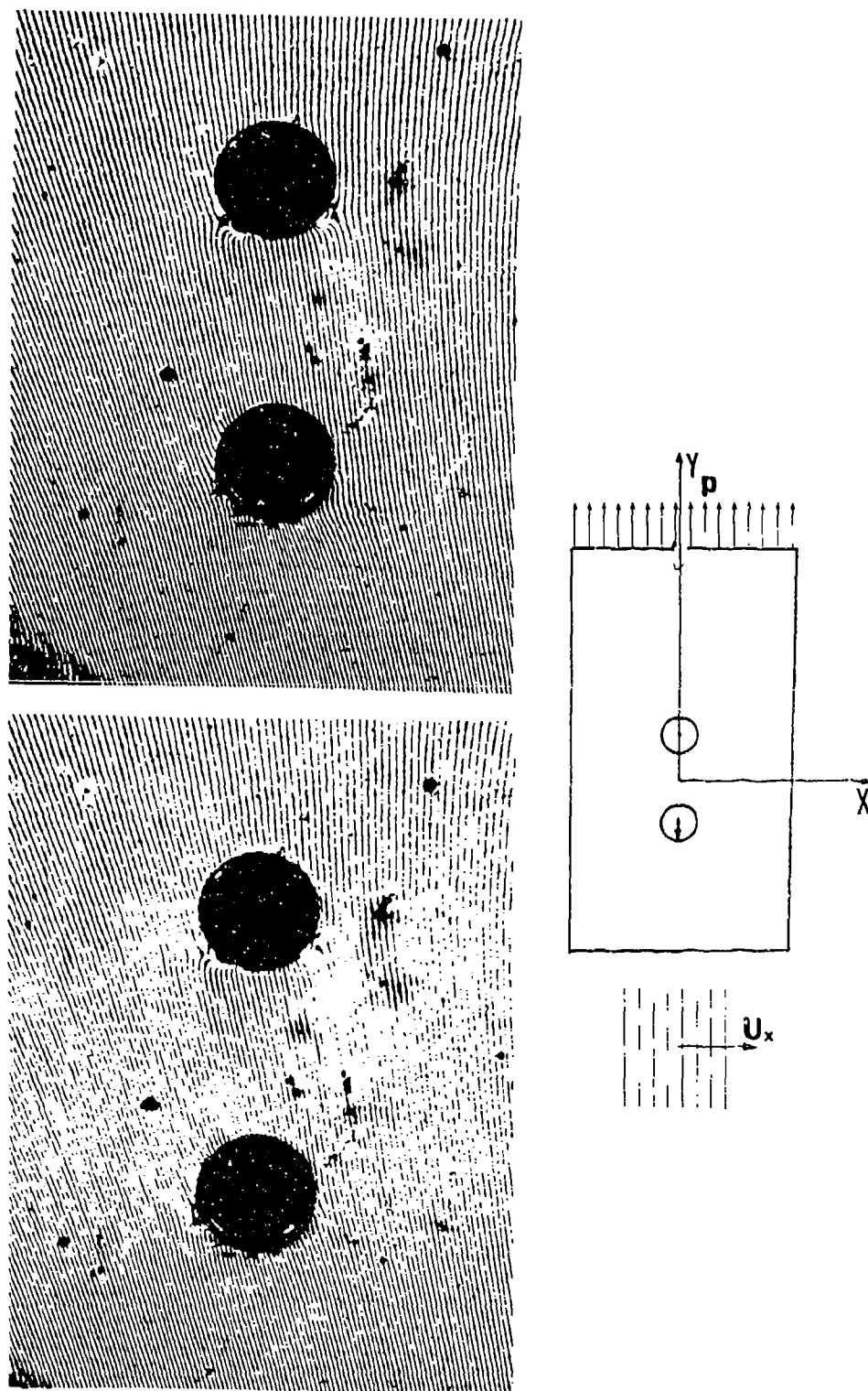


Figure 5-15. Moire Fringes of Displacement Perpendicular to Direction of Load for Specimen with Tandem Hole Array when Lower Hole is Loaded

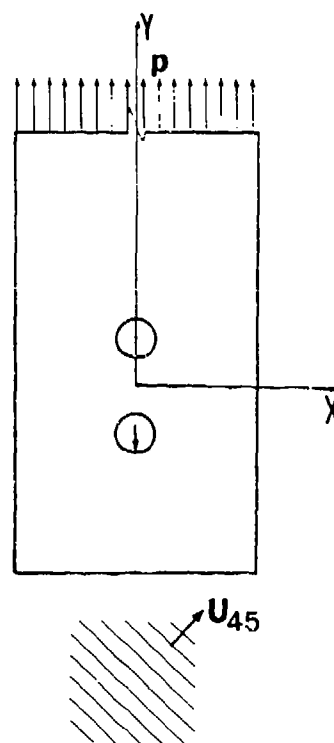
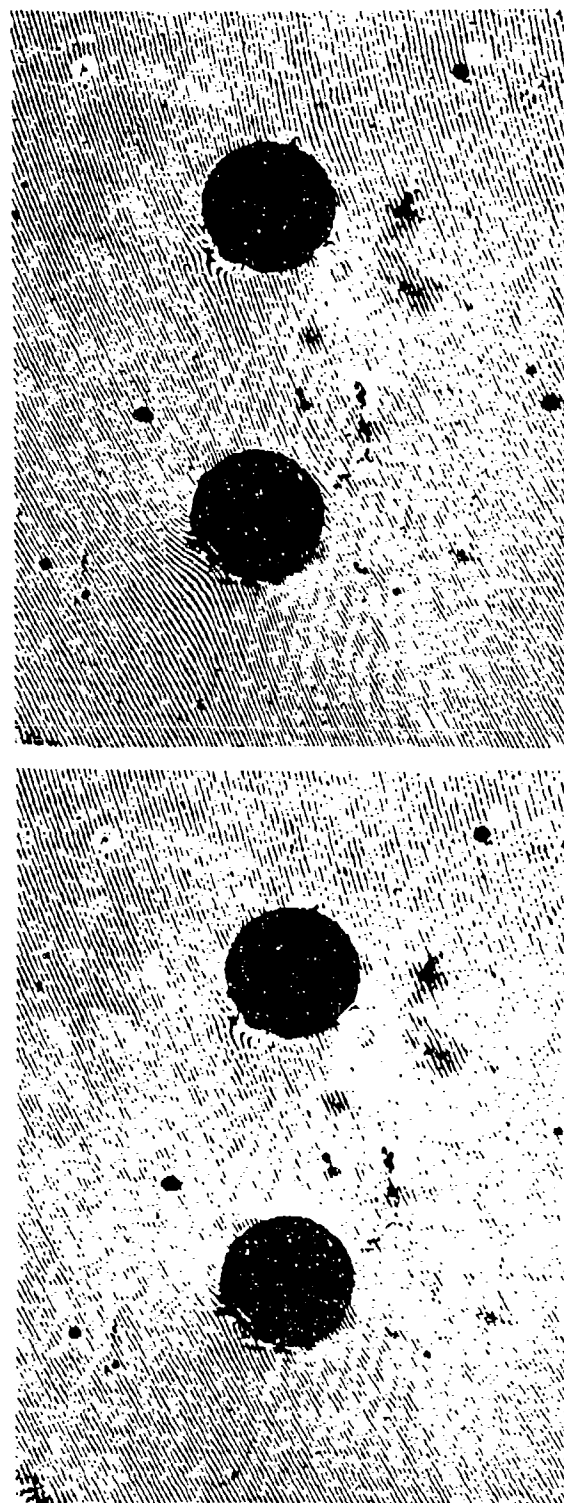


Figure 5-16. Moiré Fringes of Displacement 45° to Direction of Load for Specimen with Tandem Hole Array when Lower Hole is Loaded

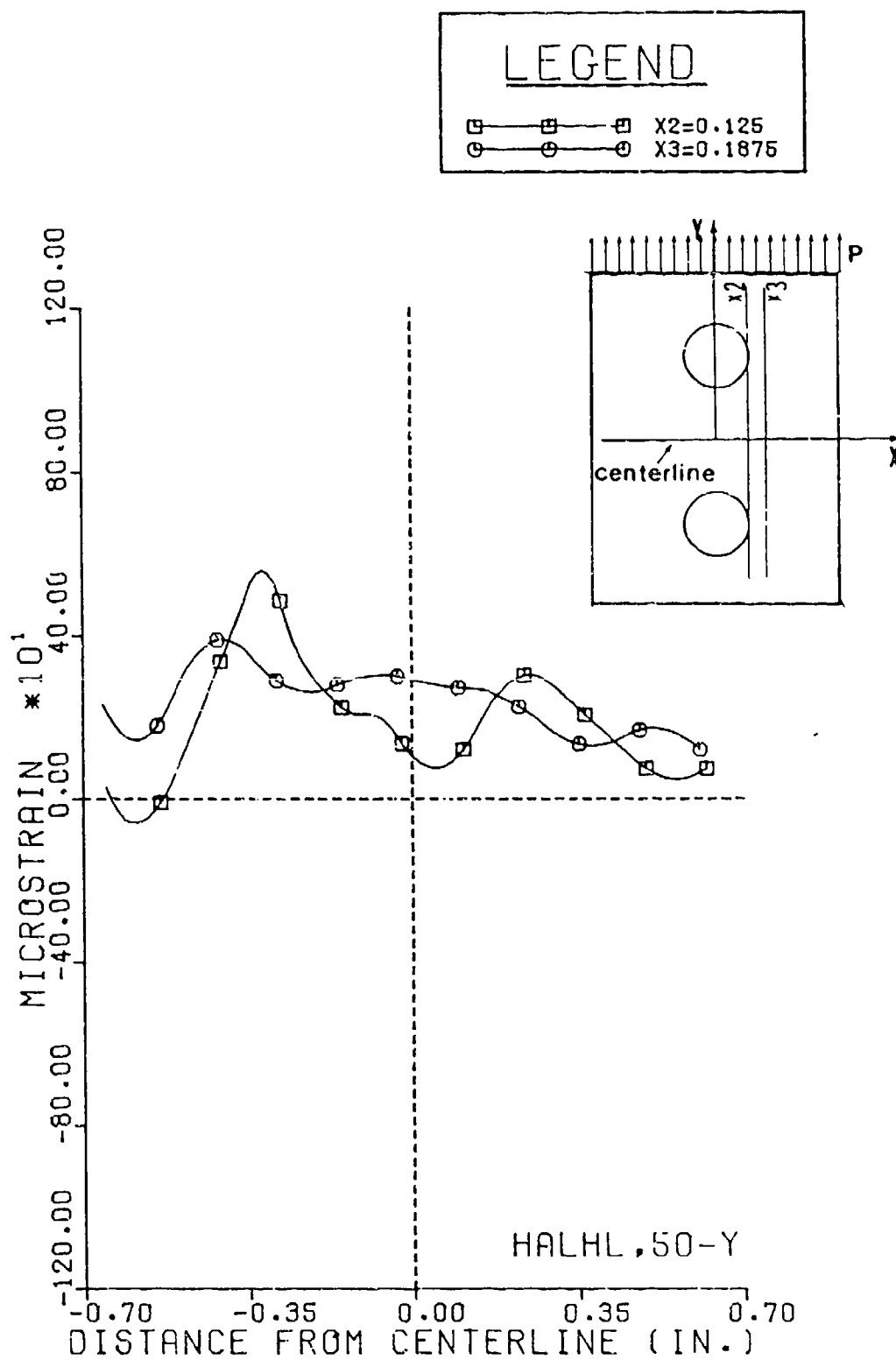


Figure 5-17. Strain ϵ_y along Lines Parallel to Direction of Load

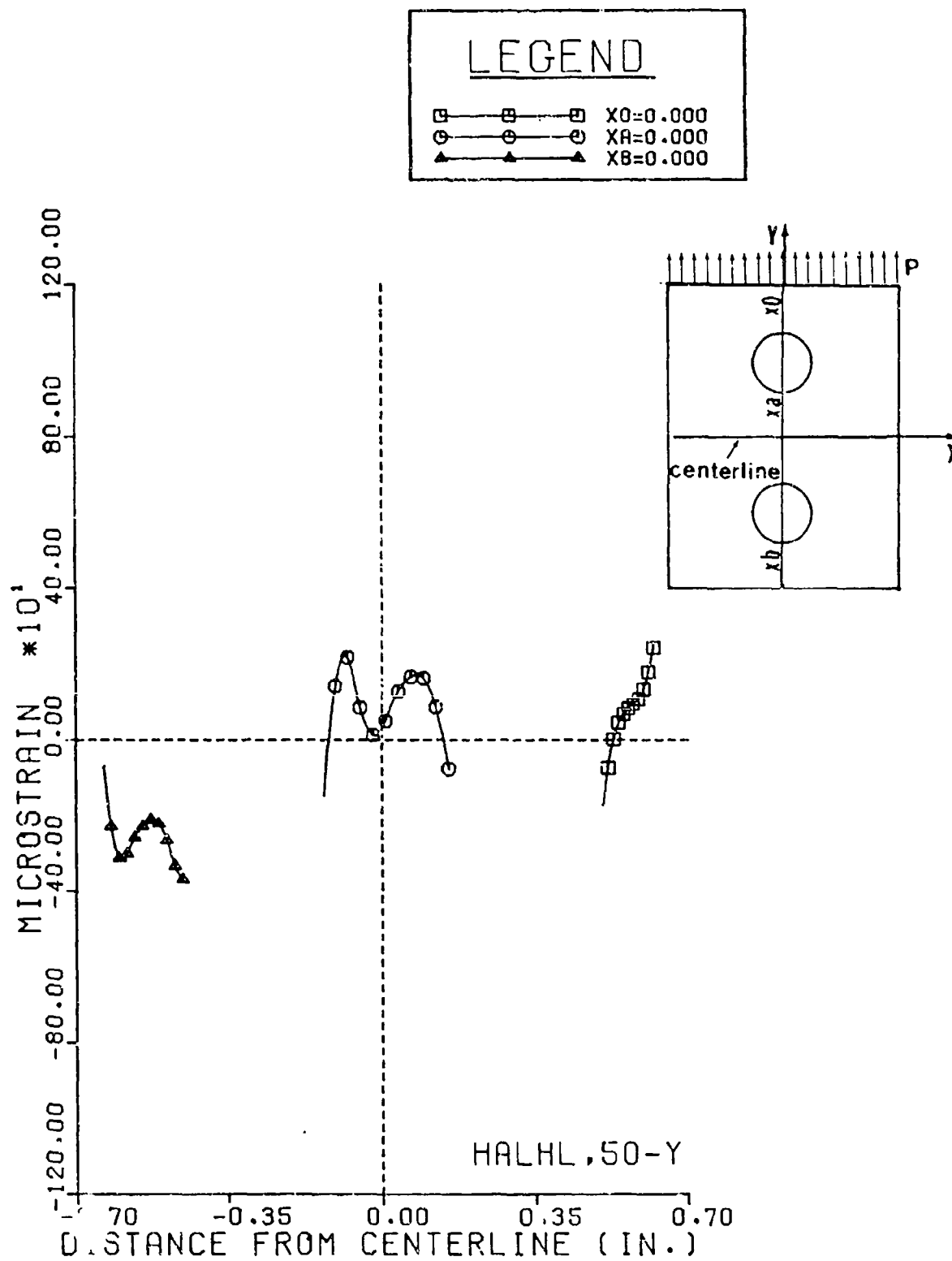


Figure 5-18. Strain ϵ_y along Lines Parallel to Direction of Load

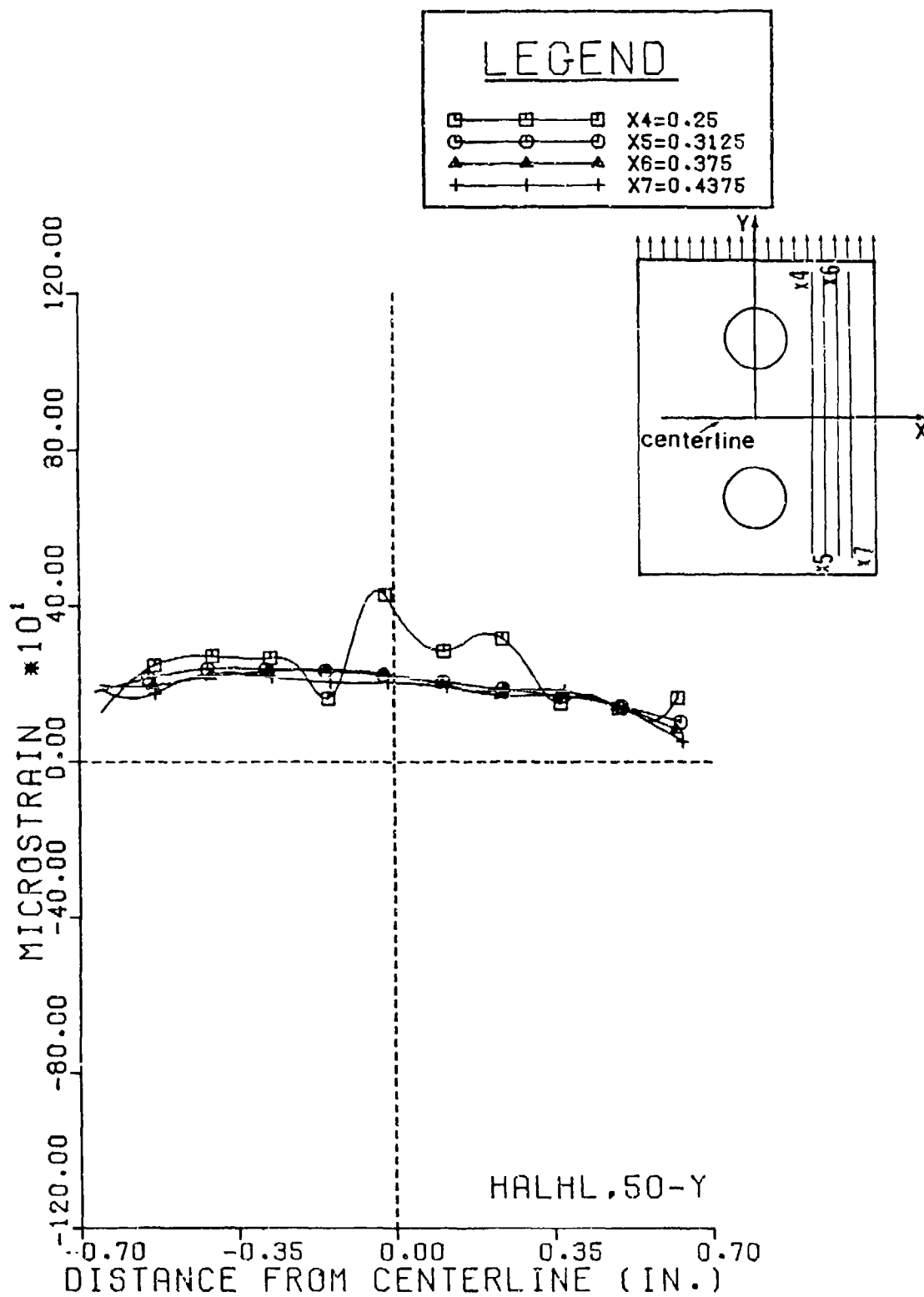


Figure 5-19. Strain ϵ_y along Lines Parallel to Direction of Load

circular cut-out has been studied by several authors. The most relevant presentation was given by Lekhnitskii [5.3]. The stress concentration factor for an orthogonally reinforced glass fiber plastic with a circular cutout loaded in tension, in the principal material direction, is found to be $k = 4.08$ at the edge of the hole. In this case the stress concentration factor at the edge of the hole in the direction of loading, agrees with the value established by Lekhnitskii [5.3]; but at the lower edge of the unloaded hole the SCF would also be negative but of different magnitude.

Figure 5-20 shows strain ϵ_x for two lines located above and below the loaded hole. There is a considerable difference in the magnitude of strain, especially between the strain at the contact edge and the strain in the upper half of the hole. A slight asymmetry is observed in the strain distribution especially for the strain above the loaded hole.

Figure 5-21 shows ϵ_{45} for lines located in the bearing region and above the lower hole. Again, the location of the maximum shear strain coincides with the points where ϵ_x and ϵ_y are zero. It is observed that ϵ_{45} above the lower hole is relatively small, compared with the strain in the bearing region. In the lower right edge of the hole, ϵ_{45} is positive, and then it increases to a maximum tensile value, after which it decreases to a negative strain. The same behavior has been observed for a single pin loaded hole [5.2].

5.4. Two Holes in Tandem: Upper Loaded

The third test was performed with the same specimen, but this time loading only the upper hole. Figure 5-22 shows a free body diagram of the joint and plates and the expected load distribution.

In this case, each net section of the two holes carry the total load, but the unloaded hole acts only as a stress raiser.

Figures 5-23, 5-24, and 5-25 show Moire fringe patterns of displacement parallel, perpendicular, and at 45° respectively to the direction of the applied load. In Figure 5-23, the number of fringes per unit of length increases considerably in the ligament regions of the upper hole. A tensile strain is present in both ligaments in the direction of loading. In Figure 5-23 there is also a noticeable decrement of the number of fringes in the bearing region of the upper hole due to the compressive strain present in that area. In Figure 5-24, analyzing the shape and number of the fringes, it can be seen that in the region of the upper hole, there exists a negative strain in the direction perpendicular to the applied loading and in the bearing region a positive strain exists in the same direction. Figure 5-25 shows the same characteristics for the strain in the upper hole in the 45° orientation.

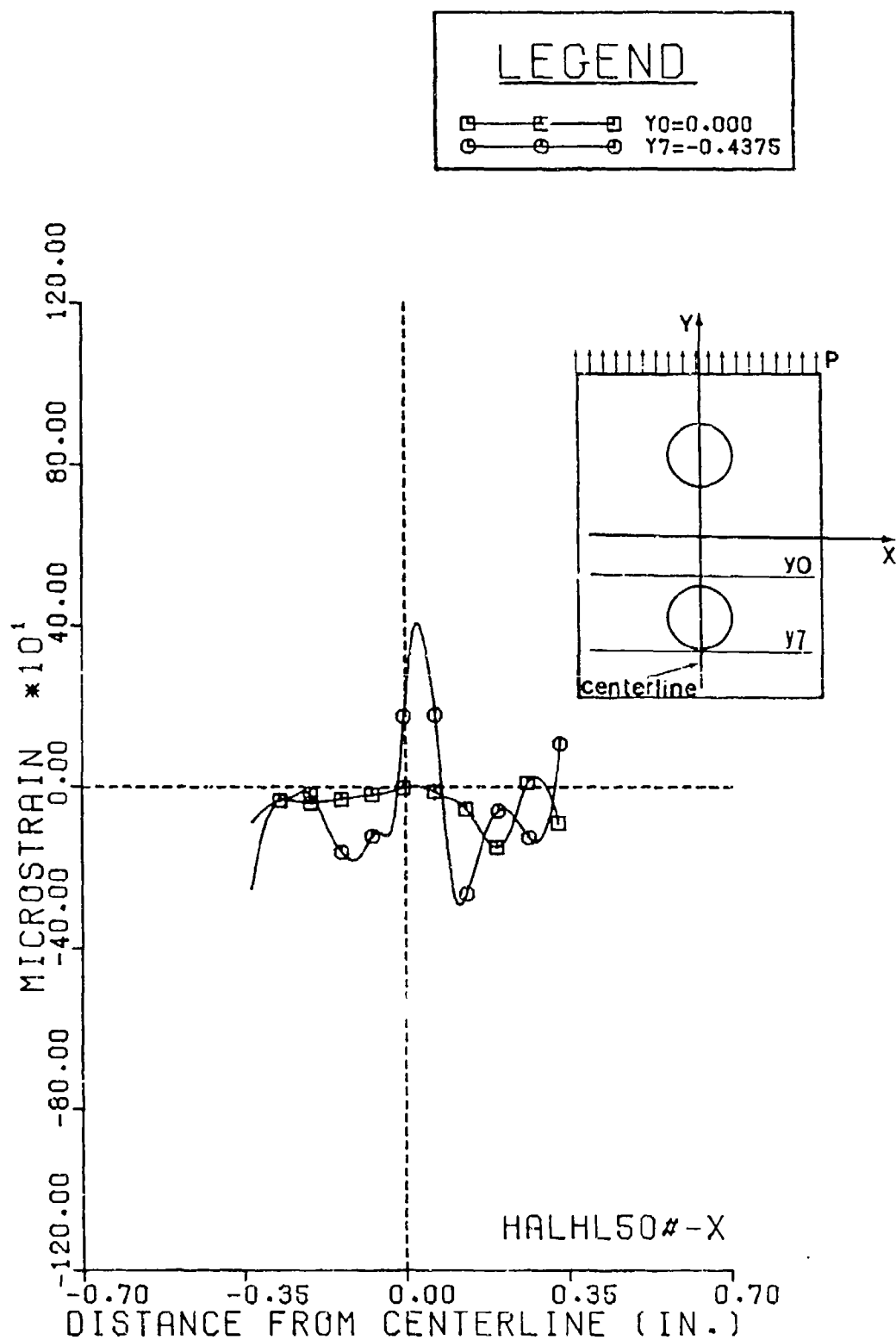


Figure 5-20. Strain ϵ_x along Lines Perpendicular to Direction of Load

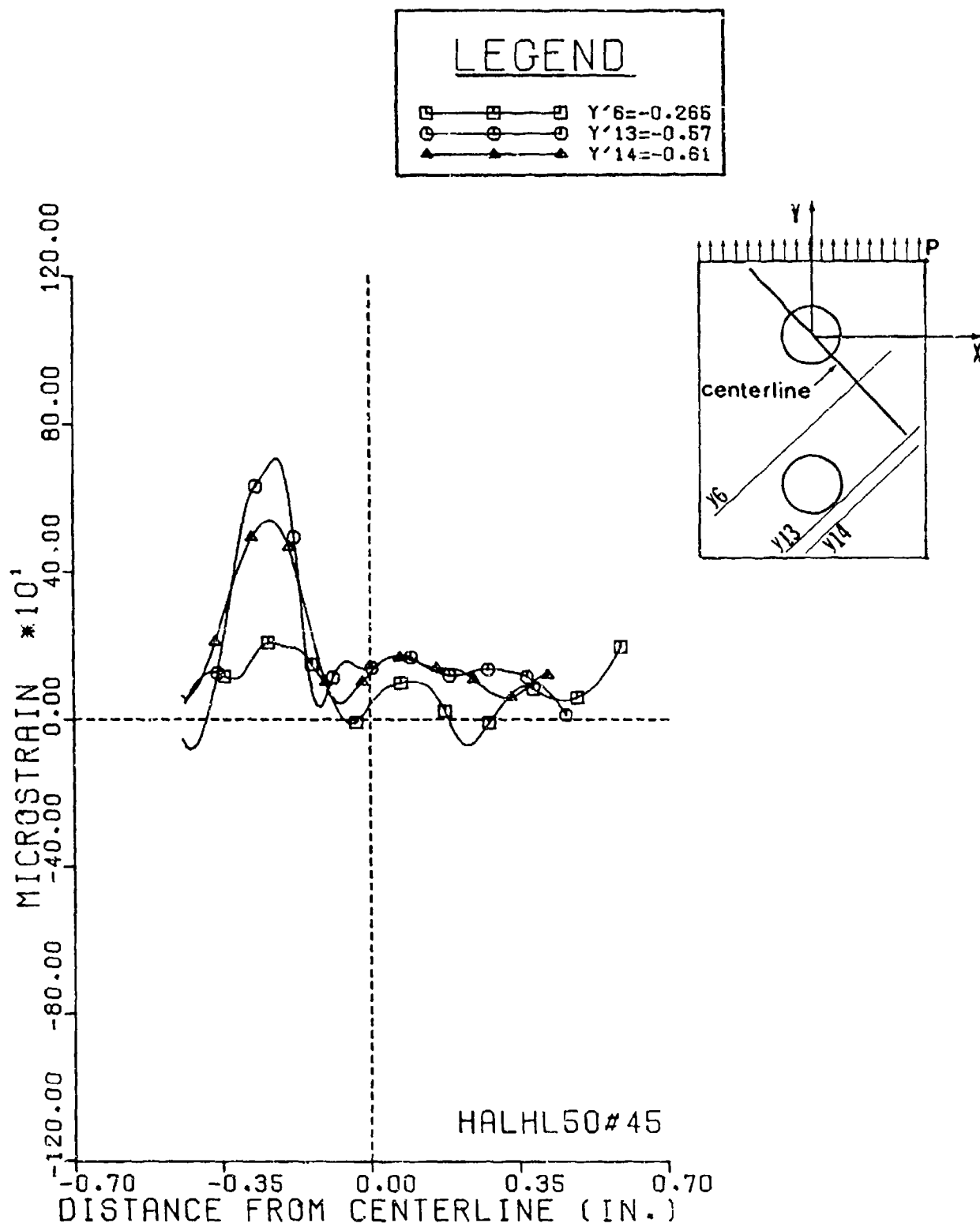
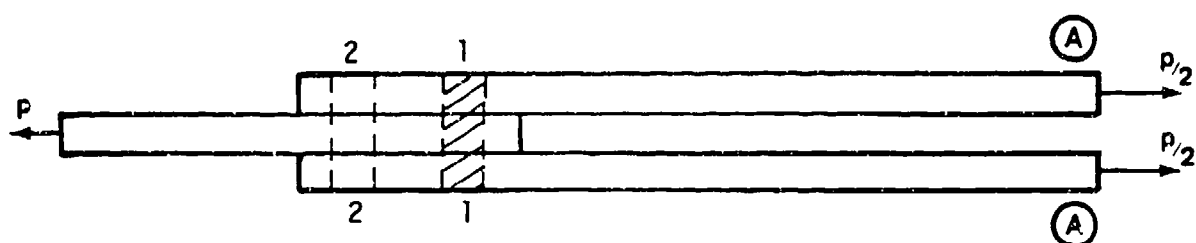
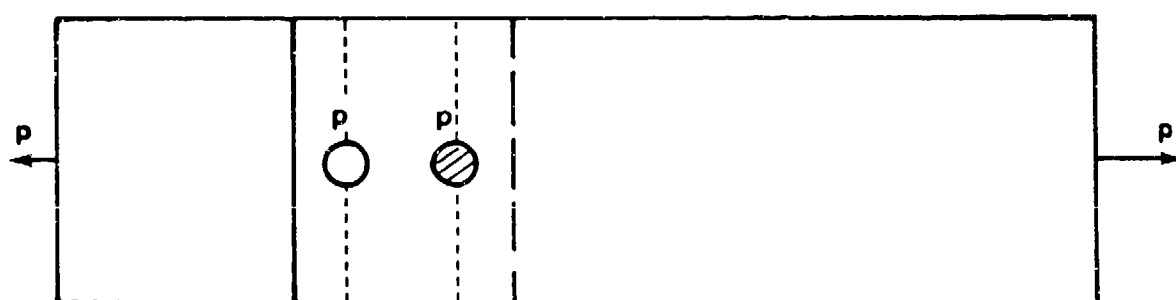


Figure 5-21. Strain ϵ_{45} along Lines 45• to Direction of Load

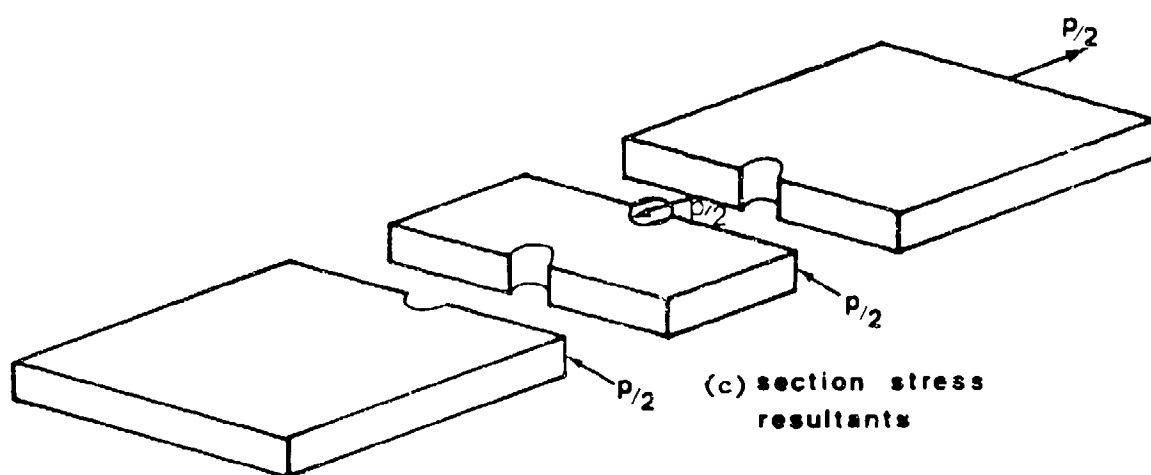


(a) Side View

section stress
resultants



(b) Top View



(c) section stress
resultants

Figure 5-22. Stress Resultants for Two Tandem Holes: Upper Loaded

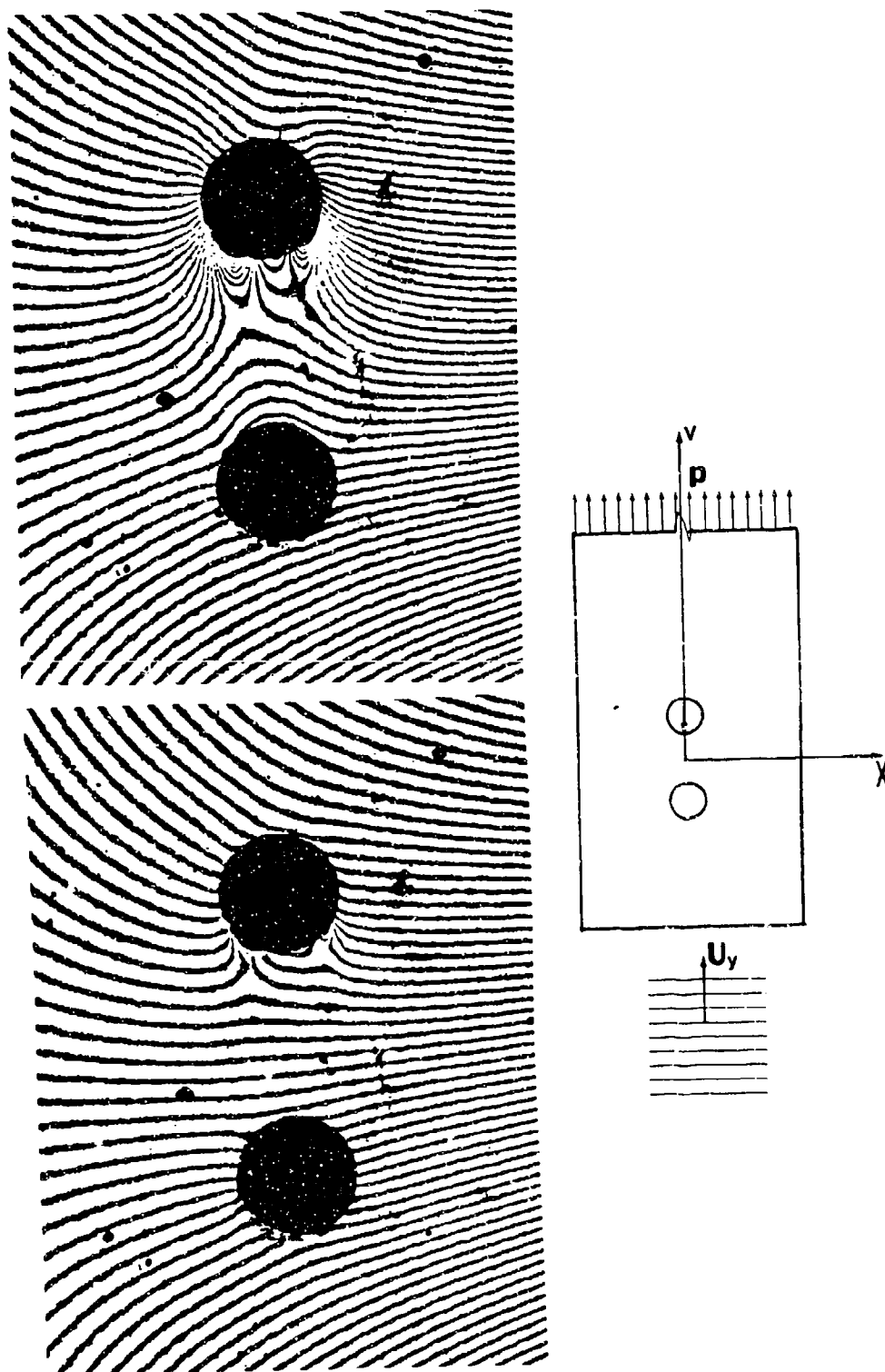


Figure 5-23. Moiré Fringes of Displacement Parallel to Direction of Load for Specimen with Tandem Hole Array when Upper Hole is Loaded

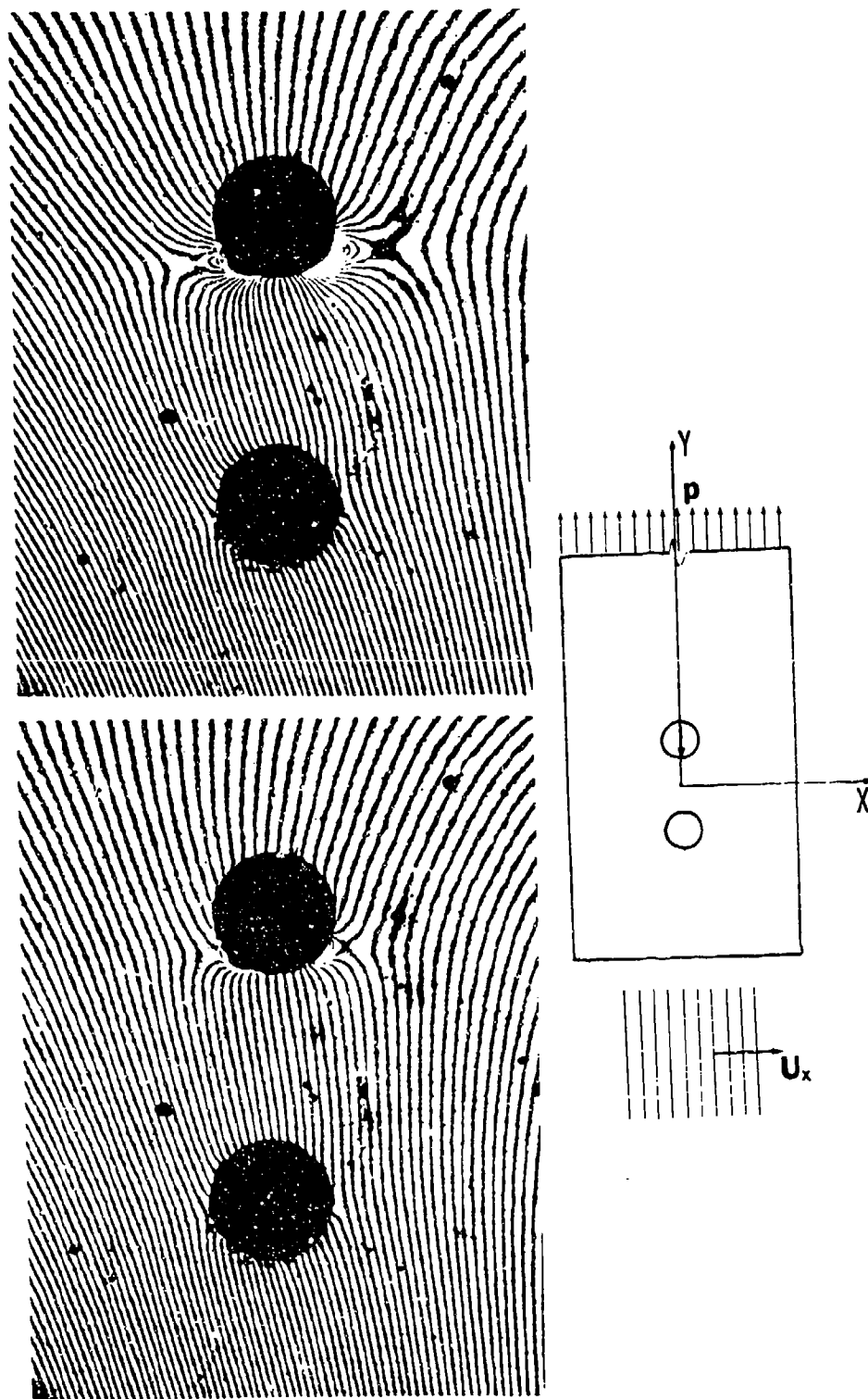


Figure 5-24. Moiré Fringes of Displacement. Perpendicular to Direction of Load for Specimen with Tandem Hole Array when Upper hole is Loaded

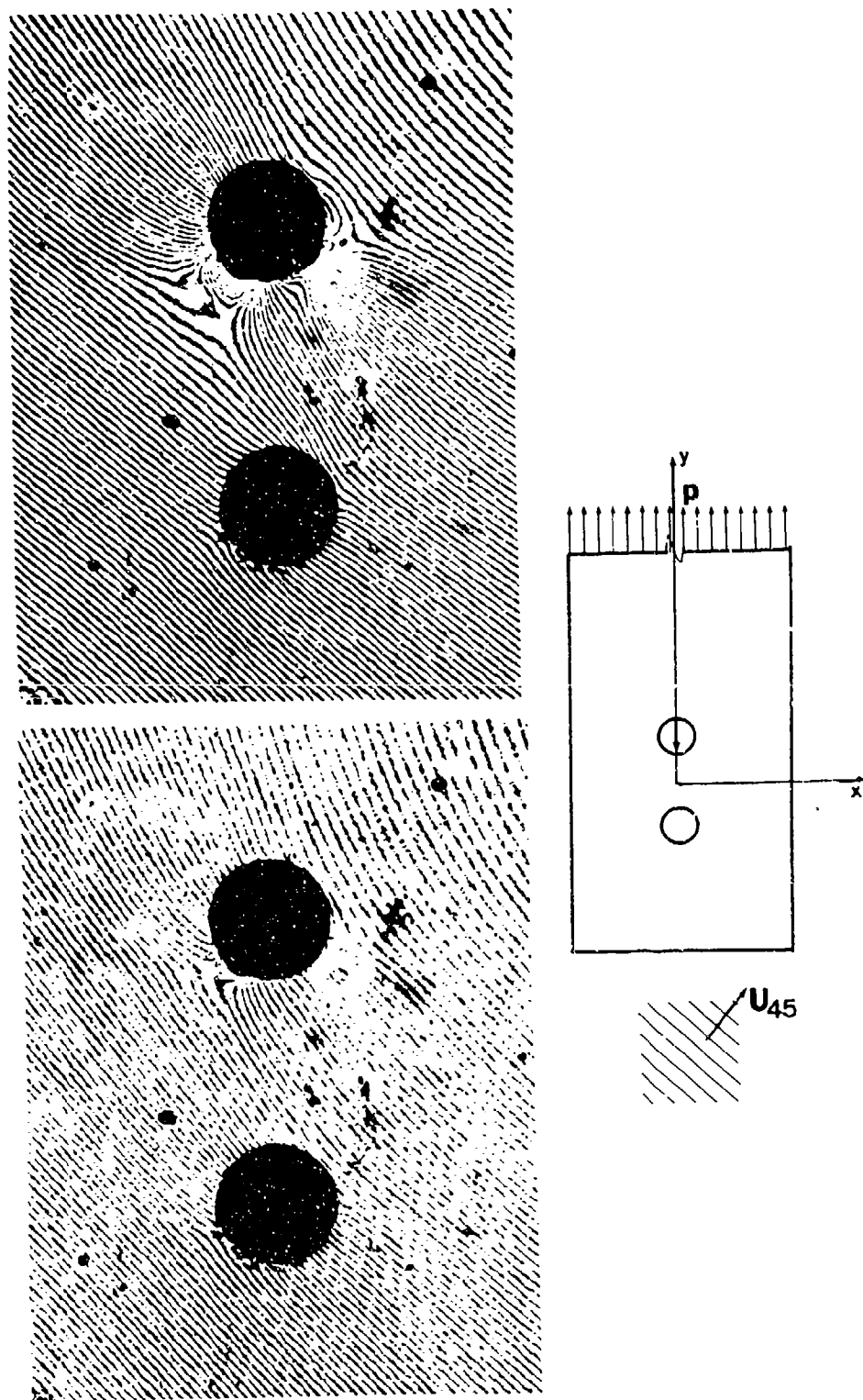


Figure 5-25. Moire Fringes of Displacement at 45° to Direction of Load for Specimen with Tandem Hole Array when Upper Hole is Loaded

Contrary to the behavior of the upper hole there is little noticeable change in number and shape of the fringes near the lower hole. Figure 5-26 shows strain ϵ_y for lines loaded in the ligament region to the right of both holes. From line $x_2 = 0.125$, the strain ϵ_y attains a maximum at $y = 0.1464$, i.e., below the horizontal diameter of the hole. Contrary to the case in which the lower hole is loaded, there is not a noticeable increase in the strain at the edge of the unloaded hole. The sign of the strain on the bearing area remains compressive even at the edge of the unloaded hole. The SCF for these two holes are: for the upper hole $k = 12.1$, and for the lower hole $k = 1.0$.

The stress distribution near the lower hole can be explained if the behavior of a plate with a circular cutout is remembered [4.24]. In the direction of loading, the SCF is positive, and this stress field is influenced by the bearing area of the upper pin-loaded hole. Thus, there exists a cancellation of signs of strains resulting in a low-level stress in the region between the two holes. Also, in the region between the two holes, there exists a point where the strain becomes zero. This point is located slightly above the unloaded hole. For lines located closer to the long edge of the specimen, the magnitude of the strain remains positive and approaches an average value.

Figure 5-27 shows strain ϵ_y for lines encompassing the ligament area and the bearing region of the upper hole. Some asymmetry is observed in the strain distribution in the ligament areas. The right-hand side appears to have a slightly higher strain than the left side. Also, the magnitude of the strain at $y_3 = 0.1875$ is higher than the strain at the edge of the hole.

Figure 5-28 shows strain ϵ_{45} for parallel lines encompassing the ligament and bearing regions of the upper hole. It is observed in lines $y_4 = -0.177$ that the strain ϵ_{45} is tensile in the ligament region but it becomes negative and it changes back to positive strain again. This peak value is associated with the maximum value of the shear strain.

ϵ_{45} behaves in a more complicated way for this case than for the single pin-loaded hole but, in the region between the two holes there exists an interaction between the compressive nature of the bearing region of the upper hole and the tensile nature of the strain in the lower hole.

5.5. Two Holes in Parallel: Both Loaded

The fourth case studied was a specimen with the two holes positioned in a row perpendicular to the direction of the load. In this case the same load was applied (444 N) using a steel cable and pulley to introduce the load to each pin. Using the assumption that each pin will transmit the same amount of load, the distribution of forces is shown in Figure 5-29.

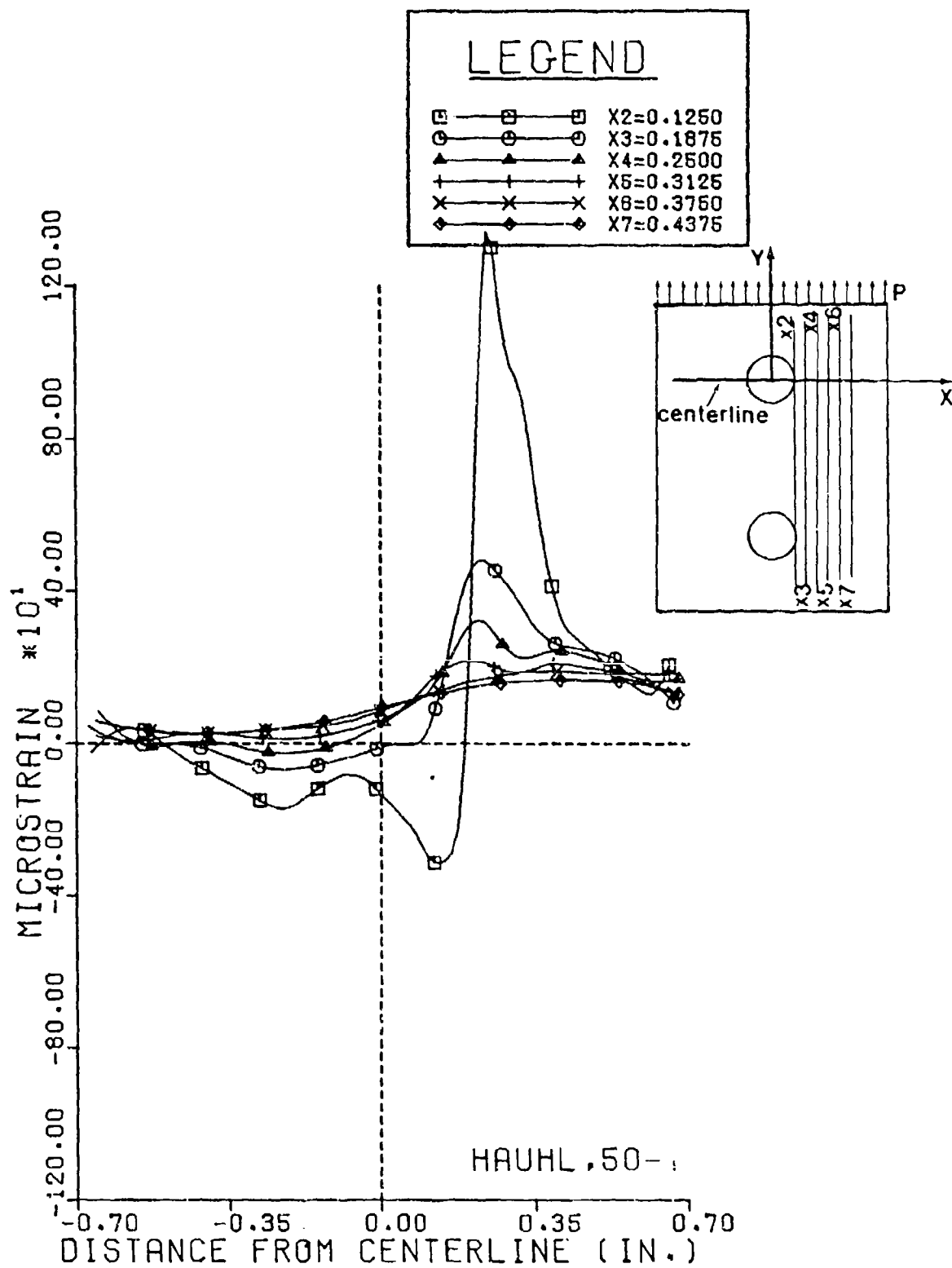


Figure 5-26. Strain ϵ_y along Lines Parallel to Direction of Load

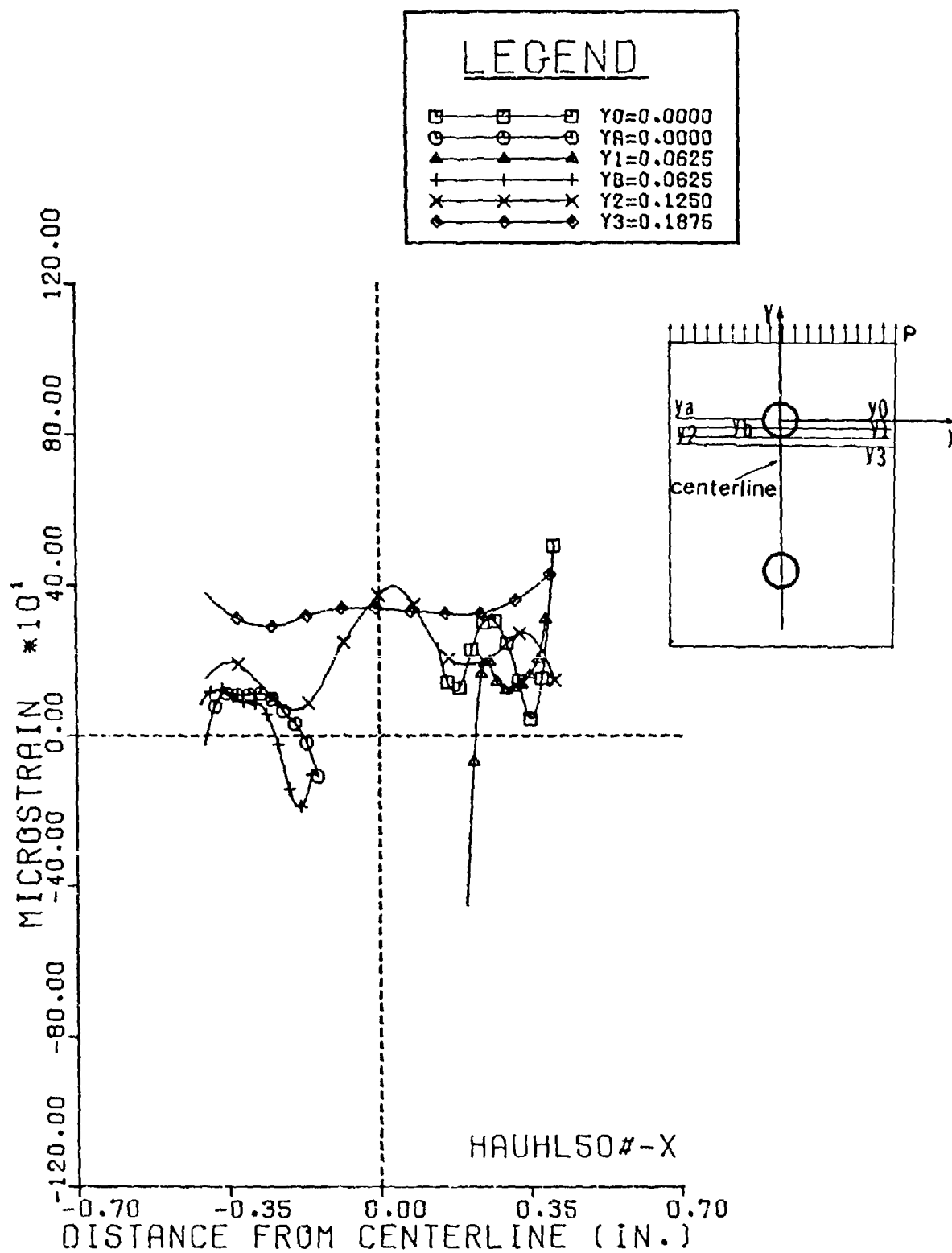


Figure 5-27. Strain ϵ_x along Lines Perpendicular to Direction of Load

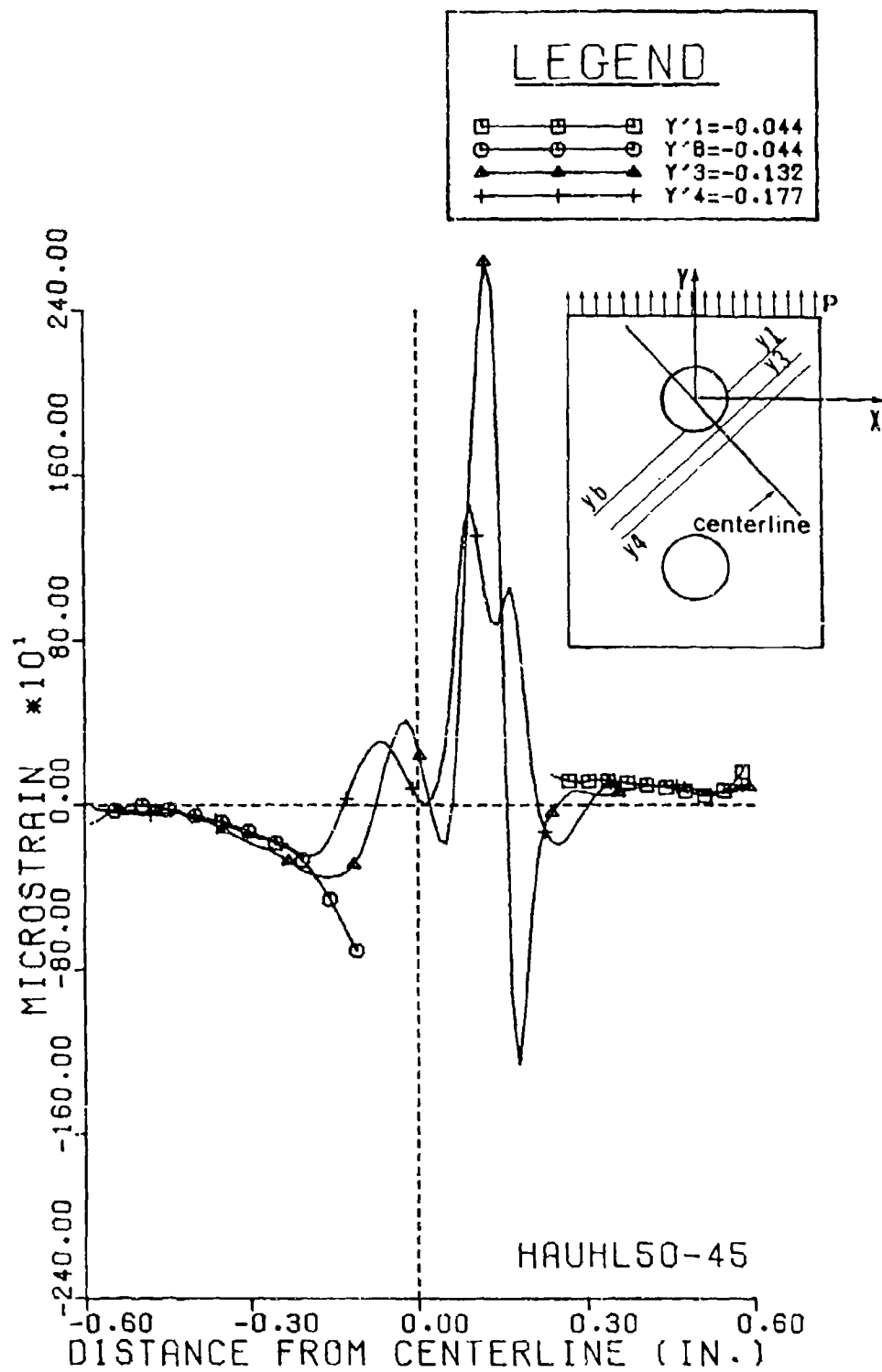
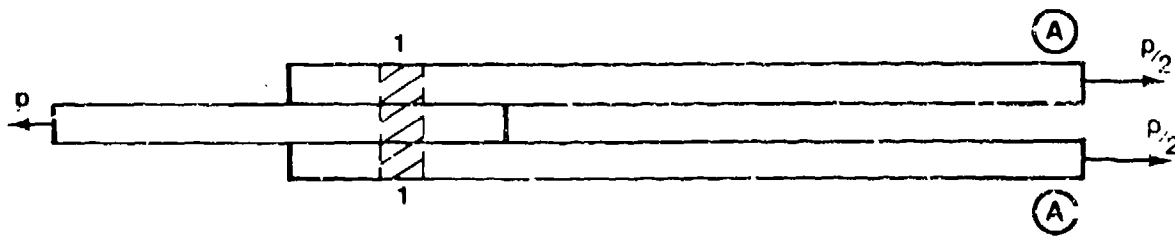
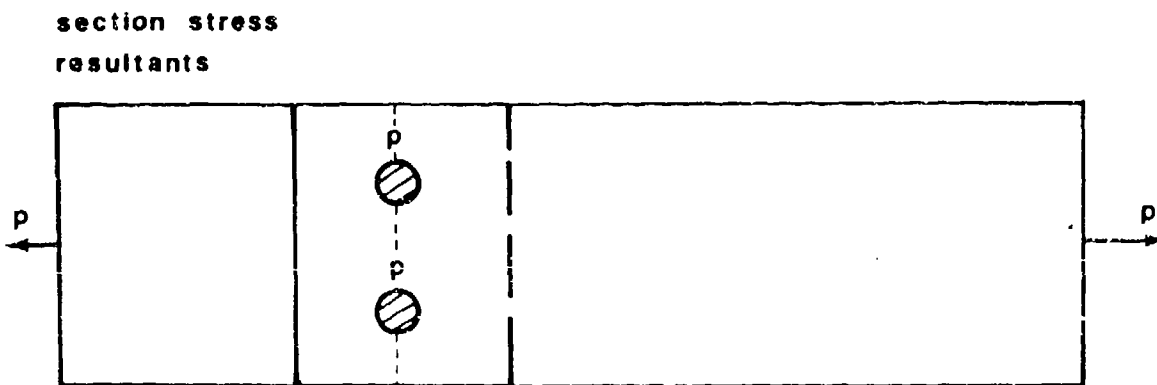


Figure 5-28. Strain ϵ_{45} along Lines 45° to Direction of Load



(a) Side View



(b) Top View

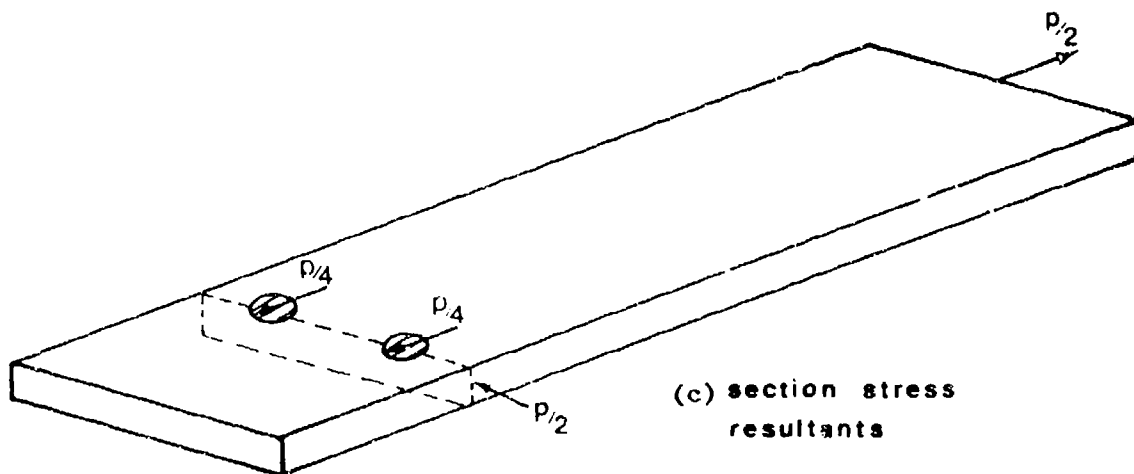


Figure 5-29. Stress Resultants for Two Parallel Holes Equally Loaded

Even though the loading could be considered symmetric, there existed some slight asymmetry in the Moire fringe patterns. Figures 5-30, 5-31 and 5-32 show the Moire fringes of displacement parallel, perpendicular, and at 45° to the direction of the load. Again, studying the change in number and shape of the fringes, it is possible to say that in the ligament region of the two holes there exists a tensile strain and a bearing strain of a negative nature.

Figures 5-33 and 5-34 show strain ϵ_y for lines located in the region between the two holes. In Figure 5-33, line $x_3 = 0.1875$, tangent to the hole, shows a tensile strain at the inner edge of the hole, then it becomes negative in the bearing region after which it becomes positive again. In Figure 5-34 the corresponding line $x_3 = -0.1875$ also shows a tensile strain at the inner edge of the left hole but it does not show any negative strain for the bearing region. Only a small decrease in the magnitude of the strain is observed. This lack of symmetry is being attributed to imperfections of the specimen. Only a slight increase of the strain ϵ_y is observed at the inner edge of the right hole.

Figure 5-35 shows strain ϵ_y for lines located above and below the right hole. For the lines located above the hole, the strain is tensile, as expected. For the lines located in the bearing region, the strain is compressive only very close to the hole edge and then it becomes positive. It should also be observed that the relative magnitude of the strain is fairly constant, both for the upper and lower portion of the hole. The stress concentration was calculated for two edges of the right hole, and at the ends of its horizontal diameter. For the left end, $K = 0.65$ and for the right end $k = 1.16$. The stress at the inner edge of the hole was lower than the far-field stress. This is perhaps an indication that most of the load is transferred through the sections located outside the two holes.

Figure 5-36 shows strain ϵ_y for lines located in the ligament area of the right side hole. Again, a very uniform strain distribution is observed. Figures 5-37 and 5-38 show strain ϵ_x for lines located above, on the ligaments, and on the bearing region of the right hole. In Figure 5-37 it can be seen that ϵ_x is compressive as expected. In Figure 5-38 ϵ_x appears as tensile, which is the correct sign for the bearing region, although some fluctuation is observed from one side of the specimen to the other.

Figures 5-39 and 5-40 show strain ϵ_{45} for lines encompassing the ligament region, the upper portion of the right hole, and part of the region between the two holes. In Figure 5-39, it is observed that strain ϵ_{45} in the ligament region, is tensile and in the region between the two holes and part of the bearing region the strain is negative, as was observed for a single hole [4.22]. In the upper portion of the right hole the strain is fairly uniform.

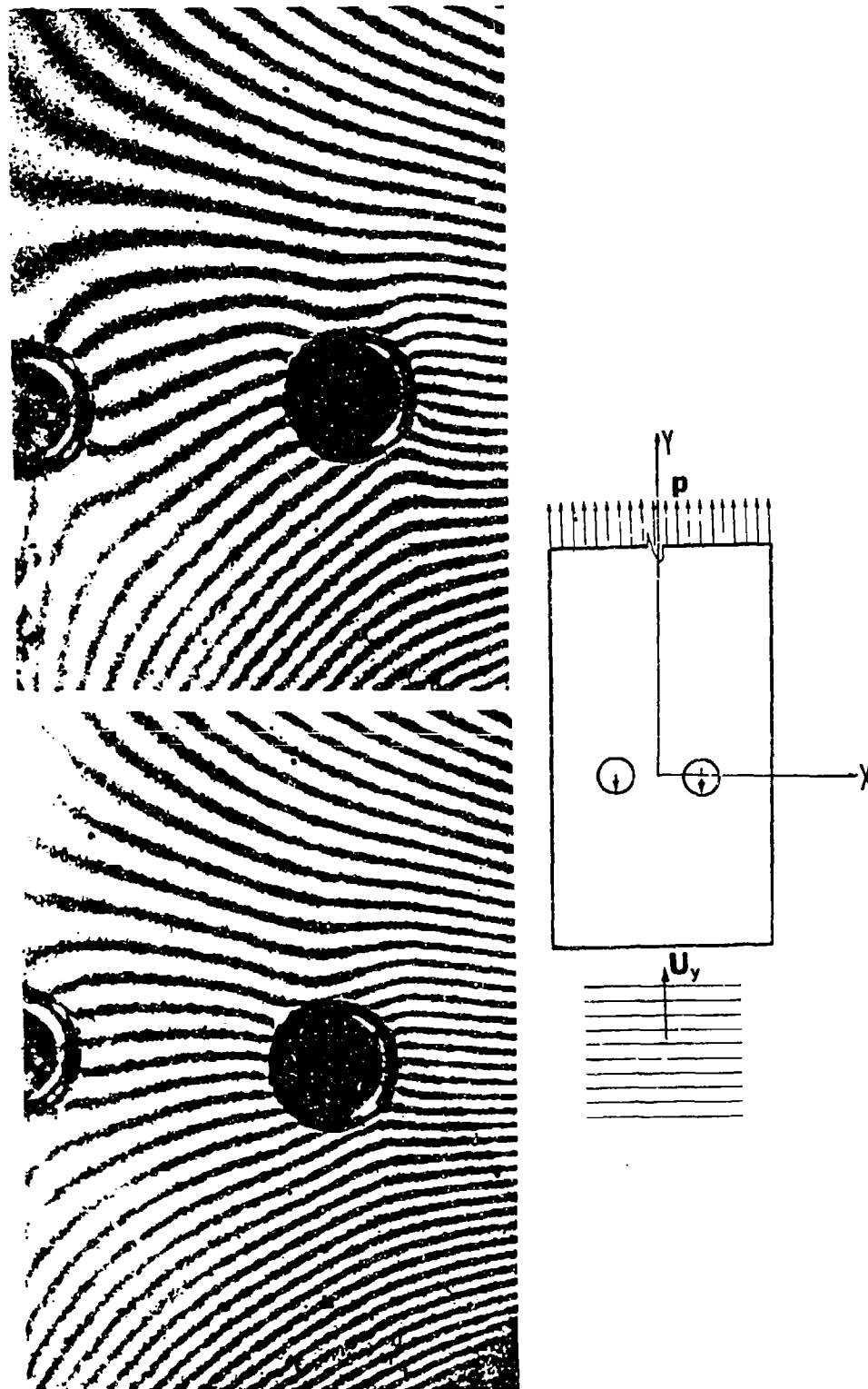


Figure 5-30. Moire Fringes of Displacement Parallel to Direction of Load for Specimen with Two-Hole Parallel Array

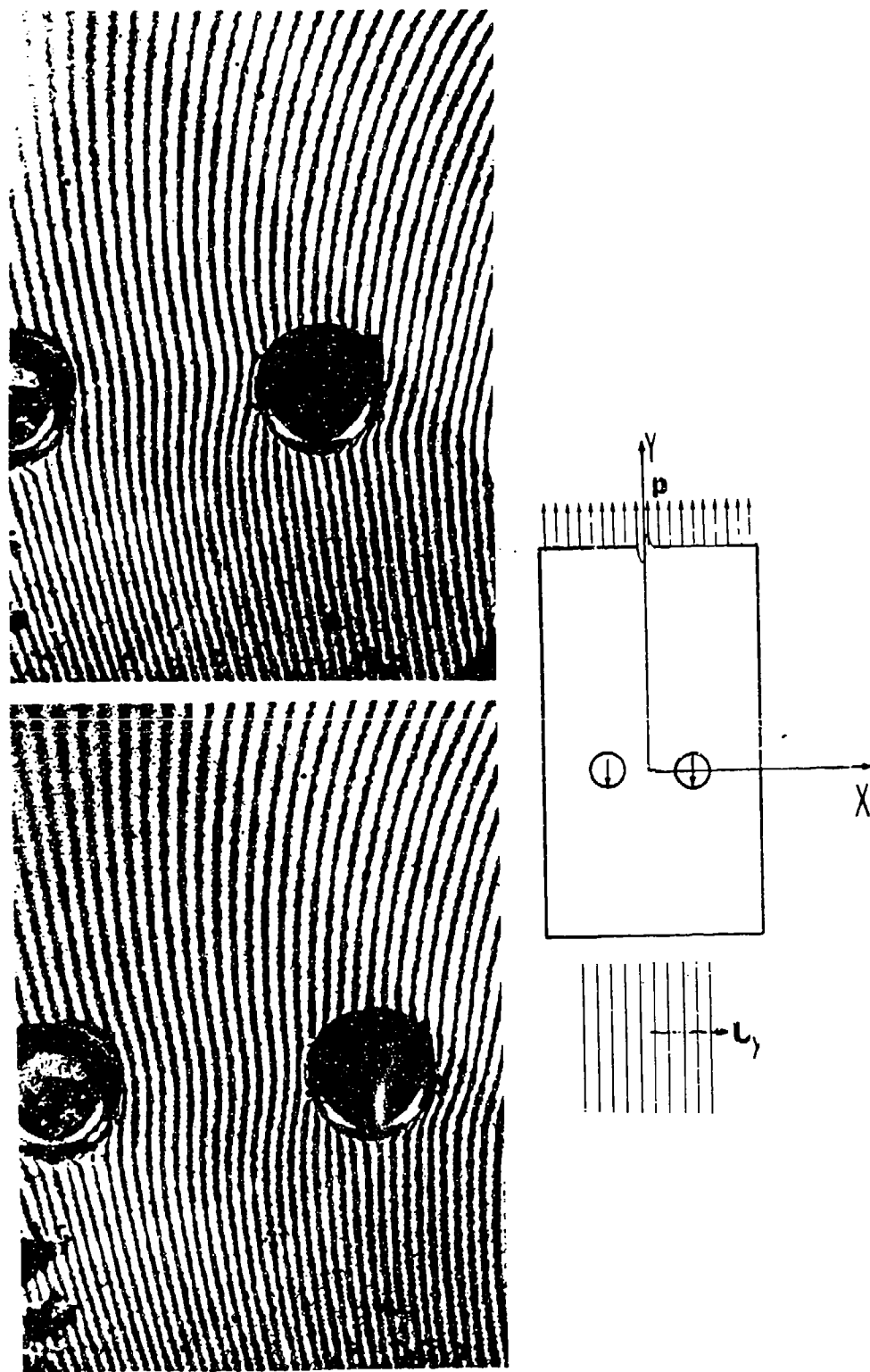


Figure 5-31. Moire Fringes of Displacement Perpendicular to Direction of Load for Specimen with Two-Hole Parallel Array

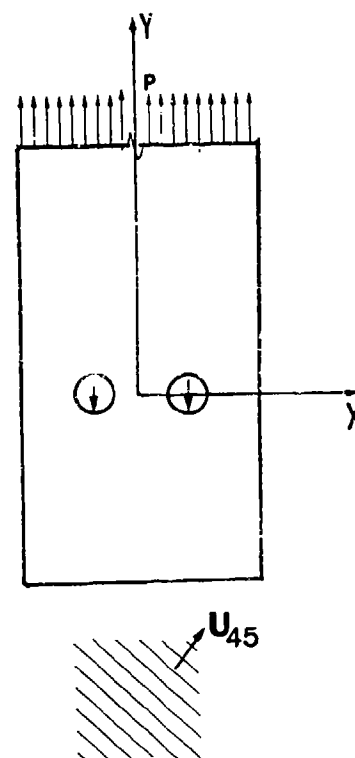


Figure 5-32. Moiré Fringes of Displacement at 45° to Direction of Load for Specimen with Two-Hole Parallel Array

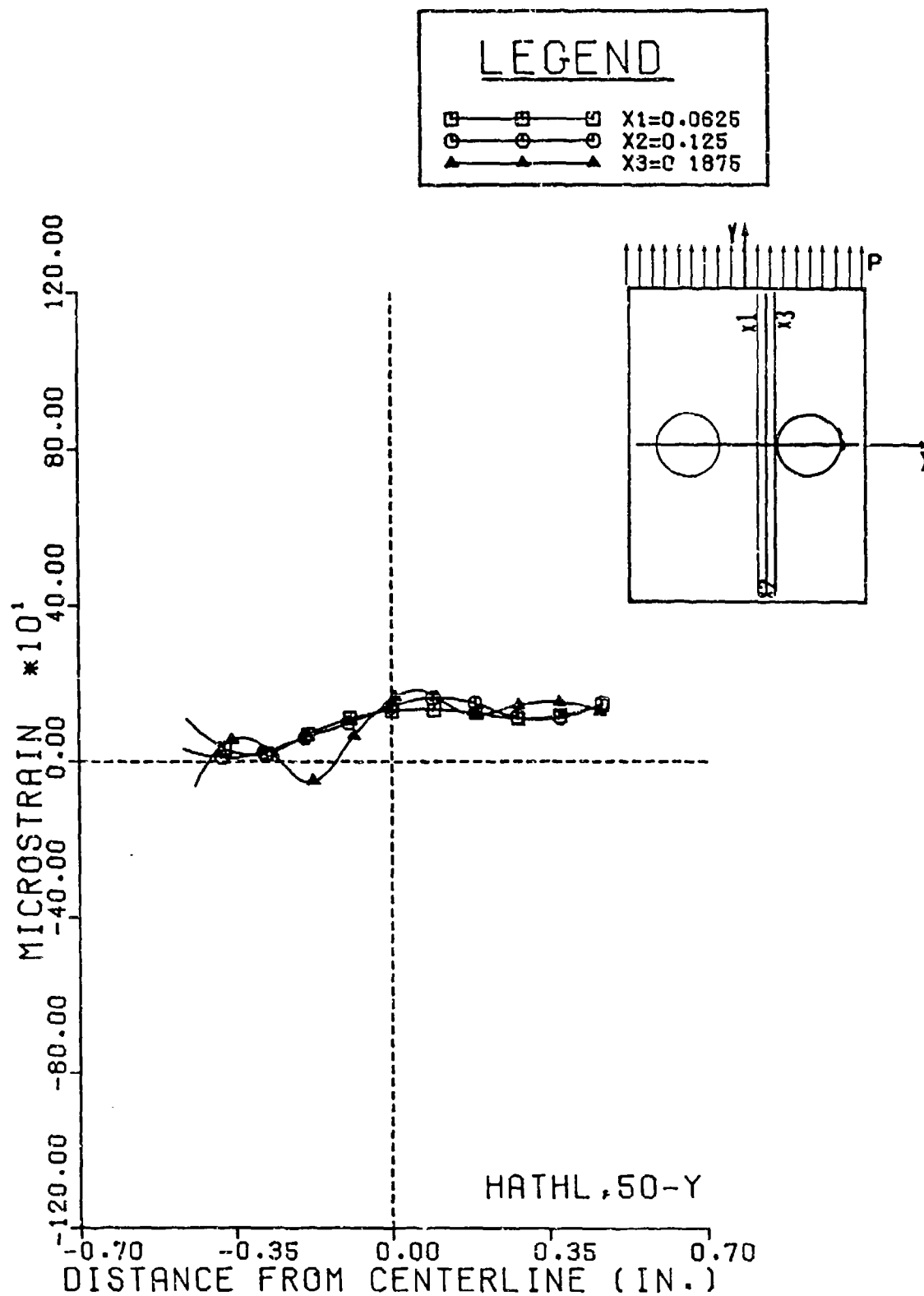


Figure 5-33. Strain ϵ_y along Lines Parallel to Direction of Load

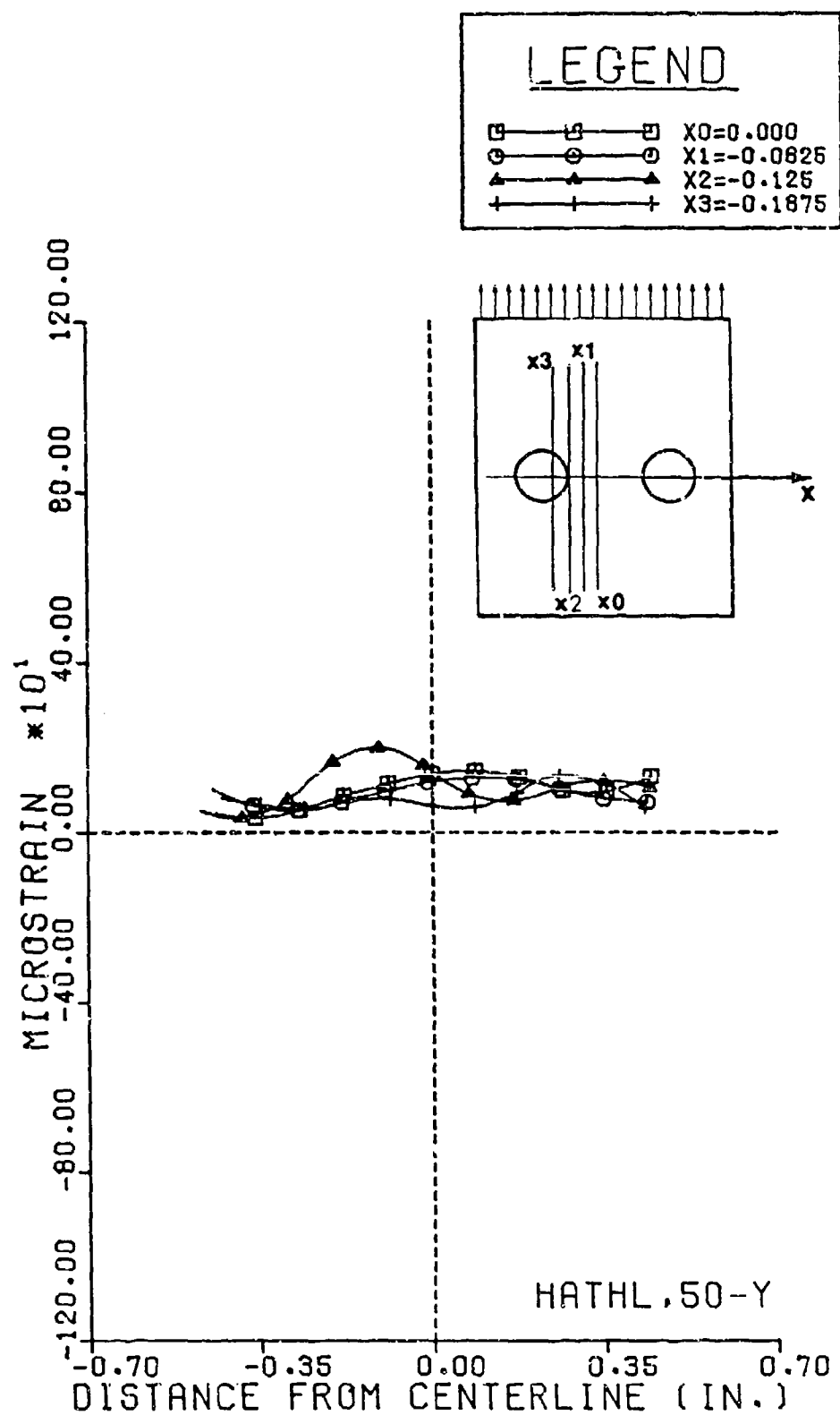


Figure 5-34. Strain ϵ_y along Lines Parallel to Direction of Load

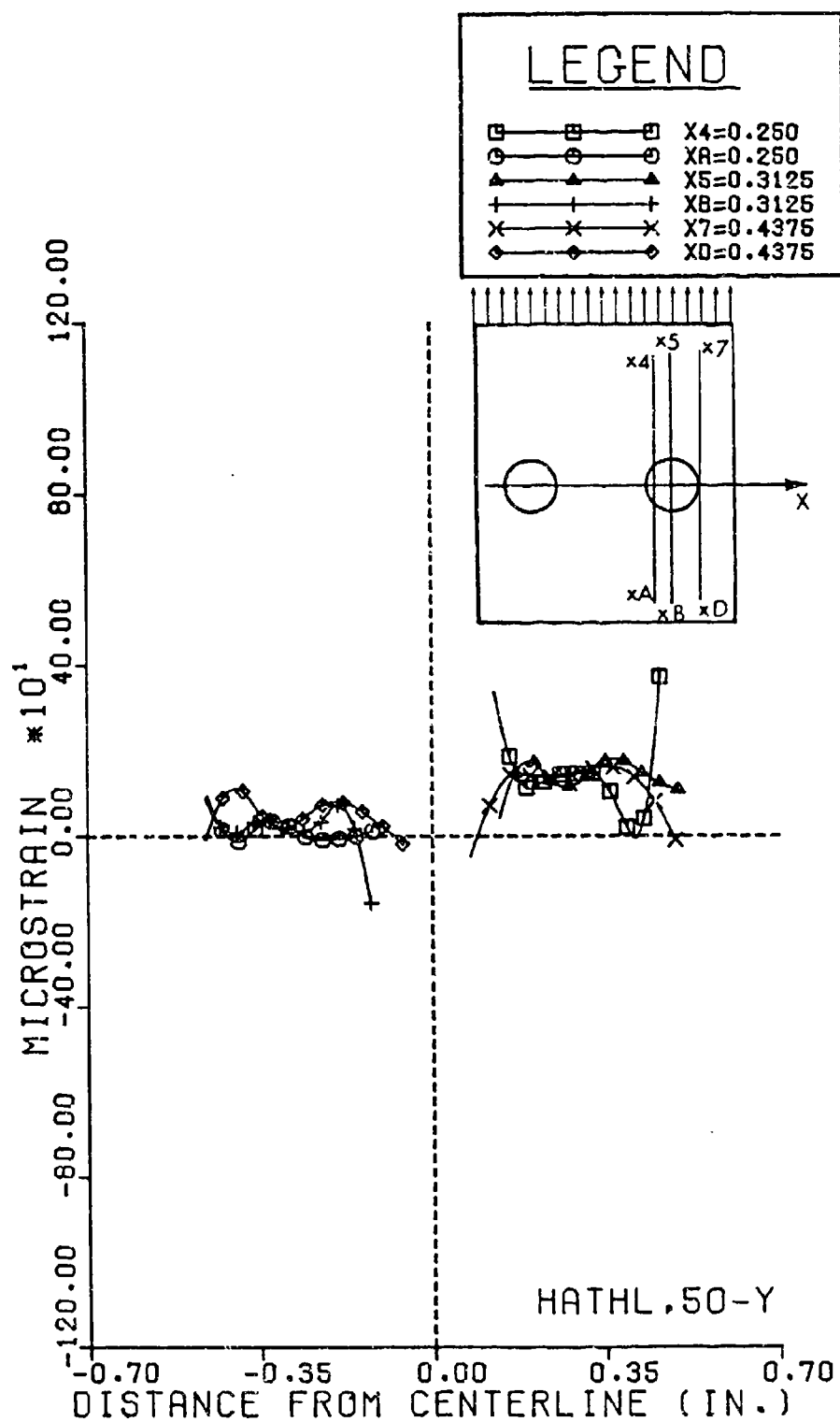


Figure 5-35. Strain ϵ_y along Lines Parallel to Direction of Load

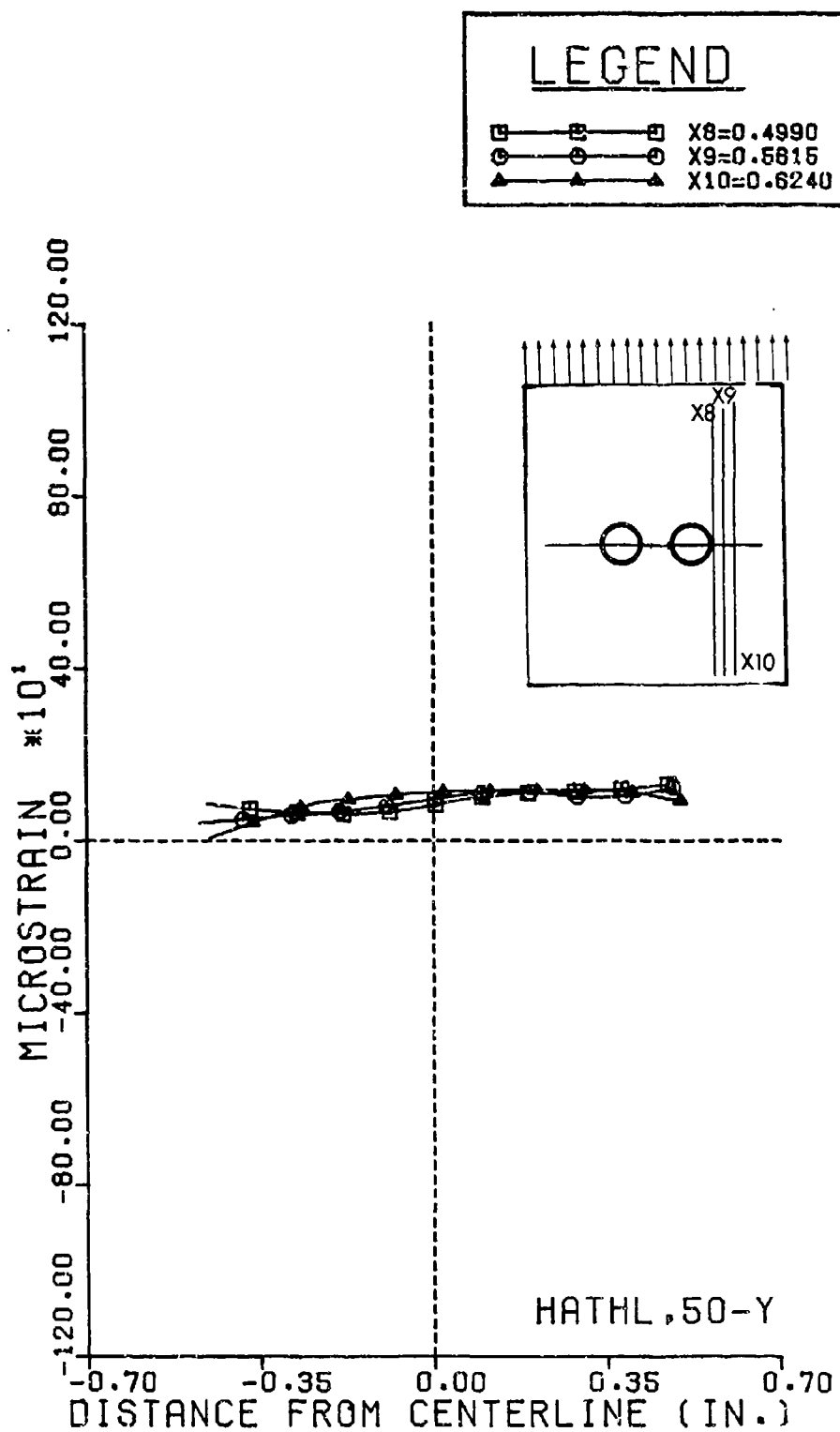


Figure 5-36. Strain ϵ_y along Lines Parallel to Direction of Load

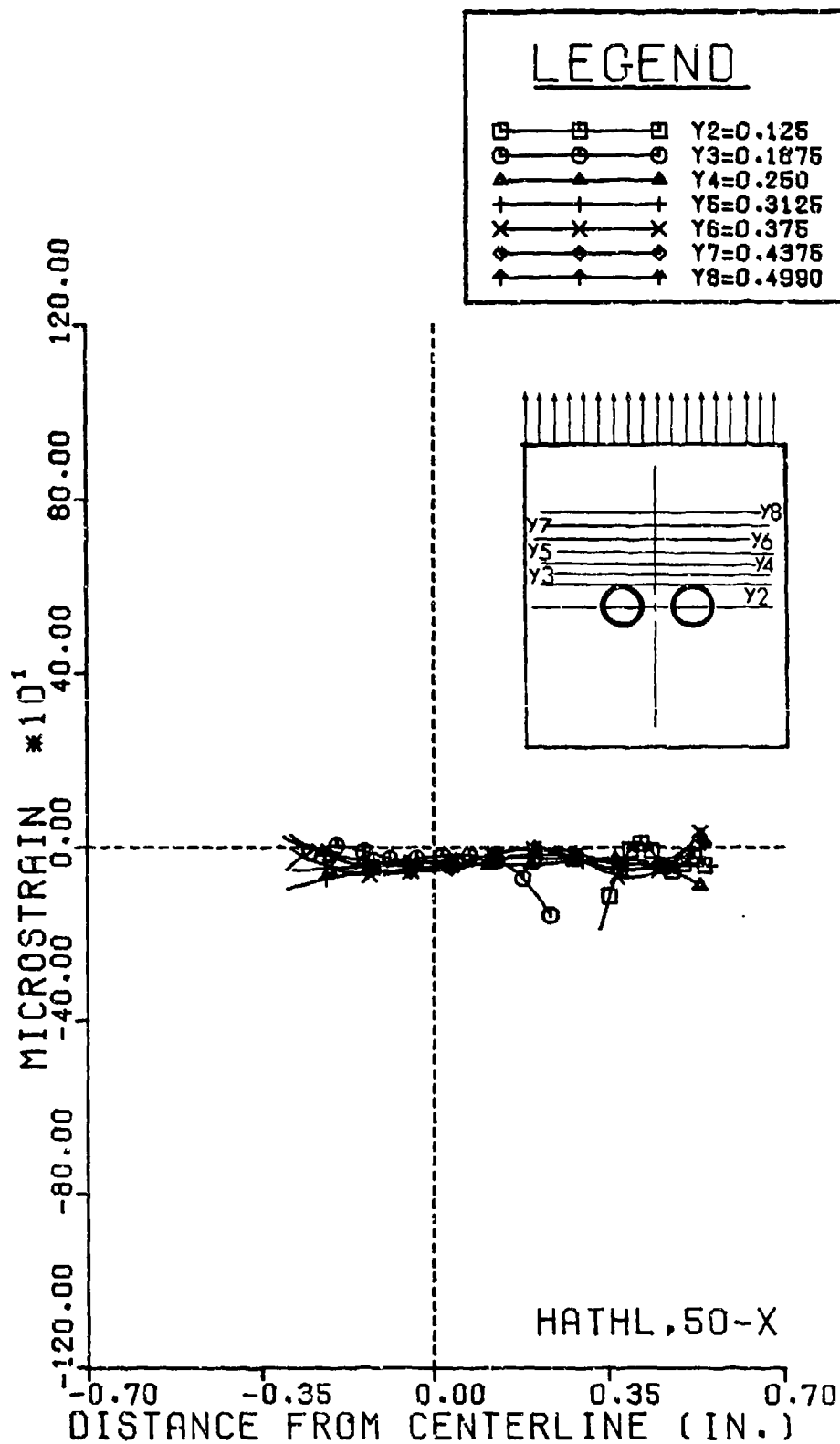


Figure 5-37. Strain ϵ_x along Lines Perpendicular to Direction of Load

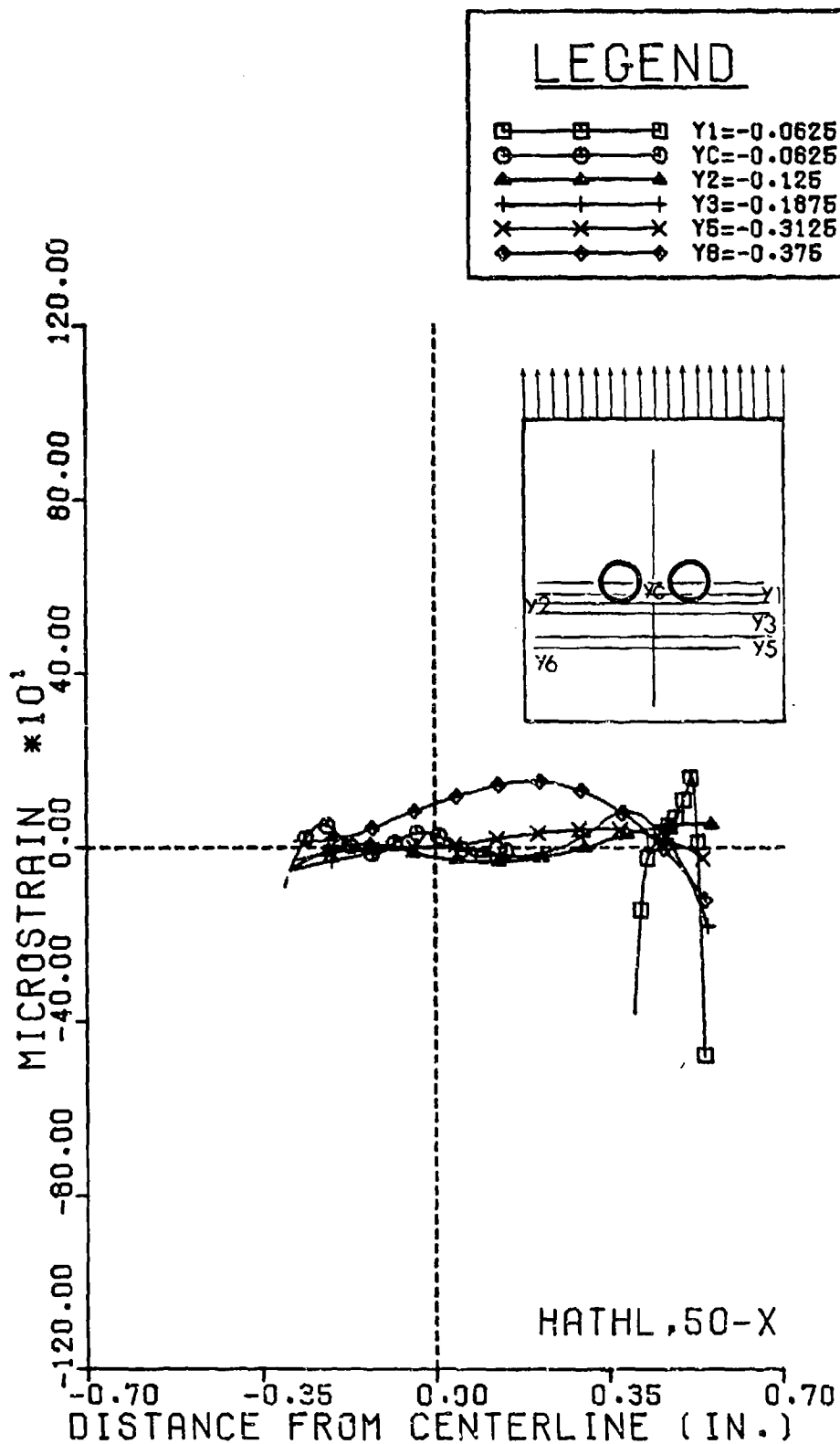


Figure 5-38. Strain ϵ_x along Lines Perpendicular to Direction of Load

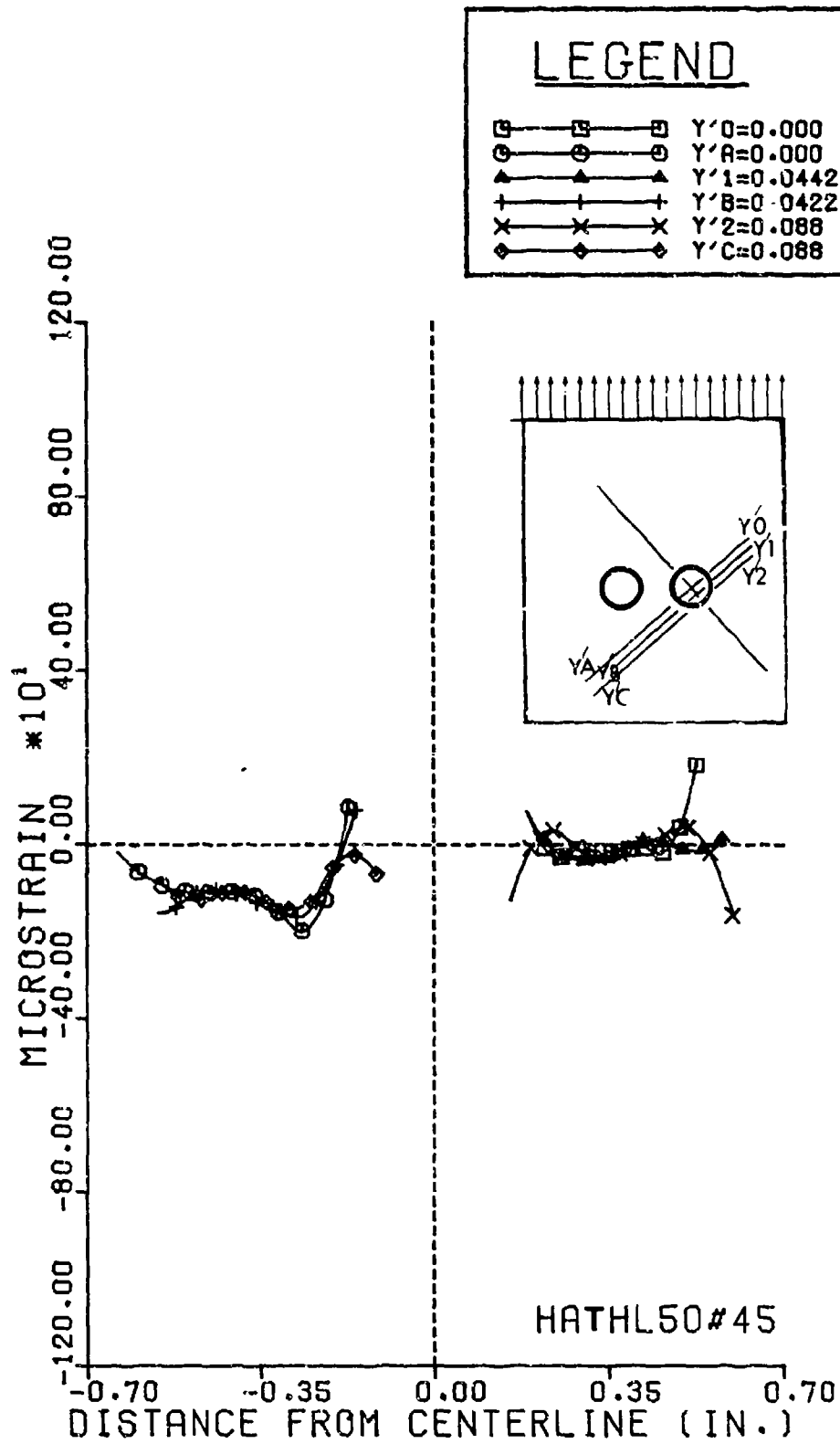


Figure 5-39. Strain ϵ_{45} along Lines 45• to Direction of Load

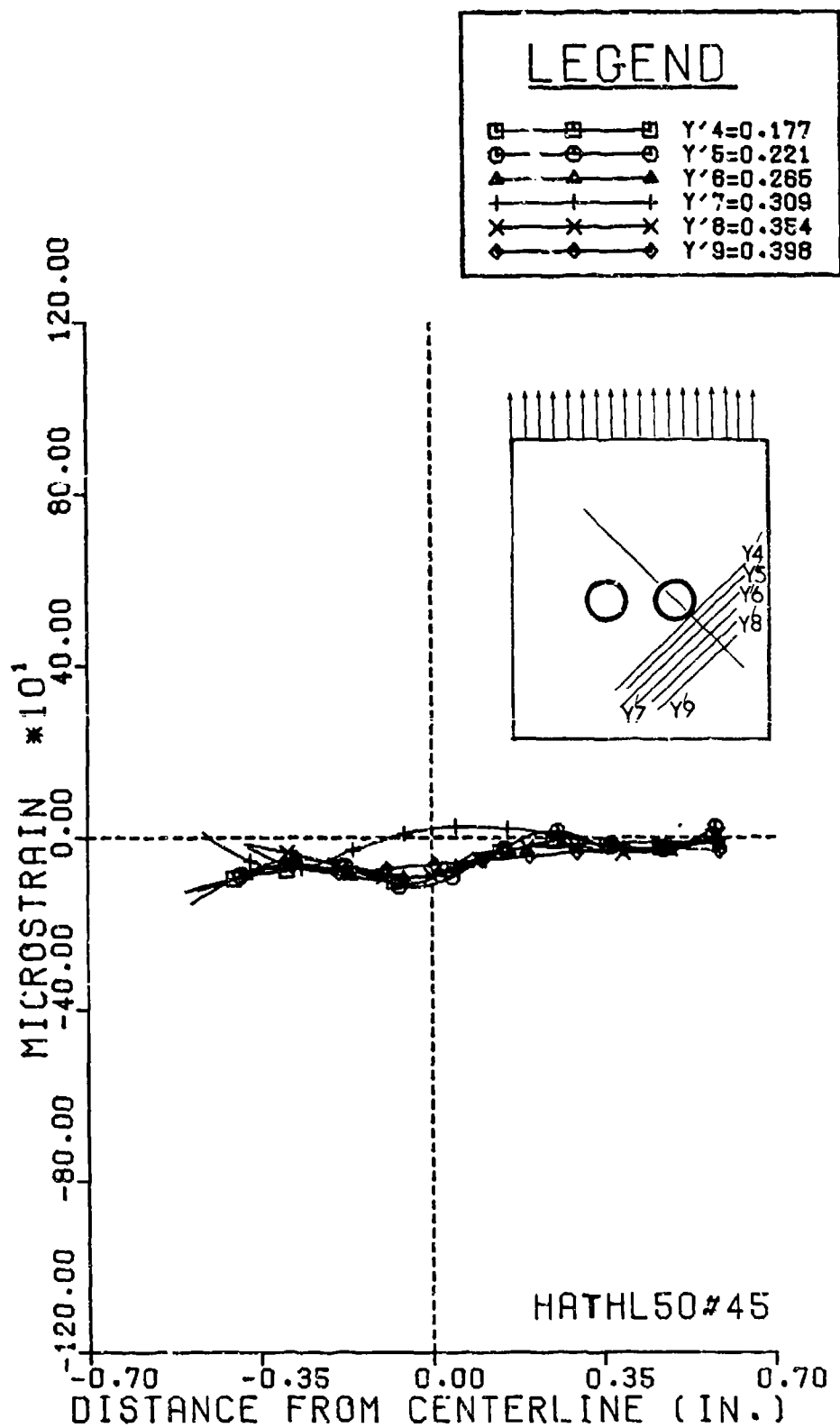


Figure 5-40. Strain ϵ_{45} along Lines 45° to Direction of Load

Figures 5-41 and 5-42 show strain ϵ_{45} for lines encompassing the region between the two holes and the bearing region. Figure 5-42 shows a negative strain in the bearing region of the two holes, but as it was noticed in the previous cases, the same uniform strain distribution prevails in the 45-degree orientation. The strain distribution for this hole array is more uniform. Even at the edges of the hole, in the bearing regions, or in the ligament region, there is not a noticeable strain concentration. In this case, it would be interesting to further study the effect of the distance between centers on the interaction of the strains between the holes.

5.6. Three Hole Staggered: Array All Loaded

A fifth experiment used a specimen with a three-hole array in a staggered configuration. All holes were loaded simultaneously with the same amount of force using a cable and pulley arrangement to equally divide the load. Figure 5-43 shows the load distribution in the pins and net sections of the specimen. As seen in Figure 5-43, the force acting in section 1-1 of plate A is $P/2$, and in section 2-2 only a portion of it. This means that the resulting tensile stress in section 1-1 is higher than in section 2-2. A very common practice in joint design is to decrease the number of holes in order to increase the net section or the amount of material in section 1-1 and to increase the strength of the joint. In the specimen used in this case, section 1-1 contains only one hole. Interest will be centered on the stress and strain concentrations at the edges of the three holes in the relevant direction, and in the interactions of strain between the three holes.

Figures 5-44, 5-45, and 5-46 show Moire fringes of displacement parallel, perpendicular, and at 45° to the direction of loading.

Figure 5-47 shows strain ϵ_y for lines located above and below the upper hole. As expected, the strain above the hole is tensile except close to the upper edge, as has been observed for a single pin-loaded hole. For the two lines in the bearing region of the upper hole a very interesting behavior is observed. The strain ϵ_y is negative only very close to the edge of the hole, and then it changes to a peak tensile strain which then decreases to an average value.

Figures 5-48 and 5-49 show strain ϵ_y along lines which are tangent to the upper hole and also to the lower ones. In Figure 5-48, $x_2 = 0.125$ is tangent to the upper hole and $y_3 = 0.1875$ is tangent to the inner edge of the lower left hole. In line $x_2 = 0.125$ there are two peak values, at $y = 0.1818$ and $y = 0.410$. These peak strains correspond to positions which are above the horizontal diameter of the upper hole; then ϵ_y becomes very uniform even close to the lower holes. In line $x_2 = 0.1875$, the peak strain occurs at $y = -0.307$, which is located slightly below the horizontal diameter of the lower left hole. In Figure 5-49, $x_2 = 0.125$ is tangent to the upper hole, and $y(-3) = -0.1875$ is tangent

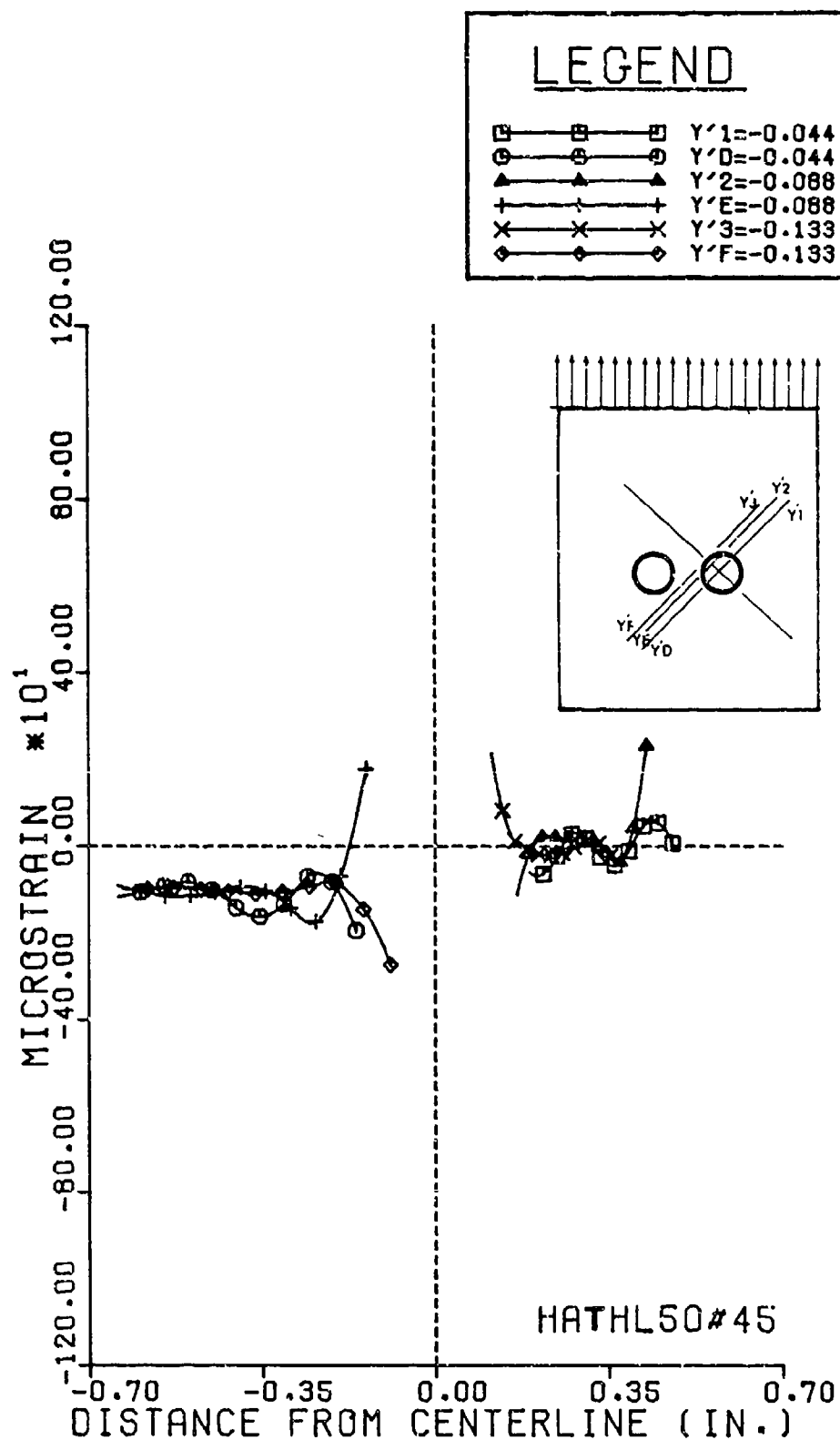


Figure 5-41. Strain ϵ_{45} along Lines 45• to Direction of Load

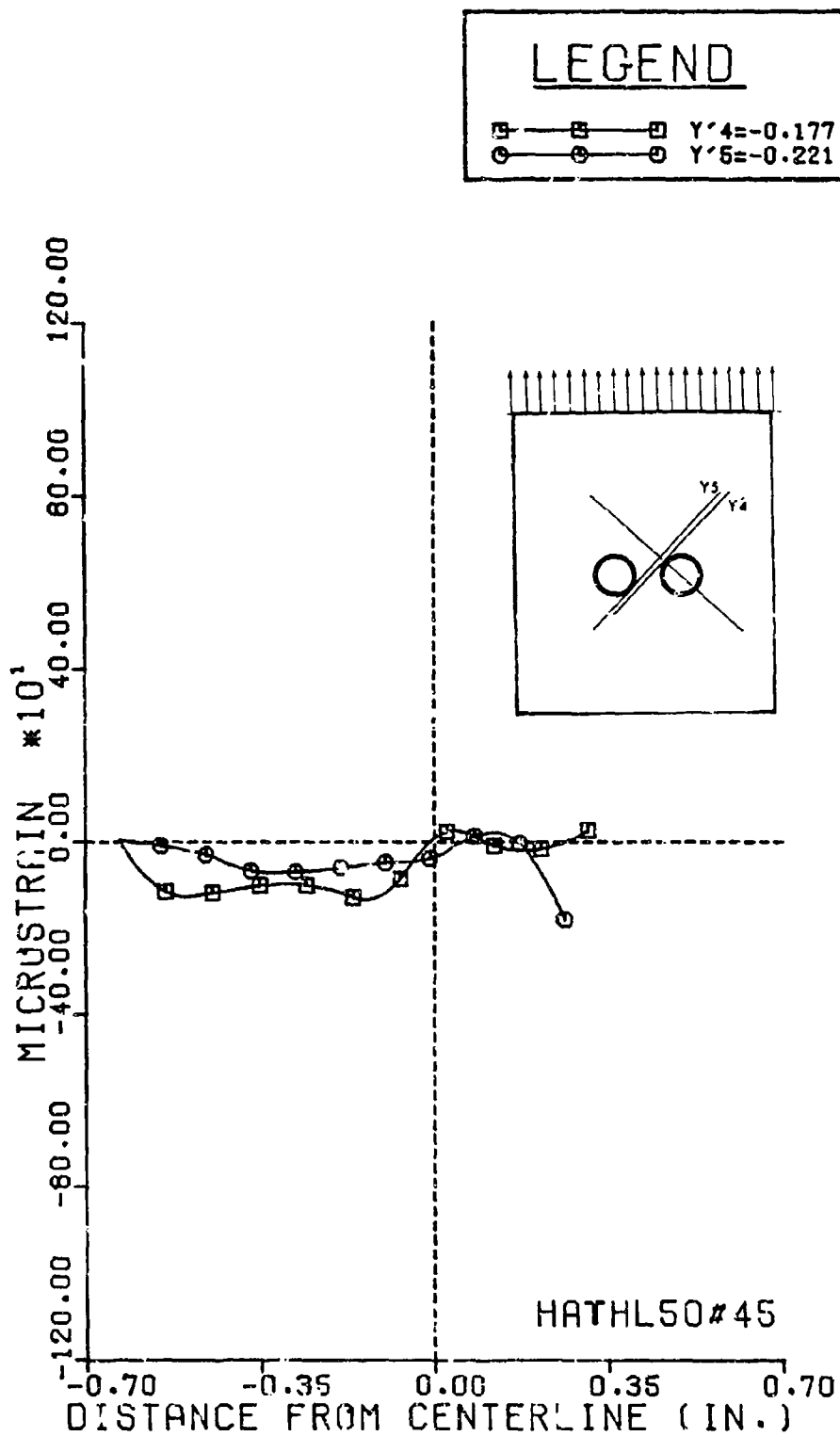
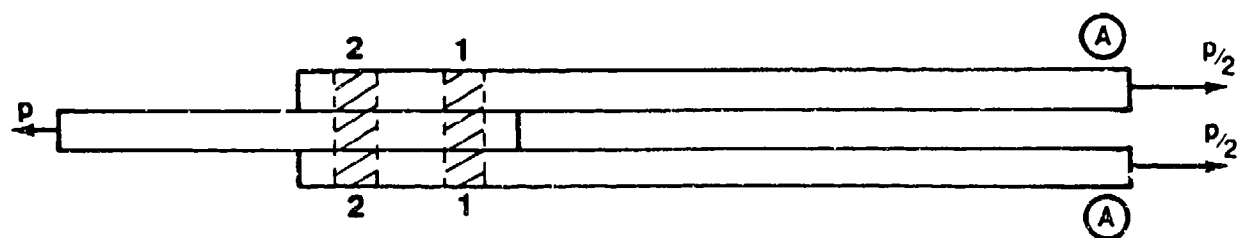
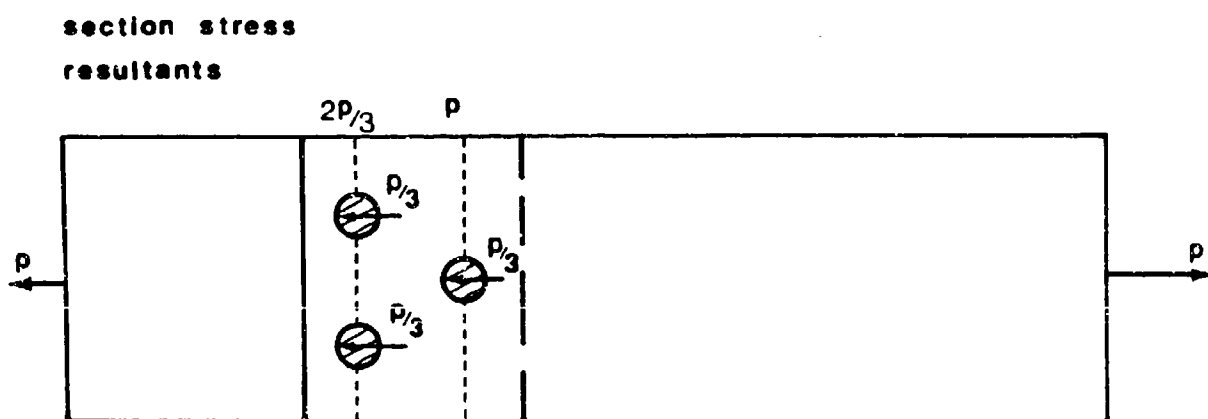


Figure 5-42. Strain ϵ_{45} along Lines 45° to Direction of Load



(a) Side View



(b) Top View

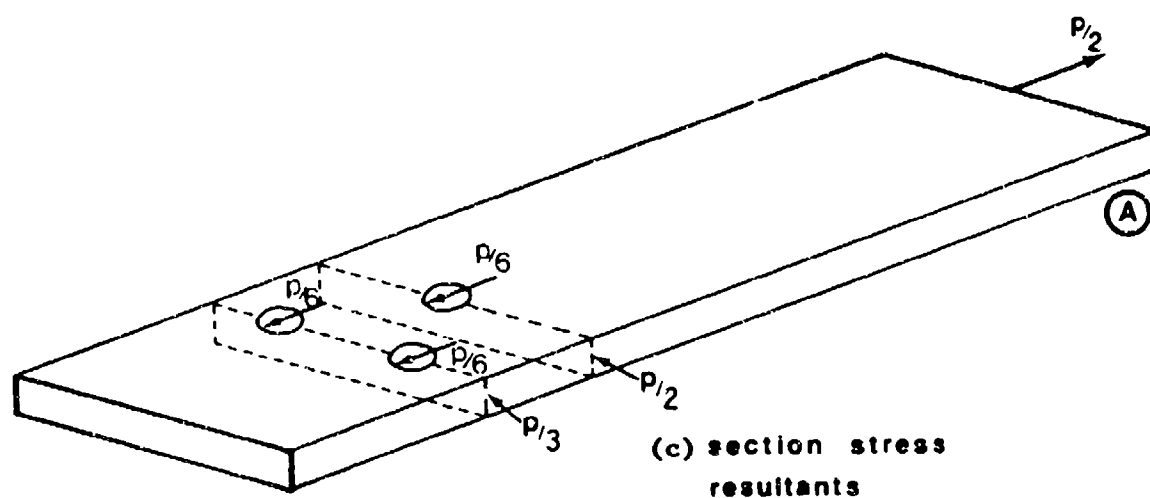


Figure 5-43. Stress Resultants for Three Staggered Holes Equally Loaded



Figure 5-44. Moiré Fringes of Displacement Parallel to Direction of Load for Specimen with Three-Hole Staggered Array

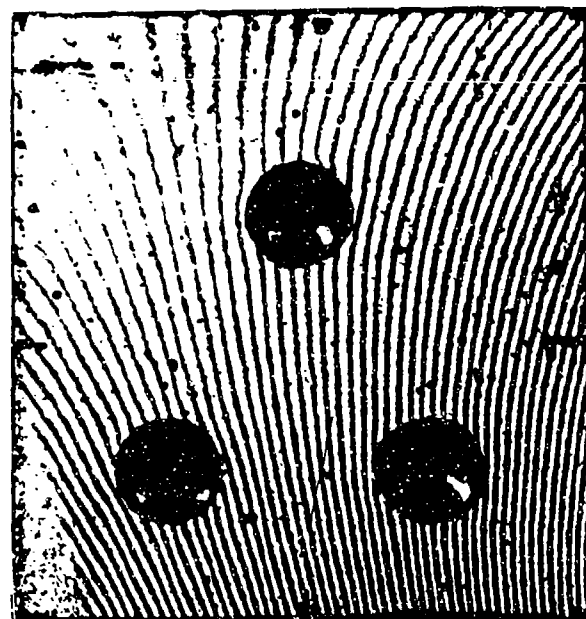


Figure 5-45. Moiré Fringes of Displacement Perpendicular to Direction of Load for Specimen with Three-Hole Staggered Array

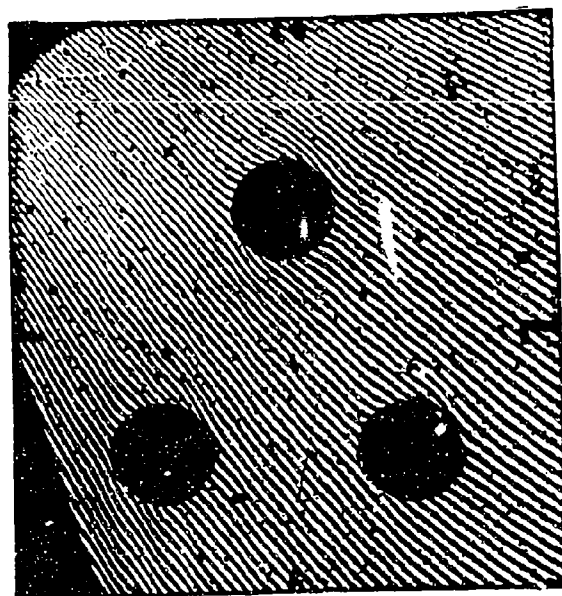
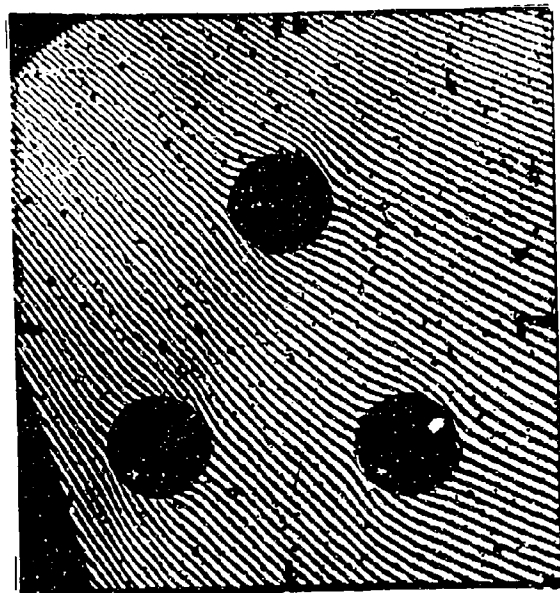


Figure 5-46. Moiré Fringes of Displacement 45° to Direction of Load for Specimen with Three-Hole Staggered Array

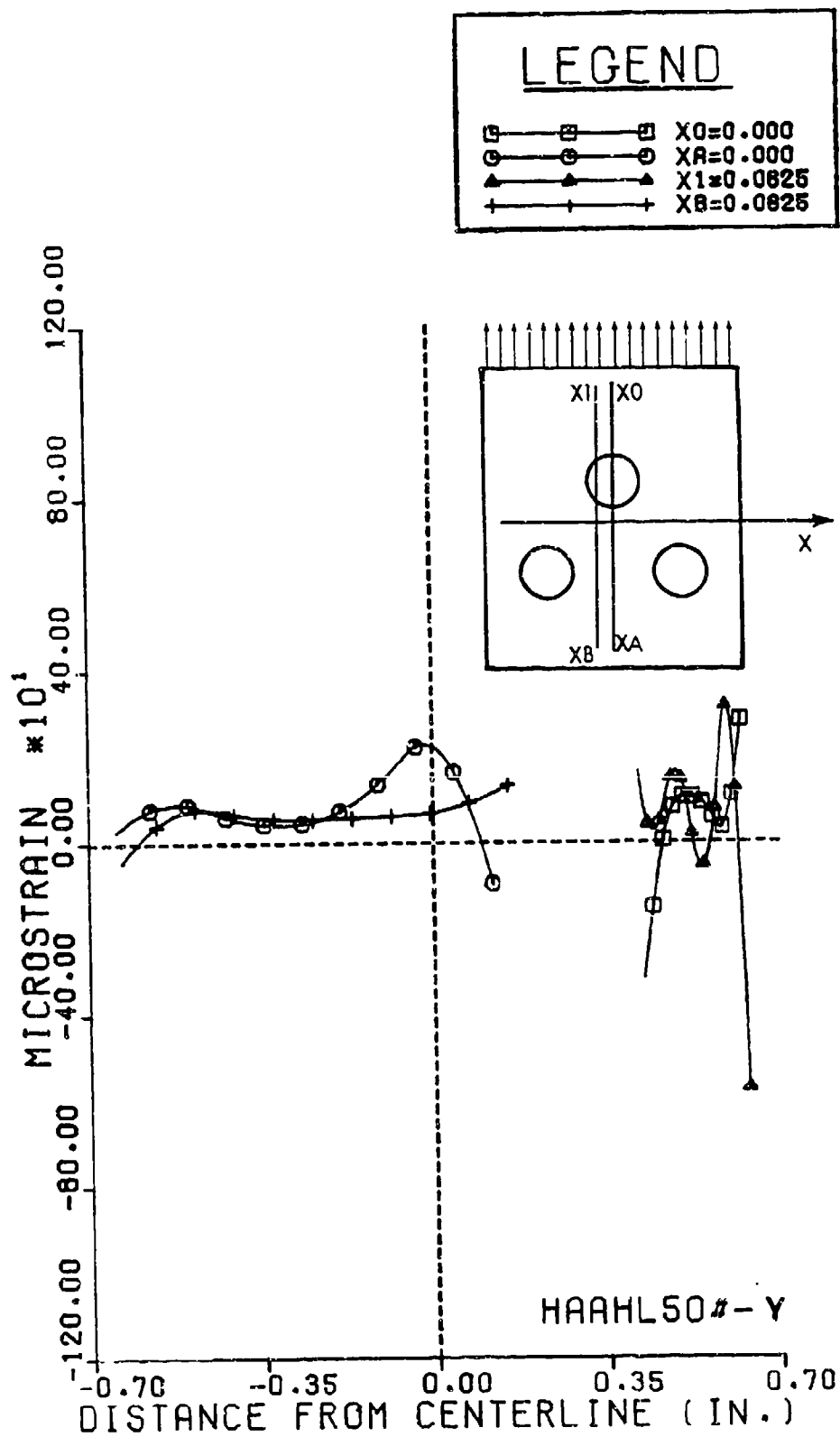


Figure 5-47. Strain ϵ_y along Lines Parallel to Direction of Load

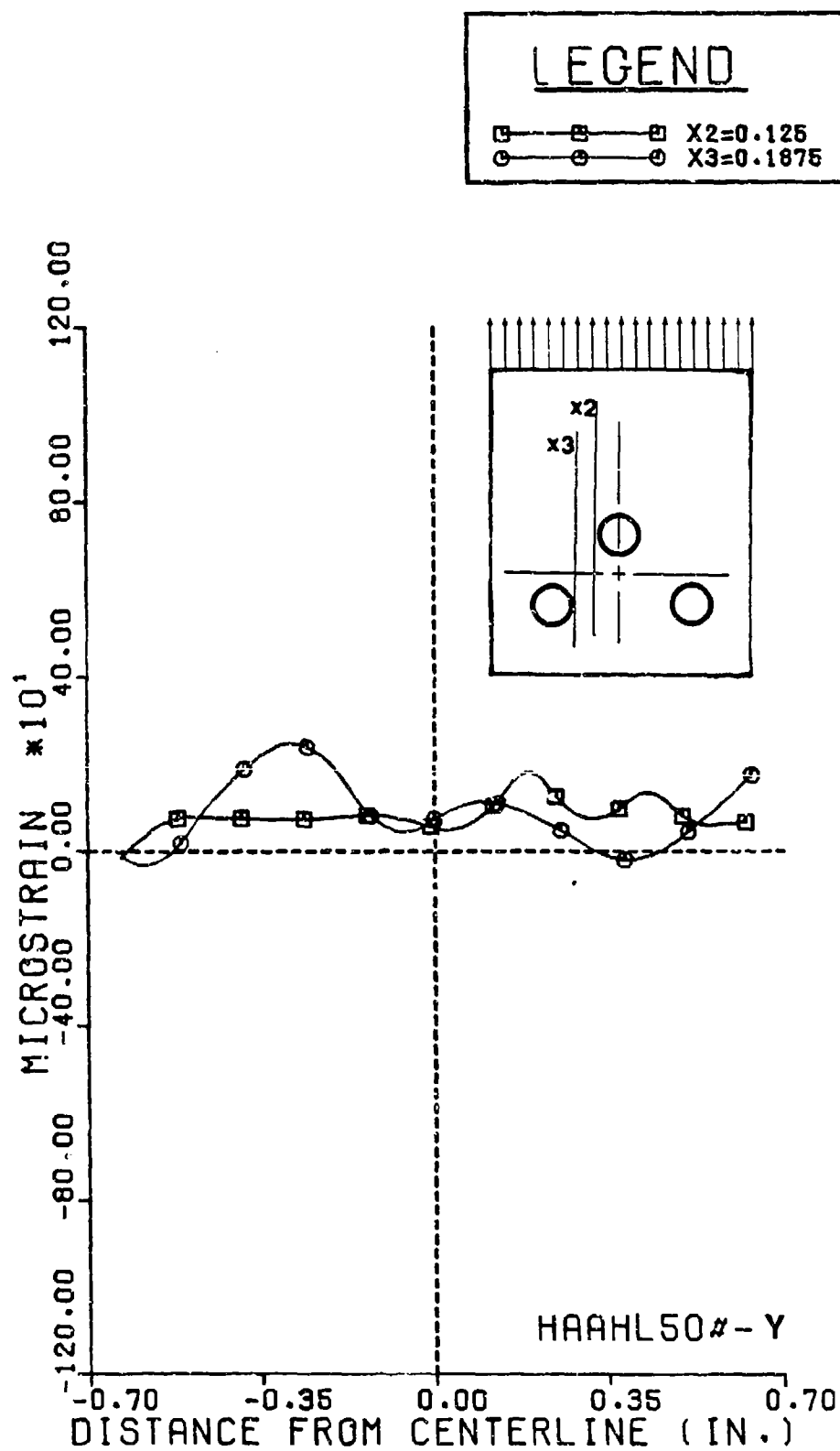


Figure 5-48. Strain ϵ_y along Lines Parallel to Direction of Load

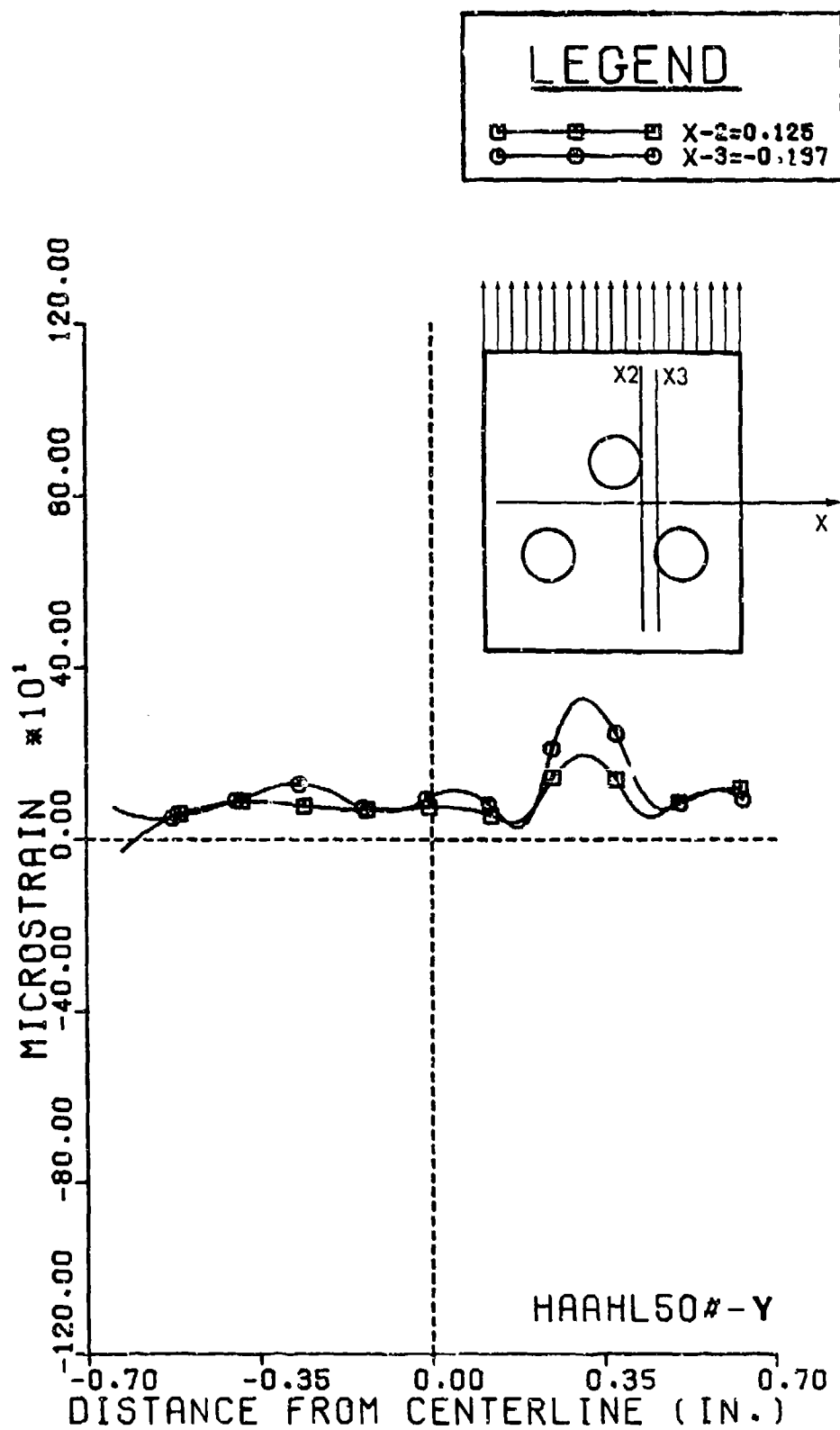


Figure 5-49. Strain ϵ_y along Lines Parallel to Direction of Load

to the inner edge of the lower right hole. For both lines, there is a peak strain value right at the horizontal diameter of the upper hole and, close to the lower right hole, the peak strain is also at its horizontal diameter.

The stress concentration factor for these three holes was calculated. At the right-side edge of the upper hole $k = 2.32$, and for the left-side edge $k = 2.17$. For the lower left hole, the stress concentration factor at its inner edge is $k = 2.95$ and for the lower right hole the stress concentration factor is $k = 1.54$. There exists only small asymmetry between the two sides of the lower holes. For the upper holes the difference between the two edges is very small.

Figures 5-50 and 5-51 show strain ϵ_y for lines located above and below the right and left lower holes respectively. In both figures a similar behavior is observed. Above the hole there exists a tensile strain, and in the bearing region there is a compressive strain at the edge of the hole. It should be pointed out that the strain in the bearing region of both the lower holes fluctuates from negative to positive, but the relative magnitude is almost the same. Another interesting point is noticed in lines $y(-5) = -0.312$ and $y(5) = 0.312$ of the two holes which show exactly the same fluctuating behavior on the upper portion (exactly the center) of both holes. This fluctuation is slightly more pronounced in the right side.

Figures 5-52 and 5-53 show strain ϵ_y for lines tangent to the lower right and left holes respectively and located in the ligament regions. They present a very uniform distribution of strain, except for line $y(-8) = -0.5$, which shows a small bump in the neighborhood of the hole. This can be attributed to material imperfections in the specimen.

As can be observed from these figures, the strain distribution in the region between the holes shows only a very small bearing region for the upper hole, and then it changes to tensile strain. There are not any high strain gradients due to the interaction of the three holes. Further study should be done in order to appreciate the effect of d/D , that is the distance between centers. Also, it should be remembered that the region between the lower holes is of a tensile nature, and right above them exists a compressive strain, which should cancel out the high tensile stress concentration of the lower holes resulting in a uniform tensile strain.

Figures 5-54, and 5-55 show strain ϵ_x for lines located in the bearing region of the upper hole. In Figure 5-54 ϵ_x appears to be negative. Also, in the region located right above each hole, lines $y(-1) = -0.062$ and $y(-2) = -0.125$ show an increase in the compressive strain for the left and right lower holes respectively. Closer to the upper hole the strain ϵ_x does not appear to have any strain gradient.

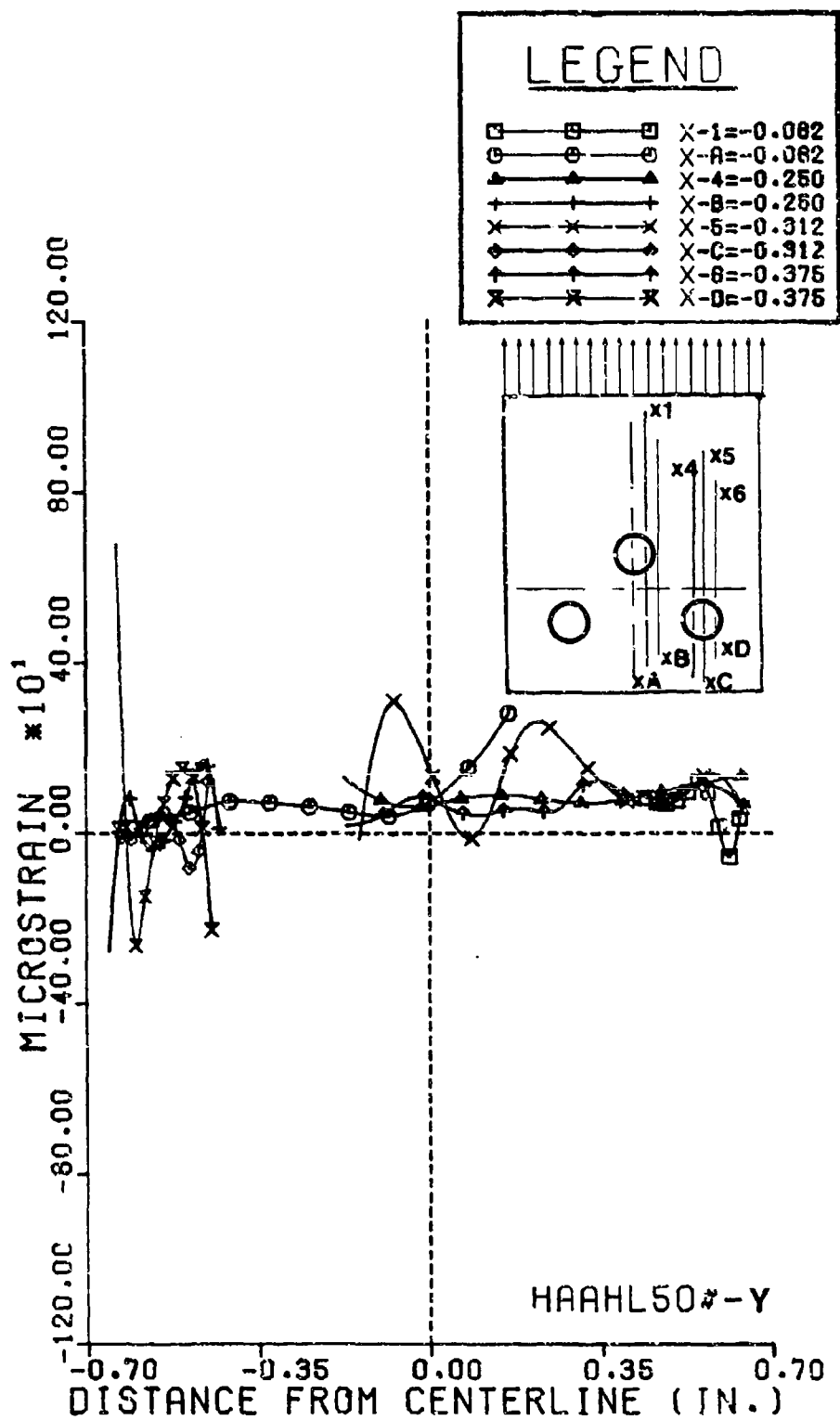


Figure 5-50. Strain ϵ_y along lines Parallel to Direction of Load

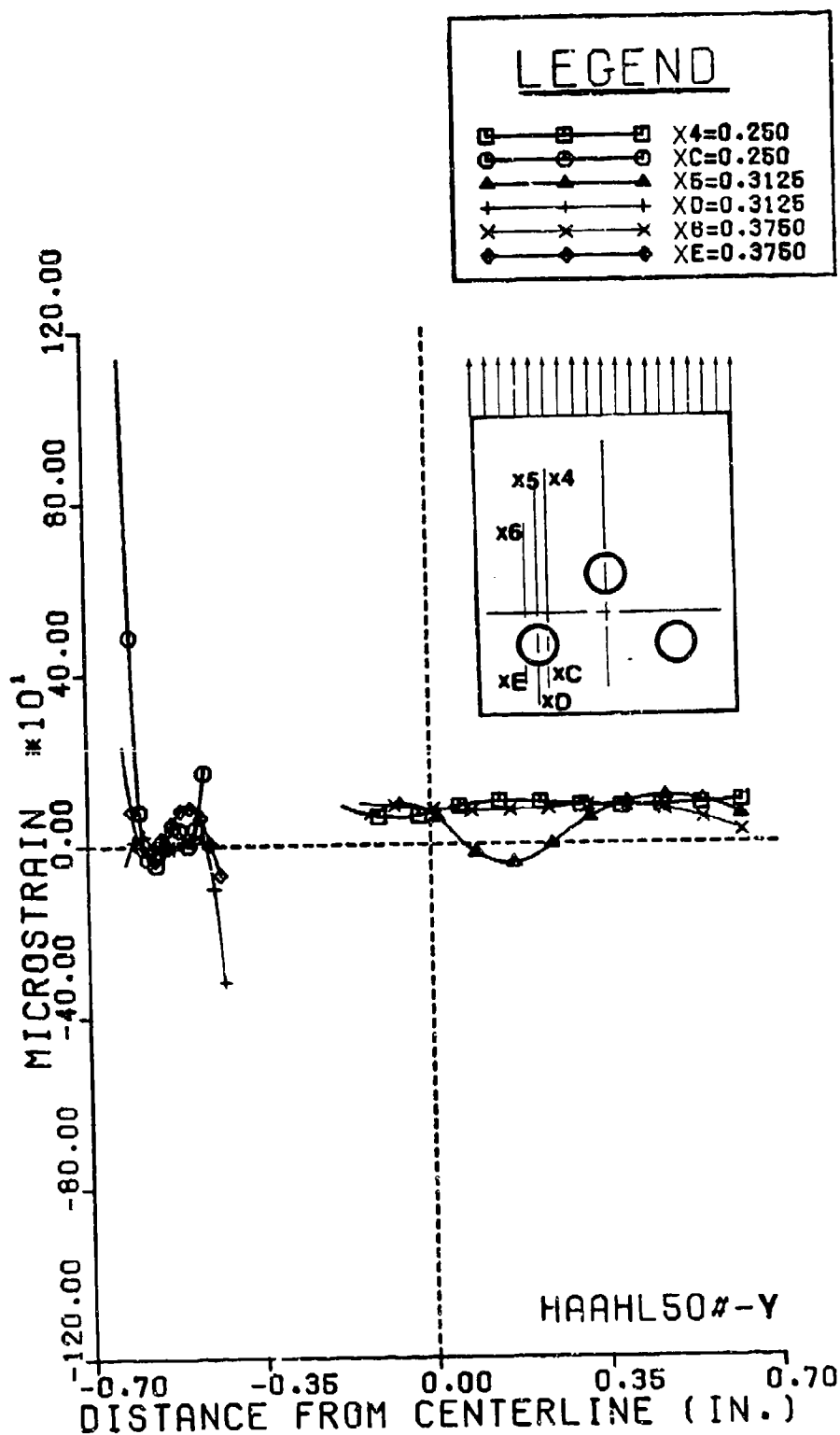


Figure 5-51. Strain ϵ_y along lines Parallel to Direction of Load

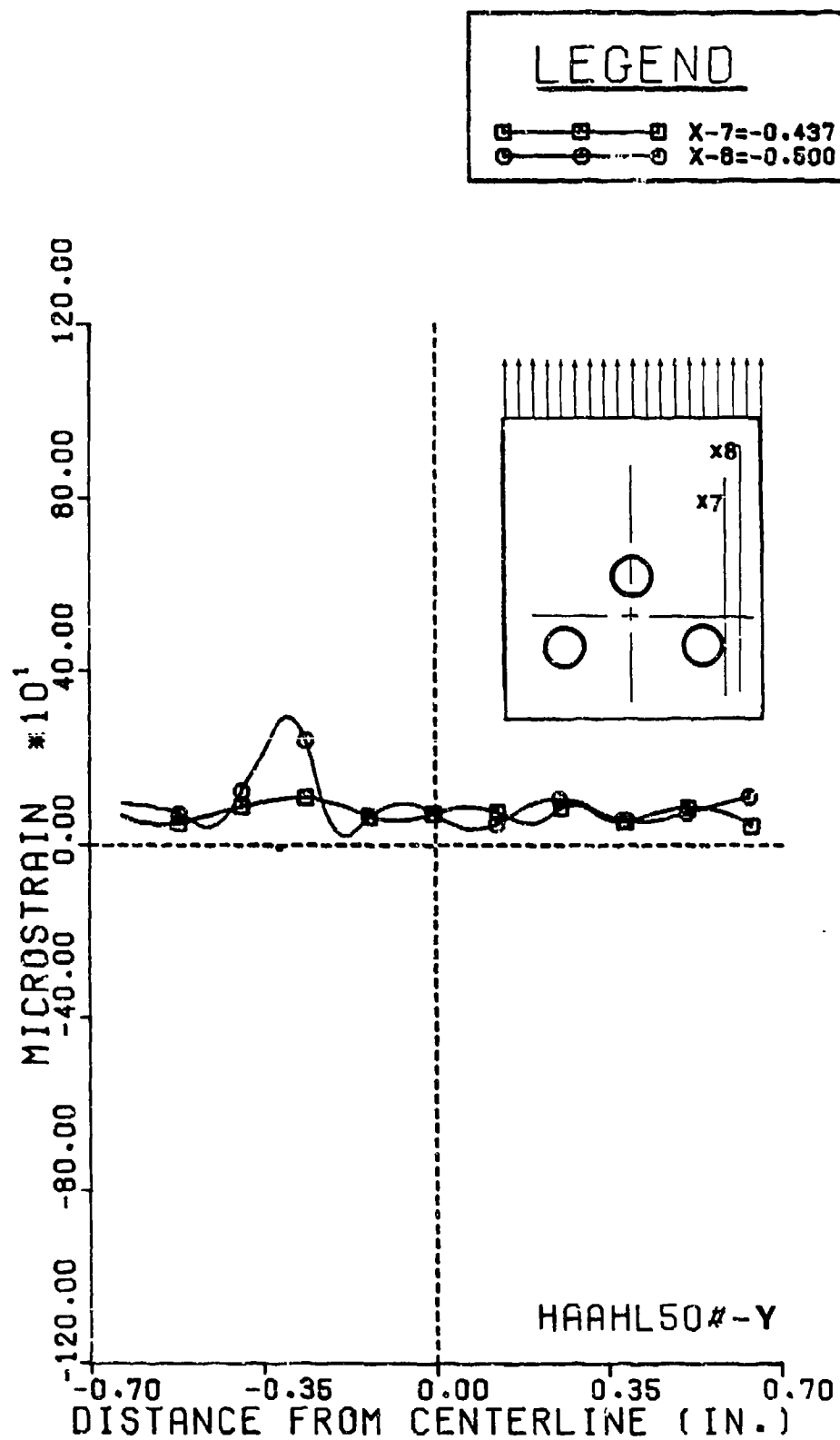


Figure 5-52. Strain ϵ_y along Lines Parallel to Direction of Load

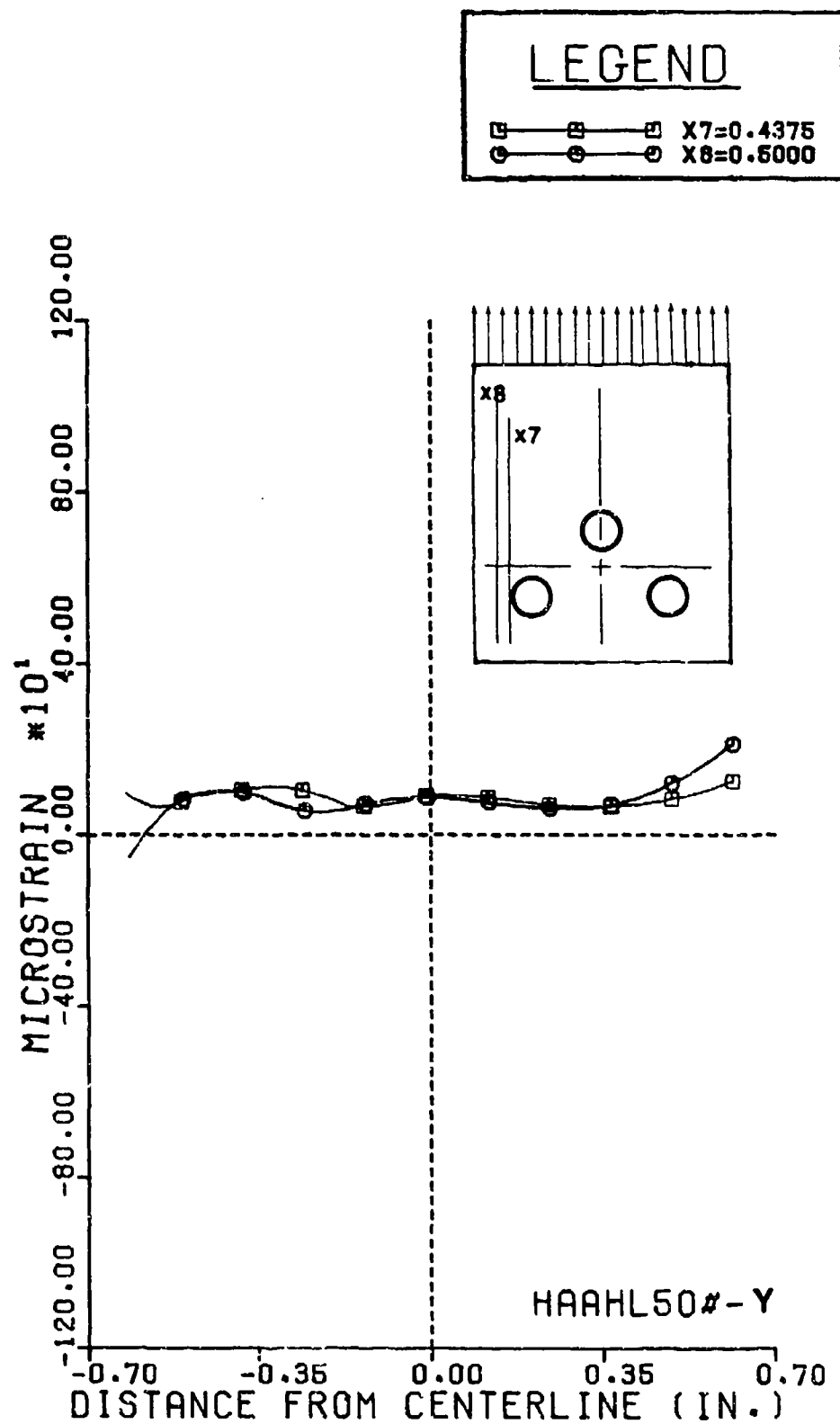


Figure 5-53. Strain ϵ_y along Lines Parallel to Direction of Load

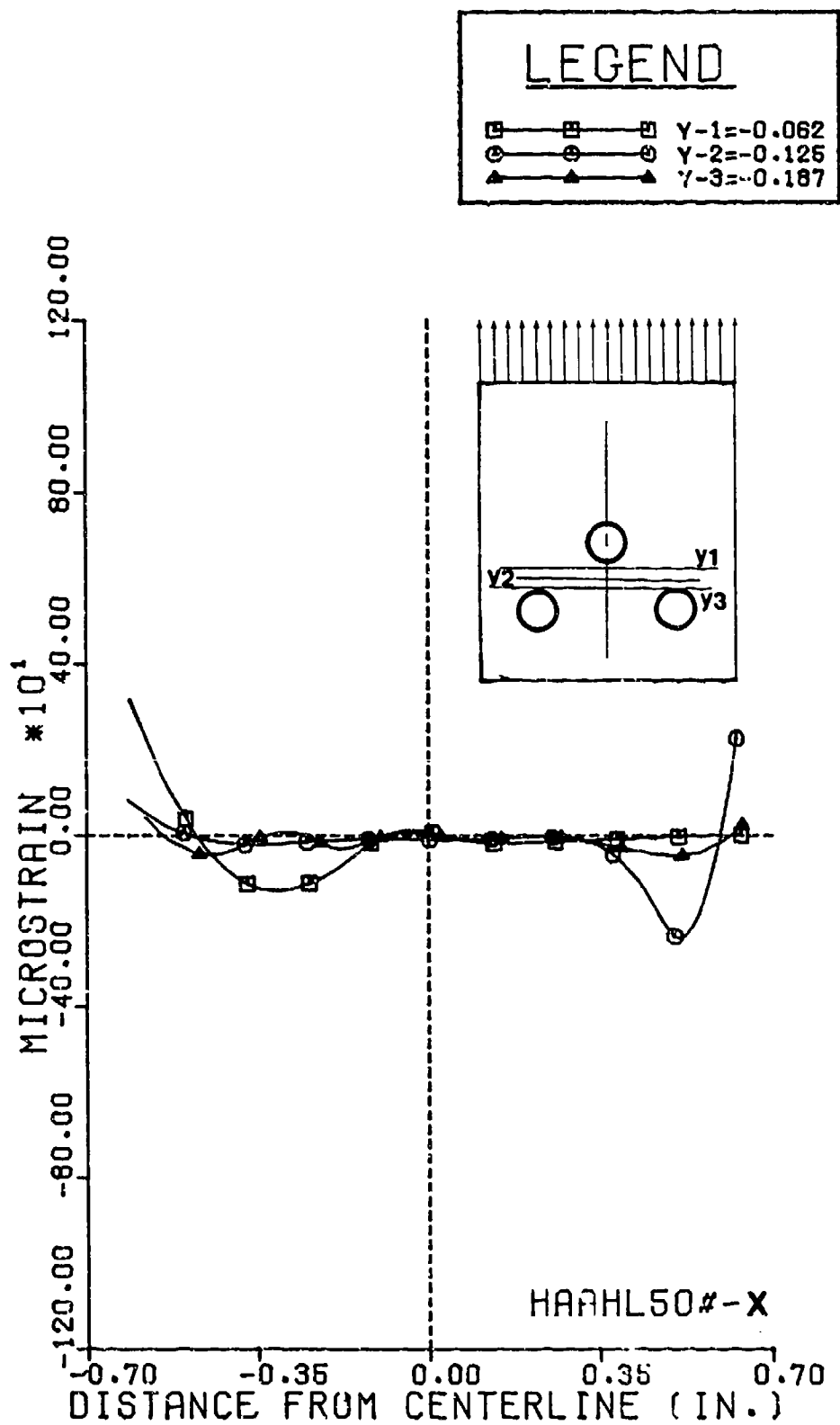


Figure 5-54. Strain ϵ_x along Lines Perpendicular to Direction of Load

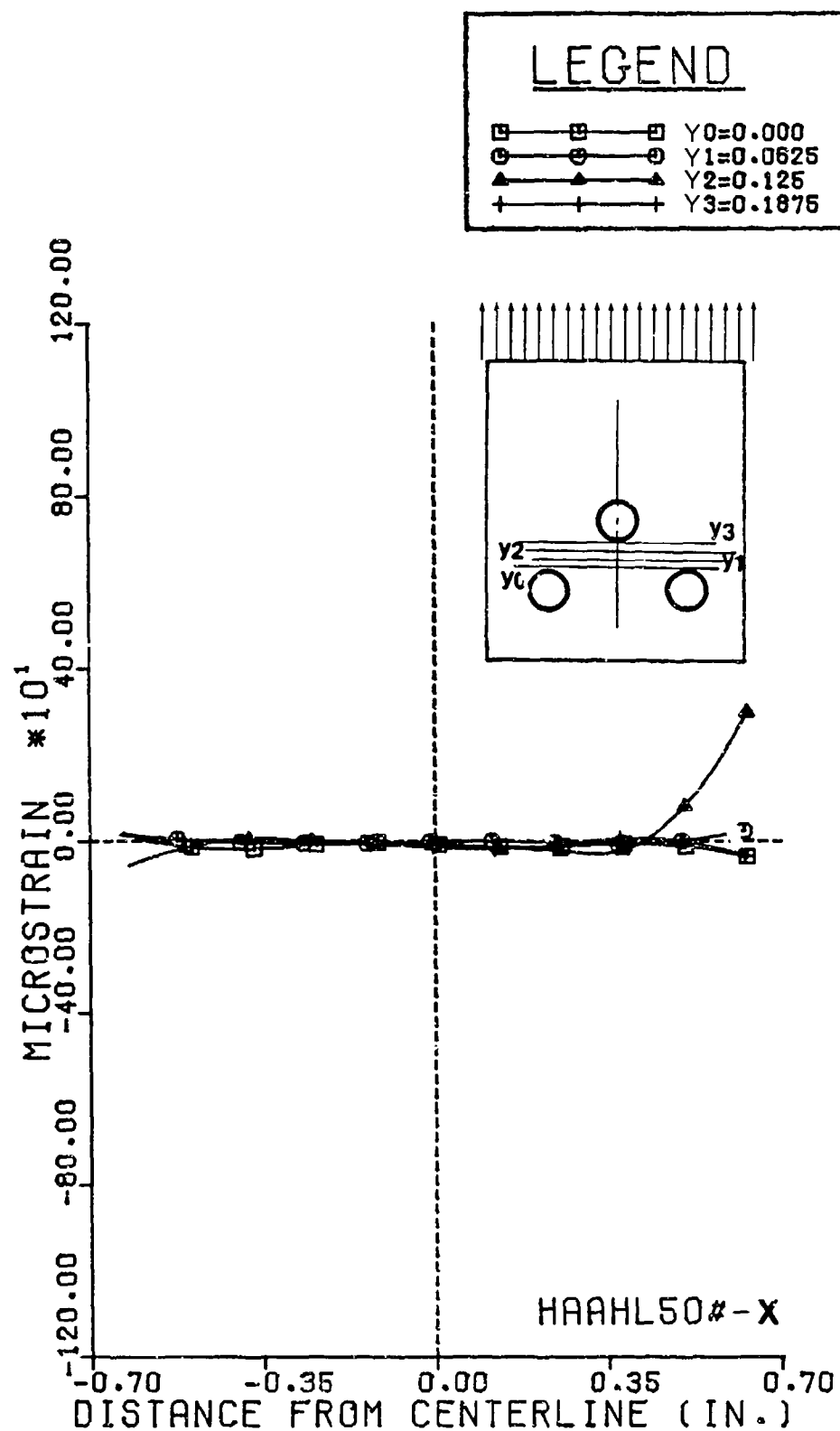


Figure 5-55. Strain ϵ_x along Lines Perpendicular to Direction of Load

Figures 5-56 and 5-57 show strain ϵ_x for parallel lines located on both sides of the upper hole and also above it. In these regions the strain distribution appears to be fairly uniform.

Figures 5-58 and 5-59 show strain ϵ_x for parallel lines encompassing the net section of the lower holes and the bearing region respectively. In Figure 5-58, lines $x(-A) = -0.25$ and $x(-B) = -0.312$ both located in the region between the two holes show a peak value of compressive strain. The interesting thing is that both peaks are displaced to both sides of the centerline. In Figure 5-59, line $x(-7) = -0.437$ shows an increase in strain ϵ_x in a point close to the bearing region of the lower right hole. Again, based on the analysis of strain ϵ_x , there is an indication of uniform strain distribution, except in the region located right above the two lower holes.

Figures 5-60, 5-61, 5-62, and 5-63 show strain ϵ_{45} for lines located in the bearing region, ligament areas, and above the upper hole. In Figure 5-60, in the region located to the right and at the bearing region, the strain is tensile and in the bearing region is highly negative at the edge of the lower left hole, but ϵ_{45} fluctuates from negative to positive. Figures 5-61 and 5-62 show similar behavior for ϵ_{45} in the ligament and bearing region of the upper hole, with tensile on the right side of ϵ_{45} , and to the right the strain fluctuates from negative to positive. Figure 5-63 also shows ϵ_{45} for lines above the upper hole, but there exists a small peak strain value in the right hand side of the specimen. This peak value could be due to material imperfections.

Figures 5-64 and 5-65 show strain ϵ_{45} for lines located in between the two holes and in the bearing region of the lower right hole. In Figure 5-64, ϵ_{45} shows peak values which should be related to maximum values of shear strains and principal strains. Figure 5-65 also shows a peak value for ϵ_{45} in the ligament region of the lower right hole.

5.7. Summary and Conclusions

Tables 5-1 to 5-3 summarize stress concentration factors for the hole arrays and load configurations studied.

Using high-sensitivity Interferometric Moire Technique the stress and strain distribution was obtained for three different directions. The stress concentration factor was calculated at only one point located at the edge of the hole in the horizontal diameter for the two- and three-hole arrays. For the two-hole array in tandem, when both holes are loaded, the stress concentration factor for the upper hole was 2.9 times higher than that at the lower hole, indicating that the load sharing between both holes is not exactly given in a ratio of 2. In the case of two holes in tandem (lower hole loaded) the stress concentration factor

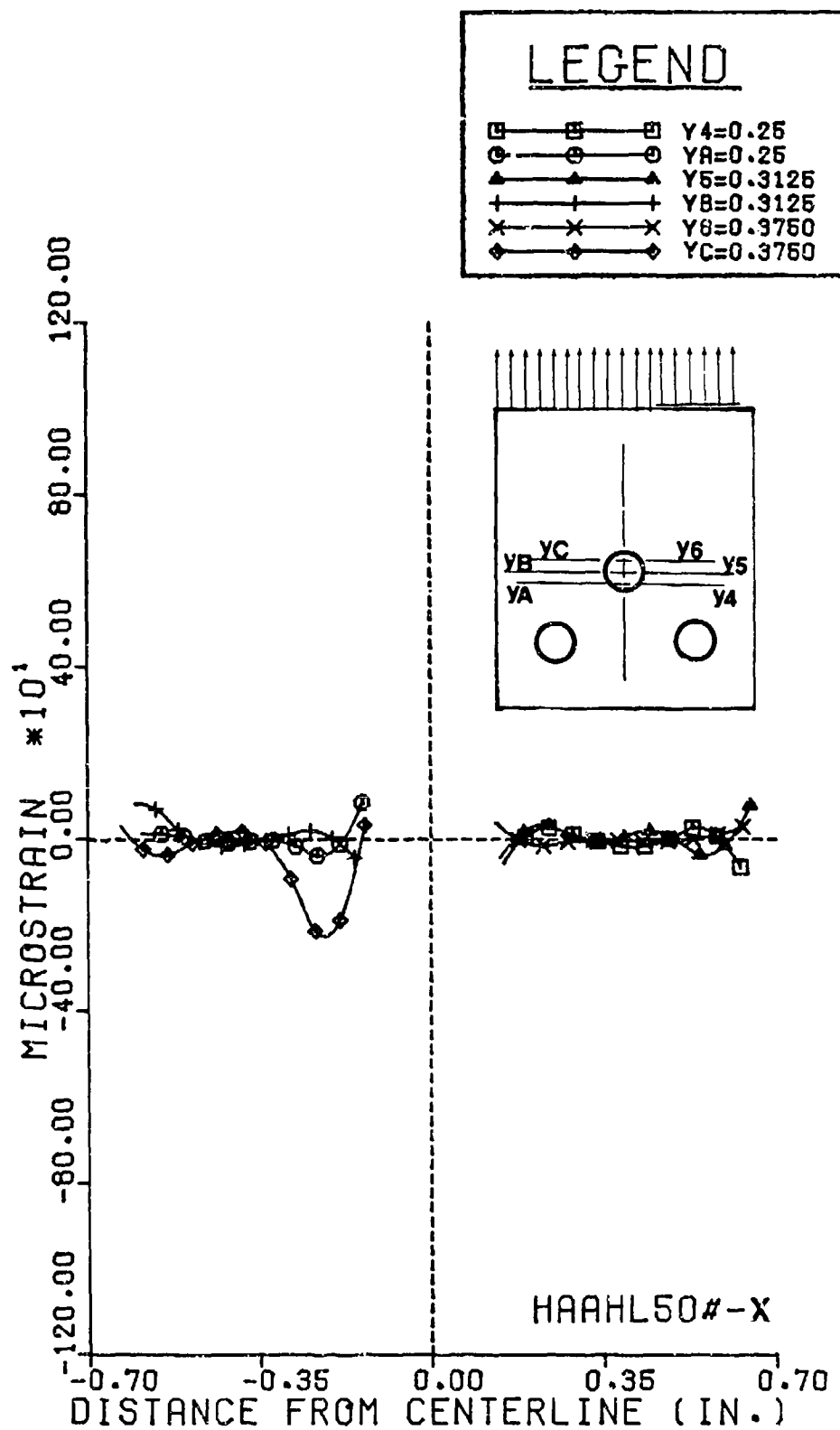


Figure 5-56. Strain ϵ_x along Lines Perpendicular to Direction of Load

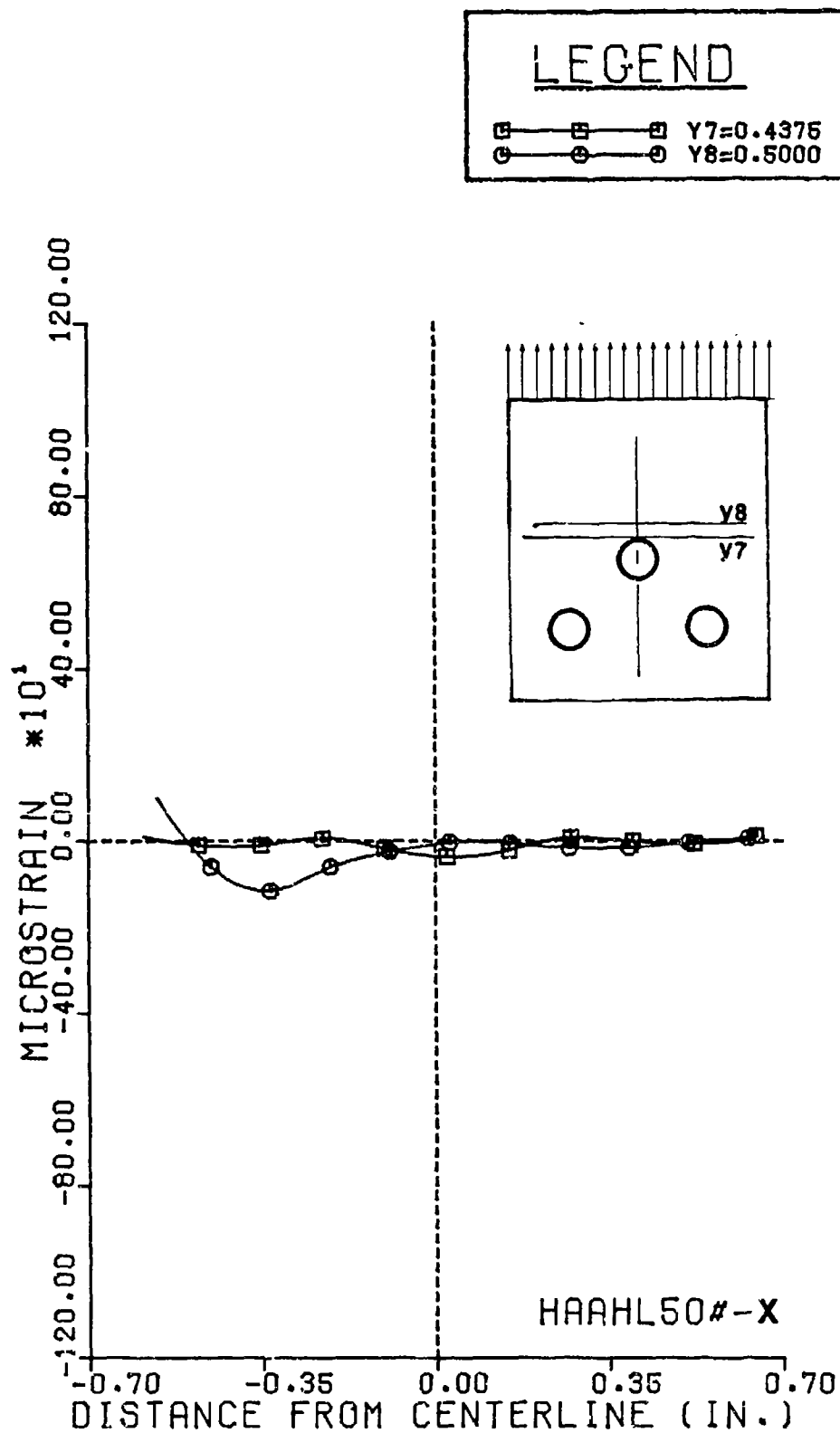


Figure 5-57. Strain ϵ_x along Lines Perpendicular to Direction of Load

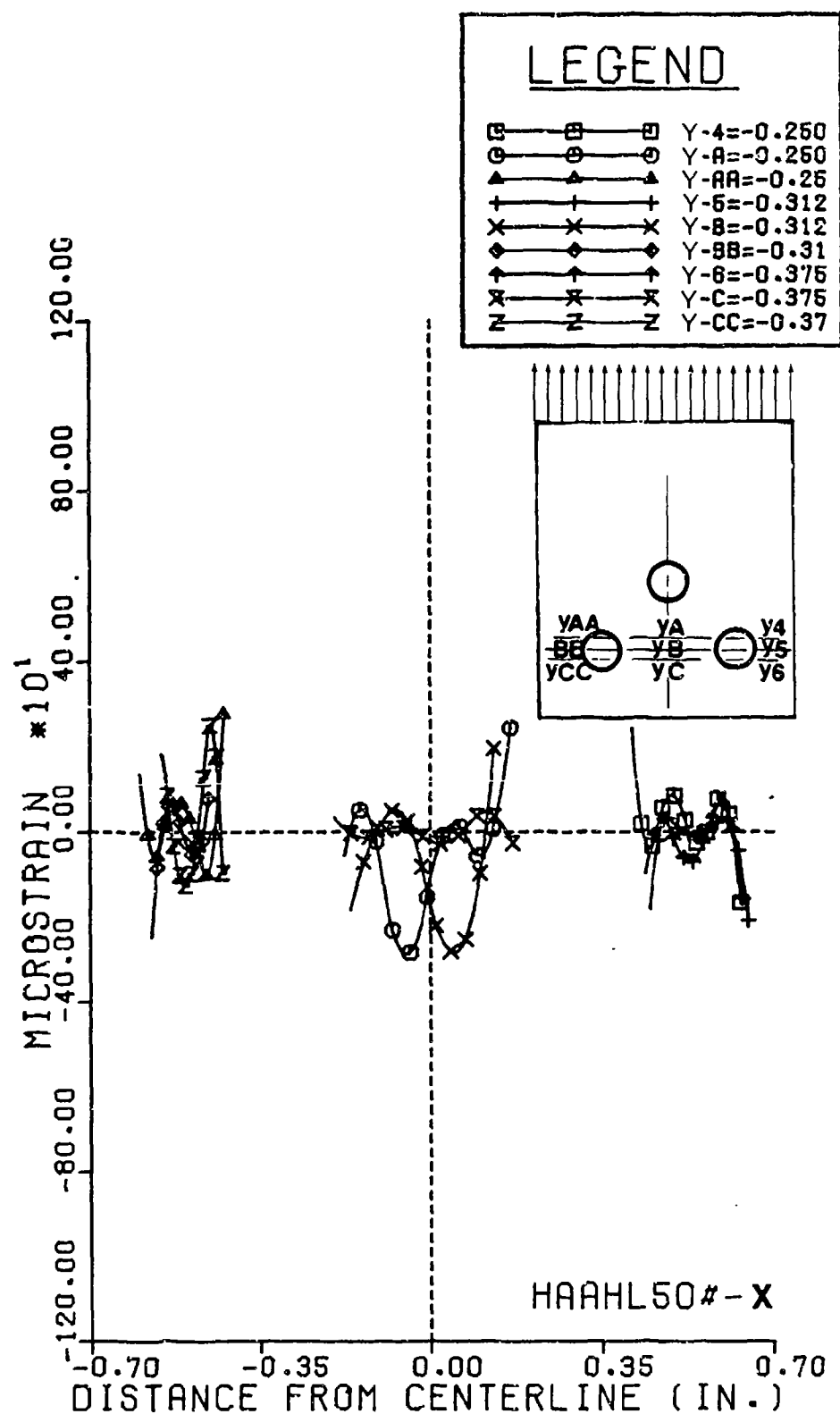


Figure 5-58. Strain ϵ_x along Lines Perpendicular to Direction of Load

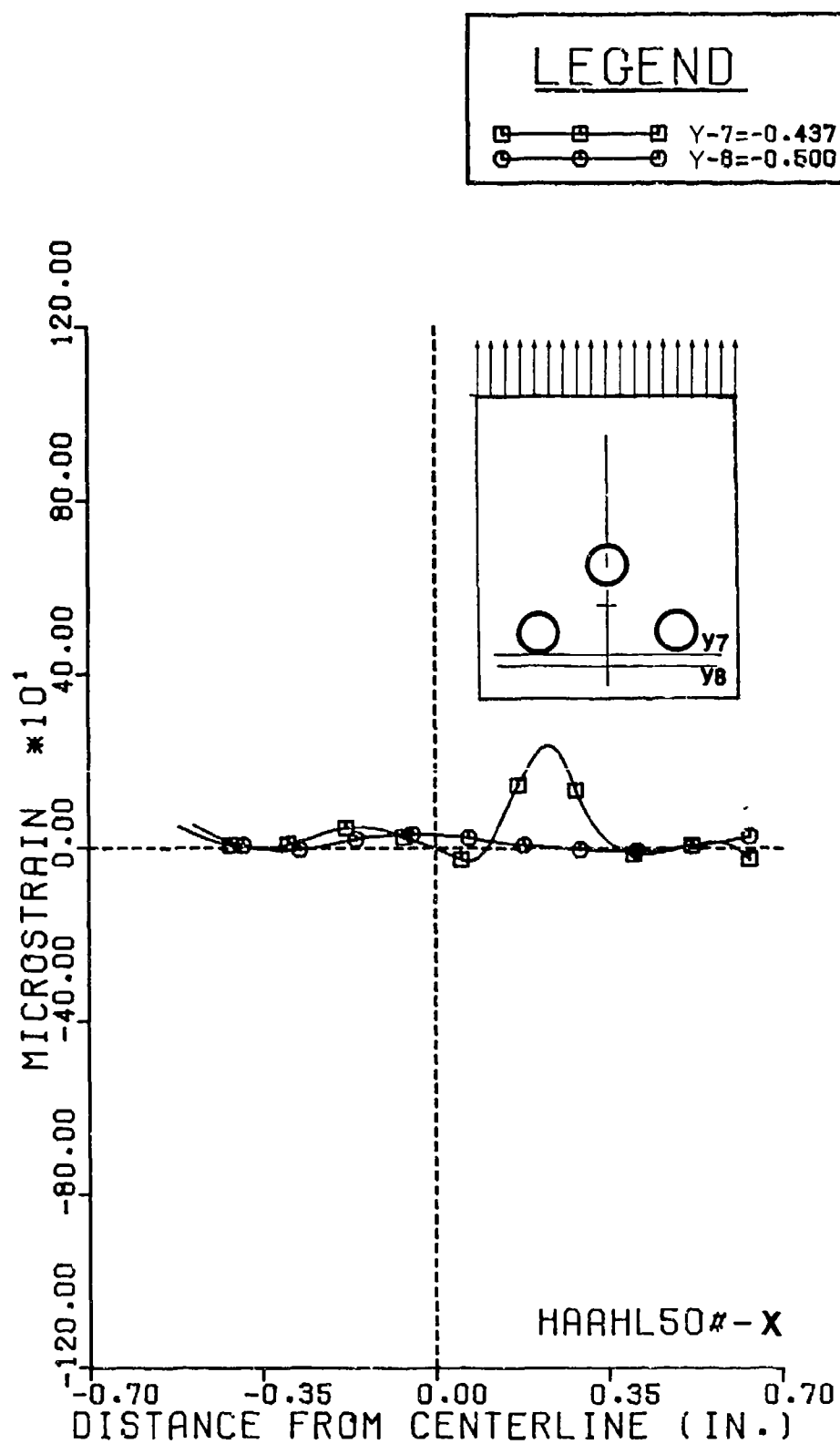


Figure 5-59. Strain ϵ_x along Lines Perpendicular to Direction of Load

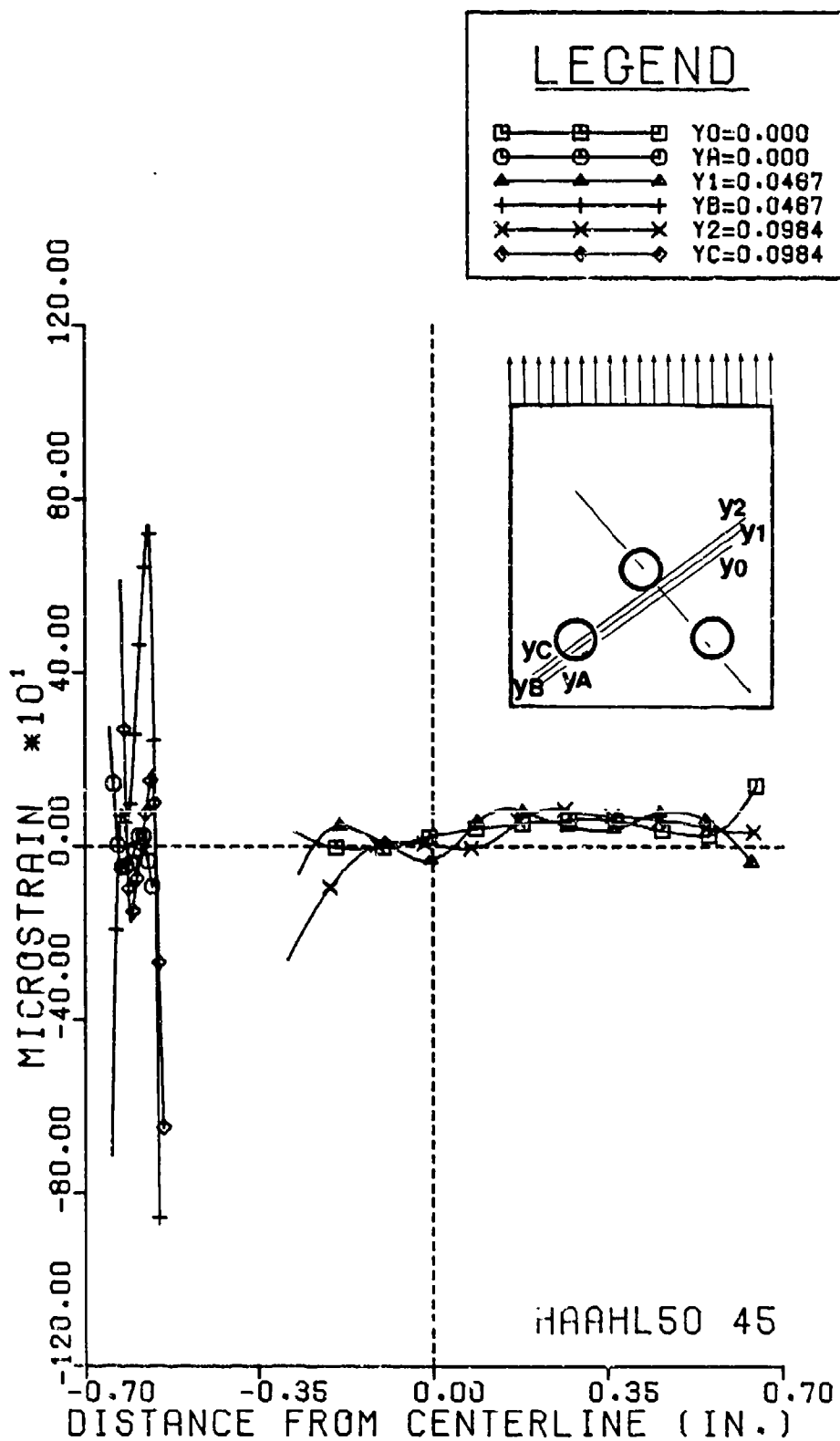


Figure 5-60. Strain ϵ_{45} along Lines 45• to Direction of Load

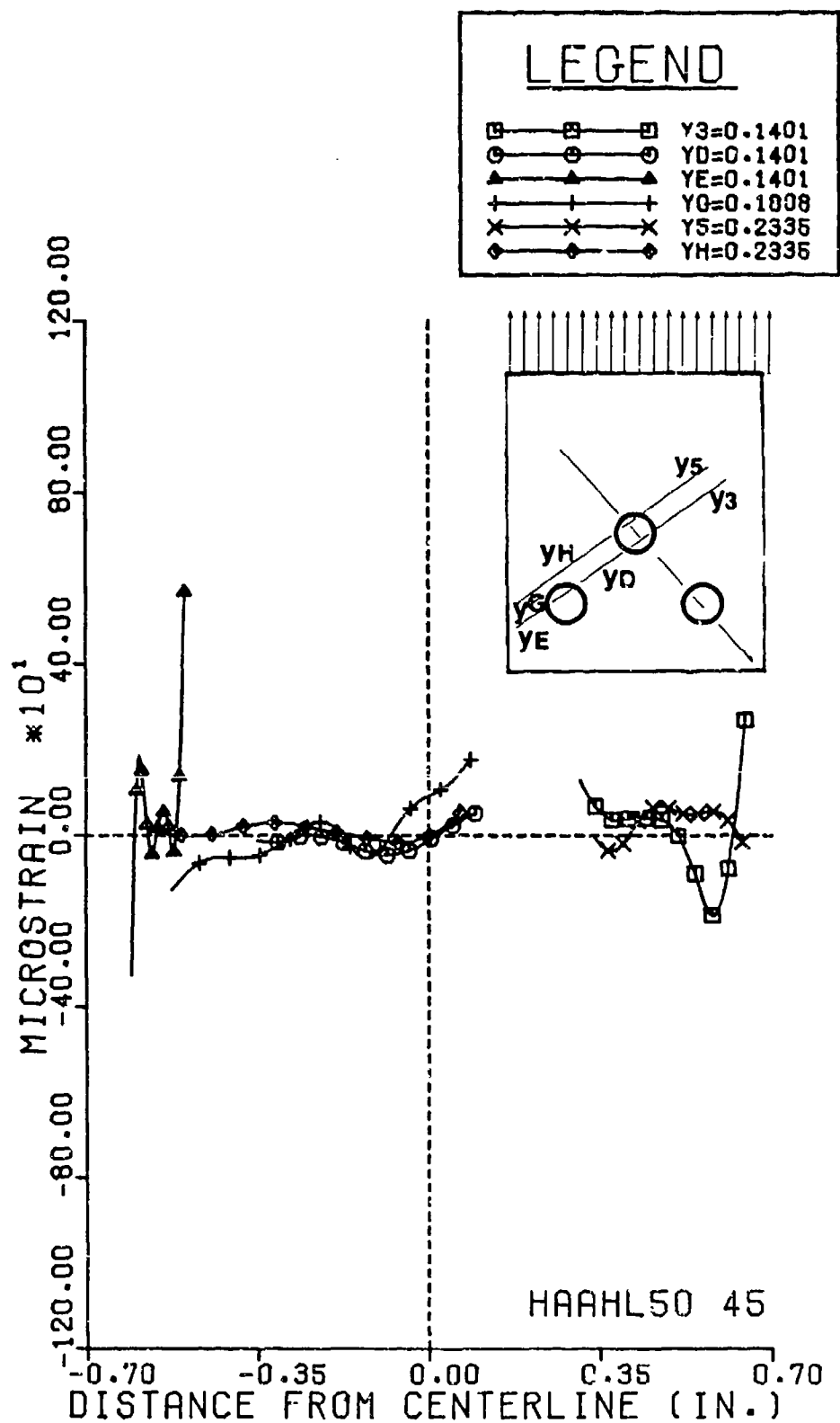


Figure 5-61. Strain ϵ_{45} along Lines 45• to Direction of Load

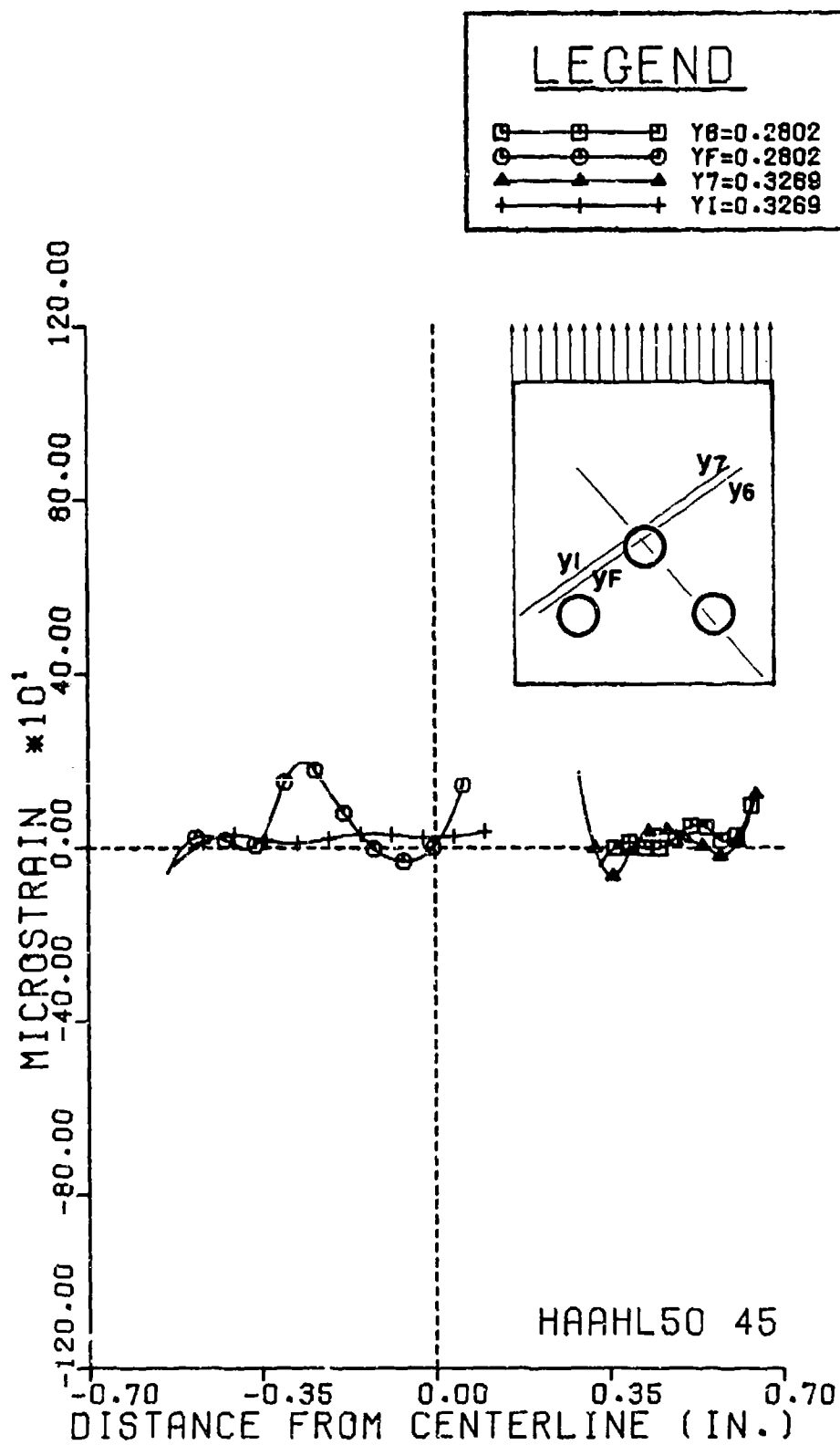


Figure 5-62. Strain ϵ_{45} along Lines 45• to Direction of Load

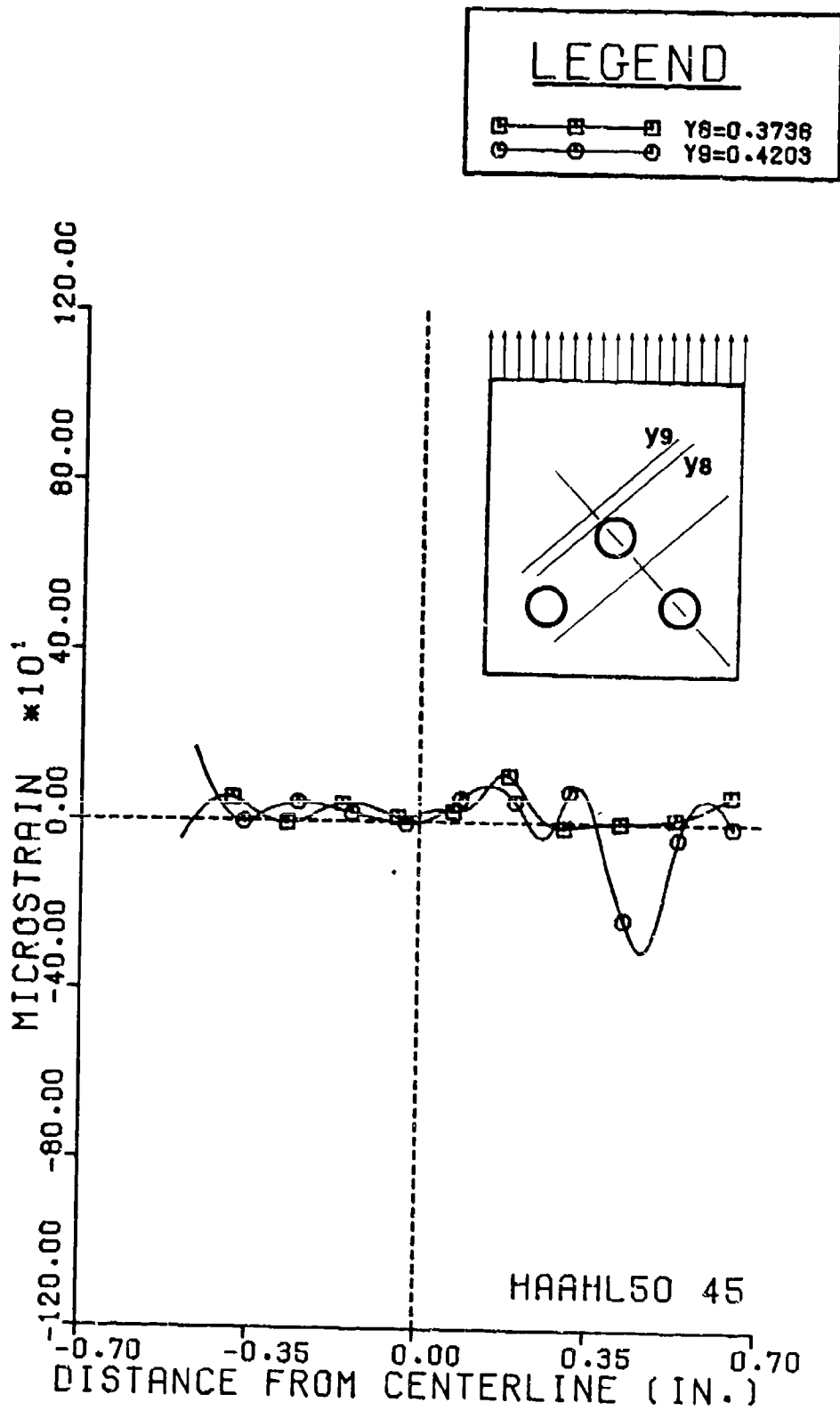


Figure 5-63. Strain ϵ_{45} along Lines 45• to Direction of Load

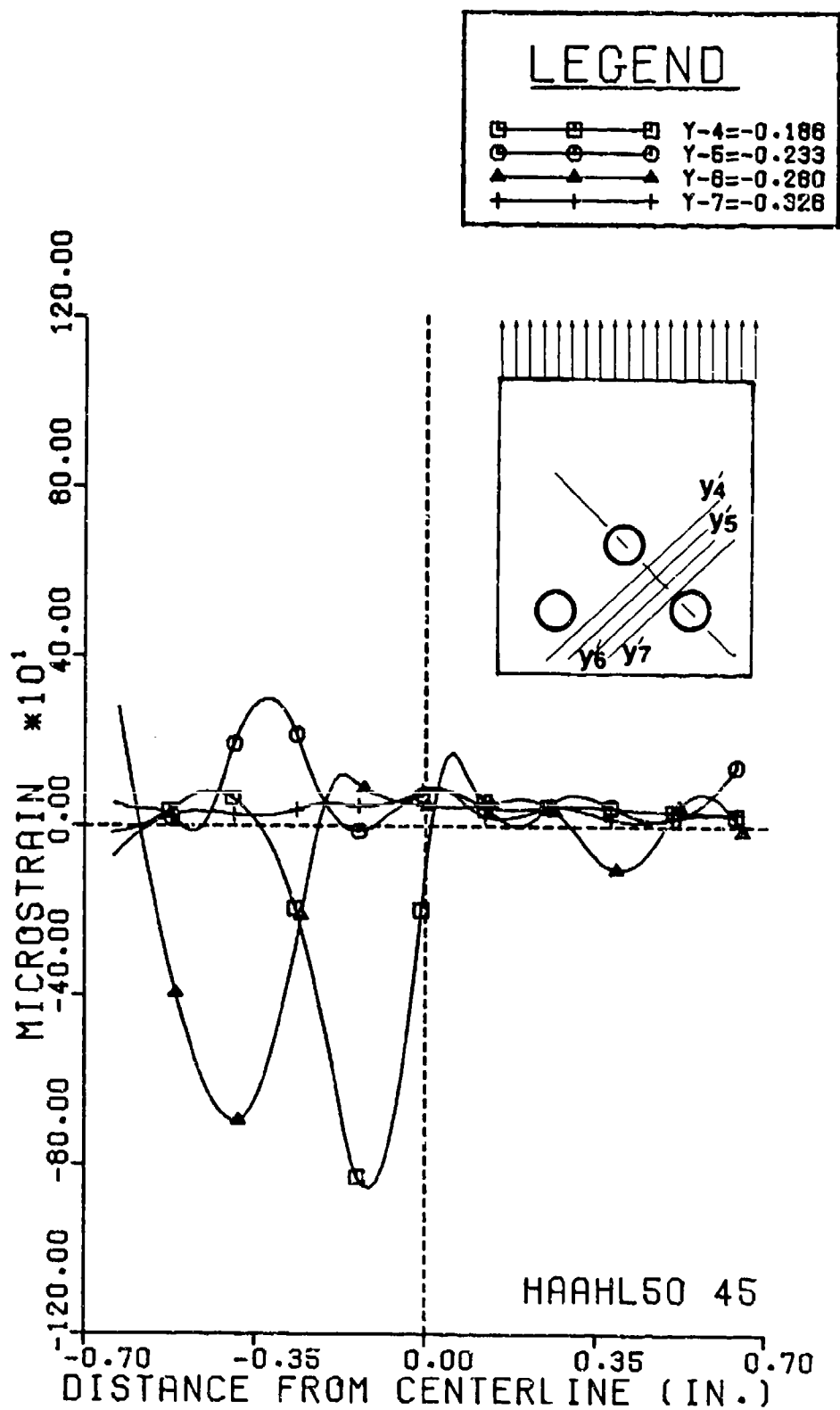


Figure 5-64. Strain ϵ_{45} along Lines 45• to Direction of Load

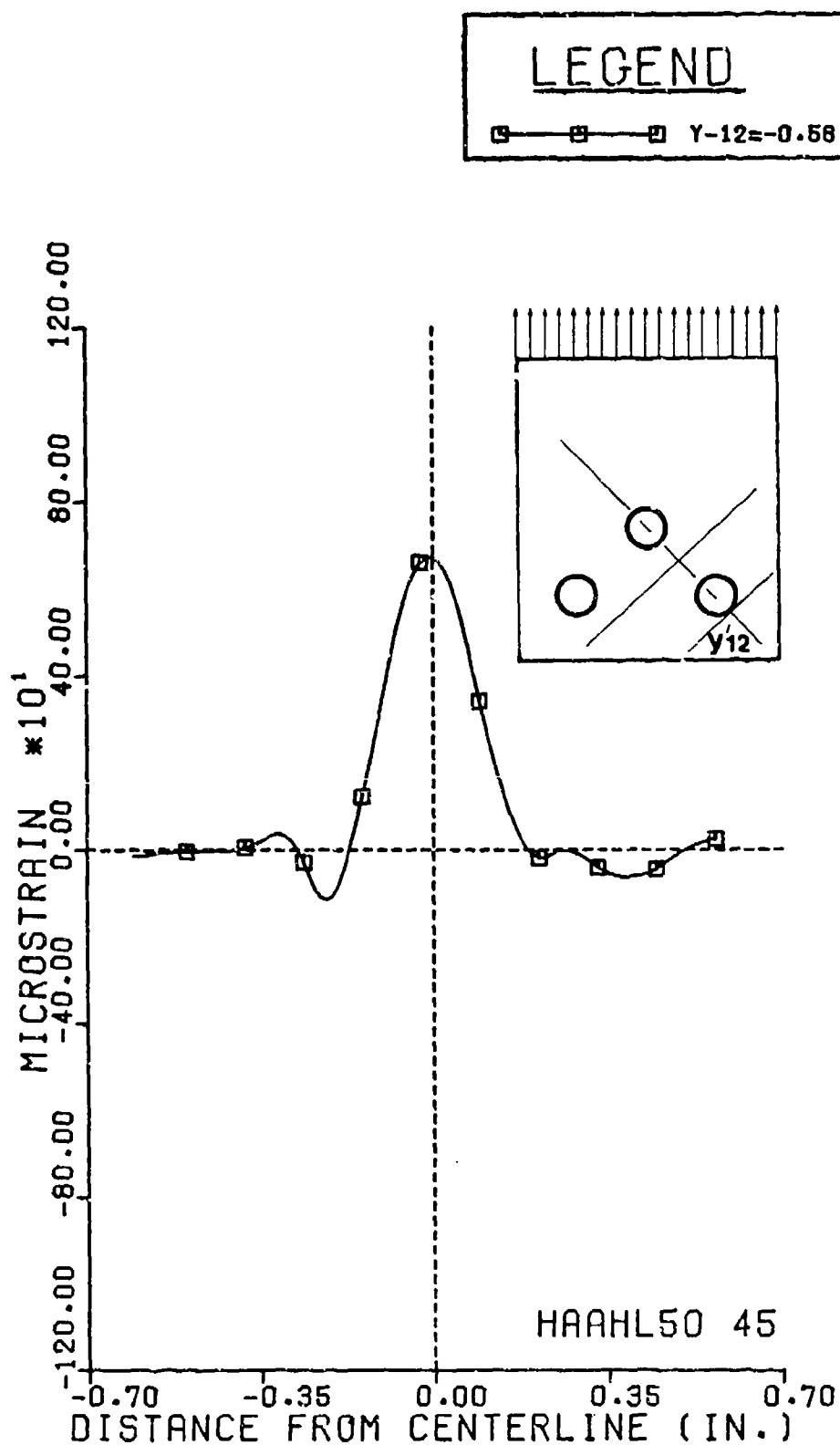


Figure 5-65. Strain ϵ_{45} along Lines 45• to Direction of Load

Table 5-1. Comparison of Stress Concentration Factors

	TWO-HOLE TANDEM			SINGLE-HOLE
	both loaded	up loaded	low loaded	
upper	5.57	12.1	4.97	14.0
lower	1.91	1.0	9.16	14.0

Table 5-2. Comparison of Stress Concentration Factors

	TWO-HOLE PARALLEL		SINGLE-HOLE
	left hole	right hole	
	0.65	1.16	14.0

Table 5-3. Comparison of Stress Concentration Factors

	THREE-HOLE ARRAY			SINGLE-HOLE
	upper hole edge	lower-left hole	lower-right hole	
left	right			
2.17	2.32	2.95	1.54	14.0

for the lower hole was 1.84 times higher than the stress concentration factor for the upper hole. Some interaction between the two holes, one of them being loaded and the other acting as a stress raiser, defines the stress and strain field in the region between them, but the influence of the hole acting as a stress raiser on the loaded one is not very large. When the upper hole is loaded, the stress concentration factor for the upper hole produces a large influence in the stress/strain field of the lower hole. The ratio of SCF between both holes is 12. For the case of the two-hole array in parallel, there is a further reduction of the net section area, and an increase in the stress concentration factor was expected at the edge of the holes. In this case, the results showed a fairly uniform distribution of stress and strain around the holes.

In the case of the three-hole array in a staggered configuration, some asymmetry was observed for the stress concentration factor. For the upper hole $k = 2.32$ and $k = 2.17$ for the right and left edges respectively, and for the inner edges of the two lower holes $k = 2.95$ for the lower right and $k = 1.54$ for the lower left. This was an indication that the right half of the specimen had a higher SCF. Also some high strain values were observed above the two lower holes in a symmetric position with respect to the specimen. The bearing area of the upper hole did have some effect on the strain field of the three holes.

If these results are compared with the result obtained by Herrera-Franco and Cloud [5.2, 5.4] for a single pin-loaded hole, where the stress concentration factor at the edge of the hole was equal to $k = 14$, then the advantage of utilizing a multihole array in a connection is evident by the reduction of SCF at each hole.

6.0. EXPERIMENTAL STUDY OF WASHERS AND CLAMPING FORCE

6.1. Objectives and Scope

The main objectives in this phase of research are:

- To gain insight into the strain field in the vicinity of bolted connections when using flat, concave, and convex load spreading washers, different clamping pressures, i.e., bolt torques, and different loads;
- To compare the strain profiles of the investigated fasteners seeking the most strain relieving concept;
- To compare the degree of strain relief between bolted connections and pin-loaded holes.

The specimens were loaded statically leaving no residual strain around the fastener after unloading. Interlaminar strains as well as strains underneath the washer were not taken into account. The bolt size of 0.25 in. in diameter, the washer's inner and outer diameters, as well as all specimen specifications, were kept constant. The experimental setup and the experimental procedures, (see Par. 4.0) were basically the same for all measurements. Attention focused on the question of which type of washer would provide the better strain relief. Having this in mind the parameters were not varied except for the applied load and the clamping force, i.e., bolt torque.

An evaluation on other design parameters (such as washer size, end effects, clamping forces etc.) is made in Par. 1.0. There, the basic behavior of bolted joints in composites is explained and reviewed from literature findings. Parameters such as hole diameter, hole tolerances, type of fit, washer dimensions, specimen to hole dimensional relations, clamping forces, etc., for this research project were kept precisely within the suggested optimal limits.

6.2. Approach to the Problem

A literature search was conducted to determine the research fields already being covered. Numerous previous investigations of mechanical joints were found. These are outlined in Par. 1.0. The findings were utilized to draw a line to unknown regions and, thus, to reduce the necessary amount of experimental work. The basic behavior derived from literature was used to establish most of the parameters of the experimental procedures and the experimental setup.

In earlier investigations strain relief was found as a measure to improve joints in composites [6.1]. This criteria was used to evaluate the tested fastener designs. The surface strain measurements necessarily had to feature whole field, biaxial data.

A highly sensitive Moire method was applied to measure the surface strain field around several mechanically fastened joints. This method was a well-developed in-house technique and had a sensitivity which is adequate for work on composites.

Starting with examining single-pin-loaded holes [6.1 through 6.8], a basis was created for comparing bolted connections. In the case of pin-loaded holes the absence of frictional forces transmitted between the contacting composite plates concentrated the force flow over the bearing region (compressive zone underneath the hole). In the case of bolted connections the force flow separates with an amount going through the bearing region and an amount being transmitted over the contacting plates. The last mentioned partial force flow is increased by increasing the clamping force. Then, the bearing stress is significantly reduced and the overall strain level is widely distributed into the vicinity of the fastener. This advantage is acquired in conjunction with an increase of interlaminar shear strain, which, in case of no or too low a lateral constraint, would be highly critical.

The very difficult task of measuring the ratio of these force flows to decide where the more efficient strain relief takes place was altered into the task of measuring surface strain distributions around the washers. Evidence that the surface strains will give a criteria for strain relief was found in several papers [6.9 through 6.15]. Extreme care was taken when accepting this conclusion. From experimental evidence, a slight imperfection in the experimental set-up was shown to cause deviations of 90 percent and more in the strain readings. Small variations like a tilted pin or bolt which usually cannot be avoided in normal applications do have such an impact since the material is build up in layers. Each layer can have separate stress and strain levels and profiles [6.16], and the strains in the surface layer may be illusory. Thus, care was taken to keep the experiments repeatable.

Interesting to note is that the results from experimental work with composites do assume a more perfect stage of experimental environment than similar work on, for example, metals. Practice shows that the material is much less forgiving to local imperfections, therefore, the evaluation of literature about experimental results dealing with composites must be done cautiously.

For this investigation three of the most relevant papers are from Stockdale and Matthews [6.17], Collings [6.18], and Crews [6.19]. They investigated failure modes of bolted connections utilizing washers. Stockdale changed washer sizes and clamping forces when loading his specimens to failure. His results show that above a minimal clamping force the bearing failure mode was out of consideration. Failure occurred at the outer edges of the washers by compression or by cracking at the hole, both apparently caused by a low shear strength. It was found that larger washer outer diameters extended the failure limit but desired weight savings and bending of the washer set an optimum value. For this investigation a value of 0.563 in was adopted (0.25 in bolt size).

A maximum clamping force must not be surpassed to avoid surface damage of the composite and bending of the plate resulting in early failure [6.20]. In this investigation a maximal force of 400 N was established.

All design parameters of specimen and setup were optimized according to the literature findings mentioned in Par. 1.0.

In order to compare the work with former similar investigations on pin-loaded holes by Herrera [6.1] the hole size was chosen to have a diameter of 0.25 in. Also, the load Herrera used for his measurements was increased exactly by a factor of two and then four when applying tensile load onto the test coupon.

6.3. Choice of Method

Measurements of surface strain distributions were required in order to investigate the possibility of strain relief either by the use of flat or a type of convex load spreading washers. The material had a flat, rather smooth and uniform surface. Out-of-plane displacements were negligible. A high sensitivity was required to examine elastic strains. Biaxial strain data and whole-field mapping of the strain field should be obtainable on the same specimen. The data should be compatible with data from Herrera, who basically used the same technique on a different fastener problem.

An already successful moire interferometry technique (see Par. 4.0 and Appendix D) was devised using a 16,256 lines per inch (lpi) phase-type grating which was applied onto the surface of the specimen. A two-beam system of coherent laser light illuminated the grating and reflected a diffraction pattern. The first diffraction orders of each beam were overlapped to create a Moire fringe pattern, by interference. From the change of this pattern, displacement and, thus, strain could be calculated utilizing a computer program [6.21]. The technique had an excellent sensitivity, and it offered an easy measurement of whole-field and biaxial strain data. The production of the grating, as well as the application of the grating onto the surface of the specimen, was a well-developed routine. Additionally, most of the equipment and know-how was readily available, which promised to make the project time and cost efficient.

6.4. Surface Regions of Interest

It is necessary to distinguish four different regions, shown in Figure 6.1, around the hole:

- The area below the hole, where the pin or bolt shank contacts the composite, is called the bearing region. Here bearing failure by compression and/or delamination can give the failed surface a brushlike appearance. Also, the locus of shear-out failure, sometimes introduced by bearing failure, is in this region. In case of using washers the primary bearing region is hidden underneath the washer. In general it is impossible to obtain

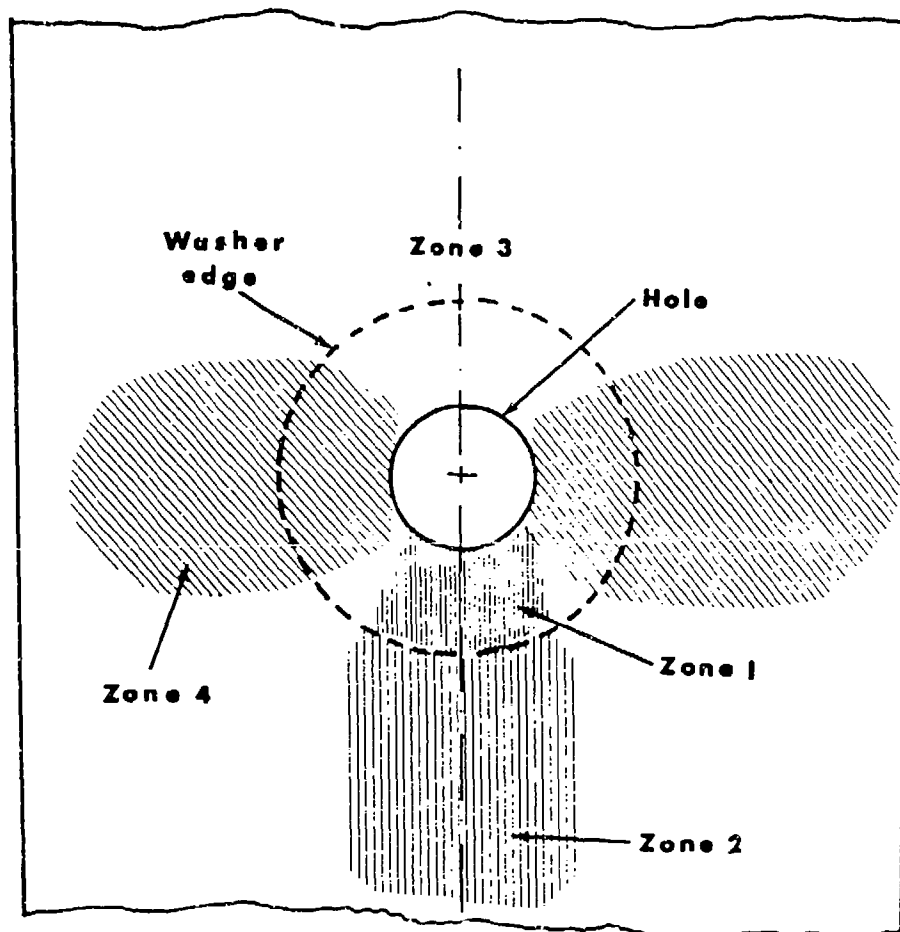


Figure 6-1. Specific Regions of Interest for Measuring Strain in the Vicinity of the Fastener

strain data from the surface area subjacent the washer with the technique.

- The area below the lower edge of the washer is called the secondary bearing region or the lower zone. For sufficient clamping pressures it is shown [6.17] that failure occurs in this zone rather than in the primary bearing region since delamination is suppressed. The failure modes are bearing (compressive damage) and/or shear-out.
- The region above the hole or washer is called the top zone.
- The regions on both sides of the hole or washer are called the ligament regions; they are the loci of net-tension failure. In the case of washers the failure might occur underneath the washer [6.17] in form of cracking at the hole if the level of lateral constraint is too low.

Owing to time limitations because of an inefficient digitizing procedure only a limited number of axes could be chosen to obtain strain profiles from. Figure 6-2 shows for all three measurement directions the positions of the axes along which strain profiles were obtained.

6.5. Influence of Misaligned Pin

A pretest series using a pin (0.25 in. diameter) to connect the composite plates was performed. Loads of 100 and 200 pounds were applied. The Moire fringe patterns are presented in Figure 6-3 for reasons of completeness. A more accidentally occurring effect caused a major deviation from strain profiles observed by Herrera [6.1], as is illustrated in Figures 6-4a through 6-4d. The deviation was caused by an axially tilted pin as shown in Figure 6-5. Since the material is laminated, the bearing region is strongly separated and shifted partially towards the inner layers of the first composite plate. This introduces compressive strain in the theoretical tension zone and the high compressive bearing strains of the lower zone are accommodated in the inner layers of the laminate.

Evidence for this explanation is given in the axial strain plot (Y-direction). Figure 6-6 shows compressive strain where there should be pure tension in the upper zone (CENTERUP) right above the hole. In the lower zone the values of compressive strain (CENTERDO) are decreasing instead of increasing. The overall strain levels at both sides in the ligament area are much too low compared with the regular case. Additionally, another factor might have reduced the peak levels. That is the different mounting method at the upper end of the specimen. Herrera used a second pin to fix the specimen. In contrast to the grips used for this investigation Herrera's method could introduce stress channels along the fibers running tangentially to the hole section, Figure 6-7.

The transverse strains exhibit similar effects but because of the low strain values they are not presented.

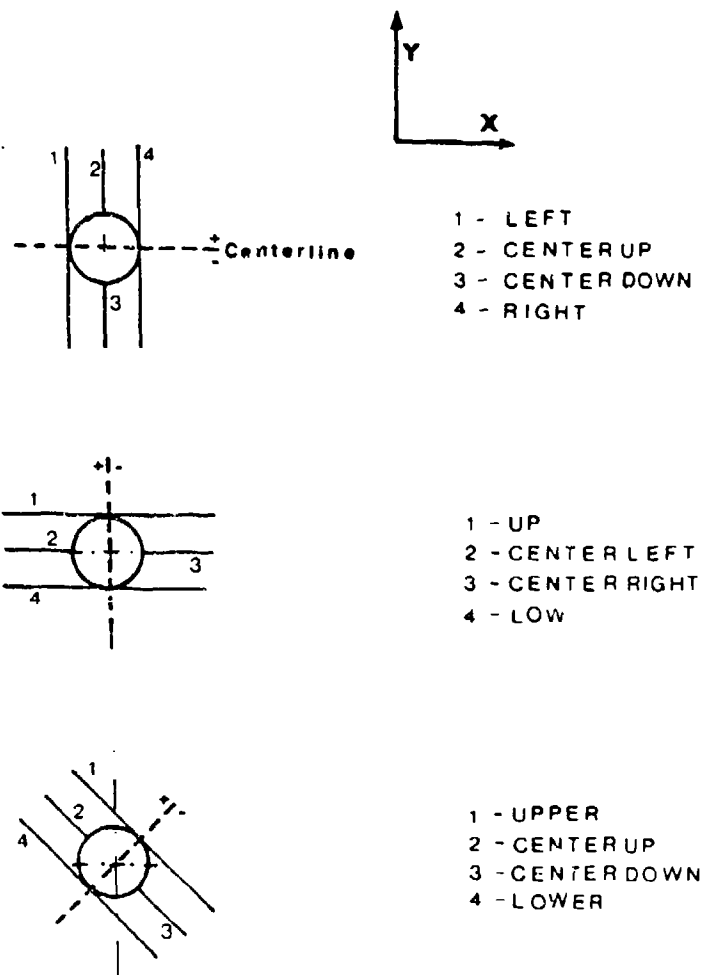


Figure 6-2. The Locations of the Chosen Axes for the Digitizing and Strain Readout are Shown and Labeled in Correlation with the Labeling in the Strain Plots

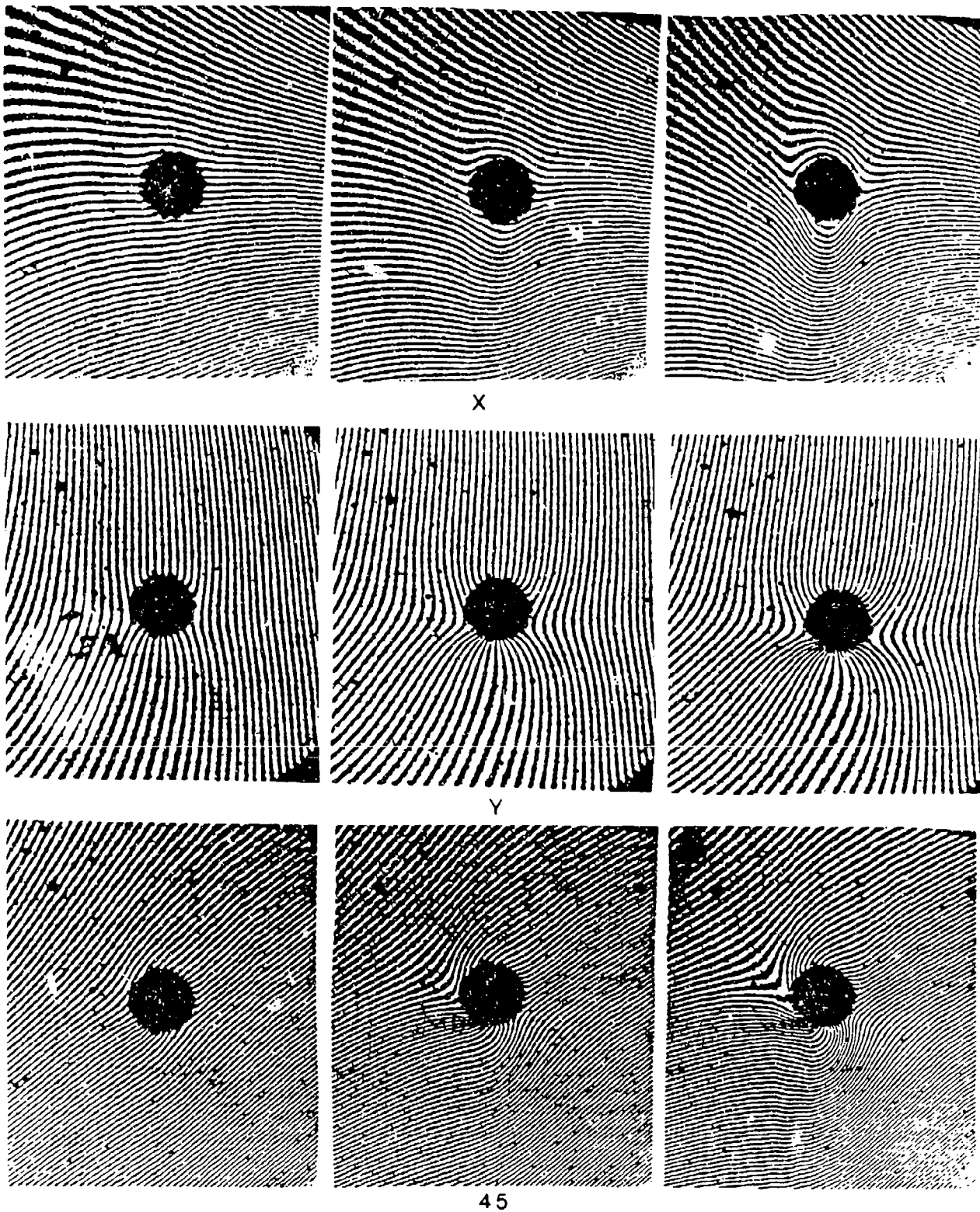


Figure 6-3. Moiré Fringe Patterns of Displacement in all Three Directions (Y, X, 45 °) for the Tilted Pin. Left: No-Load; Center: 100 lbs.; Right: 200 lbs.

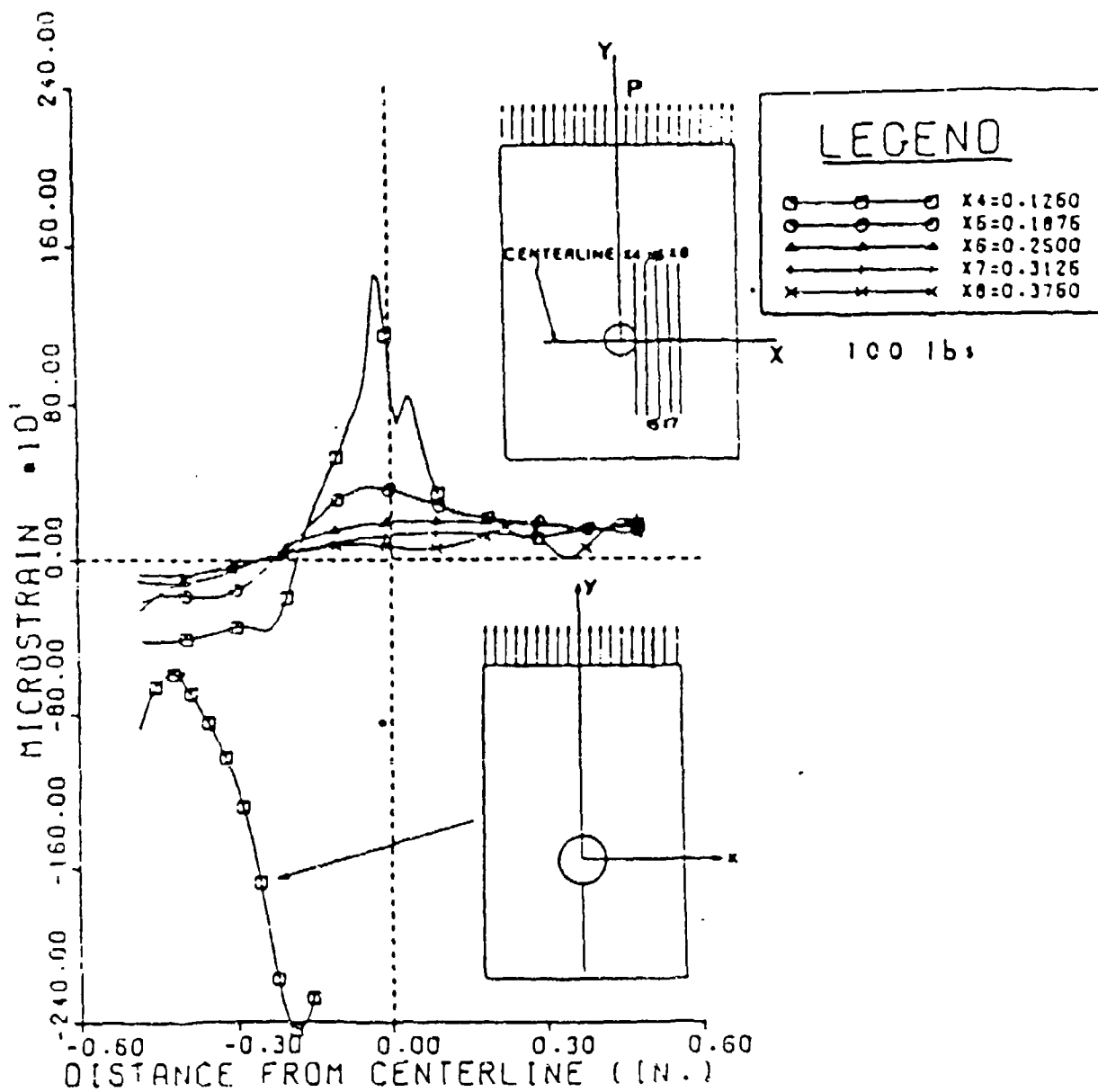


Figure 6-4a. Comparison of the Strain Profiles of a Regular Pin

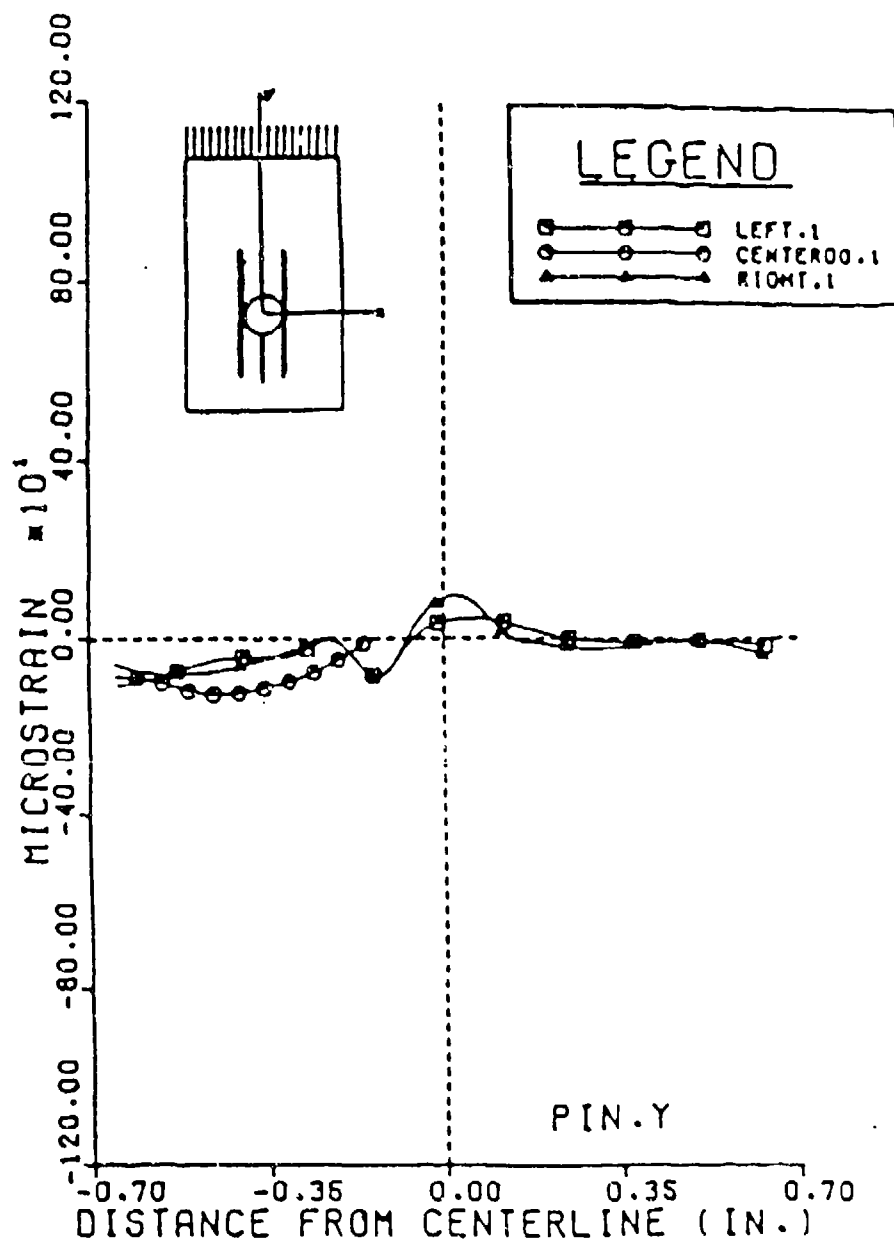


Figure 6-4b. Comparison of the Strain Profiles with a Tilted Pin

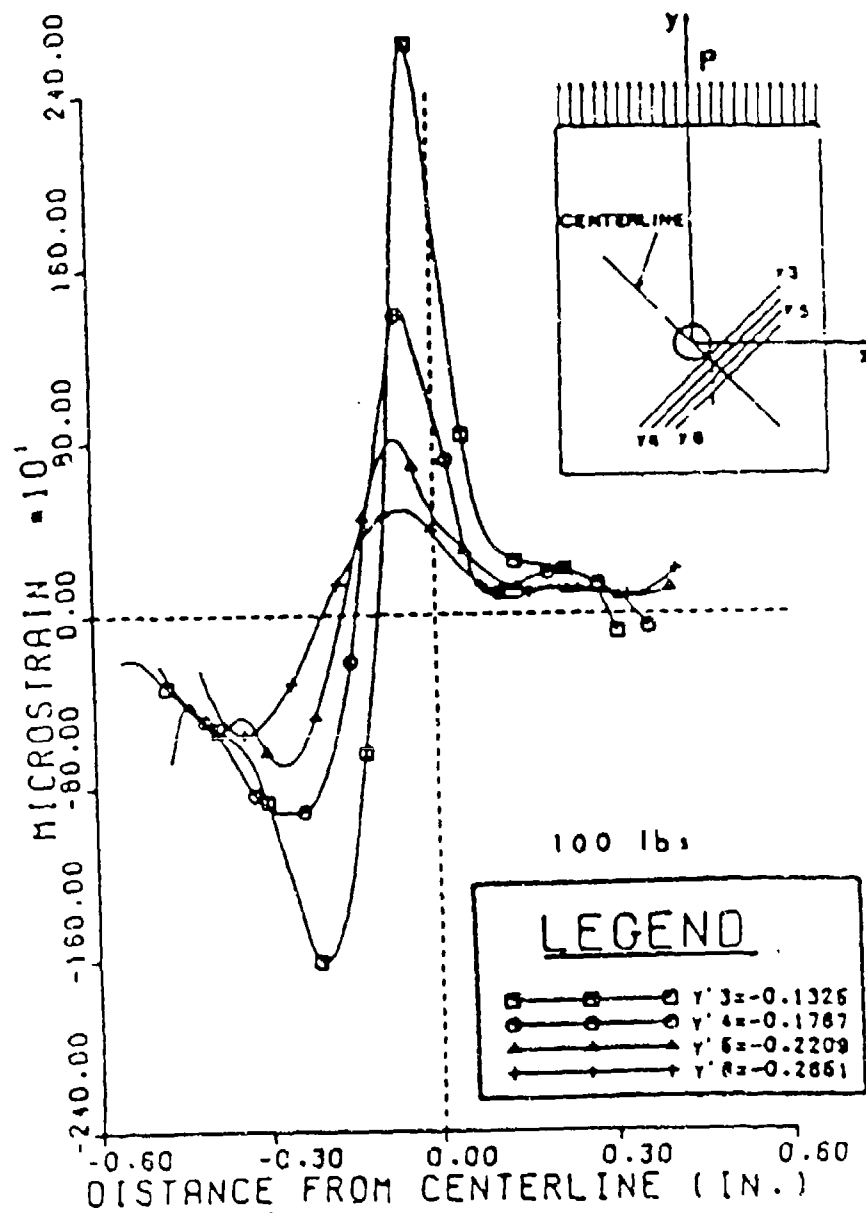


Figure 6-4c. Comparison of the Strain Profiles in the Y-Direction

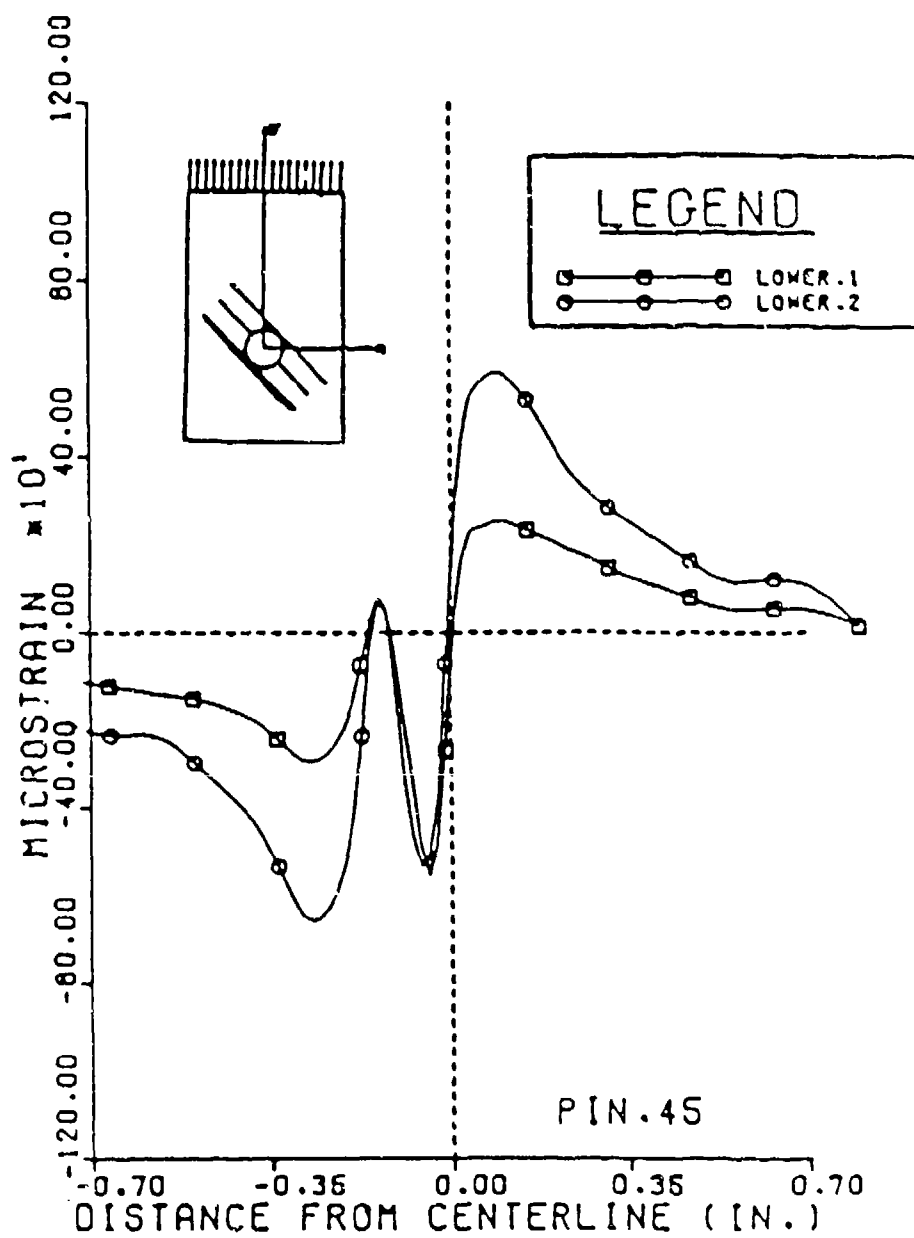


Figure 6-4d. Comparison of the Strain Profiles in the 45° Direction

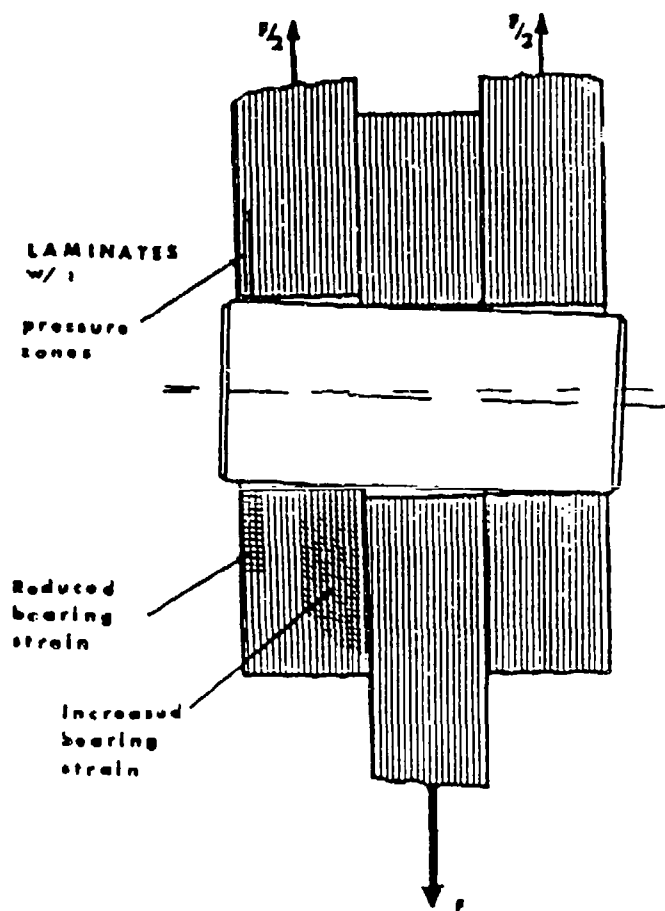


Figure 6-5. Effect of Tilted Pin-Deviation of Surface Strain by Shifted Bearing Area

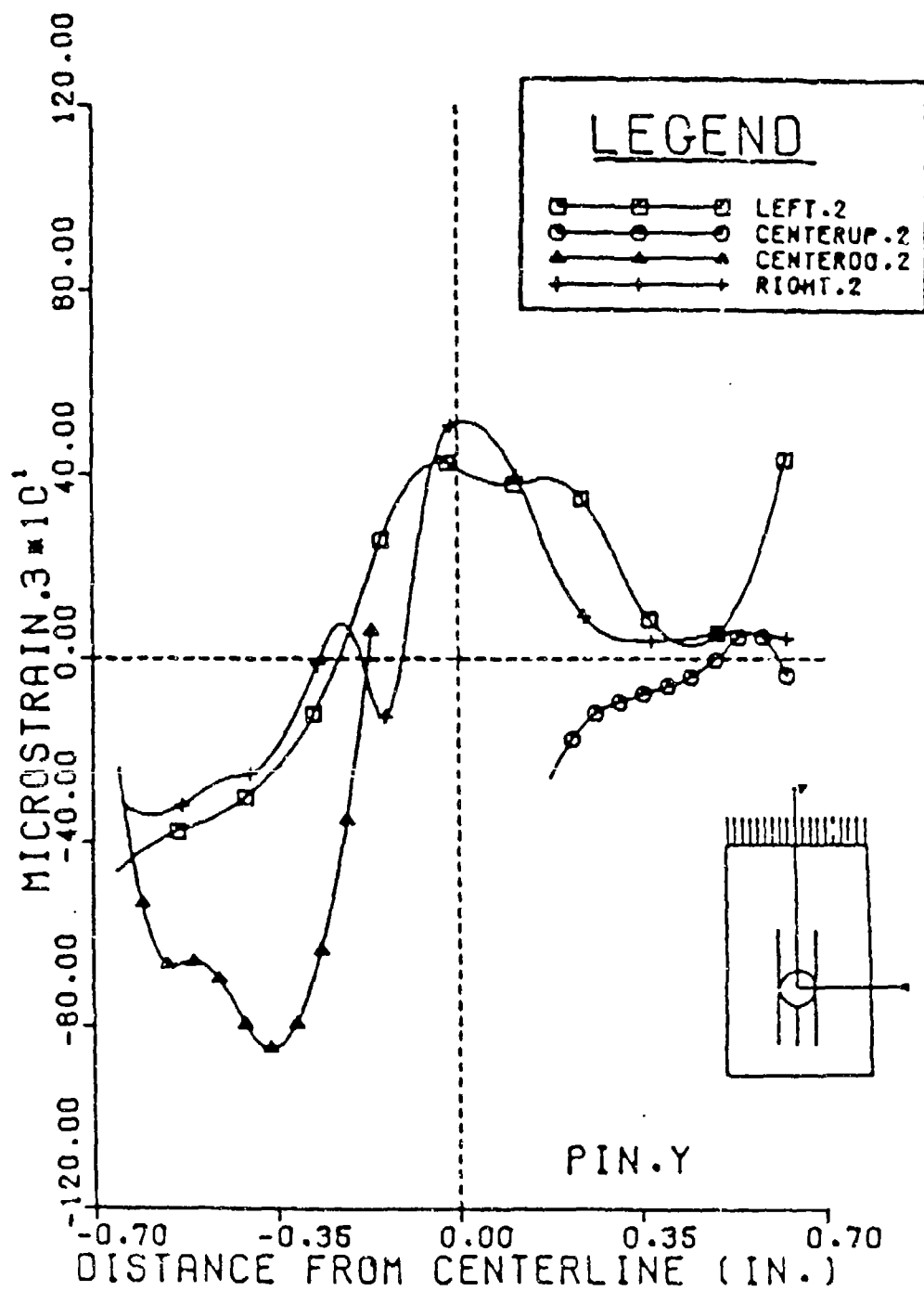


Figure 6-6. Axial Strain ϵ_y of Tilted Pin

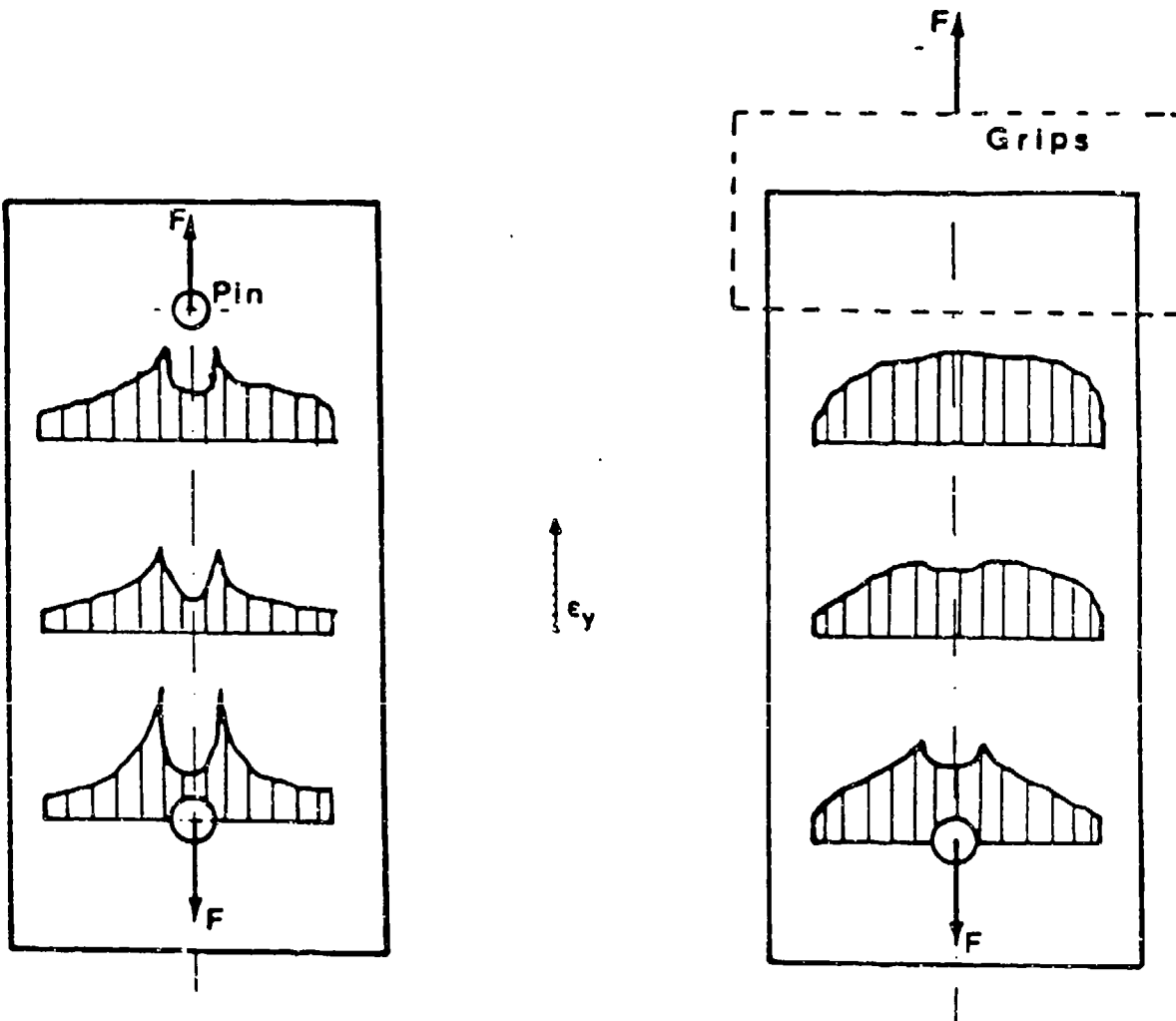


Figure 6-7. Influence of Specimen Mount onto the Axial Strain Distribution; Comparing a Pin and Grips Qualitatively

Also, the 45-degree strain profiles which indicate shear strain are showing effects caused by the tilted pin. The strain levels measured were too low and, underneath the pin, where usually the highest bearing strains create plain compressive 45-degree strains, a tensile peak is perceptible (UPPER). It is followed by a rapidly increasing compressive peak where there should be a tensile one.

There is no full bearing strain developed in the surface layer due to a tilted pin. Slight imperfections are causing tremendous deviations in the surface strains. The prediction that the surface strains are a valid criteria to evaluate joint efficiency must be used cautiously. In the later experiments extreme care was taken to avoid these errors. In order to keep the setup compatible when comparing different types of washers, the grips were carefully aligned. A clamping force transducer was built into the force flow of the bolted connection and the bolt torque was increased until the transducer indicated the desired clamping forces. Furthermore, for reasons of repeatability the introduced torque should not have any influence onto the strain field. Therefore, a thrust bearing was used to uncouple the rather destructive effects of torque from the surface laminate.

6.6. Influence of Bolt Design

Some pretest series using the assembly shown in Figure 6-8 indicated that the head of the bolt would cast a shadow in regions of interest (see Figure 6-9). The head size was reduced to a minimum. The new fringe patterns still are showing slight shadows but they are covering a negligible amount of surface.

6.7. Influence of Torque

The torquing of the bolt introduced a high rotational strain onto the surface layer of the laminate as shown in Figure 6-10. A device shown in Figure 6-11 was built which provided the application of lateral constraint without twisting the surface. This was absolutely necessary considering the extreme influence of torque compared with the almost imperceptible application of load onto the specimen.

The investigation was intended to find out about basic effects. Thus, the span between the laboratory techniques used and practical applications of regular bolts was of little direct concern. The gained results do not give directly useful information for practice except that it is not desirable to apply lateral constraint by means of bolt torque. The experiments give, though, information about some aspects relatively clearly, i.e., the effects of different types of washers upon the net surface strains. They can serve as a basis to measure the influence of strains which are produced by other influences like hole tolerances in later investigations.

6.8. Testing of Washer Designs

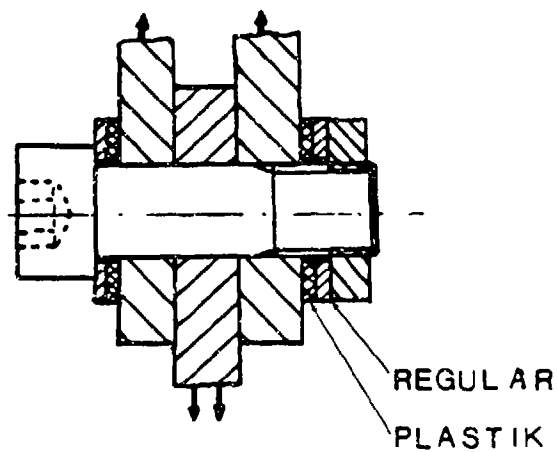


Figure 6-8. Bolt Assembly Used in Early Tests. A Standard Hex-Socket-Head was Used with Plastic Washers



Figure 6-9. Early Fringe Patterns for the Displacement in Y and 45° Directions of the Bolt

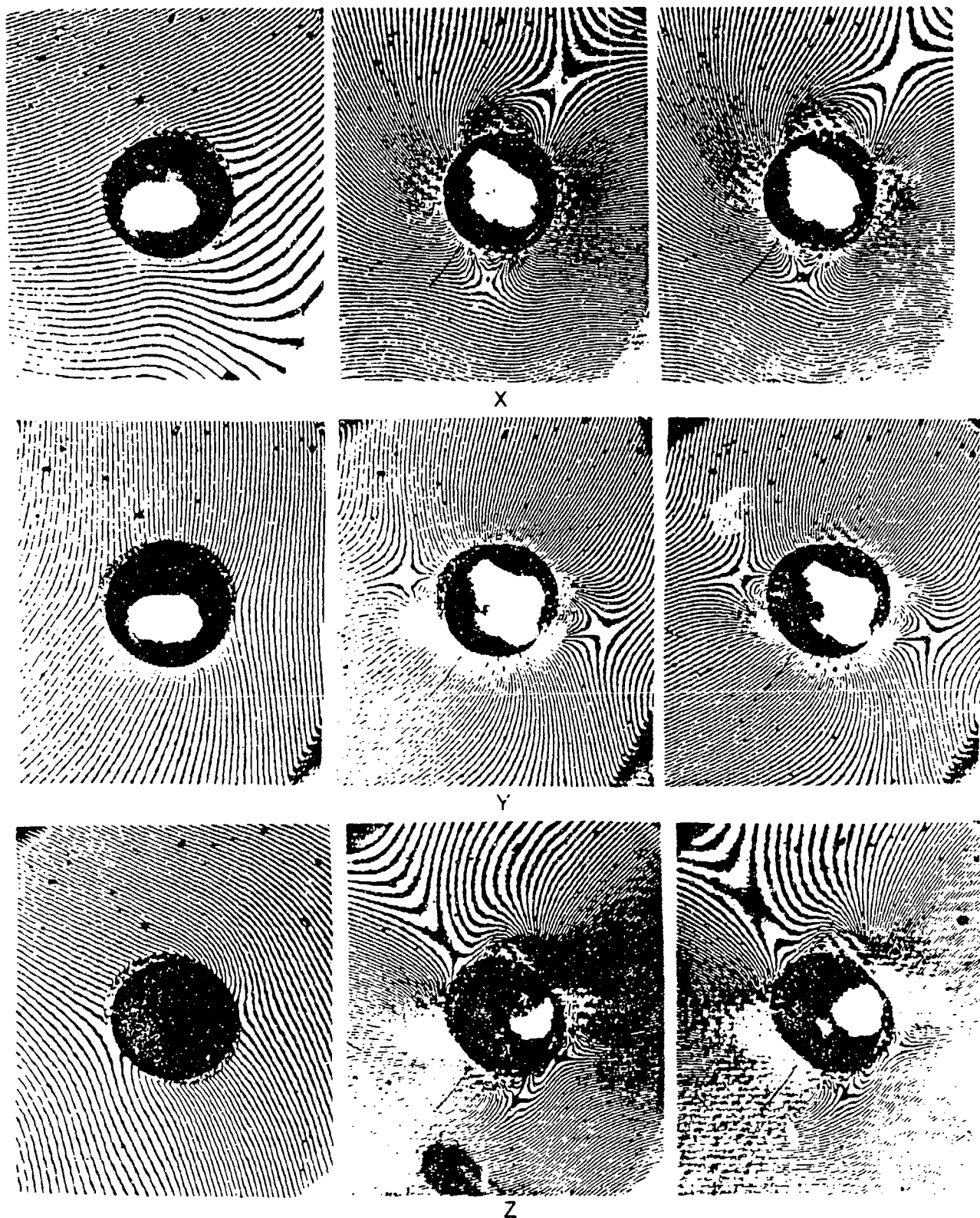


Figure 6-10. Influence of Torque onto the Displacement Field. Left: No-Load, Low Torque; Center: High Torque, No-Load; Right: High Torque, At-Load (200 lbs.)

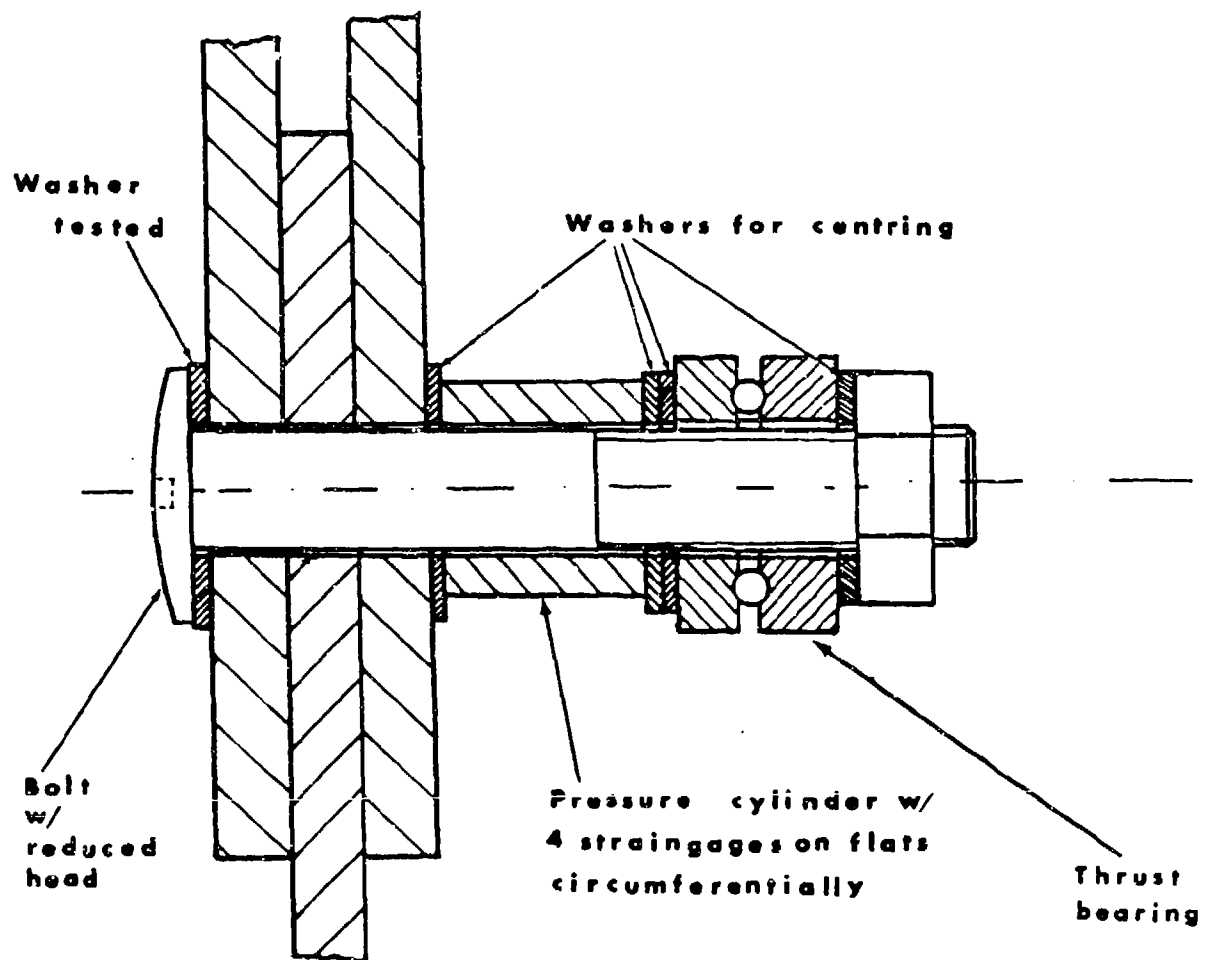


Figure 6-11. Sectional View of the Bolt and the Clamping Mechanism Integrating a Thrust Bearing and a Clamping Pressure Transducer

The three designs tested are shown in Figure 6-12. They include the flat washer (FW), the convex washer with cone base facing down (CWD), and the convex washer with cone base facing up (CWU). The clamping force was either 200 N (.LT) or 400 N (.HT). The strains were measured in three directions: axial (.Y), transverse (.X), and in 45° to both of the first directions (.45). The codes used in the lower left side of each strain plot are explained as follows:

example: CWD.HT.Y

CWD

The first three digits explain the type of washer used.

HT

The next two digits explain which clamping force was applied.

Y

The last digits explain in which direction the strain was measured.

In the legend of each strain plot the position of each strain profile is specified according to the description in Par. 6.4. The tensile loads applied on the test coupon were 200 pounds (.2) and 400 pounds (.4). The last two digits of the curve specifications in the legend give the applied load, for example:

LEFT.2 means that the curve shows the strain profile of the left axis for an applied load of 200 pounds.

The testing pattern is shown in Table 6-1, where all strain plots are identified. The identification code of the Moire fringe patterns is similar to the one of the strain plots. But an additional bit of information is needed, that being the currently applied load when the photograph was taken. The definitions are adopted from the legend.

example: FW.LT.0.45

FW

The first three digits explain the type of washer used.

LT

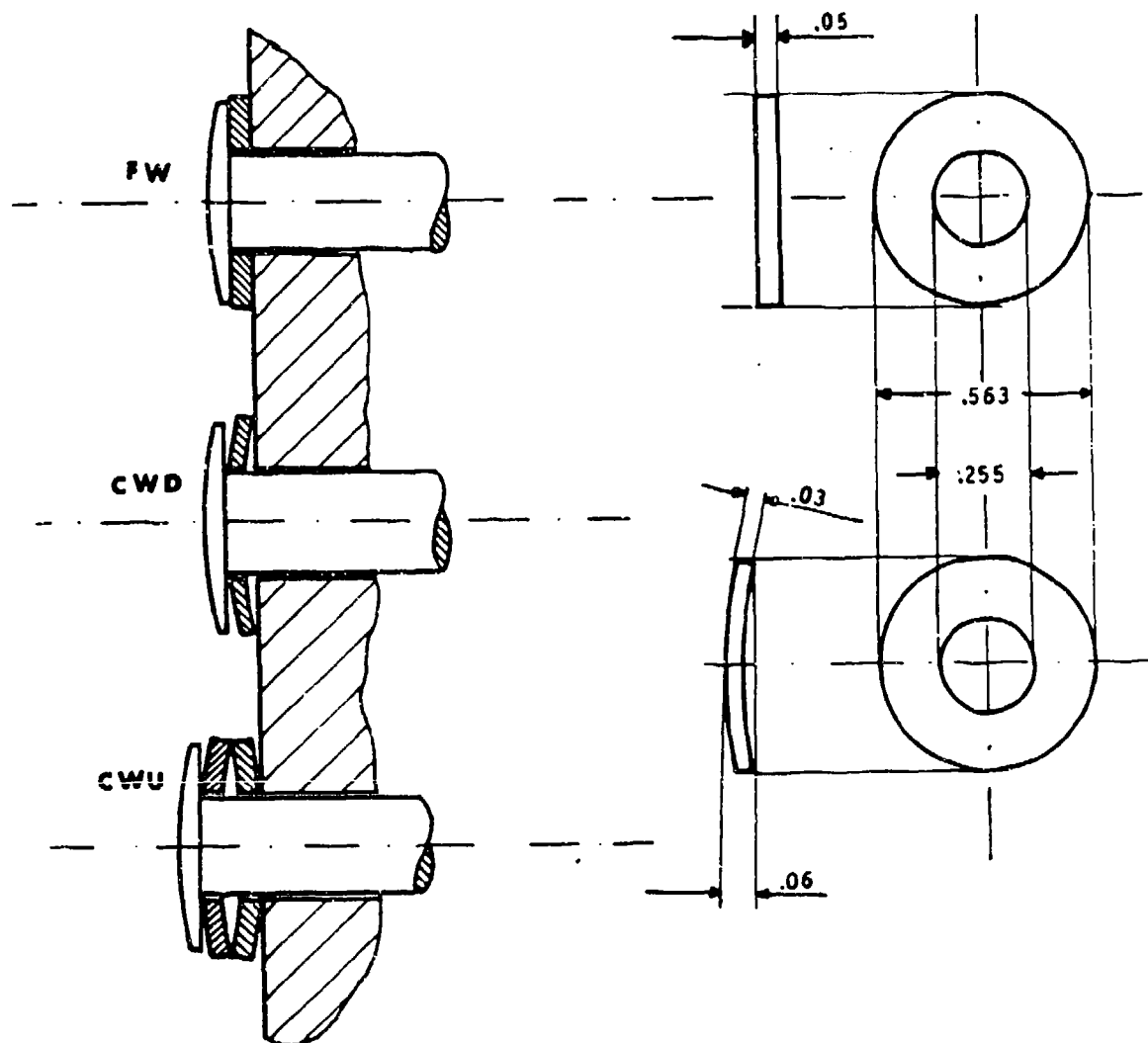
The next two digits explain which clamping force was applied.

0

The next digit explains which load was applied.

45

The last digits explain the direction of the



FW - Flat Washer

CWD - Convex Washer with Conus Base Facing Down

CWU - Convex Washer with Conus Face Facing Up

Figure 6-12. Washer Designs Tested

strain plot	testing parameters	Torque		Load (lbs)		Strain direction		
		low .LT	high .HT	200 .2	400 .4	X	Y	45°
FW.LT.X		X		X		X		
		X			X	X		
FW.LT.Y		X		X			X	
		X			X		X	
FW.LT.45		X		X				X
		X			X			X
CWD.LT.X		X		X		X		
		X			X	X		
CWD.LT.Y		X		X			X	
		X			X		X	
CWD.LT.45		X		X				X
		X			X			X
CWD.HT.X			X	X		X		
			X		X	X		
CWD.HT.Y			X	X			X	
			X		X		X	
CWD.HT.45			X	X				X
			X		X			X
CWU.LT.X		X		X		X		
		X			X	X		
CWU.LT.Y		X		X			X	
		X			X		X	
CWU.LT.45		X		X				X
		X			X			X
CWU.HT.X			X	X		X		
			X		X	X		
CWU.HT.Y			X	X			X	
			X		X		X	
CWU.HT.45			X	X				X
			X		X			X

Table 6-1. Testing Parameter Matrix Assigning each Strain Plot to a Specific Test

displacement field, i.e.
the direction of strain
measurement.

In the following paragraphs, the Moire patterns of displacement are presented in the way that three at a time are giving one strain plot. For example, the strains produced by an increase of load of 200 lbs, followed by a further increase to a total of 400 lbs, can be obtained comparing the displacement fields of CWU.HT. 2 .X (data) and CWU.HT. 4 .X (data) with CWU.HT. 0 .X (base) along their individual axes, resulting in the global strain plot CWU.HT.X.

6.8.1. Joint with Flat Washer. Figures 6-13 through 6-15 show the moire patterns and strain plots for the single bolt with flat washer.

6.8.2. Joint with Conical Washer Down. The fringe patterns and strain results for the case of the bolt with conical washer down under high torque and low torque are shown in Figures 6-16 through 6-21.

6.8.3. Joint with Conical Washer Up. These results are shown in Figures 6.22 through 6.27.

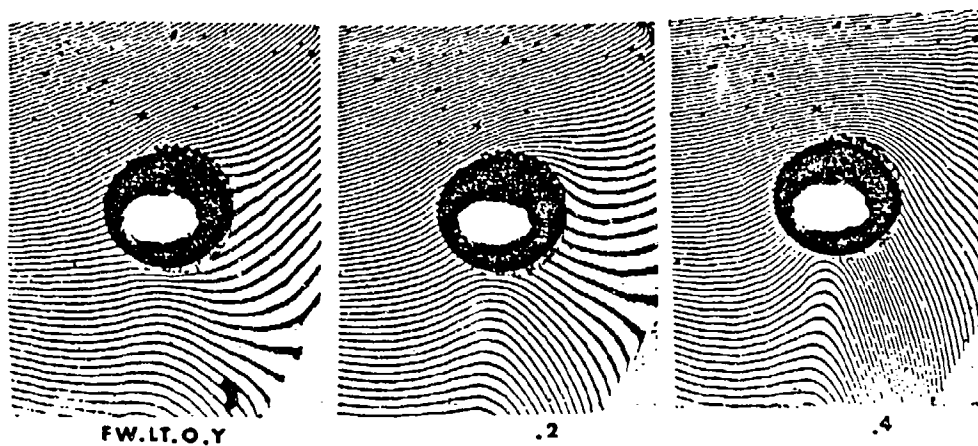
6.9. Comparison of Pin with Bolt and Washer

Strain plots from Herrera's work on simple pins were compared with the strain profiles presented above. All of the following estimates are made on the safe side. Always, the washer with the highest strains was chosen for the comparison. Assuming the same load, it was estimated that the axial peak strain levels in the ligament area of pin-loaded holes are at least 25 times higher than similar ones when using washers (see Figure 6-28). Under the same conditions the bearing strain for pin-loaded holes was estimated to be at least 35 times higher than similar strains in the lower zone of the washer, (see Figure 6-29).

In the lower zone tangential to the hole, the transverse strain peak of the pin has a value at least 30 times higher than that for the washer, (see Figure 6-30).

Since the data are not sufficient and because of the totally different behavior of washers it was difficult to find comparable data for the strains in the 45-degree direction; these are shown in Figure 6-31. In general the maximum shear strain found in Herrera's results and the corresponding value for the washers have a ratio of approximately 1: 30. The bolted connection shows a much more uniform shear strain distribution than the pin. The average value at a distance from the fastener is only 2-4 times higher for the pin than for the washer. The strain concentration factor $\sigma_{\max} / \sigma_{\text{average}}$ has a value of 13.6 for the pin and 1.6 for the washer. It is apparent that bolted connections do have significantly decreased average shear strain values with respect to the savings in axial and transverse directions when compared with pinned connections.

(a)



(b)

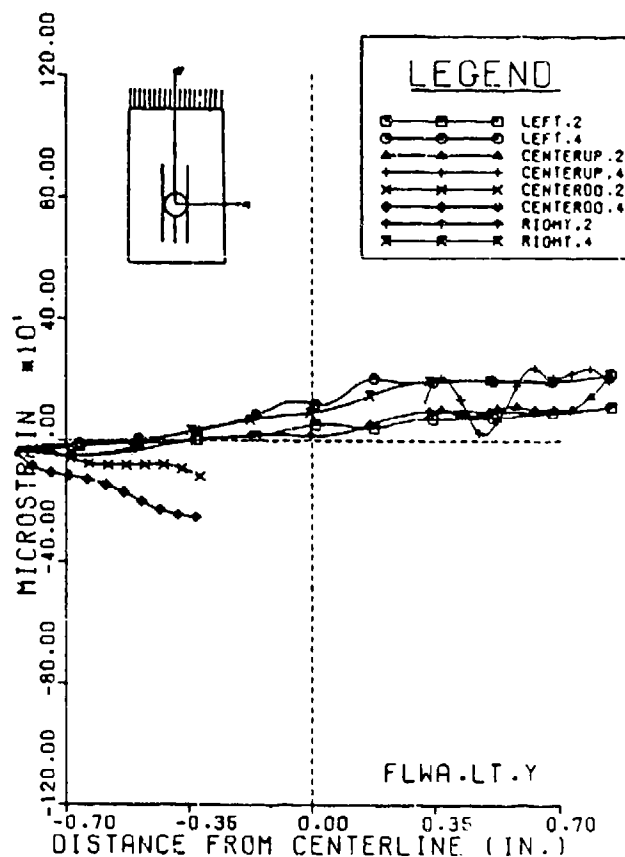


Figure 6-13. (a) Moire Fringe Pattern of Displacement in Y-direction

(b) Strain ϵ_y along Lines Parallel to the Direction of the Load^y for 200-lbs and 400-lbs loads. A Low Torque was Applied onto the Bolt

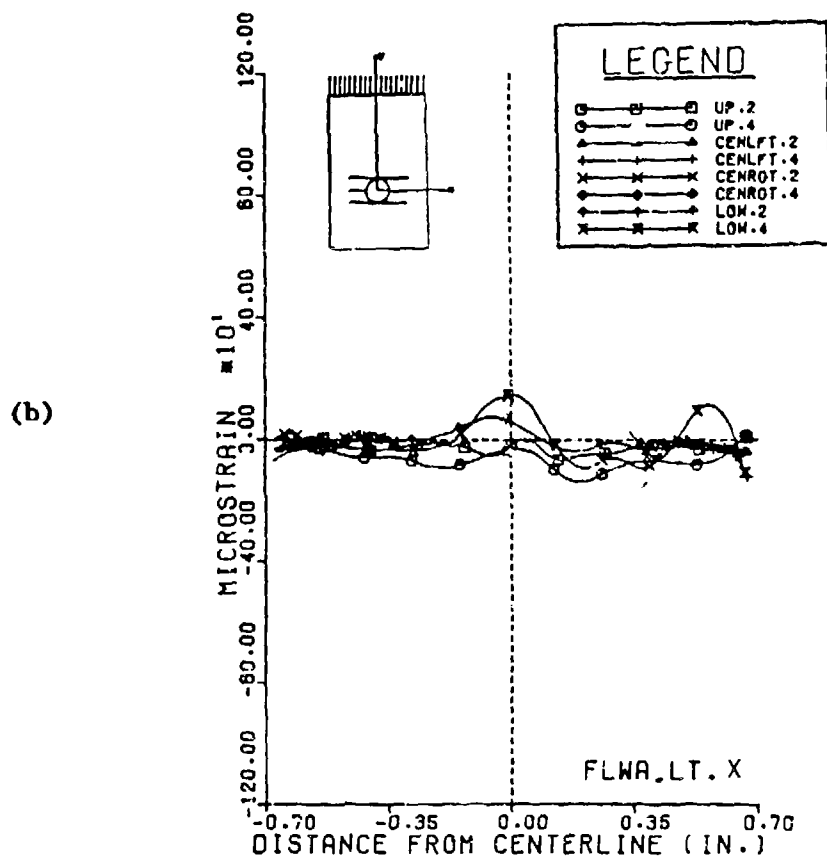
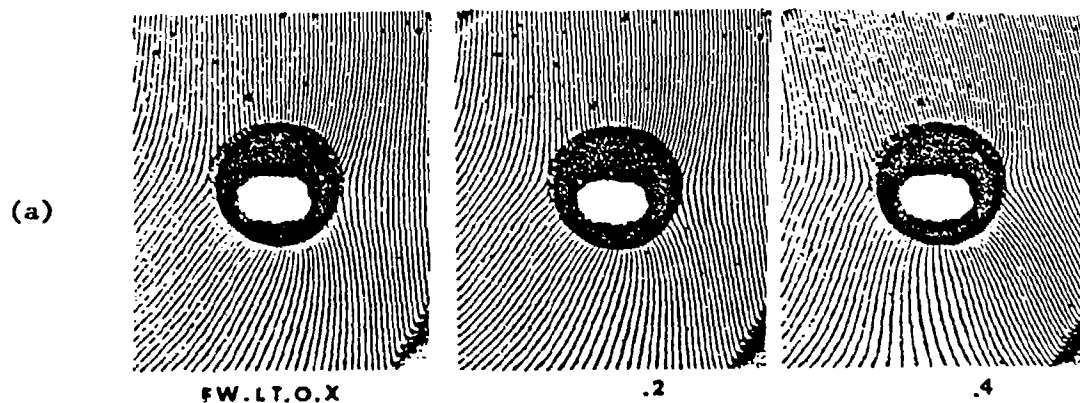
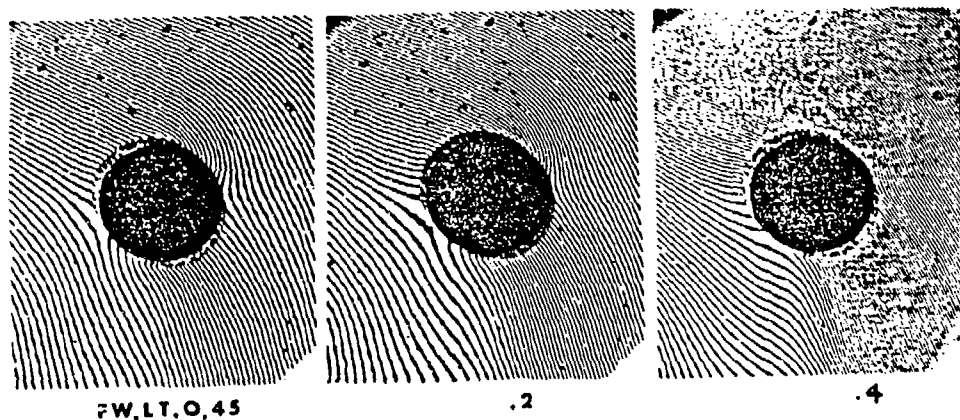


Figure 6-14. (a) Moiré Fringe Pattern of Displacement in X-Direction

(b) Strain ϵ_x along Lines Transverse to the Direction of Load for 200-lb and 400-lb Loads. A Low Torque was Applied onto the Bolt

(a)



(b)

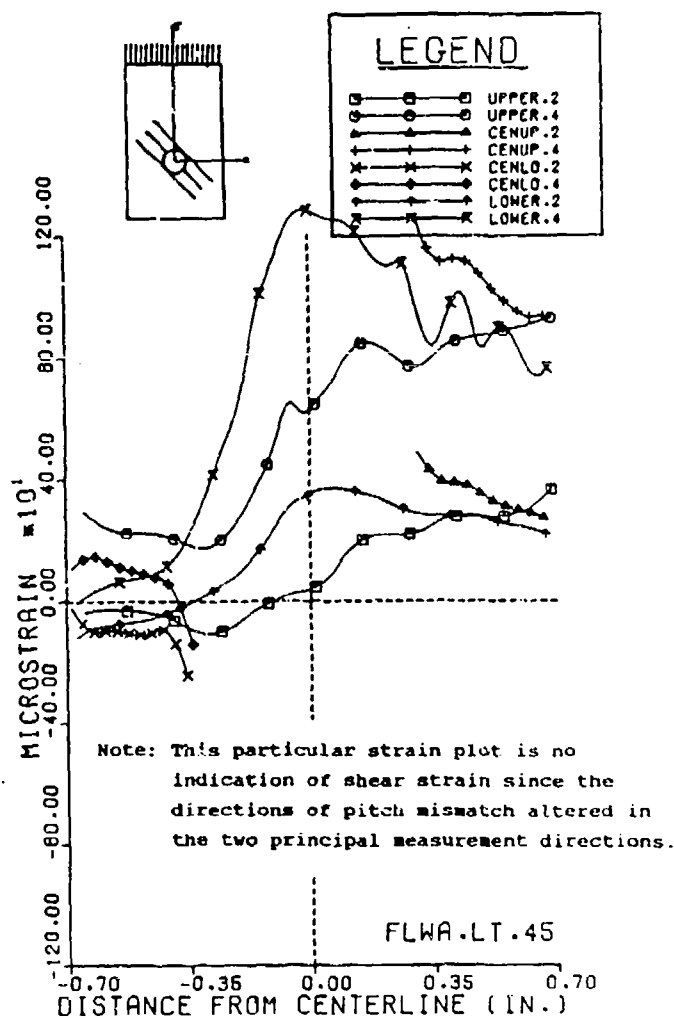


Figure 6-15. (a) Moiré Fringe Pattern of Displacement in 45°-Direction

(b) Strain ϵ_{45} along Lines 45° to the Direction of Load for 200-lb and 400-lb Loads. A Low Torque was Applied onto the Bolt

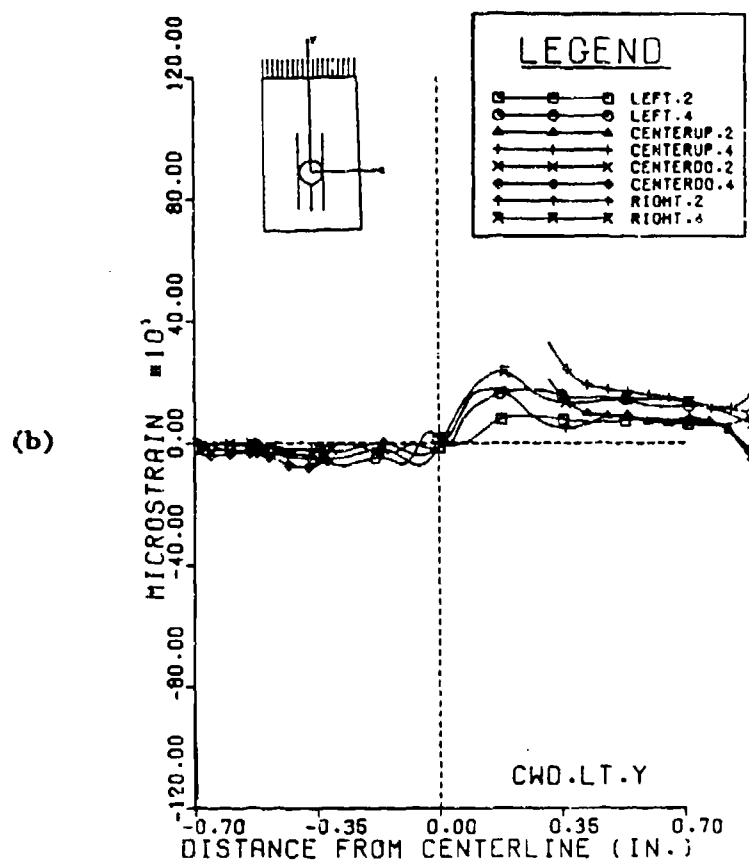
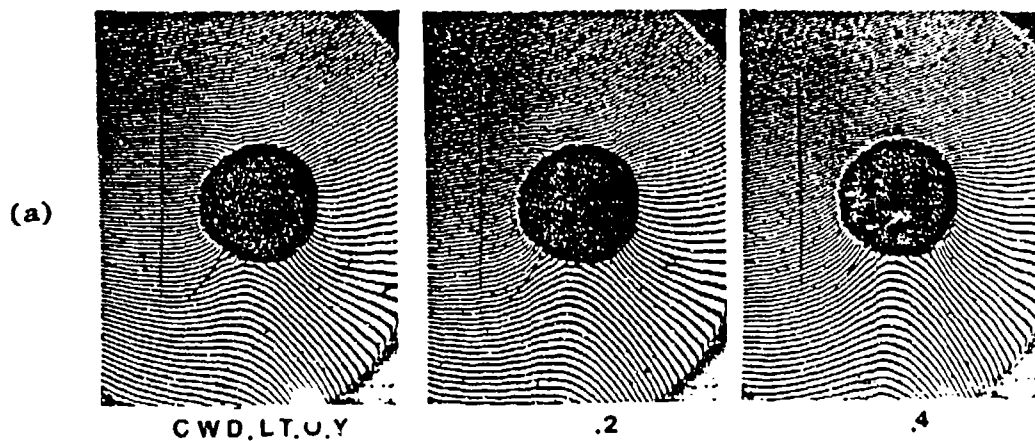


Figure 6-16. (a) Moiré Fringe Pattern of Displacement in Y-Direction
 (b) Strain ϵ_y along Lines Parallel to the Direction of Load for 200-lb and 400-lb Loads. A Low Torque was Applied onto the Bolt

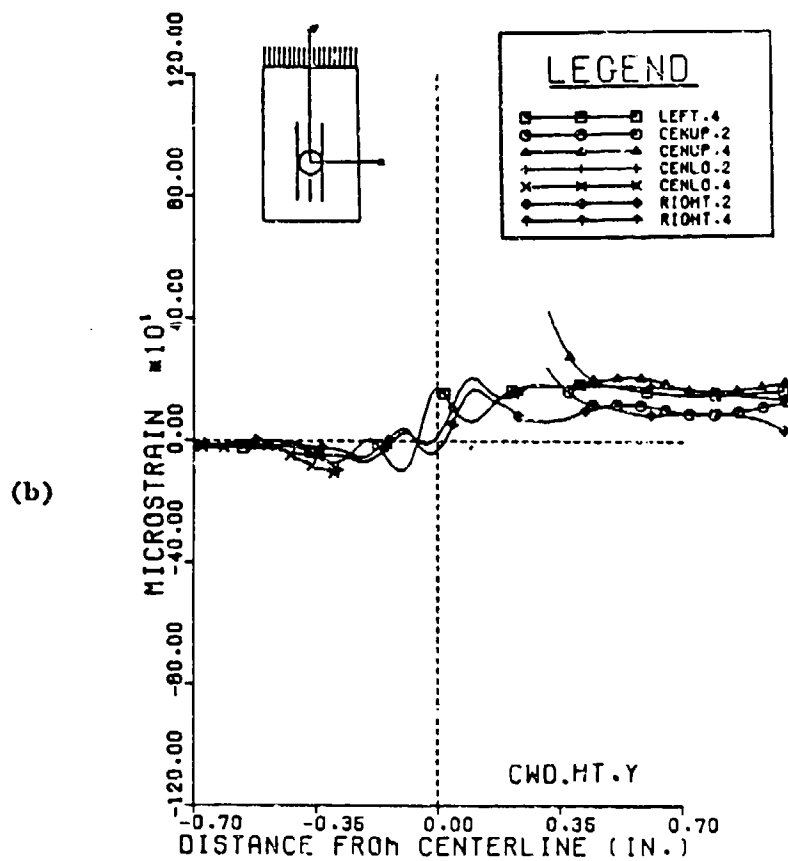
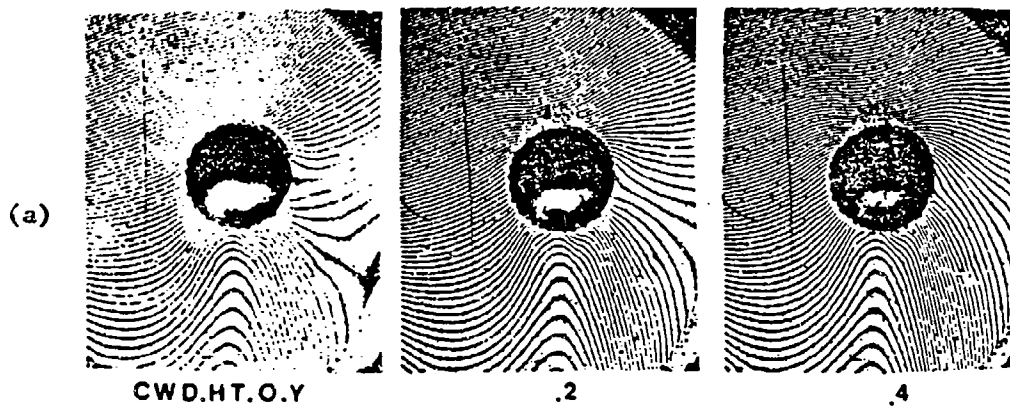


Figure 6-17. (a) Moiré Fringe Pattern of Displacement in Y-Direction
 (b) Strain ϵ_y along Lines Parallel to the Direction of Load for 200-lb and 400-lb Loads. A High Torque was Applied onto the Bolt

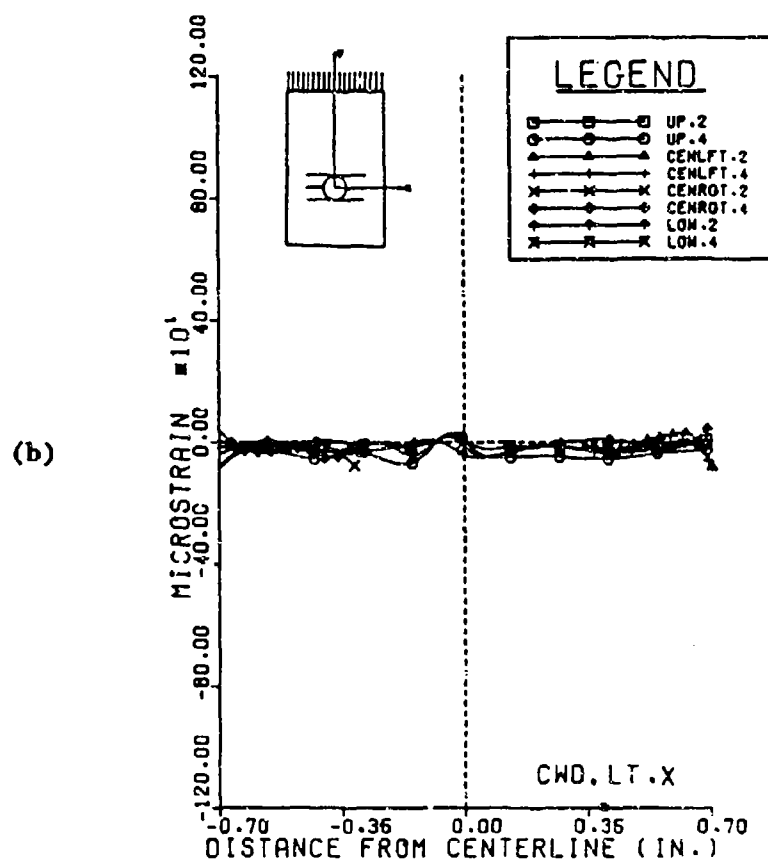
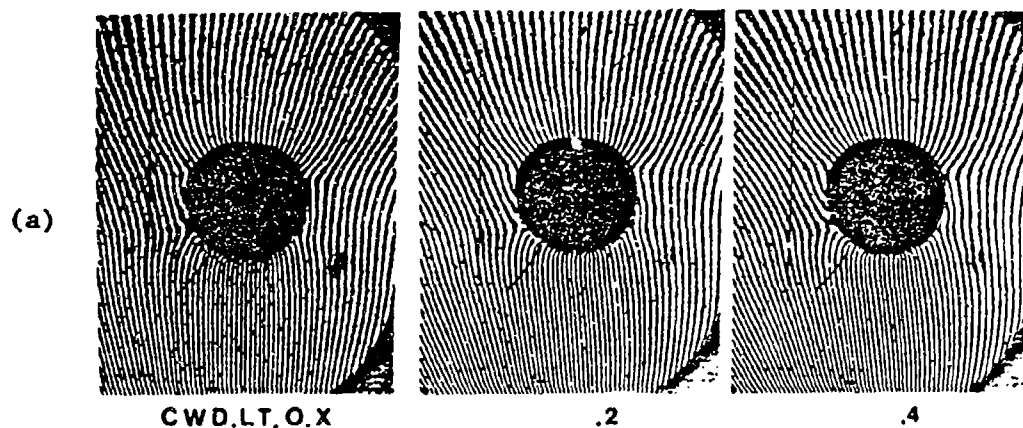


Figure 6-18. (a) Moiré Fringe Pattern of Displacement in X-Direction

(b) Strain ϵ_x along Lines Transverse to the Direction of Load for 200-lb and 400-lb Loads. A Low Torque was Applied onto the Bolt

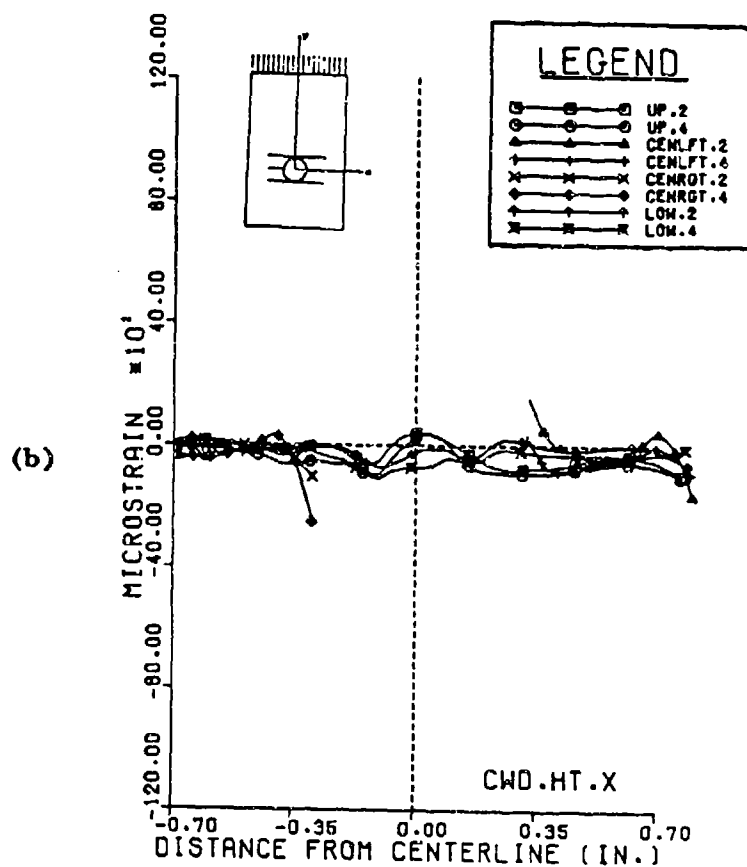
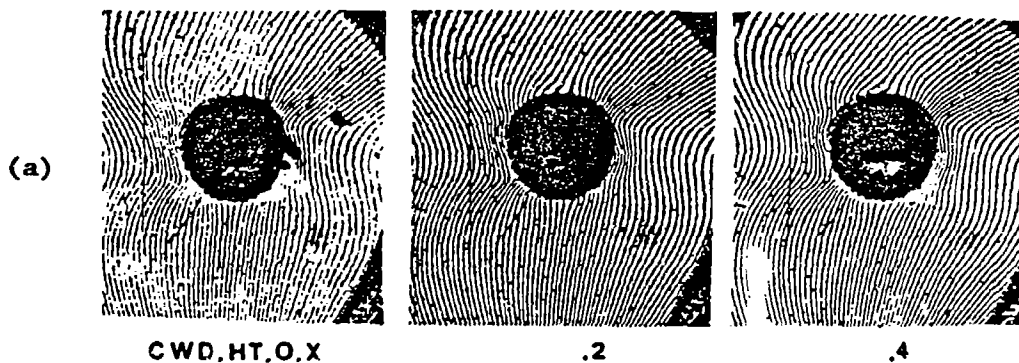


Figure 6-19. (a) Moiré Fringe Pattern of Displacement in X-Direction
 (b) Strain ϵ_x along Lines Transverse to the Direction of Load for 200-lb and 400-lb Loads. A High Torque was Applied onto the Bolt

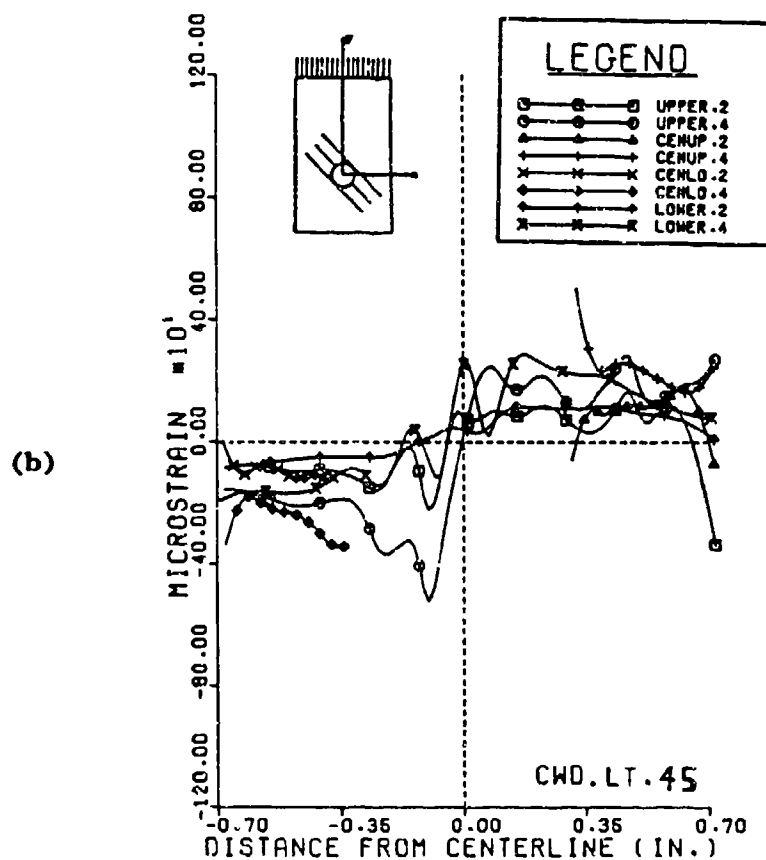
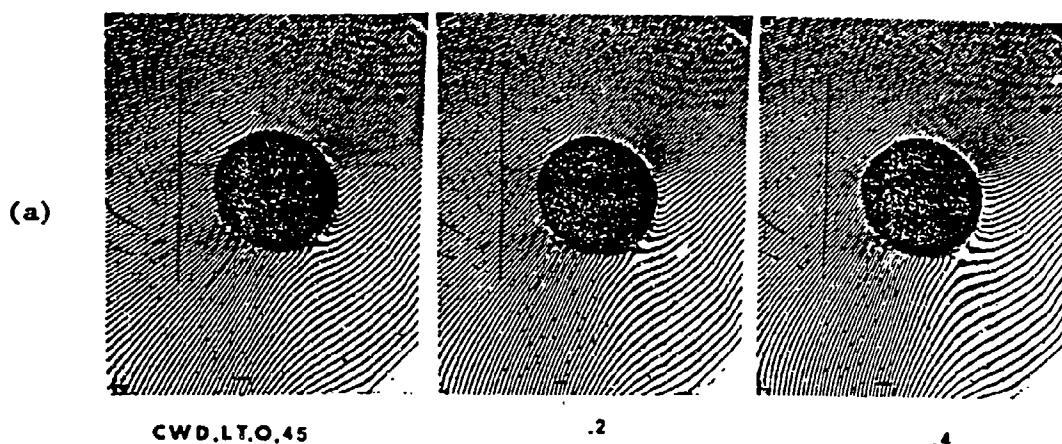


Figure 6-20. (a) Moiré Fringes of Displacement in 45°-Direction

(b) Strain ϵ_{45} along Lines at 45° to Direction of Load for 200-lb and 400-lb Loads. A Low Torque was Applied onto the Bolt

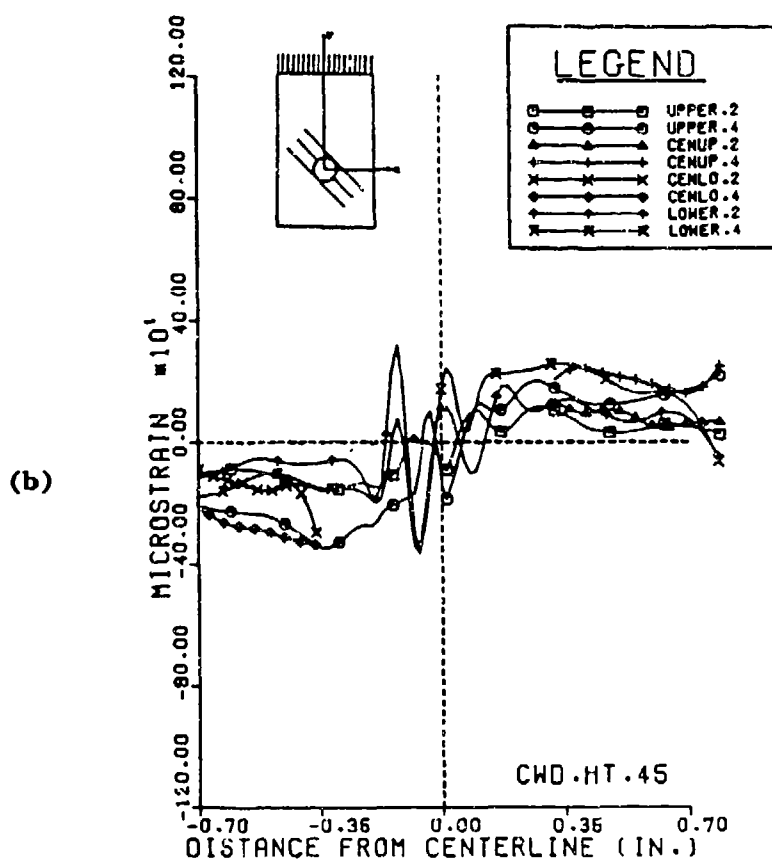
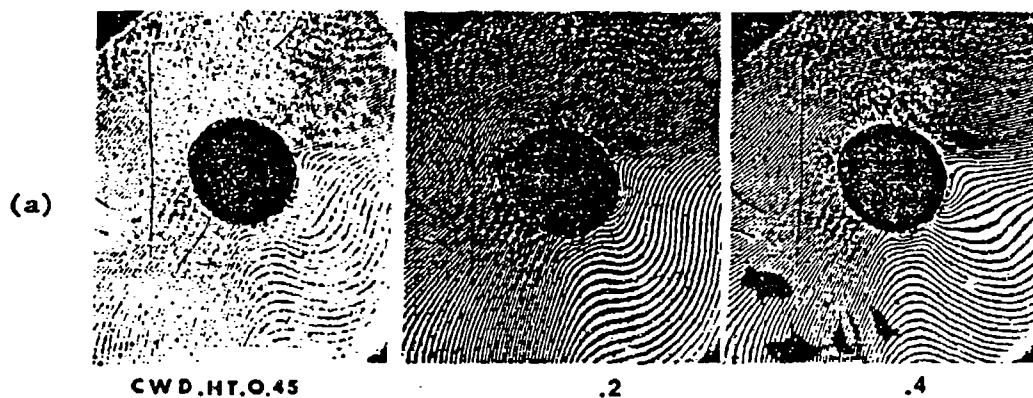


Figure 6-21. (a) Moiré Fringe Pattern of Displacement in 45°-Direction
 (b) Strain ϵ_{45} along Lines at 45° to Direction of Load for 200-lb and 400-lb Loads. A High Torque was Applied onto the Bolt

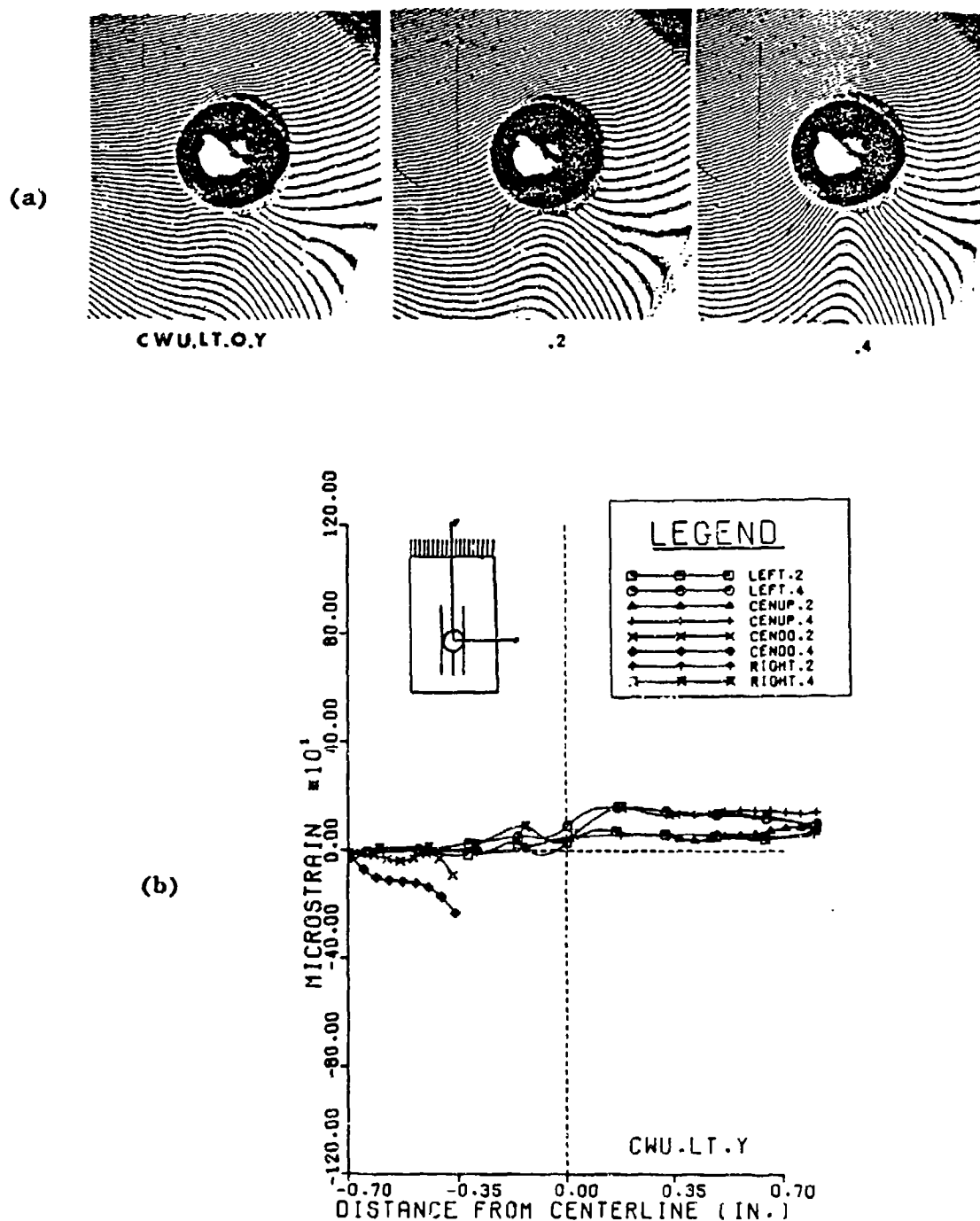
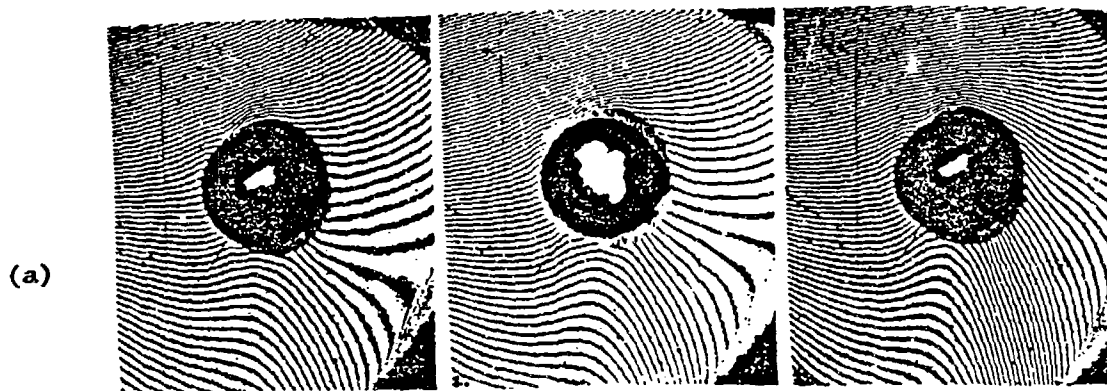


Figure 6-22. (a) Moiré Fringe Pattern of Displacement in Y-Direction
 (b) Strain ϵ_y along Lines Parallel to the Direction of Load for 200-lb and 400-lb Loads. A Low Torque was Applied onto the Bolt



CWU.HT.O.Y

.2

.4

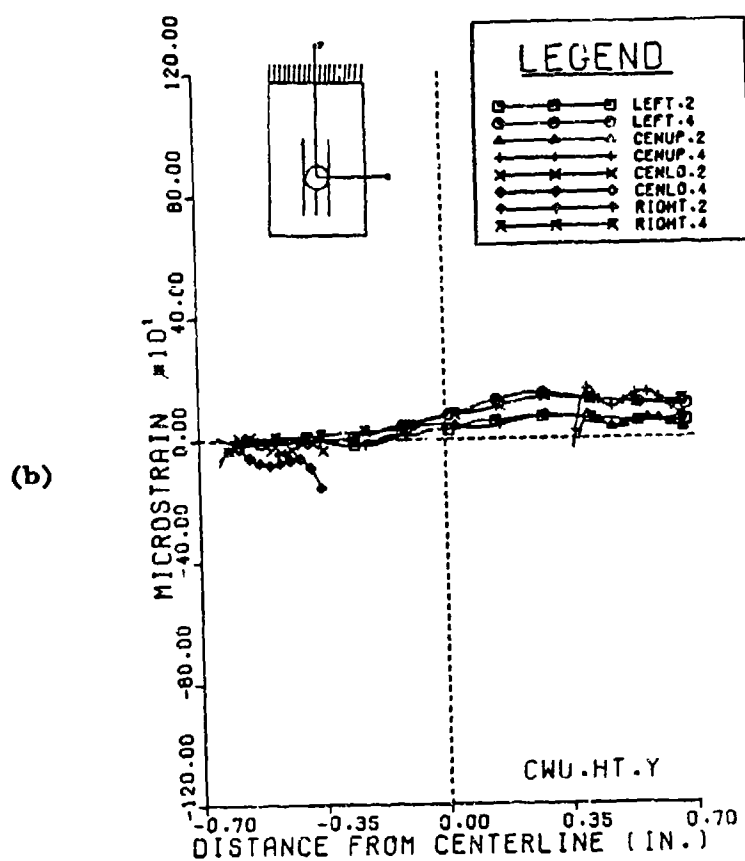


Figure 6-23. (a) Moiré Fringe Pattern of Displacement in Y-Direction
 (b) Strain ϵ_y along Lines Parallel to the Direction of Load for 200-lb and 400-lb Loads. A High Torque was Applied onto the Bolt

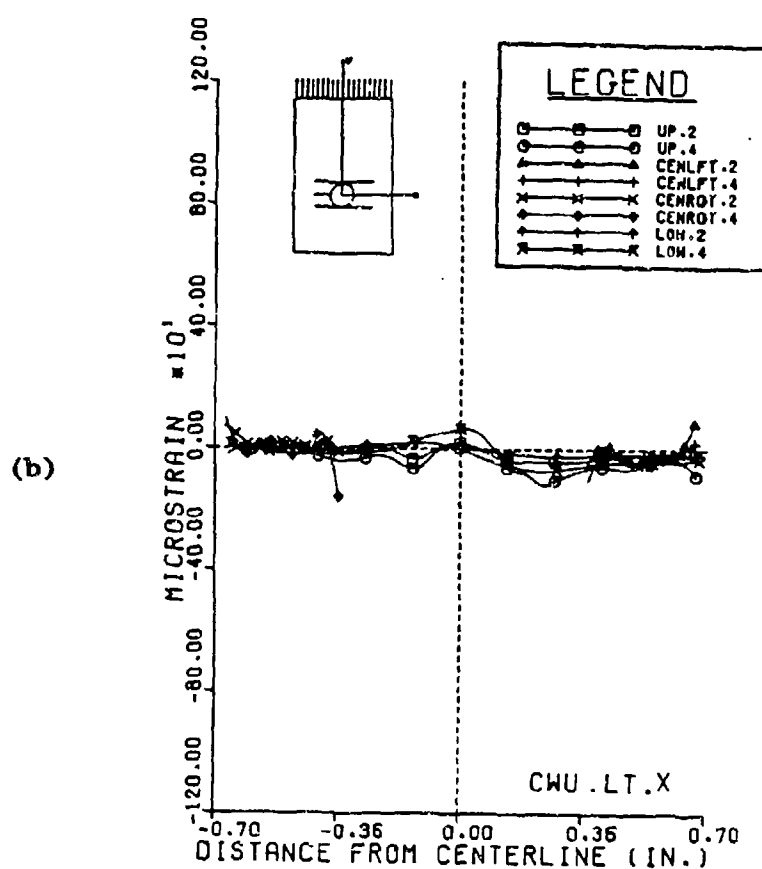
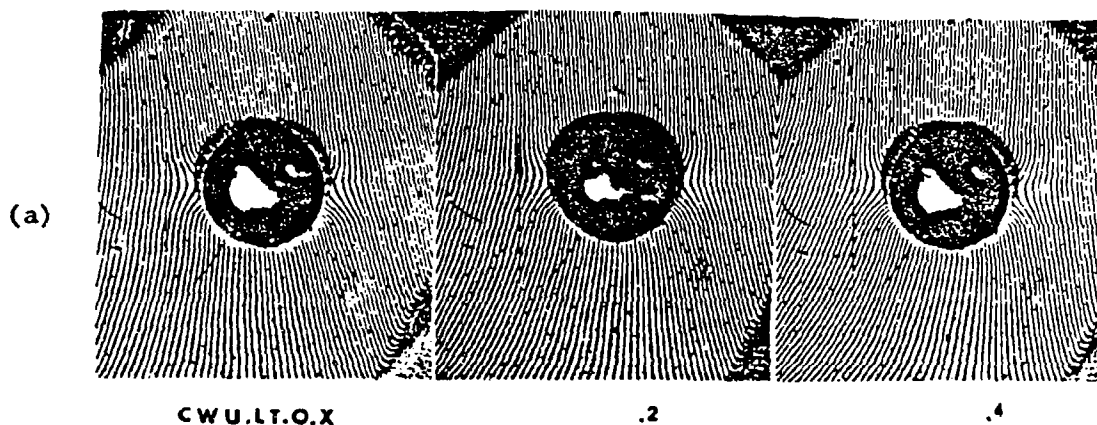


Figure 6-24. (a) Moire Fringe Pattern of Displacement in X-Direction
 (b) Strain ϵ_x along Lines Transverse to the Direction of Load for 200-lb and 400-lb Loads. A Low Torque was Applied onto the Bolt

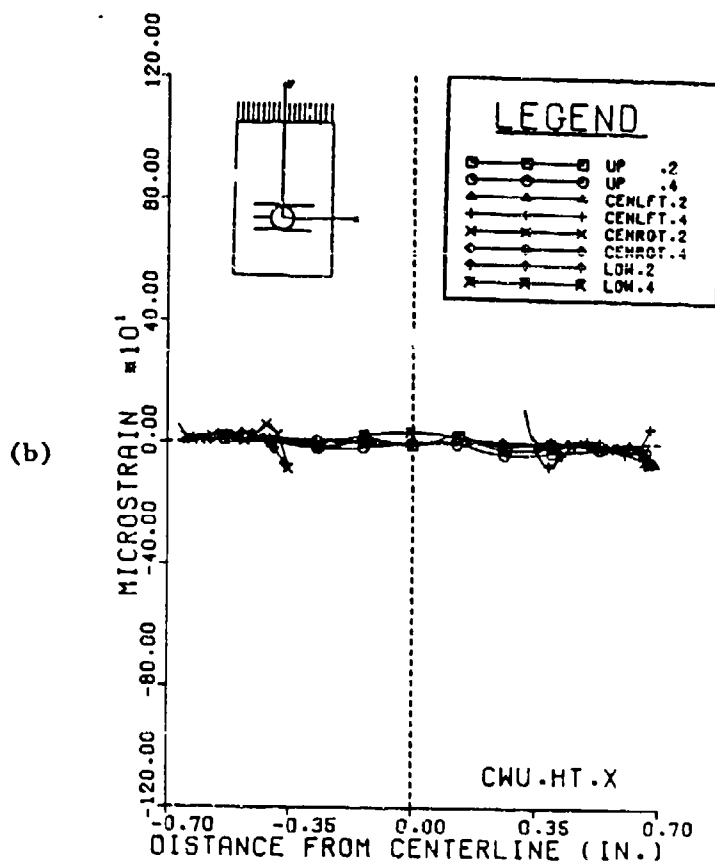
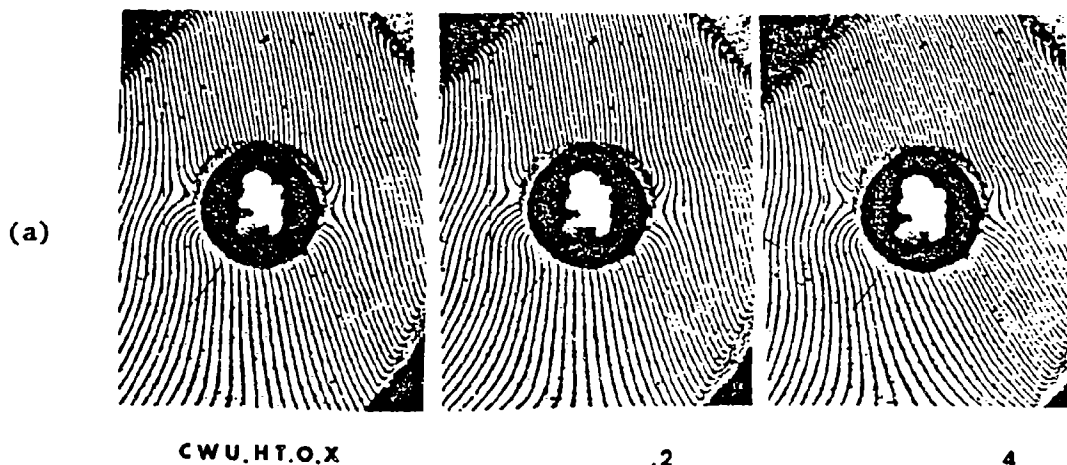


Figure 6-25. (a) Moiré Fringe Pattern of Displacement in X-Direction

(b) Strain ϵ_x along Lines Transverse to the Direction of Load for 200-lb and 400-lb Loads. A High Torque was Applied onto the Bolt

(a)

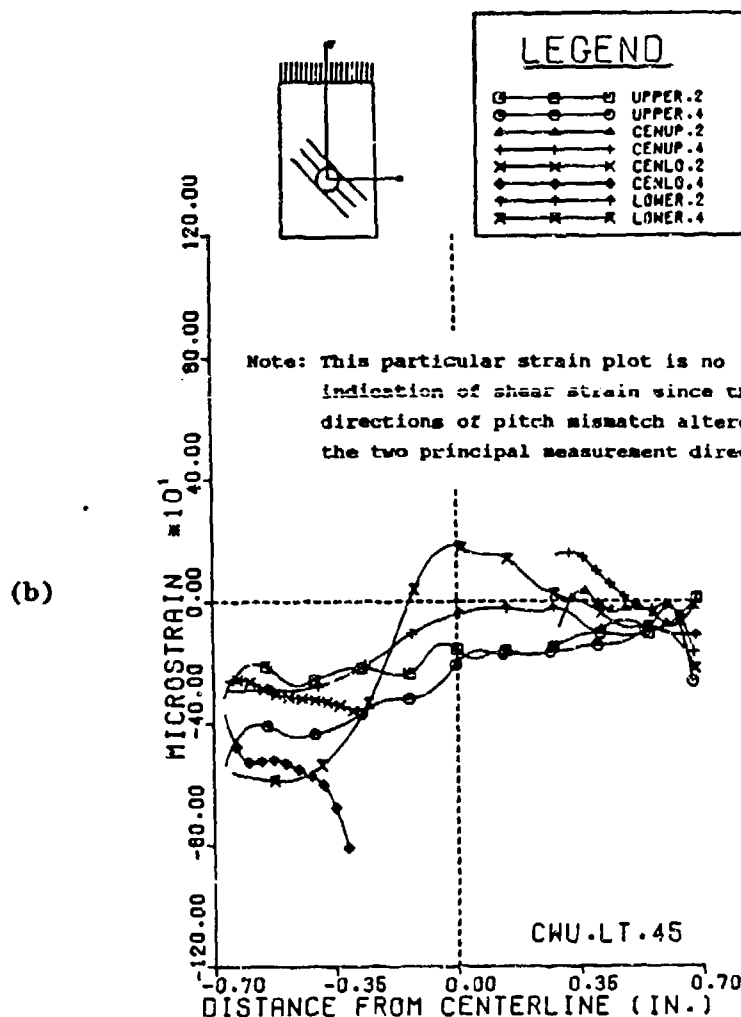
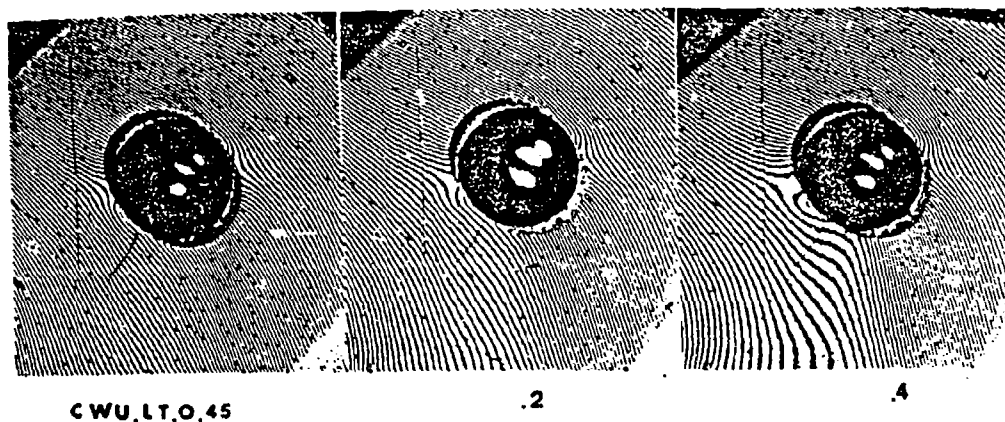
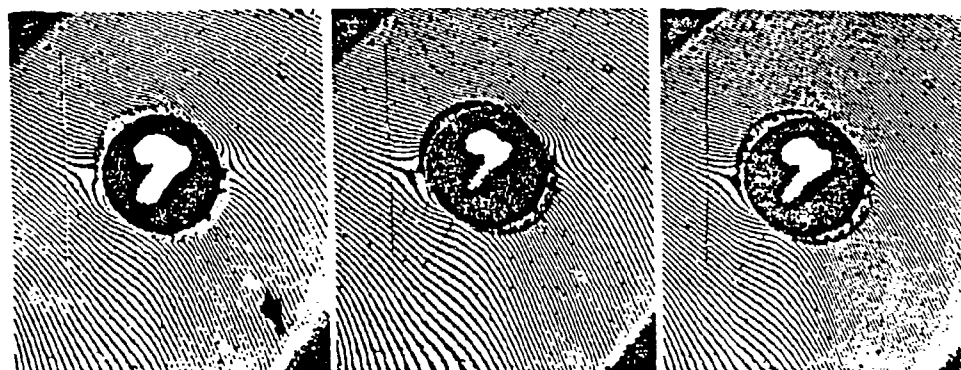


Figure 6-26. (a) Moiré Fringe Pattern of Displacement in 45°-Direction
(b) Strain ϵ_{45} along Lines at 45° to Direction of Load for 200-lb and 400-lb Loads. A Low Torque was Applied onto the Bolt

(a)



CWU.HT.0.45

.2

.4

(b)

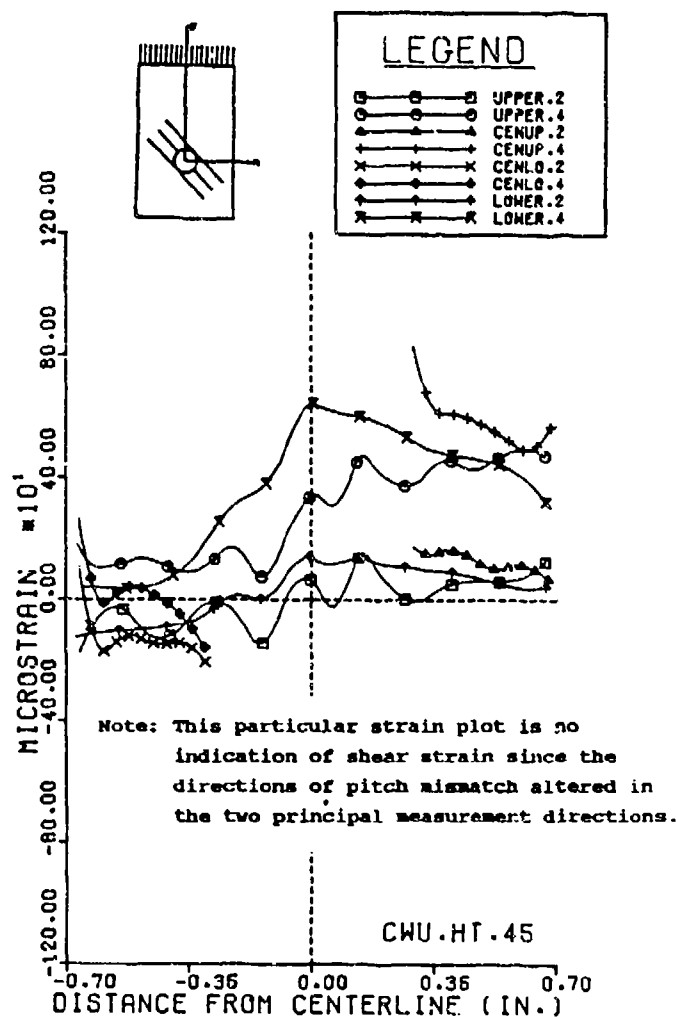
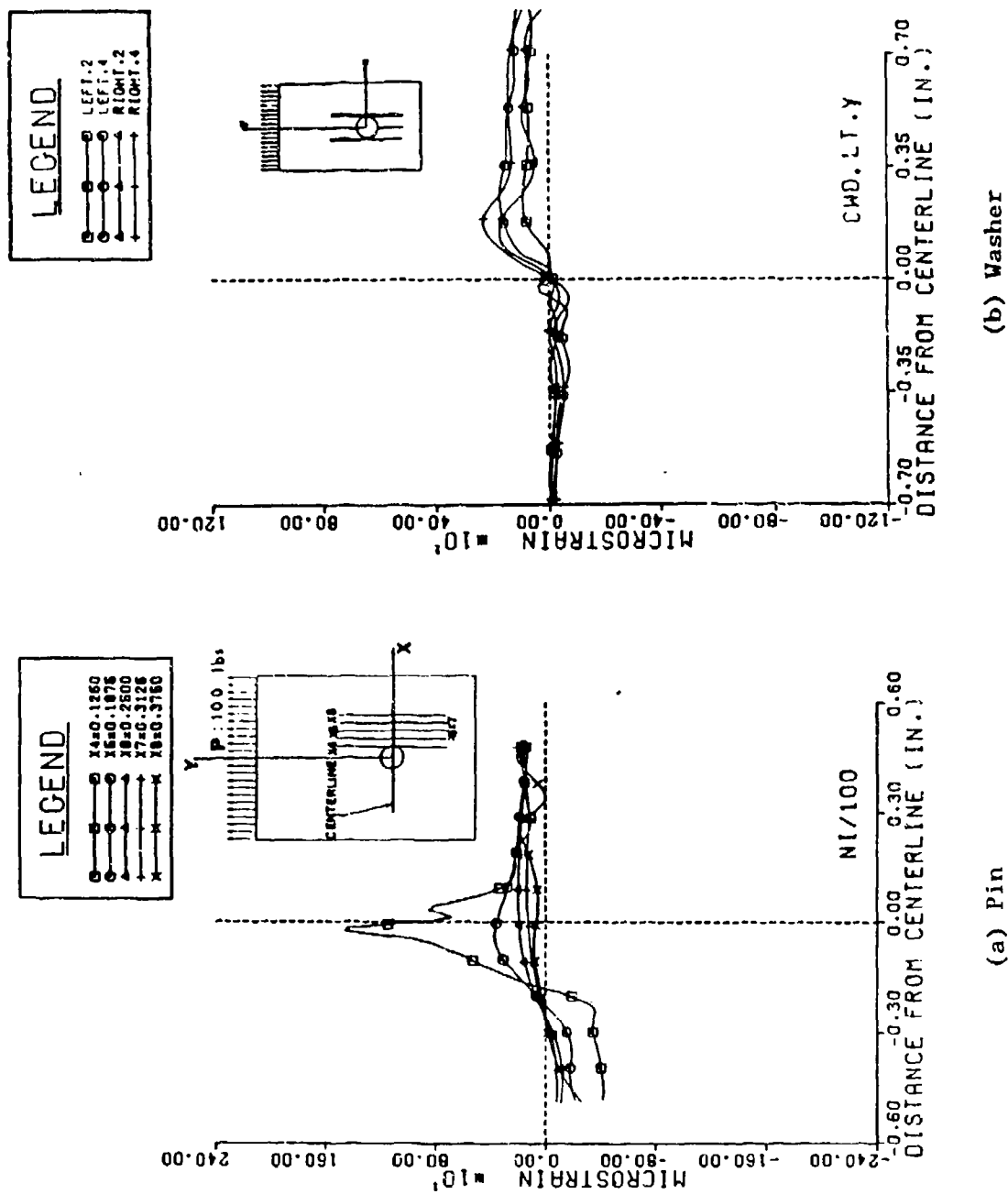


Figure 6-27. (a) Moiré Fringe Pattern of Displacement in 45°-Direction

(b) Strain ϵ_{45} along Lines at 45° to Direction of Load for 200-lb and 400-lb Loads. A High Torque was Applied onto the Bolt



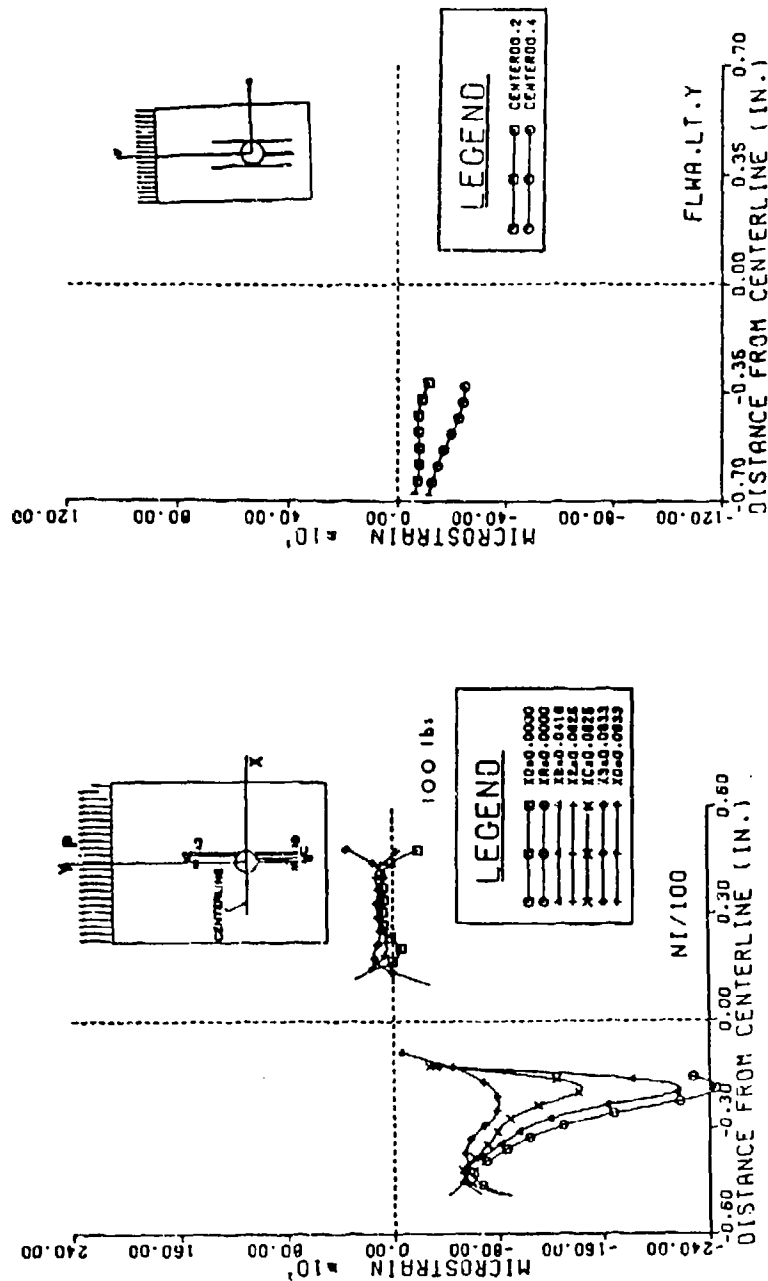
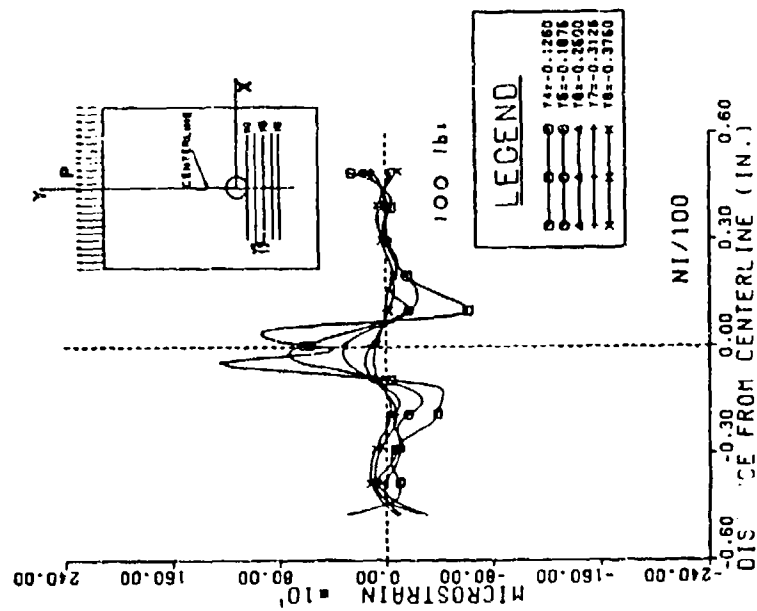
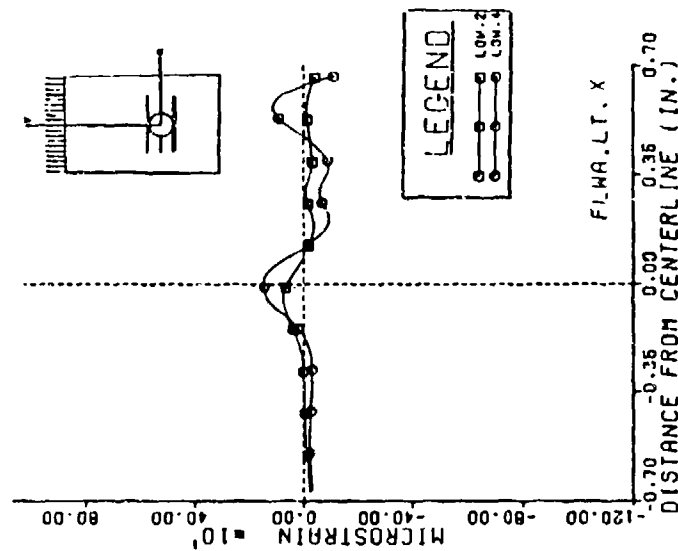


Figure 6-29. Comparison of Strain ϵ_y in the Bearing Region or Lower Zone



(a) Pin



(b) Washer

Figure 6-30. Comparison of Strain ϵ_x in the Bearing Region or Lower Zone

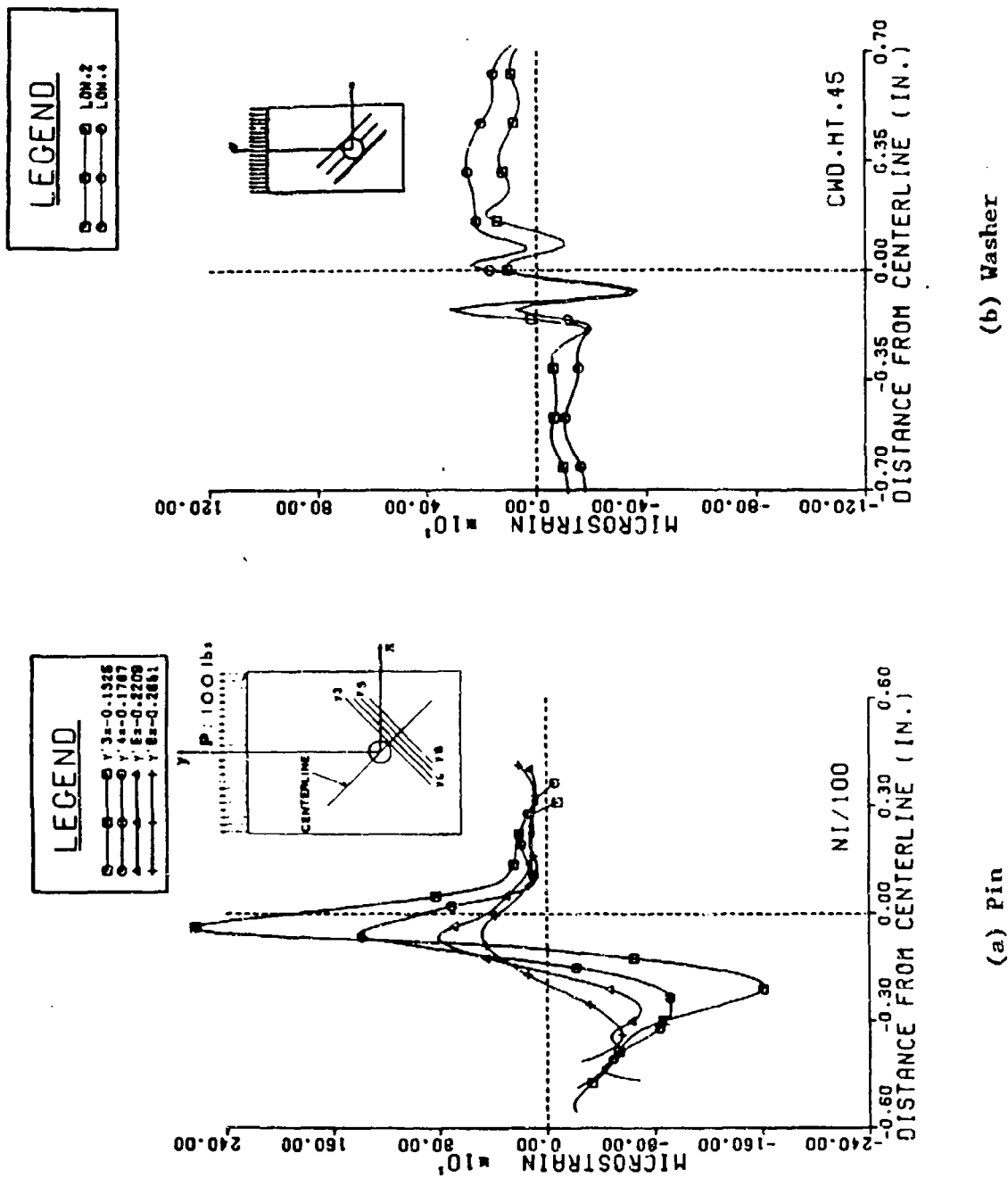


Figure 6-31. Comparison of Strain ϵ_{45} at the Locus of Shear-Out Failure

The literature findings [6.22, 6.18, 6.24, 6.25] agreed in the statement that bolted and correctly torqued connections do have 3-4 times the strength of pinned joints under the same conditions. This finding agrees very well with the fact that the shear strains are unproportionally high.

The use of washers can reduce the strain levels of axial (Y) and transverse (X) strains rather efficiently. But the shear strains cannot be reduced in the same manner. This perception is intensified when comparing the overall values of one type of washer in different directions. The 45 degree strains are showing the highest levels. A failure condition, however it is defined, is very likely to be reached first by a critically high shear.

6.10. Comparison of Different Types of Washers

Every bolted connection on which a certain torque is applied produces a lateral constraint, if not lateral trauma, in the components to be connected. For composite materials many investigations have been performed and they show that with the use of washers the joint strength increases. With increasing outer diameters of the washer the clamping pressure is more distributed and the joint strength is further improved. But weight penalties will set a natural limit to the size of the washer.

No information could be found concerning what type of washer possibly might feature the better strain relief in a tensile load situation of the connecting plates. The test results are evaluated considering the influence of design, torque, i.e., clamping force, and load in the three directions of measured strain. Attention is focused in the lower zone and the ligament area on the axial (Y) and 45 degree strain directions since the transverse values are relatively low and failure preferably occurs by delamination, compression or shear-out in the lower zone and by tensile breakage in the ligament region [6.17, 6.18, 6.22, 6.19, 6.14, 6.25, 6.26, 6.27].

Detailed comparisons are first presented with references to Figures 6-32 through 6-35. Then, in Table 6-2, the peak and average values are compared and summarized.

The bearing behavior comparing the different designs for two loads is shown in Figure 6-32. Higher torques seem to moderate bearing strains. The CWD shows the lowest values. A comparison of the different designs considering the tensile strains in the ligament area is shown in Figure 6-33. Higher torques decrease the overall strain values. The CWU-HT-washer is the best since it has the lowest strains. The CWD-washers shows a better behavior on the lower side but high peaks on the tensile side. This non-uniformity is probably due to the typically better grip of the washer into the material at the outer rim. CWD-washers do have an increased amount of lateral constraint in the primary contacting ring (see Figure 6-12). This introduces a pressure cone in the laminate and concentrates the force flow over the outer rim of the washer causing

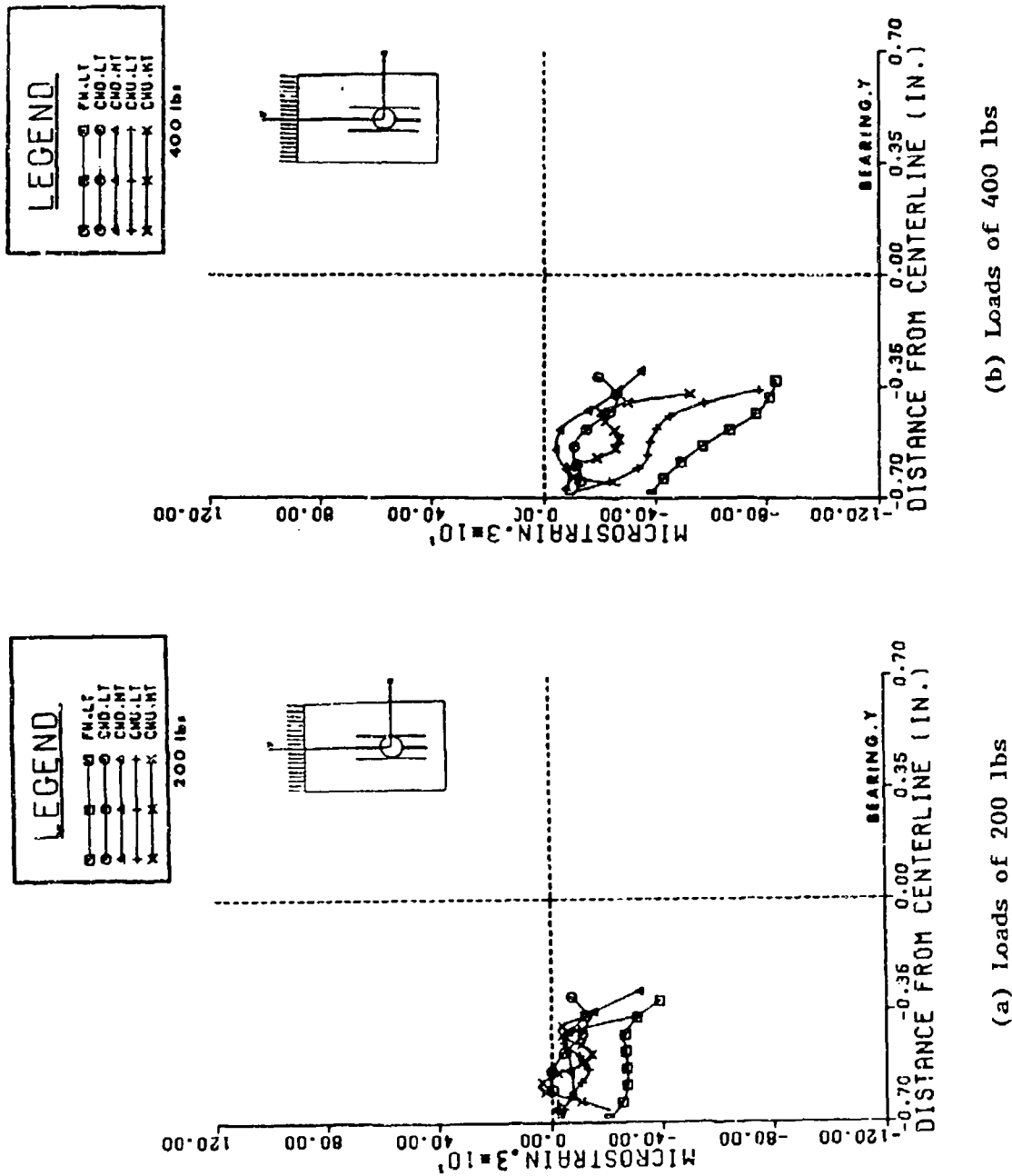


Figure 6-32. Strain ϵ_y in the Bearing Zone Comparing the Different Washer Designs

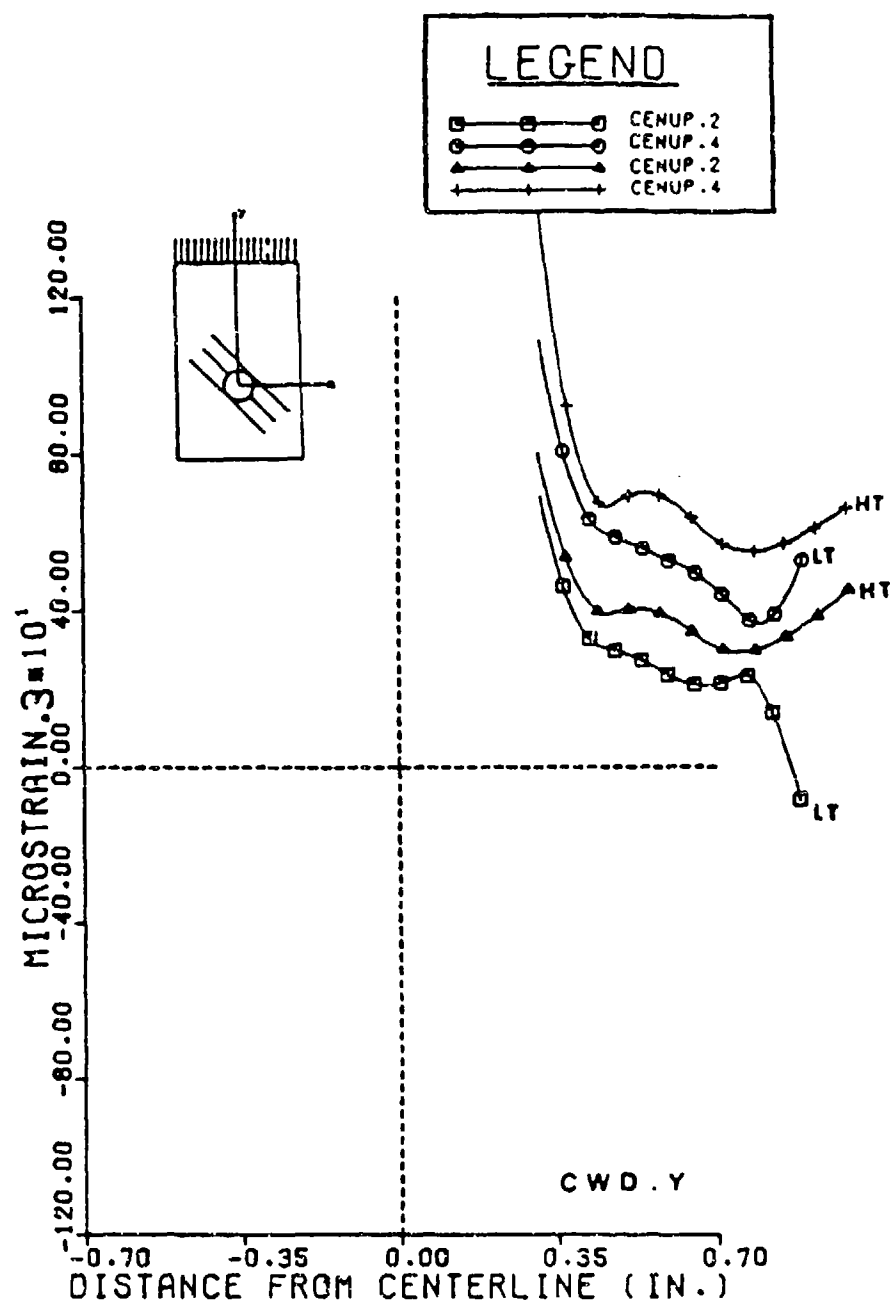


Figure 6-35. Strain ϵ_y in the Top Zone Indicating an Increase of Tensile Bearing with Higher Clamping Forces

Y	FW.LT	CWD.LT	CWD.HT	CWU.LT	CWU.HT
Bearing Strain					
peak ϵ_{\max} [10^{-6}]	-250	- 79	-105	-232	-157
	100 %	32 %	42 %	93 %	63 %
average ϵ_{av} [10^{-6}]	-157	- 49	- 42	-128	- 78
	100 %	31 %	26 %	82 %	50 %
ratio $\epsilon_{av}/\epsilon_{\max}$	1.6	1.6	2.5	1.8	2.0
Ligament Strain					
peak ϵ_{\max} [10^{-6}]	222	235	210	162	135
	94 %	100 %	89 %	69 %	58 %
average ϵ_{av} [10^{-6}]	100	87	89	98	78
	100 %	87 %	89 %	98 %	78 %
ratio $\epsilon_{av}/\epsilon_{\max}$	2.2	3.5	2.4	1.6	1.7
Top Zone					
peak ϵ_{\max} [10^{-6}]	239	328	426	152	149
	56 %	77 %	100 %	36 %	35 %
average ϵ_{av} [10^{-6}]	205	146	179	140	120
	100 %	71 %	87 %	68 %	58 %
ratio $\epsilon_{av}/\epsilon_{\max}$	1.2	2.2	2.3	1.1	1.2
Table for 400 lbs					
45°	CWD.LT.2	CWD.HT.2	CWD.LT.4	CWD.HT.4	
Lower Axis					
peak ϵ_{\max} [10^{-6}] in C	10	350	32	80	
	3 %	100 %	9 %	23 %	
peak ϵ_{\max} [10^{-6}] in A	46	117	244	250	
	18 %	47 %	98 %	100 %	
average ϵ_{av} [10^{-6}] *	101	114	228	240	
	42 %	48 %	95 %	100 %	
ratio $\epsilon_{av}/\epsilon_{\max}$ **	2.2	1.0	1.1	1.0	

Table 6-2. Comparison of Peak and Average Strain Values along the Most Interesting Axes for All Tested Washers

higher peak strains in axial and 45-degree directions above the high pressure contacting area.

The 45-degree strain profiles show several peaks, as can be seen in Figure 6-34. Apparently, they correspond with the loci of several design features. The more interesting line is the lower line (LOWER.2/.4) because of the higher values and the presence of the locus of shear-out. Basically LT- and HT-plots show the same peaks but they are developed to different levels. When the fibers happen to be underneath the washer (seen from the top of the specimen in strictly axial direction), in the middle of this zone, the first tensile strain peak in the HT-plot occurs (A). The same peak can be seen in the LT-plot with about the same value. Away from the middle towards the center there is a stripe of fibers with high compressive strain (B). In the HT-plot this peak does not increase its value even though the load increases by 100 percent. But, in the LT- curve there is a clear dependency on the load. The peak at point (C) is tangential to the rim of the hole. It is almost not perceptible in the LT-plot, but it has a very distinct value in the HT-plot. There, this value significantly increases with increasing load. At the left half of the fastener the shear-out failure must be indicated by a positive 45-degree strain peak (C,A). The ratio of these peak strains to the average strains is relatively low compared with the case of a pin-loaded hole, (see Par. 6.9). This is due to an increase of the average rather than to an increase of the peak strains. Especially at point (C), the application of torque shifts the peak strain to higher levels. Apparently, higher torques have a very deleterious influence upon the shear strains. They introduce the buildup of stress channels tangential to the rim of the hole in the axial direction. Also, the strain gradients are increased which is another sign for stress channels. With increasing lateral constraint the locus of failure by shear-out is more likely at the borderline of connected and cut axial fibers than at the outer edge of the washer (CENTERLINE).

The other 45-degree strains cannot be used to indicate shear since the orientation of the pitch mismatch during the adjustment procedure of the two principal directions alternated.

In general, a higher clamping force moderates the strain values. This is not the case in the upper zone of the CWD-washer, as shown in Figure 6-35. There, a higher tensile strain which increases with increasing lateral constraint indicates that this region also participates in transferring the load. This unique active function is produced by the increased slip resistance. It distributes the load into the area above the hole where the axial fibers are cut. For all other washers this area is carrying only very low tensile loads.

Critical values are high-bearing strains in the lower (compression) zone of the fastener and high tension in the ligament zones. Strains at 45° need more study in order to be comparable. High tensile strain values

in the upper region are more of a quality feature since it shows a good grip of the washer onto the surface releasing part of load from the lower and ligament zone.

Matthews, et al., [6.23], who was using spring washers (CWD-type), showed that "fingertight" bolts (.LT) do have about 75 percent of the strength of fully tightened bolts (.HT). This result matches with the results shown in Table 6-2. It may be concluded that surface strains, in the case of this investigation, are a good criteria to evaluate joint efficiency.

6.11. Conclusions and Recommendations

A high-sensitivity interferometric Moire technique was utilized. A review of simple concepts and equations of diffraction by a grating demonstrated how this technique could be applied to perform measurements of strain fields on the surface of specimens in order to study current problems in mechanics and structural design. A three-dimensional geometrical approach was used to present this technique and to demonstrate the mechanics of moire fringe formation. Moire patterns of displacement could be obtained for three different orientations, allowing calculation of strain in the same number of directions. The washers investigated to evaluate strain relief of bolted connections were a flat washer (FW), and two different types of convex load spreading washers (CWD, CWU). A high torque (.HT) and a low torque (.LT) were applied onto the bolt to create two definite clamping forces. Beginning with a no-load condition (.0) the test coupon was subjected to 200-pound (.2) and 400-pound (.4) tensile load.

In the following paragraphs some basic results of the washer and preload study will be reviewed in short and conclusions are drawn.

Increasing the lateral constraint by a higher bolt torque moderates the axial strains in the bearing and net-tension region significantly (see Figures 6-32 and 6-34). In the case of the CWD-type of washer, additionally, the tensile strains in the top zone opposite to the lower (compressive) bearing zone are raised. Both of these features improve the joint efficiency. With an efficiently applied torque the differences between different types of washer are less distinctive. But the considerably different behaviors which are displayed at lower torques still can be perceived.

At lower clamping forces the individual axial strain profiles show that the FW- and CWU-types of washers offer the lowest tensile values in the ligament zones but do have high compressive bearing strains (see Figures 6-32 and 6-33). At higher torques the CWU-type provides the lowest peak and average axial strain levels of all investigated washer types. Its design, though, is coupled with impractical weight penalties (see Figure 6-12) due to the fact that two washers are required. But the more moderate the clamping pressure introduced onto the surface the more relieved appear the strain profiles in the vicinity. The CWU-type has another advantage which is the suppression of delamination at the weakest spot in the laminate: the edge of the hole. There the highest

clamping pressure acts as a result of the washer's design and reinforces the low interlaminar strength. The CWD-type exhibits axially higher peak values in the ligament area but low compressive bearing strains. This is combined with a higher tensile strain in the top zone which then is participating in the load transfer. Now the almost inactive axial fibers above the hole help in distributing the load. This very advantageous behavior is improved with increased lateral constraint. But the high-pressure ring at the rim of the washer causes high shear values and large strain gradients which are worse with higher torques applied.

Strains measured in the 45-degree direction indicate shear strain values. The exact formula for calculating shear strain is given in Appendix D. At the end of this investigation there was not enough data available from the digitizing work done to make a calculation worthwhile. The needed data can be extracted from the moire patterns at a later time if desired. It would not be necessary to rerun the experiments. One would use the same fringe patterns digitize other lines of interest. The plots for the CWD-type are the only correct measurements obtained in the 45-degree direction. They show an increase of strain at the loci of possible shear-out failure with higher lateral constraint. The buildup of shear stress channels in conjunction with increasing clamping forces seems to be apparent at least in the case of CWD-type of washers. A very important fact is presented in the comparison of pin-loaded holes and bolted connections (see Par. 6.9). That is, the real problem lies in critical shear rather than in axial strains for the used material and layup.

Transverse strains have the smallest influence due to their low overall values. The application of torque does have a moderating effect. Just minor importance was attached to the evaluation of transverse strain.

Based on the results presented above, the investigators suggest an order to rate the quality of strain relief:

- CWU-HT-type is best
- FW-HT-type is second best
- CWD-HT-type is third.

Low torques are not advisable because too much strain is shifted into the bearing region risking early bearing failure. Higher torques increase shear values risking early failure by shear-out. There is an optimum value for the right amount of clamping force [6.17. 6.19].

The discussed cases always assume the application of lateral constraint without allowing the bolt torque to produce any effect in the laminate. This more theoretical condition was produced using a thrust bearing integrated into the clamping mechanism. Without this device the application of torque onto the bolt does introduce strains in the surface layer of the laminate which are substantially larger than the strains produced by applying a load. This result can easily be seen in Figure 6-11. Even with a thrust bearing, slight disturbances can be

seen when comparing the fringe patterns, especially for the fringe patterns in the 45 degree direction. How much the twisting action from the washer affects the layers subjacent the surface, and to what degree the joint efficiency will suffer is pure speculation at this time. But, it is apparent that a heavy-handed application of lateral constraint will contribute to an early failure. The problem is that a fastener which can avoid this problem must be weight-and cost-efficient and still feature easy control of the clamping force. Otherwise riveting would be the better approach.

The results and conclusions of this phase of the research project suggest concentrating in future research more on practical aspects which are more directly important for applications. These aspects include:

- Investigations on shear stress/strain distributions, especially in cases of shear stress channels; what they depend on, and means to reduce them.
- Investigations on effects of bolt torque and other application parameters like hole tolerances, bolt tilt, and surface roughness for joint efficiency. Especially, importance should be attached to reducing the twisting action introduced by bolt torque.

The first point was found important mainly due to the low accomplished strain relief in the 45-degree direction. The second point is marginal for work with composites. The material is so much less forgiving to local imperfections that in most practical applications, where these imperfections cannot be avoided, uncertainties arise as to what actually caused the failure. It will be necessary to examine to what degree imperfections can be tolerated in order to provide failure predictions that are accurate within a certain range.

7.0. MODEL FIELD STUDY

7.1. Approach

Understanding the mechanics of a problem, that is, having the relationships between load and stresses, is not sufficient to solve the design problem. The loads must be known for expected service conditions in order to scale stresses measured in the lab or determined through computation.

One of the major problems facing designers of structures is the lack of dependable data about service loads. This lack is especially serious in vehicle design, where field service conditions vary widely. Some data exist for typical autos and trucks, of course. It is an error to think that these data, when available and even when of assured dependability, can serve for the design of vehicle components made of composites. The reasons are quite simple. For one, extensive usage of composites will result in drastic changes in the ratio of sprung to unsprung mass. Also, the dynamic properties of composites, in particular the specific mass and stiffness, are much different from the values for metals. These facts suggest that fastener loads in a vehicle which is partially made of composites will probably bear little relationship with the loads obtained for a conventional vehicle.

At first it might seem that extensive strain or stress measurements should be taken directly from a vehicle under service conditions. This procedure would involve using moire interferometry and/or extensive arrays of strain gage rosettes in the field. Such an approach would be difficult, especially in dynamic field conditions. Fortunately, it is also not necessary.

A better and simpler approach is to measure service loads directly and use them as input for scaling the strains and stresses obtained from careful lab studies as have been conducted during this project. The measured fastener service loads can also be used as input for the analytical schemes as they are proven dependable by the lab measurements. In this way, an efficient synergy between field study, lab experiment, and computation is established. In the early stages at least, it seems advisable to augment the field measurement of fastener service loads with some strain gage data in order to demonstrate clearly the correlation between lab and field studies.

Note also that bolt loading may be established with reasonable accuracy from strain gages that are installed at a distance from the bolt and in sufficient number surrounding the bolt. The material properties are used to obtain the stress resultant around the fastener. The integral of the stress resultant around the strain gage boundary will be equal to the load.

With the above general approach in mind, the following objectives were established:

- Devise a transducer that can be used to measure directly bolt loads for different clamping forces;
- Calibrate the transducer in various loading situations;
- Use the transducer along with strain gages to measure bolt loads and in-plane strains in a laboratory model of a composite joint;
- Correlate the results with the strain maps obtained from the moire studies.

7.2. Bolt Load Transducer

Two transducers were designed and fabricated for this pilot study. They were to utilize resistance strain gages and standard bolts in so far as possible. Although 1/4-inch pins were used in the earlier phases of the experimental research, 3/8-inch pins were chosen for the transducers owing to the difficulties involved in installing strain gages in or on the smaller size pin. It was necessary to reshape the bolts in order to reduce stiffness and to provide protected areas in which to mount the gages.

Figures 7-1 and 7-2 show the two designs tested. Both designs offer the capability of measuring clamping force as well as in-plane load. It is only necessary to hook the gages up so that they respond to axial load and cancel bending loads. Also, both designs can give both magnitude and direction of the in-plane load vector. To accomplish this task, the gages on opposite sides of the transducer are wired into one bridge circuit, and the gages at 90-degrees to the first set are put into a second circuit. Each circuit yields the load component in the plane of the corresponding gages. These components can be combined electronically if necessary.

The main concerns with such transducer designs are sensitivity, linearity, and proof that the device is responding primarily to the load of interest (the in-plane load). The main source of concern has to do with the relatively large diameter-to-length ratio. The gages are hooked up as if they were responding to bending loads. In fact, local shear loads are large, and, owing to short moment arms, the bending strains will be small. To some extent, this concern is reduced by making the bolts hollow tubes so that bending effects are maximized. Contact stresses are also a concern, especially with the slotted configuration. At the very least, such a device must be extensively calibrated and tested. There can be no reliance upon calculated sensitivity.

Both transducers were subjected to brief preliminary tests. The one with the outside slots, as appears in Figure 7-1 was chosen for subsequent calibration.

The chosen transducer was tested in a dead-weight loading frame such as has been described in Chapter 6. It was calibrated for five different

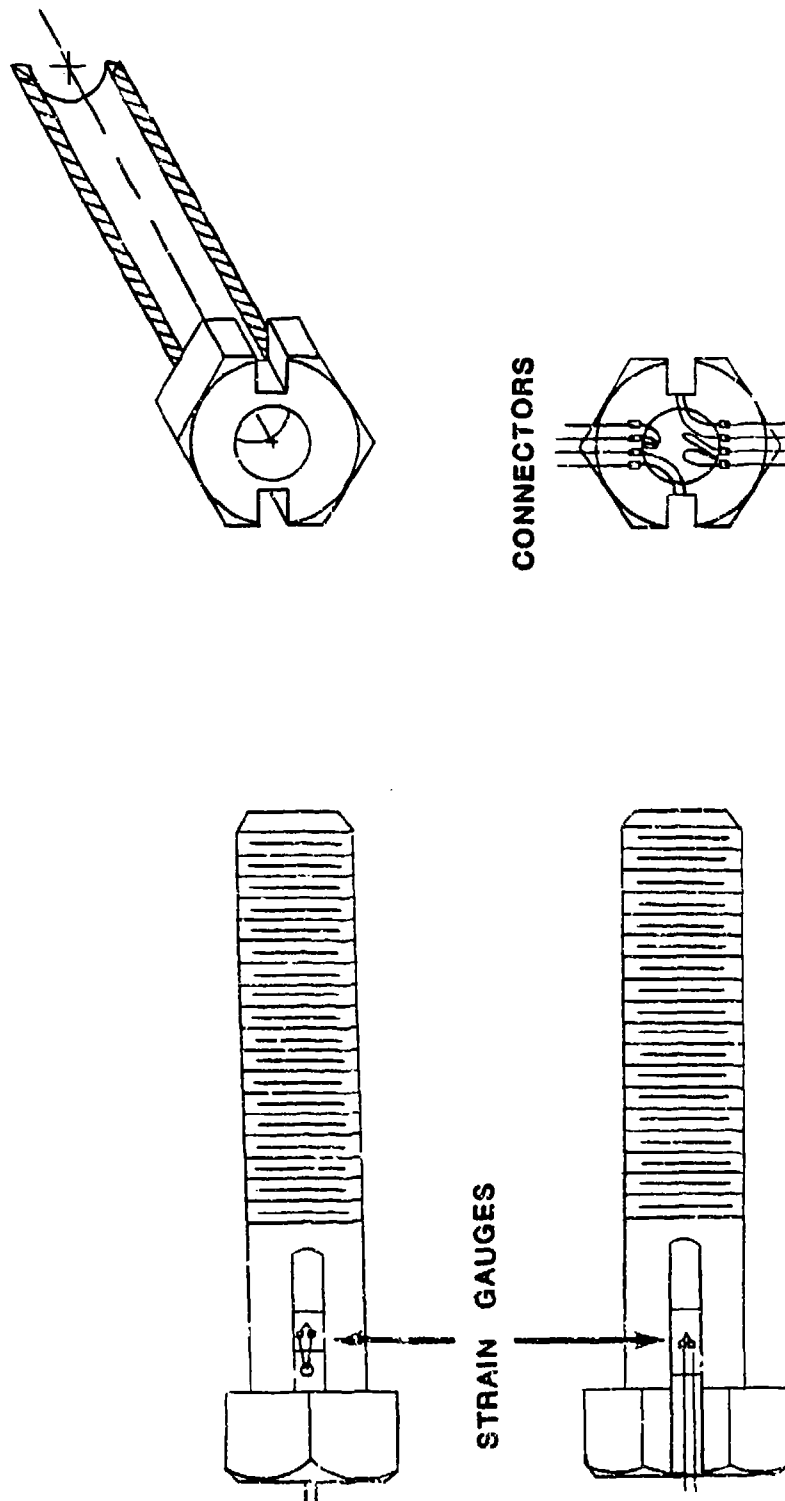


Figure 7-1. Bolt Load Transducer Designs

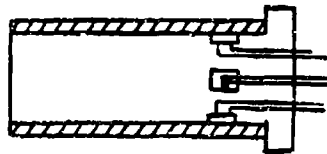
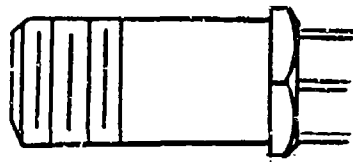


Figure 7-2. Section View Showing The Placement of Strain Gages

angular positions at minimal clamping force and for one angular position at each of 15 and 20 ft-lbs. tightening torque. The resulting calibration plots are shown in Figures 7-3 through 7-9.

While the plots show some inconsistencies, they do show that the transducer can be used to determine bolt loads to within an uncertainty of about 30 percent when it is used with one of the gage planes aligned with the load axis and when the tightening torque is known. Such an uncertainty was better than expected for the this design and for the rather crude construction. It is adequate for field determination of service loads.

The curves for the cases involving clamping force show that the output is greatly decreased as compared with the finger-tight case. Beyond that, the output does not depend greatly on the torque used, except that the onset of joint slip is clearly exhibited. This characteristic is potentially useful, as the results given in Par. 6.0 suggest that a high clamping force will reduce stress concentrations.

7.3. Strain Gage Measurements

The use of strain gages near fasteners is difficult owing to the very large strain gradients in the regions of primary interest. That is one of the reasons for choosing the moire technique as the primary investigative tool in fastener research. As mentioned above, demonstrating some correlation between single gage readings and the moire whole-field results would be useful in that it would provide an alternate to the bolt-load transducer for field measurements.

Study of Figures 6-4a through 6-4d suggests that there are certain areas that are far enough from the hole so that the strains, while small, have small-enough gradient to make RSG measurements practicable. This Figure also suggests that the single-gage measurements might be highly affected by the tilted-pin problem.

Two specimens were instrumented with resistance gages as depicted in Figure 7-10. Owing to lack of material, it was necessary to use specimens which had been used previously for moire studies of the single-pin fastener. The specimens were loaded in the dead-weight system and the strains determined using the devices mentioned in Par. 2. 0.

Table 7-1 shows the strains measured for each gage along with comparable strains obtained for each location and load from the figures mentioned above.

At first glance, the discrepancies apparent in the results are discouraging. That the strain gage results are roughly midway between the full-contact pin and the tilted-pin cases is highly significant. Upon dismantling the strain gage load system, it was found that the pins were contacting only the central layers of the composite. Recall that previously used specimens were being recycled. In one case, there had

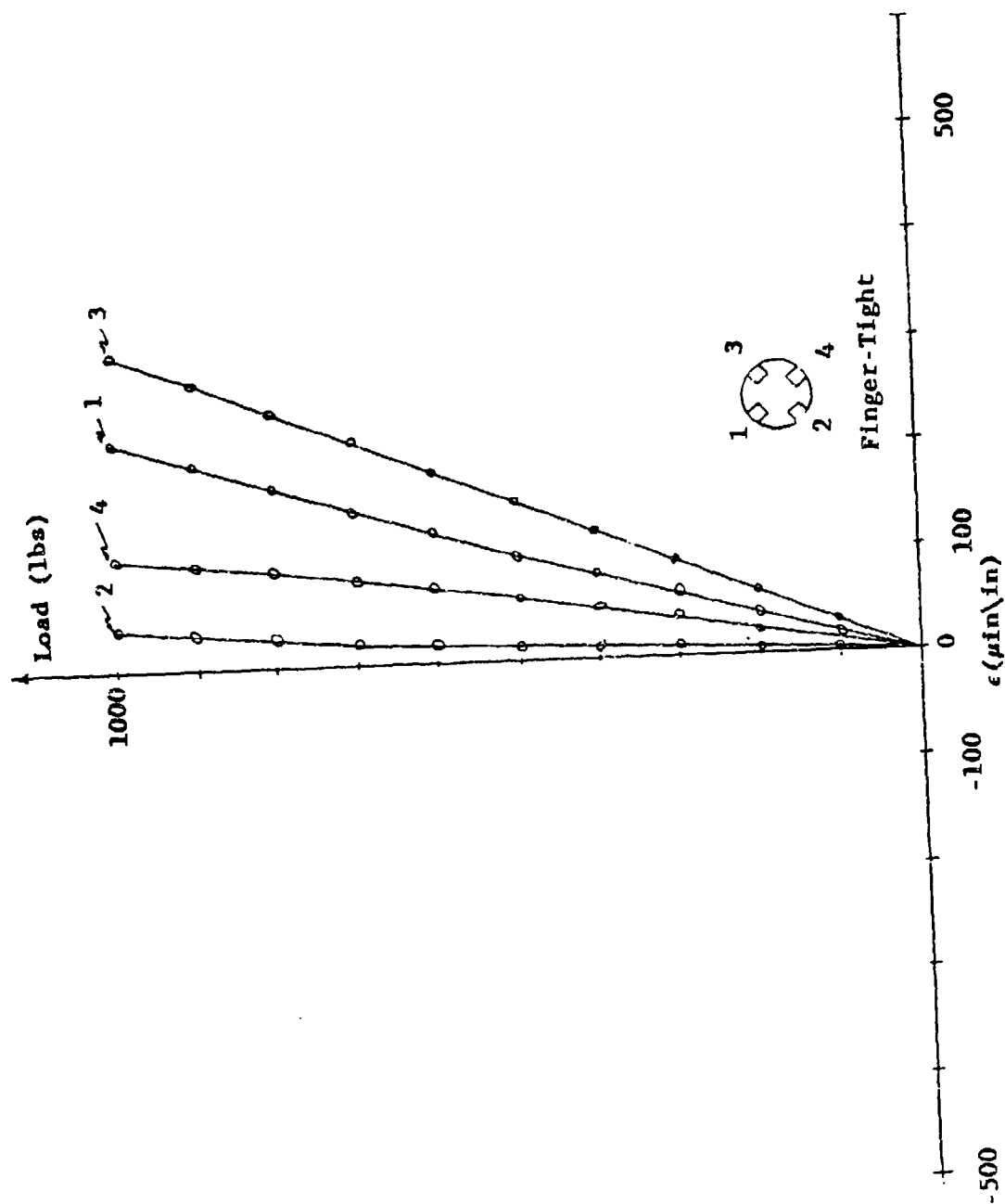


Figure 7-3. Individual Gage Outputs from Transducer in Given Orientation

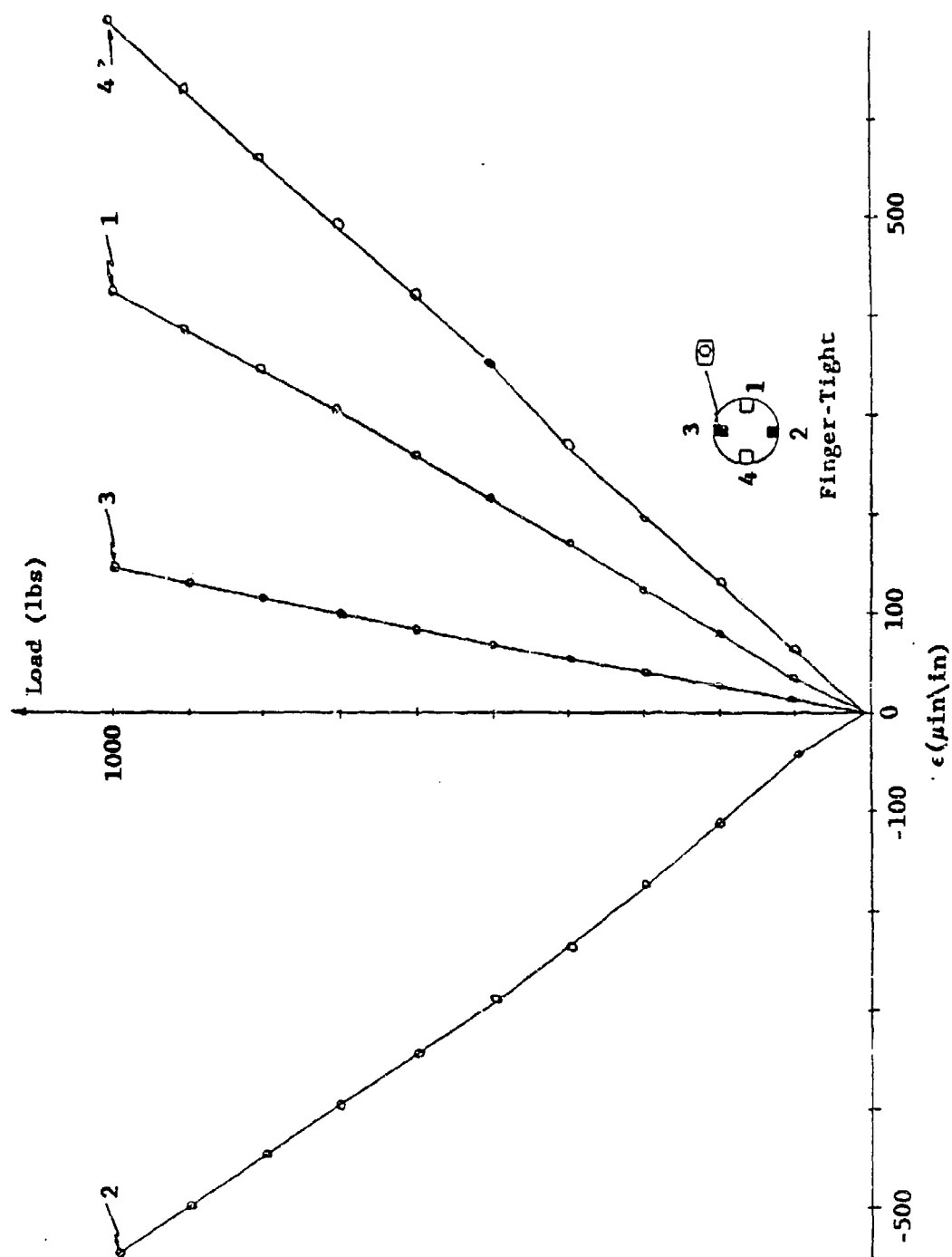


Figure 7-4. Individual Gage Outputs from Transducer in Given Orientation

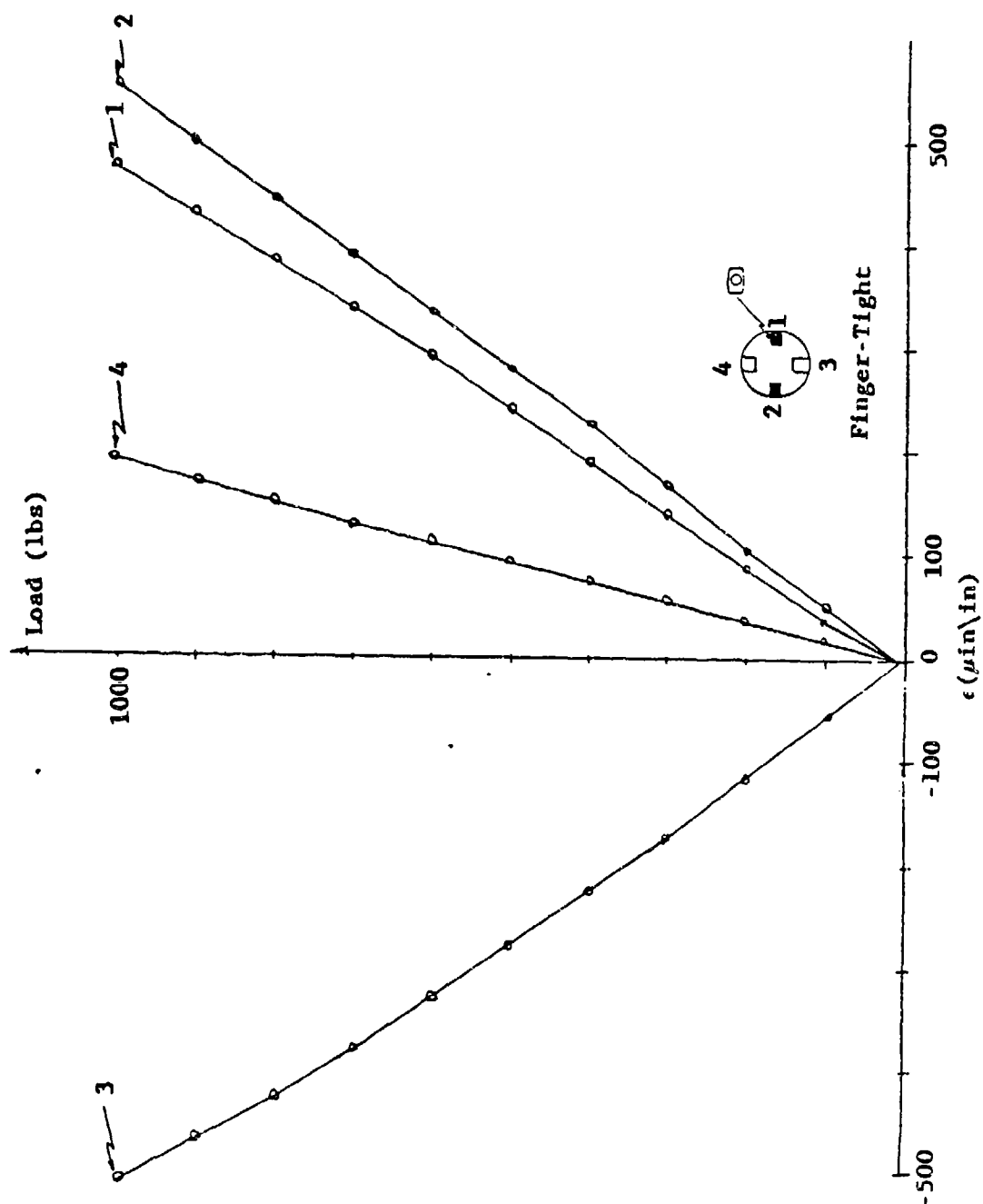


Figure 7-5. Individual Gage Outputs from Transducer in Given Orientation

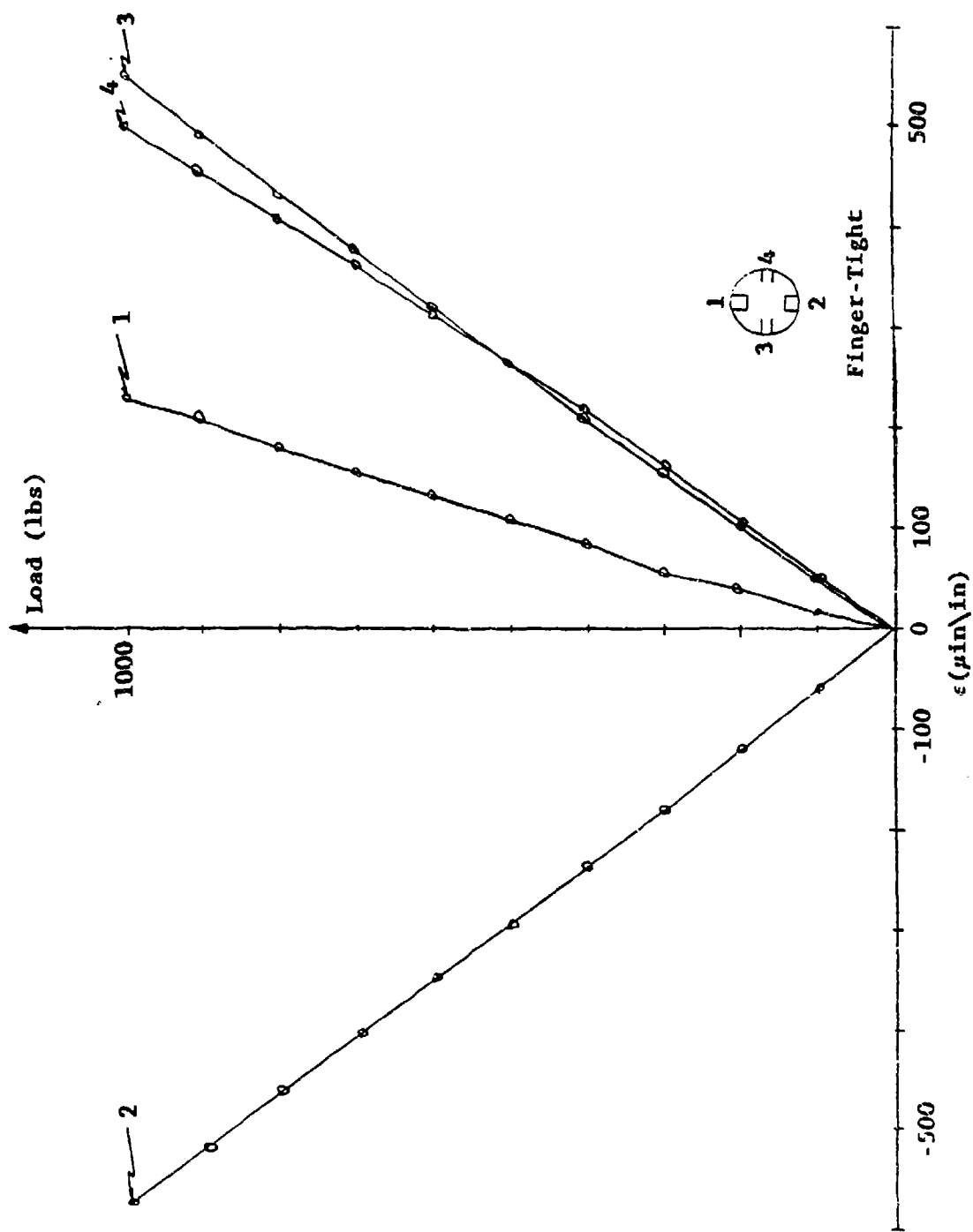


Figure 7-6. Individual Gage Outputs from Transducer in Given Orientation

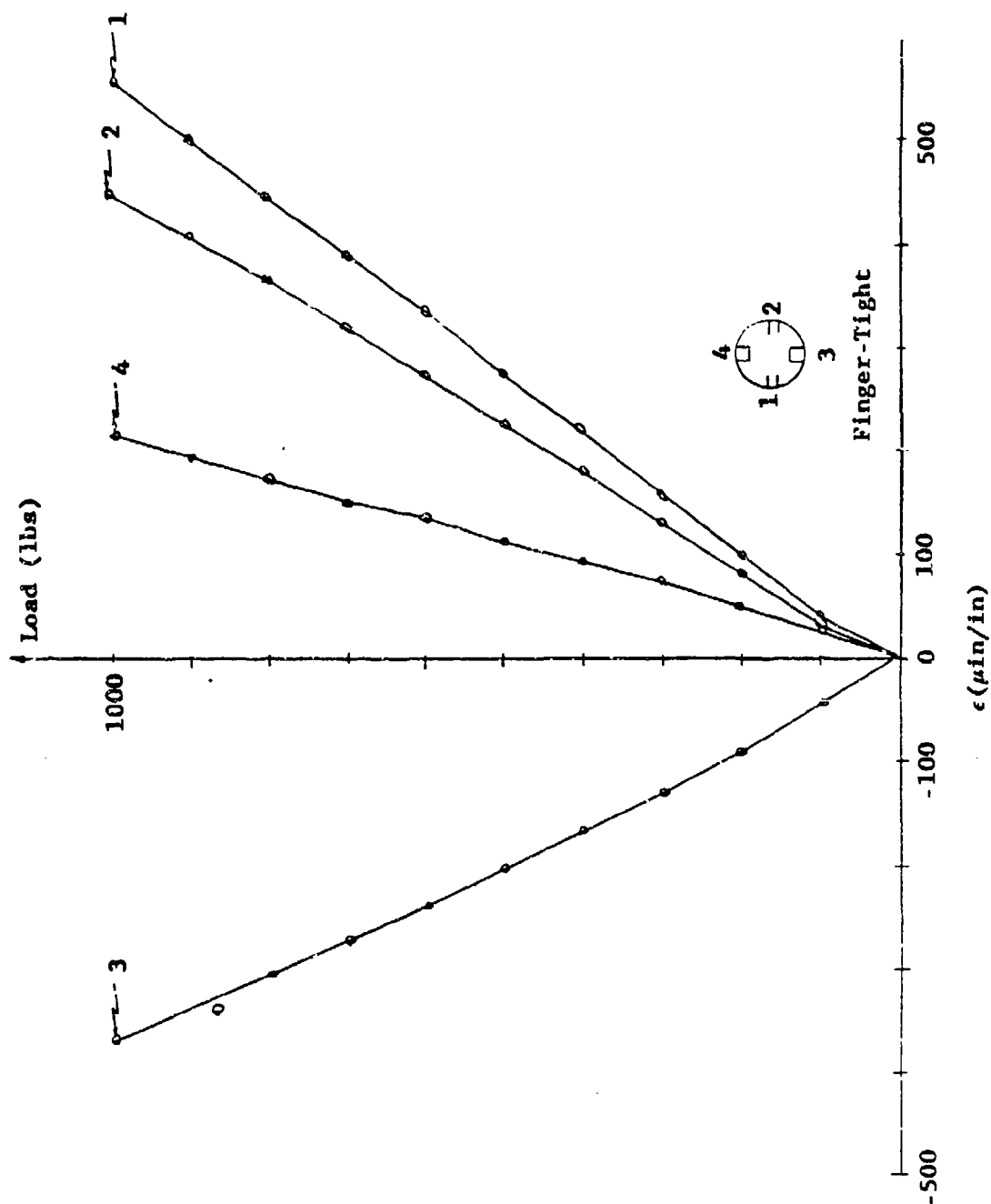


Figure 7-7. Individual Gage Outputs from Transducer in Given Orientation

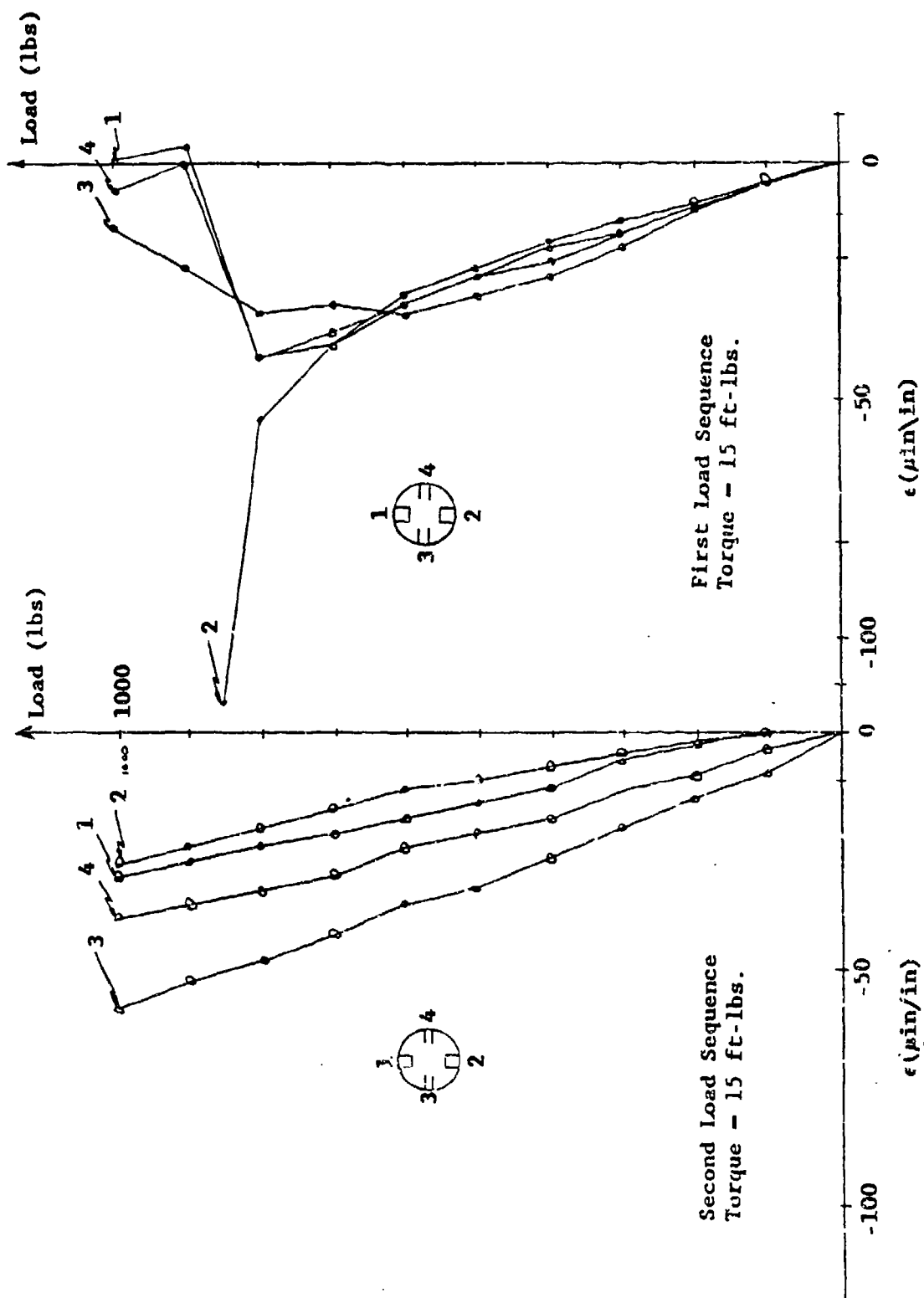


Figure 7-8. Individual Gage Outputs from Transducer in Given Orientation

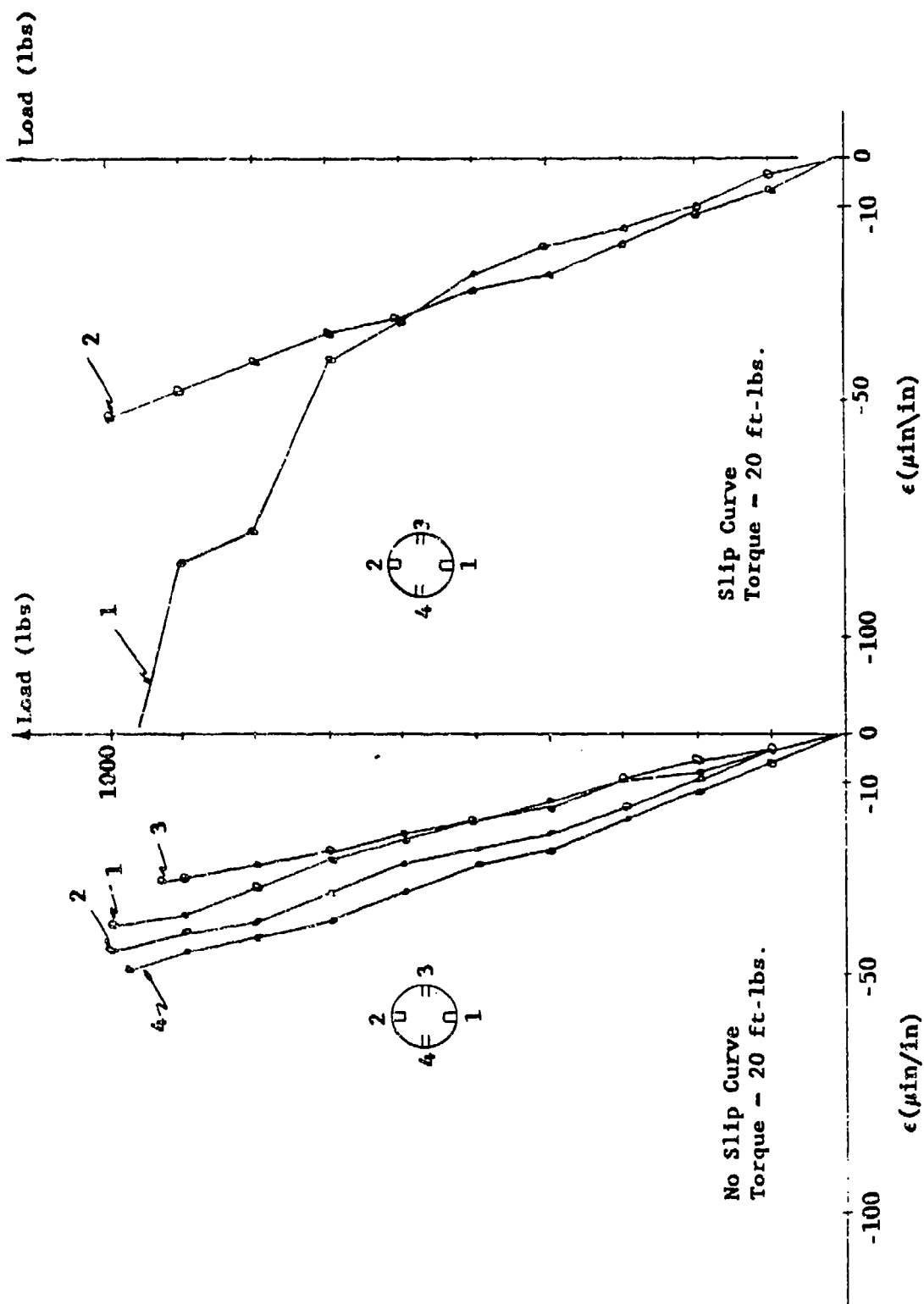


Figure 7-9. Individual Gage Outputs from Transducer in Given Orientation

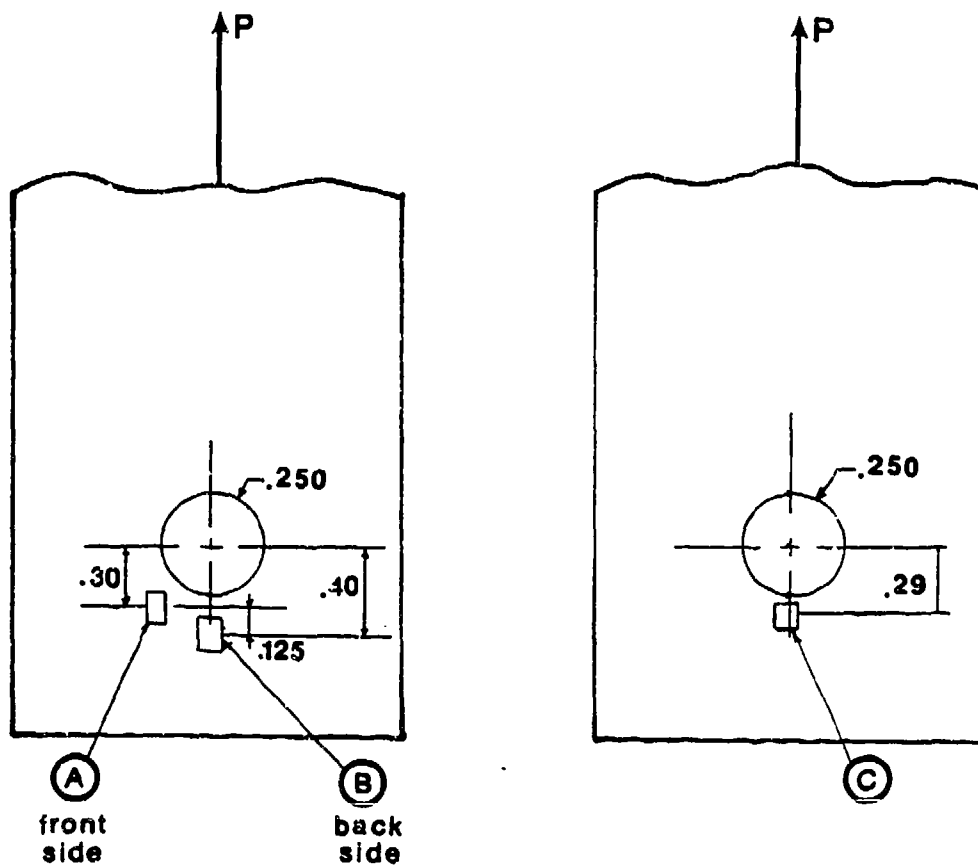


Figure 7-10. Locations of Resistance Strain Gages

LOAD lbs	LOCATION			
	GAUGE A	GAUGE B	GAUGE C	
100	RSG measured	135	175	195 (550)
	MOIRE good fit	400	480	1100
	MOIRE tilted pin	72	145	109
200	RSG measured	252	330	500
	MOIRE good fit	Not Avail.	Not Avail.	Not Avail.
	MOIRE tilted pin	Not Avail.	209	247

All Values in Microstrain.

* After Reshaping Hole, This Increased to 550 microstrain.

Table 7-1. Strain Gage Results Compared with Moire Results for Well-Fitted Pin and Tilted Pin

been some delamination near the surface. In both cases, the holes were slightly bell-mouthed. Both of these specimens were from the early days of this research program, and they had been used for demonstrations and testing of the moire setup.

The inference that the strain gage readings are attenuated by the hole shape is supported by the observation that the readings are not linear with respect to load. As the loads are increased, the surface strains increase disproportionately because the pin is brought into contact with the surface layers of the laminate.

Although it may not be significant, the measured strains are seen to be roughly equivalent to those obtained with certain types of stress-relieving inserts (7.1,7.2).

Since there was no possibility of making new specimens from the scraps of remaining material, one of the bell-mouthed holes was relieved in the midplane area with a hand reamer. Upon retesting, the strain readings were more than double the values obtained before the hole was reshaped. The results are no longer strictly comparable since, in reshaping the hole, the fit was destroyed and the hole profile was modified. This simple test does strongly support the notion that surface strain gage readings were strongly affected by the lack of full pin contact with the hole boundary.

7.4. Summary and Conclusions

This limited strain gage and transducer study yields several suggestive conclusions, as follows:

- Using single gage measurements of strain in the field would give load indications with an uncertainty of around 50 percent on the safe side provided the interpretation is on the basis of tilted-pin results;
- The well-fitted pin results given in Par. 5.0 of this report probably can be interpreted as accurate worst-case strain distributions;
- The results presented in Par. 5.0 and 6.0 for well-fitted and tilted pins probably provide suitable upper and lower bounds on the magnitudes of stresses which will be realized in comparable design situations;
- Interior strains in the poorly fitted pin case are likely comparable to surface strain for the well-fitted pin, but this point needs more study;
- Poor control of hole size and shape can have drastic effects on strain magnitudes;
- Measurements of surface strain can be catastrophically misleading for laminated composites unless test conditions are carefully known and controlled and unless care is taken in interpretation of test results;

- A bolt load transducer of the sort described will give field bolt load measurements with an uncertainty of about 30 percent provided it is properly oriented and the bolt tightening torque is known;
- The bolt load transducer will indicate both clamping force and joint slippage when clamping force is used.

This page left blank intentionally

LIST OF REFERENCES

- 1.1 Cloud, G. L., Sikarskie, D., Mahajerin, E., Herrera, P., "Theoretical and Experimental Investigation of Mechanically Fastened Composites", Technical Report No. 13004, U. S. Army Tank-Automotive Command Research Center, Warren, Michigan, 48890, 55pp., 1984.
- 1.2 Cloud, G., Herrera, P., "Experimental Study of Mechanically-Fastened Composites," Army Symposium on Solid Mechanics 1984, Army Material and Mechanics Research Center, Watertown, MA, Oct.1984.
- 1.3 Mahajerin, E., Sikarskie, D.L., "Application of the Boundary Element Method to Problems in Composites Fastening," Army Symposium on Solid Mechanics 1984, Army Material and Mechanics Research Center, Watertown, MA, Oct.1984.
- 1.4 Herrera-Franco, P., Cloud, G., "Moire Study of Mechanically-Fastened Composites," Proc. Spring 1985 Meeting of Society for Experimental Mechanics, Las Vegas, NV, June 1985.
- 1.5 Cloud, G., Herrera, P., "Experimental Study of Mechanically-Fastened Composites," Proc. Tenth Canadian Congress of Applied Mechanics, London, Canada, June 1985.
- 1.6 Herrera-Franco, P.J., A Study of Mechanically Fastened composite Using High Sensitivity Interferometric Moire Technique, Ph.D. Dissertation, Michigan State University, E. Lansing, MI 48824, 1985.
- 1.7 Herrera-Franco, P.J., Cloud, G.L., "Strain-Relief Inserts for Composite Fasteners," Proc. American Soc. for Metals - Eng. Soc. Detroit Advanced Composites Conf., Dearborn, MI, Dec. 1985.
- 1.8 Vable, M., Sikarskie, D.L., "Boundary Element Method for Plane Elastoplastic Orthotropic Problems," Abstracts, First World Congress on Computational Mechanics, Austin, Texas, Sept. 1986.
- 1.9 Vable, M., Sikarskie, D.L., "Stress Analysis in Plane Orthotropic Material by the Boundary Element Method," Submitted to International Journal of Solids and Structures.
- 1.10 Herrera-Franco, P.J., Cloud, G.L., "Experimental Analysis of Multiple-Hole Arrays of Composite Material Fasteners," Proc Spring 1986 Conference of Experimental Mechanics, Soc. Exp. Mech., New Orleans, LA, June 1986.

List of References (continued)

- 1.11 Bayer, M.H., Cloud, G.L., "Moire Study of Strains Near Washers on Composites," Proc. Fall 1986 Conference of Experimental Mechanics, Soc. Exp. Mech., Keystone, CO, June 1986.
- 1.12 Herrera Franco, P.J., Cloud, G., Zimmerman, K., "Moire Study of 2- and 3-Hole Fastener Arrays in FGRP Composite," Proc. 2nd Conf. on Advanced Composites, American Soc. Metals and Eng. Soc. Detroit, Dearborn, MI, Nov. 1986.
- 1.13 Herrera Franco, P.J., Cloud, G.L., "Moire Analysis of Two- and Three-Hole Arrays of Composite Material Fasteners," Proc. Joint BSSM / SEM International Conference, London, England, Aug. 1987.
- 1.14 Vable, M., Sikarskie, D.L., "Boundary Element Method for Mixed Boundary Value Plane Elastostatic Orthotropic Problems," To be presented at 9th International Conference on Boundary Element Method in Engineering.
- 1.15 Cloud, G., Herrera Franco, P., Bayer, M., and Zimmerman, K., "Strain Analysis of 2- and 3-Hole Fastener Arrays in FGRP," submitted for presentation and publication.
- 1.16 Godwin, E.W., and Matthews, F.L., "A Review of the Strength of Joints in Fibre-Reinforced Plastics," Composites, July 1980, p. 155.
- 1.17 Matthews, F.L., Nixon, A., and Want, G.R., "Bolting and Riveting in Fibre Reinforced Plastics," Proc. Reinforced Plastics Congress, British Plastics Federation, Brighton, November 1976.
- 1.18 Webb, A.L., "Riveting and Bolting in Carbon Fiber Composite," Symposium: Jointing in fibre reinforced plastics, Imperial College, IPC Press, London, 1978.
- 1.19 Kingston-Lee, D.M., and Rogers, K.F., "A Preliminary evaluation of Proprietary Rivets as Fasteners for Carbon Fibre Laminates," RAE Technical Memorandum Materials 243, 1976.
- 1.20 Cole, R.T., Bateh, E.J., and Potter, J., "Fasteners for Composite Structures," Composites, July 1982, p. 233.
- 1.21 Sendekyj, G.P., and Richardson, M.D., "Fatigue behavior of a Graphite-Epoxy Laminate Loaded Through an Interference-Fit Pin," Proc. of 2nd Air Force Conference on Fibrous Composites in Flight vehicle design, Tech Report AFFDL-TR-74-102 Air Force Flight Dynamics Lab, WPAFB, OH, Sept. 1974, pp. 1-10.

List of References (continued)

- 1.22 Tanis, C., and Poullos, M. , "Composite Fasteners - A Compatible Joining Technique for Fibrous Composites in Structural Design," Fibrous Composites In Structural Design, Plenum Press, New York, 1980, pp. 645-658.
- 1.23 Stockdale, J.H., and Matthews, F.L. , "The Effect of Clamping Pressure on Bolt Bearing Loads in Glass Fibre-Reinforced Plastics," Composites, January 1976, p. 34.
- 1.24 Collins, T.A. , "The Strength of Bolted Joints in Multi-Directional Cfrp Laminates," Composites, January 1977, p. 43.
- 1.25 Webb, J.N., and Smith, M.A. , "The Fatigue and Residual Strength of a Multi-Bolt Joint Between Metal and Carbon Fibre Composite," RAE Technical Report 78134, 1978.
- 1.26 Rufolo, A. , "Design Manual for Joining of Glass Reinforced Plastics," US Naval Material Laboratory report, Navship 250-634-1, August 1961.
- 1.27 Crews, J.H. , "Bolt Bearing Fatigue of a Graphite/Epoxy Laminate," Joining of Composite Materials, ASTM STP 749, American Society for Testing and Materials, 1981, p. 131.
- 1.28 Matthews, F.L., Roshan, A.A., and Phillips, L.N. , "The Bolt Bearing Strength of Glass/Carbon Hybrid Composites," Composites, July 1982, p. 225.
- 1.29 Collings, T.A. , "On The Bearing Strength of CFRP Laminates," Composites, July 1982, p. 241.
- 1.30 Soni, S.R. , "Failure analysis of Composite Laminates with a Fastener Hole," Joining of Composite Materials, ASTM STP 749, American Society for Testing and Materials, 1981, p. 145.
- 1.31 Schgjelderup, H.C., and Jones, B.H. , "Practical Influence of Fibrous Reinforced Composites in Aircraft design," Composite Materials: Testing and Design, ASTM STP 460, American Society for Testing and Materials, 1969, p.285.
- 1.32 Porter, R.M. , "Bolted Joints in Fibre Reinforced Plastics," MSC Project Report Aeronautics Dept, Imperial College, London, England 1976.
- 1.33 Saddler, C.J., and Barnard, A.J. , "The Strength of Bolted and Riveted Joints in CFRP Laminates," Westland Helicopter Ltd., Structure Research Note No. 16, 1977.

List of References (continued)

- 1.34 Dastin, S. , "Joining and Machining Techniques," Handbook of Fibreglass and Advanced Plastics Composites, edited by G. Lubin, Van Nostrand Reinhold, 1969.
- 1.35 Oleesky, S.S., and Mohr, J.G. . SPI Handbock of Reinforced Plastics Reinhold, 1964.
- 1.36 Eisenmann, J.R., and Leonhardt, J.L. , "Improving Composite Bolted Joint Efficiency by Laminate Tailoring," Joining of Composite Materials, ASTM STP 749, American Society for Testing and Materials, 1981, p. 117.
- 1.37 Kocher, L.H., and Cross, S.L. , "Reinforced Cutouts in Graphite Composite Structures," Composite Materials: Testing and Design, ASTM STP 497, American Society for Testing and Materials, 1972, p. 382.
- 1.38 Strauss, E.L. , "Mechanical Jointing in Reinforced Plastics Structures," Machine Design, Vol. 32, March, 1960.
- 1.39 Clayton,, C., and Jones, D.P. , "Further Investigations into the Effect of Countersunk Holes in a Multi-Directional CFRP Laminate using Various Fibre/Resin Combinations," British Aircraft Corp. Reports p. 137, 1976.
- 1.40 Padaver, G.E. , "The Strength of Bolted Connections in Graphite/Epoxy Composites Reinforced by Colaminated Boron Film," Composite Materials: Testing and Design, ASTM STP 497, American Society for Testing and Materials, 1972, p. 396.
- 1.41 Hart-Smith, L.J. , "Mechanically-Fastened Joints for Advanced Composites - Phenomenological Considerations and Simple Analysis," Fibrous Composites Instructural Design, Plenum Press, New York, 1980, pp. 543-574.
- 1.42 McGarry, F.J. , "Composite Structural Materials," Experimental Mechanics, Vol. 6. No. 6., p. 331, June 1966
- 1.43 VDI-Nachrichten , Nr. 14, 1986, p. 71.
- 1.44 VDI-Nachrichten , Nr. 17, 1986, p. 36.
- 1.45 VDI-Nachrichten , Nr. 17, 1986, p. 16.
- 1.46 VDI-Nachrichten , Nr. 15, 1986, p. 39.
- 1.47 VDI-Nachrichten , Nr. 24, 1986, p. 45.

List of References (continued)

- 1.48 Bickley, W. G., "Distribution of Stress Around a Circular Hole in a Plate," Phil. Trans. Roy. Soc. London, Ser. A, 227, 1928, pp 383-415.
- 1.49 Tiffen, R. and Sharfuddin, S. M., "A mixed Boundary Value Problem of Two Dimensional Elasticity," Mathematika, Vol. 11, 1964, pp. 151-154.
- 1.50 Sharfuddin, S. M., "Loaded Loose-Fitted Rough Circular Rigid Pin in a Circular Hole," Acta Mechanica, Vol. 3, No. 4, 1967, pp. 376-384.
- 1.51 Theocaris, P. S., "The Stress Distribution in a Strip Loaded in Tension by Means of a Central Pin," J. Applied Mechanics, Vol 23, 1956, pp. 85-90.
- 1.52 Waszcak, J. P. and Cruse, T. A. "Failure Mode and Strength Predictions of Anisotropic Bolted Bearing Specimens," J. Composite Materials, Vol. 5, July 1971, p. 421.
- 1.53 De Jong, Theo, "Stresses Around Pin-Loaded Holes in Elastically Orthotropic or Isotropic Plates," J. Composite Materials, Vol. 11, July 1977, pp. 313-331.
- 1.54 Wong, C. M. S. and Matthews, F. L. "A Finite Element Analysis of Single and Two-hole Bolted Joints in Fibre Reinforced Plastic," J. Composite Materials, Vol. 15, September 1981, p.481.
- 1.55 Matthews, F. L., Wong, C. M. S. and Chrysafity, C. "Stress Distribution Around a Single Bolt in Fibre-Reinforced Plastic", Composites, Vol. 13, pp 316-322, 1982.
- 1.56 Wilkinson, T. L. and Rowlands, R. E. "Analysis of Mechanical Joints in Wood," Experimental Mechanics, Vol. 21, pp. 408-414, (November, 1981).
- 1.57 Oplinger, D. W. "On the Structural Behavior of Mechanically Fastened Joints in Composite Structures," Fibrous Composites in Structural Design, Edited by Edward M. Lenoe, Donald W. Oplinger and John J. Burke, Plenum Press, New York, 1980, pp. 575-602.
- 1.58 Chang Fu-Kuo, Scott, Richard A. and Springer, George S., "Strength of Mechanically Fastened Composite Joints," J. Composite Materials, vol. 16, November 1982, p.470.
- 1.59 Yamada, S. E., "Analysis of Laminate Strength and its Distribution," J. Composite Materials, vol. 12, 1978, pp. 275-284.

List of References (continued)

- 1.60 Pradhan, B. and Ray, Kumar, "Stresses Around Partial Contact Pin-loaded Holes in FRP Composite Plates," Journal of Reinforced Plastics and Composites, vol. 3, pp. 69-84, January 1980.
- 1.61 Chang, Fu-Kuo and Scott, Richard A., "Failure of Composite Laminates Containing Pin Loaded Holes - Method of Solution," J. Composite Materials, Vol. 18, May 1984, pp. 255-278.
- 1.62 Chang, Fu-Kuo and Scott, Richard, A., "Design of Composite Laminates Containing Pin Loaded Holes," J. Composite Materials, Vol. 18, May 1984, pp. 279-289.
- 1.63 Zhang, Kai-Da and Ueng, Charles E., "Stresses Around a Pin-loaded Hole in Orthotropic Plates," J. Composite Materials, Vol. 18, September 1984, pp. 432-446.
- 1.64 Frocht, M. M. and Hill, H. N., "Stress Concentration Factors Around a Circular Hole in a Plate Loaded Through Pin in the Hole," Journal of Applied Mechanics, Vol 7, March 1940, pp. 5-9.
- 1.65 Lambert, T. H. and Brailey, R. J. "The influence of Coefficient of Friction on the Elastic Stress Concentration Factor for a Pin-jointed Connection," Aeronautical Quart., Vol. 13, 1962, pp. 17-29.
- 1.66 Jessop, H. T., Snell, C. and Holister, G. S., "Photoelastic Investigation of Plates with Single Interference-fit Pins with Load Applied (a) to pin only and (b) to Pin and Plate Simultaneously," Aeronautical Quarterly, Vol. 9, 1958, pp. 147-163.
- 1.67 Cox, H. L. and Brown, A. F., "Stresses Round Pins in Holes," Aeronautical Quarterly, Vol. 15, Nov. 1964, pp. 357-372.
- 1.68 Nisida, M. and Saito, H., "Stress Distribution in a Semi-infinite Plate Due to a Pin Determined by Interferometric Method," Experimental Mechanics, vol. 23, May 1966, pp. 273-779.
- 1.69 Oplinger, D. W., Parker, B. S., Katz, A. H., "Moire Measurements of Strain and Deformations in Pin-loaded Composite Plates," Proc. SESA 1979 Spring Meeting. San Francisco, California, May 1979.
- 1.70 Wilkinson, T.L., Fuchs, E. A. and Rowlands, R. E. "Photomechanical Determination of Stress in the Neighborhood of Loaded Holes in Anisotropic Media," Proc. 6th. Int. Conf. on Stress Analysis, Munich, 121-126, 1978.

List of References (continued)

- 1.71 Rowlands, R. E., Rahaman, M. J., Wilkinson, T. L. and Chiang, Y. I., "Single-and-Multiple-Bolted Joints in Orthotropic Material," Composites, Vol. 13, Number 3, July 1982, pp. 273-279.
- 1.72 Prabhakaran, R., "Photoelastic Investigation of Bolted Joints in Composites," Composites, Vol. 13, Num. 3, July 1982, pp. 253-256.
- 1.73 Same as ref. 1.1
- 1.74 Serabian, S. M., "Experimental Verification of Analytical Bolted Joint Methodologies," Proceedings of the Sixth Conference on Fibrous Composites in Structural Design, Army Materials and Mechanics Research Center, Watertown, Mass., AMMRC MS 83-2, November 1984.
- 1.75 Katz, Alan H., "A Semi-Automated System for Moire Strain Analysis", Proceedings of the Sixth Conference on Fibrous Composites in Structural Design," Army Materials and Mechanics Research Center, Watertown, Mass., AMMRC MS 83-2, November 1984.
- 1.76 Johnson, M., and Matthews, F.L. , "Determination of Safety Factors for Use When Designing Bolted Joints in GRP," Composites, April 1979, p. 73.
- 1.77 Devine, F.E., and Humphreys, J. , "Bolted Assembly of engineering components press moulded from sheet moulding compound," Composites, July 1982, p. 311.
- 1.78 Green, A.K., and Phillips, L.N. , "Crimp-Bonded End Fittings For Use on Pultruded Composite Sections," Composites, July 1982, p. 219.
- 1.79 Pickett, A., Hollaway, L., and Phillips, L.N. , "Analysis of a Crimped and Bonded Joint for Load Bearing Skeletal Members," Composites, July 1982, p. 257.
- 1.80 Cluley, A.P., and Scoular, R.P. , "Jointing of Components Moulded in Carbon Fibre-Reinforced Thermoplastics," Composites, January 1983, p. 19.
- 1.81 York, J.L., Wilson, D.W., and Pipes, R.B. , "Analysis of Net Tension Failure Mode in Composite Bolted Joints," J. Reinforced Plastics and Composites, Vol. 1, pp. 141-152, April 1982.
- 1.82 De Koning, C.A.M., and Van Dreumel, W.H.M. , "Mechanical Joining of Aramid Fibre Composites: An Experimental Study," J. Reinforced Plastics and Composites, Vol. 2, pp. 130-137, April 1983.

List of References (continued)

- 1.83 Pyner, G.R., and Matthews, F.L. , "Comparison of Single and Multi-Hole Bolted Joints in Glass Fibre Reinforced Plastic," *Journal of Composite Materials*, Vol. 13, July 1979, p. 232.
- 1.84 Carlsson, L. , "Interlaminar Stresses at a Hole in a Composite Member Subjected to In-Plane Loading," *Journal of Composite Materials*, Vol. 17, May 1983.
- 1.85 Lakshminarayana, H.V. , "Stress Distribution around a Semi-Circular Edge-Notch in a Finite Size Laminated Composite Plate under Uniaxial Tension," *Journal of Composite Materials*, Vol. 17, July 1983.
- 1.86 Lo, K.H., Wu, E.M., and Konishi , "Failure Strength of Notched Composite Laminates," *Journal of Composite Materials*, Vol. 17, September 1983.
- 1.87 Delale, F., Kishore, N.N., and Wang, A.S.D. , "Stress Analysis of a Composite Plate With a Circular Hole Under Axisymmetric Bending," *Journal of Composite Materials*, Vol. 18, September 1984.
- 1.88 Regalbuto, J.A., and Wheeler, O.E., "Stress distribution from Interference Fits and Uniaxial Tension," *Experimental Mechanics*, July 1970, p. 274.
- 1.89 Waszczak, J.P., and Cruse, T.A. , "Failure Mode and Strength Prediction of Anisotropic Bolt Bearing Specimen," *Journal of Composite Materials*, Vol. 5, July 1971, p. 421.
- 1.90 Grimes, G.C., Jeans, L.L., and Demuts, E. , "Sensitivity of Bonded and Bolted Joints in Composites to Load/Environmental Spectrum Variations," Fibrous Composites Instructural Design, Plenum Press, New York, 1980, pp. 619-644.
- 1.91 Gandhi, K.R. , "Analysis of an Inclined Crack Centrally Placed in an Orthotropic Rectangular Plate," *Journal of Strain Analysis*, Vol. 7, No. 3, 1972.
- 1.92 Seely, F.B., and Smith, J.O. , "Stress Concentrations Determined by Photoelastic Method," Advanced Mechanics of Materials, 1952, p. 393.
- 1.93 Wahl, A.M., and Beeuwkes, R. , "Stress Concentration Produced by Holes and Notches," *Transactions of the American Society of Mechanical Engineers*, APM-56-11.

List of References (continued)

- 1.94 Mindlin, R.D. , "Stress Distribution Around a Hole Near the Edge of a plate under tension," Proc. SESA, Vol. 5, pp. 56-68, 1948.
- 1.95 Cope, R., and Pipes, R.B. , "Design of the Spar-Wingskin Joint," Fibrous Composite Instructural Design Plenum Press, New York, 1980, pp. 603-618. 19711.
- 1.96 Daniel, I.M. , "Biaxial Testing of [0/45] Graphite/Epoxy Plates with holes," Exp. Mech., Vol. 22, No. 5, pp. 188-195, May 1982.
- 1.97 Jacob, K.A. , "Fabrication of Birefringent Anisotropic Model Materials," Exp. Mech., Vol. 22, No. 5, p. 196, May 1982.
- 1.98 Tennyson, R.C., Elliot, G., and Hansen, J.C. , "Failure Analysis of Composite Laminates Using a Tensor Polynomial Strength Criterion," University of Toronto, Institute for Aerospace Studies, Toronto, Ontario, Canada.
- 1.99 Matthews, F.L. and Hirst, I.R. , "The Variation of Bearing Strength with Load Direction," Symposium: Jointing in Fibre Reinforced Plastics, Imperial College London, England, ICP Press, 1978.
- 1.100 Coker, E. G. and Filon, L. N. G., "A Treatise on Photoelasticity", Cambridge University Press, 1931.
- 1.101 Dundurs, J., "Dependence of Stresses on Poisson's Ratio in Plane Elasticity," International Journal of Solids and Structures, Vol. 3, 1967, pp. 1013-1021.
- 1.102 Dundurs, J. and Stippes, M., "Role of Elastic Constants in Certain Contact Problems," Journal of Applied Mechanics, Vol 37, December 1970, pp. 965-970.
- 1.103 Michell, J. H., "On The Direct Determination of Stress in an Elastic Solid," Proceedings of the London Mathematical Society, Vol., 31, 1899, pp. 100-124.
- 1.104 Post, D. "Optical Interference for Deformation Measurements - Classical, Holographic and Moire Interferometry," Mechanics of Nondestructive Testing, Proceedings Edited by W. W. Stinchcomb, Plenum Publishing Corp. N. Y., 1980.
- 1.105 Post, D. and Baracat, W. A., "High Sensitivity Moire Interferometry - A Simplified Approach," Experimental Mechanics, Vol. 21, pp. 100-104, March 1981.

List of References (continued)

- 1.106 McDonach, A., McKelvie, J. and Walker, C. A. "Stress Analysis of Fibrous Composites Using Moire Interferometry," Optics and Lasers in Engineering, Vol. 1, (1980), pp. 85-105.
- 1.107 Weissman, E. ... and Post, D., "Full-field Displacement and Strain Rosettes by Moire Interferometry," Experimental Mechanics, Vol. 22 (9), pp. 324-328, (September 1982).
- 1.108 De Jong, Theo, "Stress Around Pin-Loaded Holes in Composite Materials - Recent Advances," Proceedings of the IUTAM Symposium on Mechanics of Composite Materials, VPI and State Univ., August 16-19, 1982, Edited by Zvi Hashin and Carl T. Herakovich.
- 1.109 Dallas, Richard N., "Mechanical Joints in Structural Composites," 2nd. National SAMPE Symposium, Society of Aerospace Materials and Process Engineers - Advances in Structural Composites", (1967).
- 2.1 Jones, Robert M., "Mechanics of Composite Materials," McGraw-Hill Book Company, 1975.
- 2.2 "Experimental Mechanics of Fiber Reinforced Composite Materials," by James M. Whitney, Isaac M. Daniel, R. Byron Pipes, Published by The Society for Experimental Stress Analysis, Brookfield Center, Connecticut, SESA Monograph No. 4, First Edition 1982.
- 2.3 Pagano, N. J. and Halpin, J. C. "Influence of End Constraint in the Testing of Anisotropic Bodies," J. Composite Materials, Vol. 2, 1969, p. 18.
- 2.4 R. B. Pipes, "On The Off-Axis Strength Test for Anisotropic Materials," J. Composite Materials, Vol. 7 (April 1973), p. 246.
- 2.5 Horgan, C. O., "Saint-Venant End Effects in Composites," J. Composite Materials, Vol. 16, Sept. 1982, p. 411.
- 2.6 Kulkarni, H., and Beardmore, P. , "Design Methodology for Automotive Components Using Continuous Fibre-reinforced Composite Materials," Composites, October 1980, p. 225.
- 3.1 Sikarskie, D.L., Benjumea, R., "On the Solution of Plane Orthotropic Elasticity Problems by an Integral method," Jour. App. Mech., Trans. ASME, vol. 94, pp. 801-808, 1972.

List of References (continued)

- 3.2 Cloud, G. L., Sikarskie, D., Mahajerin, E., Herrera, P., "Theoretical and Experimental Investigation of Mechanically Fastened Composites," Technical Report No. 13004, U. S. Army Tank-Automotive Command Research Center, Warren, Michigan, 48890, 55pp., 1984.
- 3.3 Lekhnitski, S.G., Theory of Elasticity of an Anisotropic Elastic Body, Holden-Day, Inc., San Francisco, 1963.
- 3.4 Snyder, M.D., Cruse, T.A., "Boundary Integral Equation Analysis of Cracked Anisotropic Plates," Int. Journal Fracture Mech., v11, pp. 315-328, 1975.
- 3.5 Sneddon, I.N., Fourier Transform, McGraw-Hill, New York, 1951.
- 3.6 Vable, M., "Making the Boundary Element Less Sensitive to Changes or Errors in the Input Data," Submitted to Int. Jour. for Numerical Methods in Engineering.
- 3.7 Vable, M., An Algorithm for Evaluating the Boundary Integral Equations in Planar Elasto-Plastic Bodies, Ph.D. Dissertation, University of Michigan, Ann Arbor, MI, 1981.
- 3.8 Irschik, H., "A Boundary-Integral Equation Method for Bending of Orthotropic Plates," Int. Jour. Solids and Structures, vol. 20, no. 3, pp. 245-255, 1984.
- 3.9 Peterson, R.E., Stress Concentration Factors, John Wiley, New York, 1974.

- 4.1 Frocht, M. M. and Hill, H. N., "Stress Concentration Factors Around a Circular Hole in a Plate Loaded Through Pin in the Hole," Journal of Applied Mechanics, vol. 7, March 1940, pp. 5-9.
- 4.2 Lambert, T. H. and Brailey, R. J. "The Influence of Coefficient of Friction on the Elastic Stress Concentration Factor for a Pin-jointed Connection," Aeronautical Quart., vol. 13, 1962, pp. 17-29.
- 4.3 Jessop, H. T., Snell, C. and Holister, G. S., "Photoelastic Investigation of Plates with Single Interference-fit Pins with Load Applied (a) to pin only and (b) to Pin and Plate Simultaneously," Aeronautical Quarterly, Vol. 9, 1958, pp. 147-163.

List of References (continued)

- 4.4 Cox, H. L. and Brown, A. F., "Stresses Around Pins in Holes," Aeronautical Quarterly, vol. 15, Nov. 1964, pp. 357-372.
- 4.5 Nisida, M. and Saito, H., "Stress Distribution in a Semi-infinite Plate Due to a Pin Determined by Interferometric Method," Experimental Mechanics, vol. 23, May 1966, pp. 273-279.
- 4.6 Dally, J. W. and Alfievich, I. "Application of Birefringent Coatings to Glass-Fiber-Reinforced Plastics," Experimental Mechanics, vol. 9, no.3, pp. 97-102 March 1969.
- 4.7 Pipes, R. B. and Dally, J. W., "On the Birefringent Coating Method of Stress Analysis for Fiber Reinforced Composite Laminates," Experimental Mechanics, vol. 12, no. 6, pp. 272-277, June 1972.
- 4.8 Prabhakaran, R., "Photoelastic Investigation of Bolted Joints in Composites," Composites, vol. 13, no. 3, July 1982, pp. 253-256.
- 4.9 Rowlands, R. E., Liber, T., Daniel, I. M. and Rose, P. G., "Stress Analysis of Anisotropic Laminated Plates," AIAA Journal, vol.12, no. 7, pp. 903-908, July 1974.
- 4.10 Hung, Y. Y., Daniel, I. M. and Rowlands, R. E., "Full-Field Optical Strain Measurement Having Postrecording Sensitivity and Direction Selectivity," Experimental Mechanics, vol. 18, no. 2, pp. 56-60, February 1978.
- 4.11 Cloud, G., "Residual Surface Strain Distributions Near Holes Which are Cold Worked to Various Degrees," Technical Report, AFML-TR-78-153, Wright-Patterson AFB, Ohio, 1980.
- 4.12 Paleebut, Somnuek, An Experimental Study of Three-Dimensional Strain Around Cold Worked Holes and in Thick Compact Tension Specimens, Ph. D. Thesis, Michigan State University, Department of Metallurgy, Mechanics and Materials Science, 1982.
- 4.13 Cloud, G, Radke, R. and Peiffer, J. "Moire Gratings for High Temperatures and Long Times," Experimental Mechanics, vol. 19 no. 10, pp. 19N-21N, October 1979.
- 4.14 Cloud, G. "Measurements of Strain Fields Near Cold Worked Holes", Experimental Mechanics, vol. 20 no. 1, pp. 9-16, January 1980.
- 4.15 Cloud, G. and Herrera, P. "Experimental Study of Mechanically Fastened Composites," Proceedings of the Tenth Canadian Congress of Applied Mechanics, The University of Western Ontario, Ontario, Canada, June, 1985.

List of References (continued)

- 4.16 Cloud, G. L., "Simple Optical Processing of Moire Grating Photographs," *Experimental Mechanics*, vol. 20, no. 8, August 1980.
- 4.17 "Moire Analysis of Strain" by A. J. Durelli and V. J. Parks, Published by Prentice-Hall, Inc. Englewood Cliffs, New Jersey, 1970.
- 4.18 Horgan, C. O., "Saint-Venant End Effects in Composites," *J. Composite Materials*, vol. 16, Sept. 1982, p. 411.
- 4.19 Collings, T. A., "The Strength of Bolted Joints in Multi-Directional CFRP Laminates," *Composites*, vol. 8, no. 1, January 1977, pp.43-55.
- 4.20 Basehore, M. L. and Post, D. "High Frequency, High Reflectance Transferable Moire Gratings," *Experimental Techniques*, vol. 8, no. 5, May 1984, pp. 29-31.
- 4.21 Hornbeck, Robert W., "Numerical Methods," Prentice-Hall, Inc., Englewood Cliffs, New Jersey 07632. 1975.

- 5.1 Hyer, M W. and Liu, D H., " Photoelastic Determination of Stresses in Multiple-Pin Connectors," *Experimental Mechanics*, vol. 23, no. 3, September 1983, pp. 249-296.
- 5.2 Herrera-Franco, P.J. A Study of Mechanically Fastened Composites Using High Sensitivity Interferometric Moire Technique Ph.D. Thesis, Michigan State University, Department of Metallurgy, Mechanics, and Materials Science, 1985.
- 5.3 Lekhnitskii, S.G., "Theory of Elasticity of an Anisotropic Body," Mir Publishers, Moscow, chapter 4, p. 186.
- 5.4 Herrera-Franco, P.J. and Cloud, G.L., " Strain-Relief Inserts for Composite Fasteners," Advanced Composites Conference, American Society for Metals, Dearborn, Michigan, December 1985.

- 6.1 Herrera, P.J. , A Study of Mechanically Fastened Composite Using High Sensitivity Interferometric Moire Technique, Ph.D. Dissertation, Michigan State University, MMM-department, E. Lansing, MI, 1985.

List of References (continued)

- 6.2 Matthews, F.L., Wong, C.M., and Chryssafitis, S., "Stress Distribution Around a Single Bolt in Fibre-Reinforced Plastic," Composites, July 1982, p. 316.
- 6.3 Pradhan, B., and Ray, K., "Stresses Around Partial Contact Pin Loaded Holes in FRP Composite Plates," J. Reinforced Plastics and Composites, vol. 3, p. 69-84, January 1984.
- 6.4 Chang, F., Scott, R.A., and Springer, G.S., "Failure of Composite Laminates Containing Pin Loaded Holes - Method of Solution," Journal of Composite Materials, vol. 18, May 1984.
- 6.5 Zhang, K., and Ueng, C.E.S., "Stresses Around a Pin-Loaded Hole in Orthotropic Plates," Journal of Composite Materials, vol. 18, September 1984.
- 6.6 Chang, K., Scott, R.A., and Springer, G.S., "Design of Composite Laminates Containing Pin Loaded Holes," Journal of Composite Materials, vol. 18, May 1984.
- 6.7 DeJong, T., "Stresses Around Pin-Loaded Holes in Elastically Orthotropic or Isotropic Plates," Journal of Composite Materials, vol. 11, March 1977.
- 6.8 Frocht, M.M., and Hill, H.N., "Stress Concentration Factors Around a Central Circular Hole in a Plate Loaded Through Pin in the Hole," presented at the Annual Meeting of The American Society of Mechanical Engineers, Philadelphia, Pa., December 1939,
- 6.9 Norwood, L.S., and Millman, A.F., "Strain Limited Design Criteria for Reinforced Plastic Process Equipment," Composites, January 1980, p. 39.
- 6.10 Cole, R.T., Bateh, E.J., and Potter, J., "Fasteners for Composite Structures," Composites, July 1982, p. 233.
- 6.11 Prabhakaran, R., "Photoelastic Investigation of Bolted Joints in Composites," Composites, July 1982, p. 253.
- 6.12 Matthews, F.L., Roshan, A.A., and Phillips, L.N., "The Bolt Bearing Strength of Glass/Carbon Hybrid Composites," Composites, July 1982, p. 225.
- 6.13 Soni, S.R., "A Comparative Study of Failure Envelopes in Composite Laminates," J. Reinforced Plastic and Composites, vol. 2, p. 34-40. January 1983.

List of References (continued)

- 6.14 Daniel, I.M., Rowlands, R.E., and Whiteside, J.B., "Deformation and Failure of Boron-Epoxy Plate With Circular Hole," *Joining of Composite Materials*, ASTM STP 749, American Society for Testing and Materials, 1981, pp. 143.
- 6.15 Oplinger, D.W. , "On the Structural Behavior of Mechanically Fastened Joints in Composite Structures," Fibrous Composites in Structural Design, Plenum Press, New York, 1980, p. 575-602.
- 6.16 Kulkarni, H., and Beardmore, P., "Design Methodology for Automotive Components Using Continuous Fibre-Reinforced Composite Materials," *Composites*, October 1980, p. 225.
- 6.17 Stockdale, J.H., and Matthews, F.L. , "The Effect of Clamping Pressure on Bolt Bearing Loads in Glass Fibre-Reinforced Plastics," *Composites*, January 1976, p. 34.
- 6.18 Collins, T.A., "The Strength of Bolted Joints in Multi-Directional CFRP Laminates," *Composites*, January 1977, p. 43.
- 6.19 Crews, J.H. , "Bolt Bearing Fatigue of a Graphite/Epoxy Laminate," *Joining of Composite Materials*, ASTM STP 749, American Society for Testing and Materials, 1981, p. 131.
- 6.20 Rufolo, A., "Design Manual for Joining of Glass Reinforced Plastics," US Naval Material Laboratory Report, Navship 250-634-1 August 1961.
- 6.21 Bayer, M.H., Cloud, G.L., "Moire to 1370° C," Proc. Spring 1986 Meeting of Soc. Exp. Mech., New Orleans, June 1986.
- 6.22 Godwin, E.W., and Matthews, F.L., "A review of the Strength of Joints in Fibre-Reinforced Plastics," *Composites*, July 1980, p. 155.
- 6.23 Godwin, E.W., Matthews, F.L., and Kilty, P.F., "Strength of Multi-Bolt Joints in GRP," *Composites*, July 1982, p.268.
- 6.24 Collings, T.A. , "On the Bearing Strength of CFRP Laminates," *Composites*, July 1982, p. 241.
- 6.25 Hyer, M.W., and Lightfoot, "Ultimate Strength of High-Load-Capacity Composite Bolted Joints," *Joining of Composite Materials*, ASTM STP 749, American Society for Testing and Materials, 1981, p. 118.

List of References (continued)

- 6.26 Soni, S.R., "Failure Analysis of Composite Laminates with a Fastener Hole," Joining of Composite Materials, ASTM STP 749, American Society for Testing and Materials, 1981, p. 145.
- 6.27 Whitney, J.M., and Nuismer, R.J., "Stress Fracture Criteria for Laminated Composites Containing Stress Concentrations," Journal of Composite Materials, Vol. 8, July 1974, p. 253.
- 7.1 Herrera-Franco, P.J., A Study of Mechanically Fastened composite Using High Sensitivity Interferometric Moire Technique, Ph.D. Dissertation, Michigan State University, E. Lansing, MI 48824, 1985.
- 7.2 Herrera-Franco, P.J., Cloud, G.L., "Strain-Relief Inserts for Composite Fasteners," Proc. American Soc. for Metals - Eng. Soc. Detroit Advanced Composites Conf., Dearborn, MI, Dec. 1985.
- D.1 "Diffraction Grating Handbook", Prepared by the Staff of the Bausch & Lomb Diffraction Grating Laboratory, Erwin G. Loewen, Director, 1970.
- D.2 Guild, G., Interference System of Crossed Diffraction Gratings, Clarendon Press, Oxford, 1956.
- D.3 Stroke, G. W., "Diffraction Gratings," Handbuck der Physik, Vol. 29, Springer, 1966.
- D.4 James, J. F. and Sternberg, R. S., "The Design of Optical Spectrometers," CHAPMAN AND HALL, LTD., 11 New Fetter, London EC4, 1969.
- D.5 Czarnek, R. and Post, D., "Moire Interferometry with ± 45 -Deg. Gratings," Experimental Mechanics, vol. 24, no. 1, March, 1984, pp. 68-74.
- D.6 Introduction to the Mechanics of a Continuous Medium, Malvern, L.E., Published by Prentice-Hall, Inc. Englewood Cliffs, New Jersey, 1969.
- D.7 Cloud, G. L., "Simple Optical Processing of Moire Grating Photographs," Experimental Mechanics, vol. 20, no. 8, August 1980.

List of References (continued)

- D.8 Basehore, M. L. and Post, D., "Moire Method for In-plane and Out-of-plane Displacement Measurements," *Experimental Mechanics*, vol. 21, no. 9, pp. 321-328, September 1981.
- D.9 Walker, C. A. and McKelvie, J. "A Practical Multiplied Moire System," *Experimental Mechanics*, vol. 8, no. 8, pp. 316-320, August 1978.
- D.10 Weissman, E. M. and Post, D., "Full-field Displacement and Strain Rosettes by Moire Interferometry," *Experimental Mechanics*, vol. 22, no. 9, pp. 324-328, September 1982.

This page left blank intentionally

APPENDIX A

Mathematical Expressions of Green's Functions

This page left blank intentionally

APPENDIX A

Mathematical Expressions of Green's Function

The Green's function H_{ijk} and U_{ik} has the following form for all relations of material constant:

$$\begin{aligned}H_{xxx} &= E_{11} T_1 + E_{12} T_2 \\H_{xxy} &= E_{21} T_3 + E_{22} T_4 \\H_{yyx} &= E_{31} T_1 + E_{32} T_2 \\H_{yyy} &= E_{41} T_3 + E_{42} T_4 \\H_{xyx} &= E_{51} T_3 + E_{52} T_4 \\H_{xyy} &= E_{61} T_1 + E_{62} T_2\end{aligned}\tag{A-1}$$

$$\begin{aligned}U_{xx} &= D_{11} T_7 + D_{12} T_8 \\U_{xy} &= D_{22} T_6 \\U_{yx} &= D_{32} T_6 \\U_{yy} &= D_{41} T_7 + D_{42} T_8\end{aligned}\tag{A-2}$$

The constants E_{ij} and D_{ij} have the following form for all relations of material constants.

$$\begin{aligned}E_{11} &= -(d_1 + d_3 - d_4)/(4\pi d_5) \\E_{12} &= -(d_1 - d_3 - d_4)/(4\pi d_6) \\E_{21} &= d_4/(4\pi) \\E_{22} &= -(2d_2 - d_1 d_4)/(4\pi d_5 d_6) \\E_{31} &= (1 + d_4/d_3)/(4\pi d_5) \\E_{32} &= (1 - d_4/d_3)/(4\pi d_6) \\E_{41} &= -1/4\pi \\E_{42} &= (d_1 - 2d_4)/(4\pi d_5 d_6) \\E_{51} &= E_{41} \\E_{52} &= -E_{42} \\E_{61} &= -d_3 E_{31} \\E_{62} &= d_3 E_{32}\end{aligned}\tag{A-3}$$

$$\begin{aligned}
D_{11} &= C_{11} E_{11} + C_{12} E_{31} \\
D_{12} &= C_{11} E_{11} + C_{12} E_{32} \\
D_{22} &= -(C_{11} E_{22} + C_{12} E_{42}) \\
D_{32} &= D_{22} \\
D_{41} &= d_3 D_{11} \\
D_{42} &= d_3 D_{12}
\end{aligned}
\tag{A-4}$$

where:

$$\begin{aligned}
d_1 &= 2(C_{12} + C_{33})/C_{11} \\
d_2 &= C_{22}/C_{11} \\
d_3 &= \sqrt{d_2} \\
d_4 &= C_{12}/C_{11}
\end{aligned}
\tag{A-5}$$

The constants d_5 and d_6 as well as some of the T 's in Eq. (A-1) change with the relationship between the material constants. Before defining them we define the following:

$$\begin{aligned}
r_x &= x(Q) - x(P) \\
r_y &= y(Q) - y(P)
\end{aligned}
\tag{A-6}$$

Where Q and P are field and source points as defined in Eq. 2. Following are the definitions of the remaining quantities for each kind of material:

CASE I: $(d_1/2)^2 > d_2$:

$$d_5 = \lambda_1 + \lambda_2 \tag{A-7a}$$

$$d_6 = \lambda_1 - \lambda_2 \tag{A-7b}$$

where $\lambda_{1,2}$ are defined by Eq. (12)

APPENDIX A (Continued)

$$\text{Let } r_1^2 = r_x^2 + \lambda_1^2 r_y^2 \quad (\text{A-8})$$

$$r_2^2 = r_x^2 + \lambda_2^2 r_y^2$$

$$T_1 = \frac{r_x}{r_1^2} + \frac{r_x}{r_2^2} \quad (\text{A-9a})$$

$$T_2 = \frac{r_x}{r_1^2} - \frac{r_x}{r_2^2} \quad (\text{A-9b})$$

$$T_3 = \frac{\lambda_1 r_y}{r_1^2} + \frac{\lambda_2 r_y}{r_2^2} \quad (\text{A-9c})$$

$$T_4 = \frac{\lambda_1 r_y}{r_1^2} - \frac{\lambda_2 r_y}{r_2^2} \quad (\text{A-9d})$$

$$T_6 = \tan^{-1} \left(\frac{\lambda_1 r_y}{r_x} \right) - \tan^{-1} \left(\frac{\lambda_2 r_y}{r_x} \right) \quad (\text{A-10a})$$

$$T_7 = \log r_1 + \log r_2 \quad (\text{A-10b})$$

$$T_8 = \log r_1 - \log r_2 \quad (\text{A-10c})$$

CASE II: $(d_1/2)^2 = d_2$: For this case $\lambda_1 = \lambda_2 = 0$ where is defined by Eq. (13)

$$d_5 = \lambda_1 + \lambda_2 = 2 \quad (\text{A-11a})$$

$$d_6 = 1 \quad (\text{A-11b})$$

$$T_1 = \frac{2r_x}{r_1^2} \quad (\text{A-12a})$$

$$T_2 = \frac{-2\lambda_1 r_x r_y^2}{r_1^4} \quad (\text{A-12b})$$

$$T_3 = \frac{2\lambda_1 r_y}{r_1^2} \quad (\text{A-12c})$$

$$T_4 = \frac{r_x^2 r_y - \lambda_1^2 r_y^3}{r_1^4} \quad (\text{A-12d})$$

APPENDIX A (Continued)

$$T_6 = \frac{r_x r_y}{r_1^2} \quad (A-13a)$$

$$T_7 = 2 \log r_1 \quad (A-13b)$$

$$T_8 = \frac{r_y^2}{r_1^2} \quad (A-13c)$$

Note that the terms T_1 , T_3 , and T_7 in Eqs. (A-12) and (A-13) would be obtained from Eqs. (A-9) and (A-10) if we substitute $\lambda_1 = \lambda_2$. But the same is not true for terms T_2 , T_4 , T_6 , and T_8 .

CASE III: $(d_1/2)^2 < d_2$: For this case, λ_1 and λ_2 are complex quantities.

$$d_5 = 2\lambda \cos \delta \quad (A-14a)$$

$$d_6 = 2\lambda \sin \delta$$

where λ and δ are defined in Eq. (14). Define:

$$\begin{aligned} r_x(\delta) &= r_x - (\lambda \sin \delta) r_y \\ r_y(\delta) &= \lambda \cos \delta r_y \end{aligned} \quad (A-15)$$

$$r^2(\delta) = r_x^2(\delta) + r_y^2(\delta)$$

$$T_1 = \frac{r_x(\delta)}{r^2(\delta)} + \frac{r_x(-\delta)}{r^2(-\delta)} \quad (A-16a)$$

$$T_2 = -\frac{r_y(\delta)}{r^2(\delta)} + \frac{r_y(-\delta)}{r^2(-\delta)} \quad (A-16b)$$

$$T_3 = \frac{r_y(\delta)}{r^2(\delta)} + \frac{r_y(-\delta)}{r^2(-\delta)} \quad (A-16c)$$

$$T_4 = \frac{r_x(\delta)}{r^2(\delta)} - \frac{r_x(-\delta)}{r^2(-\delta)} \quad (A-16d)$$

APPENDIX A (Continued)

$$T_6 = \log r(\delta) - \log r(-\delta) \quad (A-17a)$$

$$T_7 = \log r(\delta) + \log r(-\delta) \quad (A-17b)$$

$$T_8 = \tan^{-1} \frac{r_y(\delta)}{r_x(\delta)} - \tan^{-1} \frac{r_y(\delta)}{r_x(\delta)} \quad (A-17c)$$

Note the similarity of form for the terms in Eqs. (A-16) and (A-17) to those in Eqs. (A-9) and (A-10).

This page left blank intentionally

APPENDIX B

Analytical Expressions of Integrals and Singularities

This page left blank intentionally

B.1 Analytical Expressions of Integrals of Terms in the Green's Function

The functions M_{ijk} and N_{ik} in Eq. (11) are integrals of the Green's function. Since the E_{ij} and D_{ij} in the Green's functions are constants (see Eq. (A-1) and (A-2)) we need to develop expressions only for the integrals of $T_1, T_2, T_3, T_4, T_6, T_7$, and T_8 .

Let the length of the n th segment be L (see Figure B-1) and the angle which this segment makes with the x -axis be θ . Point A is the midpoint of the line segment with coordinates (\bar{x}, \bar{y}) . For all values of λ_k and δ_k ($k=1,2$) defined in Eqs. (6), (7), and (8), we define the following quantities

$$\begin{aligned} H_k^2 &= (\cos^2 \theta + \lambda_k^2 \sin^2 \theta + 2\lambda_k \sin \delta_k \sin \theta \cos \theta) \\ \cos \lambda_k &= (\cos \theta + \lambda_k \sin \delta_k \sin \theta) / H_k \\ \sin \gamma_k &= (\lambda_k \cos \delta_k \sin \theta) / H_k \end{aligned} \quad (B-1)$$

$$\begin{aligned} C_k &= \{[(x-\bar{x}) + \lambda_k \sin \delta_k (y-\bar{y})] \cos \gamma_k + (y-\bar{y}) \lambda_k \cos \delta_k \sin \gamma_k\} / H_k \\ D_k &= -\{[(x-\bar{x}) + \lambda_k \sin \delta_k (y-\bar{y})] \sin \gamma_k + (y-\bar{y}) \lambda_k \cos \delta_k \cos \gamma_k\} / H_k \end{aligned} \quad (B-2)$$

$$(R_k)_{n+1}^2 = \left(\frac{L}{2} - C_k\right)^2 + D_k^2 \quad (B-3)$$

$$\begin{aligned} (R_k)_n^2 &= \left(\frac{L}{2} - C_k\right)^2 + D_k^2 \\ (\beta_k)_{n+1} &= \tan^{-1} \left(\frac{\left(\frac{L}{2} + C_k\right)}{D_k} \right) \end{aligned} \quad (B-4)$$

$$(\beta_k)_n = \tan^{-1} \left(\frac{-\left(\frac{L}{2} + C_k\right)}{D_k} \right)$$

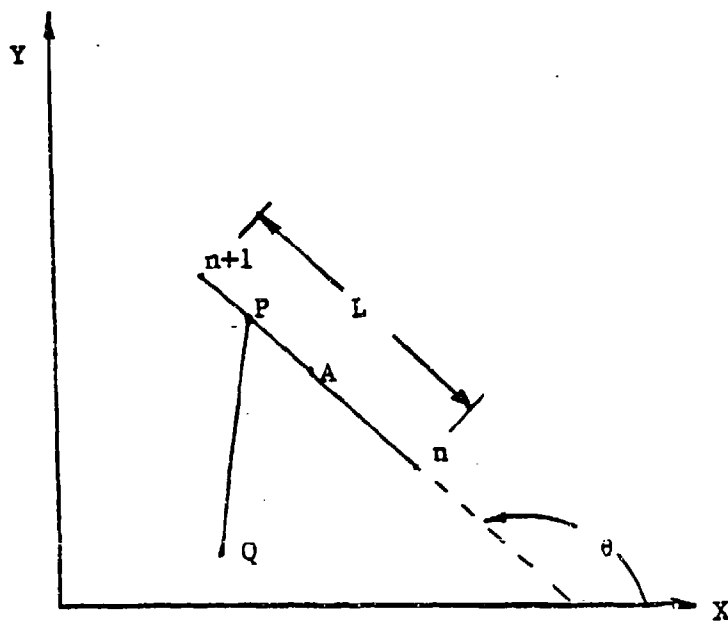


Figure B-1. Geometry of a Line Segment

APPENDIX B (Continued)

$$\Delta L_k = \log((R_k)_{n+1}/(R_k)_n) \quad (B-5)$$

$$\Delta \beta_k = (\beta_k)_{n+1} - (\beta_k)_n$$

$$J_k^{(0)} = -(\cos \gamma_k \Delta L_k + \sin \gamma_k \Delta \beta_k)/H_k \quad (B-6)$$

$$K_k^{(0)} = -(\sin \gamma_k \Delta L_k - \cos \gamma_k \Delta \beta_k)/H_k$$

$$J_k^{(1)} = -L \cos \gamma_k/H_k + C_k J_k^{(0)} + D_k K_k^{(0)} \quad (B-7)$$

$$K_k^{(1)} = -L \sin \gamma_k/H_k + C_k K_k^{(0)} - D_k J_k^{(0)}$$

For equations (B-8) through (B-10), $k = 1$

$$A_k = D_k(L/2 - C_k)/(R_k)_{n+1} + D_k(L/2 + C_k)/(R_k)_n^2 \quad (B-8)$$

$$B_k = D_k^2/(R_k)_{n+1}^2 - D_k^2/(R_k)_n^2$$

$$J_3^{(0)} = (\cos 2\gamma_k J_k^{(0)} - \sin 2\gamma_k K_k^{(0)}) + 2(A_k \sin 3\gamma_k - B_k \cos 3\gamma_k) \quad (B-9)$$

$$K_3^{(0)} = (\sin 2\gamma_k J_k^{(0)} - \cos 2\gamma_k K_k^{(0)}) - 2(A_k \cos 3\gamma_k + B_k \sin 3\gamma_k)$$

$$J_3^{(1)} = -L \cos 3\gamma_k/H_k + 2 D_k(\sin 2\gamma_k J_k^{(0)} + \cos 2\gamma_k K_k^{(0)}) + C_k J_3^{(0)} + D_k K_3^{(0)} \quad (B-10)$$

$$K_3^{(1)} = -L \sin 3\gamma_k/H_k - 2 D_k(\cos 2\gamma_k J_k^{(0)} - \sin 2\gamma_k K_k^{(0)}) - D_k J_3^{(0)} + C_k K_3^{(0)}$$

$$J_k^{(2)} = C_k J_k^{(1)} + D_k K_k^{(1)} \quad (B-11)$$

$$K_k^{(2)} = -D_k J_k^{(1)} + C_k K_k^{(1)}$$

APPENDIX B (Continued)

$$\begin{aligned}
 IL_k^{(0)} &= \frac{L}{2} [\log (H_k R_k)_{n+1} + \log (H_k R_k)_n] \\
 &\quad + H_k (\cos \gamma_k J_k^{(1)} + \sin \gamma_k K_k^{(1)})
 \end{aligned}
 \tag{B-12}$$

$$\begin{aligned}
 IT_k^{(0)} &= -\frac{L}{2} [(\beta_k + \gamma_k)_{n+1} + (\beta_k + \gamma_k)_n] \\
 &\quad + H_k (-\sin \gamma_k J_k^{(1)} + \cos \gamma_k K_k^{(1)})
 \end{aligned}$$

$$IL_k^{(1)} = \frac{L^2}{8} \Delta L_k + \frac{H_k}{2} (\cos \gamma_k J_k^{(2)} + \sin \gamma_k K_k^{(2)})
 \tag{B-13}$$

$$IT_k^{(1)} = -\frac{L^2}{8} \Delta \beta_k + \frac{H_k}{2} (-\sin \gamma_k J_k^{(2)} + \cos \gamma_k K_k^{(2)})$$

$$J_4^{(0)} = L \cos 2\gamma_k - 2H_k D_k (\sin \gamma_k J_k^{(0)} + \cos \gamma_k K_k^{(0)})
 \tag{B-14}$$

$$K_4^{(0)} = L \sin 2\gamma_k + 2H_k D_k (\cos \gamma_k J_k^{(0)} - \sin \gamma_k K_k^{(0)})$$

$$J_4^{(1)} = -2H_k D_k (\sin \gamma_k J_k^{(1)} + \cos \gamma_k K_k^{(1)})
 \tag{B-15}$$

$$K_4^{(1)} = -2H_k D_k (\cos \gamma_k J_k^{(1)} - \sin \gamma_k K_k^{(1)})$$

$$I_j^{(q)} = \int_{S_n}^{S_{n+1}} (s - s_n)^q T_j \quad q = 0, 1
 \tag{B-16}$$

The function $I_j^{(q)}$ is now defined for the various relations of material constants.

APPENDIX B (Continued)

CASE I:

$$I_1^{(q)} = J_1^{(q)} + J_2^{(q)}$$

$$I_2^{(q)} = J_1^{(q)} - J_2^{(q)}$$

$$I_3^{(q)} = K_1^{(q)} + K_2^{(q)}$$

$$I_4^{(q)} = K_1^{(q)} - K_2^{(q)}$$

$$I_6^{(q)} = -IT_1^{(q)} + IT_2^{(q)}$$

$$I_7^{(q)} = IL_1^{(q)} + IL_2^{(q)}$$

$$I_8^{(q)} = IL_1^{(q)} - IL_2^{(q)}$$

(B-17)

CASE II:

$$I_1^{(q)} = 2 J_1^{(q)}$$

$$I_2^{(q)} = (J_3^{(q)} - J_1^{(q)})/2\lambda_1$$

$$I_3^{(q)} = 2 K_1^{(q)}$$

$$I_4^{(q)} = (K_3^{(q)} - K_1^{(q)})/2\lambda_1$$

(B-18)

$$I_6^{(q)} = K_4^{(q)}/2\lambda_1$$

$$I_7^{(q)} = 2 IL_1^{(q)}$$

$$I_8^{(q)} = -J_4^{(q)}/2\lambda_1$$

CASE III:

$$I_1^{(q)} = J_1^{(q)} + J_2^{(q)}$$

$$I_2^{(q)} = K_1^{(q)} - K_2^{(q)}$$

$$I_3^{(q)} = K_1^{(q)} + K_2^{(q)}$$

$$I_4^{(q)} = -J_1^{(q)} + J_2^{(q)}$$

$$I_6^{(q)} = -IL_1^{(q)} + IL_2^{(q)} \quad (B-19)$$

$$I_7^{(q)} = IL_1^{(q)} + IL_2^{(q)}$$

$$I_8^{(q)} = -IT_1^{(q)} + IT_2^{(q)}$$

B.1.1 Evaluation of Singularity

The Green's function $H_{ijk}(Q,P)$ is singular when Q and P coincide. This happens if stresses are to be evaluated on the boundary, for example when we try to satisfy the boundary conditions of Eq. (4). The usual approach in BEM is to extract the singularity analytically and evaluate the integral in the Cauchy's principle sense. This paper takes a different approach. Since we have analytical expressions, we can use them to give the correct value of the singularity. This is accomplished by choosing the point Q on the boundary as a midpoint of a small segment of length 2ϵ . That is, in Figure B-1, Q and A are one and the same point. Thus $L_n = \epsilon$ and from Eq. (B-2), we have $C_k = 0$, $D_k = 0$, $(R_k)_{n+1} = (R_k)_n = \epsilon$, and $(\beta_k)_{n+1} = -(\beta_k)_n = \pi/2$. The computer code also calculates these values and when they are substituted in the formula, we obtain the correct value of singularity contribution.

APPENDIX C

BEM Computer Program

This page left blank intentionally

APPENDIX C

```
C*****
C    THE PROGRAM SOLVES FOR STRESSES AND DISPLACEMENTS IN PLANE ORTHO-
C    TROPIC MATERIALS. FOR ANY QUESTIONS REGARDING THE PROGRAM CONTACT
C    DR. MADHUKAR VABLE
C    MECHANICAL ENGINEERING AND
C    ENGINEERING MECHANICS,
C    MICHIGAN TECHNOLOGICAL UNIVERSITY,
C    HOUGHTON, MICHIGAN 49931
C    TELEPHONE: (906)-487-2551
C
C    THE PROGRAM READS INPUT DATA FROM UNIT 2 IN SUBROUTINE INPUT. ON
C    UNIT 6 OUTPUT IS WRITTEN IN TABULAR FORM. ON UNIT 4 OUTPUT IS
C    WRITTEN IN A FORMATED FORM, SO THAT IT CAN BE USED FOR ANY POST
C    PROCESSING.
C*****
C    COMMON/AREA1/CORD(800,2),PMAT(5,5),NCAB(150,50,2),BP(150,2),RC(800
C    1),ADF(150,2),TBC(150),NM(150),RCB(150),LEOB(4),NCA(100),MB(150),M1
C    2(100)
C    COMMON/AREA2/NLOAD,NS,NPWE,IPLANE,NN,NOB,NMAT
C    COMMON/AREA3/LENTH(800),SN(800),CT(800)
C    COMMON/AINV/FTMMB(300,300),NR(300),NC(300),XN(300)
C    INTEGER ADF,TBC,RC,RCB,BN
C    DIMENSION FTMMS(3,300),XM(2),CS(6,2,5),CD(6,2,5),P(300,5),DISP(100
C    1,2,5),SIG(100,3,5),U(300,5)
C    REAL LENTH,MAT(5,5),MU
C    CALL INPUT(NBC,P)
C    NEC2=NBC+NBC
C    NS2=NS+NS
C
C    DEFINING THE CONSTANTS OF GREEN'S FUNCTION
C
C    DO 10 I=1,NMAT
C    CALL CONST(CS(1,1,I),MAT(1,I),PMAT(1,I))
C    CALL DISCON(CS(1,1,I),PMAT(1,I),CD(1,1,I))
10  CONTINUE
C
C    TRANSFORMING POLAR TO CARTESIAN COORDINATES
C
C    CALL POLAR(CORD,RC,NN,800)
C    CALL POLAR(BP,RCB,NBC,150)
C
C    DEFINING DIRECTION COSINES OF EACH LINE SEGMENT.
C
C    BN=1
C    N=0
C    DO 40 I=1,NS
C    IF(I.GT.LEOB(BN)) BN=BN+1
C    N1=NM(I)
C    DO 30 J=1,N1
C    N=N+1
C    P1=NCAB(I,J,1)
C    P2=NCAB(I,J,2)
```

```

      DUM=CORD(K2,1)-CORD(K1,1)
      DEN=CORD(K2,2)-CORD(K1,2)
      AL=SQRT(DUM*DUM+DEN*DEN)
      LENTH(N)=AL
      SN(N)=DEN/AL
      CT(N)=DUM/AL
30  CONTINUE
40  CONTINUE

C
C   CALCULATING THE QUANTITIES NEEDED FOR IMPROVING THE CONDITION
C   OF THE MATRIX IN ALGEBRAIC EQUATIONS. THESE QUANTITIES ARE ONLY
C   DEPENDENT UPON THE GEOMETRY.
C
      CALL RIGID(NBC,XCENTO,YCENTO)

C
C   TRANSLATING THE ORIGIN OF THE COORDINATE SYSTEM TO THE CENTROID
C   OF THE BOUNDARY.
C
      CALL TRANS(CORD,XCENTO,YCENTO,NN,800)
      CALL TRANS(BP,XCENTO,YCENTO,NBC,150)

C
C   CALCULATING THE MATRIX IN ALGEBRAIC EQUATIONS FROM THE GIVEN
C   BOUNDARY CONDITIONS.
C
      CALL INTIAL(FTMMB,300,300)
      NLOAD=NLOAD+1
      DO 285 IROW=1,NBC
        XM(1)=BP(IROW,1)
        XM(2)=BP(IROW,2)
        ITBC=TBC(IROW)
        NROW=IROW+IROW-2

C
C   CALCULATING THE DIRECTION COSINES OF UNIT NORMAL
C
      CALL DIRCOS(DCOSX,DCOSY,IROW,MII)
      MSTO=MII
      IF(MII.GT.10) MII=MII/10
      NTIME=2
      IF(ITBC.LT.0) GO TO 200
      IF(ITBC.GE.22) ITBC=ITBC-22
      IF(ITBC.EQ.0) GO TO 260

C
C   CONSTRUCTING THE RIGHT HAND SIDE VECTOR FOR PURE DISPLACEMENT
C   TEST CASE
C
      XMC=XM(1)+XCENTO
      YMC=XM(2)+YCENTO
      F(NROW+1,NLOAD)=(FMAT(1,MII)+FMAT(2,MII))*XMC+FMAT(4,MII)*YMC
      F(NROW+2,NLOAD)=(FMAT(2,MII)+FMAT(3,MII))*YMC+FMAT(4,MII)*XMC
      NTIME=1
200  CONTINUE
      ITBC=ABS(ITBC)

C
C   ASSEMBLING THE ROW IN THE MATRIX FOR DISPLACEMENT BOUNDARY
C   CONDITIONS
C
      DO 255 K=1,NTIME
        CALL ASMB(XM,CD(1,1,MII),MAT(1,MII),FTMMS,NBC2,2,MII)

```

```

C
C   TRANSFORMING TO NORMAL AND TANGENTIAL COORDINATES
C
    IF(TBC(IROW).LT.22) GO TO 240
    CALL NORTAN(FTMMS,NBC2,DCOSX,DCOSY)
    DUM=P(NROW+1,NLOAD)
    P(NROW+1,NLOAD)=DCOSX*DUM+DCOSY*P(NROW+2,NLOAD)
    P(NROW+2,NLOAD)=-DCOSY*DUM+DCOSX*P(NROW+2,NLOAD)
    IF(NTIME.EQ.2) MII=MSTO-10*MII
240  CONTINUE
    DO 250 J=1,NBC2
    DO 250 L=1,2
    FTMMS(NROW+L,J)=FTMMS(L,J)-FTMMB(NROW+L,J)
250  CONTINUE
    IF(NTIME.EQ.2) MII=MSTO-10*MII
255  CONTINUE
    IF(ITBC.EQ.11) GO TO 285

C
C   CALCULATING THE ROW FOR TRACTION BOUNDARY CONDITIONS
C
260  CONTINUE
    CALL ASMB(XM,CS(1,1,MI),MAT(1,MI),FTMMS,NBC2,3,MI)
    NROW=NROW+1
    DO 265 J=1,NBC2
    FTMMS(1,J)=FTMMS(1,J)*DCOSX+FTMMS(3,J)*DCOSY
    FTMMS(2,J)=FTMMS(3,J)*DCOSX+FTMMS(2,J)*DCOSY
265  CONTINUE

C
C   CONSTRUCTING THE RIGHT HAND SIDE VECTOR FOR TESTING TRACTION
C   BOUNDARY CONDITIONS
C
    XM(1)=DCOSX+DCOSY
    XM(2)=DCOSX-DCOSY

C
C   TRANSFORMING TO NORMAL AND TANGENTIAL COORDINATES
C
    IF(TBC(IROW).LT.22) GO TO 266
    CALL NORTAN(FTMMS,NBC2,DCOSX,DCOSY)
    XM(1)=XM(1)*XM(1)
    XM(2)=XM(2)*(DCOSX-DCOSY)
266  CONTINUE

C
C   IMPOSING MIXED BOUNDARY CONDITIONS
C
    IF(ITBC.NE.1) P(NROW,NLOAD)=XM(1)
    IF(ITBC.NE.10) P(NROW+1,NLOAD)=XM(2)-FMAT(5,1)*XM(1)
    DO 275 J=1,NBC2
    IF(ITBC.NE.1) FTMMS(NROW,J)=FTMMS(1,J)
    IF(ITBC.NE.10) FTMMS(NROW+1,J)=FTMMS(1,J)-FMAT(5,1)*FTMMS(1,J)
275  CONTINUE
285  CONTINUE

C
C   IMPROVING THE CONDITION OF THE MATRIX
C
    DO 300 I=1,NBC
    IR=I+I-2
    DO 300 L=1,2
    IR=IR+1

```

```

COMP=0.
DO 287 J=1,NBC2
DUM=ABS(FTMMB(IR,J))
IF(DUM.LT.COMP) GO TO 287
COMP=DUM
IC=J
287 CONTINUE
DO 290 J=1,NBC2
FTMMS(1,J)=FTMMB(IR,J)
290 CONTINUE
LX=1
IF((IC/2)*2.EQ.IC) LX=2
CALL MODIFY(NBC,FTMMS,IC,LX)
DO 295 J=1,NBC2
FTMMB(IR,J)=FTMMS(1,J)
295 CONTINUE
300
C
C CALCULATING THE INVERSE OF THE MATRIX AND THE CONDITION NUMBER
C
CALL NORM(COND,NBC2)
CALL MATINV(NBC2,DET)
CALL NORM(DUM,NBC2)
COND=COND*DUM
C
C CALCULATING THE UNKNOWN TRACTIONS
C
DO 330 IL=1,NLOAD
DO 320 I=1,NBC2
SUM=0.0
DO 310 J=1,NBC2
IF(ABS(P(J,IL)).LE.1.0E-07) GO TO 310
SUM=SUM+FTMMB(I,J)*P(J,IL)
310 CONTINUE
320 U(I,IL)=SUM
330 CONTINUE
C
C CALCULATING THE STRESSES AND DISPLACEMENTS
C
DO 480 IROW=1,NPWSE
K1=NCA(IROW)
MII=MI(IROW)
XM(1)=CORD(K1,1)
XM(2)=CORD(K1,2)
CALL ASMB(XM,CS(1,1,MII),MAT(1,MII),FTMMS,NBC2,3,MII)
CALL QUANTY(SIG,3,IROW,FTMMS,U,NLOAD,NBC)
CALL ASMB(XM,CD(1,1,MII),MAT(1,MII),FTMMS,NBC2,2,MII)
CALL QUANTY(DISP,2,IROW,FTMMS,U,NLOAD,NBC)
480 CONTINUE
C
C PRINTING THE OUTPUT
C
WRITE(6,1010) COND
DO 490 IL=1,NLOAD
CALL OUTELS(IL,SIG(1,1,IL),U(1,IL),NBC,DISP(1,1,IL),XCENTO,YCENTO)
490 CONTINUE
C
C CALCULATING THE ERROR IN THE TEST CASE
C

```

```

CALL ERRCHE(SIG(1,1,NLOAD),NPWSE,XCENTO,YCENTO)
1010 FORMAT(/10X,22HCONDITION OF MATRIX = ,E11.4)
STOP
END
SUBROUTINE QUANTY(QUANT,NQI,IR,FTMMS,U,NLOAD,NBC)
DIMENSION QUANT(100,NQI,5),FTMMS(3,300),U(300,5)
REAL*8 SUM
NBC2=NBC+NBC
DO 30 IL=1,NLOAD
DO 20 I1=1,NQI
SUM=0.
DO 10 J=1,NBC2
SUM=SUM+FTMMS(I1,J)*U(J,IL)
10 CONTINUE
QUANT(IR,I1,IL)=SUM
20 CONTINUE
30 CONTINUE
RETURN
END
SUBROUTINE MATRIX(I,J,BN,S1S2,SM1,S2,A,FTMMS,N,IN)
C
C THIS SUBROUTINE EVALUATES THE EQ.(2-38) OF THESIS
C A(I1,I2,I3) I1=1,2,3 REFERS TO TXX,TTY,TXY
C I2=1,2 REFERS TO X,Y (LOAD SUBSCRIPT)
C I3=1,2 REFERS TO FIRST AND SECOND INTEGRALS
C
COMMON/AREA1/CORD(800,2),PMAT(5,5),NCAB(150,50,2),BF(150,2),RC(800
1),ADF(150,2),TBC(150),NM(150),RCB(150),LEOB(4),NCA(100),NB(150),MI
2(100)
COMMON/AREA2/NLOAD,NS,NPWSE,IPLANE,NN,NOB,NMAT
DIMENSION S2(4),FTMMS(3,300),SM(3,2),CM(3,2,2),A(3,3,3)
INTEGER ADF,TBC,RC,RCB,BN
N1=NM(I)
IF(J.GT.1) GO TO 15
DO 10 I1=1,3
DO 10 I2=1,2
SM(I1,I2)=0.
DO 10 I3=1,2
10 CM(I1,I2,I3)=0.
15 CONTINUE
C
C ASSEMBLY OF MATRIX MULTIPLYING CONSTANTS IN LINEAR REPRESENTATION
C
390 L=ADF(I,1)
IF(L.EQ.0) GO TO 410
NCOL=L+L-2
DO 400 I2=1,2
NCOL=NCOL+1
DO 400 I1=1,IN
SM(I1,I2)=SM(I1,I2)+A(I1,I2,1)
CM(I1,I2,1)=CM(I1,I2,1)+(-S1S2+SM1)*A(I1,I2,1)-A(I1,I2,2)
IF(J.EQ.N1) FTMMS(I1,NCOL)=FTMMS(I1,NCOL)+CM(I1,I2,1)/(S2(BN)-SM1)
1+SM(I1,I2)
400 CONTINUE
410 L=ADF(I,2)
IF(L.EQ.0) GO TO 430
NCOL=L+L-2

```

```

DO 420 I2=1,2
NCOL=NCOL+1
DO 420 I1=1,IN
CM(I1,I2,2)=CM(I1,I2,2)+(S1S2-SM1)*A(I1,I2,1)+A(I1,I2,2)
IF(J.EQ.N1) FTMMS(I1,NCOL)=FTMMS(I1,NCOL)+CM(I1,I2,2)/(S2(BN)-SM1)
420 CONTINUE
430 CONTINUE
RETURN
END
SUBROUTINE INTIAL(A,M,N)
DIMENSION A(M,N)
DO 10 I=1,M
DO 10 J=1,N
10 A(I,J)=0.
RETURN
END
SUBROUTINE POLAR(CORD,RC,NN,MDIM)
DIMENSION CORD(MDIM,2),RC(MDIM)
INTEGER RC
DO 10 I=1,NN
IF(RC(I).EQ.0) GO TO 10
DUM=CORD(I,2)*1.7453293E-02
CORD(I,2)=CORD(I,1)*SIN(DUM)
CORD(I,1)=CORD(I,1)*COS(DUM)
10 CONTINUE
RETURN
END
SUBROUTINE DIRCOS(DCOSX,DCOSY,IROW,MII)
COMMON/AREA1/CORD(800,2),PMAT(5,5),NCAB(150,50,2),BP(150,2),RC(800)
1),ADF(150,2),TBC(150),NM(150),RCB(150),LEOB(4),NCA(100),MB(150),MI
2(100)
COMMON/AREA2/NLOAD,NS,NPWSE,IFLANE,NN,NOB,NMAT
COMMON/AREA3/LENTH(800),SN(800),CT(800)
INTEGER ADF,TBC,RC,RCB,BN
REAL LENTH
N=0
DO 20 I=1,NS
N1=NM(I)
DO 20 J=1,N1
N=N+1
IS=1
IC=1
DO 10 L=1,2
K1=NCAB(I,J,L)
DX=BP(IROW,1)-CORD(K1,1)
DY=BP(IROW,2)-CORD(K1,2)
IF(DX.LT.0.) IS=-IS
IF(DY.LT.0.) IC=-IC
IF(ABS(DX).LT.1.0E-07) IS=-1
IF(ABS(DY).LT.1.0E-07) IC=-1
10 CONTINUE
IF(IS.LT.0.AND.IC.LT.0) GO TO 30
20 CONTINUE
WRITE(6,1000) IROW,BP(IROW,1),BP(IROW,2)
1000 FORMAT(/ /46X,17HTHE POINT NUMBER ,I3,22HIS NOT ON THE BOUNDARY//52
1X,14HX-COORDINATE =,F13.4/52X,14HY-COORDINATE =,F13.4)
STOP
30 DCOSX=SN(N)

```



```

DCOSY=-CT(N)
MII=MB(I)
RETURN
END
SUBROUTINE ASMB(XM,CS,MAT,FTMMS,NBC2,IQ,MII)
COMMON/AREA1/CORD(800,2),PMAT(5,5),NCAB(150,50,2),BF(150,2),RC(800
1),ADF(150,2),TBC(150),NM(150),RCB(150),LEOB(4),NCA(100),MB(150),MI
2(100)
COMMON/AREA2/NLOAD,NS,NPWSE,IFLANE,NN,NOB,NMAT
COMMON/AREA3/LENTH(800),SN(800),CT(800)
INTEGER ADF,TBC,RC,RCB,BN
REAL LENTH,MAT(5)
DIMENSION S2(4),FTMMS(3,300),CS(6,2),A(3,3,3),XM(2)
DO 290 K=1,NOB
290 S2(K)=0.
CALL INTIAL(FTMMS,3,300)
N=0
BN=1
DO 440 I=1,NS
IF(I.GT.LEOB(BN)) BN=BN+1
SM1=S2(BN)
N1=NM(I)
MBI=MB(I)
ISIG=1
IF(MBI.LT.10) GO TO 300
MBI=MBI/10
IF(MBI.EQ.MII) GO TO 310
ISIG=-1
MBI=MB(I)-10*MBI
300 CONTINUE
IF(MBI.NE.MII) GO TO 440
310 CONTINUE
DO 430 J=1,N1
N=N+1
CALL MMFT(I,J,N,CS,MAT,XM,A,IQ)
IF(IQ.EQ.2) CALL DISP(CS,MAT,N,A)
S1S2=S2(BN)+0.5*LENTH(N)
S2(BN)=S2(BN)+LENTH(N)
IF(ISIG.GT.0) GO TO 330
DO 320 I1=1,IQ
DO 320 I2=1,2
DO 320 I3=1,2
320 A(I1,I2,I3)=-A(I1,I2,I3)
330 CONTINUE
CALL MATRIX(I,J,BN,S1S2,SM1,S2,A,FTMMS,N,IQ)
430 CONTINUE
440 CONTINUE
RETURN
END
SUBROUTINE RIGID(NBC,XCENTO,YCENTO)
INTEGER BN,RC,RCB,ADF,TBC
COMMON/AREA1/CORD(800,2),PMAT(5,5),NCAB(150,50,2),BF(150,2),RC(800
1),ADF(150,2),TBC(150),NM(150),RCB(150),LEOB(4),NCA(100),MB(150),MI
2(100)
COMMON/AREA2/NLOAD,NS,NPWSE,IFLANE,NN,NOB,NMAT
COMMON/AREA3/LENTH(800),SN(800),CT(800)
REAL LENTH
COMMON/AREAR/RIG(3,300)

```

```

REAL*8 SUM
DIMENSION A(3,3,3),S2(4),SUM(10)
BN=1
NBC2=NBC+NBC
N=0
DO 5 K=1,N0B
5 S2(K)=0.
DO 10 I=1,10
10 SUM(I)=0.
CALL INTIAL(RIG,3,300)
DO 60 I=1,NS
IF(I.GT.LEOB(BN)) BN=BN+1
SM1=S2(BN)
N1=NM(I)
DO 50 J=1,N1
N=N+1
L1=NCAB(I,J,1)
L2=NCAB(I,J,2)
S1S2=S2(BN)+0.5*LENTH(N)
S2(BN)=S2(BN)+LENTH(N)
DC=LENTH(N)*(CORD(L1,1)+CORD(L2,1))*0.5
DS=LENTH(N)*(CORD(L1,2)+CORD(L2,2))*0.5
DUM=LENTH(N)**3/12.
SUM(1)=SUM(1)+DC
SUM(2)=SUM(2)+DS
A(1,1,1)=LENTH(N)
A(1,1,2)=0.
A(1,2,1)=LENTH(N)
A(1,2,2)=0.
A(2,1,1)=DS
A(2,2,1)=-DC
A(2,1,2)=DUM*SN(N)
A(2,2,2)=-DUM*CT(N)
CALL MATRIX(I,J,BN,S1S2,SM1,S2,A,RIG,N,2)
50 CONTINUE
60 CONTINUE
ST=0.
DO 65 K=1,N0B
65 ST=ST+S2(K)
XCENTO=SUM(1)/ST
YCENTO=SUM(2)/ST
DO 70 J=1,NBC
NCOL=J+J-1
RIG(2,NCOL)=RIG(2,NCOL)-YCENTO*RIG(1,NCOL)
RIG(2,NCOL+1)=RIG(2,NCOL+1)+XCENTO*RIG(1,NCOL+1)
70 CONTINUE
DO 90 I=1,NBC
IC=I+I-2
DO 80 K=1,2
IC=IC+1
SUM(4+K)=SUM(4+K)+RIG(1,IC)*RIG(1,IC)
SUM(6+K)=SUM(6+K)+RIG(2,IC)*RIG(2,IC)
80 CONTINUE
90 CONTINUE
SUM(5)=SORT(SUM(5))
SUM(6)=SORT(SUM(6))
DEN=SUM(7)+SUM(8)
SUM(1)=0.

```

```

SUM(2)=0.
DO 110 I=1,NBC
IC=I+I-2
DO 100 K=1,2
IC=IC+1
RIG(2,IC)=RIG(2,IC)/DEN
SUM(2+K)=SUM(2+K)+RIG(2,IC)
RIG(1,IC)=RIG(1,IC)/SUM(4+K)
SUM(K)=SUM(K)+RIG(1,IC)
SUM(8+K)=SUM(8+K)+RIG(1,IC)*RIG(2,IC)
100 CONTINUE
110 CONTINUE
SUM(5)=1.
SUM(6)=1.
DEN=SUM(7)+SUM(8)
SUM(7)=SUM(7)/DEN
SUM(8)=SUM(8)/DEN
DO 120 K=1,10
120 RIG(3,K)=SUM(K)
RETURN
END
SUBROUTINE MODIFY(N,FIG,IC,L)
DIMENSION S(10),FIG(3,300),ALFA(2)
COMMON/AREAR/RIG(3,300)
REAL*8 SUM(6)
LM=3-L
S(L)=RIG(3,L)-RIG(1,IC)
S(LM)=RIG(3,LM)
S(2+L)=RIG(3,2+L)-RIG(2,IC)
S(2+LM)=RIG(3,2+LM)
S(4+L)=RIG(3,4+L)-RIG(1,IC)*RIG(1,IC)
S(4+LM)=RIG(3,4+LM)
S(6+L)=RIG(3,6+L)-RIG(2,IC)*RIG(2,IC)
S(6+LM)=RIG(3,6+LM)
S(8+L)=RIG(3,8+L)-RIG(1,IC)*RIG(2,IC)
S(8+LM)=RIG(3,8+LM)
DO 10 K=1,6
10 SUM(K)=0.
DO 30 I=1,N
ICOL=I+I-2
DO 20 K=1,2
ICOL=ICOL+1
IF(ICOL.EQ.IC) GO TO 20
SUM(K)=SUM(K)+FIG(1,ICOL)
SUM(K+2)=SUM(K+2)+RIG(1,ICOL)*FIG(1,ICOL)
SUM(K+4)=SUM(K+4)+RIG(2,ICOL)*FIG(1,ICOL)
20 CONTINUE
30 CONTINUE
AX=-SUM(L)/S(L)
AY=-SUM(LM)/S(LM)
DMX=-S(2+L)/S(L)
DMY=-S(2+LM)/S(LM)
DEN=DMX*(S(4+L)+S(8+L)+S(8+L))+DMY*(S(4+LM)+S(8+LM)+S(8+LM))+S(6+
1L)+S(6+LM)
DUM=DMX*SUM(2+L)+DMY*SUM(2+LM)+SUM(4+L)+SUM(4+LM)+AX*(DMX*S(4+L)+
1S(8+L))+AY*(DMY*S(4+LM)+S(8+LM))
BETA=-DUM/DEN
ALFA(L)=AX+BETA*DMX

```

```

ALFA(LM)=AY+BETA*DMY
DO 50 I=1,N
ICOL=I+I-2
DO 40 K=1,2
ICOL=ICOL+1
FIG(1,ICOL)=FIG(1,ICOL)+BETA*RIG(2,ICOL)
IF (ABS(ALFA(K)).GT.1.0E-06) FIG(1,ICOL)=FIG(1,ICOL)+ALFA(K)*RIG(1
1,ICOL)
40 CONTINUE
50 CONTINUE
60 CONTINUE
RETURN
END
SUBROUTINE TRANS(CORD,XC,YC,N,MDIM)
DIMENSION CORD(MDIM,2)
DO 10 I=1,N
CORD(I,1)=CORD(I,1)-XC
CORD(I,2)=CORD(I,2)-YC
10 CONTINUE
RETURN
END
SUBROUTINE DISCON(C,FMAT,CD)
DIMENSION FMAT(5),C(6,2),CD(6,2)
CD(1,1)=FMAT(1)*C(1,1)+FMAT(2)*C(3,1)
CD(1,2)=FMAT(1)*C(1,2)+FMAT(2)*C(3,2)
CD(2,2)=-FMAT(1)*C(2,2)-FMAT(2)*C(4,2)
CD(3,2)=CD(2,2)
DUM=SQRT(FMAT(3)/FMAT(1))
CD(4,1)=DUM*CD(1,1)
CD(4,2)=-DUM*CD(1,2)
RETURN
END
SUBROUTINE DISP(CD,MAT,N,A)
REAL JK,KK,IL,IT,JY,KY,MAT,LENTH,JK2,KK2
COMMON/AREA1/AL2,CK(2),DK(2),H(2),CGH(2),SGH(2),JK(2,2),KK(2,2),BE
ITA1(2),BETA2(2),ALN1(2),ALN2(2)
COMMON/AREA3/LENTH(800),SN(800),CT(800)
DIMENSION JY(2),KY(2),A(3,3,3),CD(6,2),IL(2,2),IT(2,2),MAT(5)
IM=MAT(1)
DELGAM=0.
IF(IM) 10,30,20
10 C2=CT(N)*CT(N)
S2=1-C2
DUM=MAT(2)*MAT(4)*S2/(C2+(MAT(2)-MAT(4))*(MAT(2)+MAT(4))*S2)
DELGAM=ATAN(DUM+DUM)
GO TO 30
20 C2=CT(N)*CT(N)
S2=1-C2
DUM=(MAT(3)-MAT(2))*CT(N)*SN(N)/(C2+MAT(2)*MAT(3)*S2)
DELGAM=ATAN(DUM)
30 CONTINUE
L=1
40 H2=H(L)*H(L)
IL(L,1)=AL2*(ALN2(L)+ALN1(L)+ALOG(H2))+H2*(CGH(L)*JK(L,2)+SGH(L)*K
1K(L,2))
DUM=AL2*AL2
JK2=CK(L)*JK(L,2)+DK(L)*KK(L,2)
KK2=-DK(L)*JK(L,2)+CK(L)*KK(L,2)

```

```

      IL(L,2)=0.5*(DUM*(ALN2(L)-ALN1(L))+H2*(CGH(L)*JK2+SGH(L)*KK2))
      IF(IM.EQ.0) GO TO 50
      IT(L,1)=-AL2*(BETA2(L)+BETA1(L))+H2*(-SGH(L)*JK(L,1)+CGH(L)*KK(L,1))
50      IT(L,2)=0.5*(-DUM*(BETA2(L)-BETA1(L))+H2*(-SGH(L)*JK2+CGH(L)*KK2))
      IF(L.EQ.2) GO TO 60
      L=2
      GO TO 40
      CG2=CGH(1)*CGH(1)
      CG2=CG2+CG2-1./H2
      SG2=SGH(1)*CGH(1)
      SG2=SG2+SG2
      DUM=H2*DK(1)
      DUM=DUM+DUM
      DUM2=H2*LENTH(N)
      JY(1)=DUM2*CG2-DUM*(JK(1,1)*SGH(1)+CGH(1)*KK(1,1))
      KY(1)=DUM2*SG2-DUM*(JK(1,1)*CGH(1)-SGH(1)*KK(1,1))
      JY(2)=-DUM*(JK(1,2)*SGH(1)+KK(1,2)*CGH(1))
      KY(2)=-DUM*(KK(1,2)*SGH(1)-JK(1,2)*CGH(1))
60      CONTINUE
      DO 110 L=1,2
      IF(IM) 70,80,90
70      DUM1=IL(1,L)-IL(2,L)
      DUM2=IL(1,L)+IL(2,L)
      DUM3=IT(1,L)-IT(2,L)
      IF(L.EQ.1) DUM3=DUM3+LENTH(N)*DELGAM
      GO TO 100
80      CONTINUE
      DUM1=KY(L)
      DUM2=IL(1,L)+IL(1,L)
      DUM3=-JY(L)
      GO TO 100
90      CONTINUE
      DUM1=IT(2,L)-IT(1,L)
      IF(L.EQ.1) DUM1=DUM1-LENTH(N)*DELGAM
      DUM2=IL(1,L)+IL(2,L)
      DUM3=IL(1,L)-IL(2,L)
100      CONTINUE
      A(1,1,L)=CD(1,1)*DUM2+CD(1,2)*DUM3
      A(1,2,L)=CD(2,2)*DUM1
      A(2,1,L)=CD(3,2)*DUM1
      A(2,2,L)=CD(4,1)*DUM2+CD(4,2)*DUM3
110      CONTINUE
      RETURN
      END
      SUBROUTINE MMFT(I,J,N,C,MAT,X,A,IND)
      COMMON/AREA1/CORD(800,2),PMAT(5,5),NCAB(150,50,2),BP(150,2),RC(800
1) ,ADF(150,2),TBC(150),NM(150),RCB(150),LEOB(4),NCA(100),MB(150),MI
2(100)
      COMMON/AREA3/LENTH(800),SN(800),CT(800)
      COMMON/AREA1/AL2,CK(2),DK(2),H(2),CGH(2),SGH(2),JK(2,2),KK(2,2),BE
1TA1(2),BETA2(2),ALN1(2),ALN2(2)
      REAL LENTH,JK,KK,MAT(5)
      INTEGER ADF,TBC,RC,RCB
      DIMENSION A(3,3,3),C(6,2),X(2)
      DATA PIA2/1.570796327/
      IM=MAT(1)
      K1=NCAB(I,J,1)

```

```

K2=NCAB(I,J,2)
RX=X(1)-0.5*(CORD(K1,1)+CORD(K2,1))
RY=X(2)-0.5*(CORD(K1,2)+CORD(K2,2))
AL2=0.5*LENTH(N)
L=1
10 CONTINUE
DUM1=CT(N)
IF(IM.LT.0) DUM1=CT(N)+MAT(3+L)*SN(N)
DUM2=MAT(1+L)*SN(N)
H(L)=SQRT(DUM1*DUM1+DUM2*DUM2)
CG=DUM1/H(L)
SG=DUM2/H(L)
DUM3=RX
IF(IM.LT.0) DUM3=RX+RY*MAT(3+L)
DUM4=RY*MAT(1+L)
CGH(L)=CG/H(L)
SGH(L)=SG/H(L)
CK(L)=DUM3*CGH(L)+DUM4*SGH(L)
DK(L)=-DUM3*SGH(L)+DUM4*CGH(L)
DKS=DK(L)*DK(L)
CK1=(AL2+CK(L))
CK2=AL2-CK(L)
RK1=CK1*CK1+DKS
RK2=CK2*CK2+DKS
IF(RK1.EQ.0.0.OR.RK2.EQ.0.) GO TO 100
ALN1(L)=0.5*ALOG(RK1)
ALN2(L)=0.5*ALOG(RK2)
ALN=ALN2(L)-ALN1(L)
IF(ABS(DK(L)).GT.1.0E-04) GO TO 20
BETA1(L)=PIA2
BETA2(L)=PIA2
IF(CK1.EQ.0.) BETA1(L)=-BETA1(L)
IF(CK2.EQ.0.) BETA2(L)=-BETA2(L)
GO TO 30
20 BETA1(L)=ATAN(CK1/DK(L))
BETA2(L)=ATAN(CK2/DK(L))
30 DBETA=BETA2(L)-BETA1(L)
JK(L,1)=-CGH(L)*ALN+SGH(L)*DBETA
KK(L,1)=-SGH(L)*ALN-CGH(L)*DBETA
JK(L,2)=-LENTH(N)*CGH(L)+CK(L)*JK(L,1)+DK(L)*KK(L,1)
KK(L,2)=-LENTH(N)*SGH(L)-DK(L)*JK(L,1)+CK(L)*KK(L,1)
IF(L.EQ.2) GO TO 40
L=2
IF(IM.NE.0) GO TO 10
C2=CG*CG
S2=CG*SG
C2=C2+C2-1
S2=S2+S2
C3=CG*(C2+C2-1)/H(1)
S3=SG*(C2+C2+1)/H(1)
DUM1=C2*JK(1,1)-S2*KK(1,1)
DUM2=S2*JK(1,1)+C2*KK(1,1)
DK2=DK(1)+DK(1)
DUM3=CK2/RK2-CK1/RK1
DUM4=DK(1)/RK2-DK(1)/RK1
JK(2,1)=DUM1+DK2*(-C3*DUM4+S3*DUM3)
KK(2,1)=DUM2-DK2*(C3*DUM3+S3*DUM4)
JK(2,2)=-LENTH(N)*C3+DK2*DUM2+CK(1)*JK(2,1)+DK(1)*KK(2,1)

```

```

40 KK(2,2)=-LENTH(N)*S3-DK2*DUM1+CK(1)*KK(2,1)-DK(1)*JK(2,1)
CONTINUE
IF(IND.EQ.2) RETURN
DO 90 L=1,2
IF(IM) 50,60,70
50 CONTINUE
DUM1=JK(1,L)+JK(2,L)
DUM2=KK(1,L)-KK(2,L)
DUM3=KK(1,L)+KK(2,L)
DUM4=JK(2,L)-JK(1,L)
GO TO 80
60 CONTINUE
DUM1=JK(1,L)+JK(1,L)
DUM2=JK(2,L)-JK(1,L)
DUM3=KK(1,L)+KK(1,L)
DUM4=KK(2,L)-KK(1,L)
GO TO 80
70 CONTINUE
DUM1=JK(1,L)+JK(2,L)
DUM2=JK(1,L)-JK(2,L)
DUM3=KK(1,L)+KK(2,L)
DUM4=KK(1,L)-KK(2,L)
80 CONTINUE
A(1,1,L)=C(1,1)*DUM1+C(1,2)*DUM2
A(1,2,L)=C(2,1)*DUM3+C(2,2)*DUM4
A(2,1,L)=C(3,1)*DUM1+C(3,2)*DUM2
A(2,2,L)=C(4,1)*DUM3+C(4,2)*DUM4
A(3,1,L)=C(5,1)*DUM3+C(5,2)*DUM4
A(3,2,L)=C(6,1)*DUM1+C(6,2)*DUM2
90 CONTINUE
RETURN
100 WRITE(6,1000) I,J,X(1),X(2)
1000 FORMAT(3X,'RADIAL DISTANCE IS ZERO'/3X,'I=',I3,' J=',I3,' X1=',F
110.4,' X2=',F10.4)
STOP
END
SUBROUTINE INPUT(NBC,P)

```

```

C
C THIS SUBROUTINE READS THE DATA NEEDED FOR EVALUATING THE
C LINE(BOUNDARY) INTEGRAL.
C
COMMON/AREA1/CORD(800,2),PMAT(5,5),NCAB(150,50,2),BP(150,2),RC(800
1),ADF(150,2),TBC(150),NM(150),RCB(150),LEOB(4),NCA(100),MB(150),MI
2(100)
COMMON/AREA2/NLOAD,NS,NPWSE,IFLANE,NN,NOB,NMAT
COMMON/TITLE/TITLO(20)
DIMENSION P(300,5)
INTEGER ADF,TBC,RC,RCB
C
C
C TITLO - A TITLE OF LESS THAN 80 LETTERS WHICH WILL BE PRINTED
C ON THE OUTPUT.
C
C NN - NUMBER OF NODES.NODES ON THE BOUNDARY DEFINING THE
C STRAIGHT LINE SEGMENT+POINTS WHERE STRESSES ARE EVALUATED
C NOB - NUMBER OF BOUNDRIES(CLOSED).
C NS - NUMBER OF SEGMENTS OVER WHICH THE FICTITIOUS TRACTION
C IS ASSUMED TO VARY LINEARLY.

```

NMAT NUMBER OF MATERIALS IN THE PROBLEM. HAS ONLY BEEN DEBUGED
 FOR ONE MATERIAL
 NPWSE - NUMBER OF POINTS WHERE THE STRESSES ARE EVALUATED.
 LEOB(K) - LAST ELEMENT ON THE K'TH BOUNDARY OVER WHICH THE
 FICTITIOUS TRACTION IS ASSUMED TO VARY LINEARLY. WHEN
 NOB=1 THEN LEOB(1)=NS.
 NLOAD - NUMBER OF LOAD CASES FOR WHICH THE PROBLEM IS SOLVED.
 IWRITE - 0/1 IS THE INPUT DATA TO BE PRINTED OUT?(Y/N).

 FMAT(L) - MATERIAL PROPERTIES. L=1 C11 ; L=2 C12; L=3 C22; L=4 C44
 L=5 COEFFICIENT OF FRICTION.

 RC(L) - 0/1 ARE THE COORDINATES OF THE L'TH NODE POLAR.(N/Y)
 CORD(L,1) - X OR R COORDINATE.
 CORD(L,2) - Y OR THETA COORDINATE.

 NM(I) - NUMBER OF SUBDIVISION OF THE I'TH BOUNDARY DIVISION.

 NCAB(I,K,L) - NODE CONNECTION ARRAY OF THE STRAIGHT LINE SEGMENT.
 I=I'TH BOUNDARY DIVISION. J=J'TH SUBDIVISION. L=1,2
 ARE THE NODE NUMBERS OF THE STRAIGHT LINE SEGMENT
 TRANSVERSED IN POSITIVE INTEGRATION SENCE.

 ADF(I,L) - ADDITIONAL DEGREE OF FREEDOM NUMBER OF THE L'TH NODE
 ON THE I'TH BOUNDARY DIVISION.

 RCB(I) - 0/1 ARE THE COORDINATES OF THE I'TH NODE WHERE
 THE BOUNDARY CONDITIONS ARE SATISFIED POLAR.(N/Y)
 BP(I,1) - X OR R COORDINATE
 BP(I,2) - Y OR THETA COORDINATE.

 NCA(I) - NODE NUMBER OF THE POINT WHERE THE STRESSES ARE EVALUATED
 TBC(I) - TYPE OF BOUNDARY CONDITION OF THE I'TH NODE.=YX
 X,Y=0 TRACTION IN CARTESIAN COORDINATES
 X,Y=1 DISPLACEMENT IN CARTESIAN COORDINATES
 X,Y=2 TRACTION IN NORMAL AND TANGENTIAL COORDINATE SYSTEM
 X,Y=3 DISPLACEMENT IN NORMAL AND TANGENTIAL COORDINATE
 X,Y=-11 CONTINUITY CONDITION ON INTERFACE BOUNDARY

```

DO 5 I=1,100
  NCA(I)=0
  READ(2,3000) (TITLO(I),I=1,20)
  READ(2,1000) NN,NOB,NS,IPLANE,NMAT,NPWSE,(LEOB(K),K=1,NOB),NLOAD
1 IWRITE
  READ(2,1010) ((FMAT(L,J),L=1,5),J=1,NMAT)
  NS2=NS+NS
  READ(2,1020) (L,RC(L),CORD(L,1),CORD(L,2),I=1,NN)
  READ(2,1000) (NM(I),I=1,NS)
  DO 10 I=1,NS
    N2=(NM(I)/4)*4
    IF(N2.NE.NM(I)) N2=N2+4
10 READ(2,1000) (NCAB(I,K,1),NCAB(I,K,2),K=1,N2)
  READ(2,1000) (L,MB(L),ADF(L,1),ADF(L,2),I=1,NS)
  NBC=0
  DO 60 I=1,NS
    IF(ADF(I,1).GT.NBC) NBC=ADF(I,1)
    IF(ADF(I,2).GT.NBC) NBC=ADF(I,2)
  60

```



```

60 CONTINUE
  READ(2,1040) (I,TBC(I),RCB(I),SF(I,1),BP(I,2),L=1,NBC)
  N1=(NPWSE/20)*20
  IF(N1.LT.NPWSE) N1=N1+20
  READ(2,1000) (NCA(I),MI(I),I=1,NPWSE)
  DO 20 L=1,NLOAD
    READ(2,1030) (I,P(I+I-1,L),P(I+I,L),J=1,NBC)
20  CONTINUE
    WRITE(6,2000) NN,NS,NPWSE,IPLANE,ILOAD,NLOAD,NOB
    DO 25 J=1,NMAT
25  WRITE(6,2005) J,(L,PMAT(L,J),L=1,5)
    IF(IWRITE.NE.0) RETURN
    DO 30 K=1,NOB
      WRITE(6,2010) K,LEOB(K)
30  CONTINUE
      WRITE(6,2020) (L,RC(L),CORD(L,1),CORD(L,2),L=1,NN)
      WRITE(6,2025)
      WRITE(6,2030)
      DO 40 I=1,NS
        N2=(NM(I)/4)*4
        IF(N2.NE.NM(I)) N2=N2+4
40  WRITE(6,2040) I,NM(I),(K,NCAB(I,K,1),NCAB(I,K,2),K=1,N2)
      WRITE(6,2045)
      WRITE(6,2046) (I,ADF(I,1),ADF(I,2),I=1,NS)
      WRITE(6,2047)
      WRITE(6,2050) (I,BP(I,1),BP(I,2),RCB(I),I=1,NBC)
      WRITE(6,2055)
      WRITE(6,2060) (NCA(I),I=1,N1)
      WRITE(6,2065)
      RETURN
1000 FORMAT(20I4)
1010 FORMAT(5F10.4)
1020 FORMAT(3(I4,I2,2F10.4))
1040 FORMAT(3I5,2F10.4)
1050 FORMAT(2(I5,2E12.4))
2000 FORMAT(/61X,10HINPUT DATA/61X,10(1H-)/23X,25HNN =NUMBER OF
1 NODES,54X,1H=,I5/23X,25HNS =NUMBER OF SEGMENTS,54X,1H=,I5/23X,
249HNPWSE =NUMBER OF POINTS WHERE STRESS IS EVALUATED,30X,1H=,I5/23
3X,25HIPLANE=PLANE STRESS CASE?,54X,1H=,I5/16X,39H ILOAD =STA
6RTING LOAD CASE NUMBER,47X,1H=,I5/23X,44HNLOAD =NUMBER OF LOAD CAS
7ES TO BE SOLVED FOR,35X,1H=,I5/23X,27HNOB =NUMBER OF BOUNDARIES,
852X,1H=,I5)
2005 FORMAT(23X,8HMATERIAL,I3/(23X,5HFMAT(,I1,1H),72X,1H=,F10.4))
2010 FORMAT(/23X,32HLEOB =LAST ELEMENT ON BOUNDARY-,I1,46X,1H=,I5)
2020 FORMAT(/56X,20HCOORDINATES OF NODES/2X,128(1H-)/2X,2H:!,3(42H NO
1E ! RADIAL? ! COORDINATE !!)/2X,2H:!,3(42H NO. ! NO=
20 ! X-1 ! X-2 !!)/2X,128(1H-)/(2X,2H:!,3(I5,2H !,I5,4
3X,1H!,F10.4,2H !,F10.4,3H !!)))
2025 FORMAT(2X,128(1H-))
2030 FORMAT(/50X,33HNODE CONNECTION ARRAY ON BOUNDARY//5X,121(1H-)/5X,
117H:!! SEG. ! SUB- !!,4(26H DIV !! NODE-1 ! NODE-2 !!)/5X,17H:!! NO.
2 ! DIV. !!,4(26H NO. !! ! !!)/5X,121(1H-))
2040 FORMAT(5X,2H:!,I4,2X,1H!,I4,2X,2H:!,4(I3,2X,2H:!,2(I6,2X,1H!),1H!)
1/(5X,2H:!,6X,1H!,6X,2H:!,4(I3,2X,2H:!,I6,2X,1H!,I6,2X,2H:!!)))
2045 FORMAT(8X,117(1H-))
2046 FORMAT(/52X,27HPIECEWISE LINEAR CONNECTION/52X,27(1H-)/44X,44(1H-
1)/44X,44H:!! SEG.NO. ! ADDITIONAL DEGREE OF FREEDOM ! /44X,44H:!!
2 ! LEFT NODE ! RIGHT NODE !!/44X,44(1H-)/(44X,2H:!,I6,3

```

```

      3X,1H!,5X,I3,6X,1H!,6X,I3,6X,2H!)))
2047 FORMAT(44X,44(1H-))
2050 FORMAT(/45X,42HPPOINTS WHERE BOUNDARY CONDITION IS IMPOSED,/45X,42(
11H-)//44X,45(1H-)/44X,43H!! POINT          COORDINATE      !  RADIAL
2?  !/44X,45H!!          !          X-1      !          X-2      !  NO=0      !/44X,45(1
3H-)/(44X,2H! !,I5,2X,1H!,F10.4,2H !,F10.4,2H !,I5,4X,2H! !))
2055 FORMAT(44X,45(1H-))
2060 FORMAT(48X,38HNODE NUMBERS WHERE STRESS IS EVALUATED/5X,123(1H-)/(
15X,2H! !,20(I4,2H !),1H!))
2065 FORMAT(5X,123(1H-))
3000 FORMAT(20A4)
      END
      SUBROUTINE CONST(C,MAT,FMAT)
      REAL MAT(5)
      DIMENSION C(6,2),FMAT(5)
      DATA PIA4/12.56637061/
      DUM1=(FMAT(2)+FMAT(4))/FMAT(1)
      DUM2=FMAT(3)/FMAT(1)
      RAD=DUM1*DUM1-DUM2
      DUM3=SQRT(DUM2)
      MAT(1)=1.
      IF(ABS(RAD).LT.1.0E-03) GO TO 10
      IF(RAD.GT.0.) GO TO 20
      MAT(1)=-1.
      MAT(2)=SQRT(0.5*(DUM1+DUM3))
      MAT(3)=MAT(2)
      MAT(4)=SQRT(0.5*(DUM3-DUM1))
      MAT(5)=-MAT(4)
      GO TO 30
10    MAT(1)=0.
20    DUM4=0.
      IF(MAT(1).GT.0.) DUM4=SQRT(ABS(RAD))
      MAT(2)=SQRT(DUM1+DUM4)
      MAT(3)=SQRT(DUM1-DUM4)
      MAT(4)=0.
      MAT(5)=0.
30    CONTINUE
      DUM4=FMAT(2)/FMAT(1)
      DUM5=MAT(2)+MAT(3)
      DUM6=MAT(2)-MAT(3)
      IM=MAT(1)
      IF(IM.EQ.0) DUM6=DUM5
      IF(IM.EQ.-1) DUM6=2.*MAT(4)
      DUM1=2.*DUM1
      C(1,1)=-(DUM1+DUM3-DUM4)/DUM5
      C(1,2)=-(DUM1-DUM3-DUM4)/DUM6
      C(2,1)=DUM4
      C(2,2)=-(2.*DUM2-DUM1*DUM4)/(DUM5*DUM6)
      C(3,1)=(1.+DUM4/DUM3)/DUM5
      C(3,2)=(1.-DUM4/DUM3)/DUM6
      C(4,1)=-1.
      C(4,2)=(DUM1-2.*DUM4)/(DUM5*DUM6)
      C(5,1)=-1.
      C(5,2)=-C(4,2)
      C(6,1)=-(DUM3+DUM4)/DUM5
      C(6,2)=(DUM3-DUM4)/DUM6
      DO 40 I=1,6
      DO 40 J=1,2

```

```

C(I,J)=C(I,J)/PIA4
40 CONTINUE
RETURN
END

C
SUBROUTINE OUTELS(IL,SIG,U,NBC,DISP,XC,YC)
C THIS PROGRAM PRINTS OUTPUT FOR ELASTIC PROBLEMS.
C
COMMON/AREA1/CORD(800,2),PMAT(5,5),NCAB(150,50,2),BF(150,2),RC(800
1),ADF(150,2),TBC(150),NM(150),RCB(150),LEOB(4),NCA(100),MB(150),MI
2(100)
COMMON/AREA2/NLOAD,NS,NPWSE,IPLANE,NN,NOB,NMAT
COMMON/TITLE/TITLO(20)
DIMENSION SIG(100,3),U(100),DISP(100,2)
INTEGER ADF,RCB,RC,TBC
WRITE(6,900)
WRITE(6,900)
WRITE(6,2000) (TITLO(I),I=1,20)
WRITE(4,2000) (TITLO(I),I=1,20)
WRITE(6,1000) IL
WRITE(6,1010)
NCS=0
NC=0
L1=0
NS2=NS+NS
NBC2=NBC+NBC
WRITE(4,2005) NLOAD,NPWSE,NBC2,NMAT,((PMAT(K,J),K=1,5),J=1,NMAT)
WRITE(4,2010) (U(I),I=1,NBC2)
WRITE(6,1060)
DO 50 L=1,NBC
NCOL=L+L-1
WRITE(6,1070) L,U(NCOL),U(NCOL+1)
50 CONTINUE
55 CONTINUE
WRITE(6,1080)
DO 90 I=1,NPWSE
K=NCA(I)
SIG2=0.
SIG0=SQRT((SIG(I,1)-SIG(I,2))*2+(SIG(I,1)-SIG2)*2+(SIG(I,2)-SIG2
1)*2+6.*SIG(I,3)*SIG(I,3))/1.4142136
SIG1=(SIG(I,1)-SIG(I,2))*0.5
SIG1=SQRT(SIG1*SIG1+SIG(I,3)*SIG(I,3))
SIG2=(SIG(I,1)+SIG(I,2))*0.5-SIG1
SIG1=SIG1+(SIG(I,2)+SIG(I,1))*0.5
ANGLE=12.56637
IF(ABS(SIG(I,2)-SIG(I,1)).GT.0.0001) GO TO 60
IF(ABS(SIG(I,3)).LT.0.00001) GO TO 80
ANGLE=1.5708
IF(SIG(I,3).LT.0.) ANGLE=-ANGLE
GO TO 80
60 ANGLE=ATAN((SIG(I,3)+SIG(I,3))/SIG(I,2)-SIG(I,1))
IF(ANGLE.LT.0.) GO TO 70
IF(SIG(I,3).LT.0.) ANGLE=ANGLE+3.14159
GO TO 80
70 ANGLE=ANGLE+3.14159
IF(SIG(I,2).GT.SIG(I,1)) ANGLE=ANGLE+3.14159
80 ANGLE=ANGLE*28.64789
WRITE(6,1090) I,CORD(K,1)+XC,CORD(K,2)+YC,RC(K),(SIG(I,J),J=1,3).S

```

```

1160,SIG1,SIG2,ANGLE
WRITE(4,2020) RC(K),CORD(K,1)+XC,CORD(K,2)+YC,(SIG(I,J),J=1,3)
90 CONTINUE
WRITE(6,1100)
WRITE(6,900)
WRITE(6,3000)
DO 100 I=1,NPWE
K=NCA(I)
WRITE(6,3010) I,CORD(K,1)+XC,CORD(K,2)+YC,RC(K),(DISP(I,L),L=1,2)
100 CONTINUE
RETURN
900 FORMAT(1H1)
1000 FORMAT(1H1//37X,50HTHE ELASTIC SOLUTION IS GIVEN BELOW FOR LOAD CA
1SE=,I3/37X,53(1H-))
1010 FORMAT(/37X,60HTHE UNKNOWN CONSTAN 3 IN FICTITIOUS TRACTION ARE G
1IVEN BELOW)
1060 FORMAT(44X,46(1H-)/44X,46H\ BOUNDARY \ ADDITIONAL DEGREE OF FREED
10M \ /44X,46H\ NODE \ X-DIRECTION \ Y-DIRECTION \ /44X,4
26(1H-))
1070 FORMAT(44X,2H\,I6,4X,1H\,E13.4,3H \,E13.4,3H \)
1080 FORMAT(44X,46(1H-)/8X,117(1H-)/8X,117H\ S.N. \ COORDINATE
1 \ RADIAL? \ NORMAL \ NORMAL \ SHEAR \ EQUIVALENT \ PRINC
2IPAL \ PRINCIPAL \ ANGLE \ /8X,2H\,6X,109H\ X-1 \ X-2 \
3 NO=0 \ STRESS-X \ STRESS-Y \ STRESS-XY \ STRESS \ STRESS-1 \ S
4TRESS-2 \ \ /8X,117(1H-))
1090 FORMAT(8X,2H\,I4,2X,1H\,2(F10.4,2H\ ),I5,4X,1H\,6(F9.4,1X,1H\),F6
1.1,1X,2H\))
1100 FORMAT(8X,117(1H-))
2000 FORMAT(20A4)
2005 FORMAT(4I4,/(5F10.4))
2010 FORMAT(10F8.4)
2020 FORMAT(I3,5F8.4)
3000 FORMAT(1H1//60X,13HDISPLACEMENTS,/)
3010 FORMAT(10X,I5,2F10.4,I5,2F13.4)
END
SUBROUTINE NORM(PNORM,N)
COMMON/AINV/A(300,300),NR(300),NC(300),Y(300)
PNORM=0.
DO 40 I=1,N
DUM=0.
DO 35 J=1,N
DUM=DUM+ABS(A(I,J))
IF(DUM.GT.PNORM) PNORM=DUM
40 CONTINUE
RETURN
END
SUBROUTINE ERRCHE(SIG,NPWE,XC,YC)
DIMENSION SIG(100,3)
INTEGER RCB,RC,ADF,TBC
COMMON/AREA1/CORD(800,2),PMAT(5,5),NCAB(150,50,2),BF(150,2),RC(800
1),ADF(150,2),TBC(.50),NM(150),RCB(150),LEOB(4),NCA(100),MB(150),MI
2(100)
WRITE(6,2000)
DO 20 I=1,NPWE
K=NCA(I)
DO 10 L=1,3
SIG(I,L)=ABS(SIG(I,L)-1.)*100.
10 CONTINUE

```

```

WRITE(6,2010) I,CORD(K,1)+XC,CORD(K,2)+YC,(SIG(I,L),L=1,3)
20 CONTINUE
2000 FORMAT(1H1///10X,'PERCENTAGE DEVIATION FROM ONE IN STRESSES')
2010 FORMAT(10X,I3,2F12.4,5X,3F12.3)
RETURN
END
SUBROUTINE MATINV(N,DET)

```

```

C
C THIS SUBROUTINE INVERTS A NXN MATRIX
C
COMMON/AINV/A(300,300),NR(300),NC(300),Y(300)
DO 20 K=1,N
CALL PIVOT(IR,IC,K,N)
PMA= A(IR,IC)
NR(K)=IR
NC(K)=IC
DO 10 J=1,N
IF(J.EQ.IC) GO TO 10
A(IR,J)=A(IR,J)/A(IR,IC)
10 CONTINUE
A(IR,IC)=1./A(IR,IC)
DO 20 I=1,N
STO=A(I,IC)
IF(I.EQ.IR) GO TO 20
IF(ABS(A(I,IC)).LT.1.0E-07) GO TO 14
A(I,IC)=-A(I,IC)/PMA
14 CONTINUE
DO 15 J=1,N
IF(ABS(STO).LE.1.0E-07) GO TO 15
IF(ABS(A(IR,J)).LE.1.0E-07) GO TO 15
IF(J.NE.IC) A(I,J)=A(I,J)-STO*A(IR,J)
15 CONTINUE
20 CONTINUE
DO 30 J=1,N
DO 25 I=1,N
IR=NR(I)
IC=NC(I)
25 Y(IC)=A(IR,J)
DO 30 I=1,N
A(I,J)=Y(I)
30 CONTINUE
DO 40 I=1,N
DO 35 J=1,N
IR=NR(J)
IC=NC(J)
35 Y(IR)=A(I,IC)
DO 40 J=1,N
A(I,J)=Y(J)
40 CONTINUE
RETURN
END
SUBROUTINE PIVOT(IR,IC,K,N)

```

```

C
C THIS SUBROUTINE FINDS THE MAXIMUM PIVOT.
C
COMMON/AINV/A(300,300),NR(300),NC(300),Y(300)
COMP=0.
K1=K-1

```

```

      DO 30 I=1,N
      IF(K.EQ.1) GO TO 15
      DO 10 L=1,K1
      IF(I.EQ.NR(L)) GO TO 30
10    CONTINUE
15    CONTINUE
      DO 25 J=1,N
      IF(K.EQ.1) GO TO 16
      DO 20 L=1,K1
      IF(J.EQ.NC(L)) GO TO 25
20    CONTINUE
16    IF(ABS(A(I,J)).LE.COMP) GO TO 25
      COMP=ABS(A(I,J))
      IR=I
      IC=J
25    CONTINUE
      IF(COMP.LE.1.0E-08) GO TO 35
30    CONTINUE
      RETURN
35    WRITE(6,1000)
1000  FORMAT('//28X,'SINGULAR MATRIX FOUND DURING INVERSION OF SIMULTANE
      IOUS EQUATIONS.'/28X,'CHECK COORDINATES,NODE CONNECTION ,NODE NUMBE
      2RING.')
      WRITE(6,1001) K,(NR(I),I=1,K1),(NC(I),I=1,K1)
1001  FORMAT(20I5)
      STOP
      END
      SUBROUTINE NORTAN(A,N,DCOSX,DCOSY)
      DIMENSION A(3,300)
      DO 10 J=1,N
      DUM=A(1,J)
      A(1,J)=DUM*DCOSX+A(2,J)*DCOSY
      A(2,J)=-DUM*DCOSY+A(2,J)*DCOSX
10    CONTINUE
      RETURN
      END

```

APPENDIX D

Moire Interferometry

This page left blank intentionally

D.1. The Grating.

A key factor in Moire interferometry is the diffraction grating. When light is incident on a grating surface, it is diffracted from the grooves [D.1]. In fact, each grating groove becomes a very small, slit-shaped source of reflected or transmitted light. The usefulness of a grating depends on the fact that there exists a unique series of angles where, for a given groove spacing and wavelength, the light from all the facets is in phase. This can be visualized from the geometry shown in Figure D-1, which shows a plane wavefront incident at an angle α with respect to the grating normal, and diffracted at an angle β . The groove spacing is designated by d . It is easy to see that the geometrical path difference between light from successive grooves is simply $(d \sin \alpha - d \sin \beta)$. The principle of interference dictates that only when this difference equals the wavelength of light or a simple integral multiple thereof, then will the light from successive grooves be in phase, i.e. reinforce itself. At all other angles there will be destructive interference between the wavelets originating at the groove facets.

These relationships are expressed by equation D.3, known as the grating equation since it governs the behavior of all gratings:

$$m\lambda = d(\sin \alpha \pm \sin \beta_m) \quad D.3$$

where α is the angle of the incident rays with respect to a normal to the grating, β is the angle of diffraction with respect to the normal. The minus sign signifies that β is on the same side of the normal as α while the plus signifies that β is on the opposite side of the normal. λ is the wavelength of the incident and diffracted light, d is the grating constant or distance between successive grooves, m is the diffracted order, usually a small integer.

By convention, positive angles are measured positive counterclockwise from the grating normal. As they are limited by the grating surface and the diffraction equation, diffraction angles are in the range $-90 \leq \beta_m \leq +90$. Also by convention, the diffraction orders are numbered increasing in the counterclockwise direction, beginning with the zeroth order. For the zeroth order one has $m=0$ and $\sin \alpha = \pm \sin \beta$, which is Snell's law of reflection and defines the path of the direct or undiffracted light. In other words, the zeroth order always emerges at an angle which corresponds to the specular reflection angle and which is equal to the angle of incidence. The numbering of diffraction orders aids in following a diffraction sequence of a beam, particularly when two Moire gratings are involved.

Equation D.3 can be rearranged as:

$$\sin \beta_m = m\lambda f + \sin \alpha \quad D.4$$

where we can omit the \pm sign according to the convention mentioned above and $f=1/d$ is the grating frequency. Interest will be centered in the

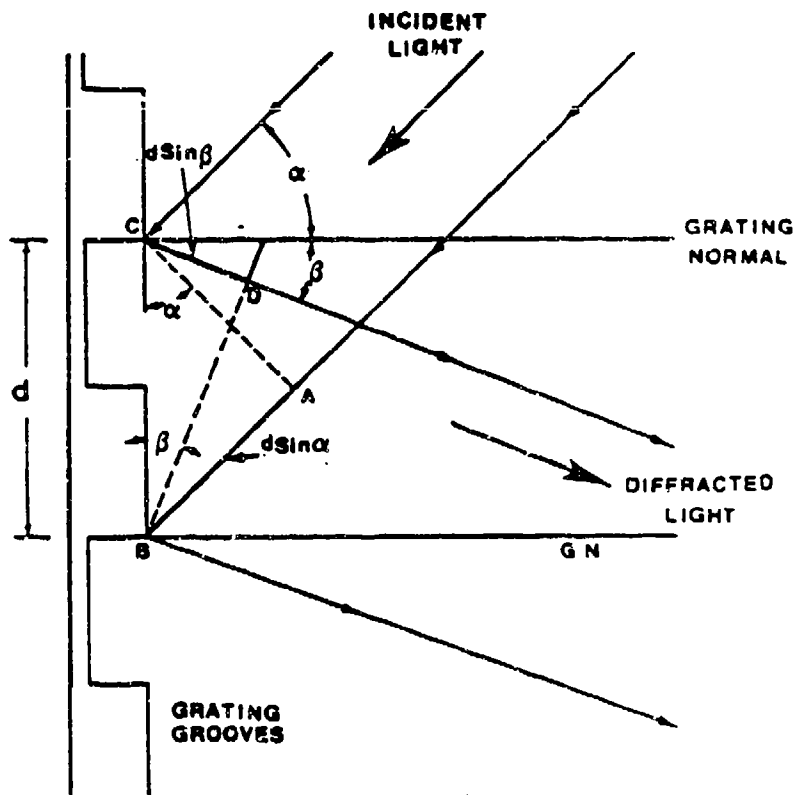
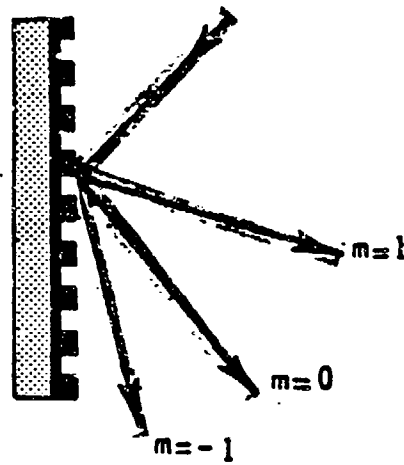


Figure D-1. Phase Relation Between Rays from Two Grating Grooves

special case of diffraction referred to as "symmetrical diffraction". This situation occurs when, for every order that emerges from the grating at an angle $+\beta$, there is another diffraction order that emerges at angle $-\beta$. If the diffraction order $m = -1$ is chosen to emerge symmetrically opposed to the zeroth order, then $\beta_{-1} = -\alpha$ and the diffraction equation D.4 reduces to,

$$\sin \alpha = \frac{\lambda}{2d} \quad \text{or} \quad \sin \alpha = \frac{\lambda}{2} f \quad \text{D.5}$$

D.2. The General Grating Equation-Oblique Incidence

D.2.1. Directional Relations.

In the description of the behavior of the grating given before, it is assumed that the incident and emergent beams both lie in the same plane. More general relations between the direction of incidence and emergence have been given by Guild [D.2]. Some of his fine explanations are adopted here.

Referring to Figure D-2, the following definitions are important:

A "principal plane" is defined as a plane normal to the surface of the grating which intersects it in a line perpendicular to the grating lines.

A "secondary plane" is a plane normal to the surface of the grating which intersects it in a line parallel to the grating lines.

An "incidence plane" is a plane formed by the incident ray and the grating normal; and a plane which is formed by emergent rays of any spectral order and the grating normal is a "plane of emergence" for that order.

To specify the direction of a ray of light in relation to the grating we use two parameters. First, the direction of the incident ray may be specified by the angle α between the ray and the normal to the grating surface, usually referred to as the angle of incidence, together with the angle ψ_1 between the plane of incidence and the principal plane.

Similarly, the direction of emergence of rays of the m th. order, may be specified by the angle of emergence, β_m , between the m th order rays and the normal to the grating plus the angle ψ_m between the plane of emergence and the principal plane.

The direction of a ray may also be specified by its inclination to any two planes, an obvious choice being the principal and secondary planes of the grating. These two inclinations for the incident ray are α' , which is the angle between the incident ray and its projection on the principal plane, and α'' , which is the angle between the incident ray and its projection on the secondary plane. The corresponding specification for the emergent ray of the m th order, are β' , which is the angle

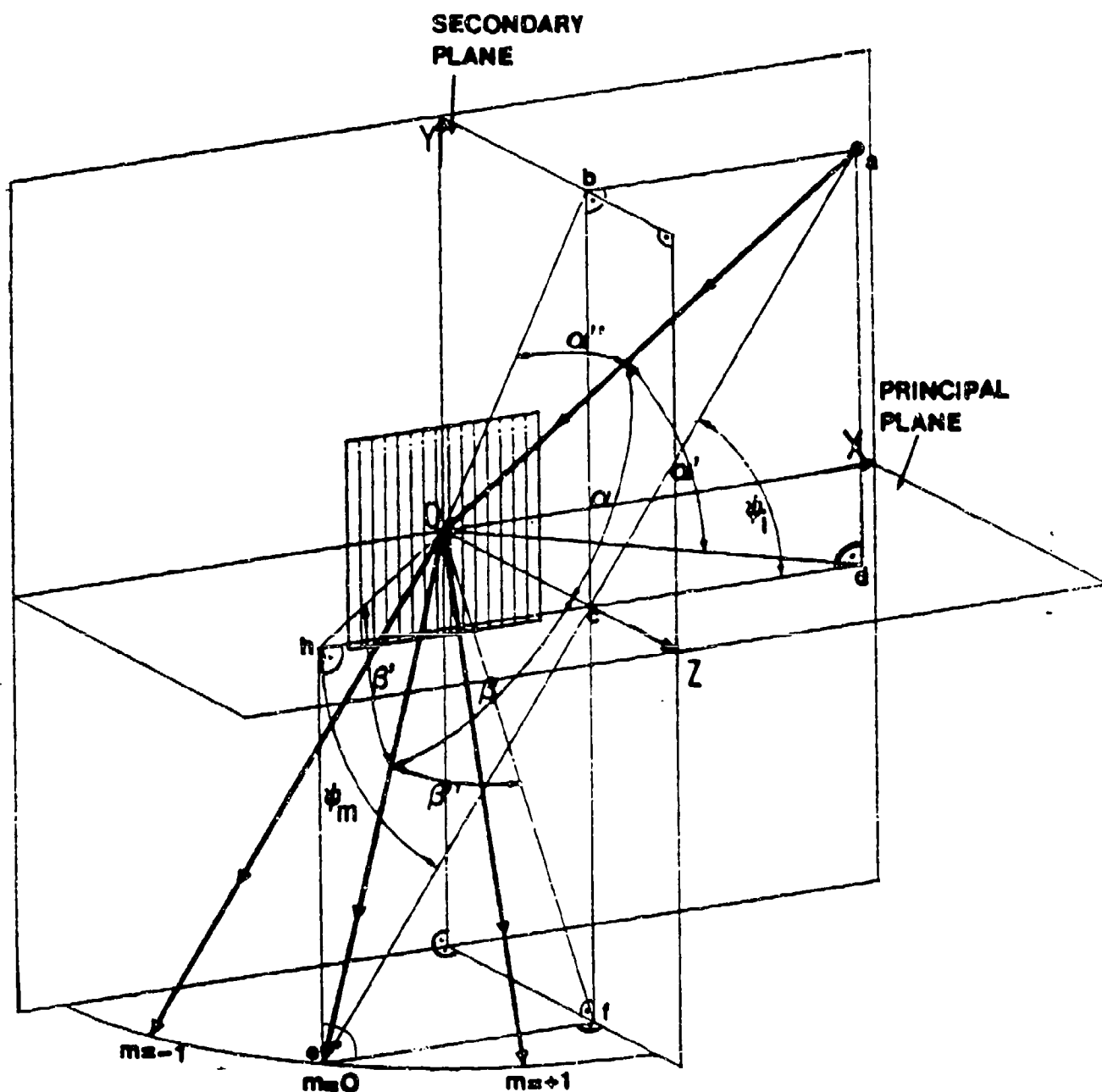


Figure D-2. Three Dimensional Geometry of the Incident and Diffracted Rays of a Grating

between the emergent ray and its projection on the principal plane, and β'' , which is the angle between the emergent ray and its projection on the secondary plane.

The geometrical relationships between these parameters are very simple and can be obtained from Figure D-2. They are given here only for completeness. First, $\sin \alpha' = ad/ao$, $\sin \alpha = ac/ao$ and $\sin \psi_1 = ad/ac$ which combined yield

$$\sin \alpha \sin \psi_1 = \sin \alpha' \quad D.6.a$$

also, $\sin \alpha'' = ab/ao$, $\sin \alpha = ac/ao$ and $\cos \psi_1 = cd/ac = ab/ac$, yield

$$\sin \alpha \cos \psi_1 = \sin \alpha'' \quad D.6.b$$

for the m th emergent order, $\sin \beta' = eh/oe$, $\sin \beta_m = ce/oe$, and $\sin \psi_m = eh/ce$,

$$\sin \beta_m \sin \psi_m = \sin \beta' \quad D.6.c$$

and $\sin \beta'' = ef/oe$, $\sin \beta_m = ce/oe$, $\cos \psi_m = ch/ce = ef/ce$, yield

$$\sin \beta_m \cos \psi_m = \sin \beta'' \quad D.6.d$$

D.2.2. Derivation of the general grating equation.

The exposition below draws heavily from Stroke's [D.3] and James and Sternberg's [D.4] fine explanations.

Consider a plane grating shown in Figure D-3 whose surface lies on the plane $z = 0$ of a rectangular coordinate system. Also, consider a ray incident on the grating at the origin of the coordinate system, with direction cosines L_1, L_2, L_3 . Let there be another ray parallel to the first, meeting the grating at point $C(x, y, 0)$. Let them both be diffracted, with direction cosines L'_1, L'_2 and L'_3 . As shown in Figure D-3, lines CA and CB are drawn from C to the first incident and diffracted rays, meeting them perpendicularly. Then CA lies on the incident wavefront, and if the outgoing rays are in the direction of a principal maximum, CB lies on a diffracted wavefront. Therefore, for constructive interference, ACB must be an integral number of wavelengths long. Let the incident waves at O and at C be:

$$L_1x + L_2y + L_3z = 0 \quad D.6.e$$

and

$$L_1x + L_2y + L_3z = CA \quad D.6.f$$

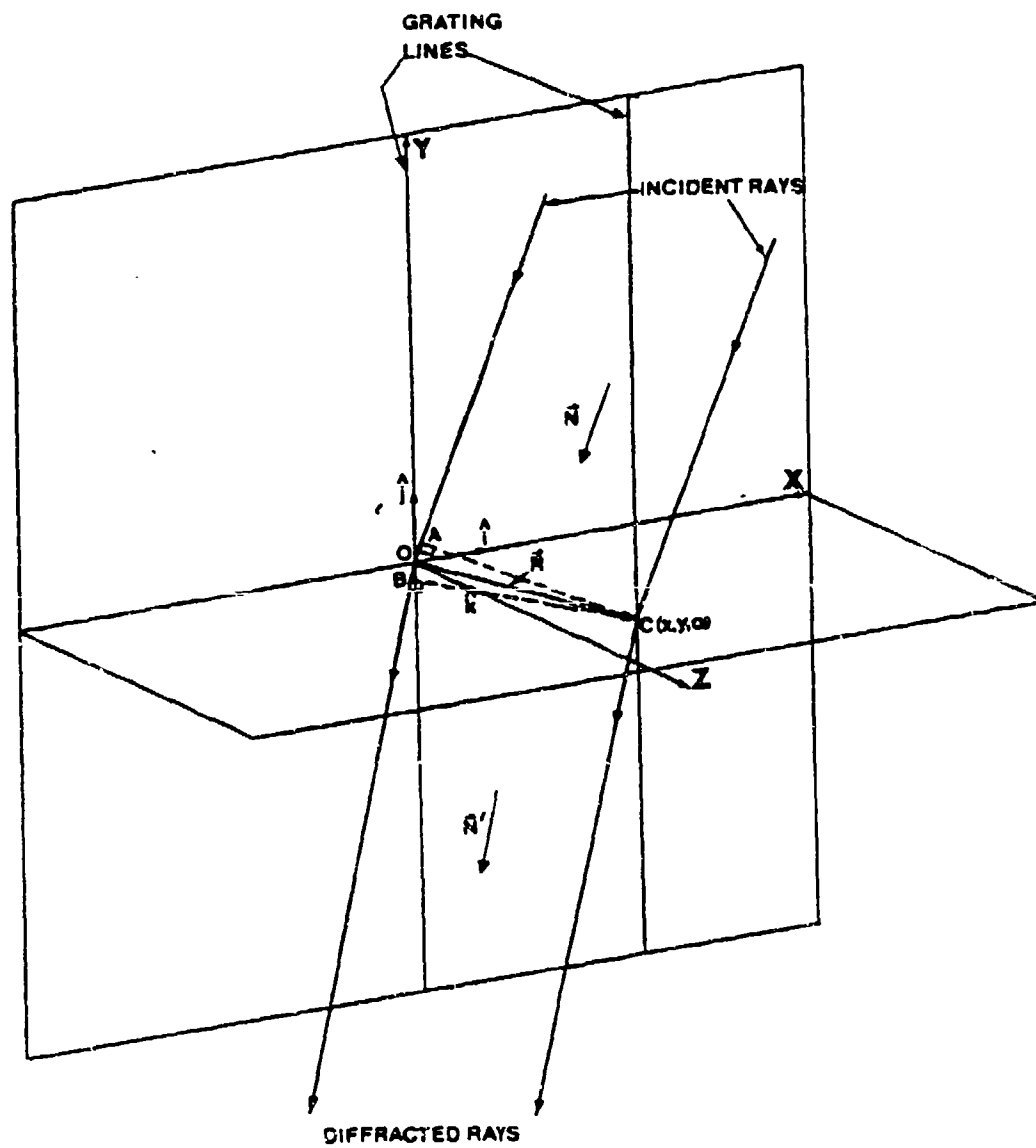


Figure D-3. Oblique Incidence on a Plane Grating

respectively. Let the diffracted rays at O and at C be:

$$L'_1x + L'_2y + L'_3z = 0 \quad \text{D.6.g}$$

and

$$L'_1x + L'_2y + L'_3z = CB \quad \text{D.6.h}$$

Let the incident wave normal be:

$$\vec{N} = n_x \hat{i} + n_y \hat{j} + n_z \hat{k} \quad \text{D.6.i}$$

or

$$\vec{N} = L_1 \hat{i} + L_2 \hat{j} + L_3 \hat{k} \quad \text{D.6.j}$$

and the diffracted wave normal be,

$$\vec{N}' = L'_1 \hat{i} + L'_2 \hat{j} + L'_3 \hat{k} \quad \text{D.6.k}$$

and on the first groove, at point C,

$$\vec{r} = d\hat{i} + y\hat{j} \quad \text{D.6.l}$$

then, for the incident beam,

$$CA = \vec{N} \cdot \vec{r} = L_1 d + L_2 y \quad \text{D.6.m}$$

and for the diffracted wave,

$$OB = \vec{N}' \cdot \vec{r} = L'_1 d + L'_2 y \quad \text{D.6.n}$$

then for constructive interference,

$$OA + OB = m\lambda \quad \text{D.6.o}$$

or

$$(L_1 + L'_1)d + (L_2 + L'_2)y = m\lambda \quad \text{D.6.p}$$

This equation must hold for any value of y, and so, the first condition for OB to be an outgoing ray is

$$L_2 = -L'_2 \quad \text{D.6.q}$$

and so

$$L_1 + L'_1 = \frac{m\lambda}{d} \quad \text{D.6.r}$$

Referring to Figure D.2, it is easy to see that

$$L_1 = \cos(\pi/2 - \alpha) = \sin \alpha$$

$$L_1' = \cos(\pi/2 + \beta'') = -\sin \beta'' \quad D.6.s$$

$$L_2 = \cos(\pi/2 - \alpha') = \sin \alpha'$$

$$L_2' = \cos(\pi/2 + \beta') = -\sin \beta'_m$$

Thus, equations D.6.q and D.6.r, can be expressed as:

$$\sin \beta''_m = \frac{m\lambda}{d} + \sin \alpha'' \quad D.6.t$$

$$\sin \alpha' = \sin \beta'_m \quad D.6.u$$

Combining equation D.6.a and D.6.b, D.6.s and D.6.t,

$$\sin \beta''_m = \frac{m\lambda}{d} + \sin \alpha \cos \psi_1$$

$$\sin \beta'_m = \sin \alpha \sin \psi_1 \quad D.7$$

Note from Figure D.2 that for $\psi_1 = 0$, $\sin \alpha'' = ad/ao = cd/ad$ and $\sin \beta''_m = ef/ce = ch/ch$, then, equation D.7 reduces to

$$\sin \beta''_m = m\lambda f + \sin \alpha \quad D.4 \text{ repeated}$$

which is the two-dimensional case.

A very important idea is demonstrated by equation D.7.b. The angle β'_m i.e the angle between the emergent ray and its projection on the principal plane is a function only of the angle of incidence α and the angle ψ_1 between the plane of incidence and the principal plane. It is not a function of the diffraction order. It is constant for any given arrangement of apparatus. This result means that the angle between the projection of any diffracted ray and the principal plane is the same. For $m = 0$, equations D.7.a and D.7.b reduce to Snell's law, that is, $\alpha = \beta_{m=0}$ and $\psi_1 = \psi_{m=0}$. Also, the sine of the angle between any diffraction order and its projection on the secondary plane will always be given by the summation of $\sin \beta''_{m=0}$ plus a quantity which depends on a multiple of the grating frequency.

It is not the inclination of the incident and emergent beams to the normal, but their inclinations to the secondary plane which are relevant to the operation of the grating. The inclination of the incident beam

to the principal plane is merely carried through to the emergent beams without modification.

For the analysis of the formation of Moire fringes, a sign convention for the diffracted rays and the angles of incidence and emergence will be adopted here. Referring to Figure D-2, a diffracted order will be positive when it propagates with a component in the +z direction and when it lies in a counterclockwise direction with respect to the zero order when viewed from the +y direction. For the incident and emergent rays, the following convention applies: the angle between the ray and the z-axis is positive when its projection on the xz-plane is rotated counterclockwise from the z-axis and it travels in the +z direction, when viewed from the +y direction. Its projection on the yz-plane follows the same convention when viewed from the +x direction. In the case of a two-direction grating, the same convention applies if x and y are interchanged.

D.3. Two Beam Interference

When two coherent beams of collimated laser light intersect at an angle 2ϕ , a volume of interference fringe planes is created. Figure D-4 shows in cross section how the two incident wavefronts combine to form a stationary system of parallel interference bands in space. The bands are not merely lines as shown, but they are planes lying perpendicular to the bisector of wavefronts and they always exhibit a sinusoidal intensity distribution. Such intensity distribution can be recorded if the two beams fall simultaneously on a screen.

The distance p between the adjacent walls of interference is calculated from Figure D-4 to be

$$p = \frac{\lambda}{2 \sin \phi} \quad D.8$$

where λ is the wavelength of the laser light, ϕ is half the angle between the propagation axes of the two beams of light. Equation D.9 can be rewritten as

$$\sin \phi = \frac{\lambda}{2} P \quad D.9$$

where P is the fringe density or number of fringes per unit of length.

D.4. Geometry of the Moire Interferometer.

Czarnek and Post [D.5] have suggested that specimen gratings with rulings oriented at ± 45 degrees to the y-axis can be used to determine the U_x and U_y displacement fields, i.e. the displacement fields in the x and y directions.

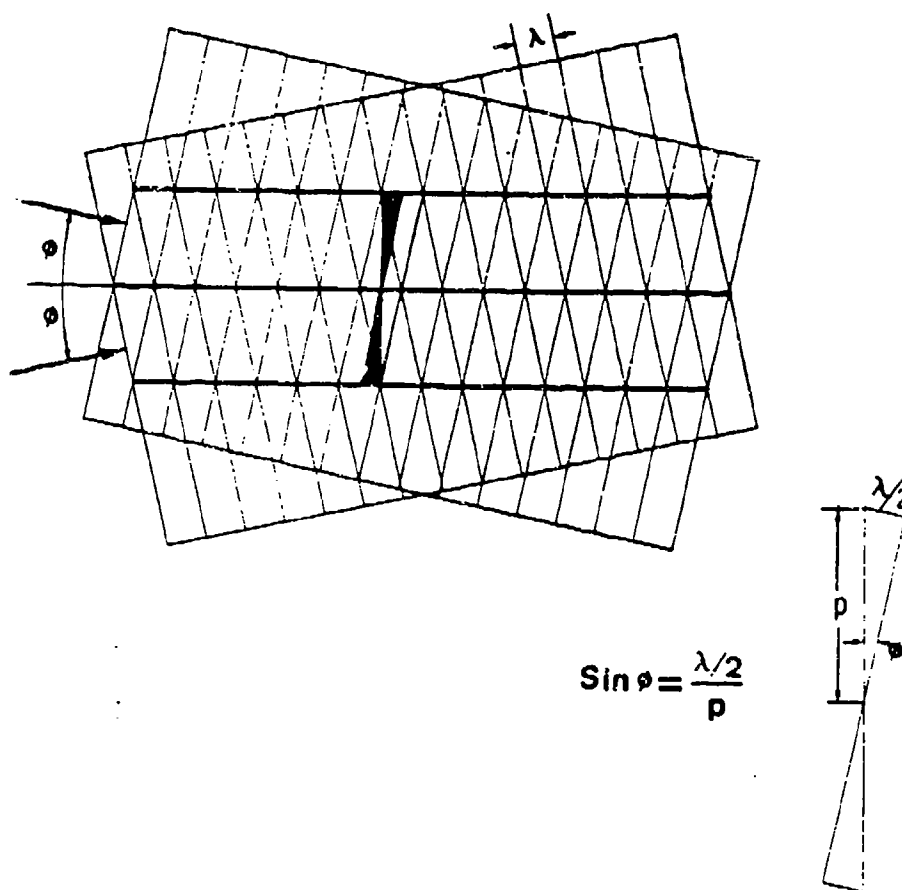
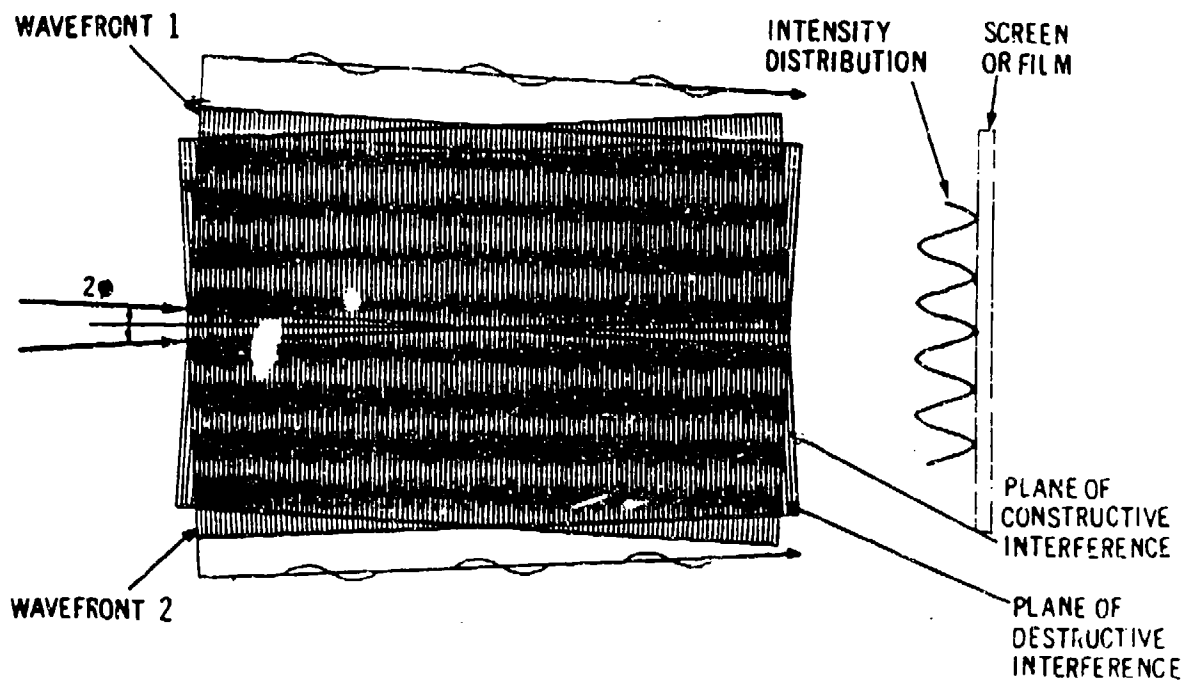


Figure D-4. Constructive and Destructive Interference Produced by the Combination of Two Wavefronts

Figure D-5 illustrates a three beam arrangement of a Moire interferometer with ± 45 degrees specimen gratings. By combining diffracted orders from beams AO and BO, deformation fields in the horizontal direction x can be visualized; the combination of beam BO and CO provides the information for the vertical y-direction, and combining beams AO and CO provides information in a third direction located at 45-degrees with respect to the x-axis.

When the specimen grating is interrogated with beams AO and BO, an interference pattern is formed. The frequency of this interference system is F, and it is calculated according to equation D.9. This interference pattern will be referred to as "the reference grating". Now, the angle between these two beams of light is,

$$AOB = 2\phi \quad D.10$$

The first diffraction order (-1) of beam AO, incident on the specimen grating x' is desired to be perpendicular to the specimen grating surface, since for an oblique diffracted order the view is foreshortened and distorted. Also, a fixed distance from the observer or camera would make focusing easier. Then, the required angle of incidence is ξ , i.e. angle AOQ. The angle 2ξ is related to the angle 2ϕ by,

$$\sin \xi = \frac{1}{\sqrt{2}} \sin \phi \quad D.11$$

Similarly, the angle of incidence for beam BO should be $-\xi$, in order for the first diffraction order (+1) to be perpendicular to the specimen grating surface.

The frequency of the specimen grating can be determined using the grating equation by letting $m = -1$, $\alpha = -\xi$ and $\beta_1 = 0$, to get: $f = \sin \xi / \lambda$. Recalling that $F = (2/\lambda) \sin \phi$, and using equation D.11 one obtains,

$$f = \frac{F}{\sqrt{2}} \quad D.12$$

The first diffraction orders (-1) and (+1) of beams AO and BO, will be referred to as AO' and BO' respectively, and they will be perpendicular to the specimen grating surface if and only if the frequencies of both gratings x' and y' are related to f as in equation D.12.

D.5. Deformation of the Specimen Grating

Consider one square formed by the intersection of two pairs of grating lines, originally parallel to the x' and y' axes as shown in Figure D-6.a. The specimen on which the grating is mounted is being deformed by the action of externally applied loads. Assume a state of plane strain parallel to the xy-plane exists at the point under consideration. In tensor form, the strain components can be written as [D.6]:

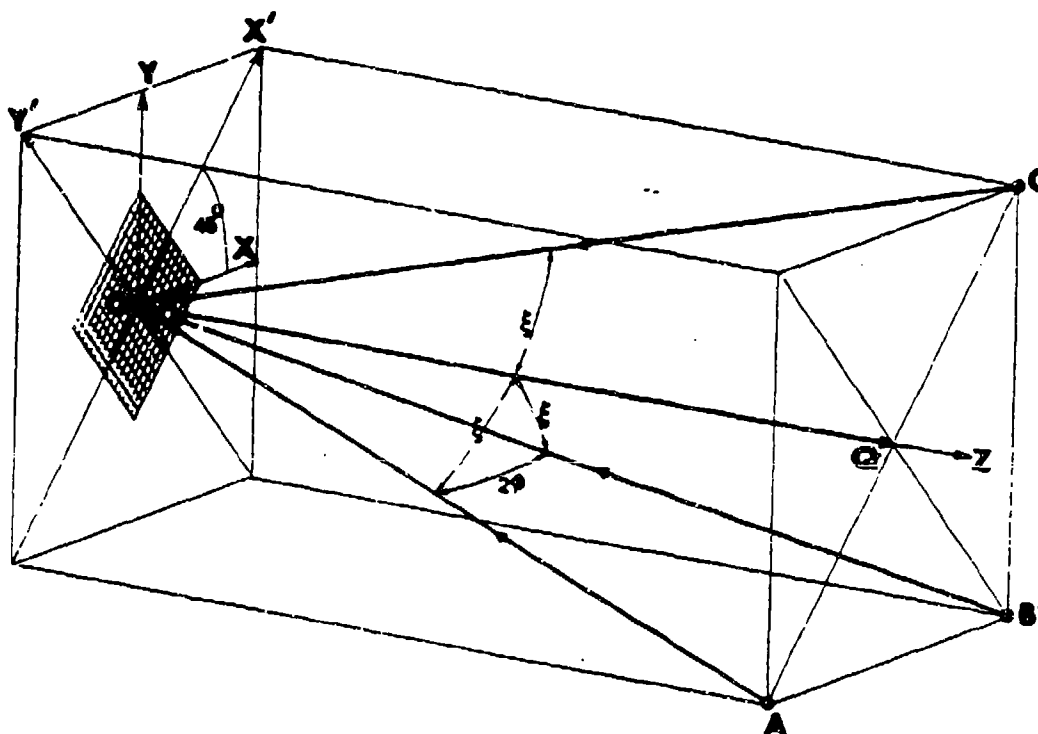


Figure D-5. Three-Beam Arrangement of the Moire Interferometer

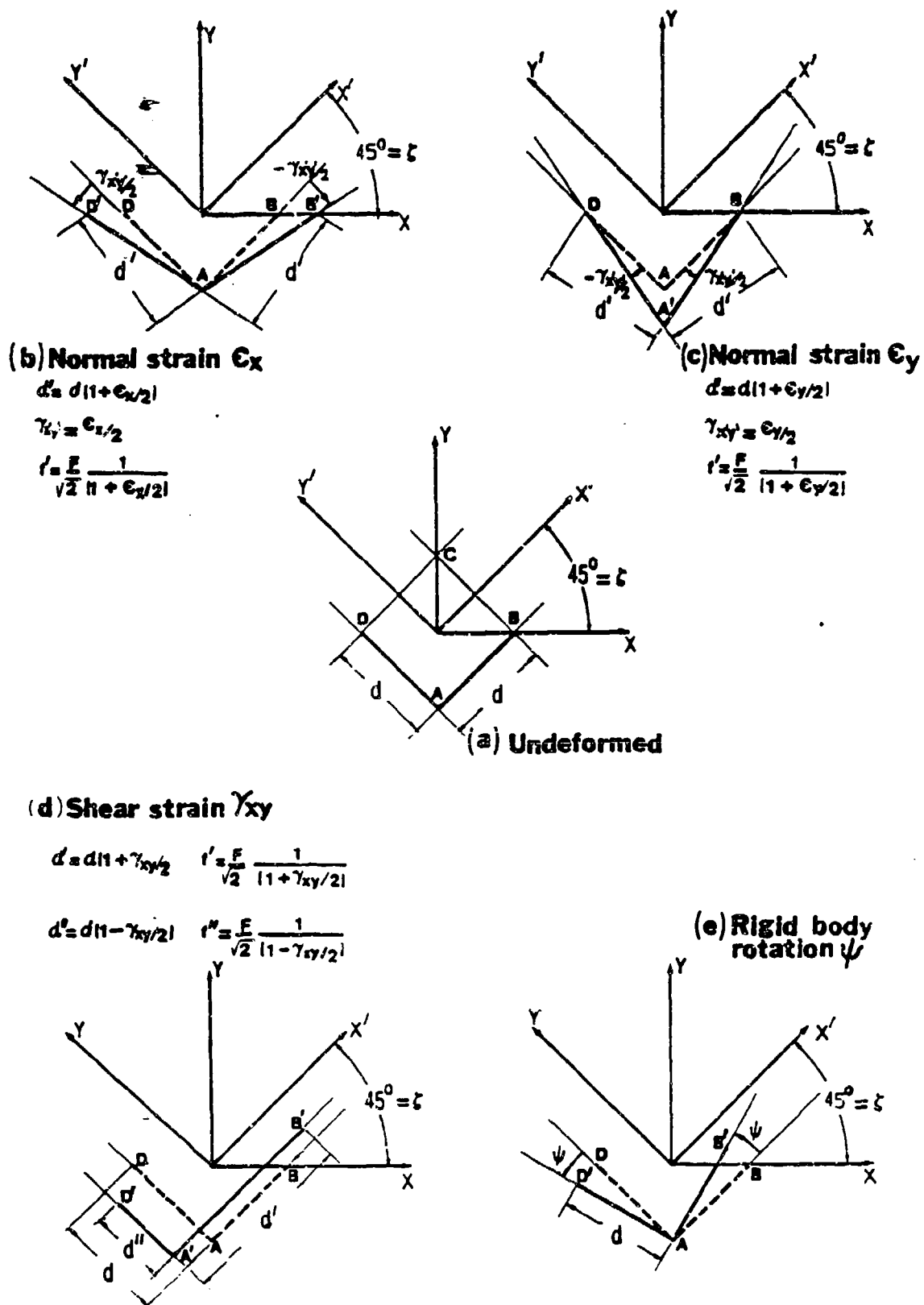


Figure D-6. Geometrical Representation of the Deformation of the Grating

$$\vec{E} = \begin{bmatrix} \epsilon_x & \epsilon_{xy} \\ \epsilon_{xy} & \epsilon_y \end{bmatrix} \quad D.13$$

ϵ_x and ϵ_y represent normal strains along the x and y axes respectively, and $\epsilon_{xy} = \epsilon_{yx} = \gamma_{xy}/2$ are the small changes in right angles whose sides were initially parallel to the x and y axes respectively. The strain along the sides of the square whose sides are parallel to the x' and y' axes can be calculated simply by applying the following transform to the strain in the specimen, since it is a second order tensor,

$$E'_{ij} = A_{ip} A_{jq} E_{pq} \quad \text{or} \quad \vec{E}' = A \vec{E} A_c \quad D.14$$

where A is the matrix of direction cosines and A_c is its transpose. Then

$$\vec{E}' = A \vec{E} A_c = \begin{bmatrix} m & n \\ -n & m \end{bmatrix} \begin{bmatrix} \epsilon_x & \frac{1}{2} \gamma_{xy} \\ \frac{1}{2} \gamma_{xy} & \epsilon_y \end{bmatrix} \begin{bmatrix} m & -n \\ n & m \end{bmatrix} \quad D.15$$

where $m = \cos \zeta$ and $n = \sin \zeta$.

$$\vec{E}' = \begin{bmatrix} \epsilon_x(m^2) + \epsilon_y(n^2) + \gamma_{xy}(mn) & (\epsilon_y - \epsilon_x)mn + \frac{1}{2}\gamma_{xy}(m^2 - n^2) \\ -(\epsilon_y - \epsilon_x)mn + \frac{1}{2}\gamma_{xy}(m^2 - n^2) & \epsilon_x(n^2) + \epsilon_y(m^2) - \gamma_{xy}(mn) \end{bmatrix} \quad D.16$$

For small strains, the principle of superposition can be used to write:

$$\vec{E}' = \begin{bmatrix} \epsilon_x(m^2) & -\epsilon_x(mn) \\ -\epsilon_x(mn) & \epsilon_x(n^2) \end{bmatrix} + \begin{bmatrix} \epsilon_y(n^2) & \epsilon_y(mn) \\ \epsilon_y(mn) & \epsilon_y(m^2) \end{bmatrix} + \quad D.17$$

$$\begin{bmatrix} y^{(mn)} & \frac{1}{2}\gamma_{xy}(m^2 - n^2) \\ xy(m^2 - n^2) & -\gamma_{xy}(mn) \end{bmatrix}$$

Each of the matrices represent the effect of ϵ_x , ϵ_y and γ_{xy} respectively, on the deformations of the grating lines. For $\zeta = 45$ degrees, this equation reduces to,

$$\vec{E}' = \begin{bmatrix} \frac{1}{2}\epsilon_x & -\frac{1}{2}\epsilon_x \\ -\frac{1}{2}\epsilon_x & \frac{1}{2}\epsilon_x \end{bmatrix} + \begin{bmatrix} \frac{1}{2}\epsilon_y & \frac{1}{2}\epsilon_y \\ \frac{1}{2}\epsilon_y & \frac{1}{2}\epsilon_y \end{bmatrix} + \begin{bmatrix} \frac{1}{2}\gamma_{xy} & 0 \\ 0 & -\frac{1}{2}\gamma_{xy} \end{bmatrix} \quad D.18$$

From these results, ϵ_x and ϵ_y will produce both extension and rotation of the grating lines, and γ_{xy} will produce extensions and contractions but not rotations. The geometrical representation of the changes in length and rotations of the sides of the square are shown in Figures D-6.a-D-6.e. The original position of the lines is indicated by dashed lines.

The results shown in equation D.18 apply to two sides of the square originally oriented along the positive direction of the x' and y' axes. From the first matrix, corresponding to the effect of ϵ_x , the two sides of the square are stretched by $\epsilon_x/2$ and the final angle between them is $(\pi/2 + \epsilon_x)$. Similarly, the second matrix, which corresponds to the effect of ϵ_y , indicates that the two sides are stretched by $\epsilon_y/2$ and that the final angle between them is $(\pi/2 - \epsilon_y)$. From the third matrix, it can be seen that γ_{xy} will produce a tensile strain $\gamma_{xy}/2$ to the line along the x' -axis and a compressive strain $-\gamma_{xy}/2$ to the line along the y' -axis, but they will remain perpendicular to each other.

If the frequency of the grating before deformation is $f = 1/d$, then the new frequency is given by $f' = 1/d'$.

D.6. Moire Fringes of Displacement U_x

D.6.1 Fringes produced by normal strain ϵ_x .

As can be seen in Figure D-7, the specimen grating is interrogated with beams AO and BO. Part of the incident beam AO will be diffracted by the

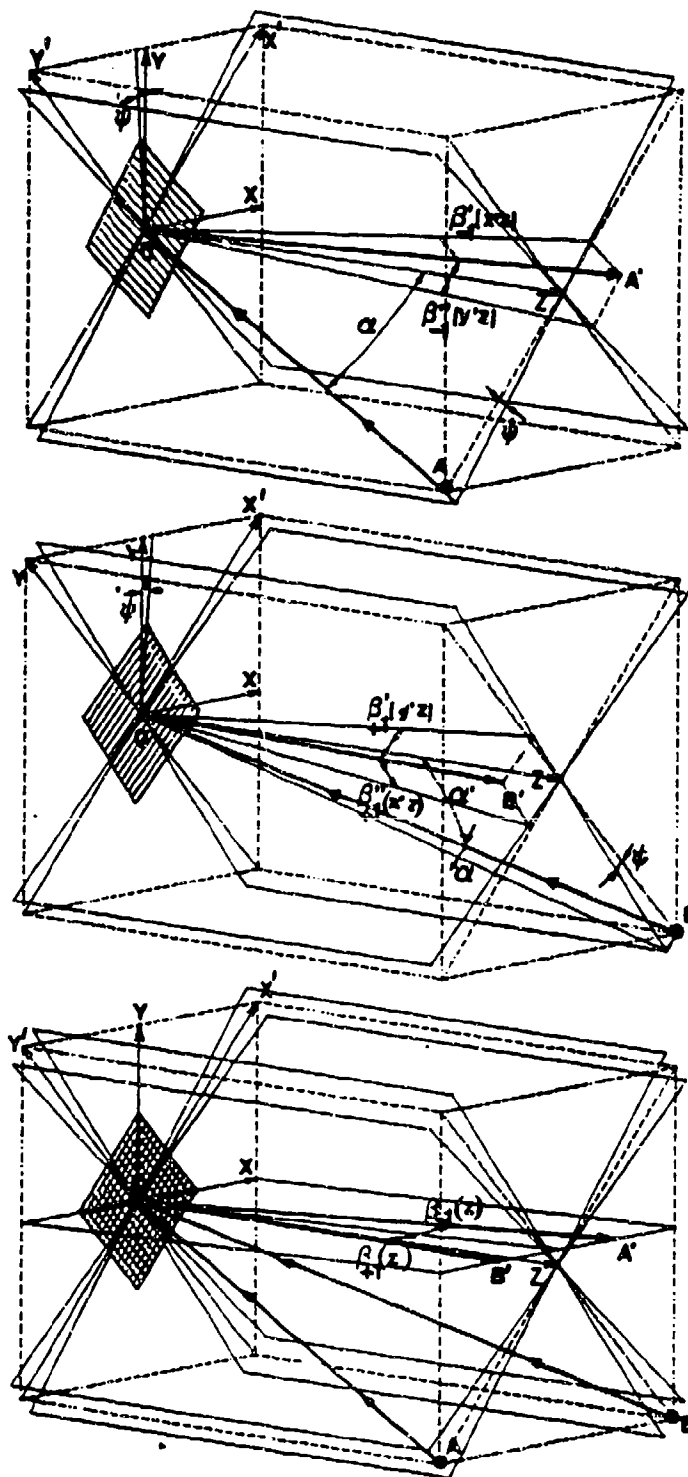


Figure D-7. Geometry of the Incident and Diffracted Rays from a Grating Deformed by ϵ_x when Analyzed by Beams AO and BO

x' grating and its -1 diffraction order will be referred to as OA'. Similarly, OB' will be the +1 diffraction order of the incident beam BO, diffracted by the y' grating.

A normal strain ϵ_x produces a change in frequency from $1/d$ to $1/d'$ (see Figure D-6.b), and it also produce a rotation of the grating lines through an angle $\gamma_{x'y'}/2$, (see Figure D.6.b). As a result the incident beams will not lie in the principal planes of their corresponding gratings. In order to determine the orientations of the emergent beams, it is necessary to use the three-dimensional grating equations. For beam AO, using equations D.7, it can be written:

$$\sin \beta_m'' (x'z) = m\lambda f + \sin \alpha \cos \psi_i \quad D.19$$

$$\sin \beta_m' (y'z) = \sin \alpha \sin \psi_i$$

Similarly for beam BO,

$$\sin \beta_m'' (y'z) = m\lambda f + \sin \alpha \cos \psi_i \quad D.20$$

$$\sin \beta_m' (x'z) = \sin \alpha \sin \psi_i$$

Note that the direction of each diffracted ray is given by the direction of its projection in the x'z and y'z planes, as indicated in parentheses. For the case of infinitesimal normal strains, the ψ_i will be small and these equations reduce to the following: for beam AO,

$$\sin \beta_m'' (x'z) = m\lambda f + \sin \alpha \quad D.21$$

$$\sin \beta_m' (y'z) = \psi_i \sin \alpha$$

and for beam BO,

$$\sin \beta_m'' (y'z) = m\lambda f + \sin \alpha \quad D.22$$

$$\sin \beta_m' (x'z) = \psi_i \sin \alpha$$

Figure D-6 and the related equations show that it is appropriate to use the same ψ_i for beams AO and BO. Then, for beam AO, let $m = -1$, $\sin \alpha = \sin \alpha = \sqrt{2} \sin \phi = \sqrt{2} (\lambda/2) F = \lambda F / \sqrt{2}$, $\psi_i = \gamma_{x'y'}/2 = \epsilon_x/2$, and $f' = (F/\sqrt{2})(1/(1 + \epsilon_x/2))$, which can be expressed as a continued fraction $f' = (F/\sqrt{2})(1 - \epsilon_x/2 + \epsilon_x^2/4 - \dots)$. Equations D.21 yield after neglecting the high order terms:

$$\sin \beta_{-1}'' = (x'z) = \frac{\lambda F \epsilon_x}{2\sqrt{2}} \quad D.23.a$$

$$\sin \beta_{-1}' (y'z) = \frac{\lambda F \epsilon_x}{2\sqrt{2}}$$

Similarly for incident beam BO, letting $m=+1$, $\sin \alpha = \sin \xi = -\lambda F/\sqrt{2}$, $\psi_1 = -\gamma_{x'y'}/2 = -\epsilon_x/2$, and f' as given above, equation D.22 yields,

$$\sin \beta_{+1}'' (y'z) = -\frac{\lambda F \epsilon_x}{2\sqrt{2}} \quad D.24$$

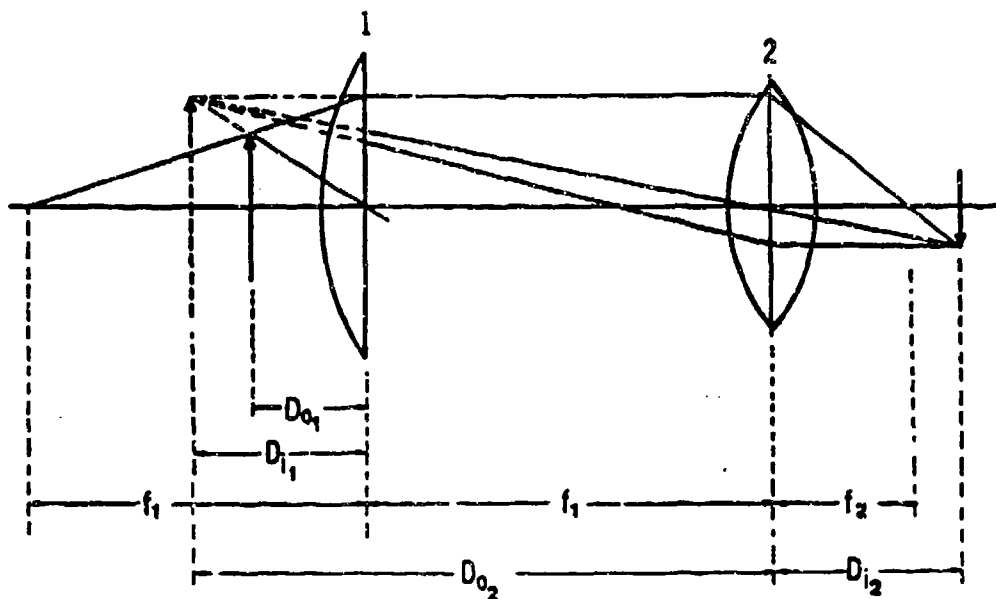
$$\sin \beta_{+1}' (x'z) = -\frac{\lambda F \epsilon_x}{2\sqrt{2}}$$

It is not difficult to show that the diffracted rays AO' and BO' lie in the xz-plane (Figure D-7) and that the sine of the angle between each of them and the z-axis is,

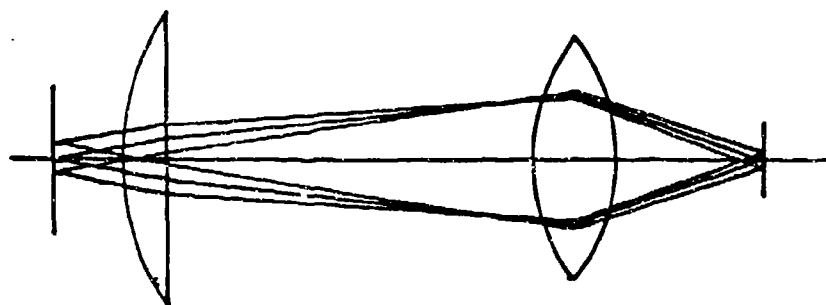
$$\sin \beta_{-1}(z) = -\sin \beta_{+1}(z) = \frac{\lambda F \epsilon_x}{2} \quad D.25$$

In an actual optical system, where a field lens decollimates beams AO' and BO', they converge to two bright points in the focal plane of the decollimating lens. Because of their angular separation, these two bright spots will be focused at a small distance apart. If they are close enough to overlap, then an interference pattern is produced. A more useful procedure is to use another lens and screen (that is, a camera) to construct images of the specimen gratings x' and y' fields with the light contained in the two diffracted wavefronts OA' and OB' [D.7]. Essentially, the camera forms two images which lie on top of one another (see Figure D-8). The degree of interference in the image depends mainly upon the relative displacement of the two focal spots in the back focal plane of the decollimator which, it must be recalled, depends upon the relative inclinations of the diffracted beams. The fringe pattern is not affected by magnification of the lens system. The ratio β'/β which governs the fringe spacing is exactly equal to M. That is, any magnification of the specimen is carried into the fringe pattern, so the ratio of fringe spacing to specimen dimension remains constant.

The image in the camera displays, then, a pattern of interference fringes which are indicative of the local spatial frequency and orientation differences between the two gratings. The resulting



(a) RAY TRACE



(b) INTERFERENCE TRACE

Figure D-8. Optical Arrangement Used to Create an Image of the Interference Pattern Produced by Two Diffracted Orders

interference system of vertical fringes, parallel to the y-axis, has a spatial frequency P_{ϵ_x} which can be calculated using equation D.9 to be,

$$P_{\epsilon_x} = \frac{2}{\lambda} \sin \beta(z) = \epsilon_x F \quad D.26$$

Equation D.23 is important because it relates the strain ϵ_x in the specimen to the known frequency F of the interference system produced by beams AO and BO, and the observed Moire fringe density P_{ϵ_x} . Therefore,

the quantity ϵ_x can be determined in terms of P_{ϵ_x} and F .

The relative displacement U_x (perpendicular to the direction of the lines of the reference grating) between a pair of points a distance p apart ($p = 1/P_{\epsilon_x}$) on two adjacent fringes of orders, say, $N = 0$ and $N = 1$ will then be,

$$U_x = \epsilon_x p = \frac{1}{F} \quad D.27$$

In general, the in-plane displacement in the direction normal to the grating lines is, in terms of the fringe order N_x ,

$$U_x = \frac{(N_x) \epsilon_x}{F} \quad D.28$$

D.6.2. Fringes due to normal strain ϵ_y .

As shown in Figure D-6.c, a normal strain ϵ_y would also change the frequency of the specimen grating, and cause the grating lines to rotate through an angle $\gamma_{x'y'}/2$.

Again using equations D.21 and D.22, it is possible to calculate the orientations of the diffracted rays with respect to the $x'z$ and $y'z$ planes.

For the incident beam AO, and letting $m = -1$, $\sin \alpha = \sin \xi = \lambda F / \sqrt{2}$, $\psi_1 = \gamma_{x'y'}/2 = -\epsilon_y/2$ and $f' = (F/2)(1 - \epsilon_y/2)$, equation D.21 yields for small angles and rotations

$$\sin \beta_{-1}(x'z) = \frac{\lambda F \epsilon_y}{2\sqrt{2}} \quad D.29$$

and

$$\sin \beta'_{-1}(y'z) = - \frac{\lambda F \epsilon_y}{2\sqrt{2}} \quad D.30$$

In a similar way for incident beam OB, letting $m = +1$, $\sin \alpha = \sin \xi = - \lambda F / \sqrt{2}$, $\psi_1 = \gamma_{x'y'} / 2 = \epsilon_y / 2$, and $f' = (F / \sqrt{2})(1 - \epsilon_y / 2)$, equation D.22 yields for small angles and deformations,

$$\sin \beta''_{+1}(y'z) = - \frac{\lambda F \epsilon_y}{2\sqrt{2}} \quad D.31$$

$$\sin \beta'_{+1}(x'z) = \frac{\lambda F \epsilon_y}{2\sqrt{2}}$$

In this case, the two diffracted rays lie in a plane parallel to the yz-plane (Figure D-9) and the sine of angle between each of them and the z-axis is (for small ψ_1),

$$\sin \beta_{-1}(z) = \sin \beta_{+1}(+1) = \frac{\lambda F \epsilon_y}{2} \quad D.32$$

Since the diffracted rays AO' and BO' in this case lie parallel one to the other, equation D.9 yields

$$P_{\epsilon_y} = 0$$

This means that when the specimen grating is interrogated by incident beams AO and BO, the normal strain ϵ_y will not contribute to the interference system.

D.6.3. Fringes due to shear strain γ_{xy}

As shown in Figure D-6.d, a shear strain γ_{xy} would induce normal strains $\epsilon_{x'}$ and $\epsilon_{y'}$ in the x' and y' directions respectively. Due to $\epsilon_{x'}$, the pitch of grating x' would increase, consequently decreasing its frequency. Similarly, due to $\epsilon_{y'}$, the pitch of grating y' would decrease and consequently increase its frequency.

Since the shear strain does not produce any rotation, the two-dimensional grating equation can be used to determine the orientation of each diffracted ray. For incident ray AO, with $m = -1$, $\sin \alpha = \sin \xi = \lambda F / \sqrt{2}$, $\psi_1 = 0$, $f = (F / \sqrt{2})(1 - \gamma_{xy} / 2)$, and for incident

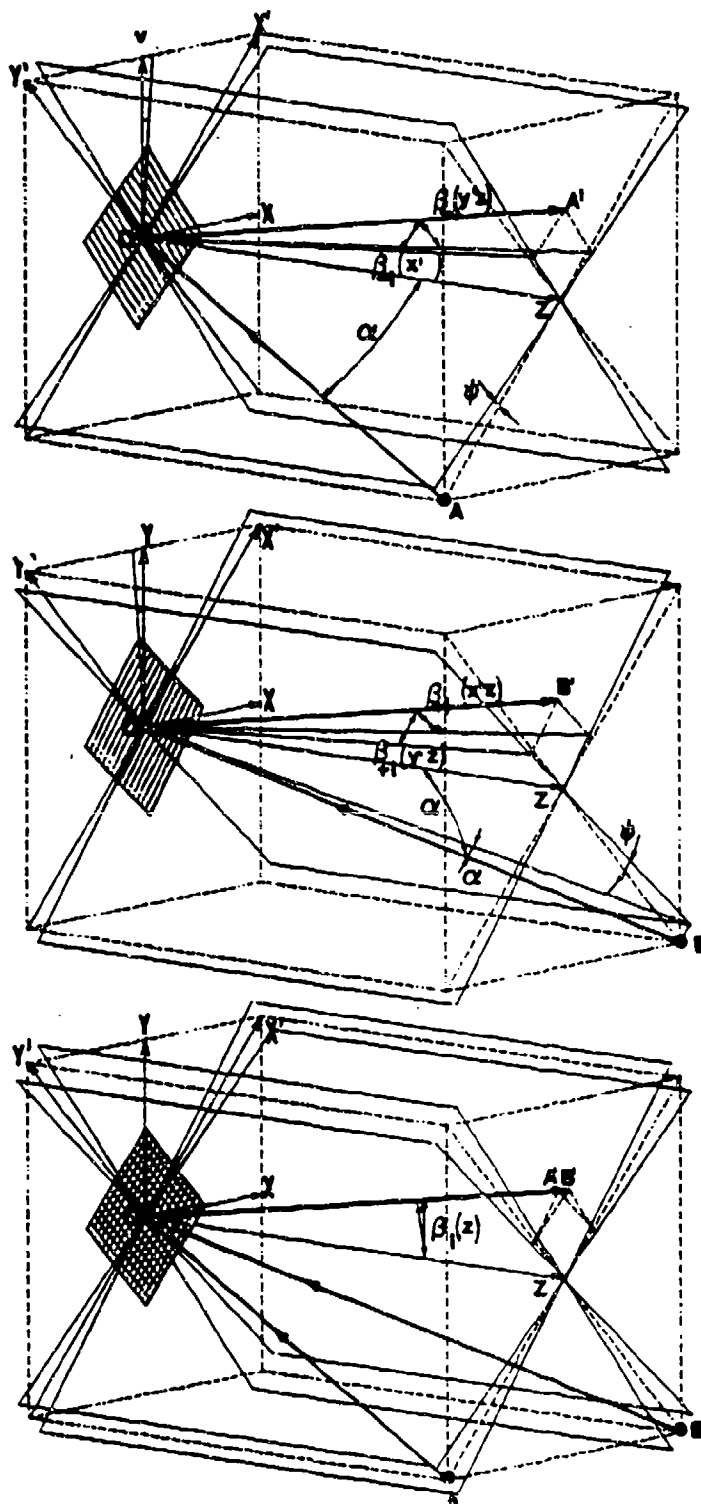


Figure D-9. Geometry of the Incident and Diffracted Rays from a Grating Deformed by ϵ_y when Analyzed with Beams AO and BO

beam OB, with $m = +1$, $\sin \alpha = \sin \xi = -\lambda F/\sqrt{2}$, $\psi_1 = 0$, and $f'' = (F/\sqrt{2})(1 + \gamma_{xy}/2)$, equation 3.4 yields,

$$\sin \beta_{-1}''(z) = \sin \beta_{+1}''(z) = \frac{\lambda F \gamma_{xy}}{2\sqrt{2}} \quad D.34$$

Using simple geometry (see Figure D-10), the sine of the angle between each of the diffracted orders and the xz-plane is found to be

$$\sin \beta = \frac{\lambda F \gamma_{xy}}{4} \quad D.35$$

The resulting interference fringe pattern is composed of horizontal fringes parallel to the xz-plane whose frequency can be calculated using equation D.9 to be,

$$P_{\gamma_{xy}} = \frac{\gamma_{xy} F}{2} \quad D.36$$

D.6.4. Fringes produced by a rigid body rotation

A rotation of the x' and y' gratings through an angle ψ , considered positive in the counterclockwise direction, causes the two diffracted rays OA' and OB' to diverge from their respective planes $x'z$ and $y'z$, but their pitch and frequency will not be disturbed. Using equations D.21.b and D.22.b, the orientations of the two diffracted rays are found to be,

$$\sin \beta_{-1}'(y'z) = \frac{\lambda F \psi}{\sqrt{2}} \quad D.37$$

$$\sin \beta_{+1}'(x'z) = - \frac{\lambda F \psi}{\sqrt{2}}$$

and the sine of the angle between each of the two diffracted orders and the xz-plane is (see Figure D-11),

$$\sin \beta_{\psi} = \frac{\lambda F \psi}{2} \quad D.38$$

Again, equation D.9 gives the frequency of the resulting interference system,

$$P_{\psi} = \psi F \quad D.39$$

D.6.5. Fringes produced by out-of-plane rotations

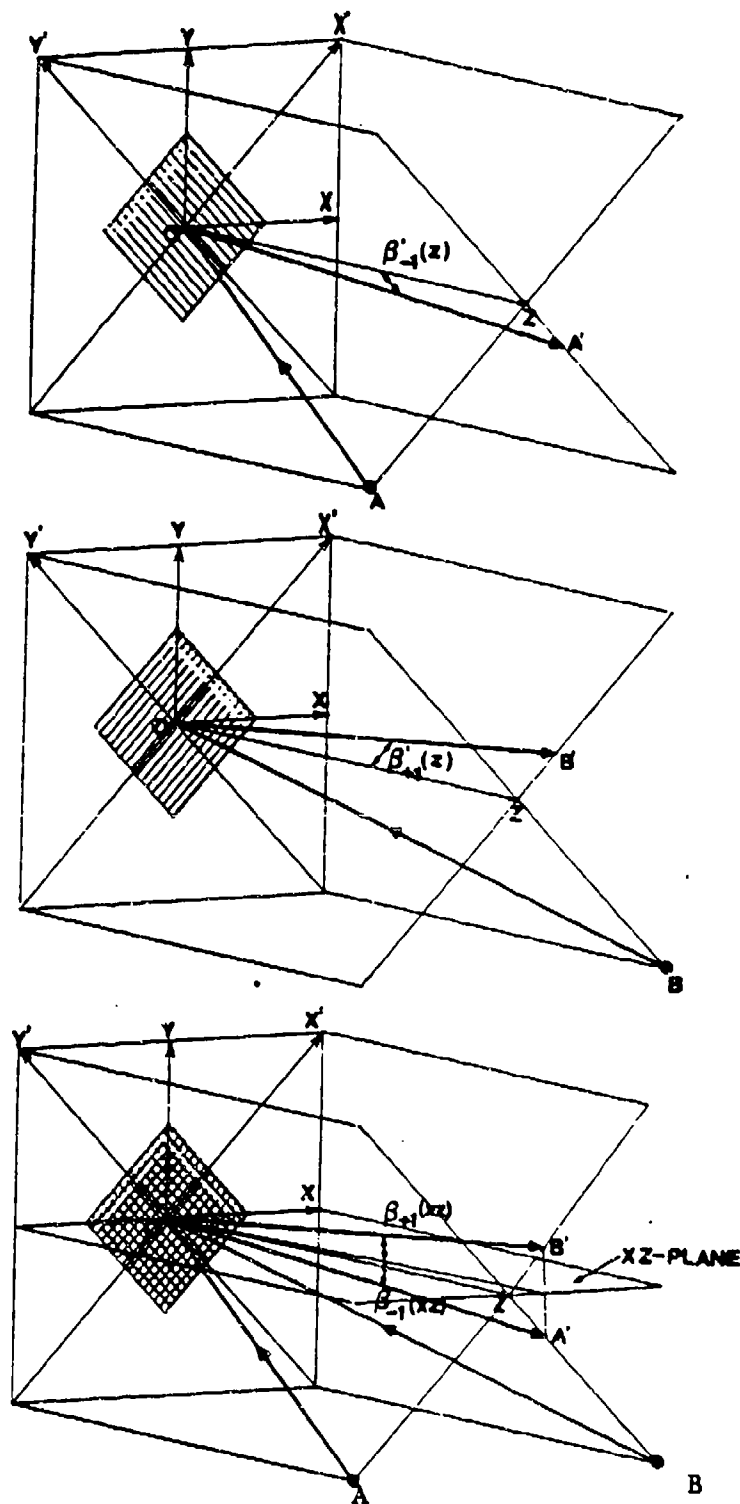


Figure D-10. Geometry of the Incident and Diffracted Rays from a Grating Deformed by γ_{xy} when Analyzed with Beams AO and BO

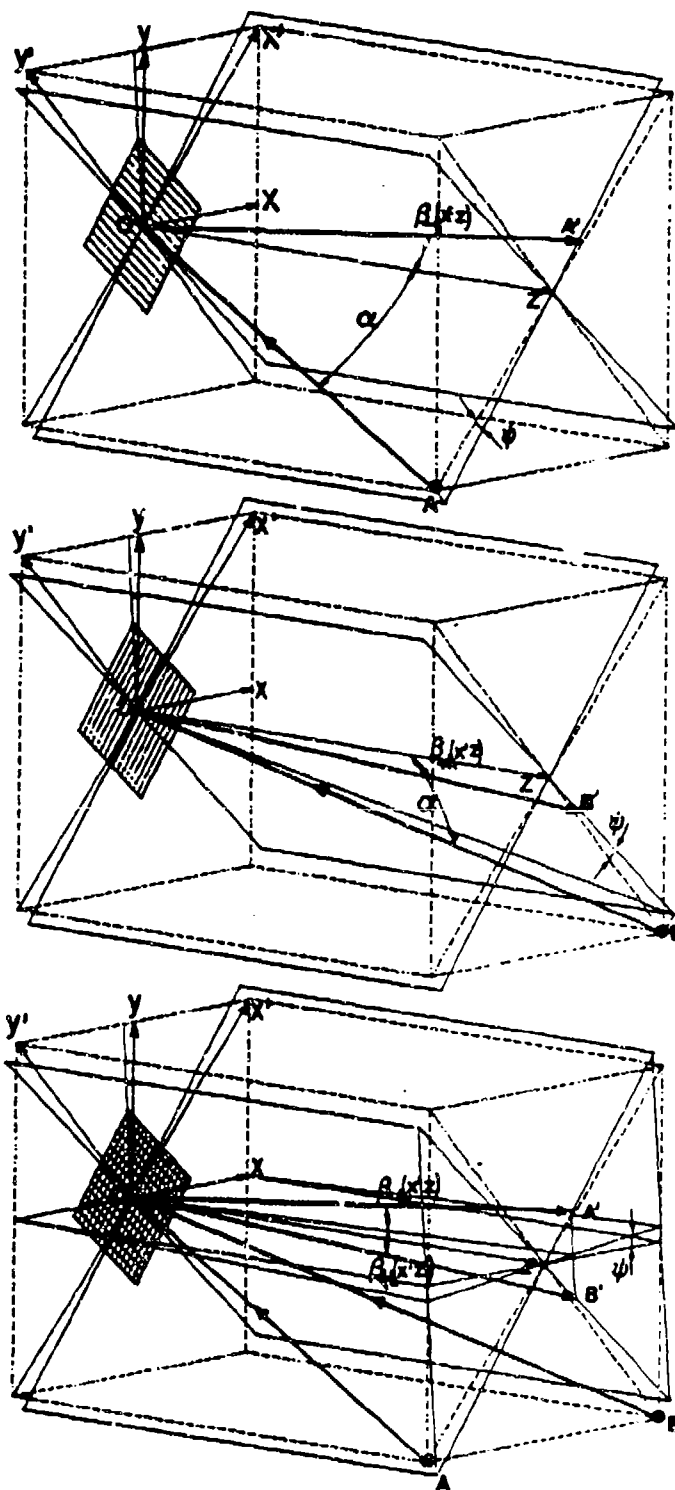


Figure D-11. Geometry of the Incident and Diffracted Rays Affected by Rigid-Body Rotation of the Grating when Analyzed by Beams AO and BO

Any small out-of-plane rotation about an in-plane axis will introduce equal deviations of beams AO' and BO' and it will not make a contribution to the interference pattern, so it can be neglected [D.5].

This analysis has shown that by interrogating the specimen grating with beams AO and BO, Moire patterns of displacement, U_x , can be obtained due to the effect of normal strain ϵ_x , shear strain γ_{xy} , and in-plane rigid body rotation ψ .

D.7. Moire Fringes of Displacements U_y .

To obtain the Moire fringes of displacements U_y , the specimen grating is interrogated with beams BO and CO. Due to the symmetry, the deformation of the grating lines will be the same as those obtained for ϵ_x , and there is no need to repeat the analysis.

D.8. Moire Fringes of Displacement U_{45} .

The displacements U_{45} , are obtained by interrogating the specimen grating with coherent beams AO and CO. The basic geometry of the Moire interferometer is reproduced again in Figure D.12.

The angle AOC is equal to 2ϵ , thus the frequency of the reference grating produced by the interference of beams AO and CO is given by equation D.9, as:

$$F_{45} = \frac{2 \sin \epsilon}{\lambda} \quad D.40$$

Using equation 3.10, it can be rewritten as,

$$F_{45} = \frac{2}{\lambda} (\sqrt{2} \sin \alpha) = 2f \quad D.41$$

i.e. exactly twice the frequency f of the specimen grating.

D.8.1. Fringes due to normal strain ϵ_x .

Due to the action of normal strain ϵ_x , the pitch of the x' grating lines will change by a factor of $(1 + \epsilon_x)$, so its frequency will decrease to $f' = (F_{45}/2)(1 - \epsilon_x)$.

Since both incident beams AO and CO lie in the $x'z$ plane, the angle of emergence of the diffracted rays can be determined using the two-dimensional grating equation D.4 or,

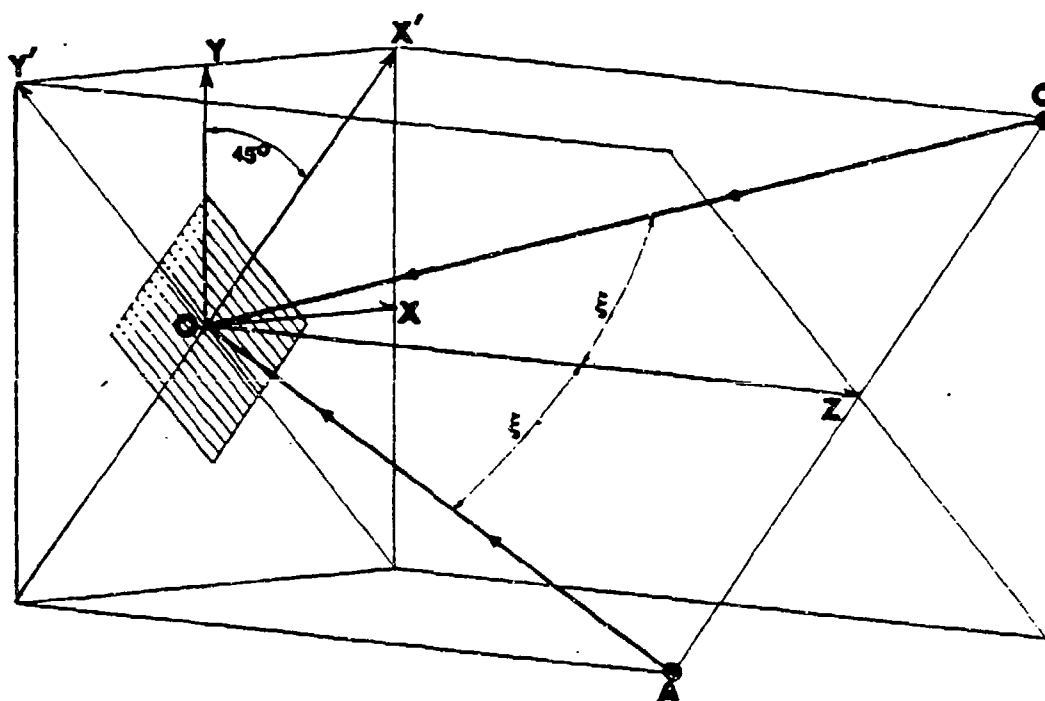


Figure D-12. Schematic of the Angles of Incidence of the Moiré Interferometer when Analyzing the Specimen Grating with Beams AO and CO

$$\sin \beta_m(x'z) = m\lambda f + \sin \alpha$$

Then for beam AO, let $m = -1$, $\sin \alpha = \sin \xi = \lambda F_{45}/2$, and f' given above, the grating equation yields,

$$\sin \beta_{-1}''(x'z) = -\frac{\lambda F_{45} \epsilon_{x'}}{2} \quad D.42$$

Similarly, for beam CO, let $m = +1$, $\sin \alpha = \sin \xi = \lambda F_{45} \epsilon_{x'}/2$, and f as above, to get,

$$\sin \beta_{+1}''(x'z) = \frac{\lambda F_{45} \epsilon_{x'}}{2} \quad D.43$$

Both diffracted rays AO' and CO' lie in the $x'z$ -plane (Figure D-13), and they are located at the same distance on opposite sides of the z -axis. The resulting interference pattern has frequency,

$$P_{\epsilon_{x'}} = F_{45} \epsilon_{x'} \quad D.44$$

and the fringes are perpendicular to the $x'z$ -plane. Again, it is seen that the frequency of the interference pattern is a function of the strain $\epsilon_{x'}$, and the frequency F_{45} of the reference grating, and the

displacement along the x' -direction is given by,

$$U_{45} = (N_{x'}) \frac{1}{F_{45}} \quad D.45$$

D.8.2. Fringes due to in-plane rotation ψ .

When the specimen grating is unstrained but undergoes a rigid body rotation in its own plane, by a small counterclockwise angle ψ , the three-dimensional grating equations D.21.b and D.22.b define the direction of the diffracted rays. For AO and CO then,

$$\sin \beta_{-1}''(x'z) = 0 \quad D.46$$

$$\sin \beta_{-1}'(y'z) = \frac{\lambda F_{45} \psi}{2}$$

and

$$\sin \beta_{+1}''(x'z) = 0. \quad D.47$$

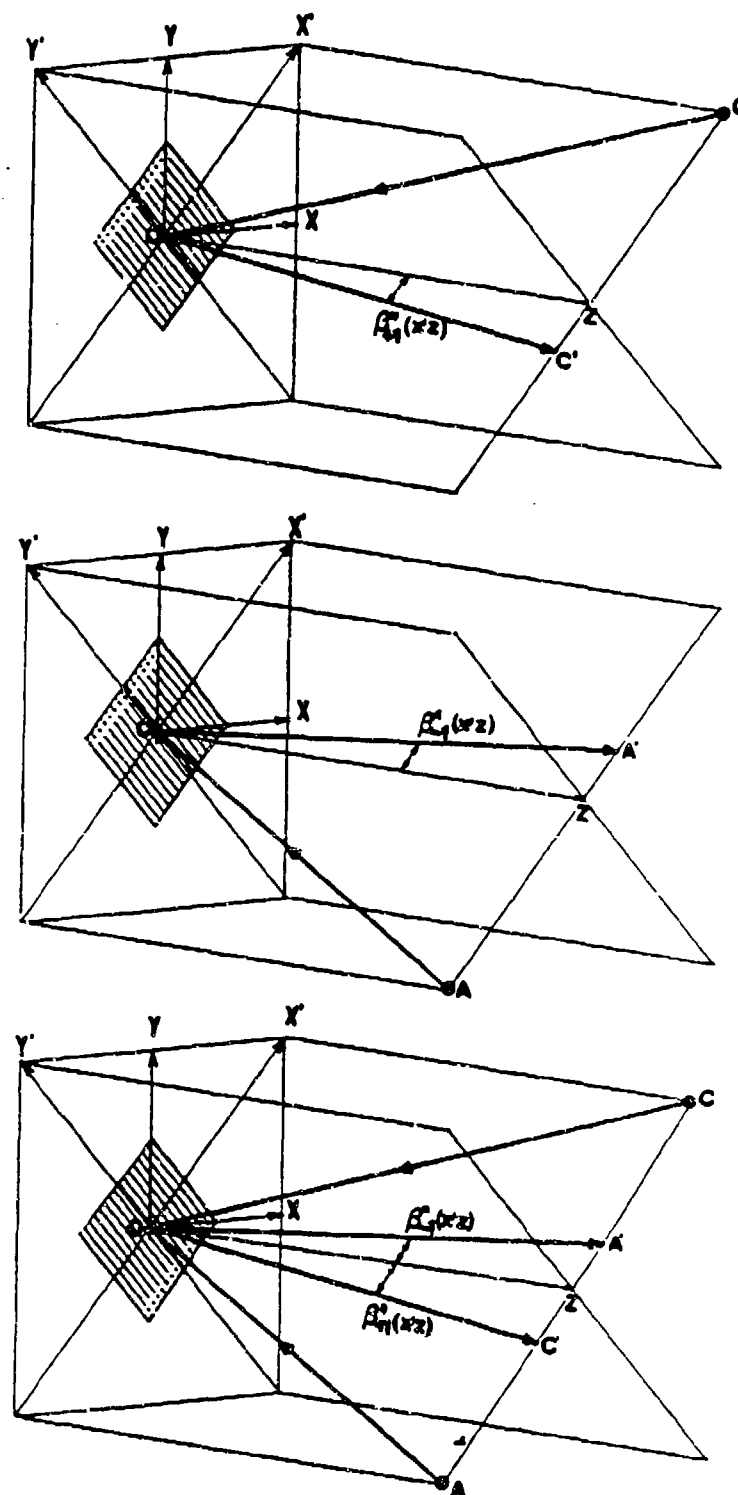


Figure D-13. Geometry of the Incident and Diffracted Rays from a Grating x' Deformed by ϵ_x , when Analyzing with Beams AO and CO

$$\sin \beta'_{+1}(y'z) = - \frac{\lambda F_{45} \psi}{2}$$

Since both rays AO' and CO' lie in the y'z-plane, at the same distance on opposite sides of the z-axis, (Figure D-14), the fringes of resulting interference pattern are perpendicular to the y'z-plane, and their frequency is,

$$P_{\psi} = \psi F_{45} \quad D.48$$

3.8.3. Fringes due to shear strain $\gamma_{x'y'}$.

A positive shear strain $\gamma_{x'y'}$, will cause the x' grating lines to rotate clockwise through an angle $-\gamma_{x'y'}/2$. Then, equation D.18.b yields,

$$\sin \beta'_{-1}(y'z) = - \frac{\lambda F_{45} \gamma_{x'y'}}{4} \quad D.49$$

and

$$\sin \beta'_{+1}(y'z) = \frac{\lambda F_{45} \gamma_{x'y'}}{4} \quad D.50$$

Again, both diffracted rays are located at the same distance on opposite sides of the z-axis (see Figure D-15), and the frequency of the resulting interference pattern is,

$$P_{\gamma_{x'y'}} = \frac{F_{45} \gamma_{x'y'}}{2} \quad D.51$$

D.8.4. Fringes due to normal strain $\epsilon_{y'}$.

When the specimen grating is deformed in the y'-direction by the action of a normal strain $\epsilon_{y'}$, the lines of the x' grating are stretched, but the frequency does not change. Then both diffracted orders leave the grating surface along its normal, and since they are parallel, the frequency of the interference pattern is equal to zero.

D.8.5. Fringes due to out-of-plane rotation.

It has been shown by Basehore and Post [D.8] that a rotation about the x'-axis causes identical angular deviations in the diffracted rays AO' and CO', but the angle between them remains unchanged. Also Walker and McKelvie [D.9], showed that a rotation about an axis perpendicular to

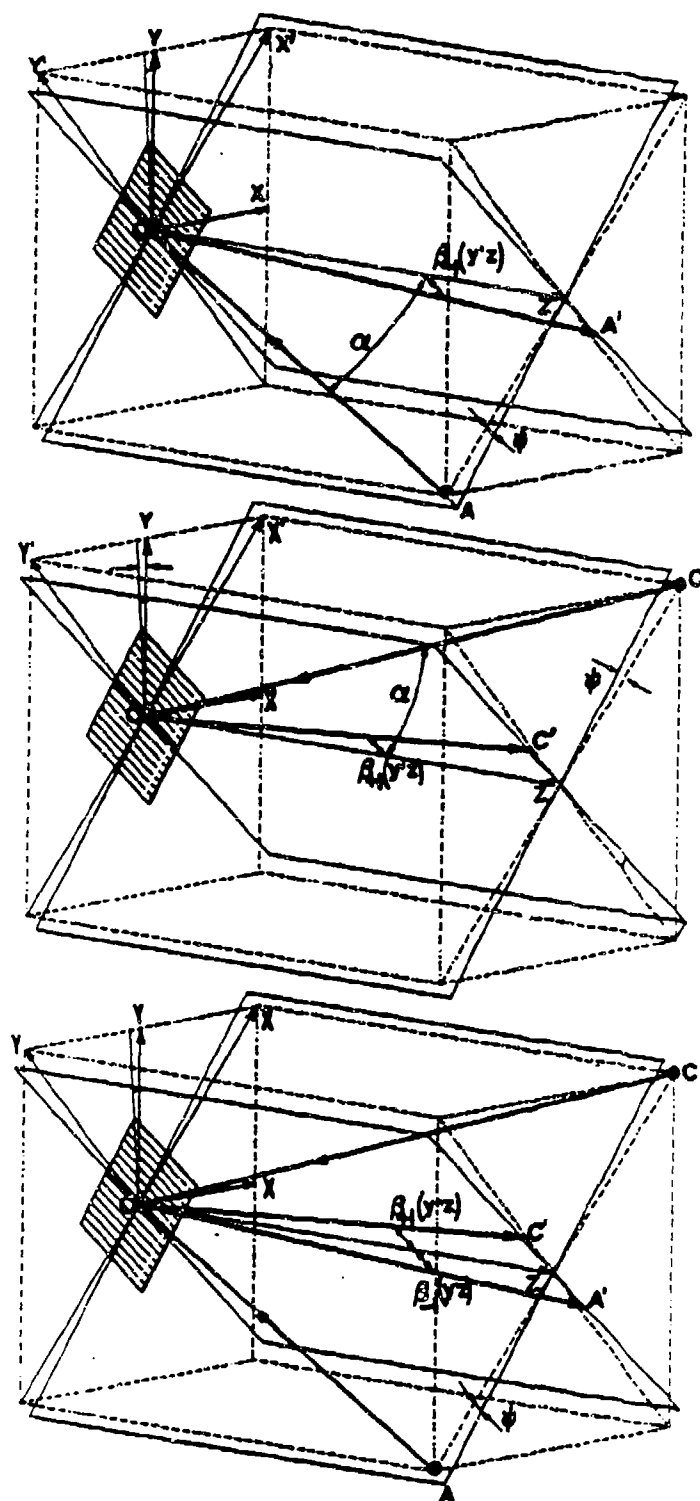


Figure D-14. Geometry of the Incident and Diffracted Rays Affected by a Rigid-Body Rotation of the Grating when Analyzing with Beams A0 and B0

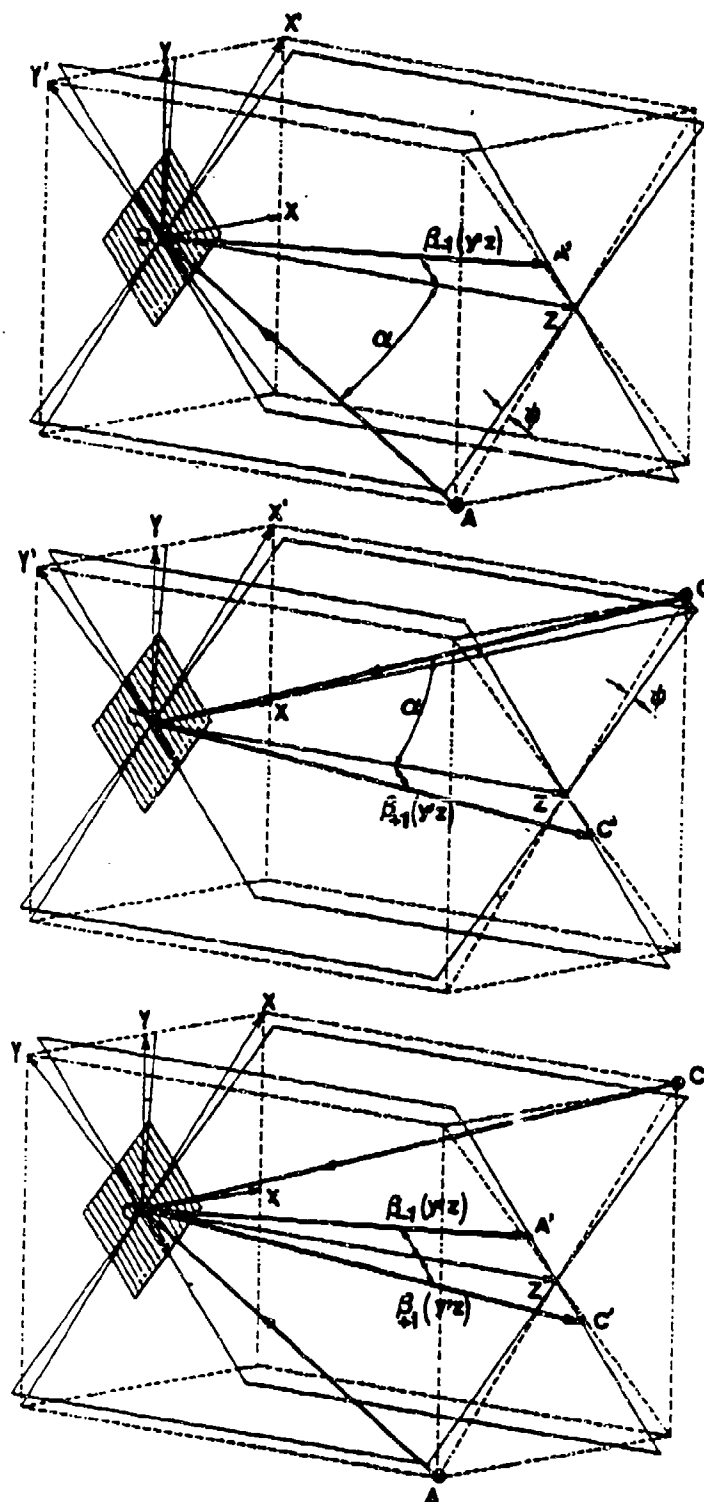


Figure D-15. Geometry of the Incident and Diffracted Rays from a Grating Deformed by $\gamma_{x'y'}$, when Analyzing with Beams AO and CO

the plane under examination will produce some fringes, but, for the case of small rotations, they are negligible.

D.9. Complete Analysis of Two Dimensional Strain Fields.

The theory presented in previous sections demonstrates that the displacement component in a given direction can be measured by interrogation of the specimen grating with different pairs of beams. That is, in order to measure U_x , the specimen grating is interrogated by beams AO and BO. Similarly, U_y is obtained by combining beams BO and CO, and U_{45} by combining beams AO and CO.

The state of strain throughout a general two-dimensional strain-field can now be determined. Recognize that there are three unknown strain components ϵ_x , ϵ_y , and γ_{xy} , at every point in "plane" elasticity problems, without distinguishing between plane stress, plane strain and generalized plane stress at this stage.

Differentiation of the displacement components with respect to the appropriate space variables yields ϵ_x , ϵ_y and ϵ_{45} , i.e. the three strain components which define the complete state of surface strain [D.6] throughout the field of view. Then,

$$\epsilon_x = \frac{1}{F} \frac{\partial N_x}{\partial x} \quad \epsilon_y = \frac{1}{F} \frac{\partial N_y}{\partial y} \quad \epsilon_{45} = \frac{1}{F} \frac{\partial N_{45}}{\partial x'} \quad D.52$$

It was also demonstrated that when interrogating the specimen grating with beams AO and BO, the resulting interference Moire pattern is formed by fringes of extension produced by normal strain ϵ_x ; and fringes of rotations are produced by shear strain γ_{xy} and the rigid body rotation ψ . It was also shown that the fringes of extension are perpendicular to the xz-plane, while those caused by the small rotations are nearly parallel to it. Also, the interference fringes created by the intersection of beams AO and BO were perpendicular to the xz-plane.

Since the quantity to be measured is a normal strain, e.g. ϵ_x , the needed final result is the gradient or spacing of the Moire fringes in the x-direction. The rotation-induced fringes run roughly parallel to the x-axis and, therefore, have no gradient in that direction. In algebraic form, the total fringe order is expressed as the sum of a part resulting from extension and another part caused by rotation:

$$N_x = (N_x)_\epsilon + (N_x)_R \quad D.53$$

$$\epsilon_x = \frac{1}{F} \frac{\partial N_x}{\partial x} = \frac{1}{F} \frac{\partial (N_x)_\epsilon}{\partial x} + \frac{\partial (N_x)_R}{\partial x} \quad D.54$$

$$\text{but } \frac{\partial (N_x)_\epsilon}{\partial x} \gg \frac{\partial (N_x)_R}{\partial x}$$

The conclusion is that rotation does not affect the measurement of normal strain.

In practice, the Moire fringe order is not separated into two parts. The rotation element merely causes the Moire strain fringes to deviate from the usual orientations parallel to the grill. This effect is clearly seen in Ffigure D.16.

The shear strain γ_{xy} could be evaluated by cross derivatives of displacements as,

$$\gamma_{xy} = \frac{\partial U_x}{\partial y} + \frac{\partial U_y}{\partial x} \quad D.55$$

The partial derivatives in the shear equation are gradients in the direction parallel to the analyzer grating lines. The gradient of the rotation-induced fringes in that direction may be at least as large as the gradient of extension-induced fringes [54]. In algebraic notation,

$$\gamma_{xy} = 2\epsilon_{xy} = \frac{1}{F} \frac{\partial N_x}{\partial y} + \frac{\partial N_y}{\partial x} \quad D.56$$

or

$$\gamma_{xy} = \frac{1}{F} \frac{\partial (N_x)_\epsilon}{\partial y} + \frac{\partial (N_x)_R}{\partial y} + \frac{\partial (N_y)_\epsilon}{\partial x} + \frac{\partial (N_y)_R}{\partial x} \quad D.57$$

$$\text{but } x = \frac{\partial (N_x)_R}{\partial y} \geq \frac{\partial (N_x)_\epsilon}{\partial y} \quad \text{and} \quad \frac{\partial (N_y)_R}{\partial x} \geq \frac{\partial (N_y)_\epsilon}{\partial x} \quad D.58$$

so the error may be very great. This situation is worsened by the lack of any direct way of estimating or eliminating the error. Thus, the rectangular strain gage rosette method involving three measurements of normal strain is superior for evaluating shear strain γ_{xy} , as,

$$\gamma_{xy} = 2\epsilon_{45} - (\epsilon_x + \epsilon_y) \quad D.59$$

This approach also circumvents the experimental difficulties associated with rigid-body motion and accidental misalignment of the reference gratings [D.10].

In order to differentiate the displacement components with respect to their appropriate space variables, graphical differentiation can be utilized. Observe that: (a) Moire fringe order can be plotted as a function of position coordinate; (b) the slope of this curve can be evaluated point by point and the result plotted; (c) when divided by the frequency of the reference grating, this last plot becomes a plot of strain along a given axis.

D.10. Use of Pitch Mismatch in Moire Interferometry

The accuracy of the in-plane Moire method depends largely on how accurately the displacement curve is plotted; and the accuracy of the displacement curve in turn, depends on the number of available points. For a given displacement field, the number of fringes depends on the grating used. The finer the grating, the greater the number of resulting fringes. Using the interferometric technique, the frequency of the reference grating and the specimen gratings can be adjusted easily to suit the problem. However, the finer the grating, the greater are the requirements in terms of handling, optical bench stability, etc. For practical purposes, it is convenient to use frequencies in the range of 15000 to 60000 lines per inch, (600 to 2400 lines per mm).

So far, it has been assumed that the reference grating and the specimen grating are related by $F = \sqrt{2} f$, and that the angle of incidence of the laser light onto the specimen grating is exactly ζ . If these conditions are not satisfied by a small difference, pitch and rotational mismatches are present. These initial differences are called "linear" and "rotational" mismatch respectively, and of course they are measured against the reference grating. The resulting fringes are called "linear mismatch fringes" and "rotational mismatch fringes". An illustration of the fringes produced by the mismatch is shown in Figure D-16.

D.10.1. Analysis of the undeformed specimen.

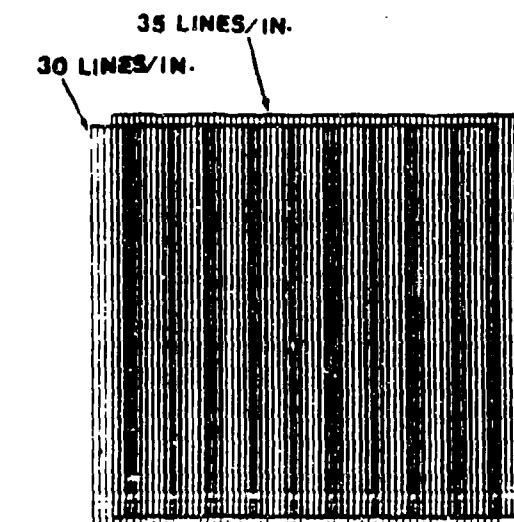
In order to illustrate the use of the mismatch, an undeformed specimen grating being interrogated with beams R0 and C0, i.e. to obtain the U_y displacement field will be considered. The relationship between the specimen grating and the reference grating frequencies is,

$$\delta F = F - \sqrt{2} f \quad D.60$$

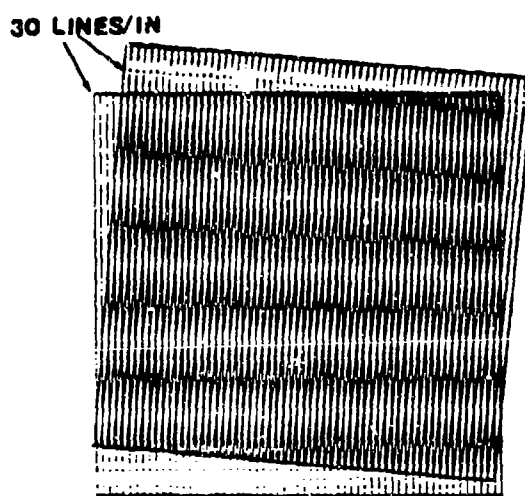
where δF is the frequency mismatch, F is the reference grating frequency, and f is the specimen grating frequency. This equation can be rewritten as,

$$f = \frac{F}{\sqrt{2}} \left(1 - \frac{\delta F}{F} \right) \quad D.61$$

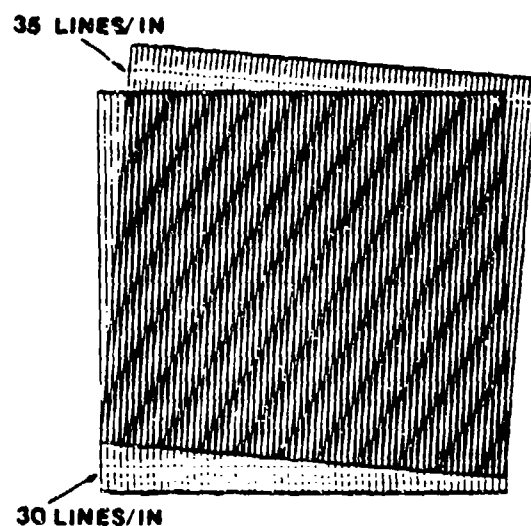
It should be noted that the second term in parentheses is a component of the frequency of the reference grating with its lines parallel to the



(a) Fringes due to
difference in
Pitch alone



(b) Fringes due to
rotation alone



(c) Fringes due to
a combination
of rotation and
difference in pitch

Figure D-16. Formation of Moire Fringes Caused by Pitch and Rotation Mismatch

xz-plane. To obtain the components along the ± 45 -degrees orientation, it should be considered the result of a rotation through 45-degrees. This will yield a component of extension equal to $\delta F/2F$ and a component of rotation of the same magnitude. The first component will produce the same effect as a fictitious tensile strain, while the second is equivalent to a fictitious rotation of the specimen grating lines. Using the three-dimensional grating equation, it is possible to determine the frequency of the resulting interference pattern. For beam BO, let $m = +1$, $\sin \alpha = \sin \xi = -\lambda F/\sqrt{2}$, $f' = (F/\sqrt{2})(1 - \delta F/2F)$, $\psi_1 = \delta F/2F$, then,

$$\sin \beta_{+1}''(y'z) = -\frac{\lambda(\delta F)}{2\sqrt{2}} \quad D.62$$

$$\sin \beta_{+1}'(x'z) = \frac{\lambda(\delta F)}{2\sqrt{2}}$$

Similarly, for beam CO, let $m = +1$, $\sin \alpha = \sin \xi = -\lambda F/\sqrt{2}$, $f' = (F/\sqrt{2})(1 - \delta F/2F)$ and $\psi_1 = -\delta F/2F$, then

$$\sin \beta_{+1}''(x'z) = -\frac{\lambda(\delta F)}{2\sqrt{2}} \quad D.63$$

$$\sin \beta_{+1}'(y'z) = -\frac{\lambda(\delta F)}{2\sqrt{2}}$$

It can be shown that the diffracted rays OB' and OC' lie in the yz-plane (Figure D-17), and the sine of the angle between them and the z-axis is,

$$\sin \beta_{\delta F}(z) = \frac{\lambda(\delta F)}{2} \quad D.64$$

The frequency of the resulting initial fringe pattern with its fringes parallel to the xz-plane is,

$$P_{\delta F} = \delta F \quad D.65$$

and the fictitious displacement is given by,

$$(U_y)_{\delta F} = \frac{1}{F} (N_y)_{\delta F} \quad D.66$$

Thus, the fictitious strain produced by the mismatch is,

$$(\epsilon_y)_{\delta F} = \frac{\partial (U_y)_{\delta F}}{\partial y} = \frac{1}{F} \frac{\partial (N_y)_{\delta F}}{\partial y} \quad D.67$$

D.10.2. Analysis of the deformed grating (strain plus mismatch).

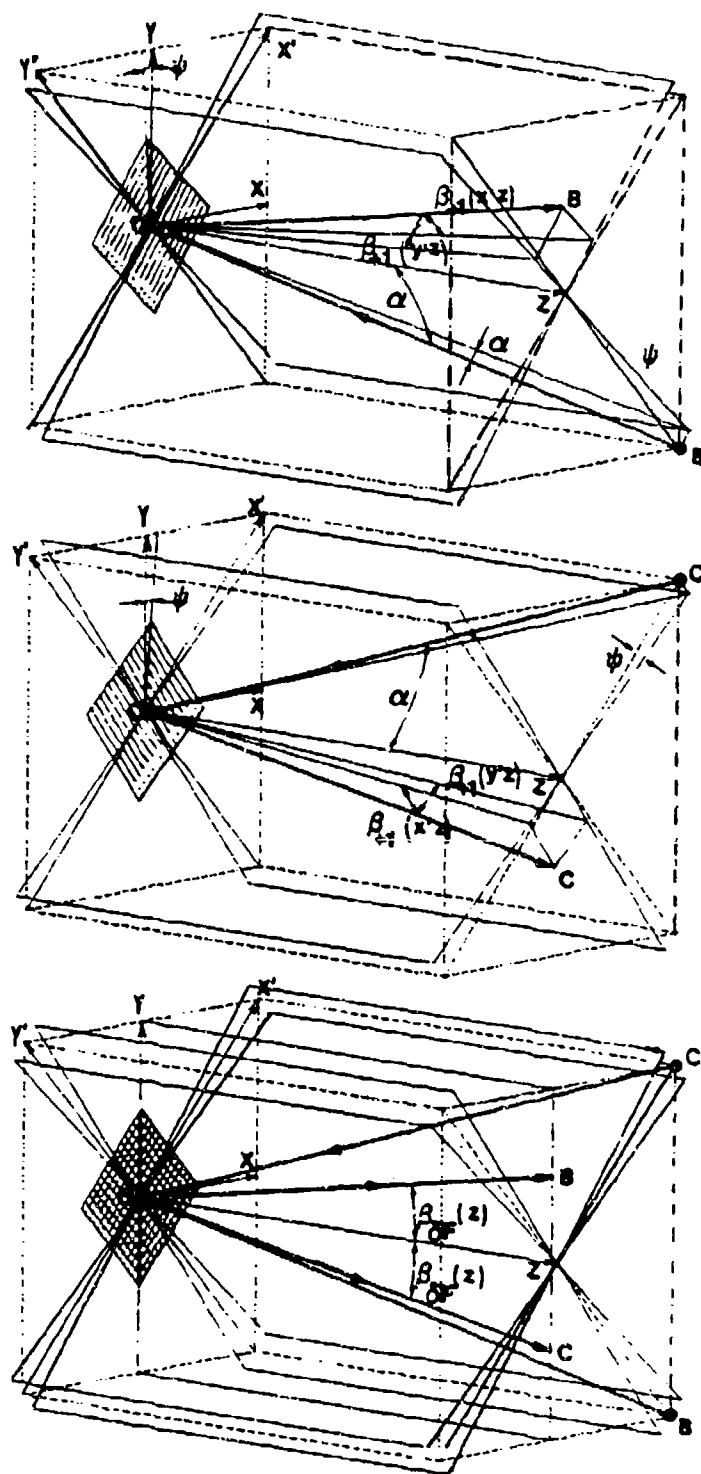


Figure D-17. Geometry of the Incident and Diffracted Rays Affected by a Fictitious Strain Produced by a Frequency and Rotational Mismatch when Analyzing with Beams BO and CO

Now, the combined effect of strain plus mismatch will be considered. In this case, $f' = (F/\sqrt{2})(1 + (\epsilon_y)_\epsilon + (\delta F)/2F)$. Then for beam BO, $\sin \alpha = \sin \xi = -\lambda F/\sqrt{2}$, $\psi_1 = (\epsilon_y)_\epsilon/2 + (\delta F)/2F$, $m=1$, the three-dimensional grating equation yields,

$$\sin \beta_{+1}''(y'z) = -\frac{\lambda F}{\sqrt{2}} \frac{(\epsilon_y)_\epsilon}{2} + \frac{\delta F}{2F} \quad D.68$$

$$\sin \beta_{+1}'(x'z) = -\frac{\lambda F}{\sqrt{2}} \frac{(\epsilon_y)_\epsilon}{2} + \frac{\delta F}{2F}$$

and for beam CO, with $m=+1$, $\sin \alpha = \sin \xi = -\lambda F/\sqrt{2}$, and f' and ψ_1 as above,

$$\sin \beta_{+1}''(x'z) = -\frac{\lambda F}{\sqrt{2}} \frac{(\epsilon_y)_\epsilon}{2} + \frac{\delta F}{2F} \quad D.69$$

$$\sin \beta_{+1}'(y'z) = -\frac{\lambda F}{\sqrt{2}} \frac{(\epsilon_y)_\epsilon}{2} + \frac{\delta F}{2F}$$

Again, the diffracted rays BO' and CO', lie in the yz-plane (Figure D.18), and the sine of the angle between each of them and the z-axis is,

$$\sin \beta_{(\epsilon + \delta F)} = \lambda F \frac{(\epsilon_y)_\epsilon}{2} + \frac{\delta F}{2F} \quad D.70$$

frequency of the resulting interference pattern whose lines are to the xz-plane is,

$$P_{(\epsilon + \delta F)} = F [(\epsilon_y)_\epsilon + \delta F] \quad D.71$$

and the displacement is,

$$(U_y)_{(\epsilon + \delta F)} = \frac{1}{F} (N_y)_{(\epsilon + \delta F)} \quad D.72$$

and the strain is,

$$(\epsilon_y)_{(\epsilon + \delta F)} = \frac{1}{F} \frac{\partial (N_y)_{(\epsilon + \delta F)}}{\partial y} \quad D.73$$

Computation of the true displacement and strain at any point follows directly from prior derivations.

$$(U_y)_t = (U_y)_{(\epsilon + \delta F)} - (U_y)_{\delta F} \quad D.74$$

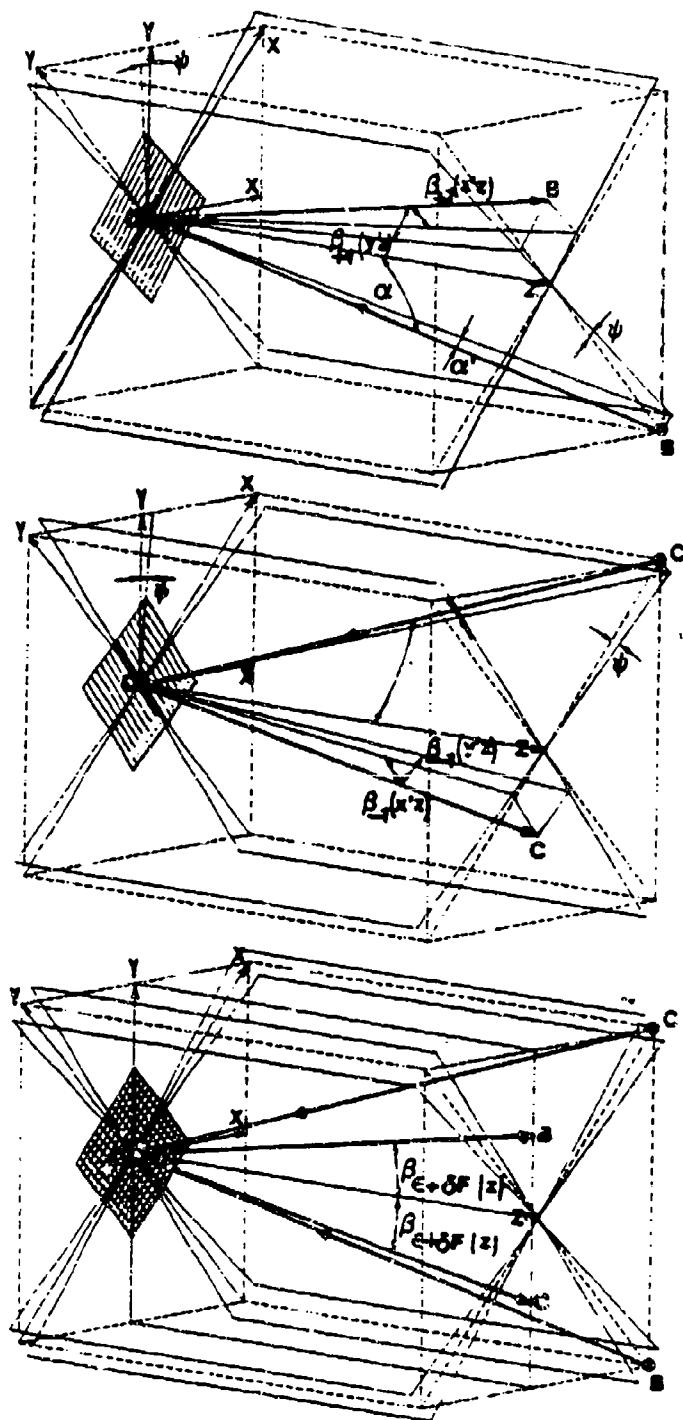


Figure D-18. Geometry of the Incident and Diffracted Rays from a Grating Affected by Strain Plus Mismatch when Analyzing with Beams BO and CO

$$(U_y)_t = \frac{1}{F} (N_y) (\epsilon + \delta F) - (N_y) \delta F$$

where $(U_y)_t$ is the true strain. The true strain ϵ_t is thus computed as follows,

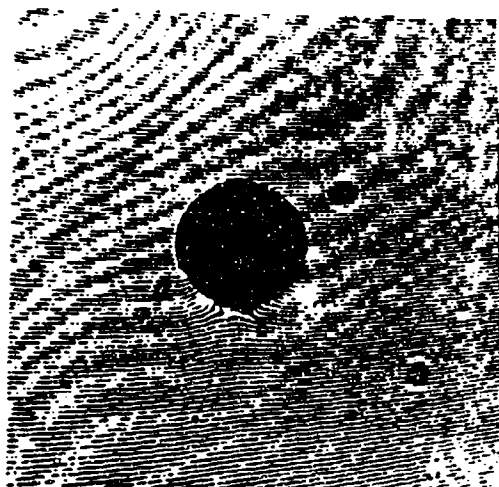
$$\epsilon_t = (\epsilon_y) (\epsilon + \delta F) - (\epsilon_y) \delta F \quad D.75$$

$$\epsilon_t = \frac{1}{F} \frac{\partial [(N_y) (\epsilon + \delta F) - (N_y) \delta F]}{\partial x} \quad D.76$$

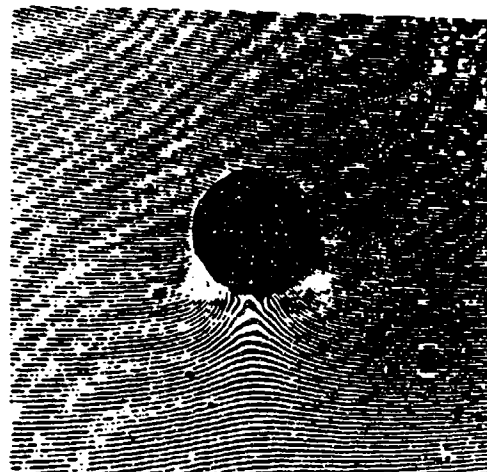
Equation D.66 demonstrates that the spacing between fringes is smaller than that given in equation D.64, which means that there is an increase in the number of fringes in a Moire measurement. Notice that the sign of the fictitious strain should be of the same sign as that of the true strain, otherwise a reduction in the number of fringes will result. Mismatch of the opposite sign can be used efficiently if its magnitude is at least twice the magnitude of the strain to be measured. Nevertheless, caution should be exercised, because the use of more mismatch would overshadow the information.

Note also that it is not absolutely necessary to know the exact size of the mismatch in order to calculate and eliminate the pitch difference and initial rotation effect. "Before strain" and "after strain" fringe photographs may be used directly. A detailed procedure for the elimination of the fictitious strain is given in Chapter 4.

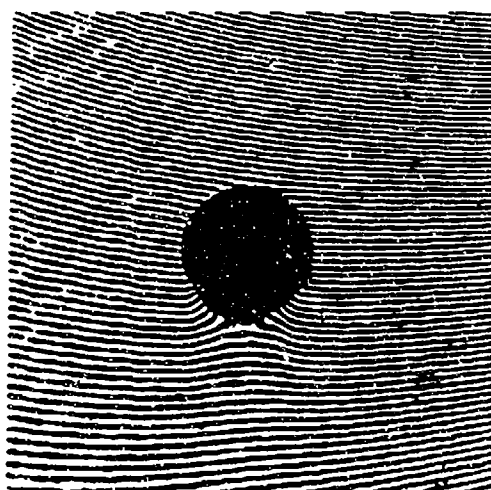
Figure D-19 shows photographs of two different amounts of mismatch for the same loading condition in a pin-loaded hole. Figure D-20 shows the strain plots obtained for these photographs, and it should be noticed that the strain plot obtained for the case of more mismatch gives a more detailed strain contour than the other case.



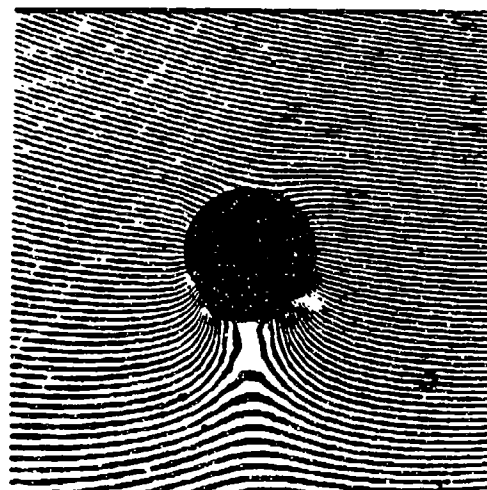
NO-LOAD



AT-LOAD



NO-LOAD



AT-LOAD

Figure D-19. Moire Fringes of Displacement for Two Different Amounts of Mismatch and Same Loading Conditions

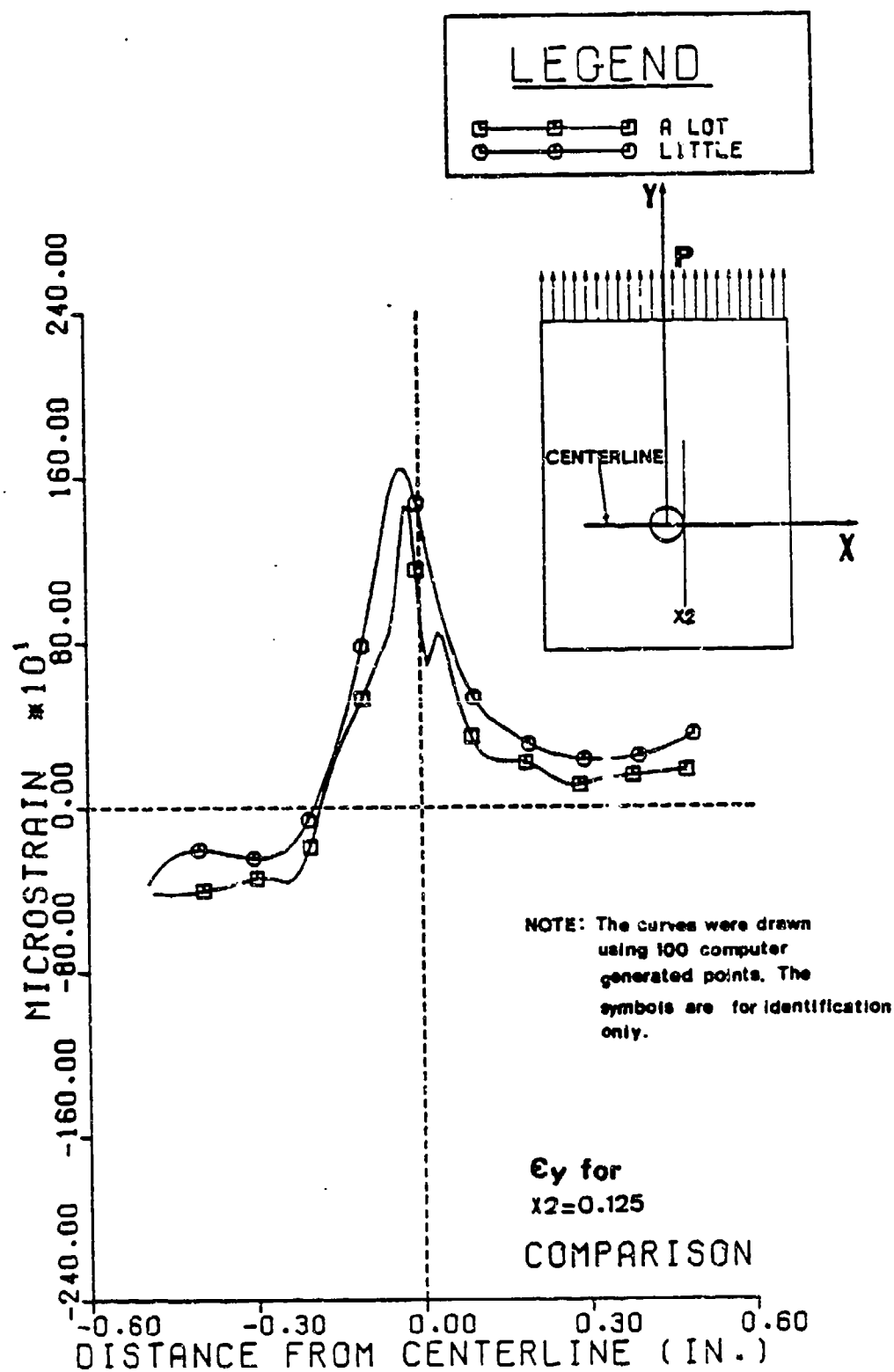


Figure D-20. Strain ϵ_y Obtained from Two Sets of Moire Patterns from the Same Specimen with Different Amounts of Mismatch

This page left blank intentionally

APPENDIX E

Processing of Agfa 8E75 Moire Submasters

This page left blank intentionally

PHOTOGRAPHIC PROCESSING OF AGFA PLATES (8E75).

1. Expose the plate for 1/5 sec. in each way (for a laser power output of about 18 mW).
2. Develop for 5 min. in HRP (1:4 dilution), or 3.25 min. (1:2 dilution).
3. Wash in running water for 15-30 seconds.
4. Fix in Kodak Fixer for double the visible clearing time, (approximately 4 min.) (*)
5. Wash in running water for 15-30 seconds.
6. Immerse in hypoclearing agent for 1 minute.
7. Wash in running water for 30 seconds.
8. Immerse in photo-flo for 30 seconds.
9. Dry in vertical position in still dry room temperature.

(*) Caution must be exercised, because fixing longer times tends to bleach the plate.

This page left blank intentionally

DISTRIBUTION LIST

Manager	2
Defense Logistic Studies	
Information Exchange	
Attn: AMXMC-D	
Ft. Lee, VA 23801	
Director	
U.S. Army Materials & Mechanics	
Research Center	
Attn: AMXMR-M	1
AMXMR-ER	1
AMXMR-S	1
Watertown, MA 02172	
PLASTECH	
Picatinny Arsenal	1
Dover, NJ 07801	
CDR	
Air Force Materials Lab	
Attn: LTM	
Attn: LLN	1
Attn: FIBEC	1
Wright-Patterson AFB, OH 45433	1
CDR	
U.S. Army TACOM	
Attn: AMSTA-DDL	13
Warren, MI 48397-5000	
Naval Material Command	1
Cede CMT0424	
Washington, D.C. 20360	
Hdq., Dept. of Army	1
Deputy Chief of Staff	
For Research, Development and Acquisition	
Washington, DC 20310	
Attn: DAMA-ARZ-E	
Mr. Donald Ostberg	1
U.S. Army Tank Automotive Command	
TACOM	
AMSTA-TMC	
Warren, MI 48397-5000	

CDR

1

U.S. Army Material Cmd

Attn: AMCMT-M

Alexandria, VA 22333

Dist-2